# Gaseous tracking detectors for academic and societal applications

David Attié

université PARIS-SACLAY

NNT : 2022UPSACL001

Habilitation à diriger des recherches

Irfu - CEA Saclay
Institut de recherche sur les lois fondamentales de l'Univers

# Gaseous tracking detectors for academic and societal applications

Habilitation à diriger des recherches de l'Université Paris-Saclay
préparée à l'Institut de Recherche sur les lois Fondamentales de l'Univers (CEA/Irfu)

École doctorale n°576 Particules, Hadrons, Energie et Noyau : Instrumentation, Imagerie, Cosmos et Simulation (PHENIICS)
Spécialité : Physique des particules

Habilitation présentée et soutenue à l'Université Paris-Saclay, le 17 octobre 2022, par

**DAVID ATTIÉ**

Composition du Jury :

| | |
|---|---|
| Laurent Serin<br>Directeur de recherche, CNRS, IN2P3/IJCLAB, France | Président |
| Alain Bellerive<br>Professeur, Université Carleton, Ottawa, Canada | Rapporteur |
| Klaus Desch<br>Professeur, Université de Bonn, Allemagne | Rapporteur |
| Fulvio Tessarotto<br>Chercheur, INFN, Trieste, Italie | Rapporteur |
| Eric Delagnes<br>Directeur, CEA, Irfu/Dédip, France | Examinateur |
| Olivier Drapier<br>Directeur de recherche, CNRS, IN2P3/LLR, France | Examinateur |

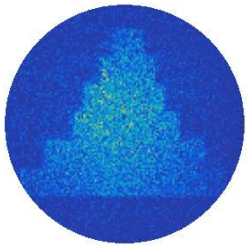

# Contents

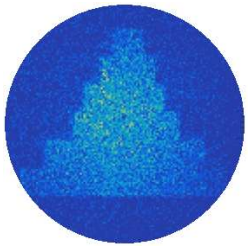

# List of Figures

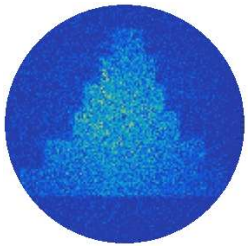

# List of Tables

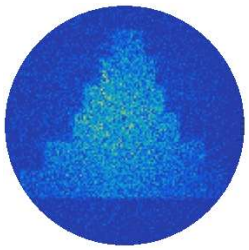

# Definition of variables and fundamental constants

## Acronymes

| | |
|---|---|
| **BMT** | **B**arrel **M**icromegas **T**racker |
| **CEA** | **C**ommissariat à l'**É**nergie **A**tomique |
| **CEBAF** | **C**ontinuous **E**lectron **A**ccelerator **F**acility |
| **FMT** | **F**orward **M**icromegas **T**racker |
| **FTT** | **F**orward **T**agger **T**racker |
| **GEM** | **G**as **E**lectron **M**ultiplier |
| **ILC** | **I**nternational **L**inear **C**ollider |
| **ILD** | **I**nternational **L**arge **D**etector |
| **LEM** | **L**arge **E**lectron **M**ultiplier |
| **MPGD** | **M**icro-**P**attern **G**as **D**etector |
| **MSGC** | **M**icro-**S**trip **G**as **C**hamber |
| **MWPC** | **M**ulti-**W**ire **P**roportional **C**hamber |
| **MVT** | **M**icromegas **V**ertex **T**racker |
| **PCB** | **P**rinted **C**ircuit **B**oard |
| **PMT** | **P**hoto**M**ultiplier **T**ube |
| **SVT** | **S**ilicon **V**ertex **T**racker |
| **THGEM** | **TH**ick **G**as **E**lectron **M**ultiplier |
| **TPC** | **T**ime **P**rojection **C**hamber |

## Definition of variables

The definition of variables used in this report is shown on Table 1 The electronic charge $e$ and the kinematic variables $\beta = v/c$ and $\gamma = 1/\sqrt{1-\beta^2}$ have their usual definitions. Constants are from *CODATA Recommended Values of the Fundamental Physical Constants:* 1998 [25]. Parenthetical numbers after the values give the 1-standard deviation uncertainties in the last digits. The convention c = 1 is used.

| Symbol | Definition | Units or Value |
|---|---|---|
| $\alpha$ | Fine structure constant $e^2/4\pi\epsilon_0 hc$ | 1/137.035 999 76(50) |
| $c, c_0$ | Speed of light in vacuum | 299 782 458 m.s$^-$1 |
| $\mu_0$ | Magnetic constant | $4\pi \times 10^{-7} N_A^{-2}$ |
| $\epsilon_0$ | Electric constant | $(\mu_0 c^2)^{-1}$ |
| | | =8.854 187 817... $\times 10^{-12}$ F.m$^{-1}$ |
| $M$ | Incident particle mass | MeV/c$^2$ |
| $M_\mu$ | Muon mass | 105.658 356 8(52) MeV/c$^2$ |
| $E$ | Incident particle energy $\gamma$Mc$^2$ | MeV |
| $T$ | Kinetic energy ($\gamma$-1)Mc$^2$ | MeV |
| $p$ | Momentum $\gamma\beta c$ | MeV/c |
| $m_e c^2$ | Electron mass $\times$ c$^2$ | 0.510 998 902(21) MeV |
| $r_e$ | Classical electron radius $e^2/4\pi\epsilon_0 m_e c^2$ | 2.817 940 285(31) fm |
| $N_A$ | Avogadro's number | 6.022 141 99(47) $\times 10^{23}$ mol$^{-1}$ |
| $z_e$ | Charge of incident particle | |
| $Z$ | Atomic number of medium | |
| $A$ | Atomic mass of medium | g.mol$^{-1}$ |
| | (Occasionally: atomic mass number) | dimensionless |
| $K/A$ | $4\pi N_A r_e^2 m_e c^2/A$ | 0.307 075 MeV g$^{-1}$.cm$^2$ |
| | | for A = 1 g.mol$^{-1}$ |
| $I$ | Mean excitation energy | eV (Nota bene!) |
| $\delta$ | Density effect correction | |
| | to electronic energy loss | |

Table 1: Definitions of most of the variables used in this report.

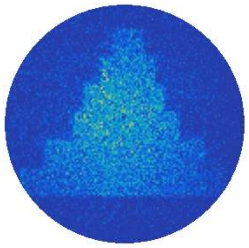

# Introduction

Fundamental physics is based on two main pillars, theoretical physics well described by mathematics and instrumental physics that relies on the development of technological and technical tools. Both are interdependent and in a constant friction. Since more than fifteen years, I spent my research time mainly in instrumental physics, in particular on gaseous detectors for particle tracking.

In this document I choose to summarize and present my work on the development of gaseous tracking detectors since 2006 in three main parts.

The first part deals with the use of gaseous detectors for particle tracking. This part shows the properties and the advantages of the gaseous detectors for particle tracking in four chapters.

In the second part, I will present my work in fundamental Physics experiments as R&D for the next tracking detectors of the future colliders, the building of a gaseous vertex tracker for a running experiment in Nuclear Physics (chapter 5) and the R&D of a 1-10 MeV spectrometer for gamma-ray Astrophysics (chapter 6).

Finally in the third part (chapter 7 & 8), I describe how I have taken advantage of the detector developments for fundamental physics experiments to answer the new needs on societal applications through muon tomography.

This introduction ensures to acknowledge my closest collaborators and particularly the students and post-docs that I have supervised, co-supervised or collaborated with. It must be added that without their contribution this work would not exist.

## • Space gamma-ray astrophysics

During my PhD in the Astrophysics Department of CEA/Irfu, from 2001 to 2005, I was in charge of the *INTEGRAL*/SPI calibration first on ground and then in space. I also contributed to the data analysis of the Vela region.

The objective of my thesis was to measure and check the performances of the telescope, in particular to validate simulations of the INTEGRAL/SPI instrument response. The presence of a significant instrumental background noise (more than 100 gamma-ray lines) coming from interaction from the cosmic rays and the instrumental equipment was found. During the data analysis of the Vela region observations, I focus on two astrophysical topics dealing with:

- the search for radioactive decays lines of titanium-44, produced by explosive nucleosynthesis, in the supernova remnant of Vela Junior and,
- the search of cyclotron resonance scattering features expected towards 25 keV and 52 keV in the accreting pulsar spectrum of the x-ray binary star Vela X-1.

The result obtained previously by COMPTEL was not confirmed considering the non-detection of the titanium-44 lines by SPI, I gave a lower limit at 4500 $km \cdot s^{-1}$ for the ejecta velocity from Vela Junior. The analysis on the research of the cyclotron lines showed that the results were very sensitive to the instrumental background.

## • R&D for future colliders

After one year of temporary teaching and research fellow (ATER) at Paris 7 Denis-Diderot University and one year as a teacher in physics science at the secondary school EPIN, I was recruited for a postdoc position between 2006 and 2008 in the particle physics department at Irfu. Although having experience in solid detectors as high purity germanium and astrophysics, I was in charge of developing an innovative gaseous detector as a time projection chamber (TPC) demonstrator based on Timepix chip readout for particle physics supervised by Paul Colas. Together with him, I joined the effort of the development a resistive bulk Micromegas for a the readout of a large TPC prototype. I remember the interaction with **Steven Turnbull** on the resistive layer simulation and data analysis.

During almost 10 years, as a technical coordinator at Irfu, I actively contributed to the design, to the construction and to the characterisation in real condition (beam test) the first large pixelated readout (500k pixels) and a large TPC with resistive bulk Micromegas detectors. Both have become a mature solution to the next generation of TPC readout. In this period of my career in science, I met decisive persons, as Xavier Coppolani, Marc Riallot and Irakli Mandjavidze which whom I continued to collaborate with later on other projects (Clas12 and muon tomography).

In order to keep the skills relating to this new technology in the lab, my position became permanent at the end of 2008, thank to the confidence given to me by Eric Delagnes. During the first years, I also took part of the Micromegas technology R&D effort enhanced by the present spirit of my colleagues in the lab. The systematic studies of the gas, pressure and amplification gas allow to optimize the Micromegas detector.

I contributed to the measurement in the lab of the **Maximilien Chefdeville** thesis from 2006 to 2009 on *Development of Micromegas-like gaseous detectors using a pixel readout chip as collecting anode* and I co-supervised **Michael Lupberger** from 2009 to 2010 for his master thesis who contributed to the Octopuce and non officially I supervised **Wenxin Wang** from 2009 to 2013 for her thesis dealing with *A Large Area Micromegas TPC for Tracking at the ILC*.

## • Clas12 experiment

I joined the Irfu's Clas12 team and I took in charge the design and the building of the cosmic test bench (2011) and I took the responsibility of the Micromeas forward tracker of the Micromegas vertex tracker (2011 to 2018). My experience in resistive readout Micromegas detector played a role in choosing this technology to achieve the required performance.

In 2012, inside the collaboration between JLab, Ohio University and INFN, I was in charge of designing, building and testing a forward tagger tracker prototype (2013) which after validation lead to the production of a final version for installation at in the Clas12 experiment at JLab. Both were installed in 2018 for operation.

## • Harpo project

In 2012, I joined the bilateral collaboration between CEA/Irfu/Dédip and CNRS/IN2P3/LLR for the HARPO project lead by Denis Bernard. My TPC expertise was appreciated. I contributed to the hiring of Philippe Gros a former post-doc at Saga University in Japan, member of the LC-TPC collaboration working on GEM technology.

My contribution was first to find a solution to keep and maintain the performance of the TPC during operation in sealed mode. This work lead to a patent with Patrick Magnier called "Device for Circulating a Gas in a Closed Circuit" (n° EP 3 054 168 B1) which was surprisingly not existing. Mickael Frotin, in charge of the mechanics on the project, was deeply involved and helped us to make in real.

After participating to the data taking in Japan and the data analysis, I gave the opportunity to **Ryo Yonamine** to work on the trigger algorithm which would be necessary in balloon flight or for a space operation.

## • Muon tomography

End of 2013, after a collaboration with Sébastien Procureur in the Clas12 Micromeas vertex tracker, he asked me to work with him on muon tomography just started in the Institute. The muon tomography activity arose from the development of multiplexed Micromegas for a cosmic test bench with a reduced number of electronics channels used for the characterisation of the Clas12 detectors.

When I started the project in 2014, the first phase of the M-Cube project was just started. Later, the idea of building and operating a CEA muon tomography telescope was discussed around the team. A year later, WatTo produced the first recognizable muon tomography picture of a large structure. This result triggered many other projects relative to muon tomography applications such as ScanPyramids, dismantling projects or R&D at CEA (G2G3, INB72, IZEN, D3DT, POMME, ...), Mimosa platform founded by the Ile-de-France region and a common lab with the company Iris Instruments. The main goal of each of these projects was mainly to produce a demonstrator to respond to a specific question.

**Héctor Gómez** as post-doc (G2G3) and **Marion Lehuraux** (D3DT) as PhD are both supervised by me. Marion will defend her thesis at the end of this year on *Development of new Time Projection Chambers for societal and academic applications: muon tomography in confined environment and T2K upgrade of the near detector.*

## • Generic Research and Development of Micromegas detectors

From 2006 up to now, I was involved in generic R&D (outside the projects) on Micromegas detectors and I would like to emphasize here only four of them:

**- X-ray polarimetry using pixelated chip and Micromegas**: the demonstration of using Timepix chip with a Micromegas detector as an X-ray polarimeter was done in 2008 and later with **Paul Serrano** with the Caliste chip with the Piggyback Micromegas.

**- Avalanche statistics studies**: with **Michael Lupberger** (Master 2 student) from 2009 to 2010 for his master thesis on *Avalanche statistics and single electron counting with a Timepix-InGrid detector.*

**- Innovative Micromegas detector**: the development with the Micromegas team at Saclay (Esther Ferrer-Ribas, Ioannis Giomataris, Fabien Jeanneau, Mariam Kebbiri) of a resistive anode deposited by an industrial process on a thin ceramic substrate which can be placed *on the back* of any readout plane that can have any granularity with a fully spark-protection.

**- Gas studies**: I am grateful to **Michal Was** (Master 1 student) for the gain systematic measurements and **Ludovic Boilevin-Kayl** (Master 1 student) for the Microbulk studies using various detector parameters (gas pressure, gas mixture and amplification gap) studies in 2014. I was the co-supervisor of both of them.

After this general overview of my work, the next chapters will described in more detail my research activities. In addition, at the end of this document, I have included five papers that I consider to be the most representative of my research. The list of these publications is given here:

- D. Attié, "TPC review", *Nucl. Instr. Methods A* **598** (2009) 89-93 [26].
- D. Attié *et al.*, "Gas pixel detector for X-ray observation", *Nucl. Instr. Methods A* **610** (2009) 178-182 [27].
- D. Attié, "Beam tests of Micromegas LC-TPC large prototype", 2011 *JINST* **6** C01007 [28].
- A. Acker *et al.*, "The CLAS12 Micromegas Vertex Tracker", *Nucl. Instr. Methods A* **957** (2020) 163423 [29].
- H. Gómez *et al.*, "Muon tomography with Micromegas: Archaeology, nuclear safety and new developments for Geotechnics", *J. Phys.: Conf. Ser.* **1312** (2019) 012013.

# First part

# Gaseous Detectors for Particle Tracking

*The most incomprehensible thing about the world is that it is comprehensible.*

Albert Einstein

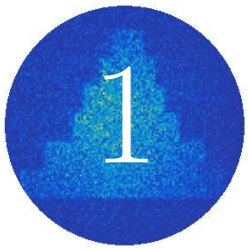

# Gaseous detectors: chronicle of a continuous technical development

Contents



## 1.1 History of detector development for subatomic Physics

The timeline of subatomic particle discovery started by J. J. Thomson with the electron in 1897 [30] (see Fig. 1.1). A few years later, physicists reveal that under certain conditions, a fast particle induces on its trajectory the condensation of supersaturated water vapour. In 1911, the Scottish physicist Charles Thomson Rees Wilson, one of the collaborators of Thomson, uses this effect to develop his cloud chamber, allowing to take a picture of charged particle tracks, like fast electrons, helping therefore their study.

The electron is considered to be the first elementary particle discovered and his study was done thanks to the ancestor of the gaseous detectors. In 1919, Rutherford found that the hydrogen nucleus is present in all other nuclei as an elementary particle so he gave to the hydrogen nucleus a special particle name ”proton”.

Following the result of Irène et Frédéric Joliot-Curie a year before, James Chadwick, in 1932, showed experimentally that the new radiation consisted of uncharged particles with the same mass as the proton and no charge. These particles were identified to be neutrons. The same year, Carl David Anderson discovered the positron by looking at his photographs taken in a cloud chamber showed quantity of electrons, as well as some tracks which seemed to correspond to particles close to the electrons, but with the opposite charge.

Later in 1936, muons were discovered by Carl D. Anderson and Seth Neddermeyer at Caltech while studying cosmic radiation.

From 1950 to 1990, most of the particles were discovered in SLAC (*Stanford Linear Accelerator Center*), in RHIC (*Relativistic Heavy Ion Collider*) of BNL (*Brookhaven National Laboratory*), at CERN (*Centre Européen pour la Recherche Nucléaire*) and others labs...

More recently, in LEP (*Large Electron–Positron Collider*) from 1989 to 2000 and later in LHC (*Large Hadron Collider*) from 2012 to today, all particles have been measured more precisely. Many experiments have used and use gaseous detectors, in particular a time projection chamber (TPC) as in ALEPH and DELPHI at LEP or ALICE at LHC.

All these discoveries would not have been possible without the emergence and the development of particle detectors.

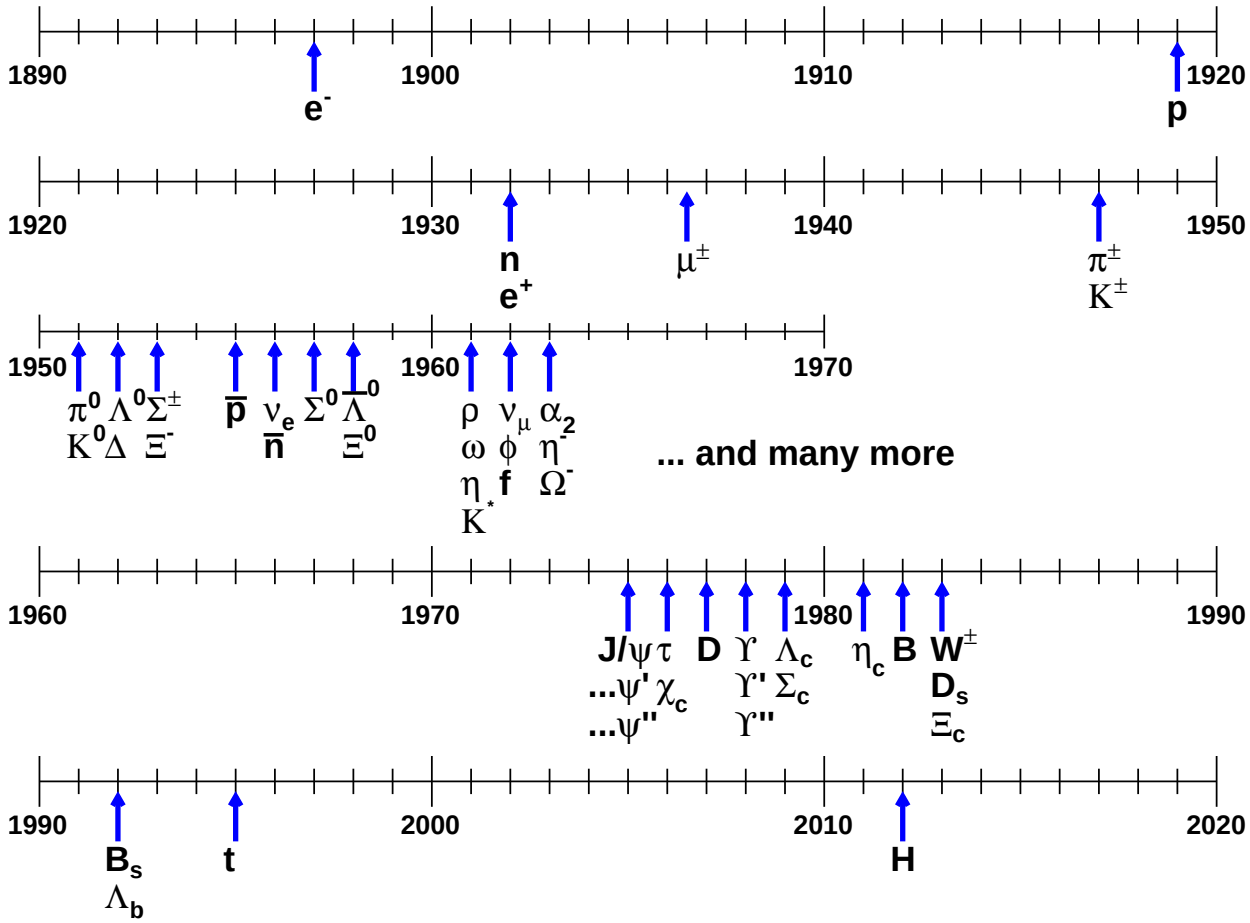


Figure 1.1: Subatomic particle discovery time line.

## 1.2 Particle detector families

Physics is a science originally based on experiments. Since more than 130 years, the discovery of particles would not have been possible without the invention and the use of particle detectors. A particle detector is a device designed to detect the passage of a particle and, generally, to deduce different characteristics (depending on the type of detector) such as its momentum, its mass, its energy, its electric charge, its lifetime or its spin.

Detectors can be divided in three families: trackers, calorimeters and timing/trigger detectors. While the calorimeter is a detector used to measure the energy of the particles, the timing/trigger detector is used to measure the time of the particle/to select the particle, trackers are particle detectors used to reconstruct the trajectory (or track) of electrically charged particles.

A **calorimeter** is a composite detector using total absorption of particles to measure the energy and position of incident particles or jets. In the process of absorption showers are generated by cascades of interactions. Calorimeters are usually composed of different parts, custom-built for optimal performance on different incident particles. Each calorimeter is made of multiple individual segmented cells, over whose volume the absorbed energy is integrated. At high energy, layers of matter of high density (tungsten for instance) are inserted between two layers of cells.

A **tracker** is a detector which measures, reconstructs the trajectories of charged particles and determines their flight paths while modifying theirs characteristics as little as possible. This is why detectors using small material budget are often selected.

A **timing/trigger detector** are detectors used to measure the arrival time, the time of flight of a particle or to quickly decide if the signals produced in the surrounding detectors will be recorded or taking into account.

These three families are summarized in Figure 1.2 and have been classified according to their function and state of matter:

- The gas-filled detectors are mainly based on ionization processes. They can be divided in four groups: ionisation counter, spark chamber, Geiger-Müller tube and proportional counter. For the proportional counter group, the charge collected after ionization in the gas depends on the intensity of the electric field (see Fig. 1.4). Theses gaseous detectors are now the most used in Physics experiments and will be described further in the following sections.

- The liquid detectors can be separated in two parts: the noble gas detectors and the scintillating liquid detectors. Whereas the operation of noble gas detectors is closed to the one of gas-filled detectors, scintillating liquid detectors are similar to the scintillating counters.

- The solid state detectors, are more suitable for energy spectroscopy than gas-filled detectors or scintillation detectors because they provide higher energy resolution largely due to the big number of charge carriers excited during the particle interaction leading to better statistics. Only 3–5 eV of energy is needed to produce an electron–hole pair in a semiconductor compared to 25-40 eV to produce an electron–ion pair in a gas-filled detector and between 100 eV and 1 keV to produce a single photoelectron ejection from the photomultiplier tube (PMT) photocathode attached to a scintillation detector (primarily due to light reflections and poor quantum efficiency at the photocathode).

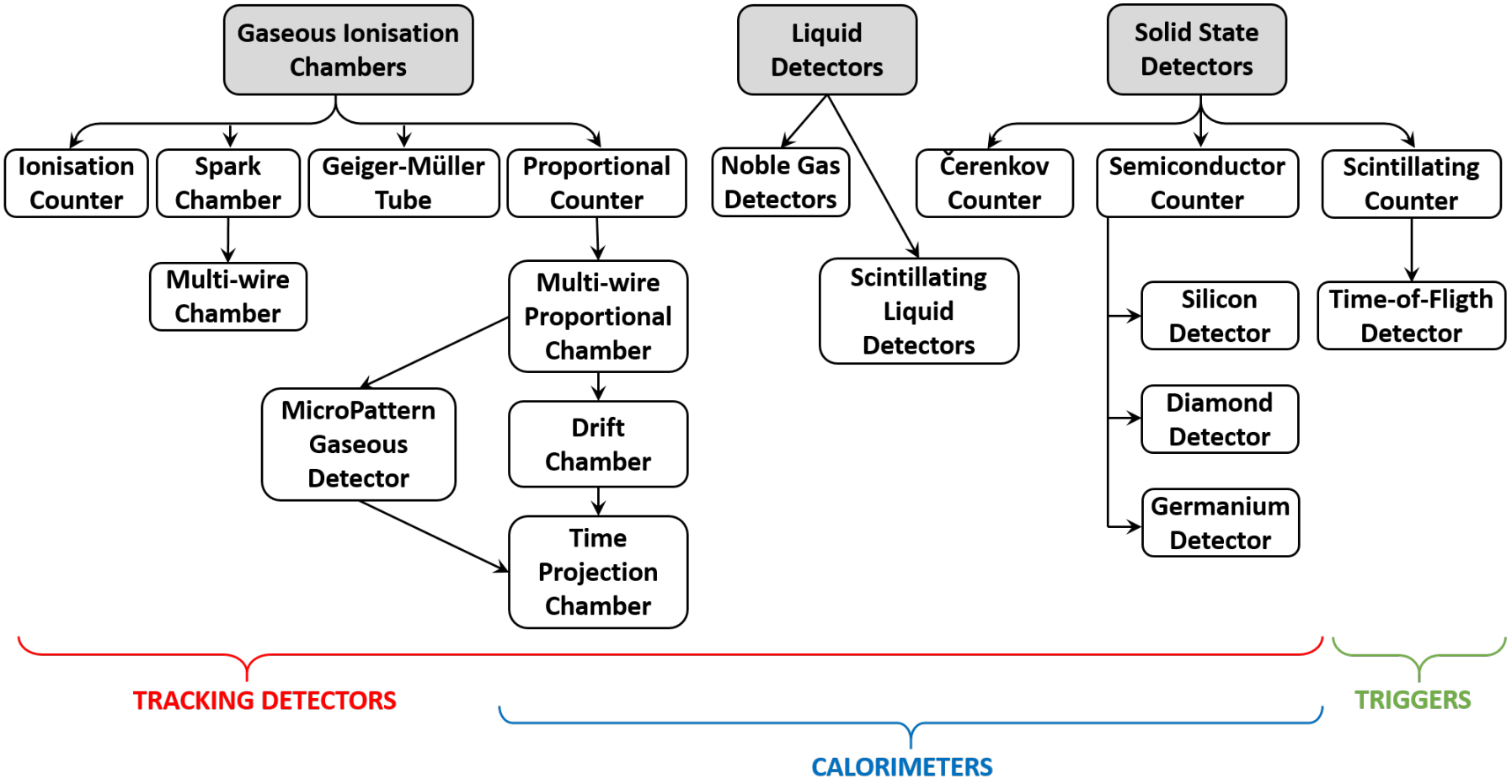


Figure 1.2: The three detector families: gaseous, liquid and solid states detectors used for tracking, calorimetry or triggering.

## 1.3 Particle detector principle

The detector principle is based on the interaction of the particle with matter. The detector medium can be solid, liquid or gaseous. A signal can be extracted by atomic excitation/ionization, by luminescence or by phonons. Most of the particle detectors are based on atomic excitation and ionization.

During interaction with the detector matter, the particle can pass through it or can be stopped. The physics phenomenon of this interaction has to produce a signal that can be amplified and be recorded by readout electronics and saved for on line and off line analysis. For proper operation, most of detectors and all electronics need to be powered and polarized. Figure 1.3 shows a general view of a detection chain.

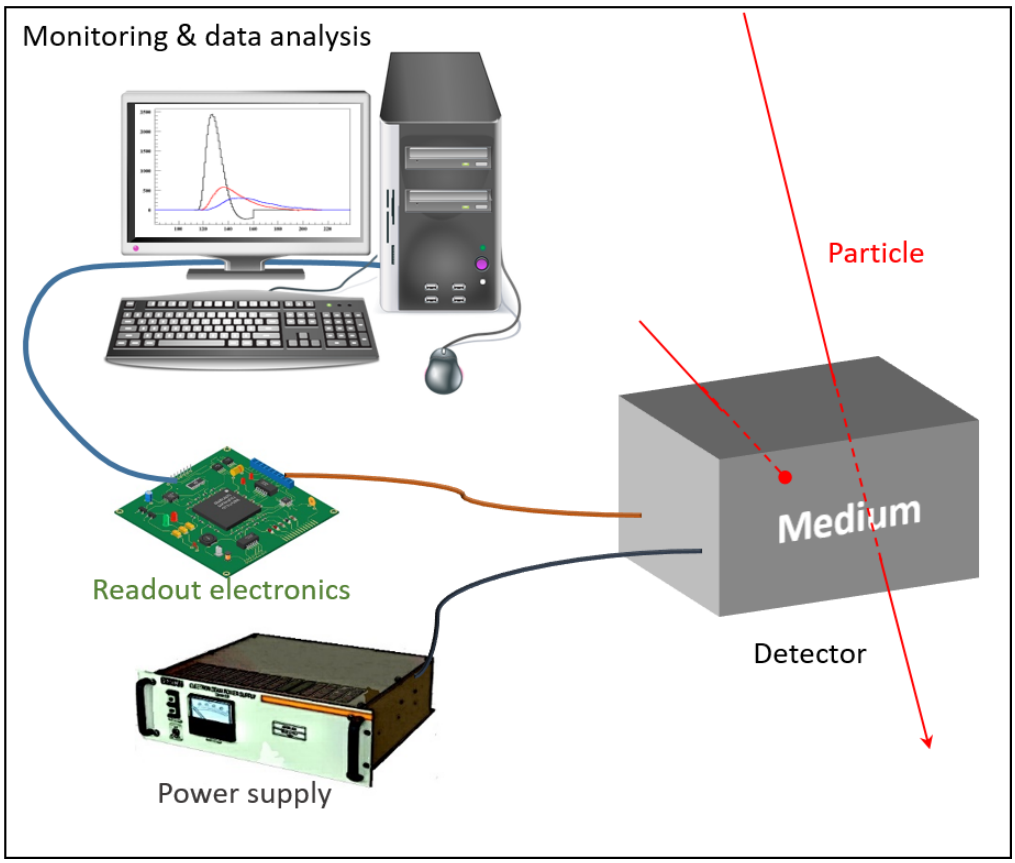


Figure 1.3: Detector principle.

The detection chain has to be matched to the signal produced by the detector. For instance, the power supply needs a correct voltage/current range and the sensitivity of their monitoring is appreciable. The input capacitance of the front-end electronics needs to be adapted.

In the following section, we will focus on the gas-filled or gaseous detectors.

## 1.4 Gaseous detectors

### 1.4.1 From Cloud Chambers to Micro Pattern Gaseous Detectors

The single wire proportional counter was invented by E. Rutherford and H. Geiger in 1908 [31]. It was used with the maximum gain in a Geiger–Müller tube in 1928 by H. Geiger and Mueller which gives their names

to the instrument [32]. They are considered as the beginning of a century of technological advancement in gas-filled detectors.

### Parallel-plate counters

Between parallel electrodes polarized, the induced currents can be described by the Ramo theorem [33] and the induced signals [34] can be obtained by simple energy conservation principles. The charge induced by the passage of a particle on parallel strips for instance depends of the position/distance of the charge with respect to the strips. The first scientist who tried to use a parallel-plate structure as a particle detector was J. Warren Keuffel in 1949 [35].

At normal temperature and pressure (NTP), a relativistic charged particle releases around 100 electron-ion pairs per centimetre in the gas. In a two-electrode parallel plate structure with a capacitance of a few tens of pF, the collection of this charge would produce a voltage signal of only a few $\mu$V, impossible to detect with simple electronics. At high electric fields, avalanches of electrons appear and increase exponentially the number of charges collected and consequently modify the amplitude and time development of the detected signals. The electron multiplication between the parallel electrodes are easy to build and operate. The size of this avalanche depends on the position of the primary ionization, and therefore the response of the counter is not proportional to the initial charge. However, the collected charge is proportional to the primary ionization for extended particle tracks. Detailed studies of the avalanche statistics are shown in [36, 37].

### Proportional counters

Proportional counter is a gaseous ionization detector, like the Geiger-Müller counter but operating with a lower voltage. While in the Geiger-Müller counter, the ionizing particle causes a maximum spark and is in saturation, in the proportional counter ionization happens in the linear mode. The influence of the electric arc created is proportional to the energy of incident particle. The single wire proportional counter was developed first by Rutherford and Geiger in 1908 [31]. Its cylindrical coaxial geometry allows the counter to provide an amplified signal proportional to the initial ionization. A thin metal wire stretched on the axis (anode) of a conducting cylinder (cathode) and insulated from it, define a difference of potential between the electrodes. The electric field in this tube is the highest at the surface of the thin wire and decreases towards the cathode. In most of the volume where the primary interaction processes produced electrons and ions, the electric field only makes them to drift respectively towards the anode and cathode. The amplification is done only nearly the anode.

Figure 1.4 shows the evolution of the pulse amplitude delivered by a single-wire counter as a function of the applied voltage for two different values of primary ionization.

### Multi-Wire Proportinal Counter

In 1968, sixty years after the single wire proportional counter, Georges Charpak invented the multi-wire proportional chamber (MWPC) [38] and was awarded by the Nobel Prize in Physics in 1992. This chamber was a revolution as the bubble chamber has a detection rate less than 1000 particles per second while MWPCs have a typical rate of $10^4$/s.mm. The MWPC also allows scientists to record and to analyse data with a computer by using the signals produced by electronics connected to the wires.

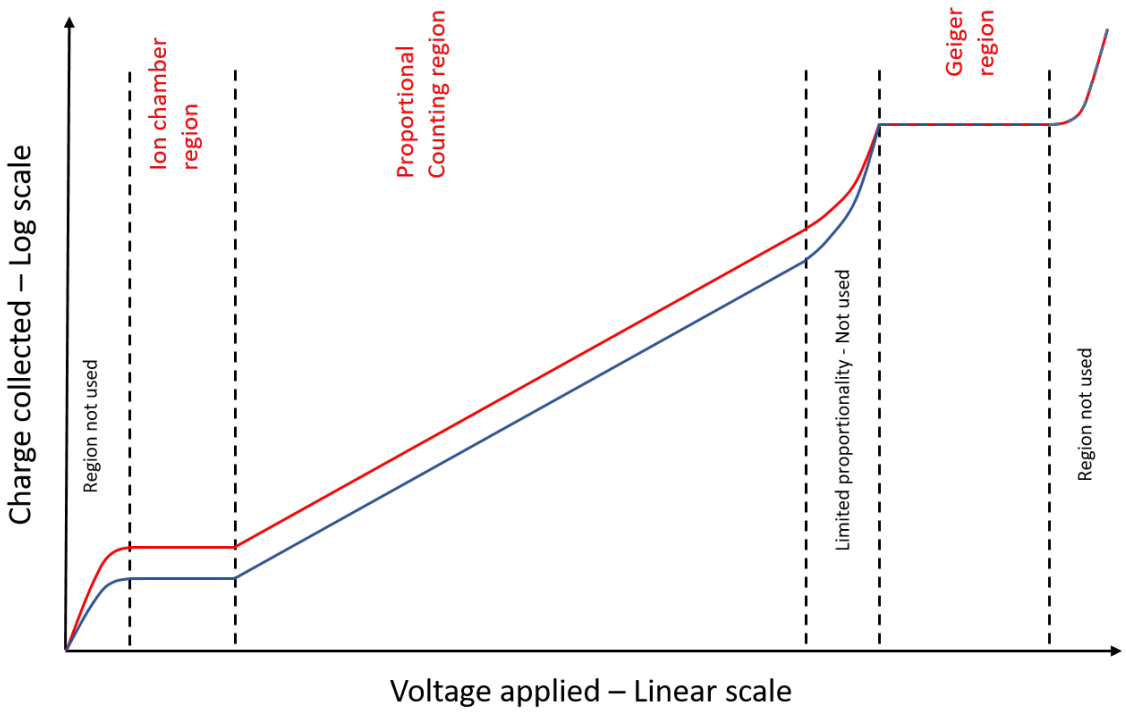


Figure 1.4: Variation of ion pair charge with applied voltage. The various region of potential shows the multiplication of the original charge by discharge processes in a tube with coaxial cylinder electrodes, inspired from [1].

The detector principle consists of an alignment of anode wires between cathode wires, all equally spaced. After the passage of an ionizing particle, the primary electrons are then attracted and amplified by the anode wires and the ions are repelled to the cathode wires. The anode electric pulses are recorded by electronics connected to the wires.

### Drift Chambers

The drift chamber (DC) is an improvement of the MWPC by measuring the drift time of the primary electrons and by giving access to a second spatial coordinate perpendicular to the anode plane. The detected signals on the various anode wires make possible to compute and record the 2D trajectory of the detected particle [39].

Unlike MWPCs, DCs need a time reference signal, $t_0$, usually given by external scintillation counters. A primary ionization electron released in the gas by a charged particle at a time $t_0$ drifts along the electric field and then reaches the anode wire or strip where it will be amplified and detected at a time $t_1$. So, the distance $d$ of the electron from the track to the anode is obtained from $d = \frac{t_1 - t_0}{v(E)}$ where $v(E)$ is the electron drift velocity for the electric field $E$.

Different kind of DCs were built between 1969 and the middle of the 90's: single wire drift chamber [40], multi-wire drift chamber (MWDC) [41] or high-accuracy drift chamber (HADC) [42].

All aspects of DCs and their general properties are presented in [9].

**Multi-tube arrays**

Drift tubes, or straw tubes in lighter version, are tubes containing a stretched wire within a gas volume [43]. When a charged particle passes through the volume electrons are extracted from the atoms of the gas by ionizing processes. These electrons are then transported by the electric field to the positively-charged wire. The geometry of drift tubes are either round, hexagonal, or rectangular. The central anode wire operating in avalanche or drift mode are very common. The tubes are typically assembled in multi-layer arrays in particle physics experiments.

**Resistive plate chambers**

Resistive plate chambers or RPCs consist of two parallel plates, a positively-charged anode and a negatively-charged cathode, both made of a very high resistivity material (either Bakelite with $\rho \approx 10^9 - 10^{11}$ Ω cm or glass with $\rho \approx 10^{13}$ Ω cm) covered with a conductive graphite coating on the outside and separated by a gas volume (gap of a few millimetres). The signal is induced by the charge motion in the gap and is read out by strips or pads located outside of the plates. With nanosecond time resolutions, RPCs are fast gaseous detectors and are usually used as trigger system for fast particles [44, 45]. Using cheap and easily available material allow this technology to be built in very large area, hundred of square meters, very suitable for muon detection in high-energy physics experiments.

### 1.4.2 Micro-pattern Gas Detectors

The micro-pattern gas detector (MPGD) are the evolution of the MPWCs introducing highly segmented readout structure in the gaseous detectors.

#### 1.4.2.1 Micro-Strip Gas Chamber

After two decades of developments on MWPC [46, 9], the idea of Anton Oed to put polarized micro-strips directly in the readout board became in 1988 the beginning of a new era of gaseous detectors when he invented the Micro-Strip Gas Chamber (MSGC) [47] thanks to the development of printed circuit board (PCB) industry. Its readout plane consists of an insulating material on which anode and cathode strips are deposited alternatively. The typical size of the anode strips and the cathode strips are respectively 10 µm and 100 µm. The electrodes alternation and the small size of the anode strips produce a very high electric field so electrons are accelerated is transferred by collisions to other electrons, generating an avalanche. This large numbers of electrons can then create a signal high enough to be read by an electronics system. The very small pitch of about 200 µm allows MSGCs to give good performances: spatial resolutions down to 30 µm, a high rate capability, a very good energy resolution (12% FWHM at 6 keV in argon) and a satisfactory gain up to $10^4$ [48].

The intrinsic discharge breakdown of the MWPC and the limited MSGC performances led to the development of new detectors. Ten years later, Ioannis Giomataris and Fabio Sauli proposed respectively with a MICRO-MEsh GAseous Structure (Micromegas) in 1996 [49] and with a Gas Electron Multiplier (GEM) in 1997 [50] as a direct improvement of the MWPC.

This improvement was the starting point of the two main families of MPGDs, by either reducing the gap between the amplification space and the readout plane or either by adding the number of amplification layers. The advantages of the MPGDs are many. They are more robust, they give fast signals (<10 ns), high gain (> 1000), low ion backflow, no E×B effect, better ageing properties and much easier manufacturing.

Since the end of the nineties, developments on both sides are going on (see Fig. 1.5).

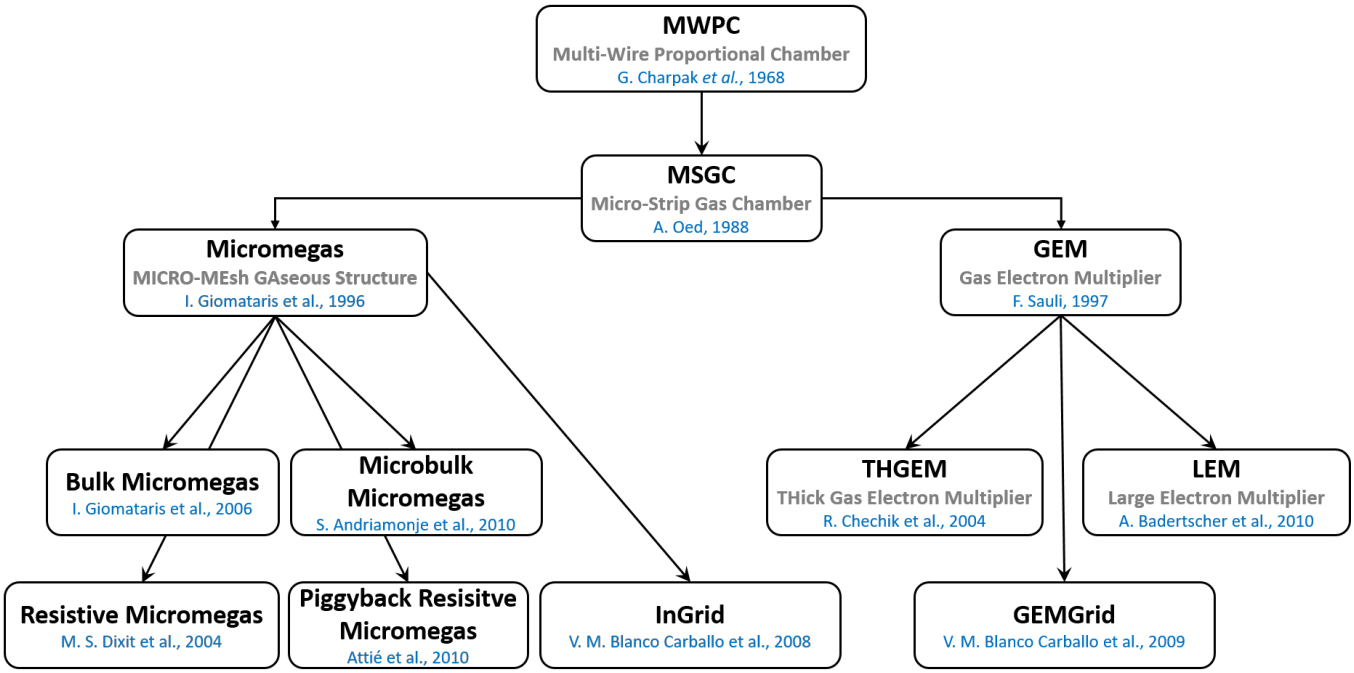


Figure 1.5: Micro-Pattern Gaseous Detectors.

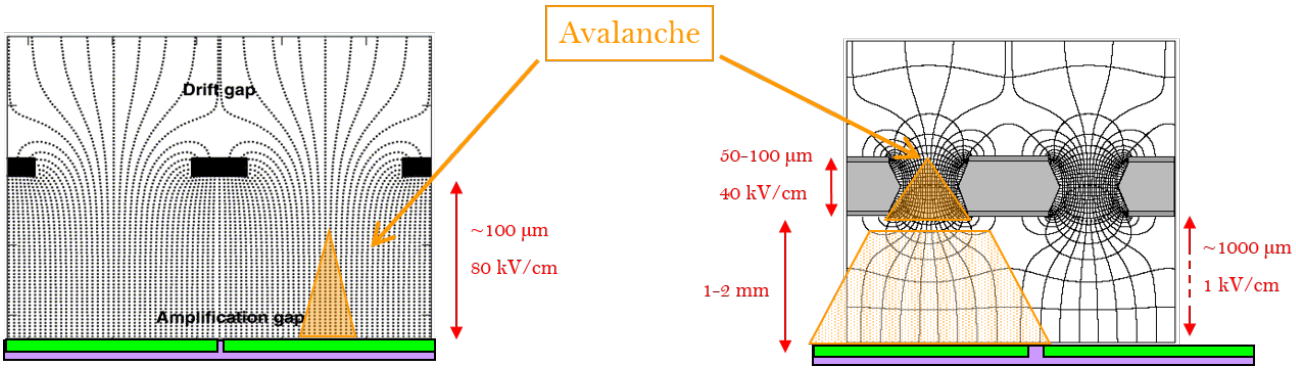


Figure 1.6: Left: Micromegas structure. Right: GEM structure.

### 1.4.2.2 GEM branch

The first main family of MPGD corresponds to the GEM detector which can be divided in three sub-families: the THick Gas Electron Multiplier [51], the Large Electron Multiplier [52] and the GEMGrid [53]. Tab. 1.1 shows the different advantages of the GEM type in term of performance criteria. The recent note of Fabio Sauli summarizes the status of latest designs, recent developments and applications of these detectors in [54].

The GEM detector is defined by two conductive layers separated by an insulating layer (50-100 $\mu$) and holes crossing them where the amplification takes place (see Fig. 1.6). Most of the time, at least three

| GEM type | Energy resolution | Spatial resolution | Robustness | Large scale |
|---|---|---|---|---|
| Standard | | | | ⋆ |
| LEM | | | ⋆ | ⋆ |
| GEMGrid | ⋆ | ⋆ | | |

Table 1.1: Advantages of the different GEM technologies.

layers are needed. Despite of the number of layers GEM detectors are easy to operate, allow low field above the readout plane and low discharge probability during operation.

#### 1.4.2.3 Micromegas branch

Micromegas detectors is the second main family of MPGD and can be divided in five sub-families: the standard Micromegas [49], the bulk Micromegas [55], the resistive (anode) Micromegas [56], the Microbulk Micromegas [57] and the InGrid [58]. These sub-families and applications have been recently summarized in [59]. Each variant of Micromegas technology improves some performance criteria (energy, spatial resolution, robustness, large area, etc.) summarized in Tab. 1.2. The resistive bulk Micromegas technology is the one filling the maximum advantages.

| Micromegas type | Energy resolution | Spatial resolution | Robustness | Large scale |
|---|---|---|---|---|
| Standard | | | | ⋆ |
| Bulk | | | ⋆ | ⋆ |
| Microbulk | ⋆ | | | |
| Resistive Bulk | | ⋆ | ⋆ | ⋆ |
| InGrid | ⋆ | ⋆ | | |

Table 1.2: Advantages of the different Micromegas technologies.

A Micromegas detector can be described as a simple metallic mesh (surface with holes) arranged at 50-150 µm above the readout anode defining the amplification gap (see Fig. 1.6). This single stage of amplification has a natural ion feedback suppression capability. The discharges which currently happen in gaseous detectors are here non destructive making this technology very robust.

The Micromegas principle consists then to divide a gaseous volume in two parts: a conversion or drift region and an amplification region using a metallic mesh (weave wires, pierced copper layer, etc.). Both regions are polarized respectively by their specific electric field: drift field $E_d$ and amplification field $E_a$ (see Fig. 1.7). $E_d$ starts from a few V/cm to a few kV/cm to separate primary electrons from their coupled ions and to make them drift to the anode while the $E_a$ should be at least a few kV/cm to a few ten kV/cm to accelerate the electron depending of the gas. When the electron speed is enough, its momentum energy can be transferred for ionizing another atom in the gas. A cascade of electron-ion pairs contributes to an avalanche.

So a signal can be recorded by a charge amplifier when the multiplication factor between the secondary electrons from the avalanche and the primary electrons is bigger than a thousand.

The mesh is usually maintained at a constant distance above the readout plane by (electrically) isolated pillars. The pillar diameters usually vary between 350 $\mu$m to 1 mm (see Fig. 1.9).

A Micromegas detector is only sensitive to electrons which can be produced in different ways (Fig. 1.7)

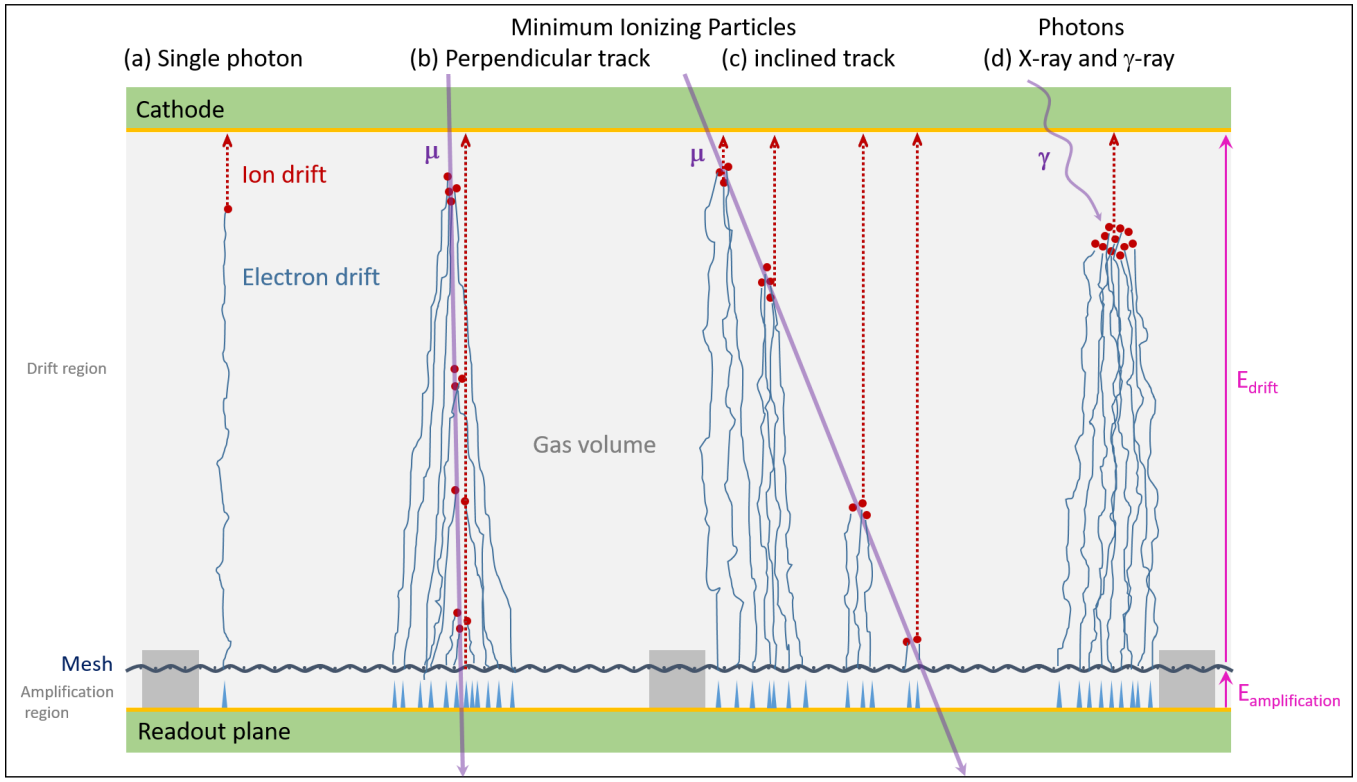


Figure 1.7: Micromegas principle (not to scale) where two electric field regions (drift region and amplification region) are defined by a metallic mesh. Examples for various events are given for: (a) single electron, (b) MIP perpendicular or (c) inclined to the readout anode and (d) a photon conversion in the gas.

(a) after a ionization of a atom by UV photon (b & c) a minimum ionizing particle crossing the detector or (d) a photon conversion (photoelectric effect) with the gas atom.

The main advantages of the Micromegas detector are listed below:

- a fast response (a few ns): resulting from a very small path, the ions need to travel (amplification gap length 100 $\mu$m) and from the very strong field, the ions are very rapidly collected at the mesh, reducing any space-charge effects,
- an intrinsic compensation of any mechanical imperfection on the stretching of the micromesh above the strips, leading to essentially stable gain. An approximation of the change in the amplification factor $G$ can be done with the amplification gap $d$ and is given by [60]:

$$\delta G/G = \alpha d \left(1 - \frac{BPd}{V}\right) \frac{\delta d}{d} \tag{1.1}$$

  for pressure $P$, applied voltage $V$ and $B$ a constant depending on the gas used. Under constant pressure, when $d$ decreases, the multiplication factor increases up to a maximum (for $d = V/B$) and then decreases for higher values of $d$. The combination of the amplification gap and the applied voltage in the Micromegas detectors helps maximizing the multiplication factor, so fluctuations due to any defects of flatness between the mesh and the anode plane are cancelled,
- a high signal capability due to constant field along the amplification region and a combination of both charge coming form ions and electrons,

- an excellent energy resolution ($\delta E/E \sim 12\%$) for a gaseous detector depending of the field ratio ($E_{\text{amp}}/E_{\text{field}}$) and the geometrical defects,
- an excellent spatial resolution depending of the readout pattern.
- a high rate capability of the order of $10^6$ counts mm$^2$.$s^{-1}$ due to the fast evacuation of the ions and the high granularity of the mesh.

The signal is induced by the charge from the electrons of the avalanche and the ions moving to the cathode electrode. Fig. 1.8 shows the fast signals recorded by a multichannel oscilloscope from a Micromegas mesh and three readout strips before any shaping. The strip signal is composed of two parts. The first part (a few ns sharp peak) corresponds to the signal induced by the movement of the electrons approaching the strip and the second part (∼100 ns time windows) corresponds to the signal induced by the ion backflow to the mesh.

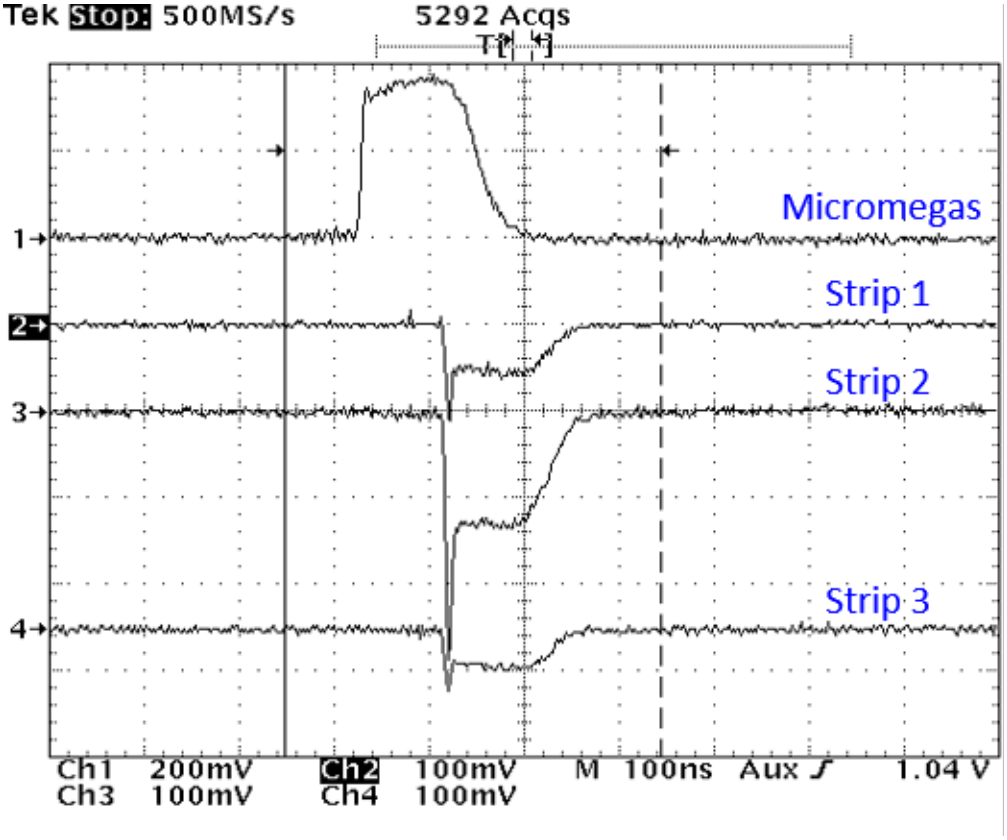


Figure 1.8: Micromegas signal and strip signal read out by an oscilloscope.

A Micromegas detector is sensitive to various events:

- low energy particles ($\alpha$ or $\beta$) which create a cloud of primary electrons inside the drift region,
- minimum ionizing particle (MIP) as cosmic muons, high energy electrons or protons,
- photons which have some probability to be converted to a photo-electron or produce a pair electron-positron if their energy is at least two times the rest electron/positron energy (511 keV).
- neutrons, if appropriate neutron converters (Boron enriched material, polyethylene, ...) are used.

### 1.4.3 Resistive Bulk Micromegas

In the following, I will focus mainly on the resistive bulk Micromegas technology for which I worked for more than a decade either using strip or pad readouts.

#### Bulk Micromegas

Since a few decades, the development and improvement of MPGD manufacturing is strongly linked to the Printed Circuit Board (PCB) technology processes which are employed to produce the detector (amplification and readout parts). In 2006, the technique of putting the Micromegas mesh in a sandwich of two layer of conventional lithography of a photoresistive film on top of the readout plane was developed [55].

So the gap (50–150 $\mu$m) is defined by one or two layers of a photoresistive film where a woven wire mesh (stretched and glued on a frame) is handled and overlapped by another layer of photoresistive film. An insulation mask with a insulation process is used and followed by a development process to define the pillars. When an intense electric field is applied between the mesh and the readout plane the mesh flatness is maintained by the height of the pillars which has an accuracy of better than a few microns.

The woven wire meshes come from the screen printing technique. The typical mesh used is the 45-18 mesh (18 µm diameter wires with an aperture of 45 $\mu$m corresponding to 400 lpi i.e. lines per inch) from the Bopp SD company. A picture of a typical bulk Micromegas zoomed close to a 500 µm diameter pillar supporting a 45-18 mesh at 128 µm from the readout plane is shown on Fig. 1.9. This 128 µm gap results from the lamination of two layers of a Dupont PC1025 photoresistive film (thickness of 64 µm). A third layer on top of the mesh encapsulates the latter.

This principle makes the bulk technology very robust and the probability of damaging the detector during mounting and testing is then very small. Also, the manufacturing processes can be done by any standard PCB company in a profitable industrial way (see Sec. 8.1.3.2).

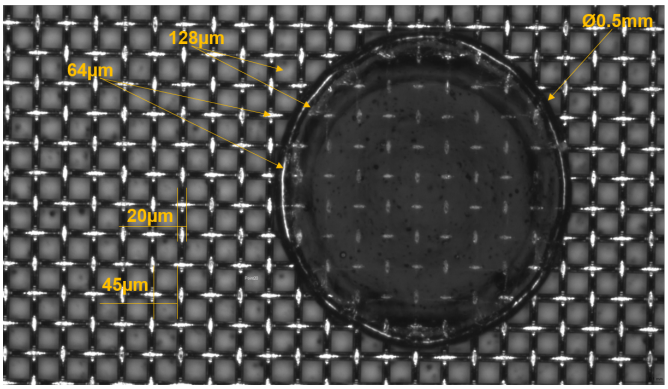


Figure 1.9: Top view of a bulk Micromegas structure near a pillar using a 45-18 (400 lpi) BOPP stainless steel screen printing mesh.

#### Resistive anode

Even being very robust, a standard (non resistive) bulk Micromegas has limited rate capability due to sparks and needs to be operated with protected electronics. So, a resistive Micromegas consist of adding a resistive coating directly on the readout plane. This resistive coating is made of two parts (see Fig. 1.11):

(1) an insulating layer (between 50 to 200 µm) and (2) a resistive layer which could be plain or made of strips (a few tens nm to a few tens microns). The resistive layer can be a Carbon Loaded Kapton of 50 µm thick, a resistive paste of a few tens $\mu$m, a polymer cover by resistive deposit by sputtering in plasma oven (Diamond Like Carbon), ...

The two main reasons of making a Micromegas resistive are:

- **spark protection** to the readout electronics by being a good quencher to natural discharges and increase the rate capability [61]. The detector can be operated with any readout system (protected or unprotected electronics) and specially the resistive layer with integrated micropixel systems (see Sec. 3.2.3.1).

- **the spread of the charge** over several readout pixels or strips allowing a good spatial resolution at low cost. The charge spreading also opens up several other possibilities as the strip readout in 2D and the multiplexing [62].

Thanks to these properties, resistive MPGDs are, for more than a decade, used to improve all the main non resistive technologies summarized in Figure 1.5.

The idea of using resistive anode Micromegas to spread the charge over several pads was initiated by Madhu Dixit (Carleton University, Ottawa, Canada) in the early 2000s [56] and extensively developed and studied leading by Paul Colas inside the ILC-TPC collaboration.

The anode, segmented in pads or in strips, is covered by a foil of insulating material, which has a thin resistive layer on its top side. So the charge deposited by the avalanche induces a signal also on the adjacent pads. The resistive layer can be approximated with a 2D RC network [2]. In this RC model the charge spread is described by a Gaussian distribution. For a point charge deposited at $r = 0$ and $t = 0$, the charge density as function of the radius $r$ and the time $t$ is given by

$$\rho(r,t) = \frac{RC}{4\pi t} e^{\frac{-r^2 RC}{4t}} \tag{1.2}$$

solution of the diffusion equation on a 2D continuous RC network

$$\frac{\partial \rho}{\partial t} = \frac{1}{RC}\left[\frac{\partial^2 \rho}{\partial r^2} + \frac{1}{r}\frac{\partial \rho}{\partial t}\right] \tag{1.3}$$

where $R$ and $C$ are respectively the resistivity and the capacitance per unit area of the resistive layer. The capacitance $C$ is defined by the glue and the resistive foil thickness giving the distance between the resistive layer and the grounded pads. These parameters $R$ and $C$ characterize the width of the induced charge spread $\sigma_t$ at a given time $t$. Considering the integration of the charge collected by a front-end electronics with shaping time $t$, this spread is approximated by the relation

$$\sigma_t = \sqrt{\frac{2t}{RC}}. \tag{1.4}$$

The surface charge density evolution with time and the resultant raw charge pulses induced on neighbouring pads obtained by simulation are shown on Fig. 1.10 for 2 mm size pads. This simple model comfortably reproduces data taken with resistive detectors.

After electronics shaping, the charge signals seen on resistive Micromegas pads are shown on Fig 1.11.

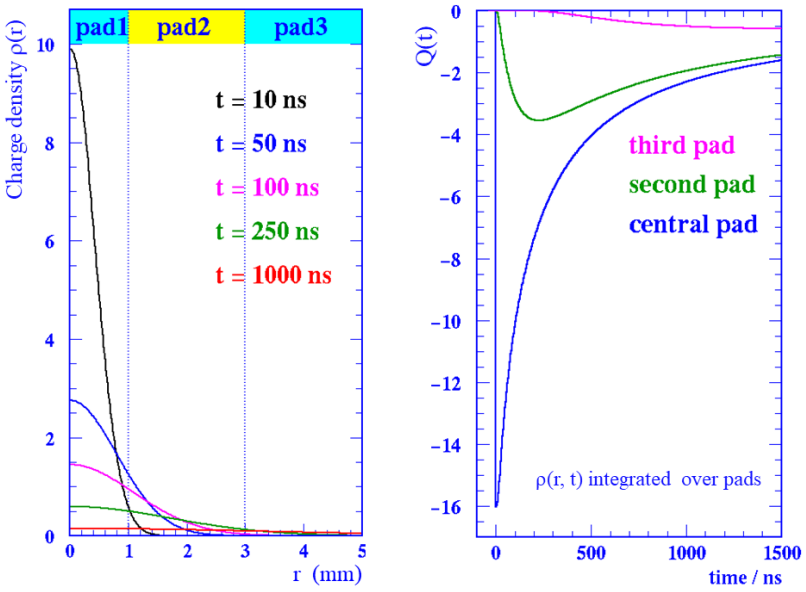


Figure 1.10: [[Left] The distribution of surface charge density is shown at five different times between 10 ns and 1000 ns. [Right] Time dependence of the charge signal seen by 3 different pads. The central pad has observed the charge avalanche directly, whereas the second and third pads have seen only the charge dispersion signals [2].

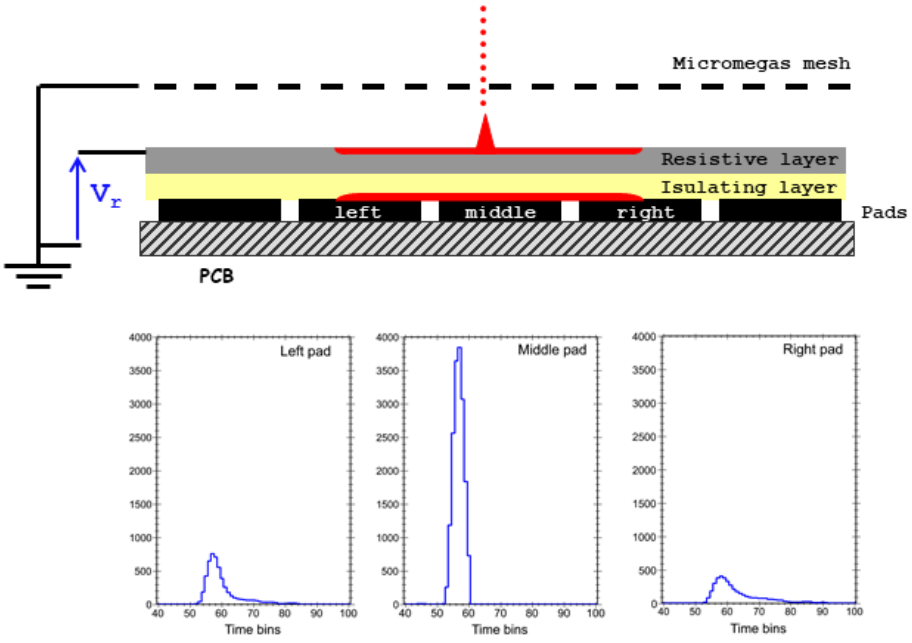


Figure 1.11: [Top] Resistive Micromegas principle. [Bottom] Pad signals recorded by an electronics after shaping.

A more elaborate physical model was introduced by Riegler recently [63]. However, the simulations require numerical calculations which struggle to converge.

# Particle interaction in gaseous detectors

Contents



## 2.1 Electromagnetic interactions with matter

The description of the interaction between matter and high energetic particles or radiation is important to understand the detection principles for particles or radiation and detector limitations (efficiency and energy, position and time resolutions).

The electromagnetic interactions of charges, fermions and photons, are described by the theory of quantum electro-dynamics (QED).

QED theory models energy loss processes in a material via scattering, expressed as exchange of virtual photons with the shell electrons of an atom, or by photon radiation. In a scattering process, the energy lost by a charged particle is transferred to the target, typically a shell electron of an atom or a molecule, making it in an excited or ionized state. After coming back to its fundamental state, free electrons, ions or excited states disappear, so the process becomes invisible to the detector.

For photons scattering processes, the photon transfers its energy to the atom increasing its wavelength and by changing the propagation directions. The photon and the atom directions define thus a scattering angle where the original photon is conserved. During the absorption processes, the photoelectric effect produces an excitation or an ionization of the atom with the photon being absorbed. In a pair production process, the photon converts into an electron-positron pair, so the original photo disappears.

To summarize, particles have different ways to lose energy in the medium when interacting with matter. Charged particles can lose energy:

- by Coulomb Scattering in Coulomb field of nucleus with small energy loss, but deflection,
- by ionization and excitation of electrons on shell,
- by radiation Bremsstrahlung effect: dominant for low masses $\rightarrow$ radiation length.
- Cherenkov effect.

When crossing matter, photons can loose energy by absorption or by attenuation. The process induced is highly dependent of the photon energy. All the possible processes are listed below:

- Photoelectric effect: $E_\gamma < 2MeV$,
- Compton effect: whatever $E_\gamma$,
- pair $e^+e^-$ production: $E_\gamma > 1,022MeV$,
- Photonuclear reaction: $E_\gamma$ at least a few MeV.

Hadrons will lose energy mainly in inelastic scattering.

In the following sections, we will focus on the gas medium used in gaseous detectors. The interactions in gas can be splitted in two part: interaction with neutral particles and interaction with charged particles.

### 2.1.1 Interaction of neutral particle

Neutral particles interact with gas in mainly two ways. The first is the thermal interaction between the neutral particle and the atoms of the gas. The second is the conversion of the particle to a charged particle been seen by the detector.

### 2.1.2 Interaction of charged particles in gas

When a charged particle crosses a detector, it will loose energy by excitation or ionization of the detector gas. The interaction of charges particles in gas are described in the next section.

## 2.2 Energy loss of charged particles

A charged particle moving through matter will interact with it in different ways, losing energy in various ways.

- **Solids, liquids and gases**: the charged particle will ionise the medium's atoms.
- **Semiconductors**: the charged particle will produce electron-hole pairs.
- **Scintillator**: the charged particle will lead to the production of light.
- **Superheated liquid**: the charged particle will leave a trail of bubbles.

The total energy loss of a charged particle can be defined as the differential energy loss divided by corresponding differential path length within a given matter (stopping power). The total energy loss is the sum of energy lost through ionization and electron-orbital excitations and the radiation energy loss by bremsstrahlung:

$$-\frac{dE}{dx} = \rho(B + RE) \tag{2.1}$$

where $\rho$ is the mass density of the matter and $E$ is the energy of the particle, $B$ is the ionizing stopping power (electron term) and $R$ is a constant characterizing the contribution of radiation process (radiation term). This formula corresponds also to the stopping power of the material [64].

In the limit that all electrons in the medium's atoms can be modelled as free, the kinetic energy $dE$ loss per unit distance travelled ($dx$) is:

$$-\frac{dE}{dx} \propto \frac{1}{\beta^2} \tag{2.2}$$

where $\beta = v/c$. This relationship can be understood by looking at the Bethe formula, derived in the following section (see A.1.3).

### 2.2.1 Primary ionization and electron clusters

In gaseous detector, the ionizing collisions occur randomly following Poisson statistics. If $k$ is the number of collision in a distance $d_k$ along the track, the probability to have an ionization is:

$$P(k) = \frac{(\frac{d_k}{k})^k}{k!} \exp -\frac{d_k}{\lambda} \tag{2.3}$$

where $\lambda = 1/(N_e \sigma_t)$ is the mean distance between clusters, $\sigma_t$ the ionization cross-sections per electron (see Fig. 2.6) and $N_e$ the electron density of the gas. The probability to find no cluster in $d_k$ is $P(0) = \exp(-d_k/\lambda)$.

In Argon, about 66% of ionizing collisions produce only a single electron-ion pair. If the primary electron is done by a collision with higher kinetic energy, one or more molecules can be ionized liberating secondary electrons. The involved kinetic energies in these secondary electrons leave them close to the first electron-ion pair, forming thereby a cluster. Hence, the ionization on small scales can be very inhomogeneous. Therefore, tracks with a sufficient length ($\sim 0.5$ m) have to be used for the determination of a mean cluster size or average ionization. The cluster size distribution is shown on Fig. 2.1 from measurements for various pure gases [3].

Most of the electron clusters along a track consist of up to ten electrons, but occasionally, the initial charged particle has enough energy, it can transfer a very large amount of energy to one single electron.

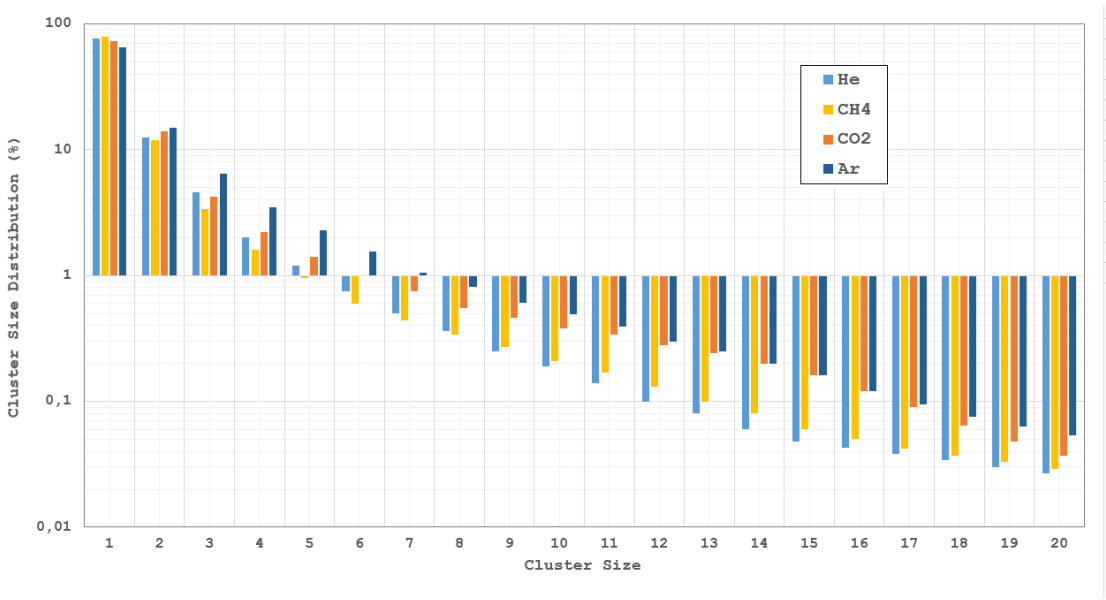


Figure 2.1: Cluster size distribution measured for several gas from [3].

These so-called delta electrons ($\delta$) are able to travel up to several centimetres in an arbitrary direction, ionizing other gas molecules on their way.

The average number per centimetre of $\delta$ electrons with the energy $E$ is approximatively inversely proportional to $E_0$: $P(E > E_0) \sim y/(\beta^2 E_0)$ cm$^{-1}$ and $E$ in keV.

In argon, $E_0 = 10$ keV, $y = 0.114$ and $P = 0.011$ cm$^{-1}$, so such $\delta$ electrons form clusters of about 100 electrons and occur in average every ten centimetres.

### 2.2.2 Energy loss per unit distance

For relativistic charged particles in the range of $0.1 \leqslant \beta\gamma \leqslant 1000$, the mean energy loss is described the term B of Eq. 2.1 which correspond to the Bethe-Bloch equation below:

$$\left\langle -\frac{dE}{dx} \right\rangle_{\text{ion}} = 2\pi N_{\text{a}} r_{\text{e}}^2 m_{\text{e}} c^2 \frac{Z}{A} \frac{z^2}{\beta^2} \left[ \ln \left( \frac{2m_{\text{e}} c^2 \beta^2 \gamma^2 W_{\max}}{I^2} \right) - 2\beta^2 - \delta - 2\frac{C}{Z} \right] \tag{2.4}$$

with

- $2\pi N_{\text{a}} r_{\text{e}}^2 m_{\text{e}}^2 c^2 = 0.1535$ MeV cm$^2$/g
- $z$ : charge of incident particle units of e
- $r_{\text{e}}$ : classical electron radius $= 2.817 \times 10^{-13}$ cm
- $m_{\text{e}}$ : electron mass
- $N_{\text{a}}$ : Avogadro's number $= 6.022 \times 10^{23}$ mol$^{-1}$
- $I$ : mean excitation potential
- $\beta$ $= v/c$ : speed of particle/speed of light in vacuum
- $\gamma$ $= 1/\sqrt{1-\beta^2}$
- $Z$ : atomic number of the absorbing material
- $A$ : atomic mass number of the absorbing material
- $C$ : shell correction factor
- $\delta$ : density factor number

This equation 2.4 describes the mean energy loss along the path for charged particles traversing matter

with an energy range between 0.1 GeV to 1 TeV. The minimum ionization value is 2.2 MeV·cm$^2$/g ($\beta\gamma \approx$ 3.5 GeV) and varies with the medium ($Z$ dependence) but occurs for all charged particles in the $3 \leqslant \beta\gamma \leqslant$ 3.5 range. The equation takes into account the particle properties, such as its charge $z$, its kinetics ($\beta$ and $\gamma$) and the maximum energy transfer per collision $W_{\max}$ which depends on the particle energy, the medium properties like its mass number $A$ and atomic number $Z$ and the mean excitation energy $I$. $\delta$ corrects for the density effect and $\frac{C}{Z}$ corresponds to shell corrections due to the structure of the atom. The equation 2.4 gives an accurate estimate for muons, pions, protons and other charged particles in the same mass range. However, heavy particles like heavy ions, large disparities up to a factor of two exist.

The maximum energy $W_{\max}$ for a particle with a mass $M$ and a momentum $M\beta\gamma c$ is given by

$$W_{\max} = \frac{2m_e c^2 \beta^2 \gamma^2}{1 + 2\gamma m_e/M + (m_e/M)^2}. \tag{2.5}$$

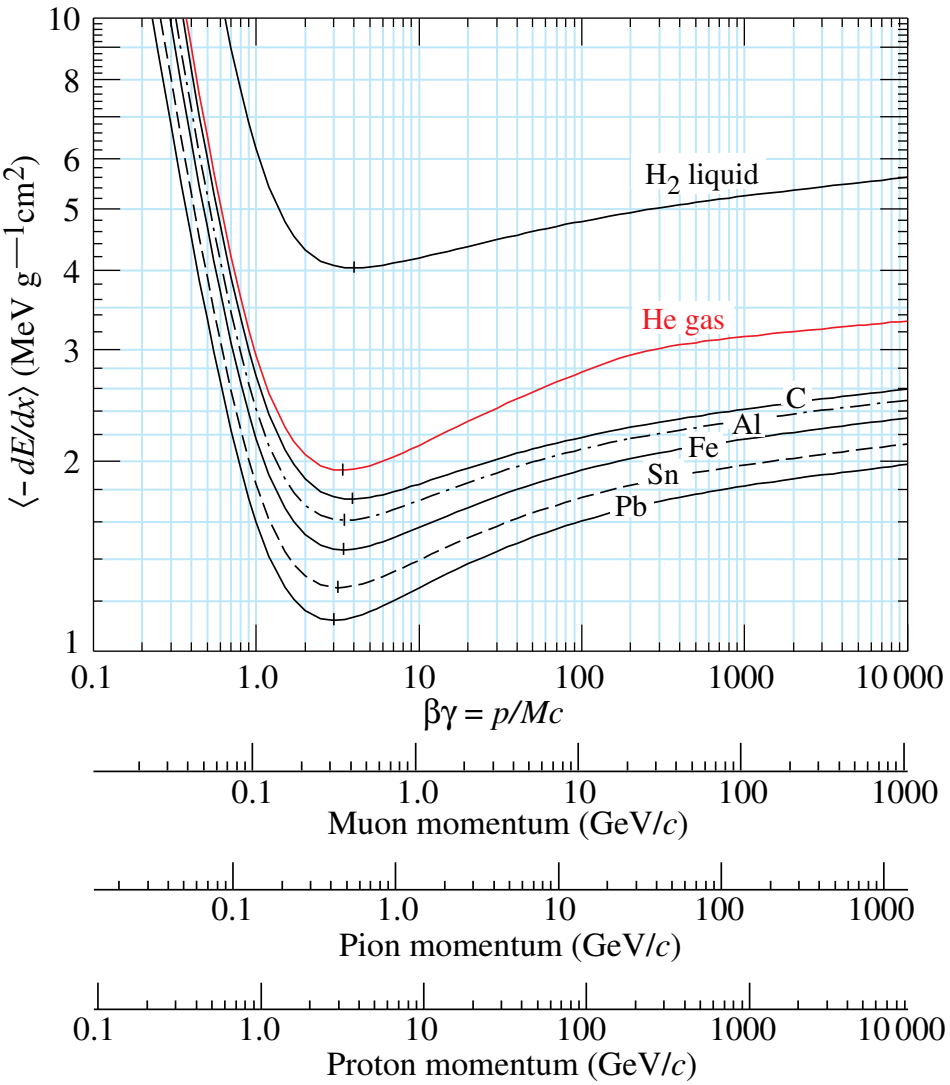


Figure 2.2: Mean energy loss rate in several material. Radiative effects, relevant for muons and pions, are not included.

Charged particles can emit Cherenkov radiation (photons) when crossing a dielectric medium with a

velocity greater than the phase velocity of light in this medium $c/\sqrt{|\epsilon|}$, with $\epsilon$ being the medium's refraction index. The angle and the wavelength of the emitted Cherenkov photon can be used for particle ID in a specific detector.

The Bethe formula describes three regions which are defined as a function of the particle velocity:

- **Low velocity regime:** $\beta\gamma < 3.5$: the stopping power ($dE/dx$) falls off as $1/v^2$ in accordance with 2.2. Slow positively charged particles can capture material's negative electrons, reducing the incident particle's effective charge, $Z$, thus reducing $dE/dx$. Negative incident particles can suffer stripping of their electrons, reducing their value of $Z$. In the range of $0.05 \leqslant \beta\gamma \leqslant 0.1$ the energy loss starts to depend on the charge of the particle where phenomenological approximations are applied which are described by Andersen and Ziegler for $0.01 \leqslant \beta\gamma \leqslant 0.05$ [65] and by Lindhard and Scharff for $\beta\gamma \leqslant 0.01$ [66, 67].

- **Minimum ionisation loss:** $\beta\gamma \approx 3.5$: the $1/(1-\beta^2)$ term in the logarithm stops the general decrease in stopping power somewhere in the range of $\beta\gamma = 3-4$. This is known as the minimum ionisation loss.

- **The relativistic rise:** $\beta\gamma > 3.5$: beyond the minimum ionisation loss $dE/dx$ begins to rise again, in fact the Bethe formula predicts it should rise indefinitely. As the incident charged particle reaches relativistic energies its transverse electric field increases, meaning more of the material's atoms are within range of the particle's electric field, leading to greater ionisation energy loss. This is known as the relativistic rise. In the highest relativistic range ($\beta\gamma > 1000$) the energy losses are dominated by radiation of Bremsstrahlung proportional to the particle's energy. Bremsstrahlung radiation is emitted when the charged particle is decelerated in the coulomb-field of a nucleus:

$$\left\langle -\frac{dE}{dx} \right\rangle_{\text{Brems}} = 4\alpha N_{\text{a}} \frac{Z^2}{A} z^2 \left( \frac{1}{4\pi\epsilon_0} \frac{\text{e}^2}{mc^2} \right)^2 \cdot \ln\left( \frac{183}{Z^{1/3}} \right) \cdot E \tag{2.6}$$

### 2.2.3 Radiation length in materials

Inelastic collisions of particles with atomic electrons in matter represents the first term of equation 2.1. So particles while crossing a medium can experience Multiple Coulomb scattering (MCS) from atom nuclei [68]. In case of single scattering where only two interactions happen, the scattering cross section is well described by Rutherford formula below:

$$\sigma(\theta) = \left( \frac{1}{4\pi\epsilon_0} \right)^2 \frac{Z^2 e^4}{M^2 c^4 \beta^4} \frac{1}{\sin^4(\theta/2)} \tag{2.7}$$

where $M$ is the mass of the medium and $\theta_0$ is the scattering angle, $\epsilon_0$ is the permittivity of free space.

For thicker medium, the number of small scatterings increase with the thickness and become MCS when the number of scattering exceeds approximately 20. The MCS angles projected on a plane follow a Gaussian distribution with a mean at zero and a standard deviation $\sigma_\theta$ given by the equation:

$$\sigma_\theta = \frac{13.6\text{MeV}}{\beta cp} \sqrt{\frac{L}{X_0}} \left( 1 + 0.038 \ln \frac{L}{X_0} \right) \tag{2.8}$$

The $L/X_0$ term is the thickness of the scattering medium in terms of its radiation length $X_0$. The radiation length of a material is thus the mean length (in cm) crossed by an electron to reduce its energy by a factor

| **Element** | **Z** | **A** [g/mol] | **Radiation Length** [g.cm$^{-2}$] (experimental) | **Radiation Length** [g.cm$^{-2}$] (analytical) | **Error**[%] |
|---|---|---|---|---|---|
| H | 1 | 1.00794 | 63.04 | 63.79 | 1.2 |
| He | 2 | 4.0026 | 94.32 | 89.95 | 4.63 |
| C | 6 | 12.0108 | 42.7 | 43.01 | 0.72 |
| N | 7 | 14.0067 | 37.99 | 38.23 | 0.64 |
| O | 8 | 15.9994 | 34.24 | 34.46 | 0.64 |
| F | 9 | 18.9984 | 32.93 | 33.16 | 0.69 |
| Ne | 10 | 20.1797 | 28.93 | 29.15 | 0.77 |
| Na | 11 | 22.9897 | 27.74 | 27.97 | 0.84 |
| Mg | 12 | 24.305 | 25.03 | 25.27 | 0.96 |
| Al | 13 | 26.9815 | 24.01 | 24.26 | 1.06 |
| Si | 14 | 28.0855 | 21.82 | 22.08 | 1.18 |
| P | 15 | 30.9737 | 21.21 | 21.47 | 1.25 |
| S | 16 | 32.065 | 19.5 | 19.76 | 1.35 |
| Cl | 17 | 35.453 | 19.28 | 19.56 | 1.47 |
| Ar | 18 | 39.948 | 19.55 | 19.86 | 1.57 |
| K | 19 | 39.0983 | 17.32 | 17.6 | 1.64 |
| Ca | 20 | 40.078 | 16.14 | 16.43 | 1.78 |
| Ti | 22 | 47.867 | 16.16 | 16.47 | 1.94 |
| Cr | 24 | 51.9961 | 14.94 | 15.25 | 2.09 |
| Fe | 26 | 55.845 | 13.84 | 14.14 | 2.17 |
| Ni | 28 | 58.6934 | 12.68 | 12.97 | 2.27 |
| Cu | 29 | 63.546 | 12.86 | 13.16 | 2.34 |
| Zn | 30 | 65.38 | 12.43 | 12.72 | 2.35 |
| Ag | 47 | 107.868 | 8.97 | 9.17 | 2.26 |
| Pt | 78 | 195.084 | 6.54 | 6.52 | 0.38 |
| Au | 79 | 196.967 | 6.46 | 6.43 | 0.53 |
| Pb | 82 | 207.2 | 6.37 | 6.31 | 0.93 |

Table 2.1: Comparison of values of radiation length for elements obtained experimentally and analytically [22].

1/e. The radiation length can be approximated by the following analytical formula:

$$\mathrm{X}_0 = 4\alpha r_e^2 \frac{N_A}{\rho A} \frac{A}{Z(Z+1)\ln\left(183Z^{1/3}\right)} = \frac{716.4\ \mathrm{g.cm}^2}{\rho} \frac{A}{Z(Z+1)\ln\frac{287}{\sqrt{Z}}} = \frac{716.4\ \mathrm{g.cm}^{-3}\cdot A}{Z(Z+1)\ln\frac{287}{\sqrt{Z}}} \tag{2.9}$$

The constant in the numerator is equal to $(4\alpha r_e^2 N_A/A) = 716.4\ \mathrm{g/cm}^{-2}$ where $\alpha$ is the fine structure constant, $r_e$ is the classical electron radius, $N_A$ the Avogadro's number. The radiation length is expressed in g.cm$^{-2}$ and we can obtain the result in cm by dividing through by the density. The magnitude of deviation of a particle is significantly dependent on $Z$ and $\rho$ of the medium.

The tables 2.1 and 2.2 give respectively the experimental and analytical values of the radiation length for a list of atoms and molecules. For example, a muon will loose $\sim 3\ (1/e)$ times its energy while crossing 6 cm of lead while 36 cm of water or 24 cm of marble are necessary.

| **Element** | **Radiation Length** [g.cm$^{-2}$] (experimental) | **Radiation Length** [g.cm$^{-2}$] (analytical) | **Error**[%] | **Density** [g.cm$^{-3}$] |
|---|---|---|---|---|
| $H_2O$ | 36.08 | 36.04 | 0.1 | 1 |
| $Al_2O_3$ | 27.94 | 27.94 | 0 | 3.7 |
| $CaCO_3$ | 24.03 | 24.02 | 0.04 | 2.8 |
| $CO_2$ | 36.2 | 36.2 | 0 | $1.84.10^{-3}$ |
| Freon-12 ($CF_2C_12$ | 23.65 | 23.65 | 0 | 1.12 |
| Cellulose acetate $(C_6H_7O_2(OCOCH_3)_3)_n$ | 38.75 | 39.11 | 0.93 | 1.42 |
| Cellulose acetate butyrate $(C_15H_22O_8)_n$ | 39.75 | 39.76 | 0.03 | 1.2 |
| Polyethylene | 44.77 | 44.78 | 0.02 | 0.89 |

Table 2.2: Comparison of values of radiation length for molecules obtained experimentally and analytically [22].

## 2.3 High-energy photons in matter

Contrary to charged particles, photons in each interaction with electrons or nuclei disappear or change dramatically their energy and direction. So, the photon flux $I$ follows an exponential law:

$$I = I_0 \exp(-\mu x) \tag{2.10}$$

where $\mu$ is the attenuation coefficient(or absorption coefficient). $\mu$ is simply the inverse of the absorption length $\epsilon$: $\mu = 1/\epsilon$. Figure 2.3 show the absorption length for various noble gases.

The processes of photon interactions in matter are discussed in the next subsections and are illustrated for Iron-55 in Fig. 2.4.

### 2.3.1 Photoelectric effect

the photoelectric effect is the absorption of a photon by an electron from an atom's shell by transferring its energy to this electron. The total photoelectric effect cross section for the photon of energy $E_\gamma > E_K$, where $E_K$ is the K-shell energy is

$$\sigma_{ph}^{K} = \sqrt{\frac{32}{\epsilon}^7}\, \alpha^4 Z^5 \sigma_{Th} \tag{2.11}$$

with $\epsilon = E_\gamma / m_e c^2$ and $\sigma_{Th} = \frac{8}{3}\pi r_e^2 = 665$ mb the cross section of Thompson scattering. The photoelectric effect cross section has sharp discontinuities when $E_\gamma$ is equal to the binding energy of the atomic shells. After a photoelectric effect in the K shell, the atomic electron is rearranged and a specific X ray photon (like $K_\alpha$ or an Auger electron is emitted.

### 2.3.2 Compton effect

Compton effect corresponds to an inelastic scattering of photons by quasi-free atomic electrons. The energy $E_\gamma^{'}$ and the angle $\theta_\gamma$ of the scattered photon are related by the formula below:

$$\frac{E_\gamma^{'}}{E_\gamma} = \frac{1}{1 + \epsilon(1 - \cos\theta\gamma)} \tag{2.12}$$

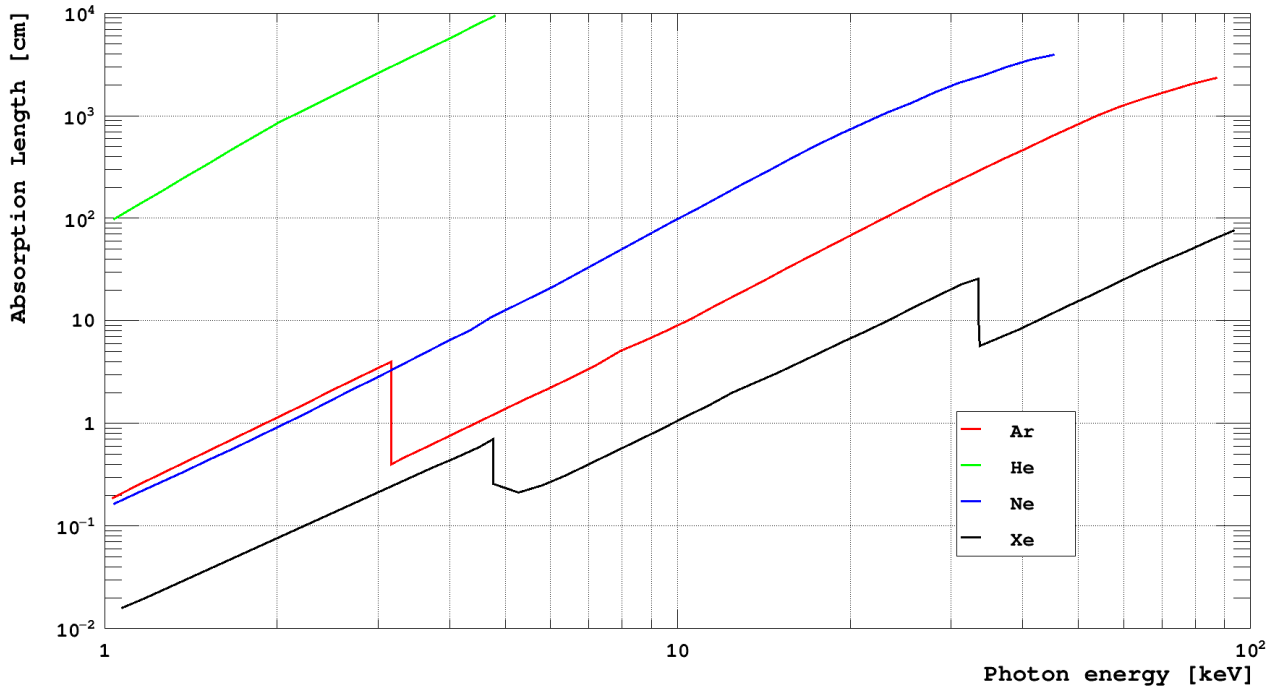


Figure 2.3: Absortpion length in various noble gases.

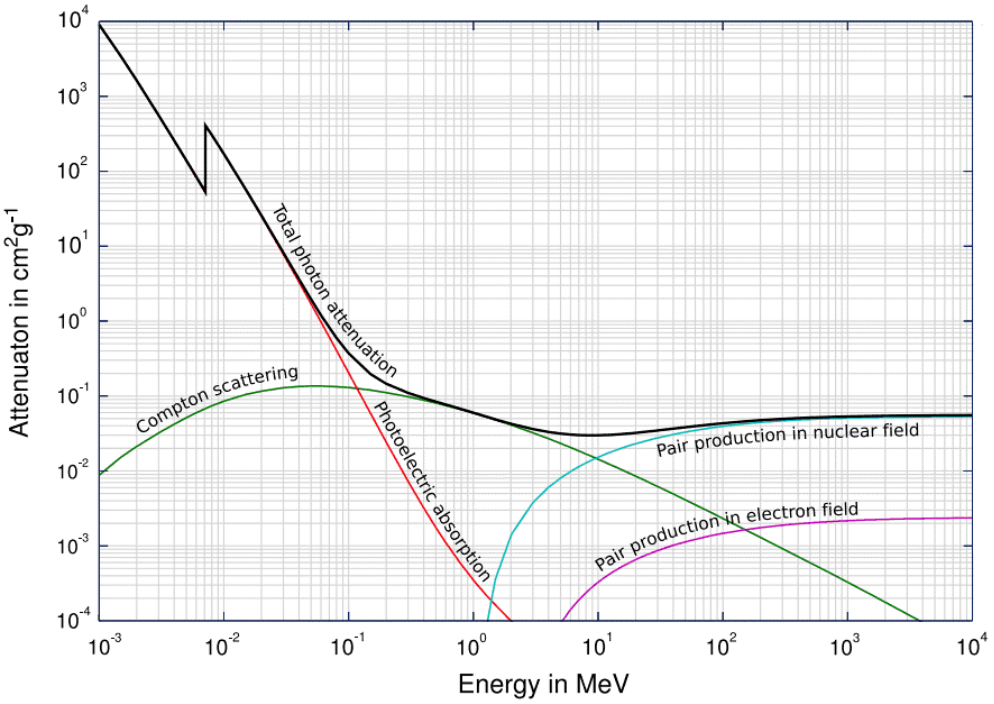


Figure 2.4: Photon attenuation in Iron depending of the energy where the three processes photoelectric absorption, Compton scattering and pair production are shown [4] with data available in [5].

with $\epsilon = E_\gamma / m_e c^2$. The total cross section of Compton scattering for one electron is derived by the integration of the Klein-Nishina formula [69]:

$$\sigma_{\mathrm{C}} = \frac{\pi r_e^2}{\epsilon}\left[\left(1 - \frac{2}{\epsilon} - \frac{2}{\epsilon^2}\right)\ln\left(1+2\epsilon\right) + \frac{1}{2} + \frac{4}{\epsilon} - \frac{1}{2\left(1+2\epsilon\right)^2}\right] \tag{2.13}$$

In the ultrarelativistic case, when $\epsilon \gg 1$, the formula for the Compton cross section is then reduced to

$$\sigma_{\mathrm{C}} = \frac{\pi r_e^2}{\epsilon}\left(\ln 2\epsilon + \frac{1}{2}\right). \tag{2.14}$$

### 2.3.3 Electron-positron pair production

If the photon energy $E_\gamma$ exceeds the threshold

$$E_\gamma \geq 2m_e c^2 + \frac{2m_e c^2}{M_{\mathrm{nucleus}}} \approx 2m_e c^2 \tag{2.15}$$

the production of an electron-positron pair becomes possible. And a screening parameter $\delta_\gamma$ is defined as

$$\delta_\gamma = 100\frac{m_e c^2}{E_\gamma}\frac{1}{\xi(1-\xi)}Z^{-1/3}, \qquad \xi = \frac{E_e + m_e c^2}{E_\gamma} \tag{2.16}$$

where $E_e$ the electron (or positron) kinetic energy. If $\delta_\gamma \ll 1$, the pair-production cross section is given by

$$\sigma_{\mathrm{pair}} = 4\alpha r_e^2 Z^2\left(\frac{7}{9}\ln\frac{183}{Z^{1/3} - \frac{1}{54}}\right). \tag{2.17}$$

The probability $\mathrm{d}w$ of photon conversion at the small path length $\mathrm{d}x$ is approximatively equal to

$$\mathrm{d}x = \frac{7}{9}\frac{\mathrm{d}x}{X_0}. \tag{2.18}$$

The energy distribution of the produced electrons and positrons is given by the differential probability

$$\frac{\mathrm{d}x}{\mathrm{d}E_+ \mathrm{d}x} = \frac{\alpha r_e^2}{E_\gamma}\frac{N_{\mathrm{A}}}{A}Z^2 f(Z, E\gamma, x(\epsilon)) \tag{2.19}$$

where $dE_+$ is the energy of the positron and $f(Z, E\gamma, x(\epsilon))$ is a dimensionless energy-partition function shown is Fig. 2.5.

## 2.4 Transport of charged particle in gases

The nature of gas-filled detectors leads to basic limitations of theirs performances. The process of detection is based on inelastic collisions between the incident particle and gas molecules. These collisions lead to excitation and primary ionization of the molecules in the medium. Knowing the location where are created these processes in the gas allow to reconstruct the track of the incident particle. The number of primary electrons $N_P$ and their space distribution (clusters) depend on the nature and energy of the particle and the gas. As primary electrons can often have enough energy to further ionize the medium, so the total number of electron–ion pairs $N_T$ is then a few times larger than $N_P$.

Table 2.3 provides values of relevant parameters in some commonly used gases at NTP for unit-charge minimum-ionizing particles.

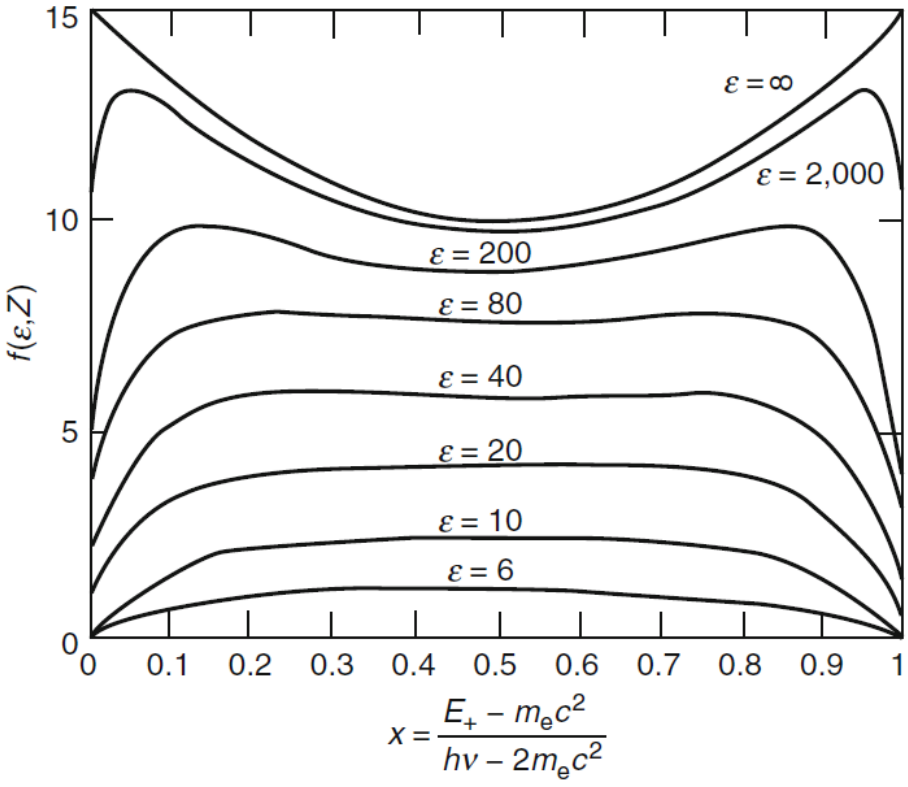


Figure 2.5: Energy partition function $f(Z, E_\gamma, x(\epsilon))$ with $\epsilon = E_\gamma/m_e c^2$.

In Argon, there is $N_P = 25$ electron-ion pairs per centimetre, so the total number of ion pairs per centimetre is $N_T = dE/dx/W_I = 2530/26 = 97$ ion pair/cm so $N_T/N_P \sim 4$.

The statistics of primary electrons determine most of the intrinsic performance of gas-filled detectors, such as efficiency, time and spatial resolutions. These processes follow the Poisson's statistics. So, the efficiency of a perfect detector with a thin layer of gas is given by $1 - e^{-N_P}$. For instance, in one mm of Ar/Isobutane (95:5), a MIP will release approximately ∼10 primary electrons and therefore it can be detected.

## 2.5 Gas mixture properties

The choice of the gas mixture depends of many parameters. Except for positive ions TPC, the properties of the gas mixture refer to the properties of electrons produced by the molecular ionization of the charge particle inside the gaseous medium. All those parameters can be simulated using the Magboltz software which solves the Boltzmann transport equations for electrons in gas mixtures under the influence of electric and magnetic fields [7].

### 2.5.1 Electron or ion drift velocity

In the absence of an external electric field, electrons and ions are thermalized (in thermal equilibrium) and their movement is described by a mean velocity $< v >$ given by the equation $1/2mv^2 = 3/2kT$ and an

| **Gas** | **Density** [$cm^{-3}$] | $E_x$ [eV] | $E_I$ [eV] | $W_I$ [eV] | $dE/dx|_{min}$ [$keV.cm^{-1}$] | $N_P$ [$cm^{-1}$] | $N_T$ [$cm^{-1}$] |
|---|---|---|---|---|---|---|---|
| He | 0.179 | 19.8 | 24.6 | 41.3 | 0.32 | 3.5 | 8 |
| Ne | 0.839 | 16.7 | 21.6 | 37 | 1.45 | 13 | 40 |
| Ar | 1.66 | 11.6 | 15.7 | 26 | 2.53 | 25 | 97 |
| Xe | 5.495 | 8.4 | 12.1 | 22 | 6.87 | 41 | 312 |
| $CH_4$ | 0.667 | 8.8 | 12.6 | 30 | 1.61 | 28 | 54 |
| $C_2H_6$ | 1.26 | 8.2 | 11.5 | 26 | 2.91 | 48 | 112 |
| $iC_4H_{10}$ | 2.49 | 6.5 | 10.6 | 26 | 5.67 | 90 | 220 |
| $CO_2$ | 1.84 | 7.0 | 13.8 | 34 | 3.35 | 35 | 100 |
| $CF_4$ | 3.78 | 10.0 | 16.0 | 54 | 6.38 | 63 | 120 |

Table 2.3: Properties of noble and molecular gases at normal temperature and pressure (NTP: 20 C, one atm). $E_X$ and $E_I$ are first excitation and ionization energies. $W_I$ is the average energy per ion pair; $dE/dx|_{min}$, $N_P$ and $N_T$ are respectively differential energy loss, primary and total number of electron-ion pairs per cm, for unit charge minimum ionizing particles. [23].

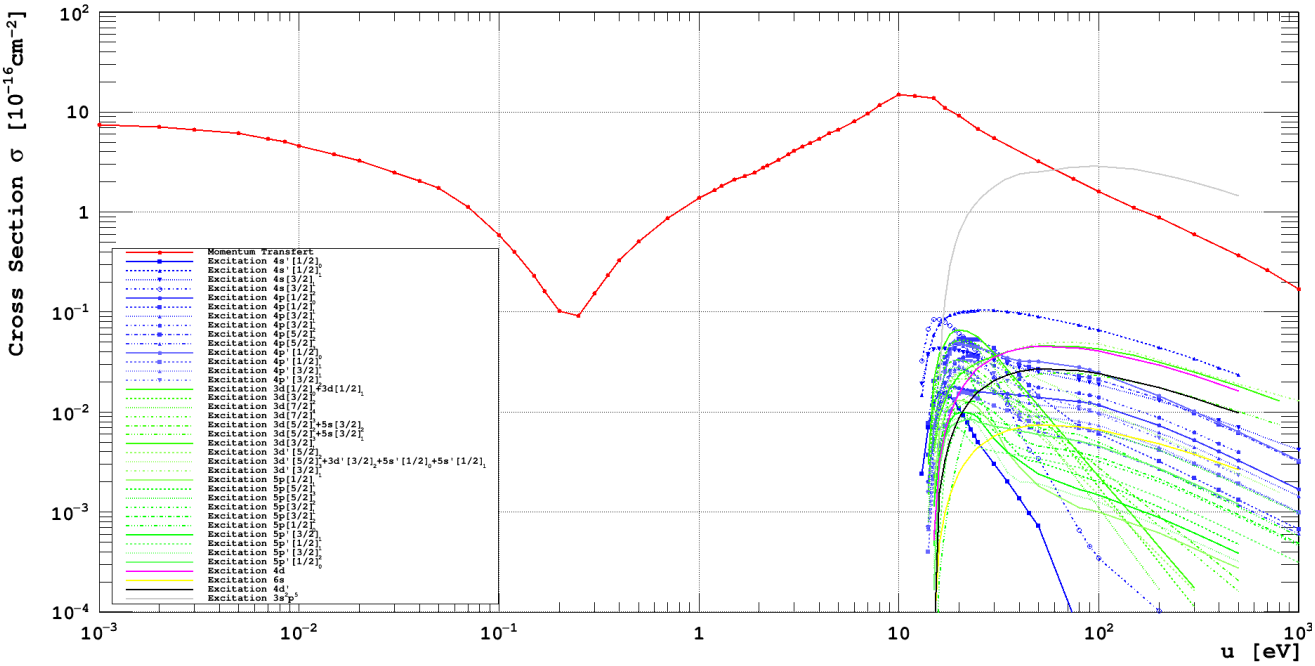


Figure 2.6: Electron cross section with elastic (red) and inelastic (other colors) contributions for argon, based on recent experimental measurements see [6].

isotropic diffusion coefficient $D$. They follow the Maxwell-Boltzmann law with a mean kinetic energy of $\epsilon = kT$ with $k$ being the Boltzmann constant and $T$ the temperature of the medium. A point like cloud of electrons or ions diffuses symmetrically in the gas. The fraction of particles $dN/N$ found in an element $dx$ at a distance $x$ from the origin after a time $t$ follows a Gaussian law:

$$\frac{dN}{N} = \frac{1}{\sqrt{4\pi Dt}} \exp\left(-\frac{x^2}{4Dt}\right) dx. \tag{2.20}$$

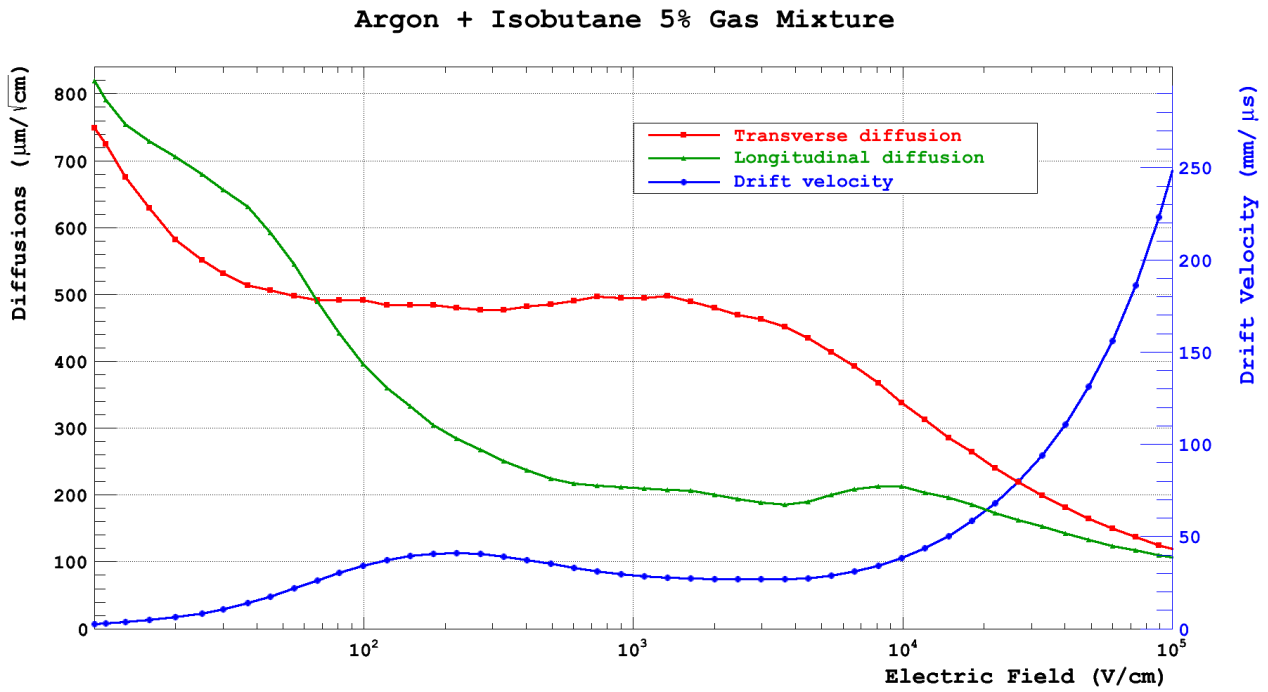


Figure 2.7: Simulated gas properties of Argon and 5% Isobutane mixture: drift velocity, transverse and longitudinal diffusions at magnetic field B=0T [7].

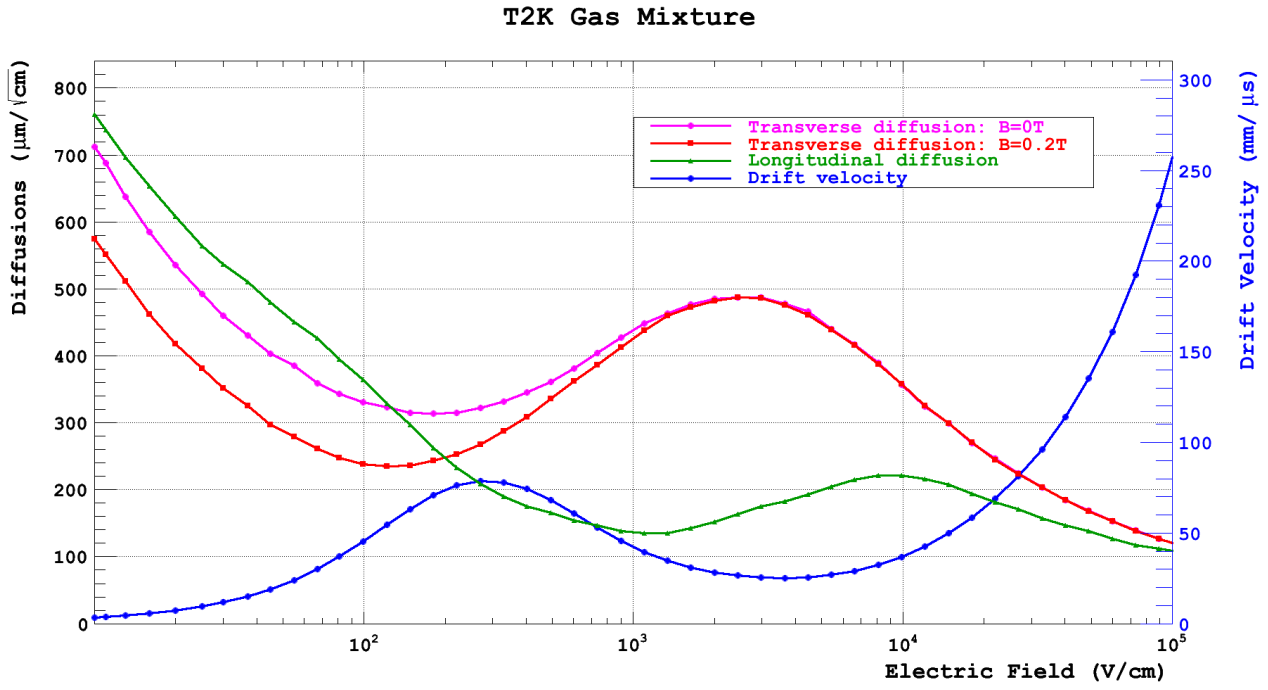


Figure 2.8: Simulated gas properties of T2K mixture: drift velocity, transverse and longitudinal diffusions at magnetic field B=0T [7].

$D$ is the gas dependent diffusion coefficient and the standard deviation of this linear diffusion $\sigma_x$ and volume diffusion $\sigma_V$ processes are given by

$$\sigma_x = \sqrt{2Dt} \quad \text{and} \quad \sigma_V = \sqrt{6Dt} \tag{2.21}$$

Fig. 2.7 and 2.8 show respectively the transverse and longitudinal diffusion in function of the electric field for the Ar+5% isobutane and T2K gas mixtures.

Under the influence of an external electric field $\vec{E}$ the electrons or ions favour a preferred direction towards the field line direction. The drift velocity of the electrons or ions $v$ defines the charge carriers mobility $\mu = v/E$

For ions, the energy increase between scatterings is largely transferred to the gas so the mobility $\mu$ is constant to a very high fields. For electrons, the scattering processes are highly dependent on the electron energy $\epsilon_k(E)$ which can be much higher than their thermal energy. The diffusion can be related to the mobility by

$$\frac{D_{ion}}{\mu_{ion}} = \frac{kT}{e} \quad \text{and} \quad \frac{D_{e-}}{\mu_{e-}} = \frac{\epsilon_k}{e} \tag{2.22}$$

In case of very low $\vec{E}$ field ($E \sim 1$ V/cm), atomic recombination can happened.

The drift velocity $\vec{v}$ of a charged particle $q$ in an electric field $\vec{E}$ and a magnetic field $\vec{B}$ is described by the Langevin equation or a the sum of forces in action:

$$m\frac{d\vec{v}}{dt} = q\vec{E} + q(\vec{v} \times \vec{B}) + \vec{Q}(t) \tag{2.23}$$

where $m$ and $q$ are respectively the mass and the charge of the particle. $\vec{Q}(t) = K\vec{v}$ describes the force due to the scattering of the particles inside the gas molecules.

So this equation has a velocity $\vec{v}_D$ averaged of many collisions as a stationary solution

$$\vec{v}_D = \mu\vec{E} + \tau\vec{v}_D \times \vec{\omega} \tag{2.24}$$

where $\tau = m/K$ is the average time between two collisions of the charged particle and the gas molecules, $\mu = q\tau/m$ is the electron mobility in the gas and $\vec{\omega} = q\vec{B}/m$ is the cyclotron frequency. Using $\hat{E}$ and $\hat{B}$ as respectively the unit vectors of the electric field and the magnetic field the Eq. 2.24 can be expanded as

$$\vec{v}_D = \frac{\mu E}{1+\omega^2\tau^2} \cdot \left[\hat{E} + \omega\tau\hat{E} \times \hat{B} + \omega^2\tau^2(\hat{E} \cdot \hat{B})\hat{B}\right] \tag{2.25}$$

**For a TPC**: the electric field is parallel to the magnetic field, which means that the second term of equation 2.25 $\omega\tau \cdot \hat{E} \times \hat{B} = 0$ and the last term can be simplified as $(\hat{E} \cdot \hat{B})\hat{B} = \hat{B} = \hat{E}$ so the equation 2.25 can be written:

$$\vec{v}_D = \frac{\mu E}{1+\omega^2\tau^2}\hat{E}(1+\omega^2\tau^2) = \mu\vec{E} \tag{2.26}$$

If there is an angle $\alpha_{E.B}$ between the electric field and the magnetic field:

$$\vec{v}_D = \frac{\mu E}{1+\omega^2\tau^2}\sqrt{1 + (1+\cos^2\alpha_{E.B}) \cdot (\omega\tau)^2 + (\omega\tau)^4 \cdot \cos^2\alpha_{E.B}} \tag{2.27}$$

The cyclotron frequency $\omega \cong 1.76 \times 10^{11}\text{s}^{-1}$ for electrons in magnetic field of $B = 1$ T.

The drift velocity $v_d$ is sensitive to contaminants and gas density (P, T). Polyatomic molecules ($CO_2$, $CH_4$, $iC_4H_{10}$, ...) added to noble gases reduce electron instantaneous velocity and cool electrons to a region where scattering cross-sections are lower so $v_d$ increases. Drift velocities are very well simulated and given in cm/µs.

The drift velocity is influenced via the electron mobility $\mu$ by gas mixture parameters like pressure or water content (see Fig. 2.12).

The shape of the drift velocity curve is explained by the Ramsauer effect [46]. For this explanation, the cross section for a collision of an electron with a gas molecule is used, which is inversely proportional to the drift velocity, since less collisions yield a faster drift. In general, the cross section decreases with the increase of the kinetic energy of the electron. But Ramsauer observed a minimum in the collision cross-section for particles with a de Broglie wave length of the order of the dimension of the gas molecules (see Fig. 2.6. The molecules become permeable for such electrons, which reach at this point a local maximum of the drift velocity. In a TPC, the drift velocity has to be large enough in order to read out the detector in a reasonable time. In addition, the drift velocity should as constant as possible so very small fluctuations of the electric field are required. Therefore, the settings are chosen to obtain a drift velocity near a maximum, since in this region the dependence on the field fluctuations would be smaller.

### 2.5.2 Electron transverse and longitudinal diffusions

The diffusion in gas is given by the diffusion constant depending of the gas mixture, the electric and the magnetic field. The diffusion constant has a great influence on the two track separation and the position resolution.

In a field, electron cloud diffuses while it drifts and the diffusion is proportional to the square root of the distance ($\sigma \propto \sqrt{d}$). So the diffusion dominates the position resolution over the drift paths. Transverse ($\sigma_{\mathrm{T}}$) and longitudinal ($\sigma_{\mathrm{L}}$) diffusions are different. The transverse diffusion ($\sigma_{\mathrm{T}}$) is suppressed when the electric ($\vec{E}$) and magnetic fields ($\vec{B}$) are parallel as electrons spiral around $\vec{E}$ field lines: $\sigma_{\mathrm{T}}(\vec{B}) \sim \sigma_{\mathrm{T}}(0)/\sqrt{1+\omega^2\tau^2}$ where $\omega = eB/m$. Figure 2.12 shows Magboltz simulations of transverse diffusion in T2K gas mixture at various B fields.

### 2.5.3 Electron multiplication and amplification

The mean free path for ionization $\lambda_i = 1/(N\sigma_i)$ is the exponentially distributed distance between collisions, $N$ is the number of molecules per unit volume and $\sigma_i$ the energy dependent total cross section for all contributing processed. $\lambda_i$ decreases exponentially with increasing electric field $\vec{E}$.

The electron amplification or multiplication, so-called gain or $G$ in a uniform electric field between two parallel plates in a gas at a pressure $P$, is described by the following equation:

$$G = N_0 e^{-\alpha.d} \tag{2.28}$$

where $d$ is the distance (or gap) between the two parallel electrodes and $\alpha$ is the first Townsend coefficient and $N_0$ is the primary number of electrons. This coefficient corresponds to the inverse of the mean free path of an electron between two ionizations. Rose and Korff introduce a good approximation of this coefficient by the formula:

$$\alpha = P.A.e^{B.P/E} \tag{2.29}$$

where $E = V/d$ is the electric field and A,B are parameters depending on the gas mixture.

The gas amplification starts when $E >\sim 5$ kV/cm ($2.5 \times 10^5$ V/m) but the threshold field for entering the amplification region is gas dependent within a large range. A simulated avalanche using Garfield++ [70] is shown Fig. 2.9.

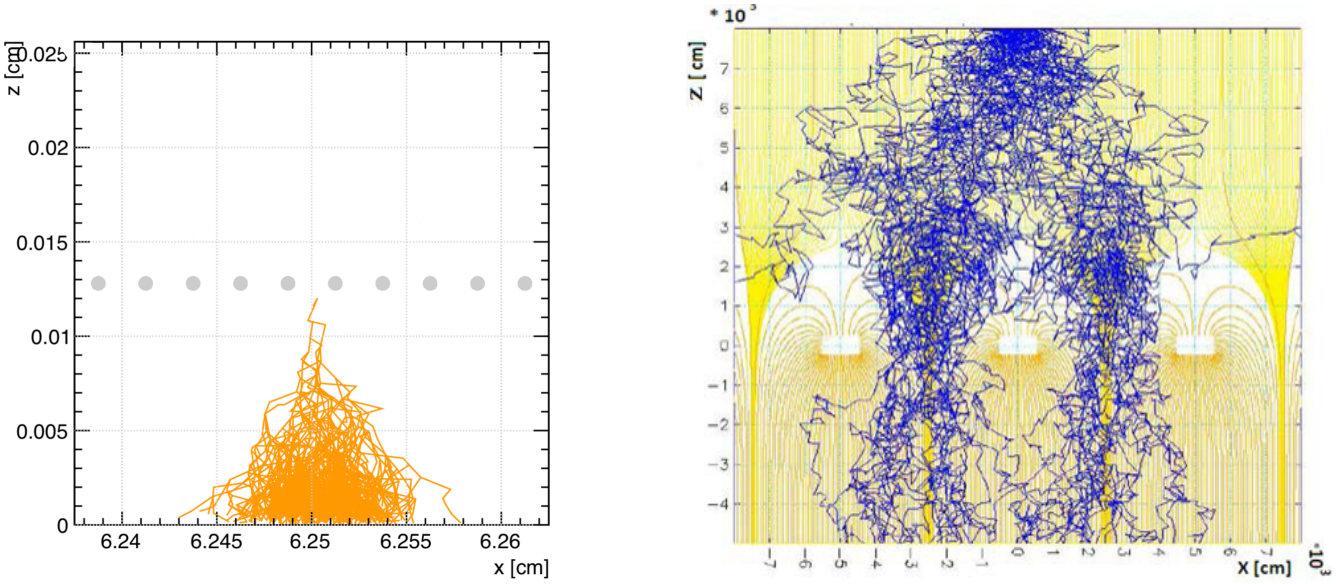


Figure 2.9: [Left] Simulated avalanche in 128 µm gap Micromegas in argon-isobutane (5%) gas mixture. The yellow paths are the trajectories of electrons coming from secondary ionizations. [Right] Simulation of electric field lines in a Micromegas grid (500 LPI) using MAXWELL 2D-SV software and electrons trajectories simulated with GARFIELD 7.10, taken from [8].

### 2.5.4 Electron loss processes

Electronegative molecules ($O_2$, $H_2O$, $CF_4$) capture electrons to form negative ions, reduce signal and impact measurement of ionization energy loss (dE/dx). Attachment and recombination are highly sensitive to contaminant concentration and differs in different primary gas mixtures.

The attenuation of air, $A_{\text{air}}$, can be written as

$$A_{\text{air}} = e^{-\sigma_{\text{air}} \cdot t_{\text{air}}} = e^{-(\sigma_{O_2} \cdot t_{O_2} + \sigma_{N_2} \cdot t_{N_2})} \tag{2.30}$$

Using the results for $N_2$ and dry air shown in Fig. 2.13, the attenuation cross-section is estimated to be $3.07 \times 10^{-17}$ cm$^2$ for $\sigma_{\text{air}}$ and $1.07 \times 10^{-17}$ cm$^2$ for $\sigma_{N_2}$. Since the fraction of $O_2$ in air is 0.209 and that of $N_2$ is 0.781, the densities of these admixtures are given by $t_{O_2} = 0.209 \times t_{\text{air}}$ and $t_{N_2} = 0.781 \times t_{\text{air}}$. Using equation 2.30 and values mentioned above, $\sigma_{O_2}$ is estimated to be $1.07 \times 10^{-16}$ cm$^2$, with the error of ±5%, which is about one order larger than the cross sections of $N_2$ and dry air [71].

### 2.5.5 Fano factor

The number of electrons produced by the conversion of a photon in a gas depends of the molecular ionisation energies and their excitation states. The mean energy per ion pair $W_i$ can be calculated from the number of primary electrons $n_e$ and the energy of the photon $E_0$ if the photon loses all its energy by ionisation:

$$W_i = \frac{E_0}{n_e} \tag{2.31}$$

In hydrocarbons and noble gases, like Ar, Kr and Xe, $E_i$ are given in Tab. 2.3. For photon energies higher than 1 keV, $W_i$ is considered to be constant.

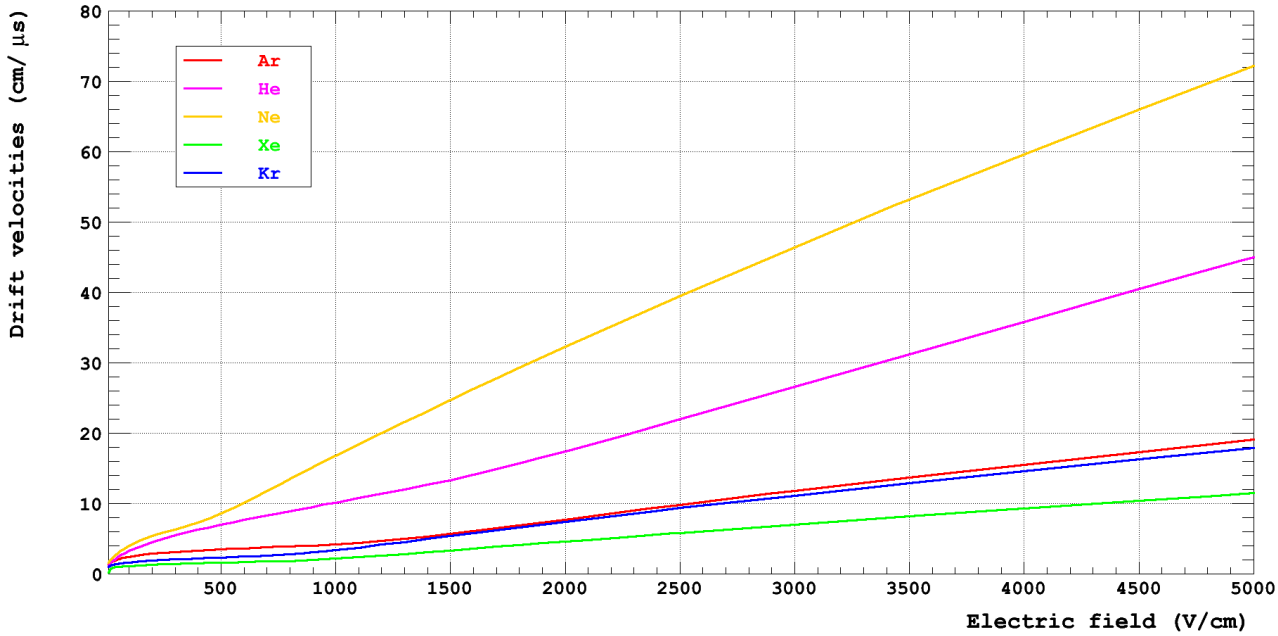


Figure 2.10: Simulated drift velocities in mono-atomic gaz at magnetic field B=0T.

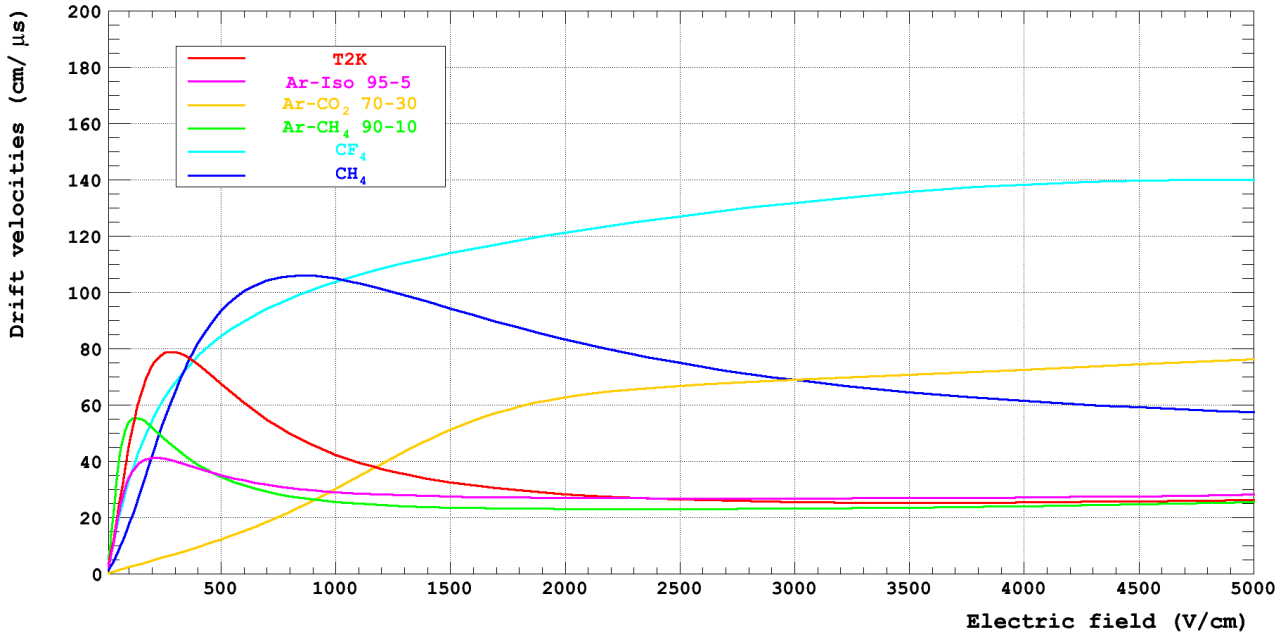


Figure 2.11: Simulated drift velocities in usual gas mixtures at magnetic field B=0T.

The number of primary electron $n_e$ follows a Poisson statistics with the variance $\sigma_{n_e}$ considering that the different steps of ionisation are independent. But as $n_e \leqslant E_0/E_i$ where $E_i$ is the ionisation potential this independence is broken. For that reason the Poisson distribution has a variance $\sigma_{n_e}$ reducing by a

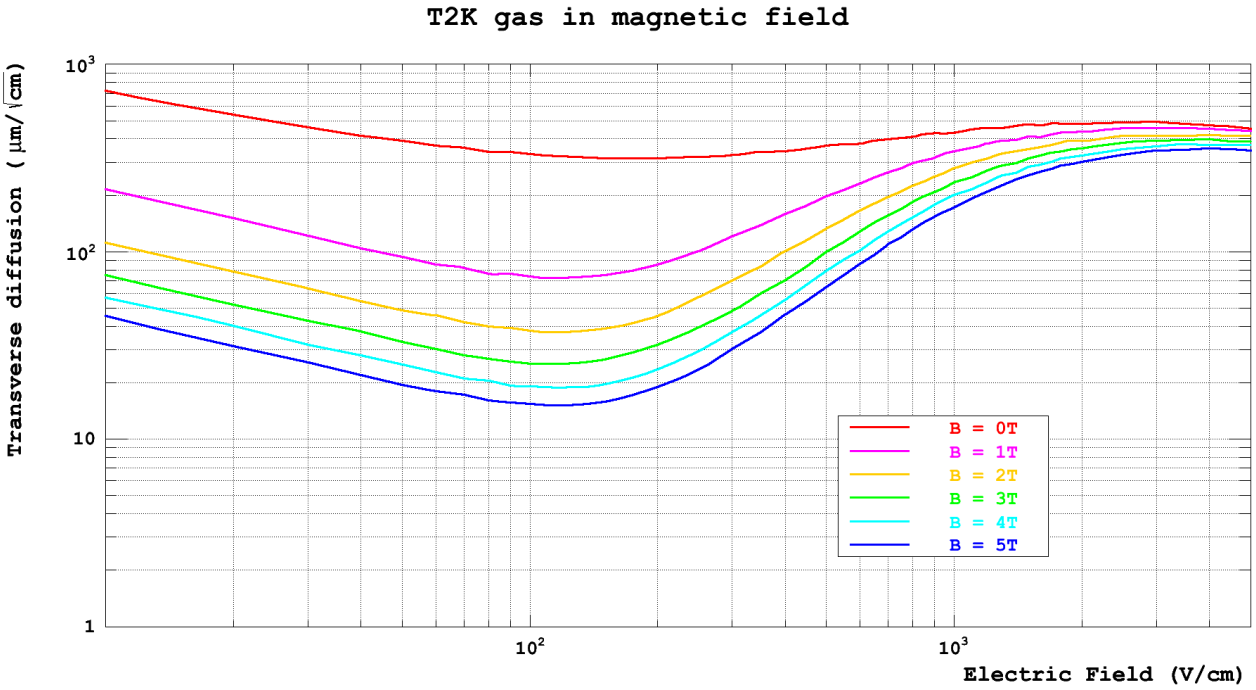


Figure 2.12: Simulated transverse diffusion in T2K (Ar-$CF_4$-$iC_4H_{10}$ 95-3-2) gas mixture at different magnetic field.

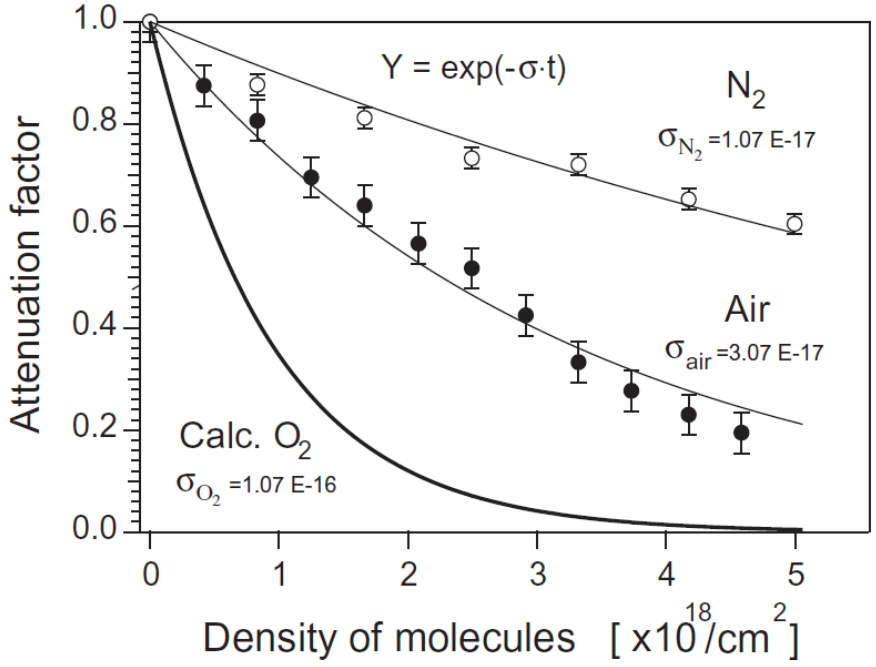


Figure 2.13: Attenuation factors for dry air and $N_2$ respectively. The attenuation factor for $O_2$ is evaluated by the results of dry air and $N_2$.

factor $F$ called *Fano factor* the number of primary electron $n_e$ defined as:

$$F = \frac{\sigma_{n_e}^2}{N_e} \tag{2.32}$$

The detection of the primary electrons $n_e$ will depend of the detector gain, to the single electron detection efficiency $\kappa$ and to the collection efficiency $\eta$. So the mean number of detected electrons $N_d$ is given by

$$N_d = \kappa\eta N_e \Rightarrow F = \left(\frac{\sigma_{N_d}}{N_d}\right)^2 \frac{N_d}{\kappa\eta} + \frac{\kappa\eta - 1}{\kappa\eta} \tag{2.33}$$

To evaluate the $F$ either the number of primary electrons or the efficiencies $\eta$ and $\kappa$ have to be know.

$F$ depends on the gas mixture and the photon energy. It is of the order of 0.15 0.2 for noble gases and 0.2-0.4 for molecular gases. Gas mixture can lead to different values, especially in Penning mixtures(see section 2.2.3). Fano factors down to 0.05 are reported in pure gases with small amount of quencher less than 1% [72].

### 2.5.6 Streamers and quenching

Ultra-violet (UV) photons are emitted by excited noble gas atoms. While photon propagation is independent of $\vec{E}$ field direction unlike electrons. UV photon absorption lengths are about $10^{-4}$ g/cm$^2$ or $\sim 0.06$ cm in Argon gas. In reasonable gas amplification fields ($< 50$ kV/cm) the mean free path in Argon for an electron before ionization is 2.7 µm while the mean free path for the photo-electric effect ($\lambda_{\text{p.e.}}$) is 2-3 cm.

By absorbing UV photons, polyatomic molecules prevent (quench) the spread of ionization processes in space (*streamers* or *sparks*). If the number charges from the avalanche reaches the *Rather limit* then space charge will induce a spark. The Raether limit is about $10^7$ to $10^8$ or defined as $\lambda\alpha < 20$ (where $\alpha$ is the first Townsend coefficient and $\lambda$ is the mean free path length for ionization).

### 2.5.7 Gas choice consideration

For a gaseous detector, the gas mixture choice is essential and has to take into account the specifications requested by the experiment. The gas mixture is mainly a noble gas with a quenching gas.

A **noble gas** is always chosen to obtain a large gas gain at a reasonable high voltage. In noble gases, electron energy is not wasted on breaking up molecules without releasing new electrons. The higher the atomic number is the lower its ionization potential (see Tab. 2.3). But Xenon and Krypton are expensive compared to argon. Hence, argon is often the noble gas chosen.

The **quenching gas** helps to stabilize the avalanche and to prevent discharges. Adding gas with complex molecule allows the absorption of the de-excitation photons produced in avalanches before they reach the closest surface and knock out new electrons.

Carbon dioxide ($CO_2$) and saturated hydrocarbons as methane ($CH_4$), isobutane (i-$C_4H_{10}$), pentane ($C_5H_{12}$) are typical molecules used as quenching gas. Typically, the more complex the molecule is, the better its quenching properties are. But, complex organic molecules have a tendency to polymerize under radiation increasing the detector ageing.

Other specific considerations could also be taken into account. Some of them are listed below:

- improvement of the electron drift velocity by adding $CF_4$,
- improvement of the electron diffusion in magnetic field by adding $CF_4$,

- prevention of ageing under radiation by adding $H_2O$, $O_2$, $CF_4$,
- reducing electron attachment by prohibiting gases with electronegative properties,
- need of enhanced gamma detection by using Xe.

# Research and Development on Micromegas Detectors

Contents



The following sections show my contribution to the systematic and specific studies of different Micromegas detector technologies. By varying the gas composition, the gas pressure and the geometric parameters (gap, hole diameter and pitch), the goals are to improve the understanding of the Micromegas concept and to find the optimal design and operation parameters depending of the application.

## 3.1 Systematic detector studies in various gas

The most significant gas detector properties is the gain described in section 2.5. The gain is given by the amplification factor between primary electrons and multiplied electrons. These electrons induced a charge signal that can be read out by a charge amplifier-based electronic chain. The energy resolution gives the precision with which the energy of the particle can be measured by the detector. The gain and energy resolution, both depend on the gas mixture, the amplification gap and the electric field configuration (absolute amplification field and ratio between drift and amplification fields). However, the energy resolution

is more sensitive to the detector geometry at microscopic scale. This section describes the methodology and the most systematic gain measurements ever done with the same Micromegas detector.

### 3.1.1 Calibration procedure using a radioactive source

Some radioactive sources provide X-ray photons which are converted to photoelectrons in the gas by photoelectric effect (see Sec. 2.3.1). The iron-55 ($^{55}$Fe) radioactive source is frequently used. Its disintegration by electron capture to $^{55}_{25}$Mn nucleus and X-ray emissions of the K-shell gives two main X-ray lines as define in table 3.1.

| | | Energy (keV) | | Relative probability (%) |
|---|---|---|---|---|
| $X_K$ | | | | |
| | $K\alpha_2$ | 5.88765 | | 51 |
| | $K\alpha_1$ | 5.89875 | | 100 |
| | $K\beta_3$ | 6.49045 | } | |
| | $K\beta''_5$ | 6.5352 | } | 20.5 |
| $X_L$ | | | | |
| | $Ll$ | 0.556 | | |
| | $L\eta$ | 0.567 | | |
| | $L\beta$ | 0.649-0.721 | | |

Table 3.1: Energy and relative probability of the X-ray lines from Fe-55 desintegration to Mn-55 nucleus.

X photons are emitted during its decays via an electron capture to Mn-55 with a half-life of 2.737 years. The nucleus transitions of $K_{\alpha_1}$ level gives X-rays with energy of 5.89875 keV and a relative probability about 51%, $K_{\alpha_2}$ level gives X-rays with energy of 5.88765 keV or $K_\beta$ level X-rays with energies of 6.49045 keV and 6.5352 keV with a combined probability about 20.5%. The energies of the $K_{\alpha_1}$ and $K_{\alpha_2}$ X-rays are so similar that they are often specified as mono-energetic radiation with 5.9 keV photon energy. The energy of 6.5 keV is also attributed to the $K_\beta$ X-rays.

An $^{55}$Fe spectrum is shown Fig. 3.1 recorded by a Micromegas detector. The main peak (on the right of Fig. 3.1) is coming from both 5.9 keV and 6.5 keV photon energies. Gaseous detectors do not have the energy resolution to separate these lines. The second peak (on the left of Fig. 3.1) is called the *escape peak* that only appears in argon-based mixtures. Indeed, the binding energies of the argon atomic K-shell electrons are 2.694 keV and 3.286 keV respectively for the $K_\alpha$ and $K_\beta$ shells with probability of 0.135 and 0.865 [73]. Photoelectric effect on the K-shell emit photoelectron which can be decomposed in two processes in competition: fluorescence and Auger electron transitions. Both produce electrons with total energy around 3 keV. Some photons from fluorescence can escape the active volume given that, at NTP, the absorption length for a photon in argon are 3.2 cm at 3 keV [74] as shown in Fig 2.3 in Sec. 2.3.

The gain is extracted by fitting the $^{55}$Fe source spectrum (see Fig. 3.1) recorded using a typical electronic chain (pre-amplifier+amplifier+ADC) with a double Gaussian with a linear background function $F$:

$$F(x; x_0^1, x_0^2, A_1, A_2, \sigma_1, \sigma_2, a, b) = ax + b + A_1 \cdot e^{-\frac{1}{2}\left(\frac{x-x_0^1}{\sigma_1}\right)^2} + A_2 \cdot e^{-\frac{1}{2}\left(\frac{x-x_0^2}{\sigma_2}\right)^2}, \tag{3.1}$$

with $A_1$, $A_2$, $x_0^1$, $x_0^2$, $\sigma_1$, $\sigma_2$, $a$ and $b$ respectively the amplitudes, the mean value (peak position corresponding to the gain), the standard deviation (proportional to the energy resolution) for both Gaussian functions

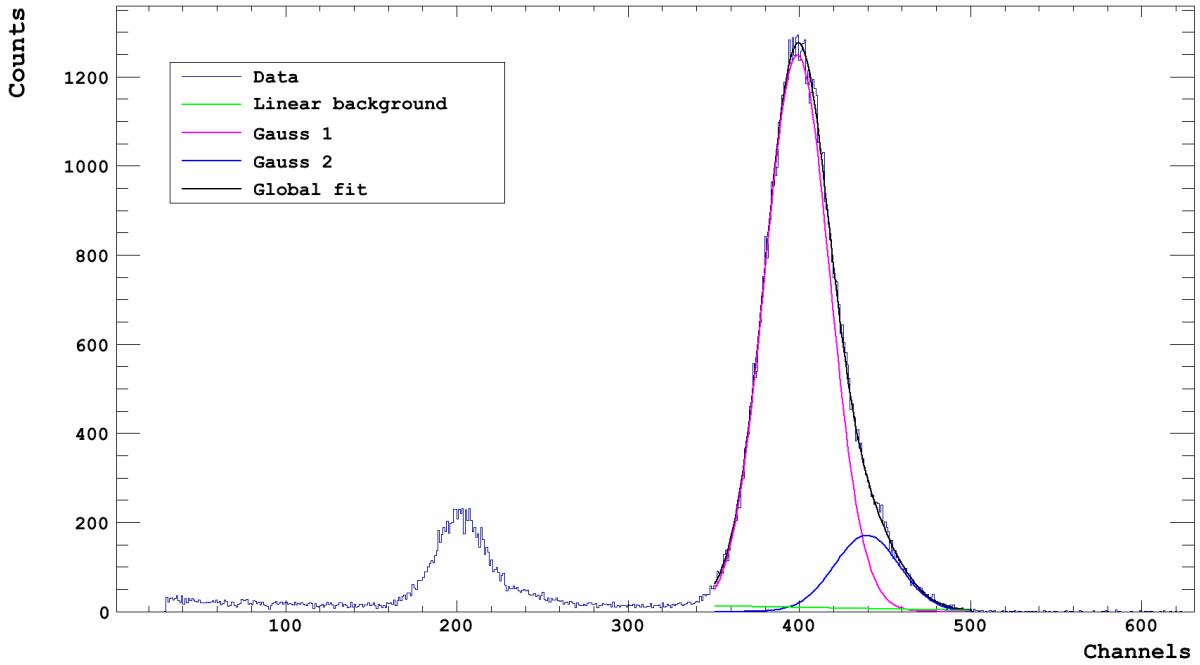


Figure 3.1: Iron-55 source taken using a Microbulk in argon + 5% isobutane. The spectrum is fitted using a specific function. This function is a sum a two gauss functions and linear function. The energy resolution extracted from the fit is 4.75% (11.18 FWHM). The position of the main Gaussian is 398.95 and the $\chi^2$/NDF is 1.01.

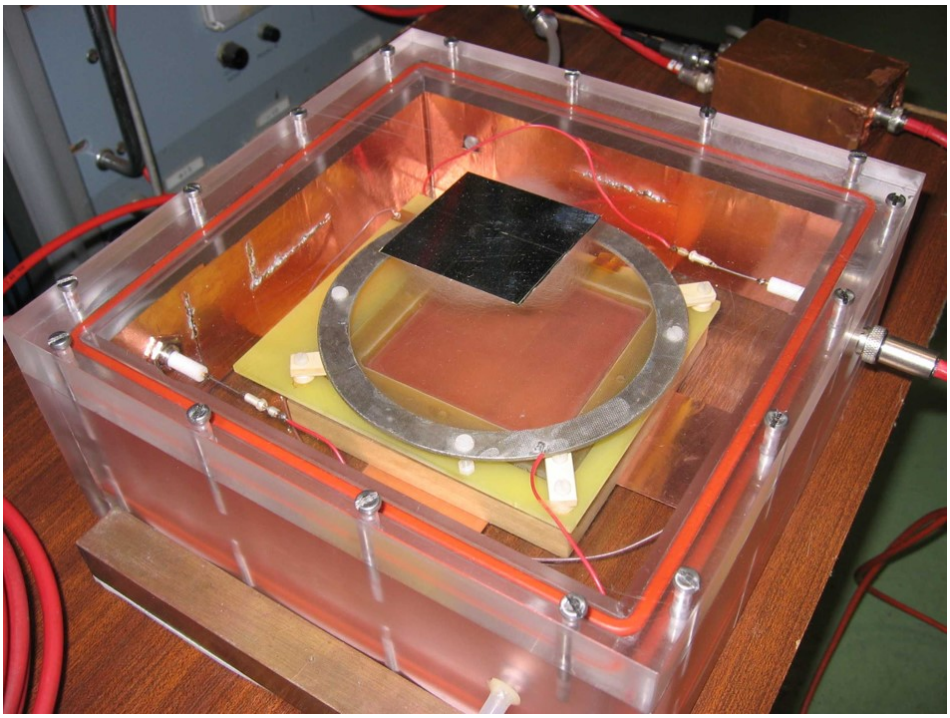

Figure 3.2: Transparent box test with a 50 µm gap copper mesh Micromegas used for the systematic gain measurements.

and a linear function (for background). All the fit parameters can be set free or some specific conditions could be added as the ratio between $A_1$ and $A_2$ or/and the mean value ratio $r_{1/2}$ between $x_0^1$ and $x_0^2$ which is expected to be equal to 5.9/6.5. Most of the time, $r_{1/2}$ was fixed.

The gain value $G$ is obtained from the $x_0^1$ (in ADC) applied in the formula:

$$G = \frac{x_0^1}{\mathrm{DR}} \frac{V_{\mathrm{Max}}}{G_{\mathrm{Ampl}}} \frac{\mathrm{CS}}{F_{\mathrm{Preampl}} \times n_e} \tag{3.2}$$

where DR is the dynamic range in ADC, $V_{\mathrm{Max}}$ ADC maximum voltage, $G_{\mathrm{Ampl}}$ is the amplifier gain and CS the charge sensitivity of the preamplifier, $F_{\mathrm{Preampl}}$ the pre-amplifier conversion coefficient and $n_e$ the number of primary electrons. If the preamplifier is an ORTEC 142B [75], the CS = 20 mV/MeV in Si equivalent. The energy required to create an electron-hole pair in Si is 3.6 eV so that 20 mV corresponds to 277778 electrons. The number of primary electrons $n_e$ from a $^{55}$Fe X-ray photon which deposits in argon + 5% isobutane is (5900/26) 227 electrons.

A calibration of the electronic chain is done using a pulse generator and a capacitor in order to cross-check the results.

### 3.1.2 Standard 50 µm gap Micromegas

A campaign of systematic gain measurements has been carried out with a 50 µm gap Micromegas made with polyimide pillars (every 2 mm) attached to a 5 µm copper layer chemically drilled of holes (30 µm diameter and 70 µm of pitch). This 6×6 cm$^2$ Micromegas grid was mounted on a frame and placed in a transparent box of 23 cm × 23 cm × 8 cm size (see Fig. 3.2). On the upper face of the transparent box, there is a 2 mm × 2 mm window in the plexiglass, this hole is covered by a 20 µm thick aluminium foil. In order to reduce the noise, the internal faces of the box were covered by large copper tape and connected to the readout electronics ground for equipotentiality. A cathode grid was put at 13 mm on top of the Micromegas using spacers. A gas mixing system was used to provide a specific gas mixture. The drift field was fixed to 200 V/cm and the gas flow at 5 L/h. The percentages of $H_2O$ and $O_2$ were monitored and always less than 200 ppm.

The method for gain extraction was done using the procedure described in section 3.1.1. These measurements are summarized in Fig. 3.3 and lead to interpretations which have been resumed below:

- The main curves present an expected logarithmic dependence with the electric field. However, for the low percentage isobutane and ethane curves, an over-exponential effect appears at high electric field. This behaviour can be explained by excess of UV photons not being absorbed by the quencher. For a large quantity of isobutane (for example 20%) this phenomenon vanishes.

- The greatest gains with a mixture of neon with 5% isobutane and 2% argon. Penning effect are known to be involved in these mixtures.

- In argon mixture, the increase in the quencher percentage results in a shift of the gain curve "to the right". The maximum gain remains about the same.

- The addition of $CF_4$ makes it possible to increase the value of the maximum drift velocity, but shifts this maximum towards greater electric fields. The gain curves are shifted to the right.

- In order to reach gain higher than a few thousands the use of hydrocarbons looks inevitable. With a single quencher the most important gains are successively for: isobutane, ethane and methane.

- No stable results were obtained using only $CF_4$ as a quencher. This mixture being very sensitive to impurities, same mixture gave different results.
- For mixture with $CO_2$ at 10%, 20% and 30% the breakdown voltage strongly depends on the amount of impurity. By cutting off the gas circulation with the $H_2O/O_2$ filtering bypass during 10 minutes, the breakdown voltage increases by 10 V resulting in a greater maximum gain. The breakdown voltages on the curves are higher than what it can be obtained without the impurities, but the rest of the points are consistent.
- Adding a small amount of complex hydrocarbon quencher (i-$C_4H_{10}$) to a large amount of constant percentage low gain quencher results in shifting the curves up, ie. the gain is greater at a fixed voltage. At the same time the maximum gain is increased. Increasing the quencher percentage at high gain gives a right shift. At a fixed voltage, the result is that the gain exhibits a maximum as a function of the percentage of the complex hydrocarbon quencher and is lower as the complexity decrease (CH4).

Three groups can be isolated, the group containing complex molecules as i-$C_4H_{10}$ (*hot gases*), the group containing more symmetric molecules (**cold gases**) as $CF_4$, $CH_4$ or $CO_2$ and a group having intermediate molecules as $C_2H_6$ and mixed molecules from the two first groups.

These measurements are one of the most accurate studies ever done with a Micromegas detector and can be seen as a reference.

### 3.1.3 Microbulk detectors

The Microbulk detector is a copper mesh built from chemical-etching technique on a single of Kapton foil cover by copper layer on both sides. Such material is currently available from suppliers from PCB industry. This manufacturing technique provides a readout anode strips and amplification structure in a single integrated structure [57]. So, the amplification gap is defined by the Kapton thickness that can be found in the market (12.5 µm, 25 µm or 50 µm). This is why three Microbulk amplification gaps, 12.5 µm, 25 µm and 50 µm, have been built by CERN workshop and characterized at IRFU. Each Microbulk is a 3.5 cm disk and has different value of hole diameter and hole pitch which are summarized in Tab. 3.2.

| Amplification gap (µm) | Hole diameter (µm) | Hole pitch (µm) |
|---|---|---|
| 12.5 | 25 | 80 |
| 25 | 30 | 100 |
| 50 | 40 | 90 |

Table 3.2: Parameters (amplification gap, hole diameter and pitch) for three different gap Microbulks.

Systematic studies using these Microbulk detectors have been performed to determine the influence the gain/resolution in function of the amplification gap, the gas mixture and the gas pressure [76]. The pressure varies from 0.5 to 1.7 bar.

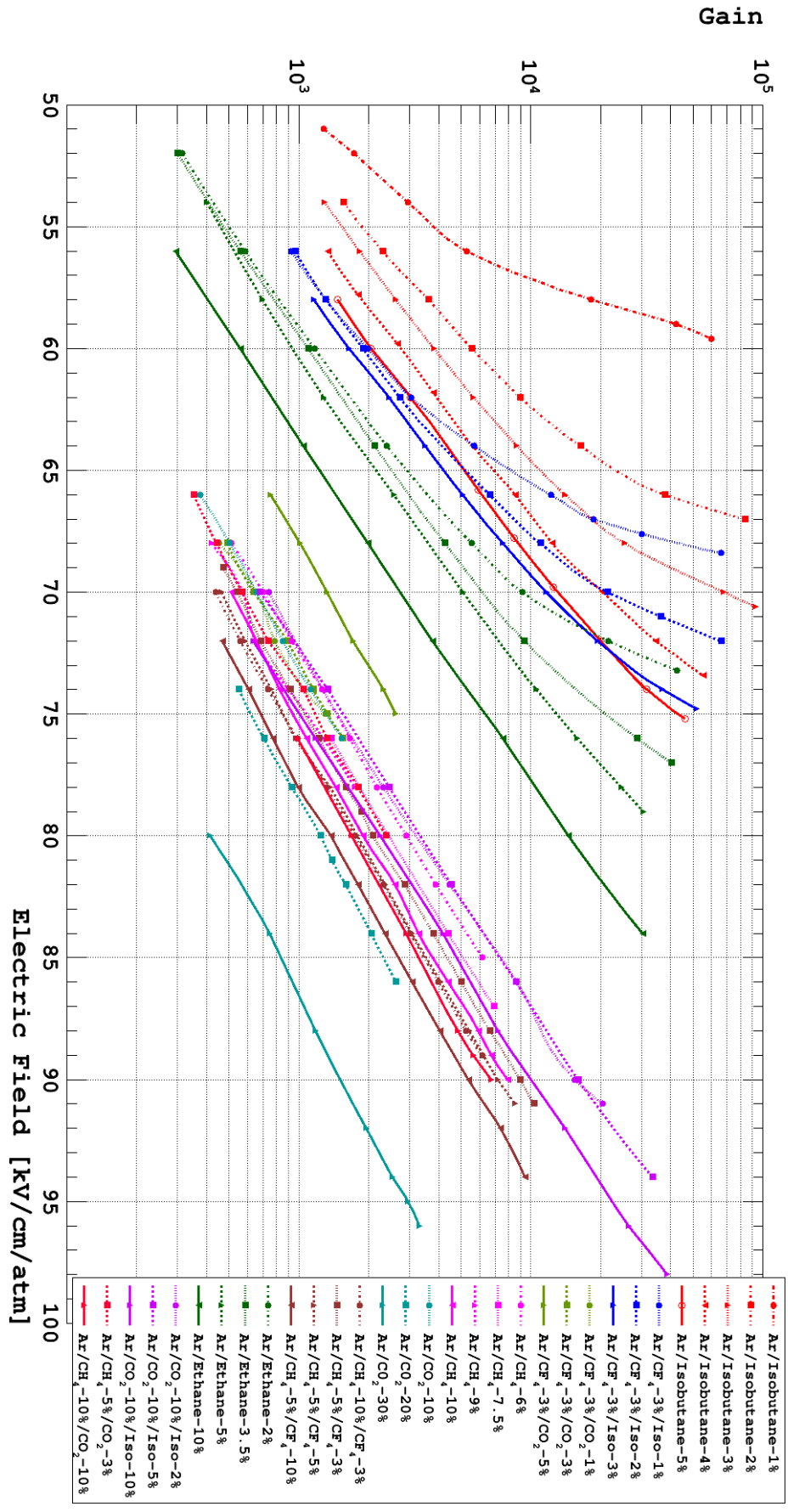


Figure 3.3: Gain curves for argon-based gas mixtures using a 50 µm gap Micromegas.

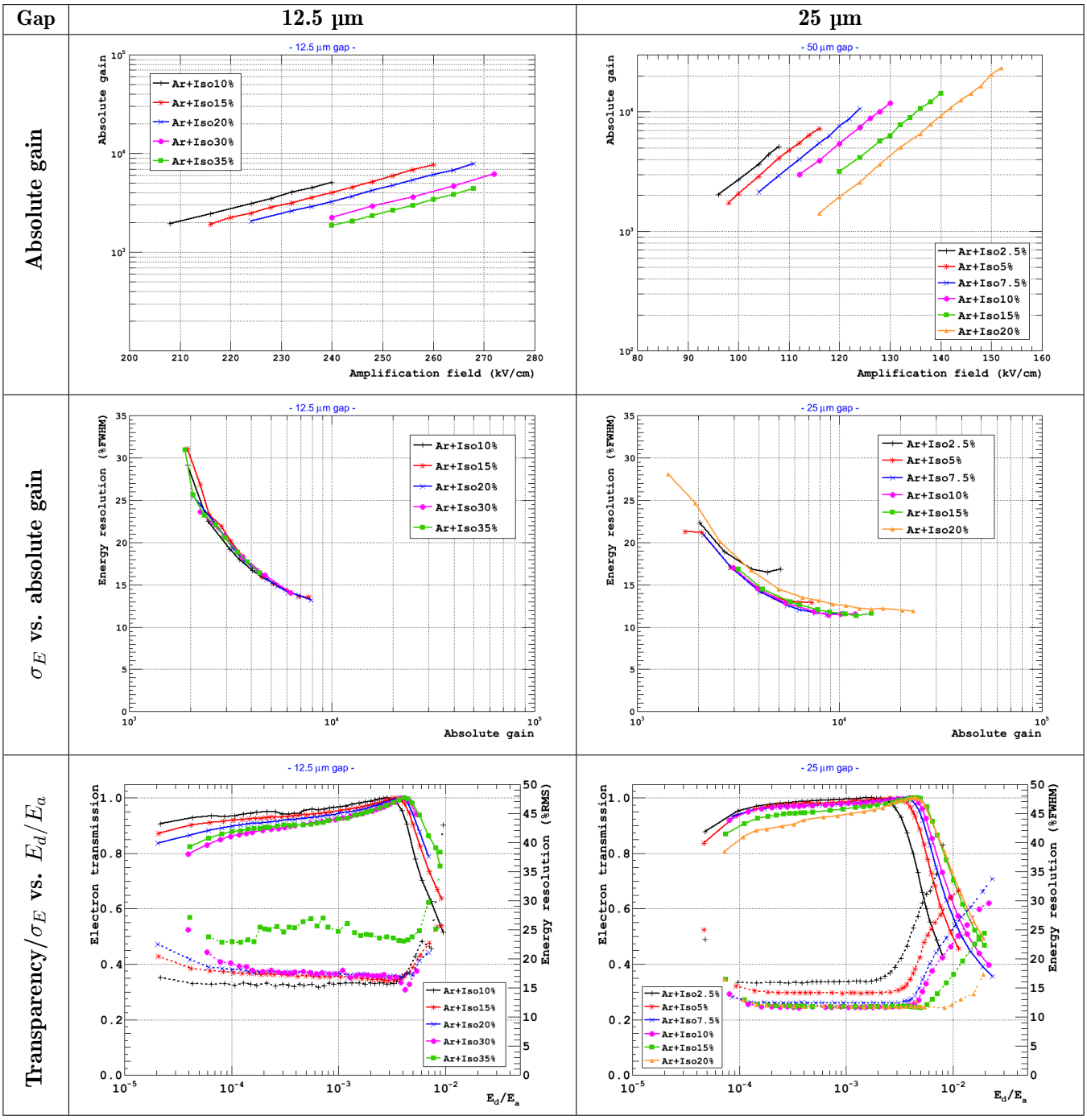


Figure 3.4: Absolute gain curves, energy resolution versus absolute gain curves and electron transmission/energy resolution (normalized gain) versus ratio of amplification fields curves for 12.5 µm and 25 µm gaps taken with Ar+Iso gas mixtures.

| Gap | Gas | Absolute gain | Energy resolution | Electron transmission |
|---|---|---|---|---|
| 12.5 µm | Ar-Iso 20% | 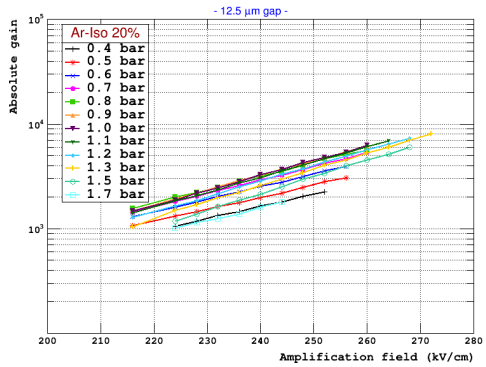 | 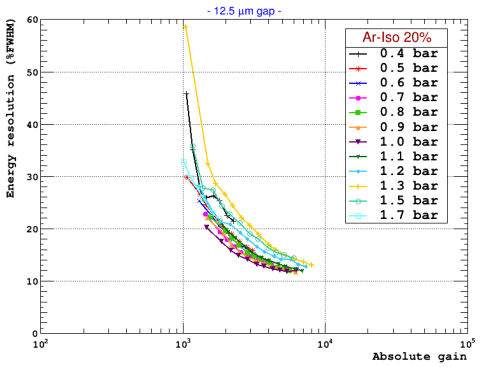 | 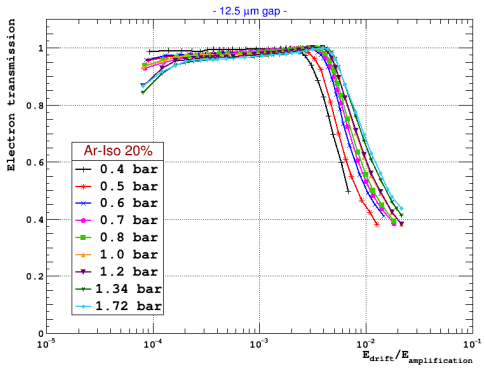 |
| 25 µm | Ar-Iso 10% | 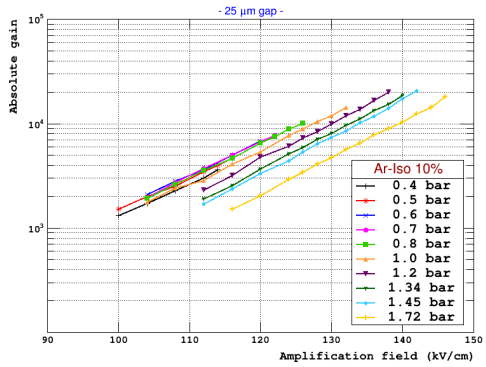 | 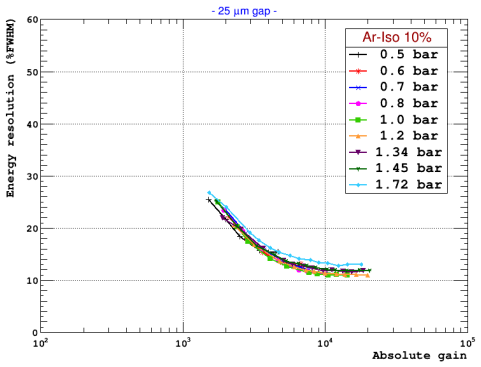 | 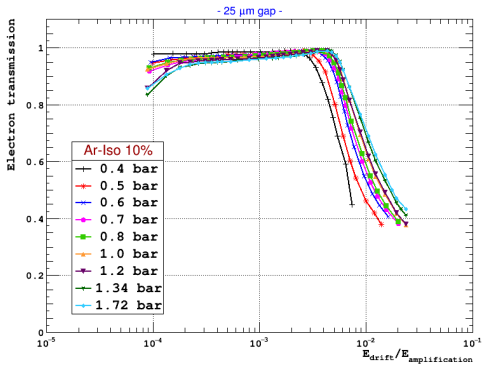 |
| 50 µm | Ar-Iso 5% | 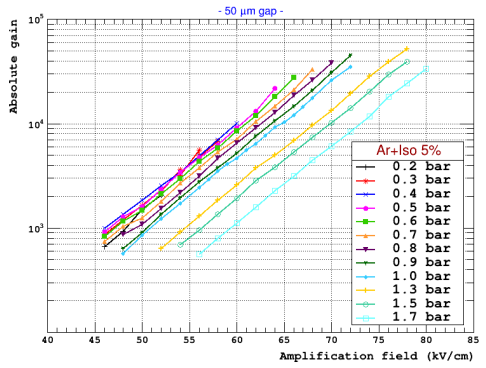 | 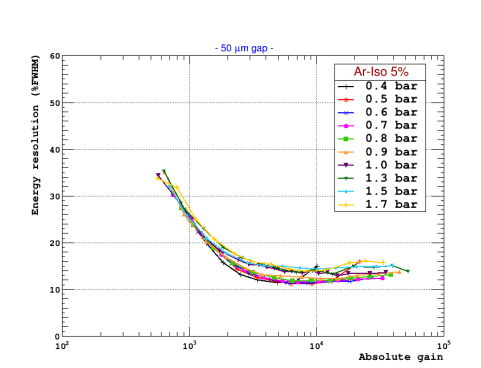 | 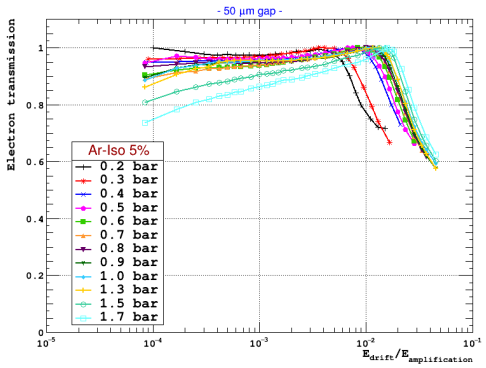 |



Figure 3.5: Absolute gain curves, energy resolution versus absolute gain curves and electron transmission (normalized gain) versus ratio of amplification fields curves for 12.5 µm, 25 µm and 50 µm gaps taken at various pressure respectively in Ar+Iso 20%, A+Iso 10% and Ar+Iso 5% gas mixtures.

The *electron transmission* (or *electron transparency*) is defined as the variation of the detector normalized gain in function of the field ratio $E_{\text{drift}}/E_{\text{amplification}}$. Under normal conditions, the electron transmission is maximal in the range where $E_{\text{drift}}$ and $E_{\text{amplification}}$ have a factor of 100 to 1000 between them.

In the past, gas mixture, gas pressure and gap dependences have been investigated in [60] for Micomegas detector. From the approximation taken from Eq. 2.29, the optimal parameters that will stabilize the operation can be determined by finding solution to the following equation:

$$\frac{\partial G}{\partial P} = G\alpha\left(1 - \frac{BPd}{V}\right) = 0. \tag{3.3}$$

The optimal pressure $P$ as solution of the previous equation for each gap $d$ is given by:

$$P = \frac{V}{Bd}, \tag{3.4}$$

where $\alpha$ is the Townsend coefficient, $B$ is the second Rose and Korff coefficient and $V$ the Micromegas voltage.

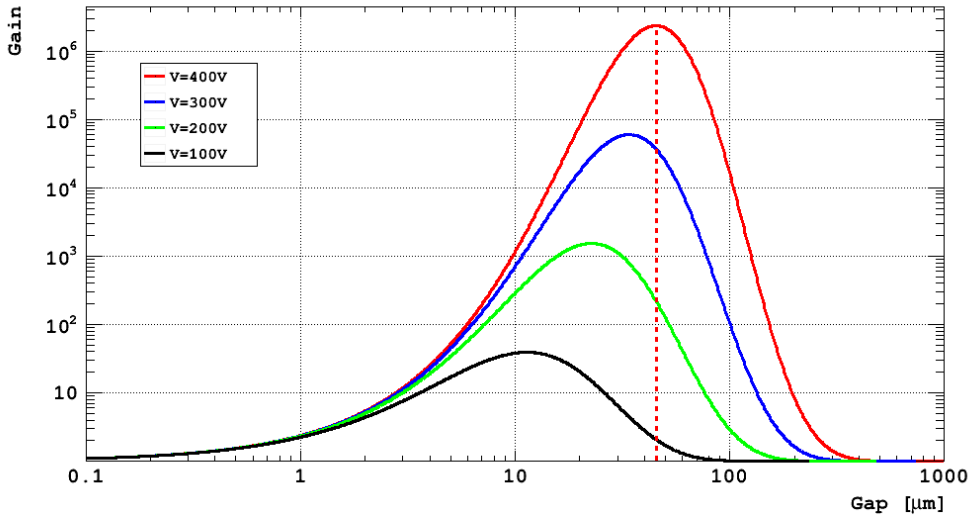


Figure 3.6: Expected gain versus the amplification for several Micromegas polarizations in argon/isobutane-5% gas mixture at atmospheric pressure. The optimal gap (maximal gain) for this gas is obtained with a 45 µm amplification gap at a voltage value of 400V.

Therefore, Micromegas gain variation for specific polarization voltages in function of the amplification gap can be evaluated for a specific gas using its own $\alpha$ and $B$ [60]. Fig. 3.6 shows that the maximal gain obtained with 45 µm gap in argon and 5% isobutane gas mixture at atmospheric pressure. This gas mixture is frequently used in Micromegas detector community by providing a wide range of stable operation with high gain. For example, in this gas mixture and with a 45-50 µm gap Micromegas, the stable gain will be at a voltage of 400 V. So for operation in pressurized gas, the use of smaller gap that 50 µm will be more appropriate.

By varying the isobutane proportion from 2.5% to 35%, the figures 3.4 shows the absolute gain, the energy resolution and the electron transparency curves for the 12.5 µm and 25 µm gap Microbulk. The maximum gain is reached respectively in argon + isobutane 20% at $8 \times 10^3$ for the 12.5 µm gap and $2 \times 10^4$

for the 25 µm gap. The best energy resolution is obtained respectively with low percentage of isobutane (10%) for 12.5 µm gap and higher percentage of isobutane (> 7.5%) for 25 µm.

That is why, the maximal gain of the different gap Microbulks have been studied with three gas mixtures argon + 5% isobutane, argon + 10% isobutane and argon + 20% isobutane.

Using the same gas mixute argon + 10% isobutane the figures 3.7 shows the normalized gain and energy resolution (top). These plots are improved when a specific gas is used for each gap as follow:

- 12.5 µm gap: maximal gain at 0.9 bar with argon + 20% isobutane;
- 25 µm gap: maximal gain at 0.7 bar with argon + 10% isobutane;
- 50 µm gap: maximal gain at 0.4 bar with argon + 5% isobutane.

The best energy resolution is obtained at the pressure where the maximal gain is reached. The gain and energy resolution curves are sensitively improved when the measurements for each Microbulk are done with a specific gas mixture (bottom plots) compared to measurements done with the same gas mixture (argon + 10% isobutane on top plots).

The absolute gain curves, energy resolution curves and electron transmission curves are shown in the Figures 3.5 and notable remarks are listed as follow:

- The gain achieved in this range are greater than 5000 for the 12 µm and $10^4$ for the 25 µm amplification gaps. For the 50 µm gap, the gains reached $3 \cdot 10^4$ and some degradation appears when increasing the pressure (see electron transmission curves in Tab. of Figures 3.5).
- The absolute gain curves flatten when the gap decreases.
- The range and the spread of the energy resolution curves also respectively decrease and increase with the amplification gap.
- The electron transmission curves are slightly pressure independent with a plateau shift changing with the pressure.
- The gas pressure impacts the flatness of the plateau and its start and its end with the field ratio $E_{\text{drift}}/E_{\text{field}}$.

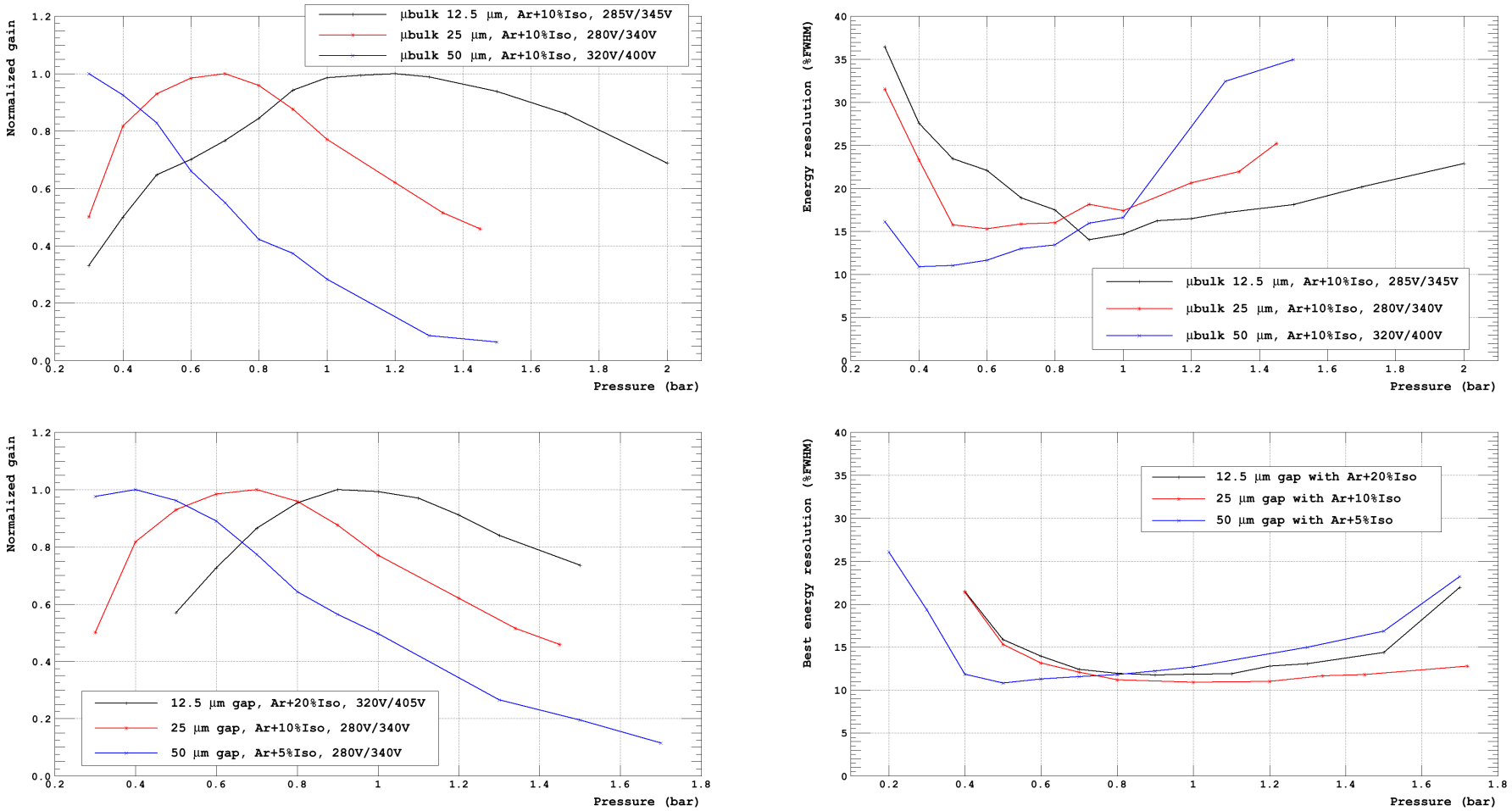


Figure 3.7: **Top**: normalized gain [left] and energy resolution [right] in function of the pressure for the 12.5 µm, 25 µm and 50 µm gap Microbulk in argon + 10% isobutane gas mixture. **Bottom**: normalized gain [left] and energy resolution [right] in function of the pressure for the 12.5 µm, 25 µm and 50 µm gap Microbulk in a specific gas mixture with argon and isobutane.

### 3.1.4 Field ratio dependence

Using the same methodology described in Sec. 3.1.1, the figures 3.8 and 3.9 show the electron transmissions (normalized gains) of respectively two large (10 cm diameter) Microbulk detectors (50 µm gap) in argon + 5% isobutane gas mixture and a standard bulk Micromegas (128 µm gap) in T2K gas mixture as function of the field ratio $E_d/E_a$ for different mesh voltages where $E_d$ and $E_a$ are respectively the drift and amplification fields.

For the Microbulk detectors (Fig. 3.8), the gain is constant in the $2 \cdot 10^{-4} < E_d/E_a < 5 \cdot 10^{-3}$ while for the bulk Micromegas detector (Fig.3.9) it is for $10^{-3} < E_d/E_a < 10^{-2}$ but the gain is lightly shifted with the mesh voltage. Indeed, at 330 V, 350 V and 370 V the gains are respectively 440, 820 and 1700.

Fig. 3.8 illustrates that even using the same detector type at the same voltage, a 30% difference is measured. This divergence can come from the environmental conditions (different temperature and pressure) or from the building processes. The energy resolution curves are minimal where the electron transmission is maximal and the decrease of the gain is linked to the increase of the energy resolution is the best.

Two regions are noteworthy:

- a region where $E_d/E_a \leq 2 \cdot 10^{-4}$: the field in the drift region becomes so low that primary electrons start to be lost (attachment, recombination);
- a region where $E_d/E_a \geq 10^{-2}$: the field in the drift region is high enough that the electron start follow the electric field lines that end up in the Microbulk mesh.

Fig 2.9 (right) illustrates the electron path (in blue) along the electric field (in yellow) close to the Micromegas mesh holes. The field ratio defines the proportion of the funnelling between the electric lines in the drift gap and the amplification gap.

## 3.2 Gas properties study

### 3.2.1 Rose and Korff's gain approximation

The Rose and Korff approximation of the Townsend coefficient given by the Eq. 2.29 in Sec. 2.5.3 can be used to fit the gain curves from Figure 3.3, $A$ and $B$ can be extracted (see Fig. 3.10). The argon/$CH_4$-10% gain curve was set as reference. The corresponding values of $A$ and $B$ extracted from the fit are given in Tab. 3.3.

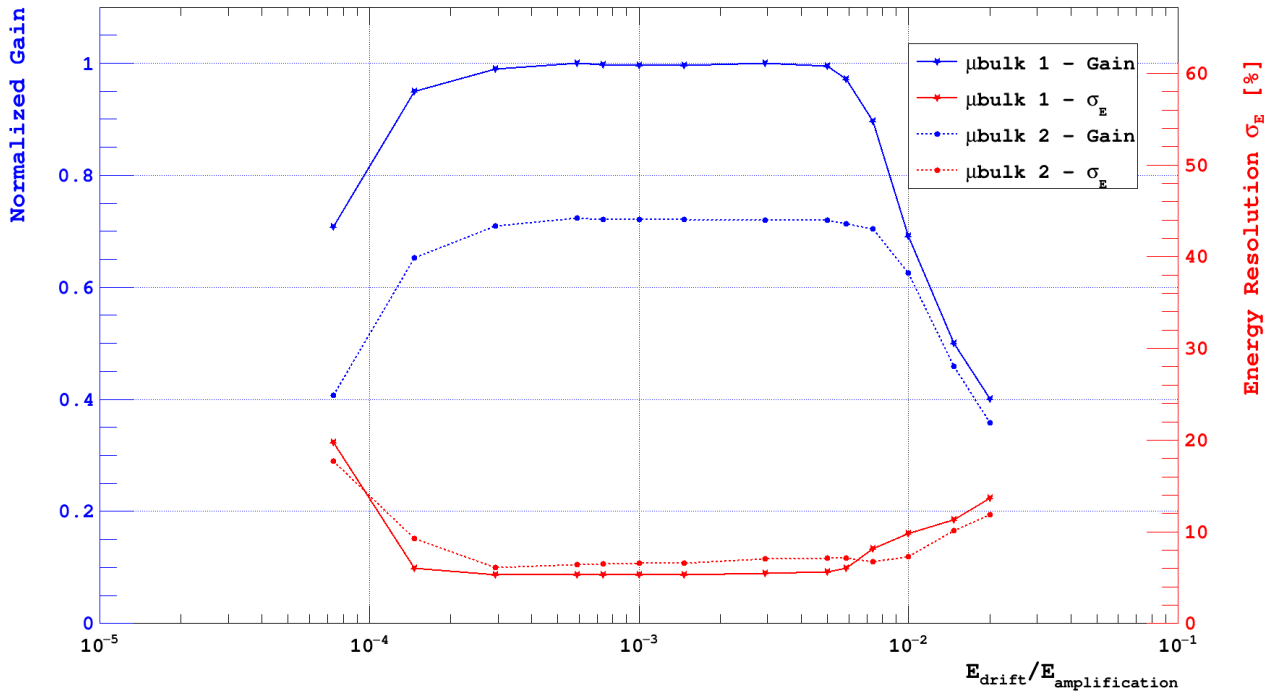


Figure 3.8: Normalized gain (electron transmission) for two supposed identical Microbulks (50 µm gap) in argon + 5% isobutane gas mixture. These curves are obtained by changing the drift voltage and fixing the amplification voltage at V=340 V.

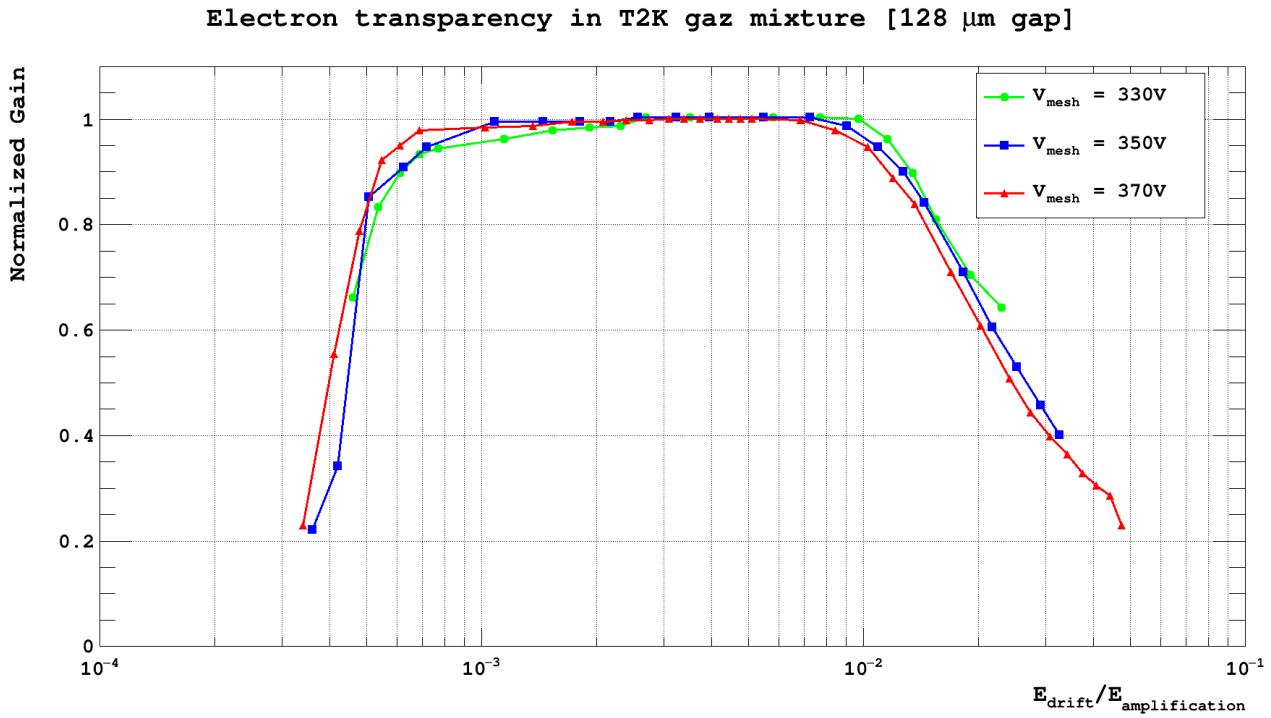


Figure 3.9: Electron transmission in a Bulk Micromegas in T2K gas mixture at various mesh voltages (gain).

| **Gas mixture** | **A** [atm.cm$^{-1}$] | **B**($10^{-2}$) [V.atm.cm$^{-1}$] |
|---|---|---|
| Ar/Isobutane-1% | 1439.3 | 5.63 |
| Ar/Isobutane-2% | 914.4 | 4.40 |
| Ar/Isobutane-3% | 707.7 | 3.94 |
| Ar/Isobutane-4% | 645.5 | 3.72 |
| Ar/Isobutane-5% | 647.2 | 3.63 |
| Ar/$CH_4$-6% | 713.4 | 2.89 |
| Ar/$CH_4$-7.5% | 777.7 | 2.93 |
| Ar/$CH_4$-9% | 705.8 | 2.81 |
| Ar/$CH_4$-10% | 691.9 | 2.76 |
| Ar/$CO_2$-10% | 638.1 | 2.77 |
| Ar/$CO_2$-20% | 680.6 | 2.63 |
| Ar/$CO_2$-30% | 839.3 | 2.56 |
| Ar/Ethane-2% | 618.8 | 3.39 |
| Ar/Ethane-3.5% | 590.6 | 3.32 |
| Ar/Ethane-5% | 632.8 | 3.36 |
| Ar/Ethane-10% | 683.3 | 3.24 |
| Ar/$CF_4$-3%/Iso-2% | 927.1 | 4.08 |

Table 3.3: Rose and Korff coefficients extracted from gain curves of various argon-based gas mixtures (see table of figures 3.10.

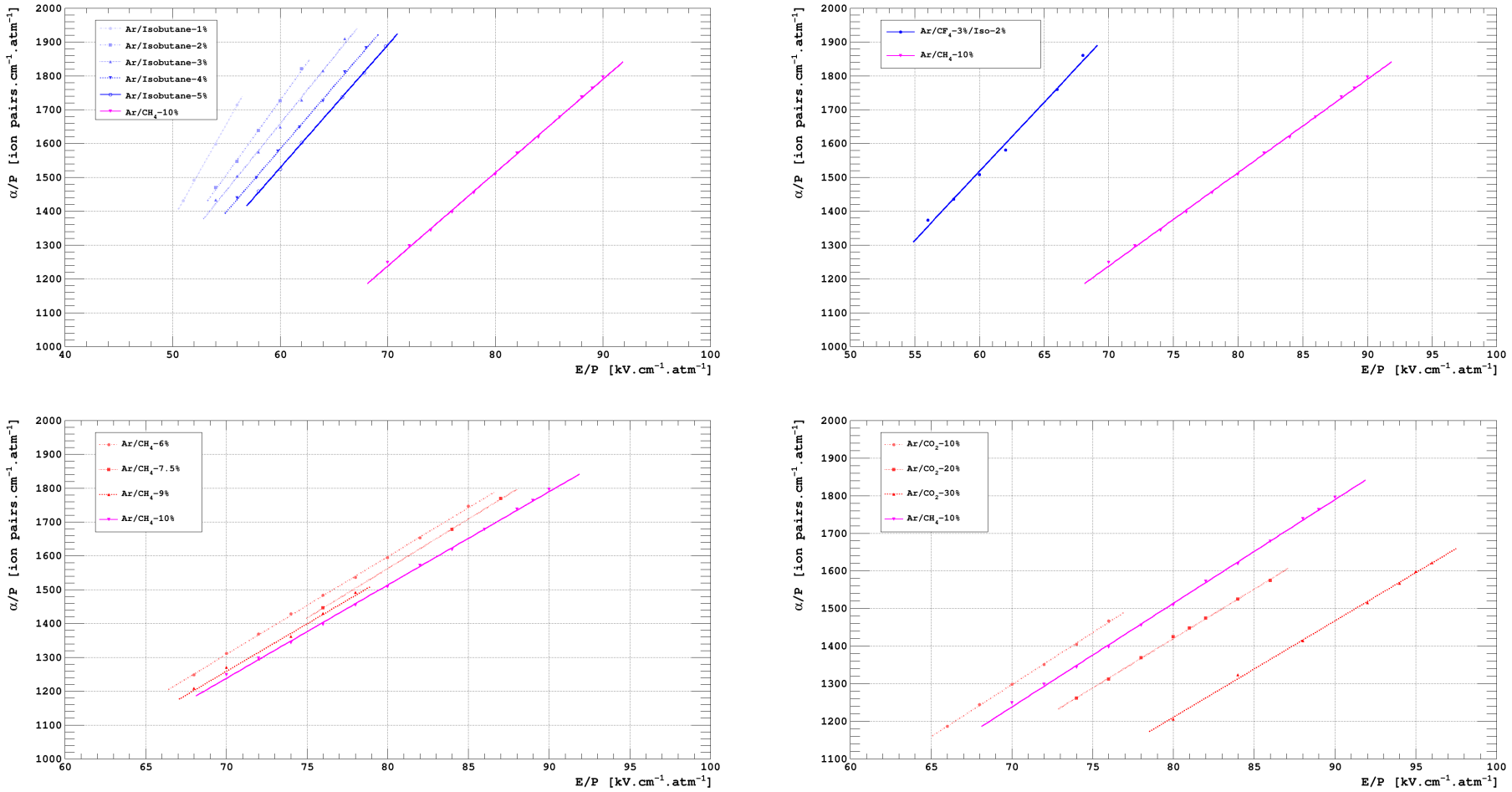


Figure 3.10: Extraction of the Rose and Korff coefficients for [Top left] argon and isobutane mixtures, [Top right] the T2K gas mixture, [Bottom left] for argon and $CH_4$ mixtures and [Bottom right] for argon and $CO_2$ mixtures. The argon/$CH_4$-10% is shown as reference.

Thus, the Rose and Korff coefficients, as a good approximation of the Townsend coefficient, can be reliably used to quickly calculate the gain with the Micromegas detector for a given gas mixture.

### 3.2.2 Penning effect

The Penning mixture is a mixture of a mono-atomic (noble) gas $A_1$ with a molecule gas $M_2$, that has lower ionization voltage than the first excited state of $A_1$. This process is called the *Jesse effect* or *Penning effect*. The ionisation of the molecule $M_2$ by excitation of the atom $A_1$ is given by the following relation:

$$A_1^\star + M_2 \longrightarrow A_1 + M_2^+ + e^- \tag{3.5}$$

The energy from the de-excitation of $A_1^\star$ is transferred to $M_2$ via collisions. If the ionisation potential of $M_2$ is low enough the latter can be ionised. So, the Penning effect can increase the primary ionisation and thus the gain. The argon + isobutane mixtures in Fig. 3.3 illustrate thoroughly this effect at high electric field and with low quencher concentration where the molecular states (vibrational and rotational) are insufficient to stabilized the avalanche.

### 3.2.3 Avalanche statistics using single electron resolution

The statistical study of the avalanche in the MPGDs is accessible by the Timepix chip giving access both to the resolution for the single electron and to the measurement of the charge deposited by each electron after multiplication. After introducing the Timepix chip, avalanche statistics measurements will be presented.

#### 3.2.3.1 The TimePix chip

The TimePix chip [77], modification of the Medipix2 chip, keeps the same layout arranged in a square matrix of $256 \times 256$ pixels of $55 \times 55$ µm$^2$. While the Medipix2 chip is able to record 2D tracks and counts the number of hits per pixels using a 14-bit counter, this counter in the TimePix chip allows to numerate the number of cycles of a clock either when the signal pass the threshold (Time-Over-Threshold or TOT mode) or when the duration between the time of the signal passing the threshold and the end of the time window. This number is thus inversely proportional to the arrival time. The clock frequency can reach 100 MHz giving a time measurement in steps of 10 ns.

A charge coming from a pixel is collected in an integration capacitance of the preamplifier. This output signal is a voltage signal. A discriminator is transforming the analog voltage signal coming from the preamplifier to a signal that can be used in the digital section of the pixel and compares the input voltage with a voltage that can be set externally via the DACs. The threshold (THL) level of the pixel can be calibrated to a number of electrons. The output voltage of the discriminator (digital) signal is a logic signal for the time the signal is over the THL in the TOT mode. In the digital section the external clock cycles are counted. As the 14-bit counter has some positions reserved for other information, the maximum number of counts is 11810 (13.5 bit). A shutter window is used to operate the chip and it can be opened and closed by an external trigger signal or by DAQ software.

There are 4 different modes of operation which are illustrated on Fig. 3.11:

- **Medipix mode**: each time the discriminator signal changes from logic 0 (low) to logic 1 (high) the counter is increased by one. This mode counts the number of charge pulses during the shutter windows time.

- **Time over threshold (TOT) mode**: as long as the discriminator signal is high the clock cycles are counted. When the discriminator signal changes to low the counting is stopped and continued if it becomes high again within the same shutter window. The length of the discriminator signal is proportional to the voltage of the preamplifier output voltage which is proportional to the charge deposited in the pixel. A calibration can be done using external test pulses to convert the TOT the absolute charge.

- **Time mode**: the clock cycles start the counting when the discriminator signal goes to logic 1 for the first time during the shutter window until the end of the shutter window. The arrival time of the charge is inverse proportional to number of clocks.

- **1$^{st}$ hit mode**: the counter is set to one by the first clock cycle when the discriminator signal is high giving that the pixel have been hit once. All other clock cycles or changes of the discriminator signal are ignored.

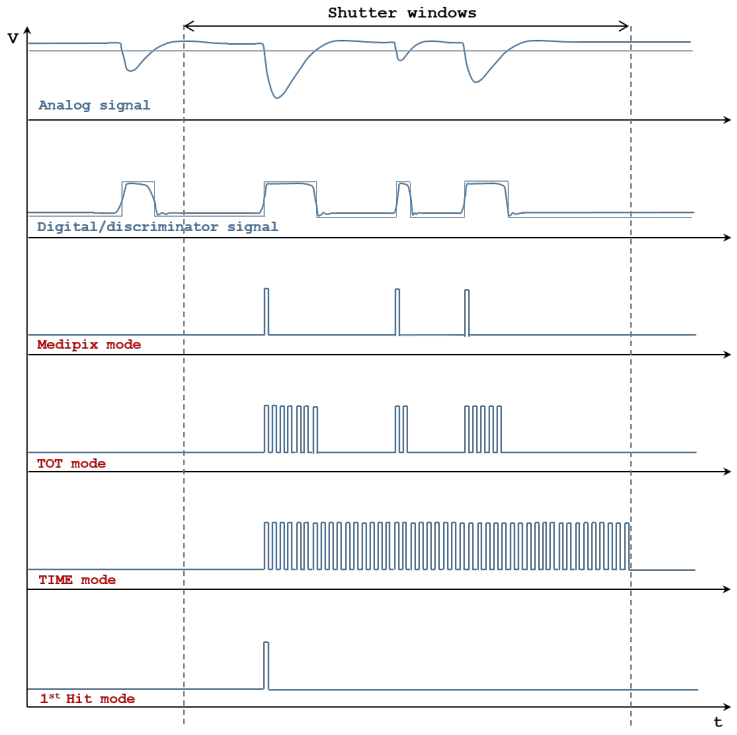


Figure 3.11: Exhaustive list of operation modes of the TimePix chip and sample signal when each mode is activated.

A *integrated grid* (InGrid) [78, 79] was developed to build a Micromegas structure by post-processing directly on top a TimePix chip. By sputtering, a conductive grid can be deposited on top of an epoxy-based photoresist substrate (SU-8) that is subsequently etched out to leave only the pillars. This lithographic process is used to align the readout pixels with the Ingrid holes so that each hole is located above a pixel. This leads to a digital Micromegas detector called Gridpix. To protect against sparks, an amorphous silicon (a-Si) layer or silicon nitride ($Si_3N_4$) layer, between 7 to 12 µm, is deposited by sputtering on the pixels before the lithographic post-processing.

#### 3.2.3.2 Avalanche statistics

The ability of the TimePix chip with an integrated Micromegas grid to detect and count the primary electrons in the gas offers a new tool for avalanche statistics studies. Gain fluctuation and single electron efficiency measurements have been performed and are presented here.

**- Gain fluctuation**

In the avalanche, the amplification of a primary charge is a statistic process. The number of electron $n_e$ (or $G$) in one avalanche is statistically distributed, so the mean gain $\overline{G}$ is the mean value of the gain distribution. The shape of this distribution is relevant for the detector performance, the energy resolution or the detection efficiency. There are many theories for the stochastic avalanche process and three are:

- Snyder's model [80]: the ionisation probability is constant and an exact solution is possible. The gain curve is an exponential distribution.
- Legler's model [81]: the ionisation probability is a step function. It is zero for low energies and constant if the electron has achieved the ionisation energy of the gas. Only after a minimum acceleration distance x0, the electrons can again ionise gas molecules.
- Alkhazov's theory [37]: the probability distribution of inelastic collision is a step function, the probability of an ionisation in an inelastic collision is not one.

The distributions of the Legler and Alkhazov models can not be expressed analytically, but moments of the distribution can be calculated. A Polya distribution is a good approximation for both models. Compared to the Legler distribution the Polya tail is longer. The Polya distribution depends on two parameters: the mean gain $\overline{G}$ (centre of the distribution) and the variance $\Theta$ of the distribution sometimes written as $m = \Theta + 1$.

$$P(G/\overline{G}, \Theta) = \frac{(\Theta+1)^{\Theta+1}}{\Gamma(\Theta+1)} \frac{1}{\overline{G}} \left(\frac{G}{\overline{G}}\right)^{\Theta} e^{-(\Theta+1)\frac{G}{\overline{G}}}, \tag{3.6}$$

$$P(G/\overline{G}, m) = \frac{m^m}{\Gamma(m)} \frac{1}{\overline{G}} \left(\frac{G}{\overline{G}}\right)^{m-1} e^{-m\frac{G}{\overline{G}}}, \tag{3.7}$$

where $\Gamma(n) = (n-1)!$ is the gamma function with $n > 0$ is an integer. Calculation of gas gain fluctuation in uniform electric field is detailed in [82].

Enough drift distance is needed to separate the electron clusters. In argon + 5% isobutane, the selection of the electron clouds corresponding (110 electrons) to the escape peak improves analysis avoiding to consider data with double hit from electron clouds from the photopeak (220 electrons). The number of clusters using TimePix with Medipix mode has been recorded event by event providing the spectrum of Fig. 3.12 by varying the grid voltage and using the procedure described on Sec. 3.1.1. The number of cluster given by the escape peak reaches a plateau for a grid voltage of 350 V.

Two other measurements were done in TOT mode. The TOT spectra fitted by the Eq. 3.7 starting from 4000 electrons are shown in Fig. 3.13. In these measurements the highest gain in Ar/Iso 95/5 was reached with an InGrid detector at $V_{grid}$ = 340V. The $\Theta$-parameters in these measurements were $\Theta_1 = 2.60 \pm 0.02$ (for the measurement with collimator and for acquisition time t=50 ms, G = $8777 \pm 14$) and $\Theta_2 = 2.68 \pm 0.04$ (for the measurement without collimator, t=1 ms, G = $7902 \pm 22$). This type of measurement is very sensitive to the condition of the data taking while the gain, the efficiency and the spread of the electrons should be maximized and the event rate should be minimized.

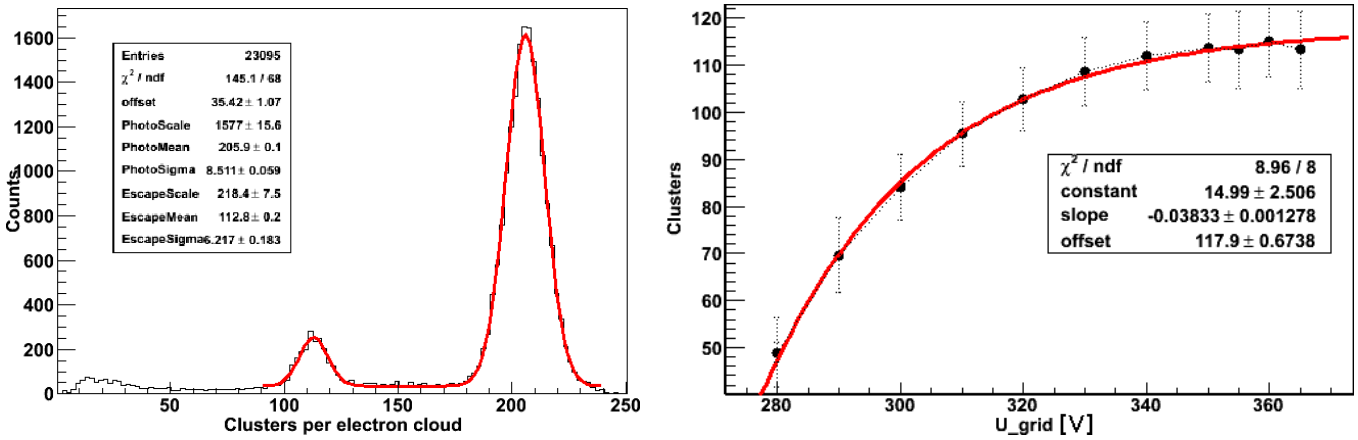


Figure 3.12: [Left] Cluster spectrum with the best resolution in photo and escape peak in Ar/Iso 95/5 with $U_{grid}$. [Right] Clusters in the escape peak as function of the grid voltage in Ar/Iso 95/5. Data points were fitted by $f(x) = -e^{ax+b} + c$.

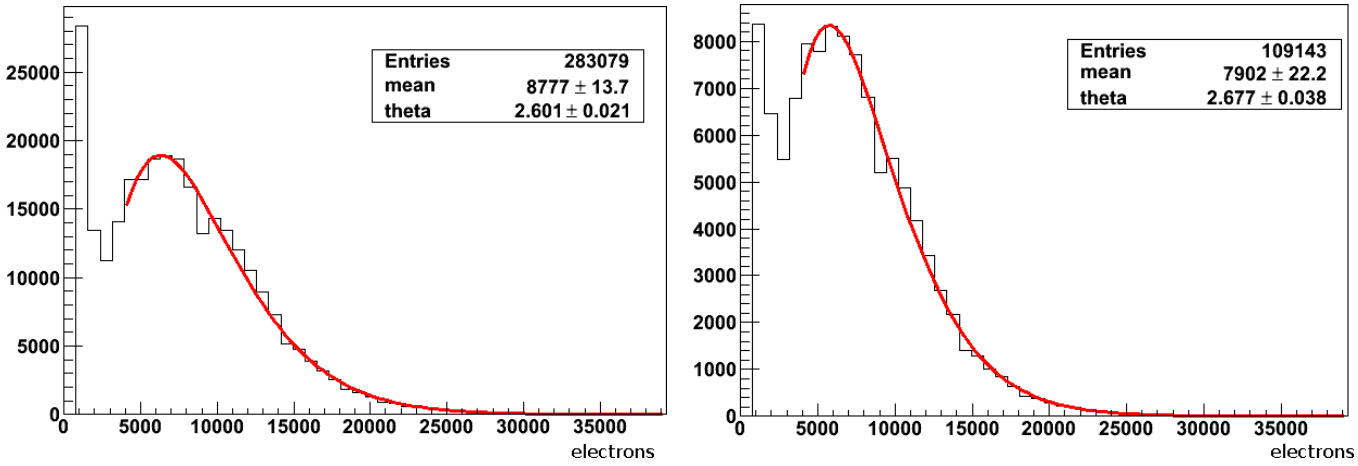


Figure 3.13: TOT spectra at $V_{grid} = 340$V,in Ar/Iso 95/5. The each spectrum has been fit by the Polya distribution from equation 3.6. [Left] With source collimation and acquisition time of 50 ms and [right] without source collimation but acquisition time of 1 ms.

**- Single electron detection efficiency**

The single electron detection efficiency $\kappa$ is given by:

$$\kappa = \int_t^\infty P(g)dg \tag{3.8}$$

where $\kappa$ is the fraction of avalanches that contain more secondary electrons than the threshold $t$ and $P(g)$ is the gain distribution given by the Eq. 3.7 which can be explicitly written as:

$$\kappa(m, \overline{G}, t) = \int_t^\infty \frac{m^m}{\Gamma(m)} \frac{1}{\overline{G}} \left(\frac{g}{\overline{G}}\right)^{m-1} e^{-m\frac{g}{\overline{G}}} dg. \tag{3.9}$$

Using the Medipix mode, the efficiency $\kappa_{\text{data}} = N_{\text{cluster}}/N^{\max}_{\text{cluster}}$ can be measured. The $N^{\max}_{\text{cluster}} = 117.9$ is given by the plateau obtained in Fig. 3.12 from the measurement of primary electrons in the escape peak. This value is assumed to be at 100% efficiency. The Eq. 3.9 is plotted for different values of the $\Theta$

parameter in Fig. 3.15. The parameter $m$ of the Polya function can be measured by fitting the curve given by the number of counted primary electrons as function of the grid voltage. The gain/threshold ratio is the mean of the TOT spectrum divided by the threshold $t$ of the TimePix chip. Thus a TOT measurement was performed for the same grid voltage. The efficiency is calculated from the Medipix mode data and the gain/threshold from the TOT data in the same way already shown in Fig. 3.13.

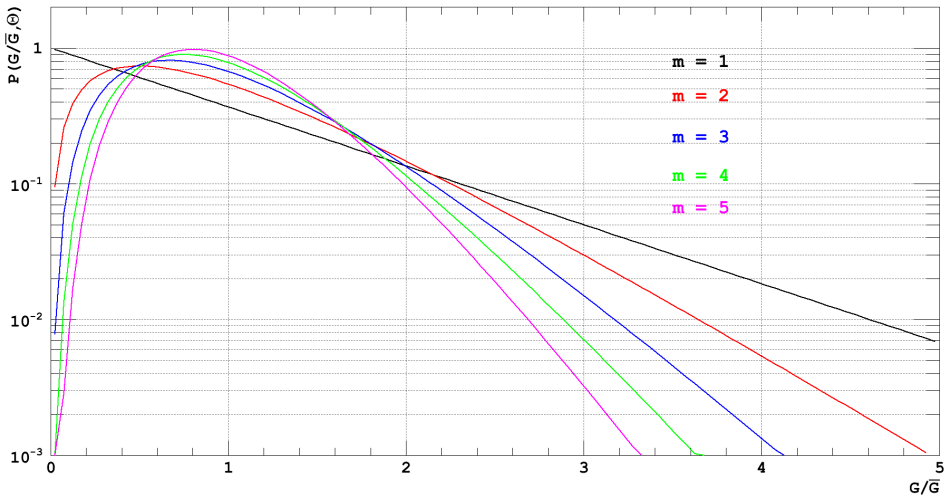


Figure 3.14: Polya distributions with different values of $m = \Theta + 1$.

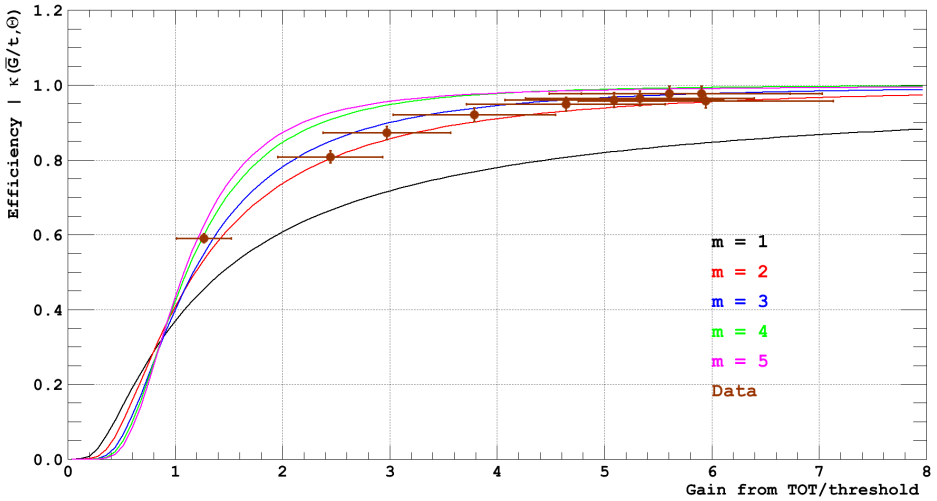


Figure 3.15: Detection efficiency with theoretical curves for Polya distributions with various $\Theta$ parameters and data points. The error on TOT is assumed to be 20%.

The medium gains in the region between 2 and 5 gain/threshold are the most interesting in this plot. The measurements indicate $2 < m = \theta + 1 < 3$. The threshold value in our measurements was of the order of 1000 electrons. As TOT calibration to electrons becomes reliable from 4000 electrons and beyond, the $\theta$ parameter of the gain distribution could not be measured directly in this region.

## 3.3 Micromegas ion backflow studies

Gaseous detectors are often limited by collateral effects (sparks, ion backflow, space charge), originating from the avalanche-induced photons and ions. The ion backflow is defined as the drift of positive ions produced in the avalanche from the amplification region towards the drift region. In TPC operation at high particle rates, the ion backflow induce space charge that may affect the electron drift by locally disturbing the electric field. Although the Micromegas mesh has the intrinsic property to naturally stop a large fraction of the secondary positive ions created in the avalanche, some of them go through the mesh. Indeed, the ions, due to their larger mass, are not affected much by the diffusion and drift along the field lines. Considering that they are emitted with the same distribution as the avalanche, most of these are collected by the mesh and only a small fraction drifts back towards the drift region.

So, the ion backflow fraction (IBF) can be defined as:

$$BF = \frac{N_b}{N_t} \tag{3.10}$$

where $N_t$ is the average number of ions produced in an electron avalanche and $N_b$ the average number of the backflowing ions. Following the previous assumptions, the dependency of the IBF on different detector parameters can be estimated through numerical simulation. In the two dimensional limit, it can be shown that,

$$BF = \frac{1}{FR}\left(\frac{p}{\sigma_t}\right) \tag{3.11}$$

Here $FR$ is the field ratio (amplification field/drift field) and p is the mesh pitch. $\sigma_t$ is related to the transverse diffusion of the electron and given by $D_t\sqrt{z}$ wherein $D_t$ is the transverse diffusion coefficient of electron and $z$ is its crossing path.

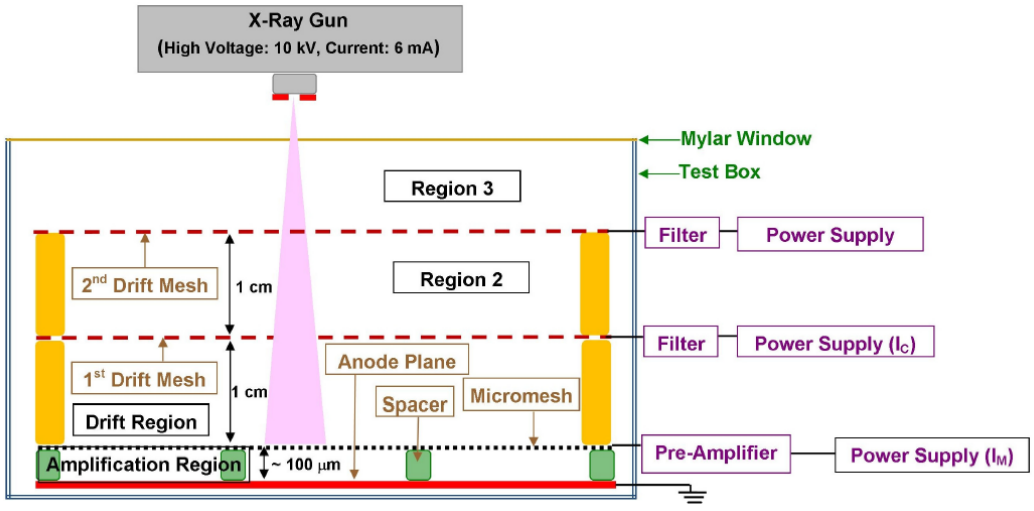


Figure 3.16: Schematic diagram of experimental setup for ion backflow measurement. A second drift mesh at a distance of 1 cm above the first one and this has been kept at the same voltage as that of the first drift mesh.

The IBF has been measured as:

$$BF = \frac{I_C - I_P}{I_M + I_C - I_P} \tag{3.12}$$

where $I_C$ is the current measured on the cathode mesh (Figure 3.16) and is proportional to the number of ions collected on the drift mesh. $I_P$ is equal to the current measured on the drift mesh without amplification

and is referred to as the primary current. $I_M$ is the current measured on the Micromegas mesh and proportional to the number of ions collected on the mesh. In our case, the primary ionization current was ignored ($\simeq$pA).

Figure 3.17 (left) shows the comparison between experimental data with and without double drift mesh. Indeed, the use of two drift meshes both polarized at the same voltage (but different power supply) cancels the field between them avoiding the perturbation of additional charges to the measurement.

Four bulk Micromegas have been built in CEA/IRFU workshop using the standard 400 LPI mesh and several layers of 64 µm-thick photoresist specifying different gap: 64 µm, 128 µm, 192 µm and 220 µm. A X-ray generator was used for the measurements in the configuration described in Fig 3.16. Simulation have been done with the Garfield simulation framework. This framework was upgraded in 2009 through the addition of the neBEM (nearly exact Boundary Element Method). This toolkit carry out 3D electrostatic field simulation in microscopic scale. Figure 3.17 (left) shows that the simulation are consistent with the 128 µm gap Micromegas when a double mesh was used in the setup and (right) for the three different gaps (64 µm, 128 µm and 192 µm) with the same mesh hole pitch of 63 µm (400 LPI) and for one different pitch of 75 µm (325 LPI) for an amplification gap of 128 µm [83].

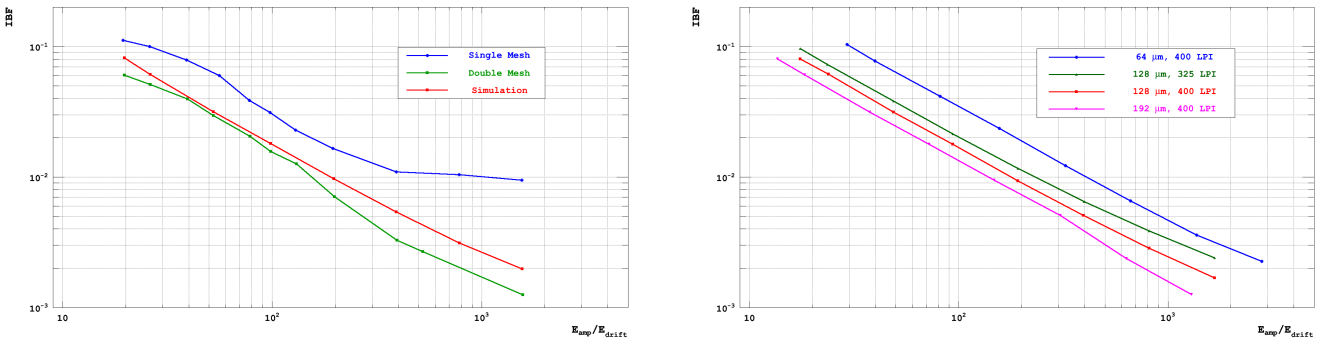


Figure 3.17: [Left] comparison between experimental data and simulation for 128 µm amplification gap and 63 µm pitch. [Right] Simulation of IBF for three different amplification gaps (64 µm, 128 µm and 192 µm) with the same mesh of 400 LPI and for one different pitch (325 LPI) for an amplification gap of 128 µm.

## 3.4 Ageing studies for Micromegas

Micromegas detectors are known to be very robust compared to MWPCs which are also limited at high flux ($10^2 - 10^3$ kHz/cm$^2$) suffering from accumulation of positive ions. The Compass experiment at Cern operated standard Micromegas detectors since 2002 starting with a flux of 450 kHz/cm$^2$ [84] to flux up to 20 kHz per pixel of $0.4 \times 2.5$ mm$^2$ (2 MHz/cm$^2$) in the detector center for the second phase started in 2015 [85]. From a certain rate, the efficiency starts to decrease due to the dead time increase [86].

The first reason why the resistive technology has been introduced and developed is to increase further the rate capability. Thus, introducing new materials in the detector, new ageing studies are required.

Typical studies of detector ageing are done by irradiating the detector for a long period of time. The integrated charge should correspond at least of few times to the expected accumulated charge of the detector during his nominal operation.

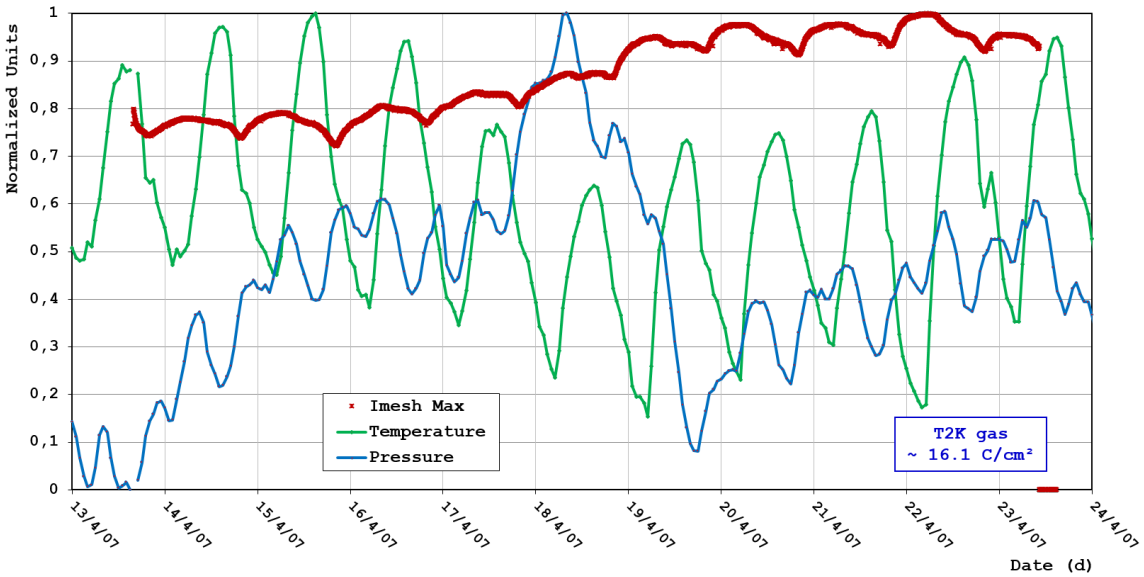


Figure 3.18: Current monitoring of a standard Micromegas mesh in argon + 5% isobutane gas mixture irradiated by an X-ray gun. The temperature and pressure variation outside the laboratory were superposed in arbitrary units.

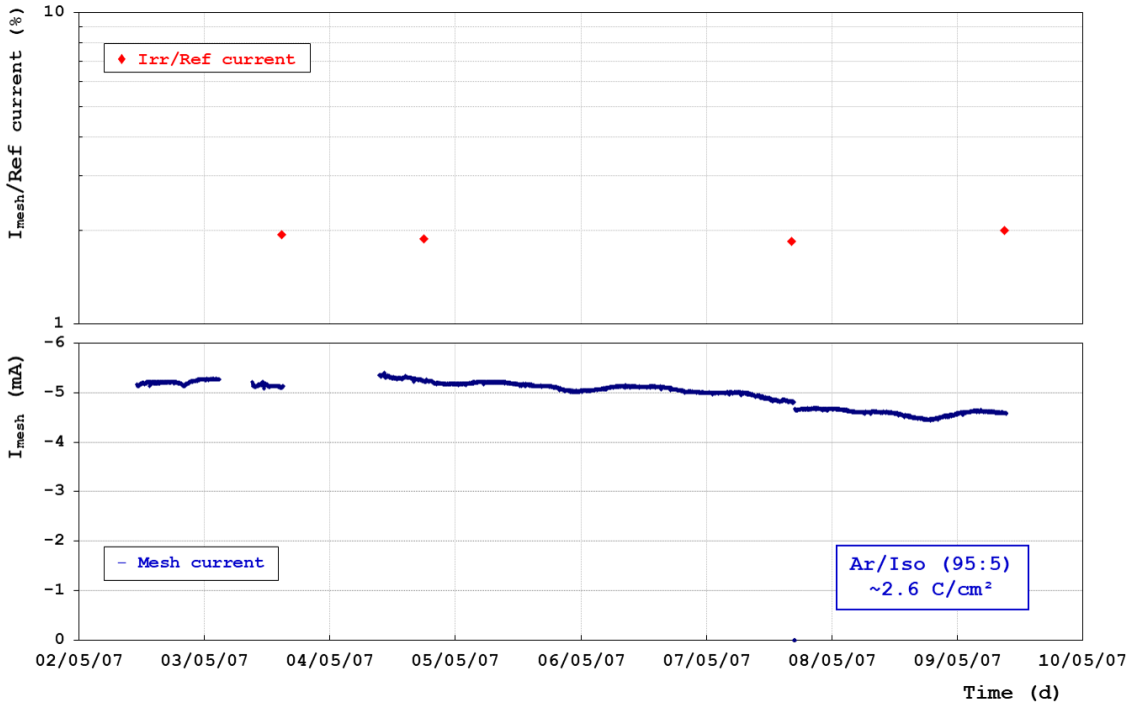


Figure 3.19: Mesh current evolution (red curve) for a period of 21 days and an integrated charge of 918 mC (more than 7×5 years of HL-LHC operation). The gain control measurements with the non exposed detector are also plotted (black circles).

### 3.4.1 Standard Micromegas

A $10 \times 10$ cm$^2$ Micromegas detector was irradiated under a X-ray gun beam (V = 9.2 kV, I = 1.9 mA) on a 0.36 cm$^2$ zone. The detector mesh voltage was set at 380 V (gain $\simeq$ 2500) in argon + 5% isobutane gas mixture. Figure 3.18 shows the current monitoring of a standard bulk Micromegas detector operating during 10 days under 16.1 C/cm$^2$ (200 years of operation for the New Small Wheel detector at LHC!). The temperature and pressure variations outside the laboratory were superposed in arbitrary units. The mesh current varied between 6.2 and 7.2 uA, the temperature between 4°C and 26,4°C and the pressure between 0.998 and 1.007 bar. The mesh current oscillation (with a day period) follows the temperature with an half day delay due to the sun exposition of the X-ray test bench every afternoon during operation.

A detector gain curve was taken before and after the test in both detector regions, irradiated and non-irradiated. A difference of 15% was found due to different environmental condition.

In order to get rid of daytime effects, the room was isolated from sunlight to be less affected temperature and pressure variations. A 10 cm$^2$ zone was irradiated only.

### 3.4.2 Resistive strip Micromegas

During the development of resistive Micromegas detector for the upgrade of the ATLAS-New Small Well, some ageing studies have been done with resistive strips bulk [87]. The mesh current was monitored during 21 days and compared to the gain of a non exposed detector (see Fig. 3.19). No significant deviation have been observed.

# Particle Tracking

Contents



In fundamental physics, a tracking detector (tracker) is a device whose main function is the reconstruction of electrically charged particle (creating tracks) while they interact with the detection medium. Tracking detectors have been developed for and, are used by physics experiments in the fields of nuclear physics, particle physics and astro-particle physics. Particle track reconstruction gives access to parameters such as the particle momentum and the particle mass. Gaseous detectors are ideal trackers thanks to their low material budget.

After introducing the families of gaseous tracking detectors, momentum measurement, particle identification and track reconstruction algorithms will be introduced.

## 4.1 Gaseous tracking detectors for Physics

Gaseous detectors used for tracking can be classified in three main families: 2D tracker, 3D tracker and 3D tracker as target.

### 4.1.1 2D tracking

The reconstruction of a particle trajectory can be done by putting slices of detection planes intermittently along its path. Thus, the $z$ position of each detection plane will be associated to the hits positions ($x$, $y$) in the latter. This configuration is suitable to minimize the electron drift in each detector ($\leqslant$5 mm) and reduce the detection time particularly in high rate particle flux.

The multi-layer Micromegas tracker built for the Clas12 experiment belongs to this category (see Sec. 5.2).

### 4.1.2 3D tracking

If the number of detection slices becomes infinite, the 2D detection planes can be replaced by a unique gas volume which gives a continuous three-dimensional track information. The $x-$, $y-$ and $z-$coordinates are measured simultaneously and continuously inside the full gas volume of the time projection chamber (TPC) described in the Sec. 4.2).

The International Linear Detector (ILD) for the future International Linear Collider (ILC) is based on a central tracker mixing a silicon vertex detector with a TPC. The R&D on a ILC-TPC concept illustrates this group (see Sec. 5.1). Similarly the vertical TPCs built and operated in the T2K experiment are also typical examples.

### 4.1.3 Time projection chamber tracker as target

Being a large volume, most of the TPC also be used as a target. In this case, pressurized gas are used to increase the cross section interaction. This kind of TPC is mainly used in rare event detection (neutrino, gamma-ray, etc.).

The idea of using TPCs in the search for weakly interacting particles (neutrino or dark matter) has been boosted by the need to maximize the amount of matter necessary to increase the detection probability.

The HARPO prototype for $\gamma$-ray astrophysics is a typical TPC as used as target to convert the sub-MeV photons to $e^+e^-$ pairs (see Sec. 6.1).

## 4.2 The time projection chamber

In order to measure simultaneously the three coordinates, the concept of TPC was introduced by David Nygren in 1974 [88, 89]. The TPC is a simple gas-filled drift chamber with one or two endplates to read out the signals (anode) and a cathode to polarize the gas volume. A field cage is necessary to ensure in it a homogeneous and constant electric field. The gas volume can have a cylindrical shape (usually in collider experiments) or a parallelepipedal shape (in low energy rare event experiments).

The TPC principle, illustrated in Fig. 4.1, is based on the following steps which happen in chronological order:

- A charged particle ionizes the gas atoms while crossing the medium.
- Primary electrons coming from ionization drift in the direction of the electric field $E$ to the anode.
- The magnetic field $B$ parallel to the electric field $E$ limits the electron diffusion and allows momentum measurement.

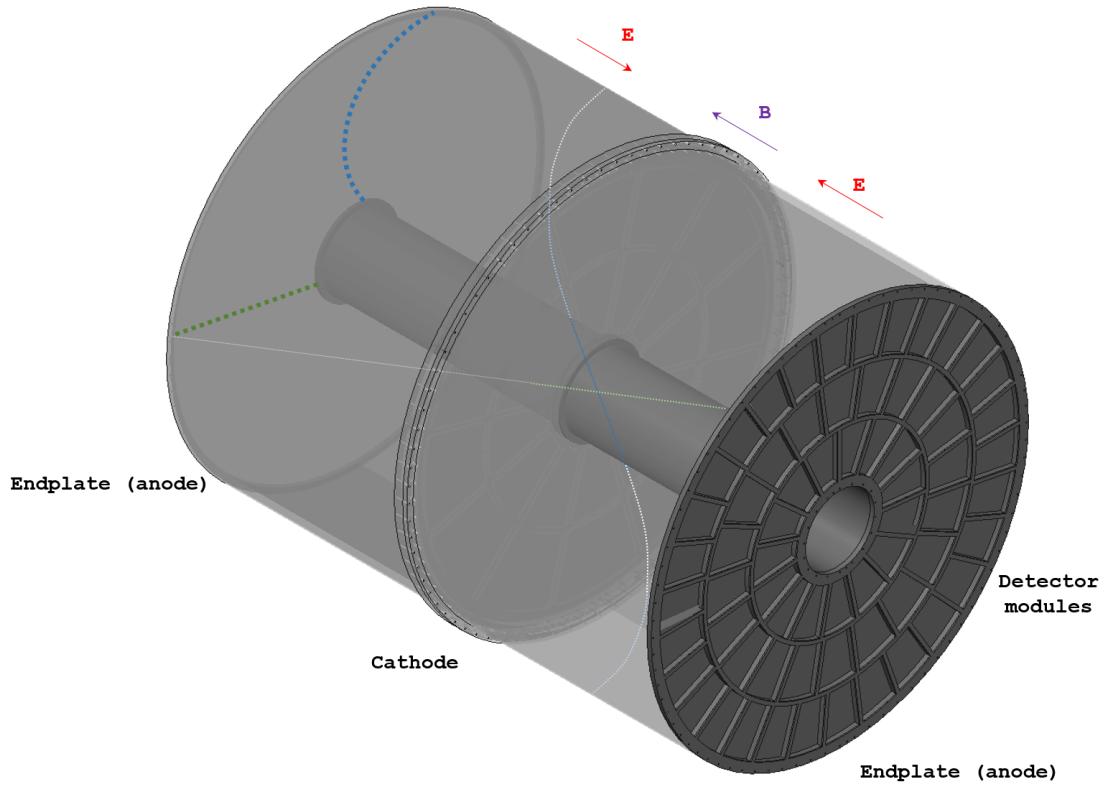


Figure 4.1: Cylindrical time projection chamber with two endplates used in collider experiments. The magnetic and electric fields are collinear. Each enplate is a disk assembled with detector modules.

- Primary electrons drifted to the anode are amplified at the anode.
- Readout electronics connected to strips or pads record the signal with time information giving access to the $x, y$ and $v_{\text{drift}} \times t = z$ coordinates.

With the help of a high magnetic field, a TPC provides simultaneously momentum measurement and particle identification (PID) with the same detector volume. As the signals are read out only on the anode plane, the number of electronics channels can stay reasonable even for large detectors. The endplate is segmented in detector modules. Each detector module consists of an amplification structure (MWPC or MPGD), a segmented readout elements (strips, pads or pixels) and a readout electronics which can be deported using connection cables.

Since the first events taken by this three-dimensional tracking device in 1983 (in PEP4 experiment at SLAC), several experiments have used TPC as their main tracker. The TPCs of the main experiments have been summarized in the following tables 4.1 and 4.2 with their specific characteristics (size, magnetic field, gas mixture, readout configuration, etc.). These tables shows the success of this concept during the last decades and the various configuration adapted for each experiment.

The three identical vertical T2K-TPC and the High Angle T2K-TPC will be discussed in Sec. 5.3.

Most of the TPC parameters are interdependent. For instance, the gas mixture choice affects the electron drift velocity and the gas amplification; the volume size affects the drift field, the total number of pads and the momentum measurement. To optimise these parameters to fulfil the performance needed by the experiment, full scale simulations are mandatory.

Table 4.1: Characteristics and performance of some TPC - Part 1. [24]

| | Experiments | | | | | | | | |
|---|---|---|---|---|---|---|---|---|---|
| **Parameters** | **PEP4** | **TRIUMF** | **TOPAZ** | **ALEPH** | **DELPHI** | **NA35** | **EOS/HISS** | **NA49 VTX** | **NA49 MAIN** |
| **Operation date** | 1982/1984 | 1982/1983 | 1987 | 1989 | 1989 | 1990 | 1992 | 1995 | 1995 |
| **Inner/Outer radius** (m) | 0.2/1.0 | ∼0.15/0.50 | 0.38/1.1 | 0.35/1.8 | 0.35/1.4 | 2.4/1.25 (L/W) | 1.5/0.96 (L/W) | 2.5/1.5 (L/W); 2x | 4/4 (L/W); 2- |
| **Max. drift length** (L/2) (m) | 1 | 0.34 | 1.1 | 2.2 | 1.34 | 1.12 vert. | 0.75 (H) | 0.67 vert. | 1.1 vert. |
| **Magnetic field** (T) | 0.4/1.325 | 0.9 | 1 | 1.5 | 1.23 | 0 | 1.3 | 1.5 | 0 |
| **Gas** | $Ar/CH_4$ | $Ar/CH_4$ | $Ar/CH_4$ | $Ar/CH_4$ | $Ar/CH_4$ | $Ar/CH_4$ | $Ar/CH_4$ | $Ne/CO_2$ | $Ar/CH_4/_2$ |
| **Mixture** | 80/20 | 80/20 | 90/10 | 91/9 | 80/20 | 91/9 | 90/10 | 90/10 | 90/5/5 |
| **Pressure** (atm) | 8.5 | 1 | 3.5 | 1 | 1 | 1 | 1 | 1 | 1 |
| **Drift field** (V $cm^{-1}$ $atm^{-1}$) | 88 | 250 | 100 | 110 | 150 | 120 | 120 | 190 | 175 |
| **Electron drift velocity** (cm $\mu s^{-1}$) | 5 | 7 | 5.3 | 5 | 6.69 | 5 | 5.5 | 1.3 | 2.3 |
| $\omega\tau$ | 0.2/0.7 | 2 | 1.5 | 7 | 5 | 0 | 0.5 | 1 | 0 |
| **Pads size** w - L (mm - mm) | 7.5 × 7.5 | (5.3-6.4) × 19 | (9-11) × 12 | 6.2 × 30 | ∼7 × 7 | 5.5 × 40 | 8 × 12 | 3.5 × (16 , 28) | (3.6, 5.5) × 40 |
| **Max. no. 3D points** | 15-straight | 12 | 10-linear | 9 + 12-circular | 16-circular | 60 + 30 | 128 | <150 | 90 |
| **dE/dx**: Max. no. samples/track | 183 | 12 | 175 | 148 + 196 | 192 | 60 | 128 | <150 | 90 |
| **Sample size** (mm atm); w or p | 4 × 8.5; wires | 6.35; wires | 4 × 3.5; wires | 4; wires | 4; wires | 40; pads | 12 | 16, 28 | 40 |
| **Gas amplification** | 1000 | 50 000 | | 3000-5000 | 5000 | | 3000 | 20 000 | 5000 |
| **Gap** a-p; a-c; c-gate[a] | 4; 4; 8 | 6 | 4; 4; 8 | 4; 4; 6 | 4; 4; 6 | | 4; 4; 6 | 3 , 2; | 2,3; 3;6 |
| Pitch a-a; cathode; gate | 4; 1; 1 | | 4; 1; 1 | 4; 1; 2 | 4; 1; 1 | 4; 1; 2 | 4; 1; 2 | 4; 1; 1 | 4; 1;1 |
| **Pulse sampling** (MHz/no. samples) | 10/455, CCD | only 1 digitiz., ADC | 10/455, CCD | 11/512, FADC | 14/300, FADC | 12.5 / | 10/256, SCA | /512 | /512 |
| **Gating**[b] | 1984 o. on tr | . 1983 o. on tr. | o. on tr. | synchr. cl. wo. tr | static | | o. on tr. | o. on tr. | o. on tr. |
| **Pads**, total number | 15 000 | 7800 | 8200 | 41 000 | 20 000 | 11 000 | 15 000 | 74 000 | 108 000 |
| **Performance** | | | | | | | | | |
| $\Delta x_T$ (µm)-best/typ. | 130-200 | 200/ | 185/230 | 170/200-450 | 180/190-280 | 300-800 | 300 | 150 | 150 |
| $\Delta x_L$ (µm)-best/typ. | 160-260 | 3000 | 335/900 | 500-1700 | 900 | 250-450 | | | |
| **Two-track separation** (mm), T/L | 20 | | 25 | 15 | 15 | 18 | 25 | | 10 |
| $-\delta p/\delta p^2$ $(GeV/c)^{-1}$ : TPC alone; high p | 0.0065 | | 0.015 | 0.0012 | 0.005 | | 1 | | |
| $dE/dx$ (%) Single tracks/in jets | 2.7/4.0 | | 4.4 / | 4.4 / | 5.7/7.4 | /6 | /4 | <4 : VTX + Main | |
| **Comments** | strong E - B effect | a in single PCs | chevron pads | circular pad rows | circular pad rows only pad r.o. | B = 0 only | pad r.o. only pad r.o. | Krm calibration only pad r.o. | up to1200 tr. |

*a*: a = anode, p = pads, c = cathode grid

*b*: o. on tr.: gate opens on trigger; cl. wo. tr. : opens before collision and closes without trigger; static : closed for ions only

Table 4.2: Characteristics and performance of some TPC - Part 2. [24]

| Parameters | Experiments | | | | | | |
|---|---|---|---|---|---|---|---|
| | **CERES/NA45** | **STAR** | **HARP** | **ALICE** | **T2K** | **ALICE-II** | **HA-TPC T2K** |
| **Operation date** | 1999 | 2000 | 2001 | 2009 | 2010 | 2020 | 2021/2022 |
| **Inner/Outer radius** or L/W (m) | 0.6/1.3; L = 2 | 0.5/2.0 | 0.1/0.41 | 0.85/2.5 | 2.2/0.7 (H/L); 3× | 0.85/2.5 | 2.2/0.7 (H/L); 3 × |
| **Max. drift length** (L/2) (m) | 0.7 rad. | 2.1 | 1.6 | 2.5 | 0.9 W | 2.5 | 0.9 W |
| **Magnetic field** (T) | " Bz < 0.7; Br < 0.3 " | 0.25/0.5 | 0.7 | 0.5 | 0.2 | 0.5 | 0.2 |
| **Gas** | $Ne/CO_2$ | $Ar/CH_4$ | $Ar/CH_4$ | $Ne/CO_2/N_2$ | $Ar/CF_4/i\text{-}C_4H_{10}$ | $Ne/CO_2/N_2$ | $Ar/CF_4/i\text{-}C_2H_{10}$ |
| **Mixture** | 80/20 | 90/10 | 91/9 | 90/10/5 | 95/3/2 | 90/10/5 | 95/3/2 |
| **Pressure** (atm) | 1 | 1 | 1 | 1 | 1 | 1 | 1 |
| **Drift field**(V $cm^{-1}$ $atm^{-1}$) | 200-600 | 140 | 111 | 400 | 200 | 400 | 200 |
| **Electron drift velocity** (cm $\mu s^{-1}$) | 0.7-2.4 | 5.45 | 5.2 | 2.7 | 7 | 2.7 | 7 |
| $\omega\tau$) | ; | 1.15/2.3 | 3.3 | <1 | 0.7 | <1 | 0.7 |
| **Pads size** (w × L, mm × mm) | 10 chevron | 2.85 × 11.5 | 6.5 × 15 | 4×7.5 | 6.9×9.7 | 4×7.5 | 6.9×9.7 |
| | 6.2 × 19.5 | | 6 × 10/15 | | 6 × 10/15 | | |
| **Max. no. 3D points** | | 13 + 32-straight | 20 | 63 + 64 + 32 | 72 × 3 | 63 + 64 + 32 | 72×3 |
| **dE/dx**: Max. no. samples/track | | 13 + 32 | 20 | 63 + 64 + 32 | 72 × 3 | 63 + 64 + 32 | 72×3 |
| **Sample size** (mm atm); w or p | | 11.5 + 19.5; pads | 15 | 7.5 + 10 + 15; pads | 9.7 | 7.5 + 10 + 15; pads | 9.7 |
| **Gas amplification** | 8000 | 3000/1100 | 20 000 | 20 000 | ∼1000 | 20 000 | ∼1000 |
| **Gap** a-p; a-c; c-gate[a] | 3;3;6 | 2; 2; 6/4; 4 ; 6 | 5;5;6 | 2; 2; 3/3; 3; 3 | 0.128 | 2; 2; 3/3; 3; 3 | 0.128 |
| **Pitch** a-a; cathode; gate | "6; 2; 2" | 4; 1; 1/4; 1; 1 | 4; 2; 2 stagg. | 2.5; 2.5; 1.5 | | 2.5; 2.5; 1.5 | |
| **Pulse sampling** (MHz/no. samples) | | 9.6/400 | 10/>300, FADC | 5-10/500-1000, ADC | /512 SCA | 5-10/500-1000, ADC | /512 SCA |
| **Gating**[b] | o. on tr. | o. on tr. | o. on tr. | o. on tr. | none | o. on tr. | none |
| **Pads, total number** | 78 000 | 137000 | 4000 | 560000 | 125000 | 560000 | 125000 |
| **Performance** | | | | | | | |
| $\Delta x_T$ (µm)-best/typ. | 230/340 | 300/600 | 600/2400 | spec:800/1100 | 600 (1m drift) | spec:800/1100 | 600 (1m drift) |
| $\Delta x_L$ (µm)-best/typ. | dr = 400/640 | 500/1200 | 3.5 | spec:1100/1250 | | spec:1100/1250 | |
| **Two-track separation** (mm) | | 8 - 13/30 | | | | | |
| $-\delta p/\delta p^2$ $(GeV/c)^{-1}$: TPC alone; high p | 1 | 0.006 | 0.2/0.45-0.50 | spec:0.005 | spec: <10; | spec:0.005 | spec: <10; |
| **dE/dx** (%): single tracks/in jets | | 7.4/7.6 | 16 spec: | spec:4.9/6.8 | <10 / | spec:4.9/6.8 | <10 / |
| **Comments** | Radial TPC<br>No field wires | No field wires<br>>3000 tracks | el. crosstalk | No field wires<br>< 20 000 tracks | Micromegas r.o. | No field wires | Micromegas r.o. |

*a*: a = anode, p = pads, c = cathode grid

*b*: o. on tr.: gate opens on trigger; cl. wo. tr. : opens before collision and closes without trigger; static : closed for ions only

## 4.3 Momentum measurements in a magnetic field and multiple scattering

The determination of a charged particle momentum can be performed by measuring the bending of its trajectory in a uniform magnetic field $\vec{B}$. The Lorentz force $\vec{F} = q\vec{v} \times \vec{B}$ applied to a point charge due to electromagnetic fields for a particle in motion perpendicular to a constant magnetic field $B$ can be written as (see Fig. 4.2, left):

$$\frac{mv^2}{R} = qvB. \tag{4.1}$$

The 2D or 3D tracking detector will measure the trajectory before and after (or inside) a magnetic field and determine the bending radius $R$.

In a TPC (cylindrical drift chamber), the momentum determination is given by

$$\frac{mv^2}{R} = evB \Rightarrow p = eB \cdot R \tag{4.2}$$

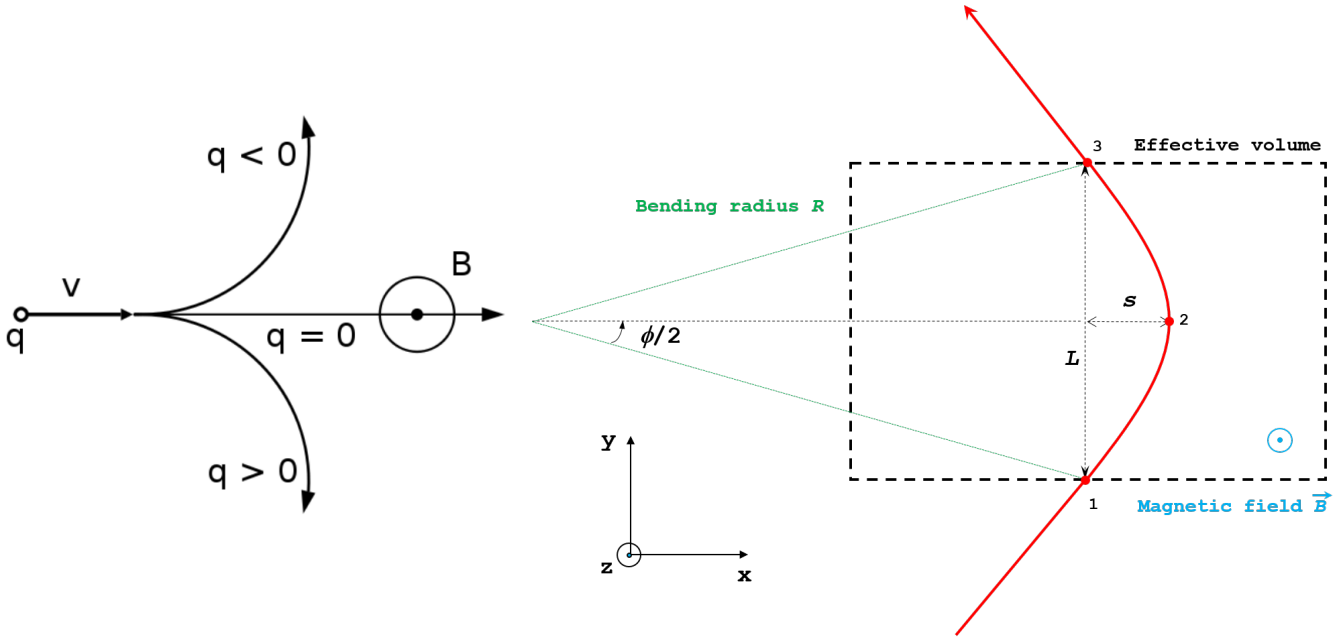


Figure 4.2: Bending of a charged particle in magnetic field $B$ perpendicular the plan.

If the particle energy is defined in GeV/c, the momentum can be simply measured by the relation:

$$p\left[\frac{GeV}{c}\right] = 0.3B[T]R[m] \tag{4.3}$$

where $B$ and $R$ are respectively given in Tesla and meter. Since $R$ is much larger than $L$ for particles in the GeV range, the sagitta $s$ of the trajectory written in function of the transverse momentum $p_T$:

$$\begin{aligned} s &= R\left(1 - \cos\frac{\phi}{2}\right) \approx R\frac{\phi^2}{8} \quad \text{with} \quad \sin\frac{\phi}{2} \approx \frac{\phi}{2} = \frac{L}{R} \\ s &= \frac{L^2}{8R} = \frac{0.3}{8}\frac{L^2 B}{p_T} \end{aligned} \tag{4.4}$$

The sagitta $s$ is measured using the relation $s = x_2 - (x_1 + x_3)/2$ where $x$ is measured at the entrance $x_1$, in the middle $x_2$ and at the exit $x_3$ of the field region in Fig. 4.2 (right). If a particle with charge $q$

and a momentum $\overrightarrow{p} = (p_r, p_\phi, p_z)$, the transverse momentum $p_T = \sqrt{p_r^2 + p_\phi^2}$ crossing a uniform magnetic field $\overrightarrow{B} = (0, 0, B_z)$ parallel to the electric field $E$, over a length $L$.

$$\frac{L}{2\rho} = \sin\frac{\theta}{2} \approx \frac{\theta}{2}, \tag{4.5}$$

$$s = \rho\left(1 - \cos\frac{\theta}{2}\right) \approx \rho\frac{\theta^2}{8} \approx \frac{0.3}{8}\frac{L^2 B}{p_T}. \tag{4.6}$$

The momentum measurement precision $p_T$ can then be deduced from 4.6:

$$\frac{\sigma_{p_T}}{p_T} = \frac{L^2}{8Rs}\cdot\frac{\sigma_s}{s} = \frac{L^2}{8R}\cdot\frac{\sigma_s}{L^4/(64R^2)} = \frac{\sigma_s}{L^2}\cdot 8R = \frac{\sigma_s}{L^2}\cdot\frac{8p}{eB}. \tag{4.7}$$

Large path length $L$ and large magnetic field with good sagitta measurement allow a precise momentum measurement.

The measurement uncertainty increases linearly with $p_T$. Uncertainties $\sigma_s$ depend on number and spacing of track point measurements. For equal spacing and large $N$ equidistant measurements, the expression becomes [90]:

$$\sigma_s = \frac{\sigma_{r\phi}}{8}\sqrt{\frac{720}{N+5}}. \tag{4.8}$$

Finally, the momentum $p$ is given by:

$$\left(\frac{\sigma_p}{p}\right)^2 = \left(\frac{\sigma_{p_T}}{p_T}\right)^2 + \left(\frac{\sigma_\theta}{\sin\theta}\right)^2. \tag{4.9}$$

## 4.4 Energy Loss and Particle Identification with dE/dx

Particles can be identified with the help of their momenta and their specific energy loss. A TPC is able to measure both and to perform therewith a complete particle identification (PID). As described in the previous section, the momentum is obtained by measuring the curvature of the track in the magnetic field. The average specific energy loss of a particle crossing matter and causing ionization is described by the Bethe-Bloch formula (See 2.4). It is based on three assumptions: first, the transfer of energy does not change the direction of flight of the ionizing particle, second, the gas molecules are at rest and third, the ionizing particle is much heavier than an electron.

The mean energy loss by moderately relativistic charged heavy particles is well described by the Bethe equation below:

$$\left\langle -\frac{dE}{dx}\right\rangle = Kz^2\frac{Z}{A}\frac{1}{\beta^2}\left[\frac{1}{2}ln\frac{2m_e c^2\beta^2\gamma^2 W_{\max}}{I^2} - \beta^2 - \frac{\delta(\beta\gamma)}{2}\right] \tag{4.10}$$

with

The particle energy (or velocity) can also be obtained by means of one of the other methods:

- time-of-flight (TOF) measurements,
- detection of Cherenkov radiation or
- detection of transition radiation.

Each of these methods provide PID not only for charged hadrons, but also for charged leptons. Muons and pions are not well separated due to their similar masses ($m_\mu \approx m_\pi$), but muons can be easily identified by other means.

· $K = 2\pi N_a r_e^2 m_e^2 c^2 = 0.1535$ MeV cm$^2$/g
· $z$ : charge of incident particle units of e
· $r_e$ : classical electron radius $= 2.817 \times 10^{-13}$ cm
· $m_e$ : electron mass
· $N_a$ : Avogadro's number $= 6.022 \times 10^{23}$ mol$^{-1}$
· $I$ : mean excitation potential
· $\beta$ $= v/c$ : speed of particle/speed of light in vacuum
· $\gamma$ $= 1/\sqrt{1-\beta^2}$
· $Z$ : atomic number of the absorbing material
· $A$ : atomic mass number of the absorbing material
· $C$ : shell correction factor
· $\delta$ : density factor number

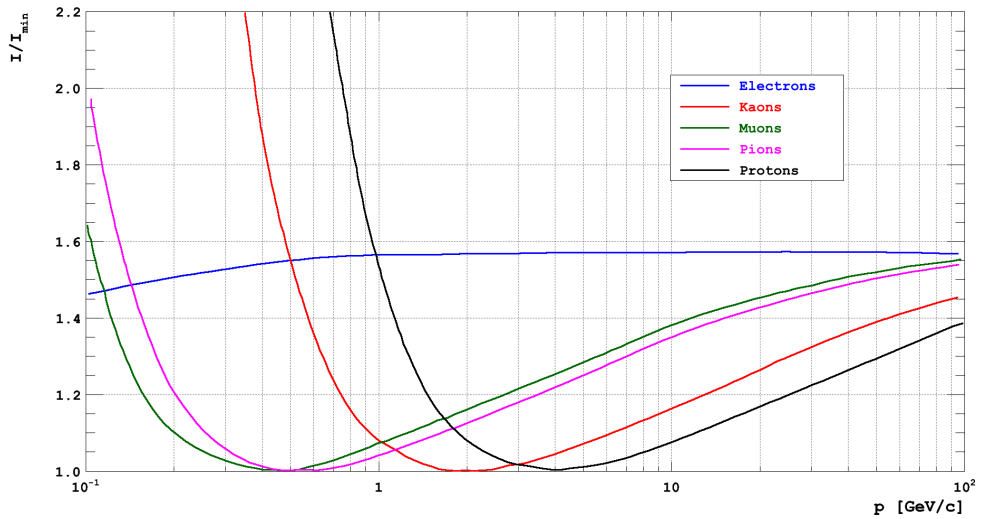


Figure 4.3: Most probable values of ionization (normalized to the minimum value) in argon at atmospheric pressure as function of the momenta of known stable particles [9].

## 4.5 Track reconstruction algorithms

Track reconstruction algorithms can be classified in three method families: combinatorial methods, local methods and global methods.

### Combinatorial methods

All possible data points are fitted using a track model. If the fit is good, the track candidate is accepted and the track reconstruction is done using the fit parameters and the track model. This is the simplest and most time requiring method. It is usually applied when the statistics is very poor as it is in a multilayer detection system. If the detector has different layers, the number of combinatorial tracks is approximately proportional to $N^\alpha$ where $N$ is the number of tracks equal to the number of points in one layer, and $\alpha$ is the number of layers. With 1000 tracks in 4 layers this gives $10^4$ combinations. The number of combinations can be reduced by using additional knowledge of the track geometry. This leads to the more appropriate tracking algorithms, the local and global methods.

**Local methods**

Many processes of track-finding exist and are independent. A few points generate an initial track candidate. An interpolation or an extrapolation of additional points are collected are used. When more points can be found the track candidate is assumed to be good, otherwise the track candidate is discarded. Local methods always contain unsuccessful track candidates, that's why the same points have to be used in several combinations. Therefore the complexity in time rises faster than linear with the number of points. The processing depends on the ordering of the points and the initial track candidate (i.e. Kalman filter, DBScan).

**Global methods**

All data points are processed by the algorithm in the same way. Global methods can be seen as transformation (space change, convolution, ...). The algorithm produces directly a list of tracks matching the original data. The processing complexity of a global method is proportional to the number of points within an event. Compared to local methods, global methods do not depend on the order of the processing of the points (starting point) like the Hough Transform.

### 4.5.1 The Kalman filter

The Kalman filter is a step-by-step algorithmic procedure based on a recursive and locally linear quadratic estimator, which is equivalent to the global least squares method, but taking into account the requirements of a complex modular detector [91]. An initial estimation of the track parameters is used and extrapolated to the next measured point. A comparison of the extrapolation is made with the measurement and the updated track parameters are derived.

To describe the evolution of the measurement state vector $\tilde{p}_k$ at position $k$, the previous measurement state vector $p_{k-1}$ at position $k$-1, the equation

$$\tilde{p}_k = \boldsymbol{f}(p_{k-1}) + w_{k-1}, \tag{4.11}$$

where the suffix $k$ denotes the position at which the state is given on the tilde over $p$ is the true value. $\boldsymbol{f}(p_{k-1})$ is the propagation in the ideal case without process noise $w_{k-1}$. If the process noise has no bias $\langle w_{k-1} \rangle = 0$ and a covariance can be given by $\boldsymbol{Q}_{k-1} = \langle w_{k-1} w_{k-1}^T \rangle$.

A measurement vector $m_k$ is used to describe the observed values at position $k$. The relation between the measurement vector $m_k$ and the state vector $p_k$ can be written

$$m_k = h_k(\tilde{p}_k) + \epsilon_k, \tag{4.12}$$

where $h_k(\tilde{p}_k)$ is the projector which is the true measurement vector if the random error due to the noise $\epsilon_k$ is absent. If the random measurement has no bias $\langle \epsilon_k \rangle = 0$. A covariance can be given by

$$\boldsymbol{V}_k = \boldsymbol{G}^{-1} = \left\langle \epsilon_k \epsilon_k^T \right\rangle. \tag{4.13}$$

To estimate effectively the state of the system using measurement vectors, the Kalman filter takes physical effects into account and predicts, filters and smooths the state vectors $\tilde{p}_k$ at each step $k$.

#### 4.5.1.1 Prediction

Before the measurement at position $k$, the random process noise for this position is not known. To extrapolate the state vector and its covariance from the position $k$-1 to the site $k$, only the first term of equation 4.11 is used:

$$p_k^{k-1} = \boldsymbol{f}(p_{k-1}^{k-1}) = \boldsymbol{f}(p_{k-1}) \tag{4.14}$$

$$\boldsymbol{C}_k^{k-1} = \boldsymbol{F}_{k-1}\boldsymbol{C}_{k-1}\boldsymbol{F}_{k-1}^T + \boldsymbol{Q}_{k-1} \tag{4.15}$$

where $\boldsymbol{Q}_{k-1}$ is the covariance matrix for the process noise between position $k$-1 and $k$ and the propagator matrix $\boldsymbol{F}_{k-1}$ and the projector matrix $\boldsymbol{H}_k$ are two application specific derivatives

$$\boldsymbol{F}_{k-1} \equiv \frac{\partial \boldsymbol{f_{k-1}}(p_{k-1})}{\partial p_k^{k-1}} \tag{4.16}$$

$$\boldsymbol{H}_k \equiv \frac{\partial \boldsymbol{h_k}(p_k^{k-1})}{\partial p_k^{k-1}} \tag{4.17}$$

which are derived from system and measurement equation.

#### 4.5.1.2 Filtering

The filtered state vector $p_k$ and its covariance matrix $\mathbf{C}_k$ at position $k$ is given by

$$p_k = p_k^{k-1} + \boldsymbol{K}_k\Big(m_k - h_k(p_k^{k-1})\Big) \tag{4.18}$$

$$\boldsymbol{C}_k = \Big[\Big(\boldsymbol{C}_k^{k-1}\Big)^{-1} + \boldsymbol{H}_k^T\boldsymbol{G}_k\boldsymbol{H}_k\Big]^{-1} \tag{4.19}$$

where $p_k^{k-1}$ is the predicted state vector, $\boldsymbol{K}_k = \boldsymbol{C}_k\boldsymbol{H}_k^T\boldsymbol{G}_k$ the Kalman gain matrix, $m_k$ the residual of the measurement with respect to the measurement vector $h_k\left(p_k^{k-1}\right)$, $\boldsymbol{C}_k^{k-1}$ the covariance matrix for the predicted vector and $\boldsymbol{G}_k \equiv (\boldsymbol{V}_k)^{-1}$.

#### 4.5.1.3 Smoothing

After more information at subsequent position $k$+1 to $n$ are collected, the state vector at position $k$ can be re-evaluated and further improved. This process is called smoothing. The goal here is to work out an inverse recurrence formula that gives the smoothed state vector at position $k$ based on the smoothed stated vector at position $k$+1 and the filtered state vectors at position $k$ and $k$+1. The smoothed state vector at position $k$ and the smooth covariance matrix for $p_k^n$ are

$$p_k^n = p_k + \boldsymbol{A}_k\big(p_{k+1}^n - p_{k+1}^k\big) \text{ with } \boldsymbol{A}_k = \boldsymbol{C}_k\boldsymbol{F}_k^T\big(\boldsymbol{C}_{k+1}^k\big)^{-1} \tag{4.20}$$

$$\boldsymbol{C}_n^k = \boldsymbol{C}_k + \boldsymbol{A}_k\big(\boldsymbol{C}_{k+1}^n + \boldsymbol{C}_{k+1}^k\big)\boldsymbol{A}_k^T \tag{4.21}$$

#### 4.5.1.4 Inverse Kalman filter

A point in the middle at position $k$, after the filtering process from position 1 to position $n$ and smoothing process from position $n$ to position 1 performed, the processor named inverse Kalman Filter is called to realize this function. The Kalman Filter can be done without using the information of position $k$ but a

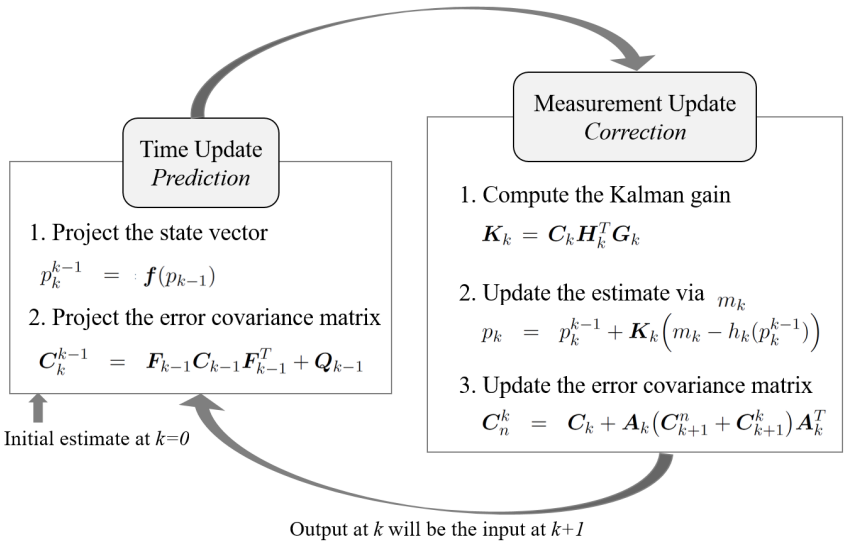


Figure 4.4: Kalman filter procedure.

better way is that makes full use of the previous results with position $k$ by using the inverse Kalman Filter applying the following formulae:

$$p_k^{n*} = p_k^n + \boldsymbol{K}_k^{n*}\left(m_k - h_k(p_k^n)\right) \text{ with } \boldsymbol{K}_k^{n*} = \boldsymbol{C}_k^n \boldsymbol{H}_k^T \left(-\boldsymbol{V}_k + \boldsymbol{H}_k \boldsymbol{C}_k^n \boldsymbol{H}_k^T\right)^{-1} \tag{4.22}$$

$$\boldsymbol{C}_k^{n*} = \left(1 - \boldsymbol{K}_k^{n*}\boldsymbol{H}_k\right)\boldsymbol{C}_k^n = \left[\left(\boldsymbol{C}_k^n\right)^{-1} - \boldsymbol{H}_k^T \boldsymbol{G}_k \boldsymbol{H}_k\right]^{-1} \tag{4.23}$$

Compared with the formulae of the processor of filtering, the difference is the sign in front of $\boldsymbol{G}_k$ or $\boldsymbol{V}_k$, which indicates the negative weight due to the eliminated information of the position $k$.

For each point a matrix of size equal to the track parameters is inverted, so the computation time is $Nd^3$ instead of $N^3$ ($N$: number of measurements and $d$: number of track parameters). The comparison allows outliers rejections which can also be used during pattern recognition.

The Kalman filter algorithm was systematically used in the data analysis of LP-TPC and T2K Upgrade beam tests.

### 4.5.2 The RANSAC algorithm

The Random Sample Consensus (RANSAC) algorithm introduced by Fischler & Bolle, for fitting a model to experimental data containing a significant percentage of important errors or aberrant data [92] where many of the common robust estimation techniques such as M-estimators and least-median squares are less efficient. This algorithm is well-adapted to noisy data or such as multiplexed readout place.

The RANSAC was used in the data analysis of D3DT where the multiplexed pads were considered to be noisy signals.

### 4.5.3 The Hough transform

The Hough transform is a pattern recognition technique invented in 1962 by Paul Hough. The simplest application can detect the lines present in an image, but modifications can be made to this technique to

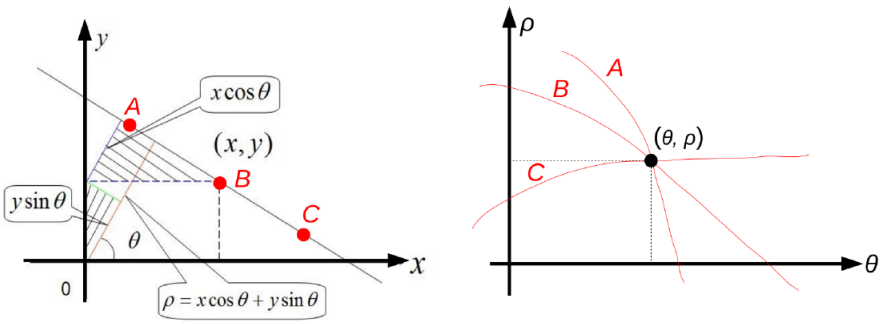


Figure 4.5: Hough transform principle [Left].

detect other geometric shapes: it is the generalized Hough transform developed by Richard Duda and Peter Hart in 1972.

For tracking reconstruction the goal is to search for and detect lines that might be present in an image. The principle behind the Hough Transform is that there are an infinite number of lines passing through a point, the only difference of which is the orientation (angle). For every straight line that passes through a point (e.g. B) in Fig. 4.5 left, can be defined by an $\theta$ and $\rho$.

The purpose of the transform is to determine which of these lines are the most frequent in the analysed image. In order to determine that two points are on the same potential straight line, a representation of the line that allows a comparison in this context is created. So a curve of $\rho$ as a function of $\theta$ is found for all lines passing through this point as shown in Fig. 4.5 right with $x\cos(\theta) + y\sin(\theta)$ ($A$, $B$ et $C$ dans la Fig. 4.5 right) passing through a point $(\rho, \theta)$ fixed (Fig. 4.5 right) in the Hough. This point is identical with the straight line $y = ax + b$ when the point $(\theta, \rho)$ is found, the line can be reconstruct in the real space. All points $(x, y)$ on the straight line can be calculated by:

$$x = \rho \times \cos(\theta) + \lambda \times \sin(\theta) \tag{4.24}$$

$$y = \rho \times \sin(\theta) - \lambda \times \cos(\theta) \tag{4.25}$$

where $\lambda$ is a variable which parametrises the position on the straight line. By removing $\lambda$ of this equation system, the relation between $(\rho, \theta)$ for each point in the real space $(x, y)$ from where a curve can be drawn in the Hough space $(\rho, \theta)$. The matching values $\rho$ and $\theta$ corresponding to the line is where all the curves corresponding to all the points in the real space are crossing (Fig. 4.5 right).

The Hough transform was used in the data analysis of HARPO TPC and D3DT.

Nowadays, state of the art in track fitting are techniques based on the Kalman filter. But a lot of more methods and techniques are available: broken line fit, multiple scattering fit, use of templates, etc.

## Second part

# Academic Applications: from Nuclear and Particle Physics to Astrophysics

*Itard remains convinced that one is savant only through experience, lucid only through doubt, intelligent only through acceptance of the limits of acquired knowledge.*

*Itard demeure convaincu qu'on n'est savant que par l'expérience, lucide que par le doute, intelligent que par l'acceptation des limites du savoir acquis.*

Lucien Malson

# High energy Physics Experiments

Contents



## 5.1 TPC R&D for the International Linear Collider

### 5.1.1 Physics in ILC

The International Linear Collider (ILC) is an electron-positron collider for the exploration of the Higgs couplings, top-quark and fundamental interactions beyond the Standard Model. The ILC machine is based on superconducting solid niobium cavities using accelerating fields of 35 MV/m or more [93]. This lepton collider concept is a precision measurement machine which would be complementary to the Large Hadron Collier (LHC) located in Geneva in operation since 2008. A possible site for ILC have been recently proposed in Japan's Tohoko region [94].

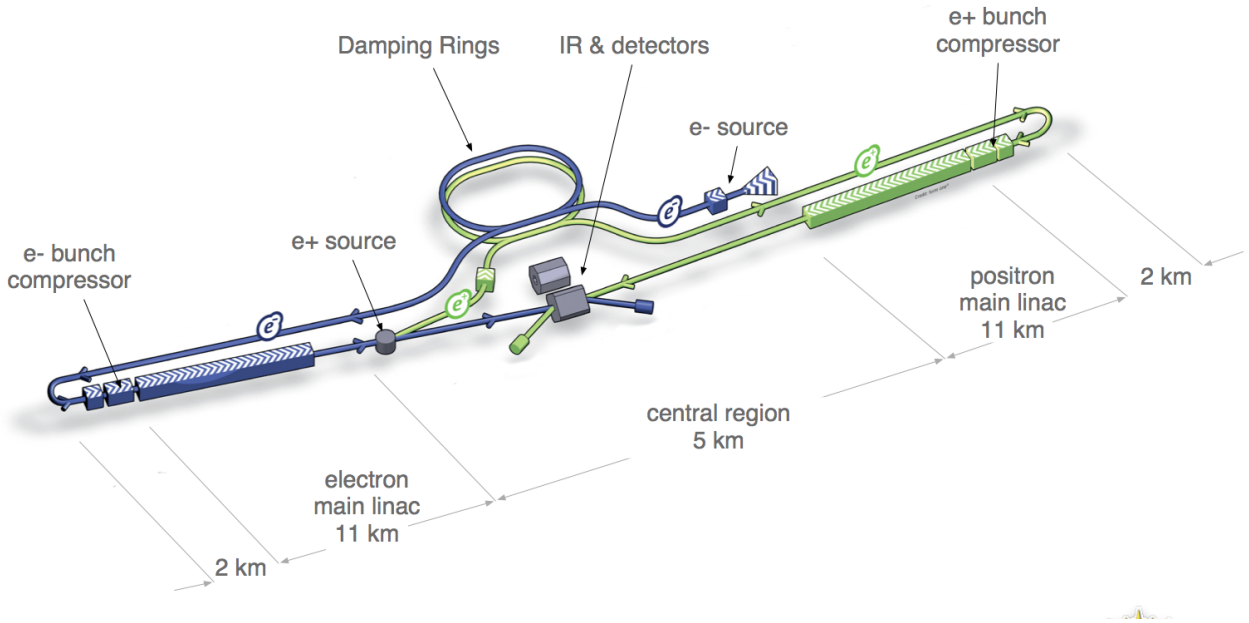


Figure 5.1: (Basic layout of the International Linear Collider.

The centre-of-mass energy of ILC will be between 200 and 500 GeV with an upgrade option to 1 TeV. Polarised electron and positron beams will collide at a crossing angle of 14 mrad. The overall length will be about 31 km. Two detectors (ILD & SiD) will be alternately moved into the beam position with a *push-pull* scheme. Figure 5.1 shows the overview sketch of the design for the ILC.

The ILC bunch structure is composed of trains with a repetition rate of 5 Hz. The train composed of 2625 bunches with $2 \times 10^{10}$ particles has a duration of 1 ms, followed by a gap of 199 ms. This gap time is very convenient for a TPC leaving time to primary electrons to drift to the anode.

ILC aims to provide precise measurements of the top quark mass, CP-violating effects [95] and Higgs couplings.

The Higgs sector consists of three major Higgs boson production processes: $e^+e^- \to ZH$ (*higgsstrahlung*), $e^+e^- \to \nu_e\overline{\nu_e}H$ (*W fusion*) and $e^+e^- \to e^+e^-H$ (*Z fusion*) [10]. These three processes have large production cross sections in the region of the 230-500 GeV CM energy (Fig. 5.2, left). For each, many Higgs decays modes, such as $H \to b\bar{b}$, $WW^\star$, $c\bar{c}$, $\tau\tau$ and $\gamma\gamma$ where high efficiency (Fig. 5.2, right) are expected.

Also, an $e^+e^-$ collider has two notable features. The first one is that such collider can provide longitudinal polarized electron and positron beams. Beam polarization has an effect on the cross sections, since the polarized $e_L$ and $e_R$ have different SU(2)xU(1) quantum numbers. The ILC expects to provide 80% polarization in the electron beam and 30% polarization in the positron beam, with the possibility in both cases of rapidly switching the polarization orientation. The second one is that the nominal center of mass energy of $e^+e^-$ collisions is affected both by initial-state radiation (ISR) and by radiation from the beam-beam interaction (*beamstrahlung*). Beamstrahlung and ISR broaden the $e^+e^-$ CM energy distribution (a few percent at energies up to 500 GeV). They also produce photons that induce hard $\gamma\gamma$ and $e_\gamma$ reactions. Those processes are often the major source of background events, in particular for many types of searches. The rate of these events is energy dependent.

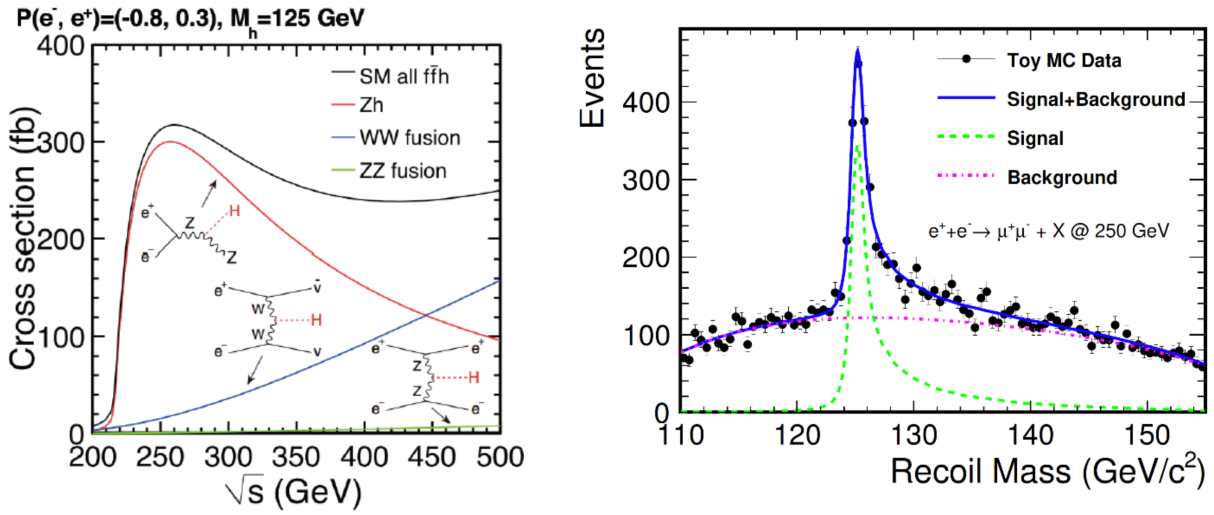


(a) (b)

Figure 5.2: (a) The processes to produce Higgs particles at the ILC Higgs factory [10]. (b) Reconstruction of Higgs particle distribution with the recoil mass technique for the process: $e^+e^- \to ZH$ followed by $Z \to \mu^+\mu^-$ decay for $m_h = 125$ GeV with 250 fb$^{-1}$ at collision energy of 250 GeV, based on Ref.[11]

### 5.1.2 Resistive Micromegas in 5T magnet as proof of concept

In close collaboration with Carleton University, the CEA/Irfu contributed to the development of the resistive Micromegas technology as a solution for the ILD detector concept. This effort required a dozen of test beam campaigns that were done between 2007 and 2015 at DESY facility. The first one was done in a 5T magnet with cosmics as a proof of concept.

The Carleton TPC prototype was designed with a drift length of 15.7 cm (see Fig. 5.3, left) to fit the 28 cm diameter 5T magnet at DESY [96]. A $10 \times 10$ resistive Micromegas with a 50 µm gap was used for the amplification. The readout plane was a matrix of 128 pads in 9 rows. The central 7 rows with a total of 126 pads in 18 columns were used for tracking, the other two rows for triggering. The resistive technology was a structure of 1 MΩ/□ surface resistivity Cermet (Al–Si alloy) coated 25 µm Mylar film laminated to the readout plane with a 50 µm thick insulating adhesive.

The pad signals were read out using ALEPH TPC charge preamplifiers and digitized directly without an intermediate shaper/amplifier using 200 MHz 8-bit FADCs.

Two different gas mixtures were tested. The first, Ar:i$C_4H_{10}$/95:5 gas mixture, was chosen as reference to compare with the previous KEK measurements at 1 T [97]. The second, so-called T2K gas, Ar:CF4:iC4H10/95:3:2, is a possible candidate for the ILC TPC where the drift velocity $v_{\text{drift}} = 7.9$ cm/µs at 270 V/cm instead of $v_{\text{drift}} = 4.2$ cm/µs for Ar:i$C_4H_{10}$/95:5 gas mixture (see Fig. 2.7 & Fig. 2.8).

Cosmic ray data were taken during four weeks. An event example is shown in Fig. 5.4. The independence of the spatial resolution $\sigma_{r\phi}$ with the gain more than 2500 at magnetic field $B = 0$T and the spatial resolution with the gas mixture at $B = 5$T is shown in Fig. 5.5. More details are available in [98].

This test was a success and triggered a decade of beam tests in the DESY infrastructure under construction. These beam test campaigns are summarized in Tab. 5.1.

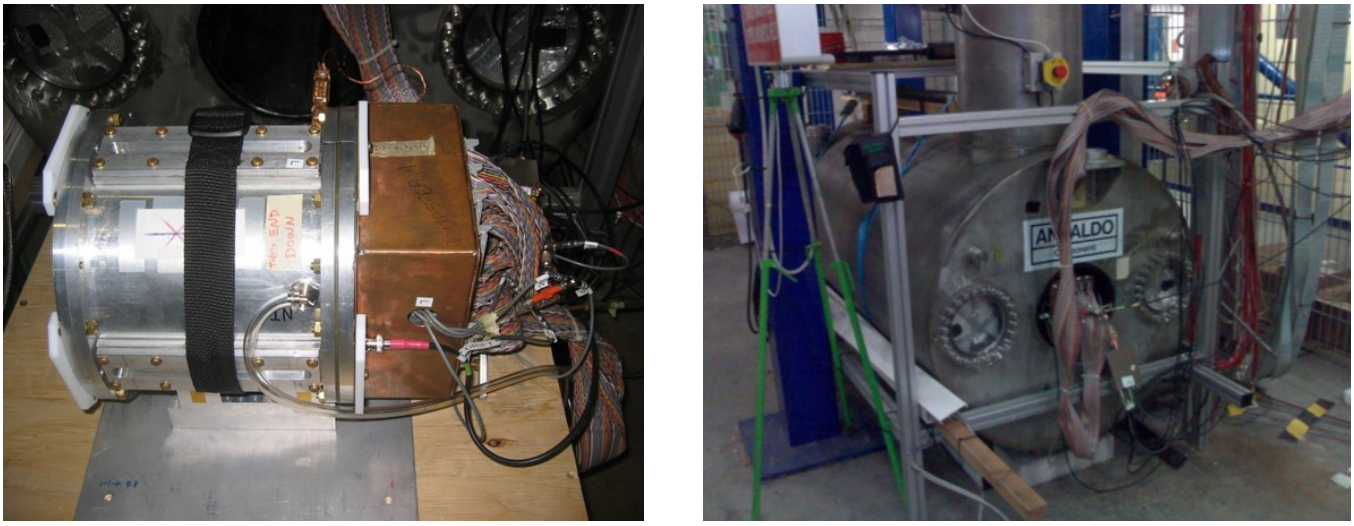

Figure 5.3: [Left] Carleton TPC and DESY 5T magnet [right].

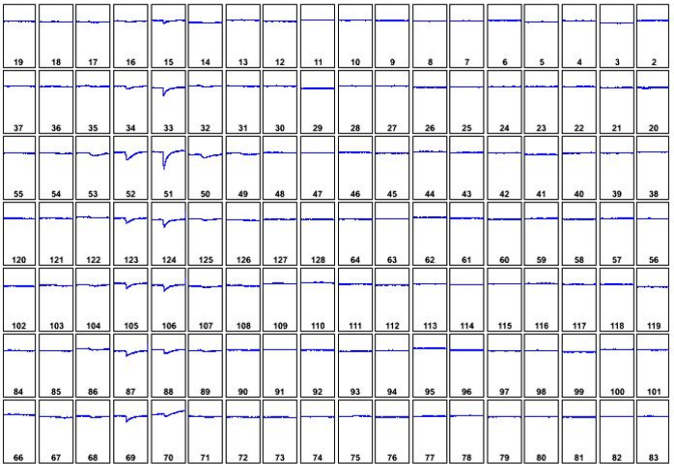

Figure 5.4: Cosmic event from the Carleton in the 5T magnet.

### 5.1.3 Data taking with Resistive Micromegas

After a first testing the resistive Micromegas demonstrator in a 5T magnet at DESY in 2007, the other beam tests took place in the LP-TPC also at DESY-II in T24 area.

#### 5.1.3.1 Large Prototype of the LCTPC collaboration

In 2007, the Linear Collider TPC collaboration (LCTPC) was founded. The goal of the LCTPC collaboration is to unify the international efforts to build a high-performance TPC for the ILC physics up to 1 TeV centre-of-mass energy and to provide common infrastructure and tools to facilitate these studies. The detailed description of LCTPC can be found in the LCTPC Memorandum of Agreement [99]. From the beginning, CEA/Irfu is an active member of this collaboration by contributing to the detector R&D (resistive Micromegas, pixelated readout, cosmic trigger, simulation, data taking and data analysis).

In the framework of the LCTPC collaboration, a large prototype TPC (LP-TPC) was designed, built,

| Date | Module | | Electronics | Cooling | Description |
|---|---|---|---|---|---|
| | Technology | Nb | | | |
| 2008 Nov.-Dec. | Standard | 1 | T2K cards | - | One Micromegas module with resistive anode |
| 2009 May-June | Standard & CLK 5 MΩ/□ | 1,1 | T2K cards | - | Single Micromegas modules<br>Laser photo-dot cathode calibration |
| 2009 Nov.-Dec. | CLK 3 MΩ/□ | 1 | T2K cards | - | Test of external S-Tracker with Micromegas module |
| 2010 March | CLK & Ink 3 MΩ/□ | 1,1 | T2K cards | - | Micromegas module with different resistive coatings<br>using the movable stage of the PCMAG |
| 2010 December | Timepix/Ingrid | 1 | Timepix | - | Ingrid Octopuce test |
| 2011 May | CLK 3 MΩ/□ | 1 | Integrated | - | Test of integrated electronics<br>on a CLK resisitve Micromegas module |
| 2012 July | CLK 3 MΩ/□ | 6 | Integrated | Air | Test with 6 CLK resisitve Micromegas TPC modules<br>with integrated electronics |
| 2013 Jan.-Feb. | CLK 3 MΩ/□ | 7 | Integrated | Air | Test with 7 CLK resistive Micromegas TPC modules<br>with integrated electronics |
| 2014 February | CLK 3 MΩ/□ | 7,2 | Integrated | $2PCO_2$ | Test with 7 CLK resistive Micromegas modules<br>with $2PCO_2$ cooling, laser calibration,<br>runs with 2 Ingrid modules |
| 2015 March | CLK & DLC 3 MΩ/□ | 7 | Integrated | $2PCO_2$ | Test with 6 CLK & 1 DLC resistive Micromegas<br>modules with $2PCO_2$ cooling |
| 2018 November | DLC 3 MΩ/□ | 4 | Integrated | $2PCO_2$ | Test with 4 DLC resistive Micromegas modules<br>with $2PCO_2$ cooling |

Table 5.1: Test beam campaigns between 2008 and 2018 using the large prototype of TPC at DESY facility.

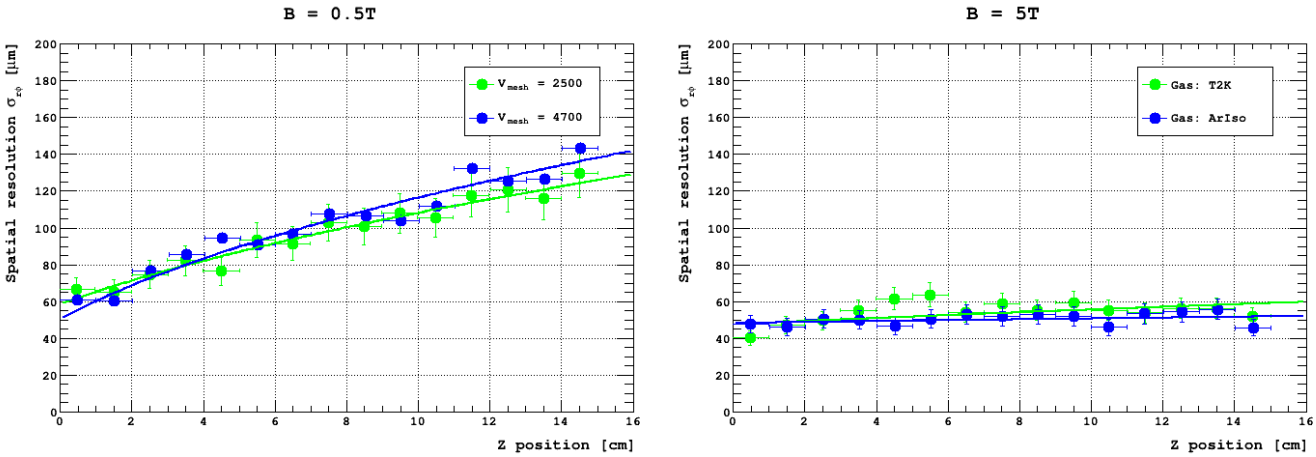


Figure 5.5: Spatial resolution $\sigma_{r\phi}$ using the Carleton TPC: [left] at 0.5 T in T2K gas mixture with two Micromegas gain 2500 and 4700 ; [right] at 5 T in Ar:Isobutane/95:5 and T2K gas mixtures

.

commissioned and tested with the help of the European funding EUDET (Detector R&D towards the international linear collider) [100]. This prototype was developed by the collaboration to test new technologies and techniques which will be necessary to build a large TPC with the performances required for the International Linear Detector (ILD) [101]. The ILD concept use a TPC as the main tracker. The momentum resolution expected for the TPC only in a magnetic field of 3.5T is $\delta(1/p_t) \simeq 9 \times 10^{-5}$/Gev/c which means $\sigma_{\text{point}} < 100$ µm in $r\phi$ and $\sigma_{\text{point}} < 0.4 - 1.4$ mm in $z$ and a resolution in $dE/dx \simeq 5$ %.

The LP-TPC was designed to be equipped with up to seven active and exchangeable readout modules ($\simeq 24 \times 17$ cm$^2$) allowing to test any MPGD technology. The LP-TPC is 60 cm long with an enplate of ≃80 cm diameter (see Fig 5.6) corresponding to the available volume inside the refurbished Persistent Current superconducting MAGnet (PCMAG) where the magnetic field (up to 1T) is homogeneous. This PCMAG which has a thin coil and wall (0.2 $X_0$) and no return yoke was initially designed for airborne experiments. Since 2008, the PCMAG was used in the test beam environment at DESY with the LP-TPC. In 2011, the cooling system was upgraded by adding cryo-coolers at 4 and 10 K to easily cool the magnet without external liquid helium with a closed circuit system. The test beam infrastructure in the T24/1 area at the DESY-II was funded by the EUDET consortium.

#### 5.1.3.2 LP-TPC test beam campaigns

The resistive Micromegas test beam campaigns aims to study resistive technology as solution for ILD detector concept.

The resistive technique is made of a thin film (typically 50 µm) laminated to the readout pad plane with an intermediate insulating spacer (between 50 to 200 µm) presented in Sec. 1.4.3.

The three resistive Micromegas technologies that have been evaluated are described below:

- **Resistive ink**: the resistive layer is done with an industrial screen-printable paste (ESL resistive paste [102]) by screen printing on a insulated film (as polyimide film). The ink thickness is a few ten microns. It is the most easier to produced. The nominal resistivity can can vary between a few Ω/□ to a few MΩ/□.

- **Carbon Loaded Kapton** (**CLK**): the resistive layer is a 50 µm polyimide film used in flexible printed circuits. Even if this technology provides the best resistivity and thickness homogeneity, the CLK have been developed by DuPont for military purposes, so it is very difficult to get supplies of it.

- **Diamond Like Carbon** (**DLC**): the amorphous carbon (a-C) resistive layer is obtained with high energy precursive carbons (plasmas, sputter deposition, arc deposition, ...) rapidly cooled or quenched on a colder surface. The homogeneity and the reproducibility of the DLC resistivity is fallible, but it is known to be a resistant, stable and a hard material. The resistivity depend of the thickness and the doping.

At that time, a specific chip named AFTER have been designed and produced [103] to readout MPGD in vertical TPC of the T2K experiment [104]. The T2K electronics based on AFTER chips is a low-noise (700 e-) electronics dedicated to MPGDs was available. This electronics is very versatile thanks to a dynamic range from 120 to 600 fC, a pre-amplifier-shaper with a 100 ns to 2 µs tunable peaking time, a 511-cell analogical full wave sampling by switch capacitor array (SCA) at sampling frequency up to 100 MHz and a zero suppression capability. The AFTER chip architecture is shown in Fig. 5.7.

The first test beam campaigns were dedicated to the choice of resistive technology and the electronic cards available were limited, so only a single resistive Micromegas module was used at a time. Some resistive technologies were tested up to seven modules. The resistive technology tested were the following: CLK 5MΩ/□, CLK 3MΩ/□, Ink 3MΩ/□ and DLC 3MΩ/□.

As the original T2K electronics provides 1728 channels with 4 AFTER chips per FEC and 6 FECs per FEM, the Micromegas readout plane of a module was designed with a matrix of $24 \times 72$ pads in a keystone shape to minimize the dead space between the module on a circular endplate (see Fig. 5.6, left). Each pad has an horizontal pitch between 2.85 and 3.17 mm and an vertical identical pitch of 6.84 mm. The space between pads are 0.1 mm in both direction (Fig. 5.6, right).

Before 2011, the measurements were done with a set of the original T2K electronics cards (see Fig) and further using an integrated electronics design on purpose. The *integrated* electronics was designed and built thanks to the absence of protection circuitry and the direct wire bonding of four AFTER chips on a front-end-card (FECi). A new front-end mezzanine card (FEMi) were also designed with a keystone shape to read out 6 FECis (see Fig. 5.10 & Fig. 5.11).

Figures 5.12, 5.14 and 5.16 show three electron beam events taken with 7 CLK resistive Micromegas modules in magnetic field (B = 1T) with the corresponding 3D display 5.13, 5.15 and 5.17. These events have a charge spreading over several pads compared to Fig. 5.9.

During the tests, the position of the TPC with respect to the beam was changed by moving the table on which the magnet containing the TPC was attached. This moving table gives a position precision of about 100 µm.

Several properties were validated during these tests: gain, spatial resolution, electronics spark protection, efficiency and long-term operation.

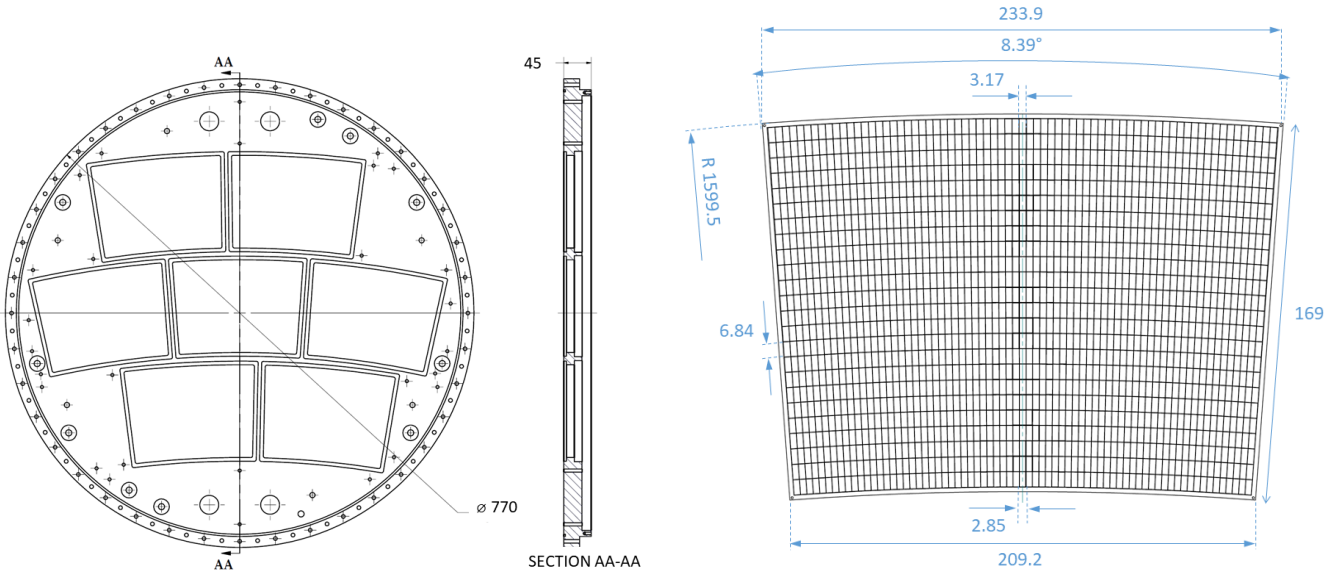


Figure 5.6: Drawings of the endplate with seven emplacements [left] and the Micromegas pad plane [right] for the large prototype of TPC.

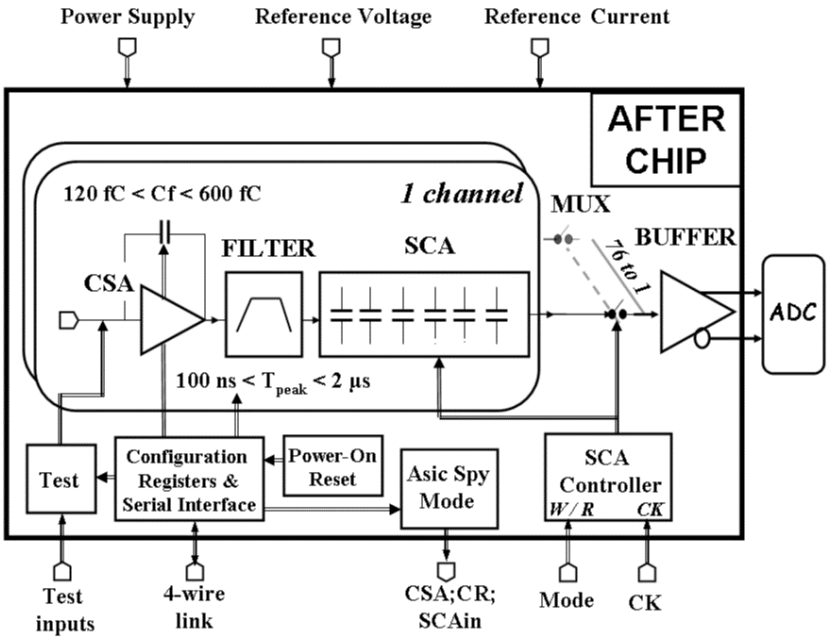


Figure 5.7: Versatile AFTER chip architecture. Each channel includes a 511-cell SCA using 4-switches high dynamic range analog memory cells and a read amplifier.

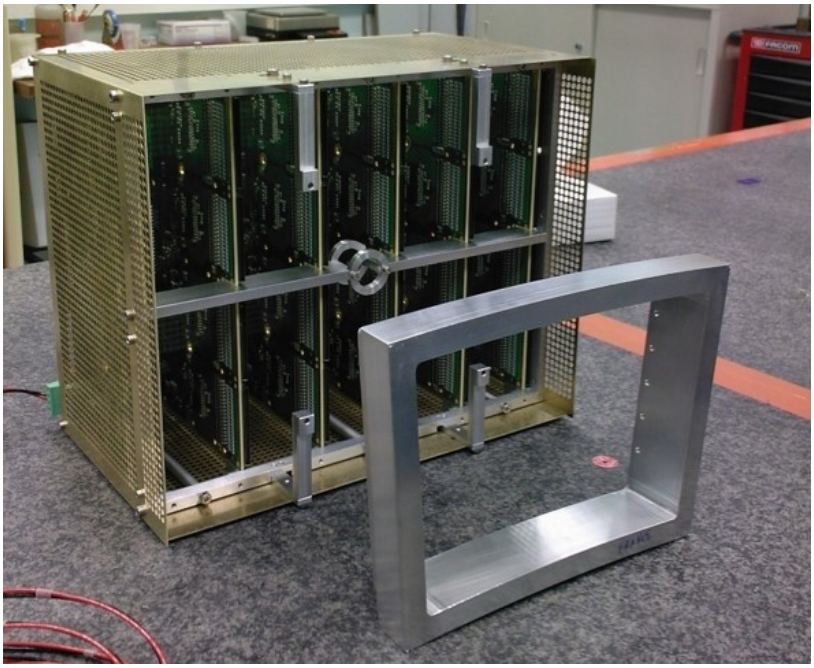

Figure 5.8: Original T2K electronics with light shielding in from of a mechanical frame.

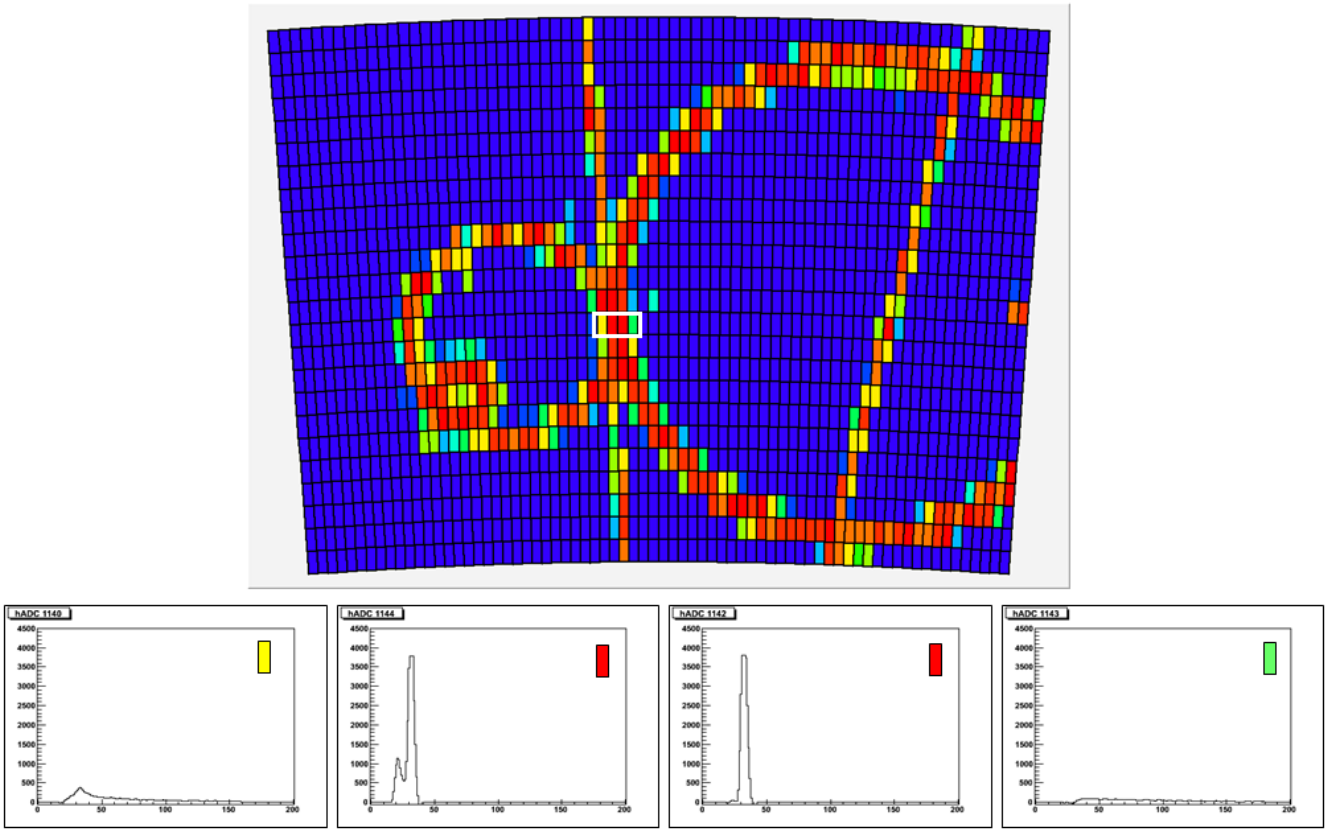


Figure 5.9: [Top] 5 GeV electron event in a resistive Micromegas in magnetic field of 1T at DESY facility. [Bottom] Signals spread on the main and the neighbouring pads are shown for selection of pads

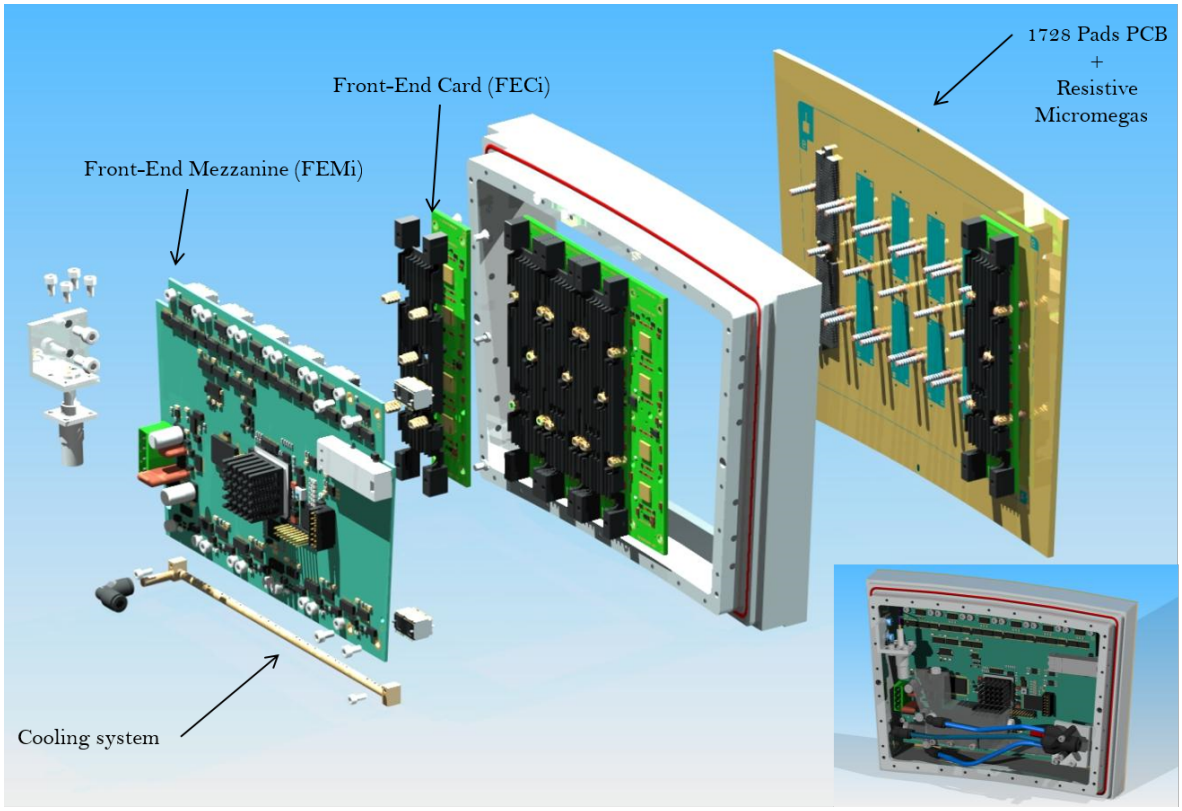


Figure 5.10: Exploded view of the resistive Micromegas module for the LP-TPC with the integrated electronics based on AFTER chips and composed of one Front-End Mezzanine (FEMi) and 6 Front-End Cards (FECi) directly connected to the readout board.

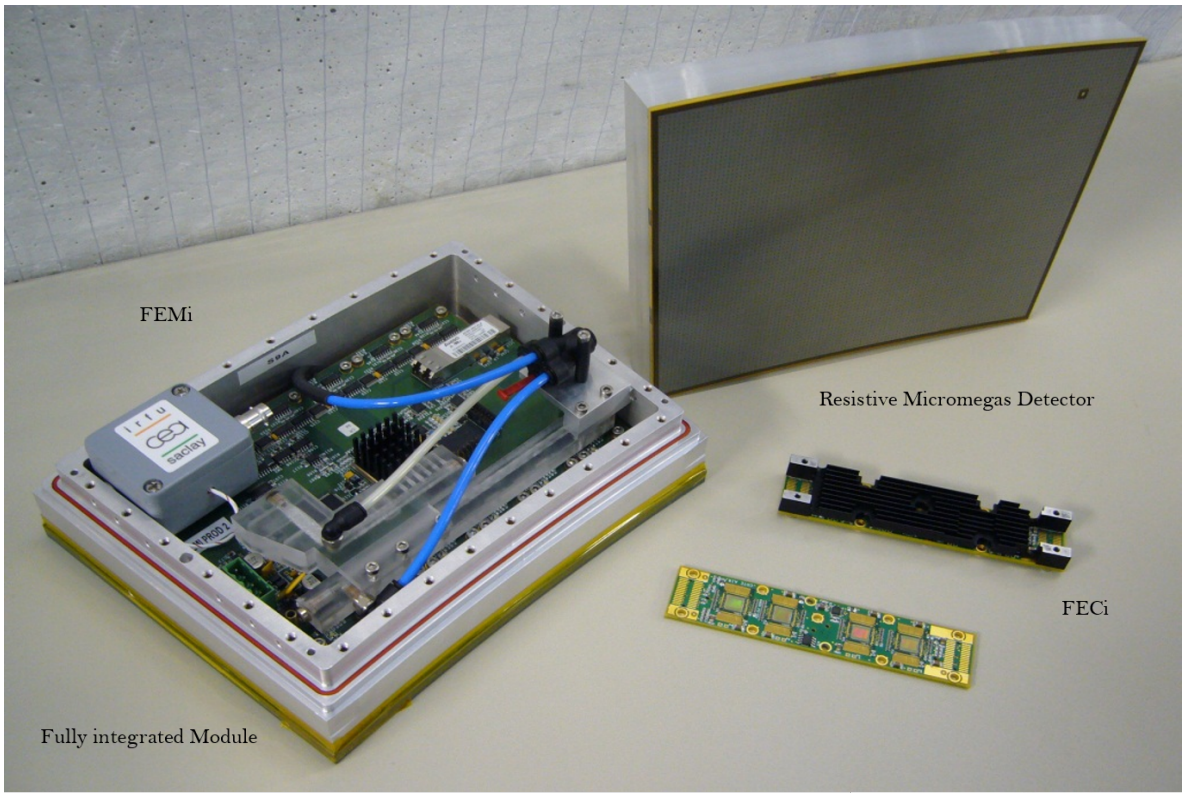


Figure 5.11: Resistive Micromegas module with fully integrated. A FECi is shown with and without cooling plate.

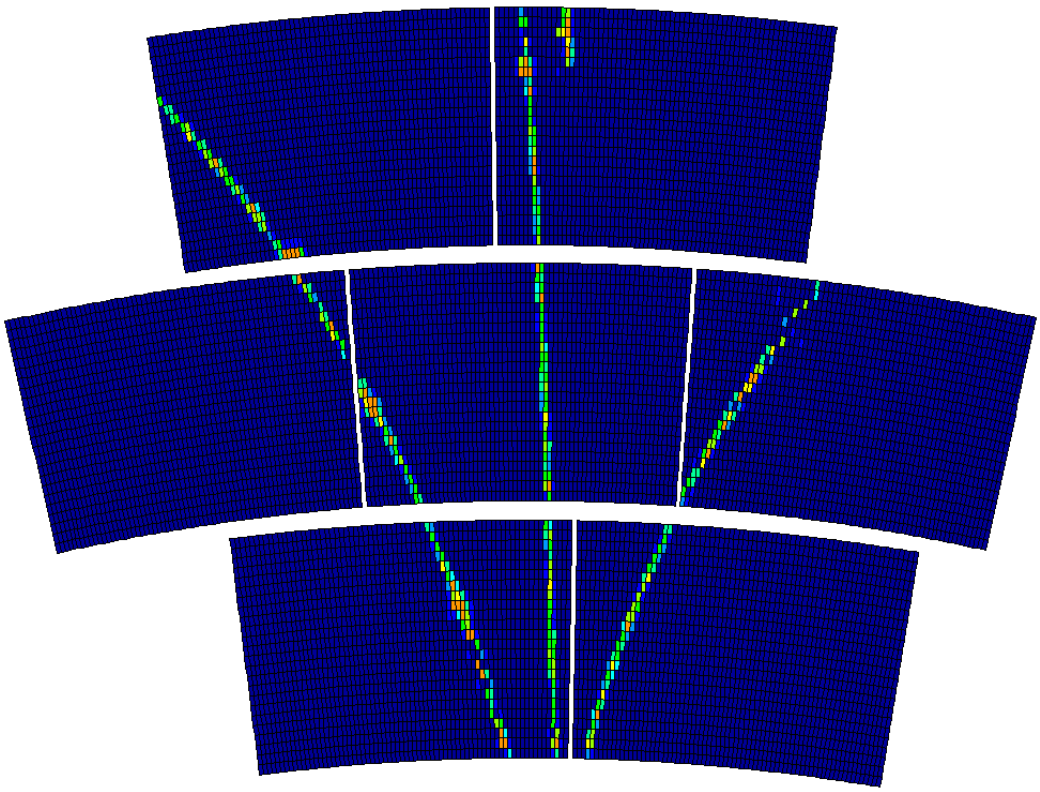

Figure 5.12: Picture of 4 GeV electron beam event recorded by the 7 modules (Run 3050, evt 33).

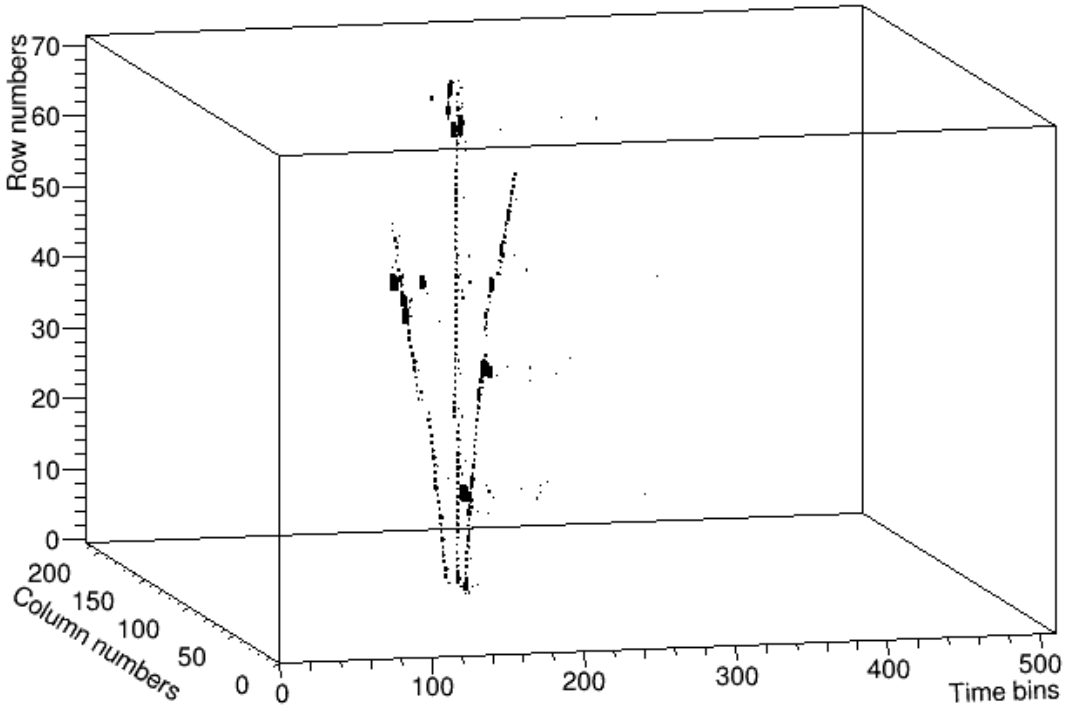


Figure 5.13: 3D picture of 4 GeV electron beam event recorded by the 7 modules (Run 3050, evt 33) same event Fig. 5.12.

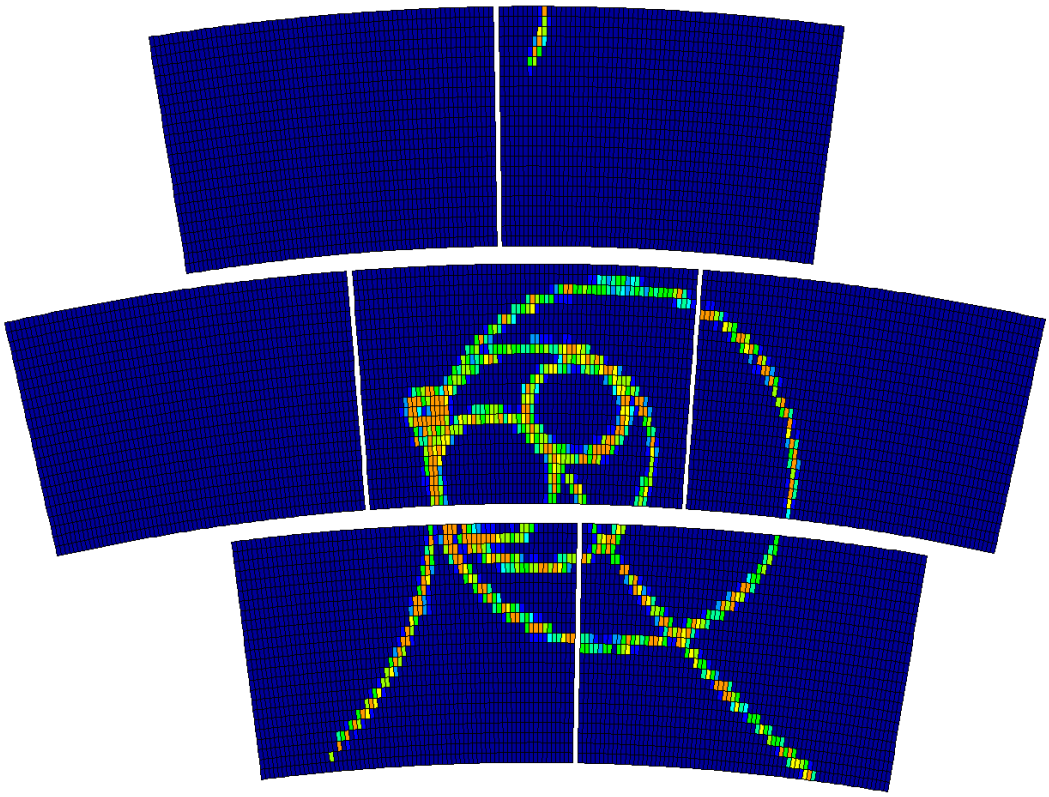

Figure 5.14: Picture of 4 GeV electron beam event recorded by the 7 modules (Run 3036, evt 164).

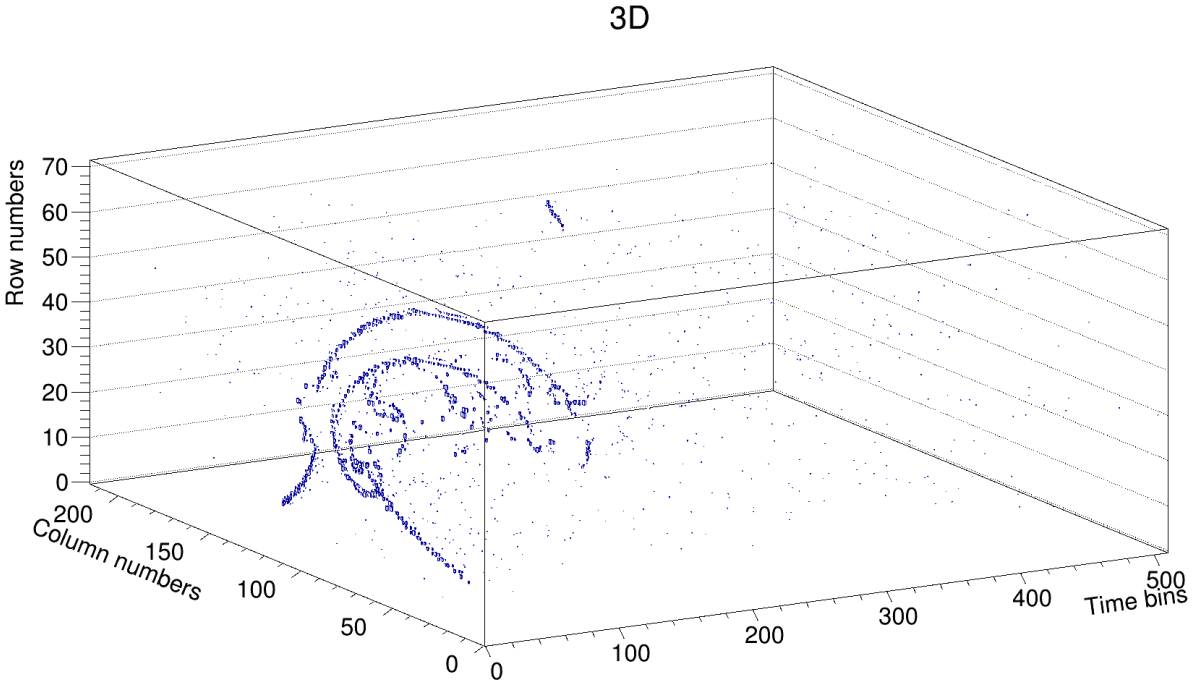


Figure 5.15: 3D picture of 4 GeV electron beam event recorded by the 7 modules (Run 3036, evt 164) same event Fig. 5.14.

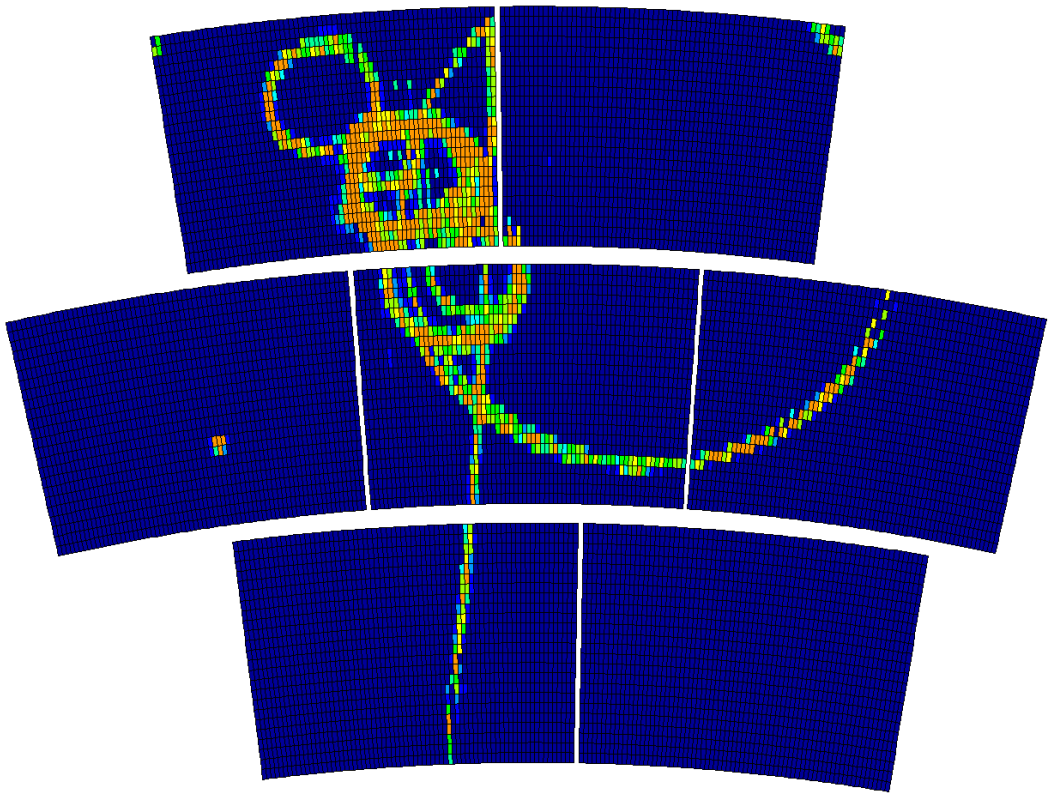

Figure 5.16: Picture of 4 GeV electron beam event recorded by the 7 modules (Run 3036, evt 194).

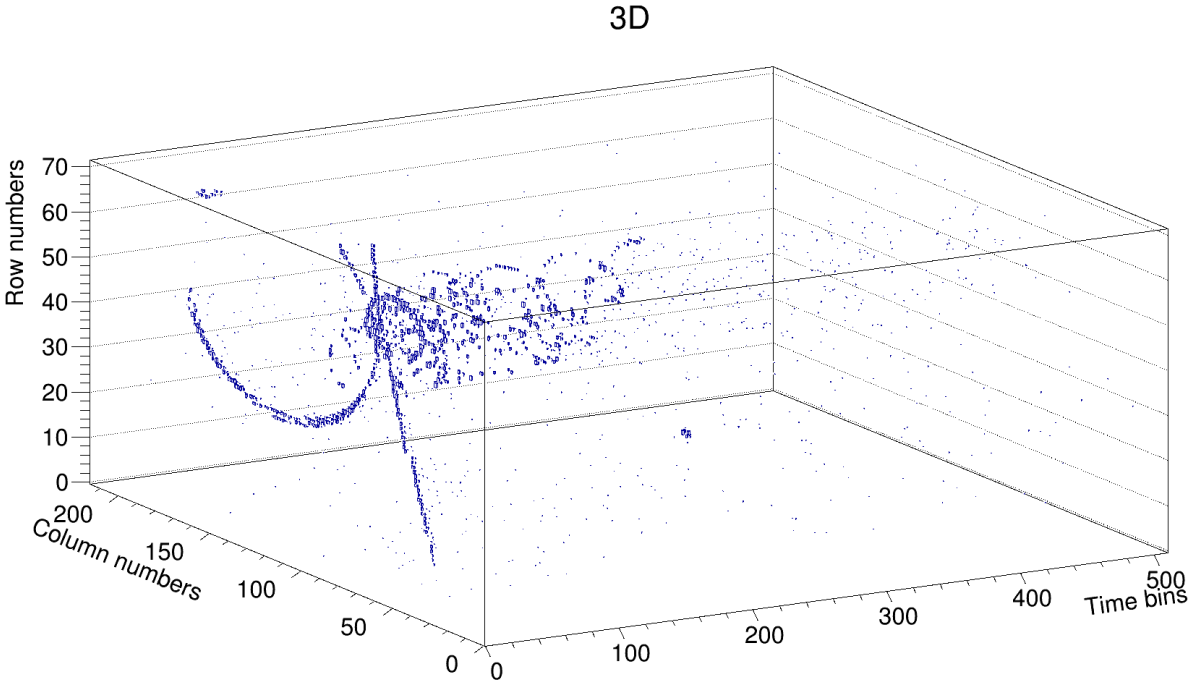


Figure 5.17: 3D picture of 4 GeV electron beam event recorded by the 7 modules (Run 3036, evt 194) same event Fig. 5.16.

### 5.1.4 Data analysis

#### 5.1.4.1 Software framework

Since 2012, multi-modules which have been tested simultaneously with the LP-TPC were analysed using MarlinTPC in the ILCSOFT software framework [105]. This software is carried along by a group at DESY but anyone from the ILC community can contribute in particular to analyse data from its set-up. To implement the MarlinTPC software, the following packages, which are provided as a part of the ILCSOFT, are required:

- **Linear Collider Input Output** (LCIO): each sub-detector group takes data using a specific electronics and produces with it own format then a conversion is done to the LCIO format file [106]. For the resistive Micromegas, the readout electronics is AFTER chip and the data file format is .acq described in [107]. The LCIO software toolkit provides an event data model (EDM) and persistency format for physics and detector simulations. It was developed as a joint effort and has been adopted by all of the detector concepts for both ILC and CLIC. The container classes named collection of data objects store one or more objects of these data classes. The following data classes are used in our analysis.
  - `TrackerRawData`: it is generic class for raw tracker data without any correction applied. CellIDs are used to decode the readout channel and an arbitrary length vector for the ADC values is stored as a complete spectrum, as well as the time bin ID of the first valid sample of spectrum. During our data taking, multiple modules are mounted on the endplate and each module has 1726 channels. Two integer CellIDs are used: CellID1 is used as the physics channel of the pad in each module and CellID2 is used as the module number to denote the identification of the module.
  - `TrackerData`: same as TrackerRawData, except the type of ADC values stored in the vector. The ADC values are calibrated by applying all electronics related corrections 108 like pedestal subtraction and stored as float values in the vector instead of short integer values in TrackerRawData.
  - `TrackerPulse`: extracted from TrackerData to get the reconstructed pulse information. In this thesis, the maximum value in one spectrum is used as the amplitude of this channel and the corresponding time bin is used as the time of this channel.
  - `TrackerHit`: used to store the information of reconstructed measured hits in each row, such as the hit position and error matrix.
  - `Track`: this class stores the reconstructed track parameters and the coordinate of the reference point.
- **GEometry Api for Reconstruction** (GEAR): Gear is a geometry description toolkit for ILC reconstruction software [106]. It uses a XML file to define the geometry parameters of the detector. In our case, it is used to provide the geometry of LP-TPC, as well as the pad size of each Micromegas module.
- **Modular Analysis & Reconstruction for LINear collider** (Marlin): is a C++ software framework for ILC, based on LCIO. The main goal of Marlin is to facilitate the modular development of reconstruction and analysis code. It is implemented by different processors via a XML steering file. The steering file provides the parameters of the active processors and gives the order of the process calls. In each processor, the LCIO collections are read and written as input/output.

- **Modular Analysis & Reconstruction for LINear collider TPC** (MarlinTPC): this framework is a special package based on Marlin common software framework for the TPC at ILC [108]. It provides for the LC-TPC collaboration the simulation, the digitisation, the analysis, and the reconstruction of TPC to handle multiple readout modules on its endplate. To obtain the spatial resolution, the Kalman Filter is used to fit the tracks. One of the goals of MarlinTPC is to ensure that most of the code can be shared among the different groups and the results can be easily compared despite of many different readout structures, electronics, amplification systems used in different groups.

#### 5.1.4.2 Drift velocity

The drift velocity can be determined by changing the beam position in the TPC with the beam perpendicular to the drift direction along $z$.

Fig. 5.18 shows the drift times measured with beam data as function of the drift distance $z$ for several peaking times and at two different drift fields. The time bin was 40 ns for an electronic sampling frequency of 25 MHz. The *low* drift field (140 V/cm) and the *standard* drift field (230 V/cm) give respectively drift velocities of 58 µm/ns and 76 µm/ns in the T2K gas mixture.

At electric field $E_{drift}$ = 230 V/cm, the simulated drift velocity by Magboltz (75.48 ± 0.03 µm/ns for T2K gas with 140 ppm of water and a system pressure of $10^5$ Pa) was in agreement with the measured drift velocity (75.6 ± 0.2 µm/ns).

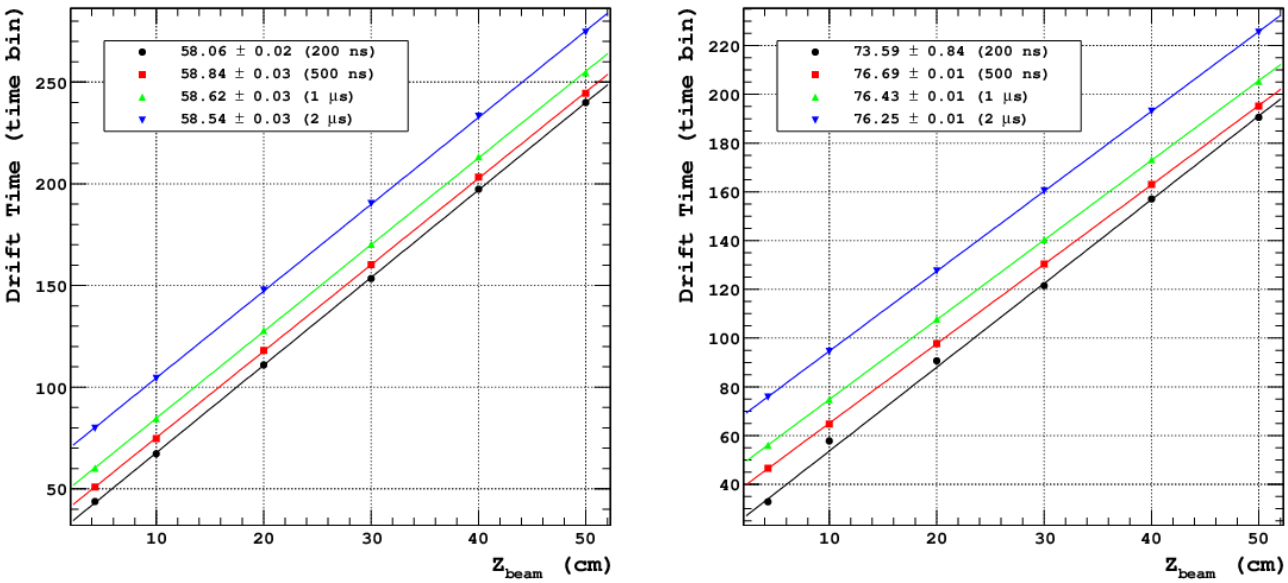


Figure 5.18: Determination of drift velocities (in µm/ns) for several electronics peaking times for two drift field conditions: low drift field condition (140 V/cm) on the left figure and standard drift field condition (230 V/cm) on the right figure. Each time bin is 40 ns for a sampling frequency of 25 MHz.

#### 5.1.4.3 Pad response function calibration

**- Pad response function**

In order to accurately calculate track position on the readout plane, the pad response function (PRF) need to be extracted from the data, for each row and for each $z$. The normalized PRF is fitted by the empirical function $f_Z^{PRF}$. This function is the ratio of two symmetrical $4^{\text{th}}$ order polynomials:

$$f_Z^{PRF}(x; N, a_2, b_2, a_4, b_4) = N\frac{1 + a_2x^2 + a_4x^4}{1 + b_2x^2 + b_4x^4}. \tag{5.1}$$

The coefficients $a_2$, $a_4$, $b_2$ and $b_4$ can be expressed in terms of the full width half maximum $\Gamma$, the base width $\Delta$ of the PRF, and two scale parameters $a$ and $b$ [109]. The track fitting parameters are determined by fitting the PRF to the pad amplitudes for the full event by $\chi^2$ minimization.

$$a_2 = -\left(\frac{2}{\Delta}\right)^2 (1 + a) \tag{5.2}$$

$$a_4 = \left(\frac{2}{\Delta}\right)^4 a \tag{5.3}$$

$$b_2 = \left(\frac{2}{\Gamma}\right)^2 \left[1 - b - 2(1 + a)\left(\frac{\Gamma}{\Delta}\right)^2 + 2a\left(\frac{\Gamma}{\Delta}\right)^4\right] \tag{5.4}$$

$$b_4 = \left(\frac{2}{\Gamma}\right)^4 b \tag{5.5}$$

$$\tag{5.6}$$

All these parameters depend on the drift distance $z$. But more parameters mean more time to find the right parameters for the different drift distance fitting and more correlation between the parameters.

Since 2012, a new function was used as the PRF:

$$f_Z^{PRF}(x, r, w) = \frac{e^{-4\ln 2(1-r)\frac{x^2}{w^2}}}{1 + 4r\frac{x^2}{w^2}} = f_Z^{PRF}(x, a, b) = b^2\frac{e^{-\frac{x^2}{2a^2}}}{x^2 + b^2}. \tag{5.7}$$

It is a combination of a Gaussian with a Lorentzian function. When $r = 1$, the PRF becomes pure Lorentzian and when $r = 0$, the PRF becomes a pure Gaussian. Both the Lorentzian and the Gaussian share the same width parameter $w$. As this function can be rewritten in function of $a$ and $b$ has only two parameters compared to the equation 5.1 the fit parameters lead to a better convergence with easier usage [110].

The PRF procedure is the following, with indexing events $i_e$, columns $i_x$ and rows $i_y$, for a given event in the pad ($i_x$, $i_y$) of centre $y_{i_x,i_y}^{pad}$ has the signal amplitude $A_{i_e,i_x,i_y}$. The normalized signals is defined as $\rho_{i_e,i_x,i_y} = A_{i_e,i_x,i_y}/A_{i_e,i_x}^{Cluster}$, the weighted cluster position is defined as

$$y_{i_e,i_x}^{Weight} = \sum_{i_y} \rho_{i_e,i_x,i_y} y_{i_x,i_y}^{pad}$$

and the track position at column level $y_{i_e,i_x}^{track}$ is set initially as $y_{i_e,i_x}^{track} = y_{i_e,i_x}^{Weight}$ The following three stages process are repeated $n$ times until convergence:

- Step 1: for all $i_e$, $i_x$ and $i_y$ the profile histogram $\rho_{i_e,i_x,i_y}$ projected to $\left[y_{i_e,i_x}^{track} - y_{i_x,i_y}^{pad}\right]$ is built
- Step 2: the profile histogram is fitted with the function $f^{PRF}(x; a_2, b_2, a_4, b_4)$

- Step 3: $y_{i_e,i_x}^{track}$ is fitted minimizing the

$$\chi^2_{i_e,i_x}(y^{track}_{i_e,i_x}) = \sum_{i_y}\left[\frac{\rho_{i_e,i_x,i_y} - f^{PRF}(y^{track}_{i_e,i_x} - y^{pad}_{i_x,i_y})}{\sqrt{\rho_{i_e,i_x,i_y}}}\right]^2$$

During the beam tests the comparison of the PRFs between resistive Kapton and resistive ink technologies (Fig. 5.20) show a better fit of the PRF on the CLK detector data compared to the ink detector at drift distance $z = 5.7$ cm. Figure 5.22 (right), the spatial resolution for resistive ink detector is 130 $\mu$m compared to the 68 $\mu$m with the resistive CLK detector.

**- Pad response function calibration**

Given that no external hodoscope was used during the tests, an estimation of the track position is necessary to calibrate (determine the coefficients of) the PRF per row in function of drift distance $z$. The technique uses an iterative approach which requires an initial guess of the PRF parameters. It relies on internal consistency of the data to ensure an appropriate PRF is found. To start the process, the track position is seek by using the pad with the largest amplitude in each row. A linear least squares fitting is used to fit these positions.

Figure 5.19 describes step by step the procedure used in the iterative calibration process. Initial guesses for the first PRF parameters are required. The initial set of PRF parameters was then used to perform all the track fitting in the run. After tracks have been fit to all the successful events, the values

$$\Delta x = x_{\text{track}} - x^i_{\text{pad}},\ A_{\text{Norm}} = \frac{A_i}{A_{\text{track}}} \tag{5.8}$$

where $x^i_{\text{pad}}$ is the pad position in the row direction and $x_{\text{track}}$ is the track position in this row, $A_i$ is the pad amplitude. $\Delta x$ and $A_{\text{Norm}}$ were recorded for each pad with an amplitude greater than some threshold value, determined by noise. $\Delta x$ is the distance between the $i^{\text{th}}$ pad (located at $x_{\text{pad}}$) and the track (located at $x$ track). $A_{\text{Norm}}$ is the normalized amplitude of the $i^{\text{th}}$ pad, $A_i$ is the amplitude of the $i^{\text{th}}$ pad, and $A_{\text{peak}}$ is the peak amplitude corresponding to

$$A^i_{\text{peak}} = \frac{\sum_j^m \frac{A^i_j f^{\text{PRF}}(x^i_j)}{\sigma^2_{A^i_j}}}{\sum_j^m \frac{\left(f^{\text{PRF}}(x^i_j)\right)^2}{\sigma^2_{A^i_j}}} \tag{5.9}$$

The error $\sigma_{A^i_j}$ was set to the square root of the pad amplitude.

The values $\Delta x$ and $A_{\text{Norm}}$ are then used to create a scatter plot of $\Delta x$ versus $A_{\text{Norm}}$. An example of such a scatter plot is shown in Fig. 5.20. These scatter plots compare the PRF from all events in a run for data taken with both resistive CLK module and resistive ink module.

From the fit new PRF parameters and $\chi$new$^2$ value of the fit are calculated with the following formula:

$$\chi^2_{\text{track}} = \sum_i^n \chi^2_{\text{row}} = \sum_i^n \sum_j^m \left[\frac{A^i_j - A^i_{\text{peak}} f^{\text{PRF}}(x^i_j - x_{\text{track}})}{\sigma^2_{A^i_j}}\right]^2 \tag{5.10}$$

To determine whether the new parameters better describe the data $\chi^2_{\text{new}}$ is compared to the total chi-square value of the previous iteration $\chi^2_{\text{old}}$.

If $\chi^2_{\text{new}} < \chi^2_{\text{old}}$ then the function $f^{\text{PRF}}$ is defined by the last parameter obtained by the fit and these parameters are used as the initial guess of the next iteration. Otherwise, if $\chi^2_{\text{new}} > \chi^2_{\text{old}}$, the iterative process is ended and the parameters become the properly calibrated PRF parameters. In the case of the first iteration where no $\chi^2_{\text{old}}$ value is available, the comparison is skipped and a second iteration is automatically conducted.

The PRF functions parameters depend on the drift distance $z$. In particular, the PRF is expected to become wider with increasing of the drift distance due to diffusion and charge dispersion.

#### 5.1.4.4 Alignment

Distortions are caused by the misalignment of the position of modules, the misalignment between the axis of the magnetic and electric fields, and the local electric field imperfection at the junction of the modules and the frame of the endplate.

Figures 5.25, 5.26 and 5.27 illustrate the effects before and after alignment for CLK modules in 2013 beam tests. The residuals in $r\phi$ left after biais correction are still around 250 µm.

The beam passes through three modules and each module has 24 rows. The transfer between two modules is clearly seen. The distortions have a 'S' shape and are caused by the misalignment of the position of modules. The misalignment is between the axis of the magnetic and electric fields, and the local electric field imperfection at the junction of the modules and the frame of the endplate. The residuals $\Delta_{r\phi}$ is less than 50 µm except on the edge of a module which should come from a defect in the TPC enplate.

The distortion is influenced by $E \times B$ effect which is more clearly significant for the residuals $\Delta_{r\phi}$ in the 2015 data where the mesh was not grounded.

#### 5.1.4.5 Biais correction

The residual is the deviation of the measurement hit position in one row with respect to the position of the real track crossing this row. It can be separated into two parts: the symmetrical deviation part and the asymmetrical part. The symmetrical part includes the diffusion of the electrons passing a certain drift distance and the measurement error. In this part, the average deviation of all events is approximated to zero. The asymmetrical part is caused by the imperfect construction of the resistive anode due to local variations in the RC parameters. Each row has a position dependent systematic error associated with its track position determination. A bias correction is calculated to account for this systematic error before the final resolution of the detector is measured. Bias corrections are calculated separately for each row. They are calculated as a function of position along a row and are made up of averaged row residuals. To get the value used for the bias correction, the row residual and the fitting track are required. The row residual is calculated by

$$\Delta x = x_{\text{track}} - x_{\text{hit}} \tag{5.11}$$

where $x_{\text{hit}}$ is the hit position measurement in this row and $x_{\text{track}}$ is the corresponding track crossing position in this row in one event. The $x_{\text{track}}$ is calculated by the equation 6-0-5 and the is calculated by minimizing the chi-square in the equation 5.10 and $x_{\text{hit}}$ minimizing the following equation

$$\chi^2_{\text{track}} = \sum_j^m \left[ \frac{A_j - A_{\text{peak}} f^{\text{PRF}}(x_j - x_{\text{hit}})}{\sigma^2_{A_j}} \right]^2 \tag{5.12}$$

Then, the row residual $\Delta$ with the track $x_{\text{track}}$ of each event is filled in a profile histogram for each row. Figure 6-5 gives an example of the profile histogram. The Y-axis displays the mean value of the row

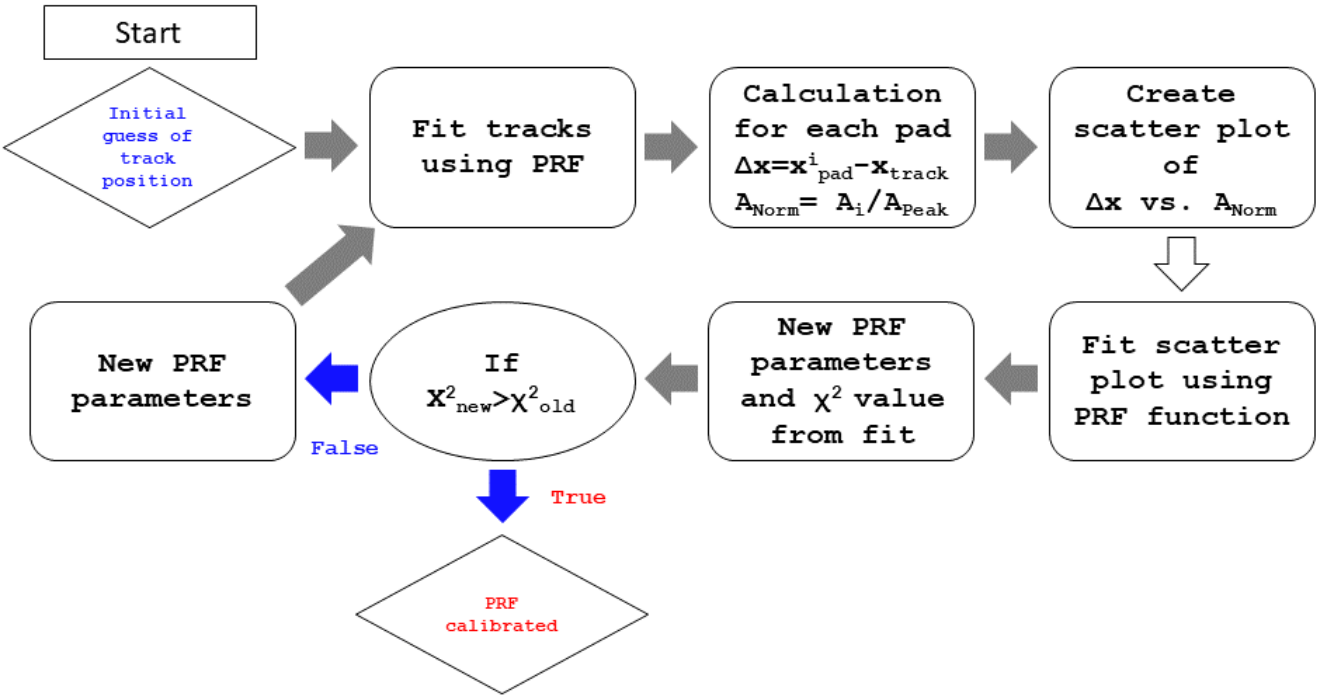


Figure 5.19: Procedure for PRF calibration.

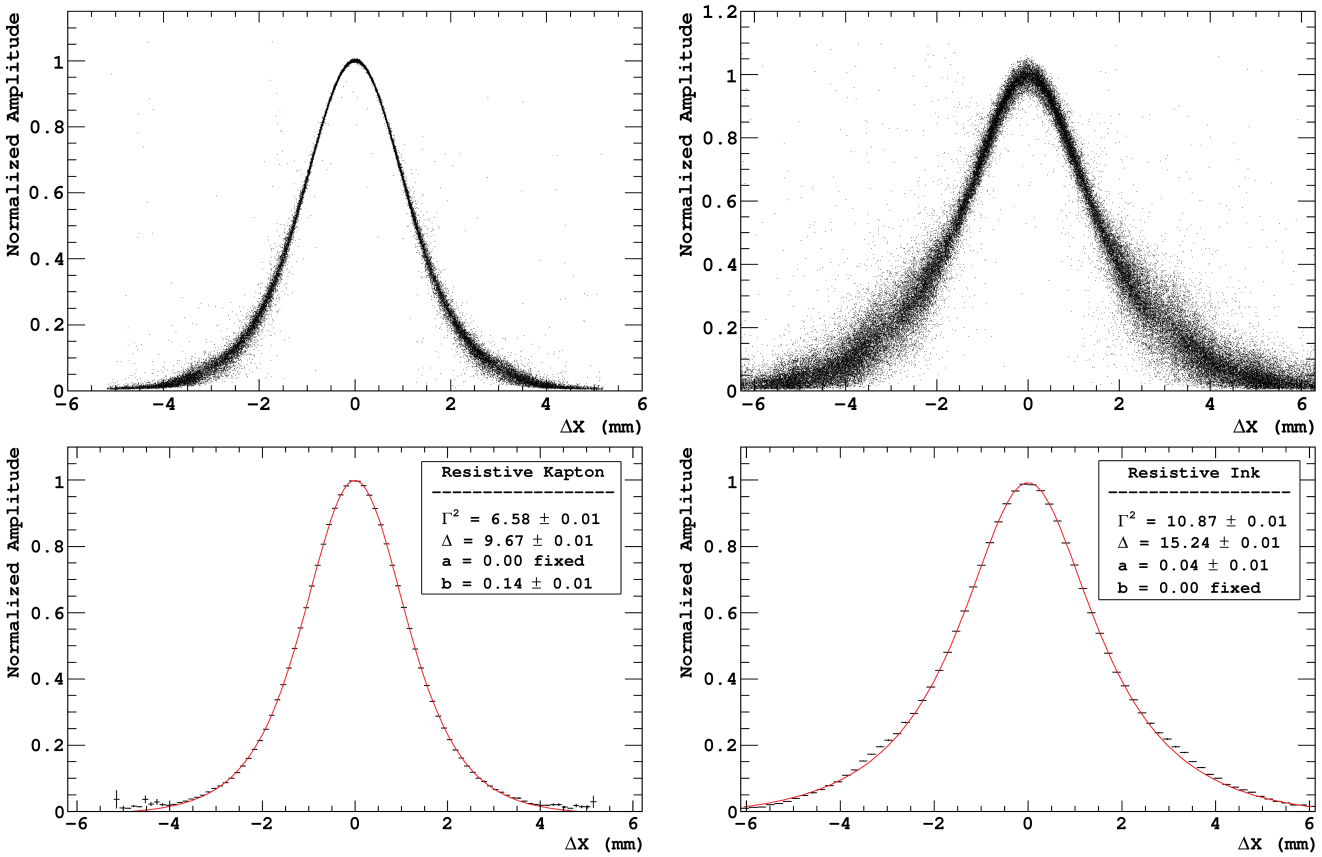


Figure 5.20: Comparison of the pad response functions (PRFs) from resistive bulks with a magnetic field of 1T, with Carbon-loaded kapton (left figure) and resistive ink (right figure) technologies.

residual when a track crosses the corresponding position in this row. This mean value is used as the value of the bias correction. Then, the equation to calculate the measurement hit $x_{\text{hit}}$ becomes as following from the equation Eq:ChiHit.

$$\chi^2_{\text{track}} = \sum_j^m \left[ \frac{A_j - A_{\text{peak}} f^{\text{PRF}}(x_j - x_{\text{hit}} + \text{Biais(track)}_i}{\sigma^2_{A_j}} \right]^2 \tag{5.13}$$

where $\text{Biais(track)}_i$ is the correction function of this row obtained for the profile histogram.

#### 5.1.4.6 Spatial resolution determination

The spatial resolution is defined as the deviation between the real track and the measurement hit position extracted from the PRF. No external equipment was available to precisely measure the track position, so a fitting track is used to estimate the spatial resolution. After the bias correction, the residual for each row is calculated in two ways: $\Delta_{\text{in}}$ is called the inclusive track fit residual and $\Delta_{\text{ex}}$ is called the exclusive track fit residual. For a test row, the first way is to fit track including the test row and the second way is to fit track excluding the test row. The inclusive and exclusive residuals are calculated using the following equation respectively:

$$\Delta_{\text{in}} = x^{\text{in}}_{\text{track}} - x_{\text{hit}} \Delta_{\text{ex}} = x^{\text{ex}}_{\text{track}} - x_{\text{hit}}. \tag{5.14}$$

The residual $\Delta$ of the test row is calculated by the following equation taken from [111]:

$$\Delta = \frac{\Delta_{\text{in}}}{|\Delta_{\text{in}}|} \cdot \sqrt{\Delta_{\text{in}} \times \Delta_{\text{ex}}}. \tag{5.15}$$

The standard deviation from Gaussian fit of the distribution of the residual $\Delta$ is used to estimate the spatial resolution of the test row.

To get the general evaluation of the spatial resolution of the detector, a weighted average of rows is used:

$$\sigma = \frac{\sum \sigma_i \times \frac{1}{\delta\sigma_i^2}}{\frac{1}{\delta\sigma_i^2}} \tag{5.16}$$

where $\sigma_i$ is the spatial resolution of row $i$ and is the associated $\delta\sigma_i$.

The spatial resolution are plot as function of the drift distance $z$ and can be fitted by the following function:

$$\sigma = \sqrt{\sigma_0^2 + \frac{C_{\text{d}}^2 \times z}{N_{\text{eff}}}} \tag{5.17}$$

Where $\sigma_0$ is the spatial resolution at $z = 0$, $C_{\text{d}}$ is the transverse diffusion coefficient and $N_{\text{eff}}$ is the effective number of electrons.

#### 5.1.4.7 Field distortions

Figure 5.28 and 5.29 shows respectively the residuals $\Delta_Z$ and $\Delta_{r\phi}$ without and with magnetic field after bias correction using 3 MΩ/□ DLC resistive Micromegas. The one from 2015 has the mesh polarized by the power supply and the DLC grounded, while the one from 2018 has the DLC polarized by the power supply and the mesh grounded. In this configuration, the field between the resistive layer and the readout pad is not zero which improve the signal collection in the pad. The field in the TPC drift region is also improved allowing specific gain for each detector.

#### 5.1.4.8 dE/dx resolution

By using tracks passing through three modules, the $dE/dx$ can be evaluated. The $dE/dx$ resolution is shown in Fig. 4.3 as a function of track length. For the ILC TPC size, the requirement is 5%.

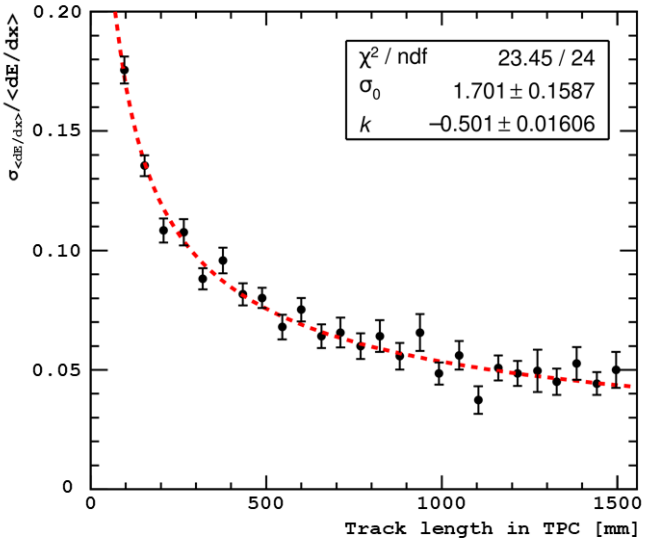


Figure 5.21: The dE/dx resolution as a function of the track length for 5 GeV electrons. The red line is a power law.

| **Module** | **R** (MΩ/□) | $\mathbf{B}_{\text{field}}$ (T) | **Peaking time** (ns) | **Resolution** $\sigma_{r\phi}$ (µm) | $\mathbf{N}_{\text{eff}}$ |
|---|---|---|---|---|---|
| CLK4 | 3 | 0 | 200 | 49.3±5.2 | 37.4±0.4 |
| CLK5 | | | | 55.7±1.1 | 37.8±0.1 |
| CLK | 5 | | 500 | 53.6±4.9 | 37.5±0.4 |
| | | 1 | | 61.0±0.5 | 38.1±0.4 |
| Ink | 3 | | | 89.2±2.2 | 49.8±3.5 |
| DLC | | | 200 | 57.4±1.5 | 24.7±0.6 |

Table 5.2: Summary of the spatial resolution results

Tab. 5.2 summarises the spatial resolutions obtained from the data analysis taken with various resistive technologies during the DESY beam tests. Each technology reaches a spatial resolution below 100 µm at zero drift distance, the requirement for the ILC-TPC. An extrapolation at a drift distance of 2.35 m in 3.5 T magnetic field (ILD-TPC) gives the single hit resolutions $\sigma_{r\phi} \leq 100$ µm and $\sigma_z \simeq 400$ µm.

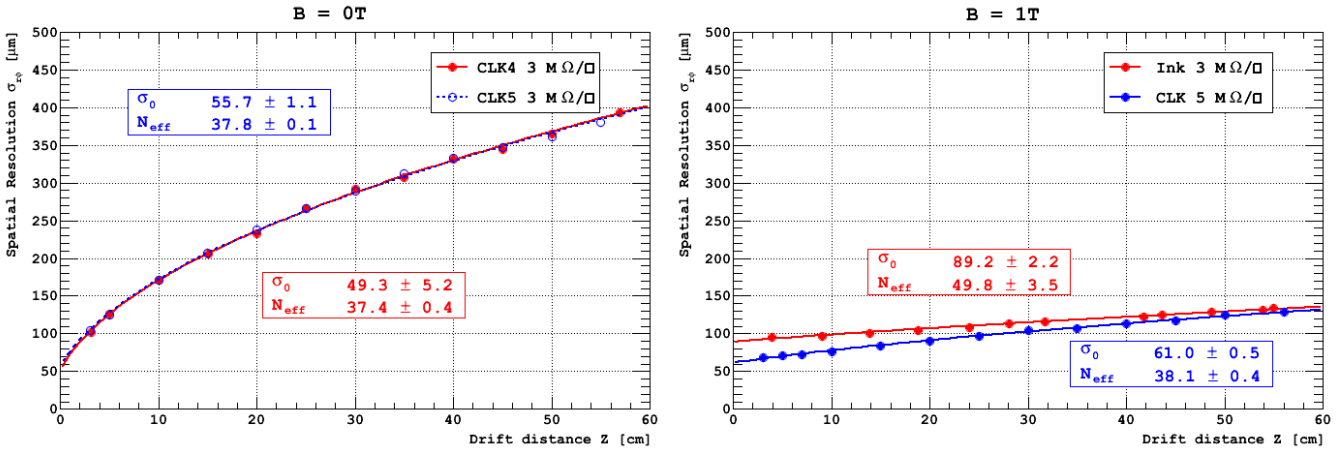


Figure 5.22: Spatial resolution $\sigma_Z$ in function of drift distance for two resistive CLK modules (3 MΩ/□) at B = 0T [Left]. Same for one resistive ink module (3 MΩ/□) and resistive CLK module (3 MΩ/□) at B = 1T.

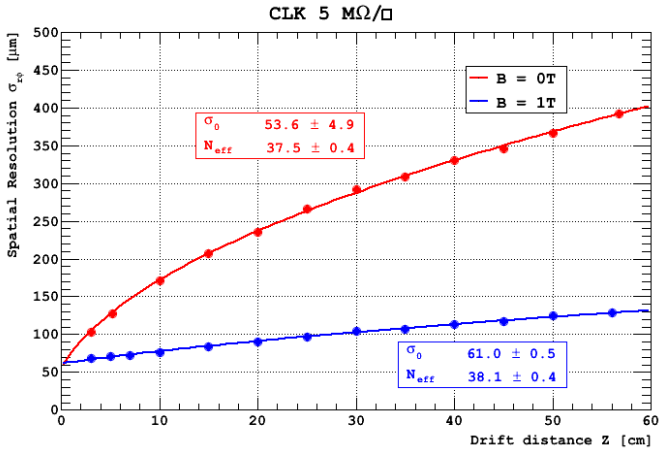


Figure 5.23: Spatial resolution with magnetic field (1 T) in blue and without magnetic field in red for CLK Micromegas.

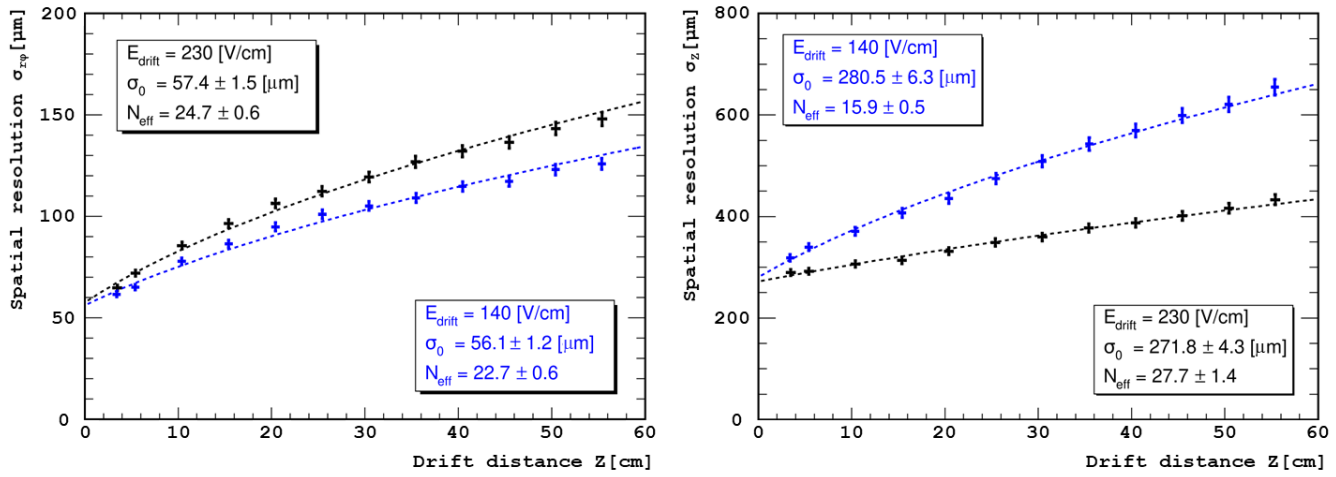


Figure 5.24: Spatial resolution in $z$ and $r\phi$ as a function of the measured drift length, in black for a drift field of 230 V cm$^{-1}$ and in blue for 140 V cm$^{-1}$.

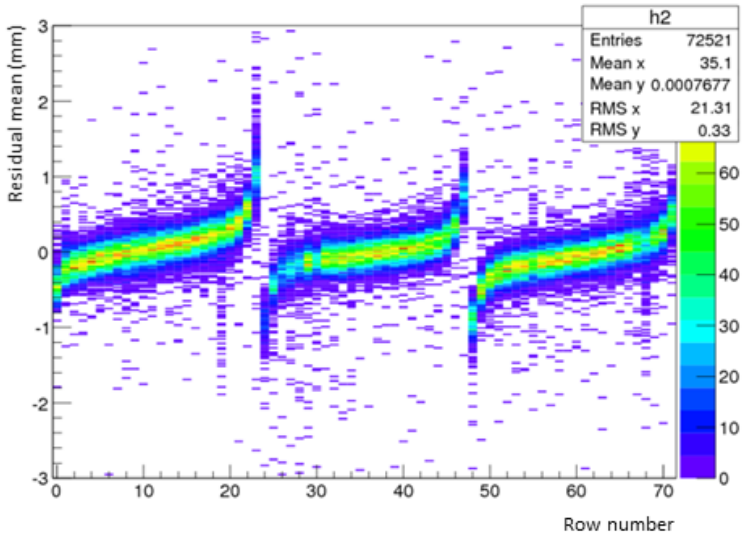


Figure 5.25: Displacement before alignment.

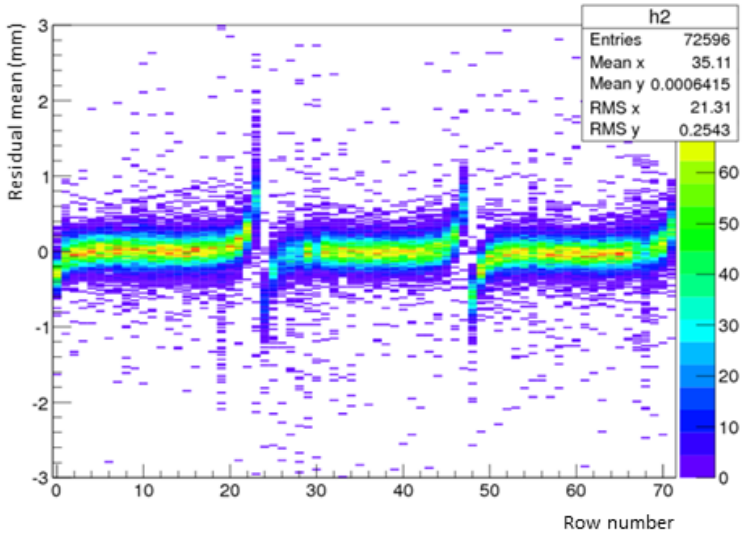


Figure 5.26: Displacement after alignment.

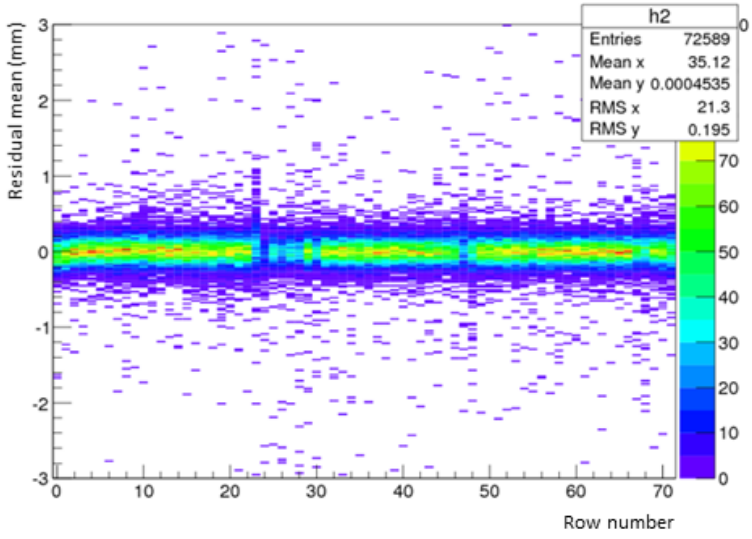


Figure 5.27: Displacement after alignment and bias correction.

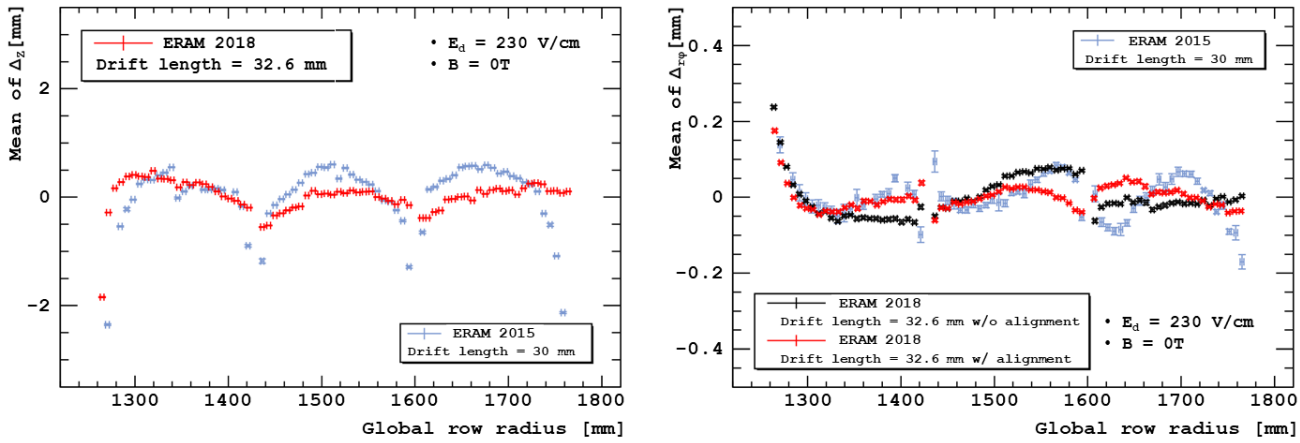


Figure 5.28: Distortions B=0T with beam around $z \simeq 3$ cm. [Left] Residuals $\Delta_Z$ and [right] residuals $\Delta_{r\phi}$ for DLC resistive Micromegas of 2015 in blue and 2018 in red with alignment (and without alignment in black).

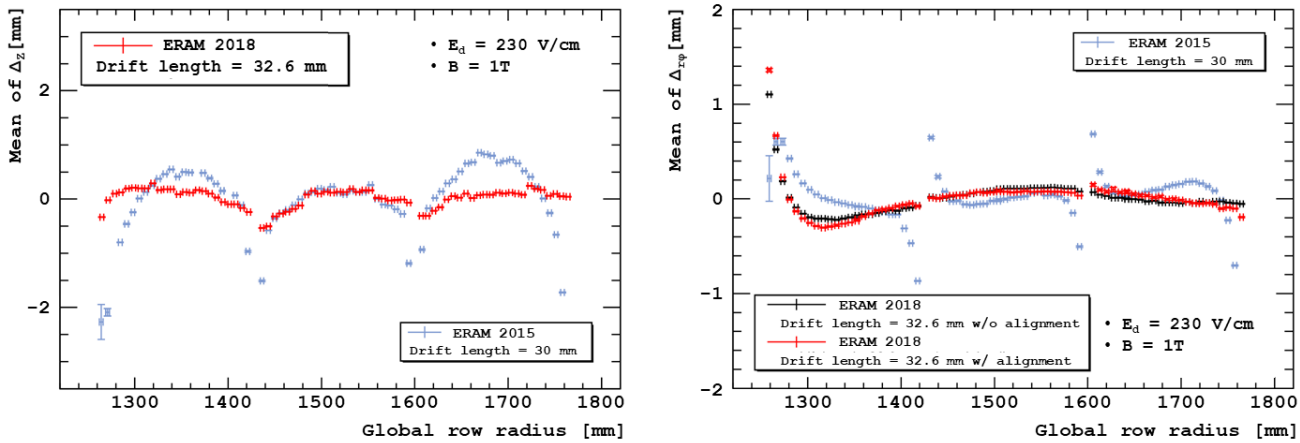


Figure 5.29: Distortions B=1T with beam around $z \simeq 3$ cm. [Left] Residuals $\Delta_Z$ and [right] residuals $\Delta_{r\phi}$ for DLC resistive Micromegas of 2015 in blue and 2018 in red with alignment (and without alignment in black).

### 5.1.5 The Octopuce: single electron efficient TPC

In close collaboration with Nikhef (National Institute for Nuclear Physics and High Energy Physics) in Amsterdam, a board able to read eight InGrid TimePix chips was designed, built and named *Octopuce*. A specific module which handle a mother PCB glued on a frame that can be mounted on the endplate of the LCTPC prototype. This mother PCB carries connection for the power supply, the chips signal and a daughter PCB where 8 TimePix + Ingrids chips (see Sec. 3.2.3.1) are wired bonded and a guard plate to provide a uniform electric field in the TPC (see Fig. 5.31.a-d).

The MUROS-2 (Medipix-2 re-Usable Read-Out System) [112], an interface between the Medipix-2/TimePix PCB and a National Instrument DIO-653X PC card, was used to interact with the TimePix chips but it could only read out eight chips. The MUROS-2 was produced at Nikhef (see Fig. 5.31.e).

The data from the chips is shift from one chip to the next one. If one chip is damaged it can be

bypassed. This is not possible for the first and the last chip. Eight InGrid chips were glued and bonded on a second daughter PCB. The InGrids were made by University of Twente. The HV connections of the InGrids were additionally fixed with a drop of silver glue (see Fig 5.31.f).

Data taking in a specific test beam campaign has been done in December 2010. It was the first 500k pixel TPC operating in 1T magnetic field in T2K gas. Some events are shown in Fig. 5.32 at 1 and 20 cm drift distance.

The track length was computed in order to obtain the distribution of the number of primary electrons per track centimeter shown on Fig. 5.30. A Landau distribution was used to fit the distribution given a Most Probable Value of MPV = 28.09 ± 0.13 $cm^{-1}$ compared with the tabulated values for the Ar-iC4H10-CF4 (95:2:3) gas mixture (27.44) which differs only of 2%.

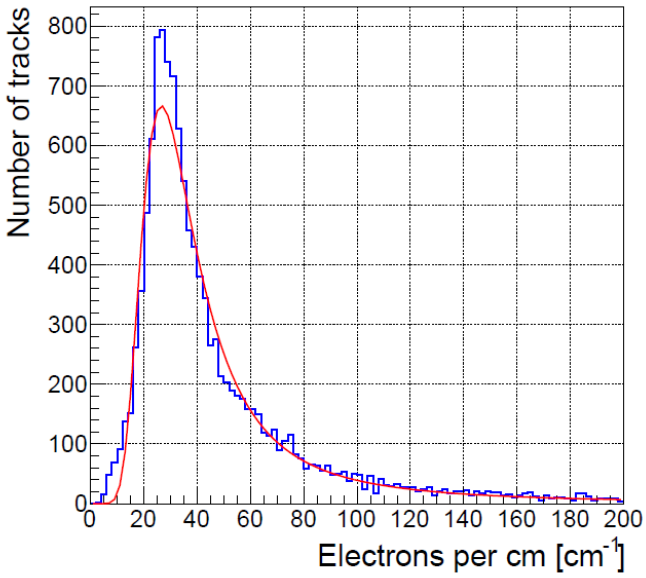


Figure 5.30: Distribution of the number of primary electrons per centimeter fitted by a Landau.

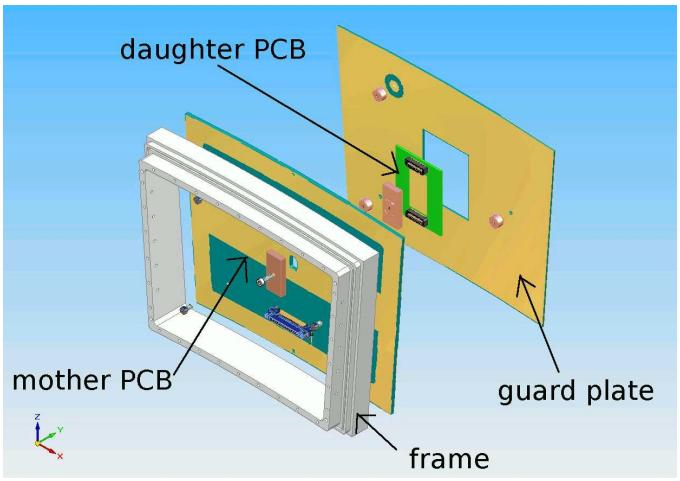


(a)

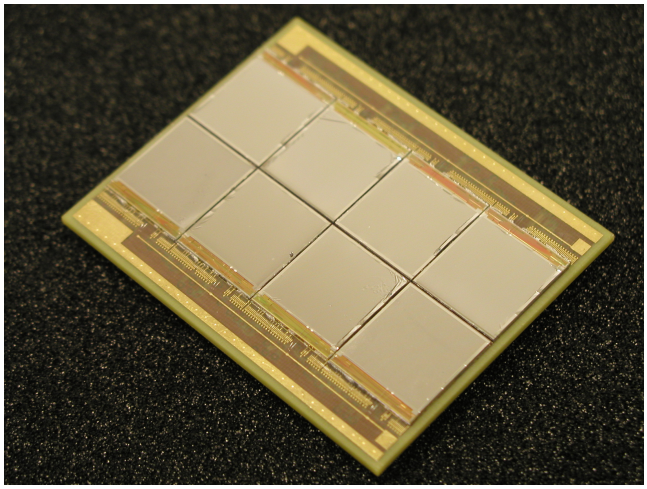

(b)

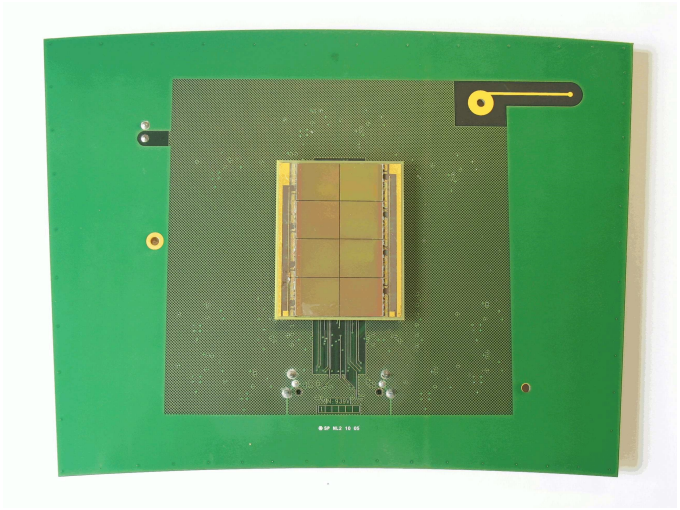

(c)

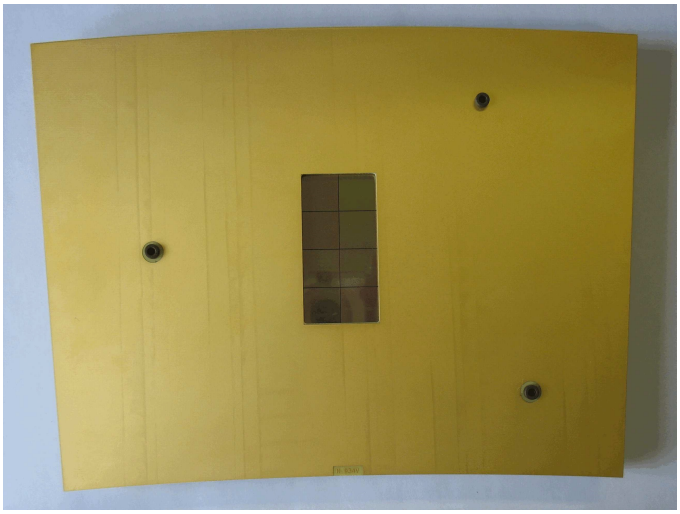

(d)

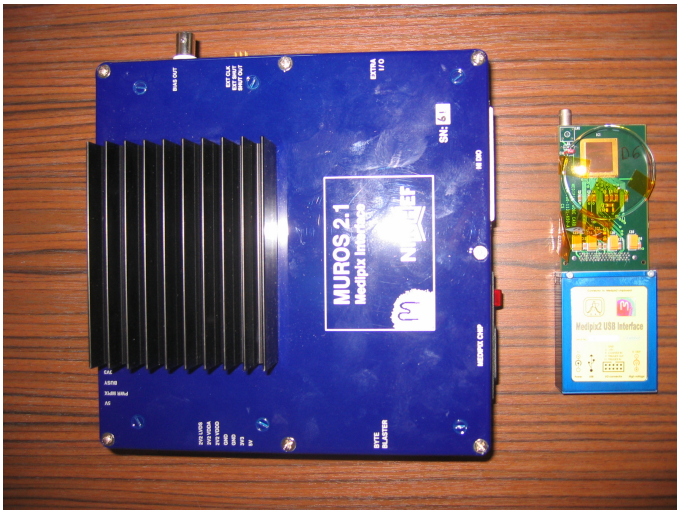


(e)

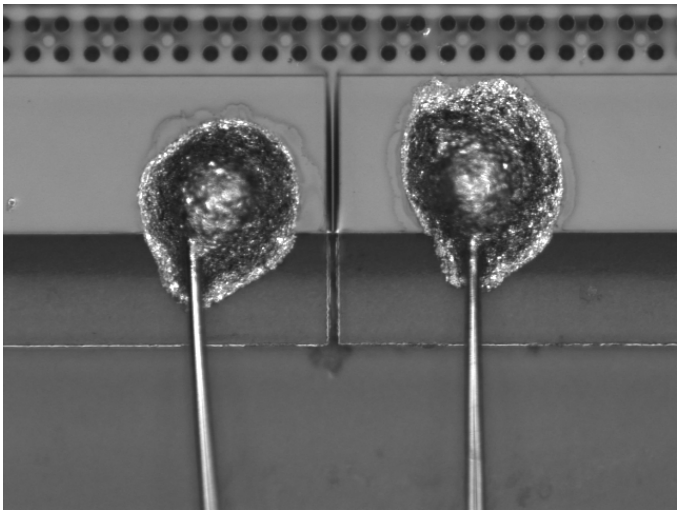

(f)

Figure 5.31: (a) Drawing of the full setup of the Octopuce module. (b) Daughter board with 8 TimePix chip + InGrids wire bonded. (c) Mother board and daughter boards connected together. (d): Guard plate mounted on the mother PCB, the daughter PCB and the eight chips are visible in the window in the centre. (e) Interface MUROS 2.1 used to connect the module to the computer via a NI card. (f) HV wire bonds on the grid of one of the InGrids additionally fixed with a drip of silver glue.

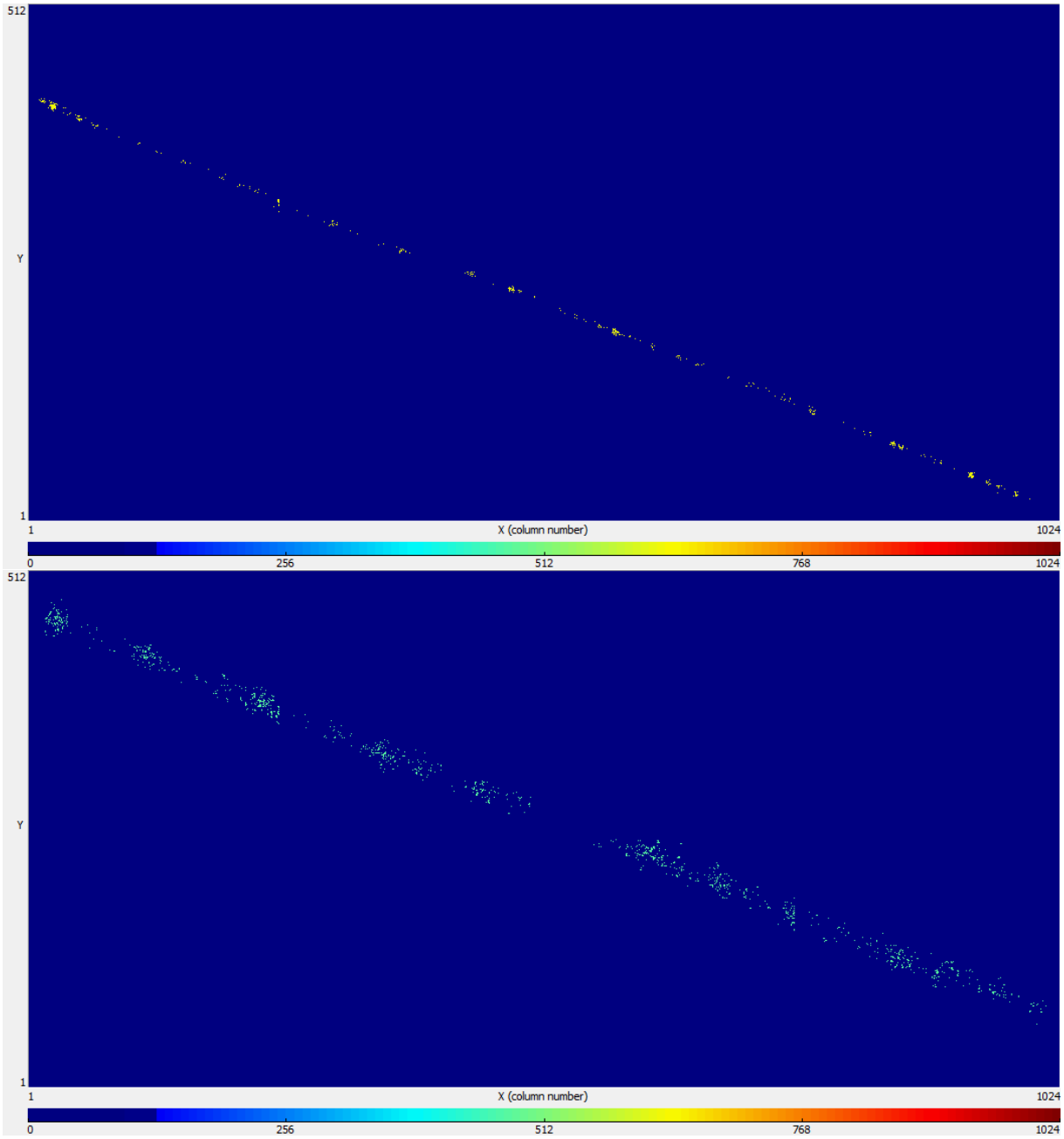


Figure 5.32: Octopuce events taken at DESY with 5 GeV electron beam at 1 cm [top] and 20 cm [bottom] of drift distance in the LP-TPC.

## 5.2 CLAS12 Micromegas Trackers

### 5.2.1 Spectrometer for hadronic physics

The CEBAF Large Acceptance Spectrometer for operation at 12 GeV beam energy (CLAS12) [113] is an experiment in Hall B at Jefferson Laboratory. Its aim is to study electro-induced nuclear and hadronic reactions. This spectrometer provides efficient detection of charged and neutral particles over a large

fraction of the full solid angle from reactions between hydrogen nuclei from a target and a 11 GeV electron beam at luminosities of $10^{35}$ $cm^{-2}s^{-1}$ over a wide kinematic range. For this reason the spectrometer has been divided into two parts:

- a central tracker for the detection of baryons with moderate momentum and polar angle $\theta$ between 35 and 125°;
- a forward tracker to cover the region between 5 and 35°.

The Hall B of the Thomas Jefferson National Accelerator Facility (commonly called Jefferson Lab or JLab [114] in Virginia, USA) aims to test theories of nucleus structure as Generalized Partons Distribution (GPD) theories or quarks and hadrons confinement theories by using a new CEBAF (Continuous Electron Beam Accelerator Facility) Large Acceptance Spectrometer in a 12 GeV electron beam energy (CLAS12).

#### 5.2.1.1 Micromegas Vertex Tracker

The Micromegas Vertex Tracker (MVT) was designed to improve the baseline design of the of the CLAS12 spectrometer. The MVT is made of a Barrel Micromegas Tracker (BMT) and a Forward Micromegas Tracker (FMT). The BMT consists of six layers of cylindrical resistive bulk Micromegas detectors, three layers with strips along the beam axis (Z strips) that provide information about the azimuthal angle of the particle and three layers with circular strips (C strips) perpendicular to the beam axis that significantly improve the polar angle determination.

The FMT consists of six flat resistive bulk Micromegas disks stacked together. The disks are all identical and assembled with a 60°rotation between them, giving 3 angles of strips (0°, 60°, and 120°). The FMT is attached to the end flange of the BMT. The Fig. 5.33 shows a complete transparent view of the MVT which has been entirely designed and built under the responsibility of the the CEA/Irfu team.

#### 5.2.1.2 Forward Micromegas Tracker

I was responsible of the design, the production and the installation of the FMT.

Each Micromegas detector of the FMT is a 450 mm diameter disk with a 50 mm diameter hole and an active area of 1024 parallel readout strips (525 µm pitch with 120 µm between two strips). The specification was to have as low as possible radiation length. For FMT is was estimated to be less than 1% $X/X_0$ ($0.15X/X_0$ per detector) with a high particle rate of ∼30 MHz.

The active area of the FMT is divided in two independent resistive strips zones, the inner ring with $86 < \varnothing < 166$ mm and the outer ring with $168 < \varnothing < 380$ mm. Each of the two parts can be independently energized so that the inner region can be turned off in the case of a very high flux of charged particles.

The distance between the readout strips of two consecutive disks is 10.5 mm. Each disk consists of an assembly of two 0.2-mm-thick PCBs glued on a 2mm Rohacell foam backing to form the readout plane and a 0.2 mm PCB for the drift plane glued on two cylindrical frames that define the 5 mm gas volume. The inner frame is made of PEEK (thermoplastic resin: polyether ether ketone) and the outer frame of aluminium. Both define the chamber and are attached to the readout plane using stainless steel screws. High voltage connections and associated filter circuits are located on the disk edge diametrically opposed from one another. The signals are read out via 16 Samtec MEC8 connectors.

Since the magnetic field is parallel to the drift field in the FMT, the drift electrons are not affected by the Lorentz angle effect. In order to improve the timing resolution, a mixture of 80% argon + 10%

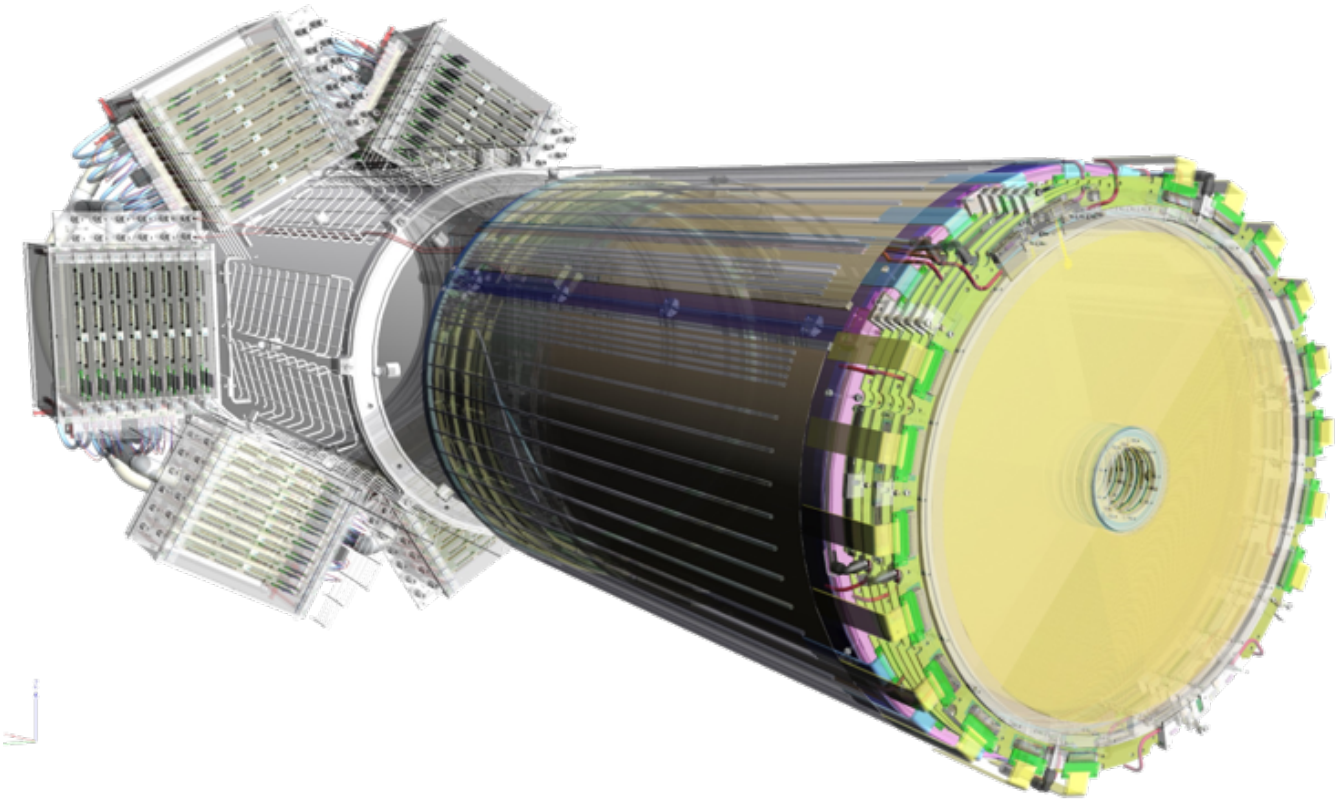

Figure 5.33: Clas12 Micromegas Tracker designed and built at Irfu.

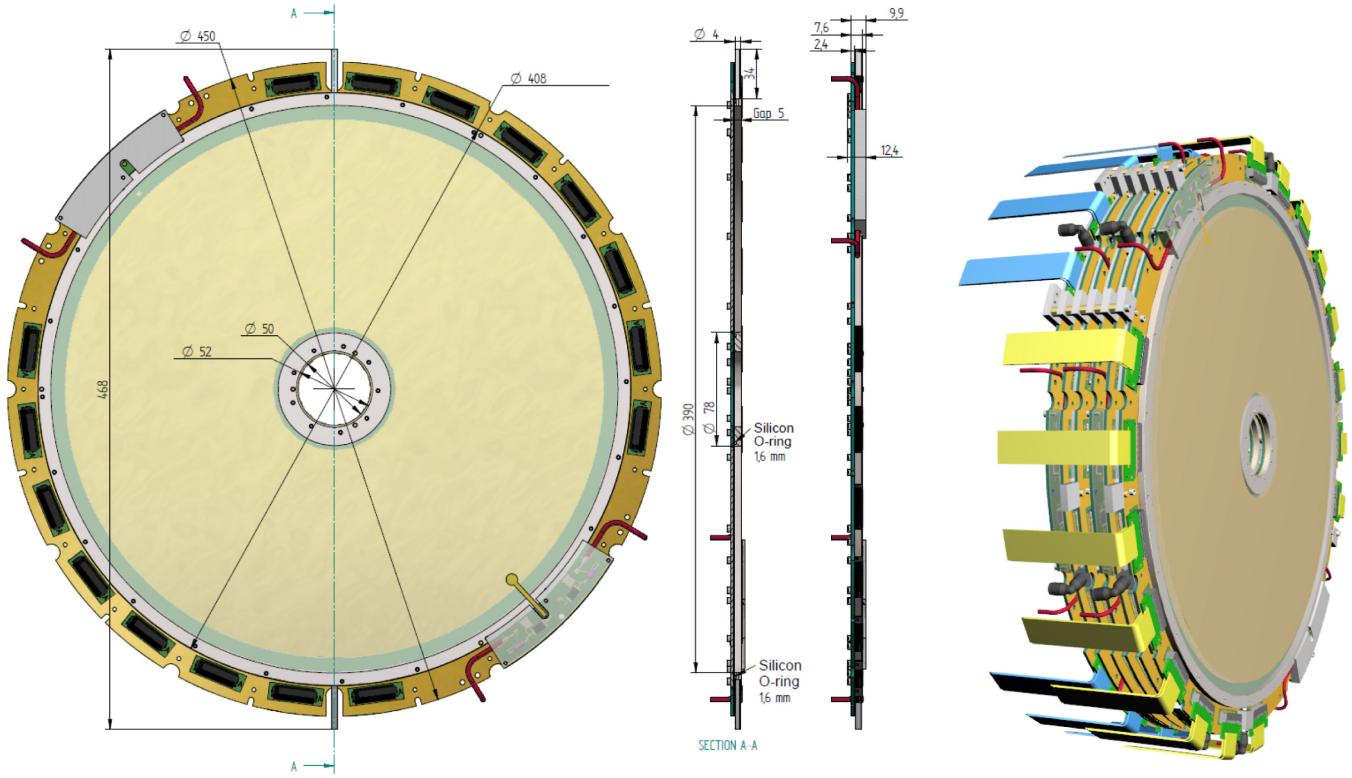


Figure 5.34: CLAS12 Forward Tracker made of six identical resistive bulk Micromegas disks assembled together.

isobutane + 10% $CF_4$ allows for an increase of the drift velocity compared to 90% argon + 10% isobutane mixture used in the BMT.

#### 5.2.1.3 The Forward Tagger Tracker

I was also responsible of the design, the production and the installation of the CLAS12 Forward Tagger (FT-Trk). The FT-Trk consists of two double-layers of Micromegas detectors are located in front of the FT-Hodo. Having two gaseous detectors permit an efficient background rejection and track reconstruction with a low material budget. Each layer is composed of a double-sided Micromegas disk built on a common printed circuit board (PCB). The first layer is rotated to the second layer of 60°. For each layer, the strips of one side is perpendicular to the other side strips. The track, perpendicular to the beam $z$-axis) is given in $(x, y)$ coordinates. To limit the number of electronics channels to 768, the pitch chosen was at 500 µm, corresponding to a spatial resolution better than 150 µm. The drift length is 5 mm and the amplification gap 128 µm. The two double-layers, centered on the beam axis, cover polar angles from 2.5 to 4.5 with an active area defined between a 70 mm inner radius and a 143 mm outer radius (see Fig. 5.35). More details are described in [115].

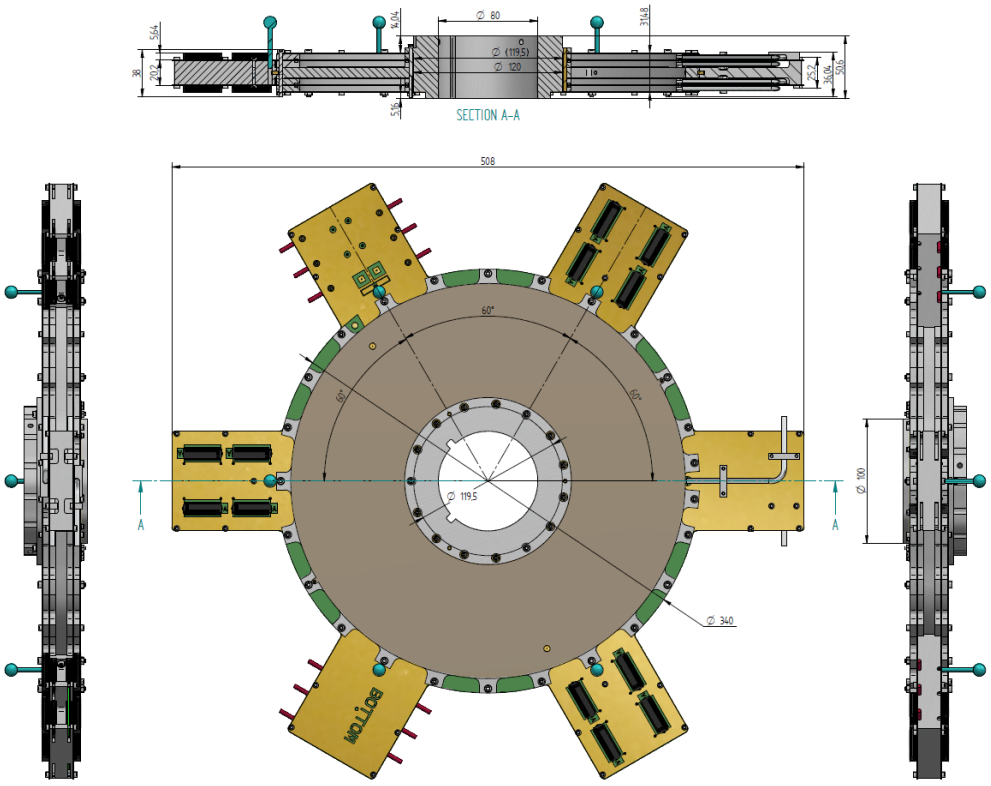


Figure 5.35: Clas12 Micromegas Tagger Tracker designed and built at Irfu.

### 5.2.2 Cosmic bench

A cosmic test bench was designed and built for the CLAS12 detector characterization. Four 50 × 50 $cm^2$ 2D multiplexed resistive strips Micromegas detectors were used for the hodoscope (see section Muon Tomography). The triggering system was two plastic scintillators of 60 × 60 $cm^2$ in coincidence. During the

first years, a set of original T2K electronics was used to read out the detectors both the ones from the hodoscope and the one that was in characterisation.

Such test bench is very convenient because there is no need to reserve beam test slots. As soon as a prototype or a production detector is ready, it can be tested at any time. So, the 2D efficient can be extracted giving information to the location on the detector of the problem if it exists. The hodoscope spatial resolutions were from 250 to 500 µm depending on the multiplexed detector versions (v1 et v2).

The 2D efficiencies of the Forward detectors from the production can be seen on Fig. 5.39. From 450 V the efficiency is maximal whatever electronics is used (spark protected or unprotected Front-End Unit or FEU) shown on Fig. 5.40). At lower strip voltage, the efficiency measured with the unprotected electronics is higher. The FEU electronics is based on Dream Asics. This electronics is a dead-time less electronics designed for the project at CEA/Irfu (see Sec. A.2) [29].

Six detectors fully operational have been delivered to J-Lab in Sept. 2016 with a radiation length of 0.70% $X/X_0$. Using the cosmic test bench, the efficiency of each detector was measured at 98% in their active area (see Fig. 5.40) with a spatial resolution better than 200 µm and a time resolution better than 20 ns (both limited by tracking of the test-bench).

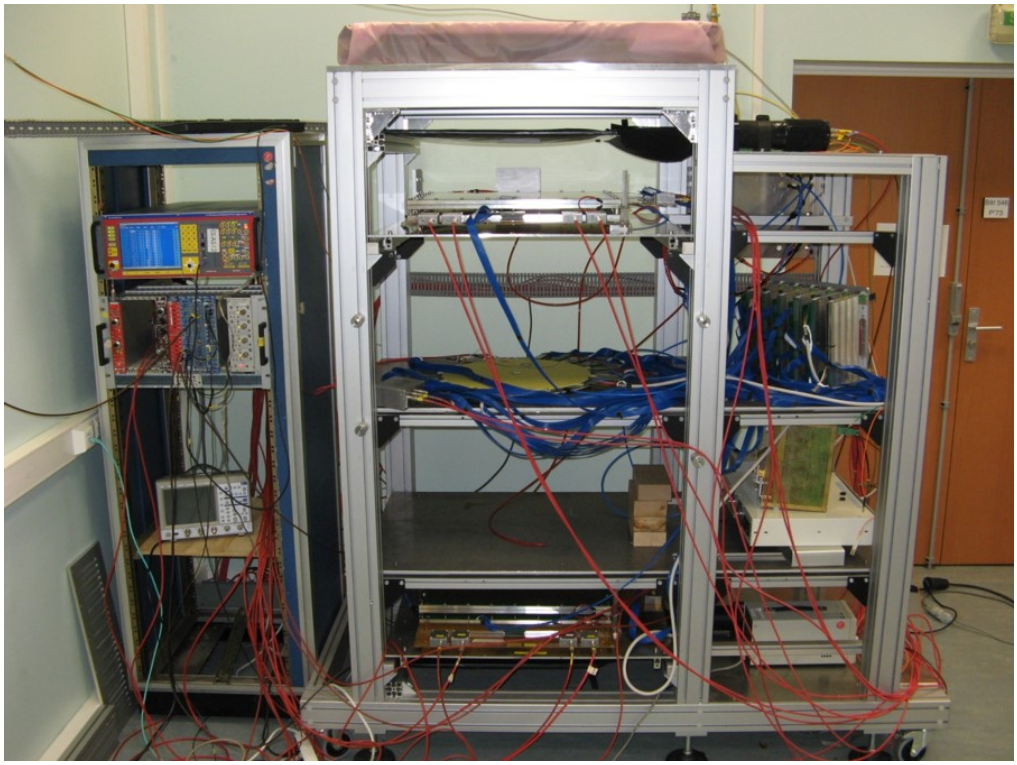

Figure 5.36: Cosmic bench designed and built for CLAS12 detector characterization. The Forward prototype is in operation using an hodoscope made of multiplexed Micromegas detector prototypes.

### 5.2.3 Resistive strip study and choice

To ensure the particle rate capability of the Forward detector ($\simeq$30 MHz). A full-size detector prototype was built and characterized with 100 k$\Omega/\square$ resistive strips with ladders in inner region and without ladders in outer region (see Fig. 5.37). The ladders are supposed to homogenise the resistivity. But, in both cases

the measured efficiency was measured to be identical at the same voltage.

Fig. 5.38 shows the current recorded on the power supply channels connected to the internal and the external zones in function of the X-ray gun current. The gas was ar-i$C_4H_10$-$CF_4$ (80:10:10). At 360 V, the or the curves are linear for both zone, but starting from 400 V, a charging up of the strip bend the curves. The effect is more pronounced with the strips with ladders in the internal zone.

To reduce this effect, the resistive strips without ladders have been chosen. This choice was also taken for muon tomography detectors.

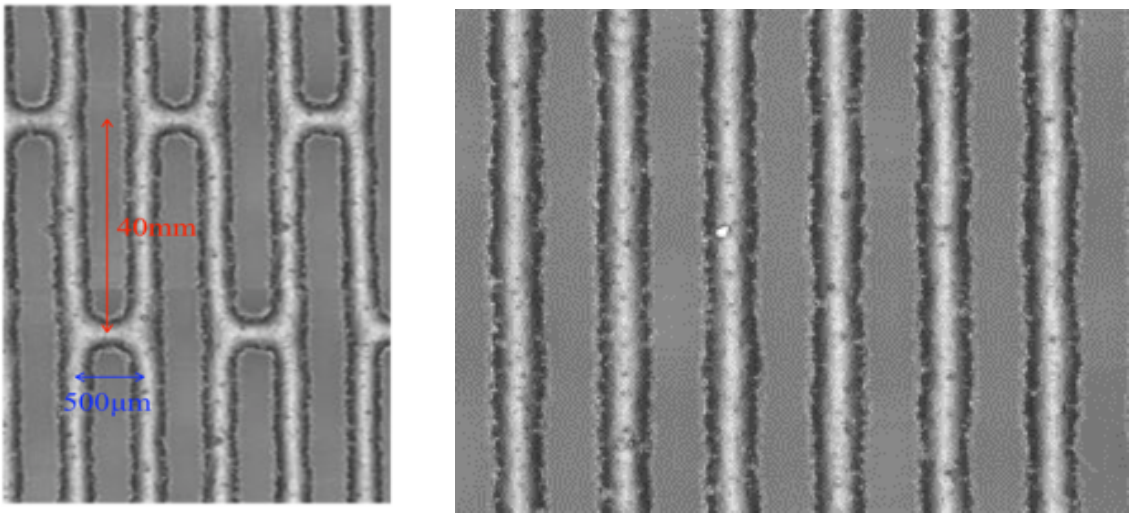


Figure 5.37: Resistive strips [left] with ladders and [right] without ladders.

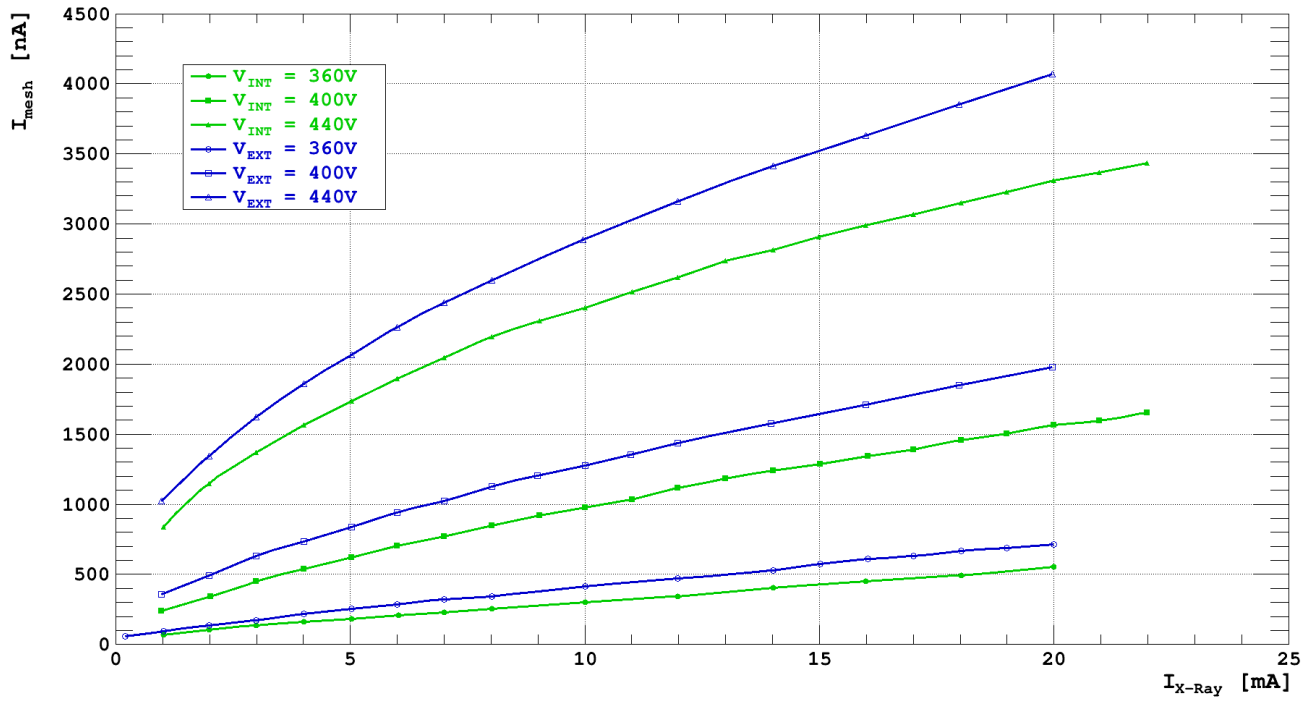


Figure 5.38: Charging up effect study with X-ray gun. Green lines: data taken using a prototype of resistive strips without ladders. Blue lines: data taken using a prototype of resistive strips with ladders.

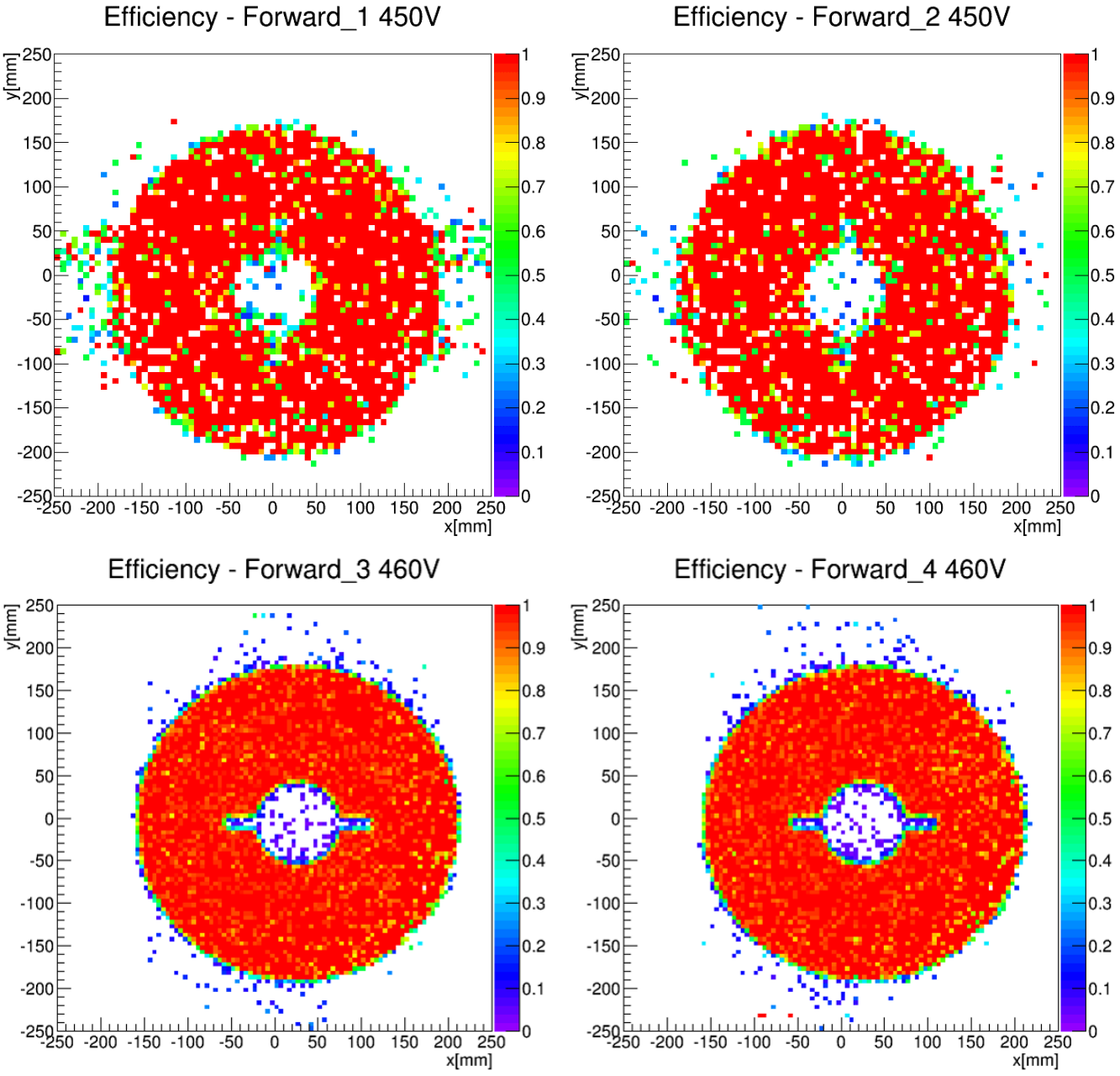


Figure 5.39: Micromegas forward detector 2D efficiency. At 460 V the event statistics was ten times the one at 450V.

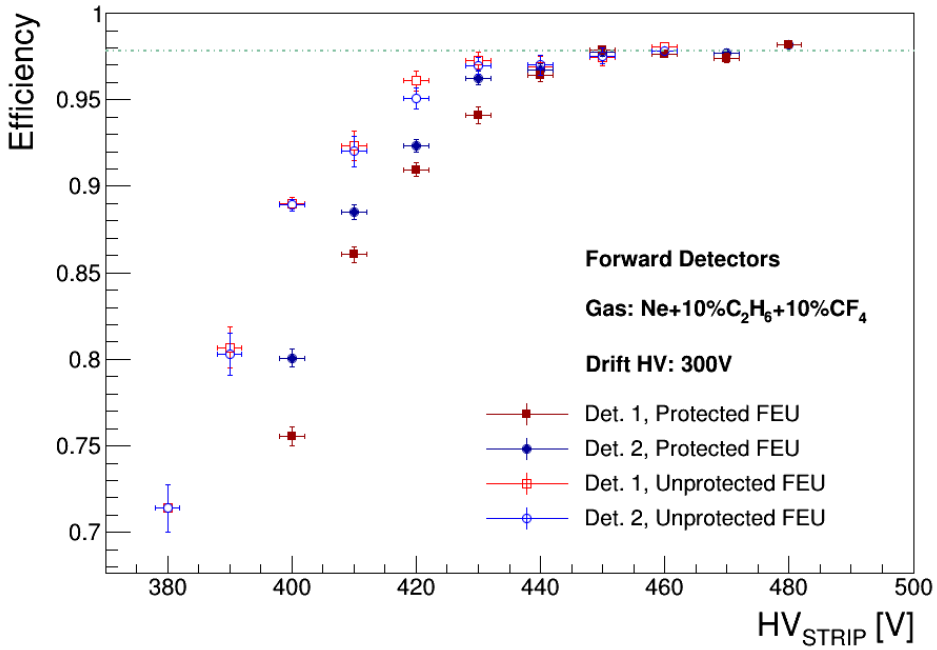


Figure 5.40: FMT efficiency with the strip polarization and two electronics card versions: unprotected and protected FEUs. The best efficiency is obtained at 450 V.


Figure 5.41: Micromegas Central Tacker and Silicon Vertex Tracker during installation at Hall B of Jefferson Laboratory in October 2017.

## 5.3 T2K TPC Upgrade

### 5.3.1 Context and specifications

The T2K (Tokai to Kamioka) experiment is a long-baseline neutrino oscillation using a muon neutrino $\nu_\mu$ beam produced by the JPARC accelerator facility in Japan. The near detector (ND280), located at 280 m from the source and 295 km far from the detector SuperKamiokande, is essential to fully understand the properties of the beam and to measure the cross sections. The main objective is the measurement of the angle $\theta_{13}$ of the neutrino mixing matrix.

T2K provided the first evidence of non-zero mixing angle $\theta_{13}$ and discovered the appearance of electron neutrinos in a muon neutrino beam [116]. Combining T2K data with precise measurement from reactor experiments, T2K has recently reported hints of large Charge-Parity (CP) violation in the leptonic sector [117], excluding CP-conservation at about the $2\sigma$ Confidence Level.

In January 2010, CEA/Irfu delivered three vertical TPCs equipped with Micromegas detectors ($3 \times 24$) and a full readout system based on AFTER chip electronics (see Sec. A.2). Since 2011, the ND280 data allows the beam monitoring (neutrino flux measurement) before the neutrino oscillations, a fundamental input for the physics case. ND280 is a magnetized multi-purpose detector that measures the neutrino flux and the neutrino–nucleus interaction cross-section.

The present ND280 consists of two main parts: an upstream detector (P0D) and a downstream tracker which includes two Fine Grained Scintillators (FGD) interleaved with three vertical TPCs. The P0D and the tracker are surrounded by an electromagnetic calorimeter (ECAL) and by the UA1 magnet providing a 0.2 T magnetic field.

At the end of 2022, the upgrade of the beam power from 500 kW to 750 kW encouraged the T2K collaboration to upgrade the detectors for a second phase of the experiment (T2K-II). In this context, ND280 will be upgraded by replacing the Pi-Zero detector (P0D) with two High-Angle TPCs (HA-TPCs) and a new tracker Super-Fine Grain Detector (Super-FGD). This upgrade will improve the detection of particles transverse to the beam, for which the acceptance of the current tracker is small (see Fig. 5.42). This new tracker system will also be surrounded by six Time-of-Flight modules. This new detector configuration will increase the angular acceptance of ND280, being close to the full $4\pi$ phase-space accessible at SuperKamiokande and improve the reconstruction of hadronic part of the neutrinos interactions. The total target mass will also be higher helping the neutrino interactions. The systematic uncertainties will be reduced from 6% to 4% so the measurement of neutrino oscillations will be achieved at a higher significance of $3\sigma$ level. The performance specifications for these new HA-TPCs are the same as the current three vertical TPCs (v-TPCs) [104]: momentum resolution $\delta(p_\perp)/p_\perp < 0.1 p_\perp$ [GeV/c], space point resolution $\simeq 700$ µm and $dE/dx < 10$ %.

The HA-TPC, with overall dimensions of $2 \times 2 \times 0.8\text{m}^3$, will be equipped with 32 encapsulated resistive anode bulk Micromegas detectors.

### 5.3.2 Development of resistive Micromegas prototype

The choice of the bulk Micromegas module had to meet two requirements. The first one is reduce the dead space taken by the original electronic cards plugged perpendicular to the endplate of the three vertical TPCs (v-TPCs) and the second one is to keep at least the same performance of the vertical TPCs.

So, a compact electronics limits the number of electronic channels and requires the used of resistive Micromegas technology developed since more than 10 years inside the LCTPC collaboration (see Sec. 5.1.3.1). Indeed, the charge spreading between neighbouring pads brought by the resistive technology improves the

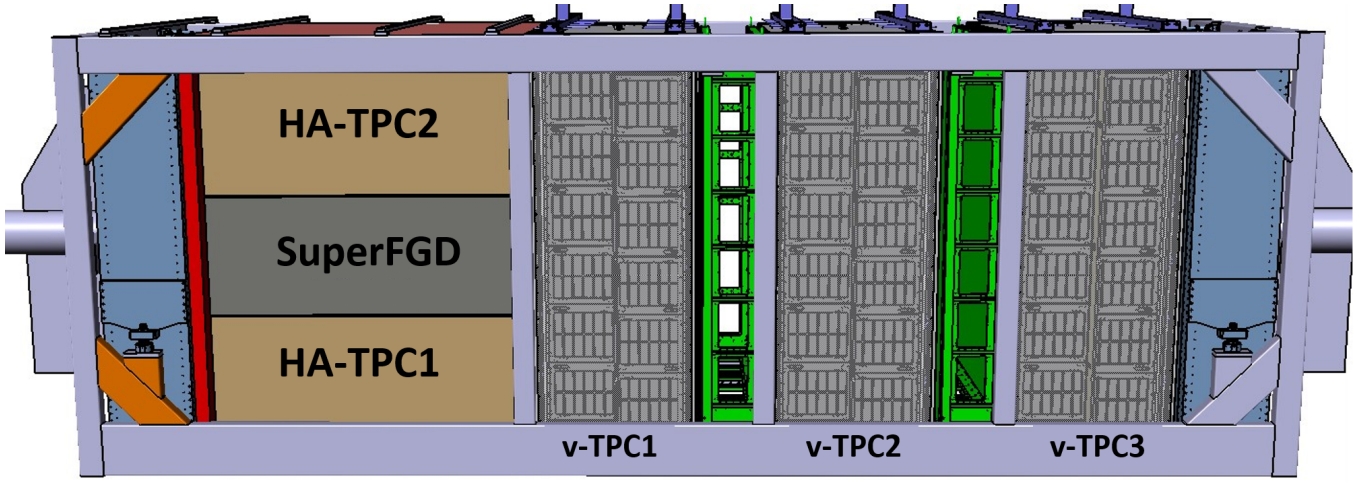


Figure 5.42: ND280 upgrade configuration. On the left side the two new high-angle TPCs surrounding the SuperFGD for the upgrade and on the right side the three existing vertical TPCs installed in 2010.

| **Parameter** | **v-TPC** | **HA-TPC** |
|---|---|---|
| **Overall size X×Y×Z** (m) | 0.8×2.2×1.8 | 2.0×0.8×1.8 |
| **Number of TPC** | 3 | 2 |
| **Micromegas module type** | Standard | Resistive |
| **Micromegas module number** | 24 | 16 |
| **Micromegas module size Y×Z** (cm) | 36×34 | 42×34 |
| **Pad rows × pad columns** | 48×36 | 36×32 |
| **Pad size Z×Y** (mm) | 6.85×9.65 | 10.09×11.18 |
| **Pads number per module** | 1728 | 1152 |
| **Pads number per TPC** | 41 424 | 18 432 |
| **Gas mixture** (%) | Ar-$CF_4$-i$C_4H_{10}$ (95-3-2) | |
| **Drift distance** (cm) | 90 | |
| **Magnetic field** (T) | 0.2 | |
| **Electric field** (V/cm) | 275 | |
| **Drift velocity** (cm/µs) | 7.8 | |
| **Transverse diffusion**(µm/$\sqrt{\text{cm}}$) | 265 | |
| **Signal sampling** (MHz) | 25 | |
| **Number of time samples** | 511 | |

Table 5.3: Parameter comparison between the vertical-TPC and the new high-angle TPC for the T2K-ND280 detector upgrade.

spatial resolution to be better than the pitch/$\sqrt{12}$ obtained with a smaller number of pads. The resistive technology bring also spark protection allowing a safe operation by a capacitive coupling readout. The cumbersome anti-spark protection circuitry necessary in the case of the standard (non resistive) Micromegas readout can be removed allowing to put the electronics card directly on the back of the module and to give a larger active volume.

#### 5.3.2.1 ERAM detector module description

This new detector module, named encapsulated resistive anode bulk Micromegas (ERAM), consists of a resistive bulk Micromegas detector glued on an aluminium frame on which the readout electronics is fixed directly on its backside. The bulk Micromegas [55] is built with the standard SD45/18 304L woven mesh micromesh [118] on top the resistive layer.

Compared to the v-TPC detector, the ERAM detector has 1152 (instead of 1728) pads of $10.09 \times 11.18$ mm$^2$ ($6.85 \times 9.65$ mm$^2$) disposed in a matrix of 36 ($48 \times 36$) of $42 \times 38$ cm$^2$ ($36 \times 34$ cm$^2$). The pad plane is covered by a resistive layer made with an insulated layer (50 µm APICAL polyimide foil pressed with 150 µm glue) with diamond-like carbon (DLC) deposition by electron beam sputtering. This resistive layer technology enables to spread the charge over several pads in order to improve the spatial resolution. To guarantee a charge dispersion over at least two pads, a DLC resistivity of at most 400 kΩ/□ was chosen.

The signals induced to the detector pad plane through the resistive layer are read out by two new front-end electronic cards (FECs) using AFTER chips (8 per FEC) and one new front-end mezzanine (FEM), both mounted on the back of the detector (see Fig. 5.43 where a set of new electronic cards is shown on the back of an ERAM detector in the cosmic test bench).

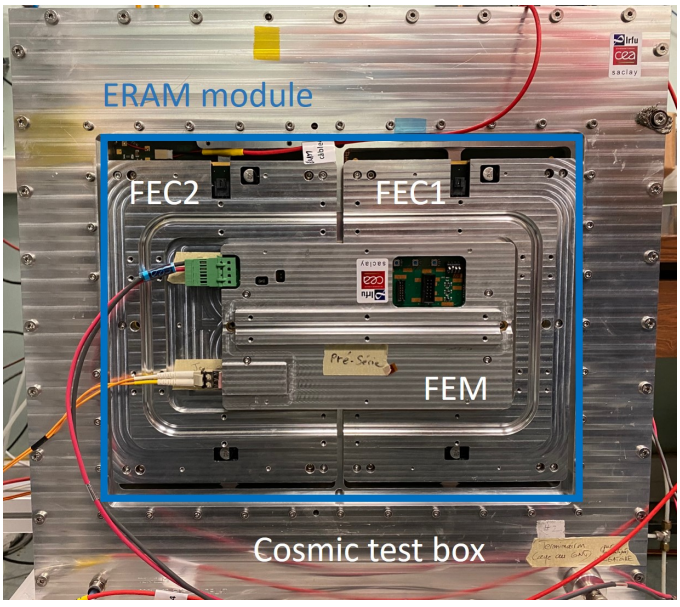


Figure 5.43: ERAM detector seen from its backside. The FEM is connected on top of both FEC for signal readout.

#### 5.3.2.2 Cosmic and X-ray test benches

In order to characterize and to validate the first production detectors, two test benches were set up in our laboratory. The first is a cosmic bench and the second is an X-ray bench using an iron-55 source to automatically scan the detector pad by pad. Both benches are shown in Fig. 5.44 and are described below:

- **The cosmic bench** is made of a couple of photomultiplier+scintillator ($50 \times 20$ cm$^2$) in coincidence hold by a mechanical structure on either side of a test box ($50 \times 49 \times 20$ cm$^3$) with 15 cm drift distance with field degrader designed to integrate an ERAM module. At least 100k events were taken at various DLC voltages (from 330V to 370V) using the cosmic trigger. Only single and purely vertical tracks

were selected rejecting empty and multiple track events (∼25%). A typical events can be seen on the left of Fig. 5.45 (left).

- **The X-ray test bench** was provided and was programmed by the Warsaw University of Technology. The chamber has a 3 cm drift distance and stands with a robotic X-Y-Z arm system on an optical breadboard of 120×60 $cm^2$ holding a 250 Mbq 55Fe X-ray source. After each installation of a new detector, an alignment procedure has to be performed in order to ensure the position of the source with respect to the center of each pad. A 1.5 mm diameter collimation hole in front of the source assures that the majority of photo-electron arrives on the targeted pad. About 4 minutes are necessary to produce a spectrum with enough statistics (Fig. 5.45, right) with the 100 Hz internal trigger, so 4 days are needed to perform automatically a full scan of the 1152 pads. Most of the frames were empty and so were ignored. A Gaussian fit gives an energy resolution of ∼ 9%.

Both test benches were fed with the T2K gas mixture with a gas flow of 10 L/h. The X-ray bench was moved to Cern and it is now the only one used to validate the next detectors from the production.

#### 5.3.2.3 Characterisation before production

By using data taken at a DLC voltage of 350V from both test benches (cosmic and X-ray), gain maps were performed by accumulating signals for the two first ERAM detectors (ERAM-01 and ERAM-02 from the production). Figure 5.50 shows the gain maps obtained in this two configurations. The RMS of the X-ray gain maps are respectively 9.8% and 13.9% for the ERAM-01 and ERAM-02 detectors. A gain deficit (of a factor 2) on the right-top side of the ERAM-02 is clearly seen in both data set.

The cluster multiplicity, the relative gain and the spatial resolution was extracted from the ERAM-01 detector with two shaping time (200 ns and 412 ns) and compared to the results from the ERAM-P2 (second prototype) which had an insulator layer of 200 $\mu$m and a DLC resistivity of 200 Ω/□. A pad response function method (described in [119]) was used to extract the spatial resolution with the cosmic data. At a typical gain of 1300 ($V_{DLC}$ = 350 V) and a peaking time of 412 ns, the spatial resolution is 300 $\mu$m at zero drift distance and the same with the ERAM-P2 at 200 ns. By increasing the peaking time to 412 ns, the time resolution (Z resolution) will be improved keeping the performance (∼ 370 $\mu$m spatial resolution) well below the T2K specifications.

#### 5.3.2.4 Beam test campaigns

Two beam test beam campaigns were performed at DESY in 2019 and 2021. The data were used to characterize the charge spreading and to produce its map. Spatial resolution better than 600 µm and energy resolution better than 9% were obtained for all incident angles. These performances fulfil the requirements for the upgrade of the ND280 TPC. More details on the data taking and the results are, respectively, available in [120] and in [119].

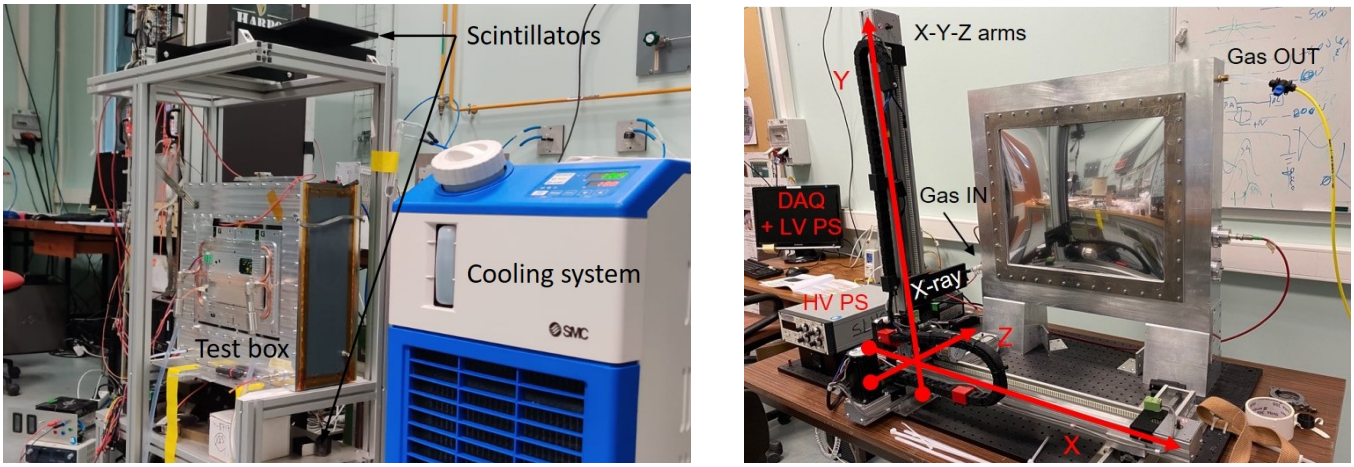


Figure 5.44: Test benches in the laboratory: [left] cosmic bench with the cooling system and [right] automatic X-ray bench behing an automatic robotic X-Y-Z arm system.

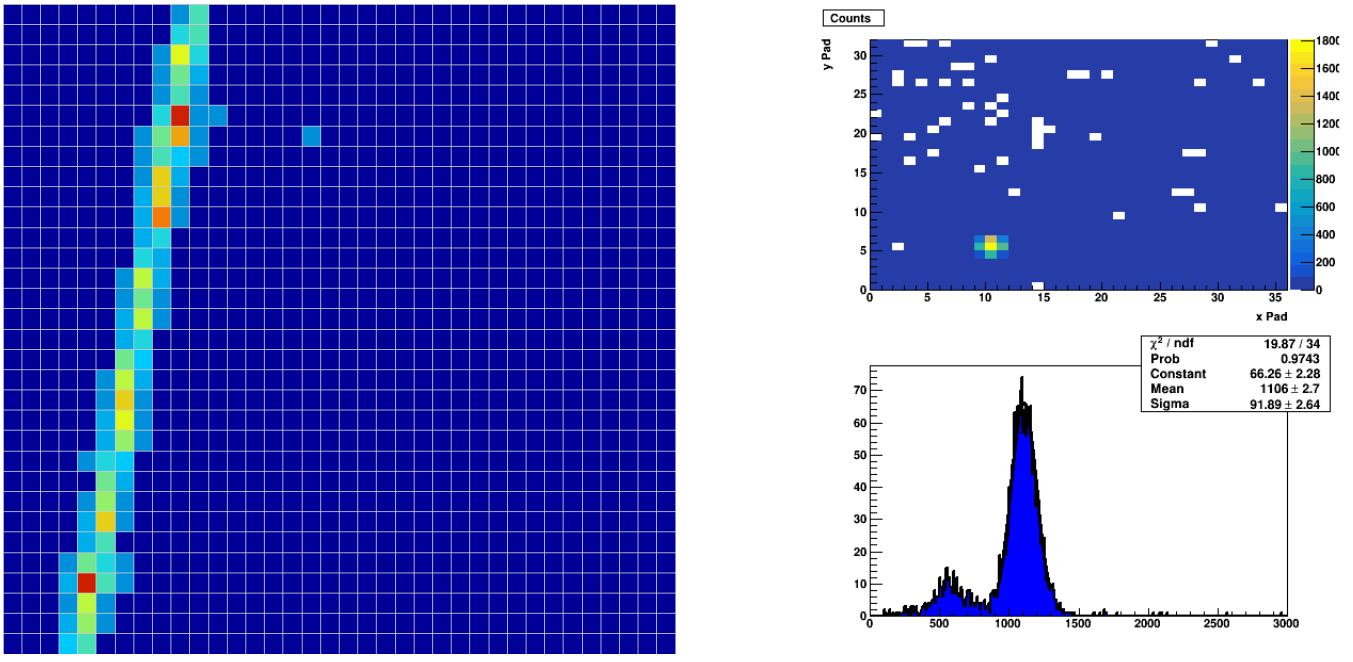


Figure 5.45: Left: cosmic test bench event. Right: spectrum extracted from X-ray run.

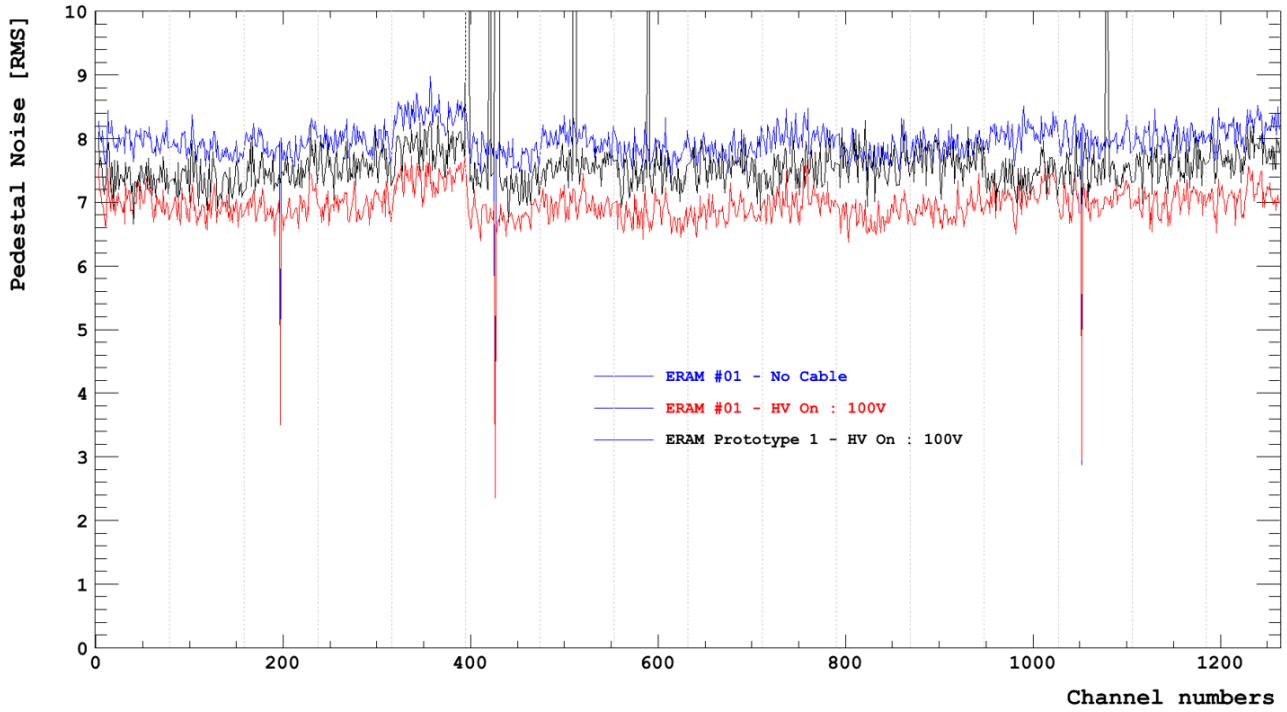


Figure 5.46: Pedestal noise improvement of the ERAM prototype after additional groundings (with the module frame (MF), with the crate) and adding a cover plate on the HV filter.

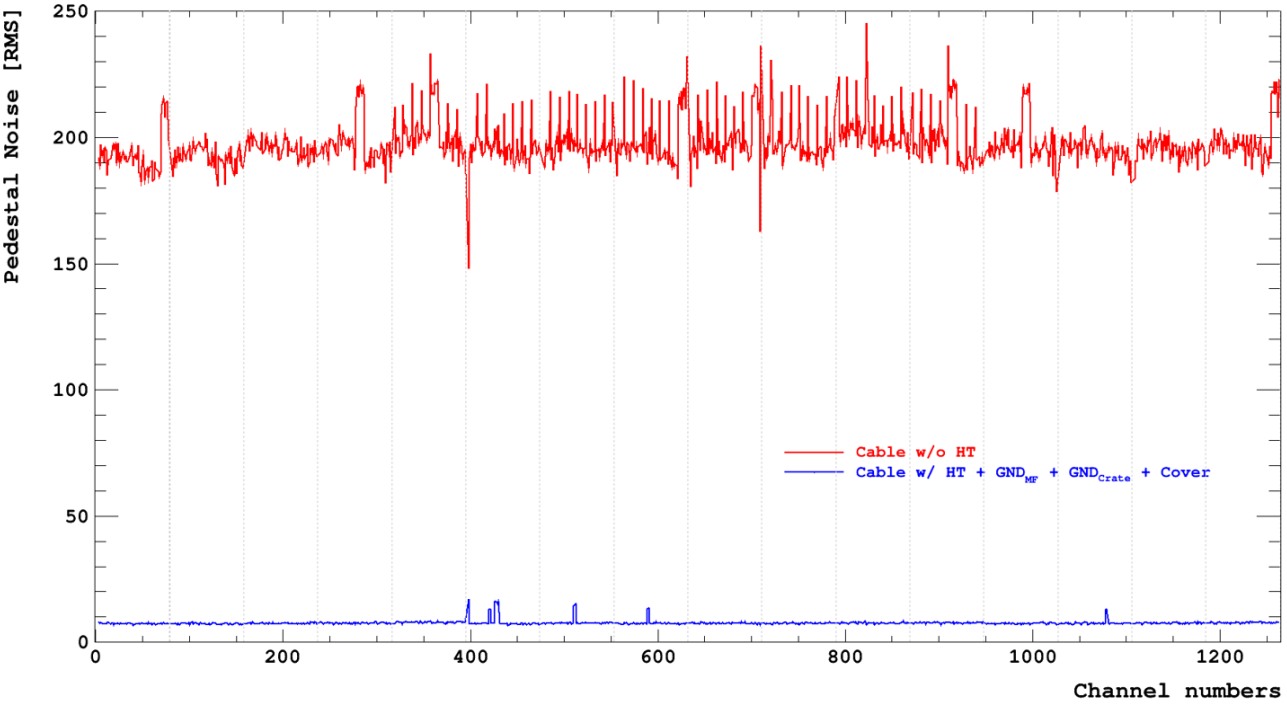


Figure 5.47

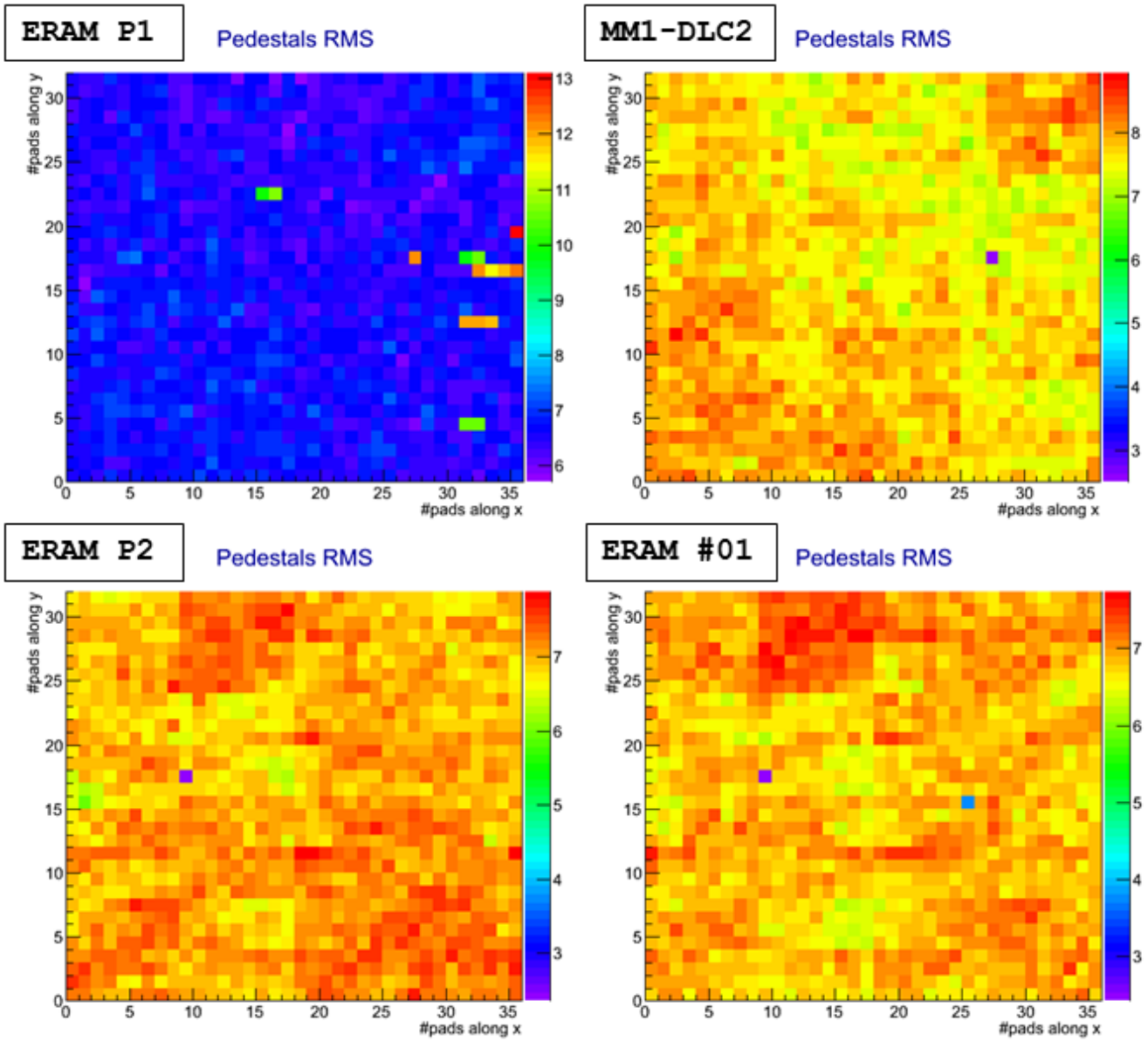


Figure 5.48: Pedestal RMS maps of four detectors: three detectors prototypes MM1-DLC2, ERAM-P1 and ERAM-P2, and a the first detector production ERAM-#01.

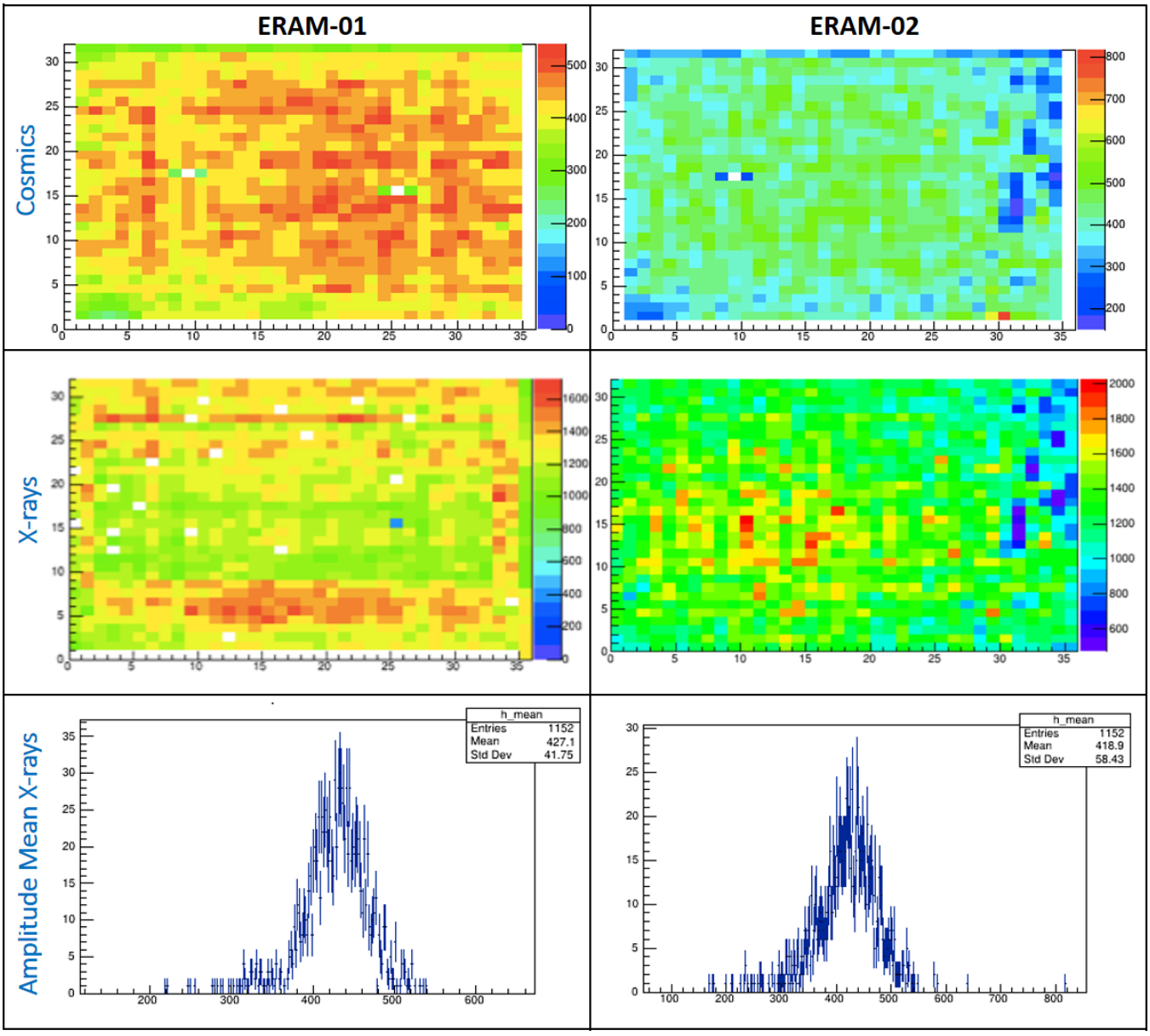


Figure 5.49: Gaim maps of ERAM01 and ERAM02 taken from cosmic and X-ray data.

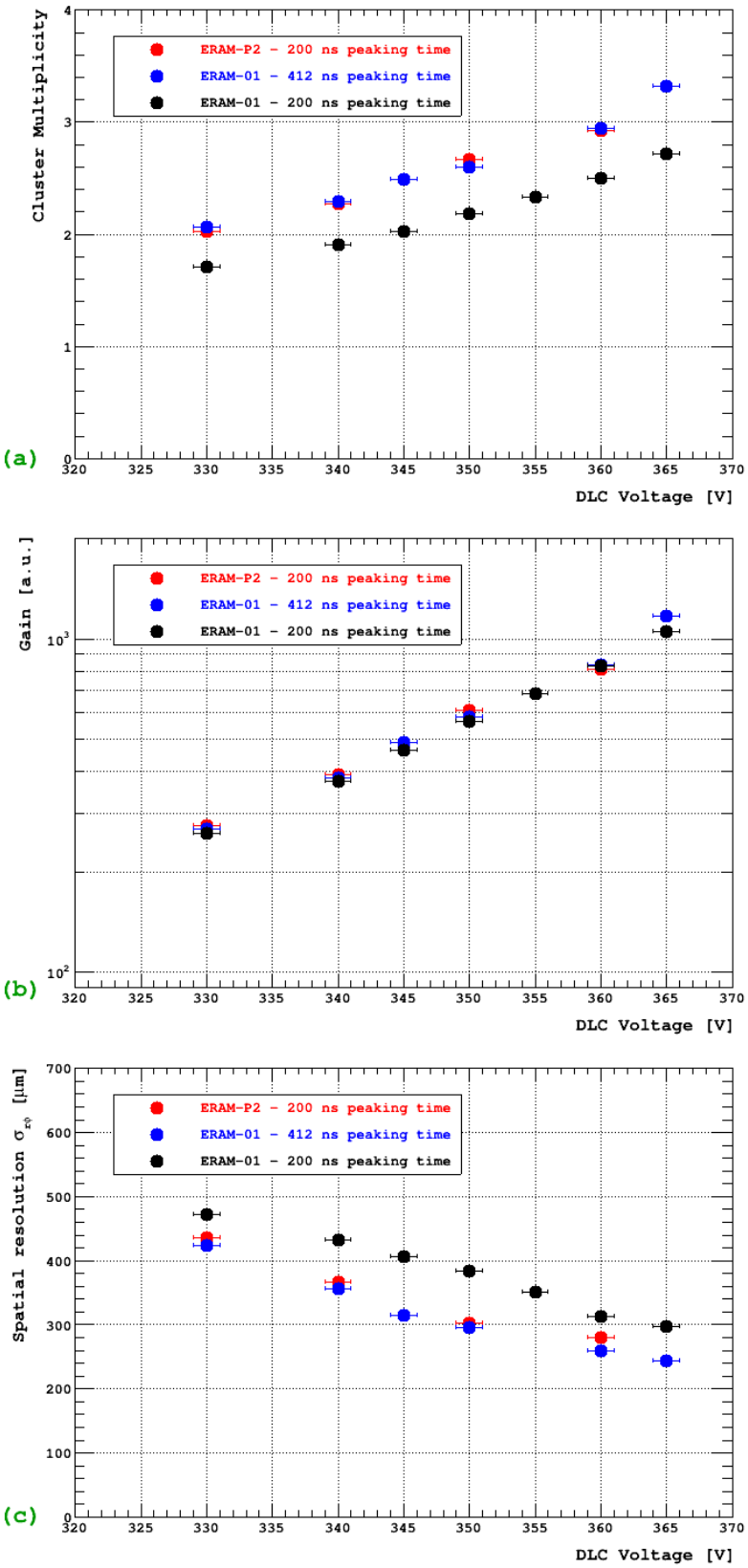


Figure 5.50: a) Cluster multiplicity, b) Gain and c) spatial resolution for ERAM prototype P2 at 200 ns peaking time (red) and ERAM01 at 200 ns peaking time (black) and 412 ns peaking time (blue).

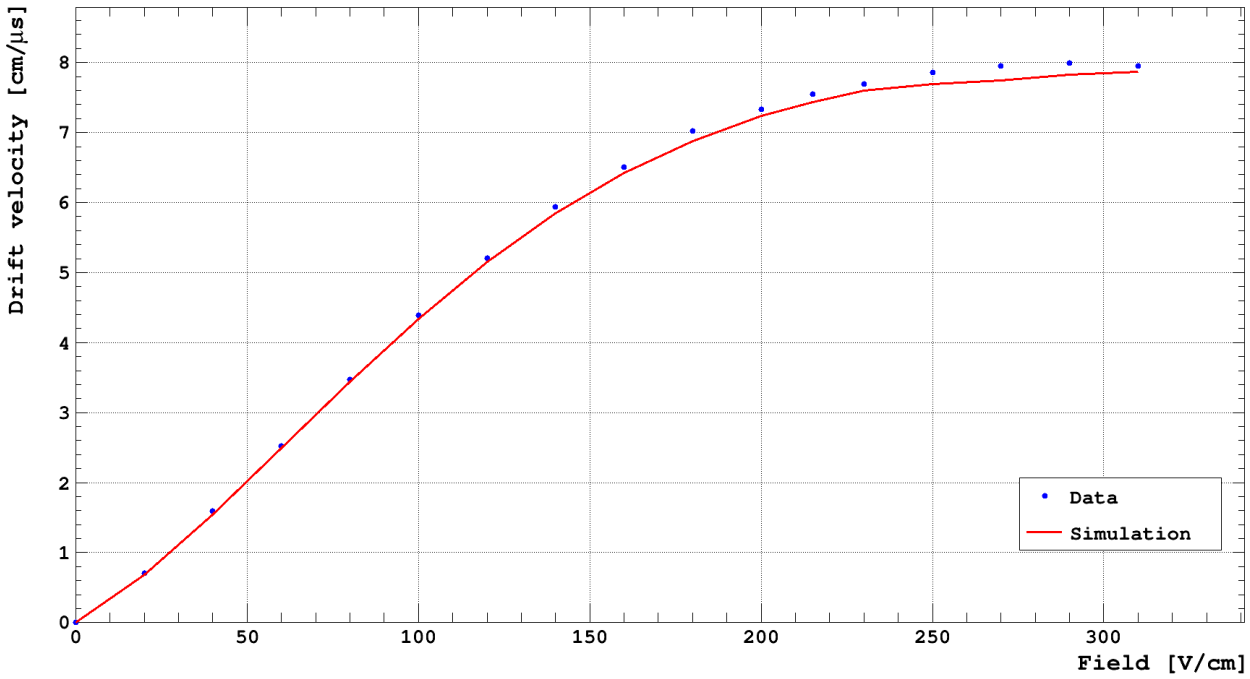


Figure 5.51: Measurement of the drift velocity using test beam data changing the beam position.

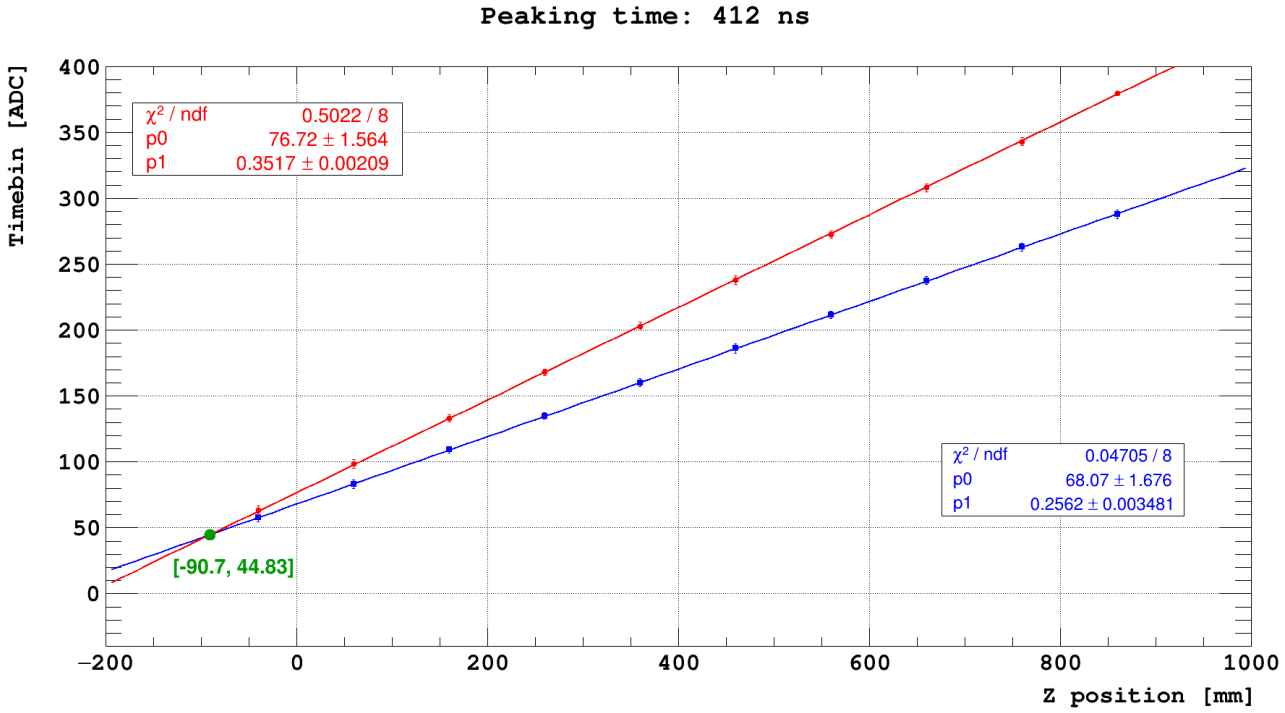


Figure 5.52: Determination of $t_0$ using test beam data.

# High energy Astrophysics

Contents



## 6.1 HARPO, a TPC prototype for gamma-ray astronomy

### 6.1.1 Description

High-energy astrophysics suffers from the lack of precise measurements in the energy range between the high-efficiency range of Compton telescopes ($< 0.1$ MeV) and that of e+e- pair conversion telescopes ($> 100$ MeV). Furthermore no significant polarisation measurement of a cosmic source has ever been performed in the gamma-ray energy range. Existing pair telescopes suffer from a very bad angular resolution at low energies ($1 < E < 100$ MeV) because of the multiple scattering of the electron and of the positron in their tungsten converters. For the same reason the polarimetric information is lost. The use of a low-density homogeneous active target has been proposed as a good solution to overcome these limitations [121, 122].

The linear polarisation $P$ of the high energy photons is a key parameter in the models to understand the mechanisms involved: model of proton hadronic interaction on matter at rest: $\pi \longrightarrow \gamma$ have no polarisation ($P = 0$), while model of leptonic radiative processes (synchrotron, inverse Compton) emits polarized $\gamma$-rays photons ($P = 70\%$). The way to discriminate the two models is the measurement of $P$. The Fig. 6.2 shows an Active Nucleus Galaxy model (left) and the model dependence of the maximum degree of polarization for an high-synchrotron-peaked blazar RX J0648.7+1516 (right) [123].

An *Hermetic Argon Polarimeter* (HARPO) prototype has been built to validate the concept. The National Agency (ANR) funded the project from 2014 to 2018. It consists of a 30-cm cubic vessel filled with high-pressure argon-based gas operating as a target and a tracking detector in TPC mode read out by MPGD technologies. The readout plane is composed of two times 288 strips of 1 mm pitch in the two perpendicular directions (X and Y) connected to electronic chain sampled at 33 MHz allowing 3D point resolution of about 1 $mm^3$. The electronic chain is composed of a T2K TPC front-end card, a FEMINOS back-end card for each axis, both connected to a Trigger Clock Module for synchronisation and data collection [124].

The TPC was filled with a mixture of 5% of $iC_4H_10$ in argon and was operated at 220 V/cm of electric field to drift the primary electrons to the readout plane composed by an hybrid MPGD detector (two GEM foils and a bulk Micromegas) on top of the strips in order to extend the dynamic range in the pressurized gas. A 128 µm gap bulk Micromegas detector with a pressure more than 2 bars have an operation range with too small margin in gain. The addition of two GEM foils allows to recover a much larger operating margin.

The detector, the electronic chain and its innovative trigger system called FAST (*Fully Automated Switched Trigger*) makes use of the FPGA of a modified PMm2 trigger card [125] to generate up to 16 trigger lines built with combinations of the signals from the 12 PMTs, Micromegas mesh signal, and an external trigger [126]. The HARPO prototype has been described in details in [127, 128]. The HARPO prototype principle and design are shown on Fig. 6.1.

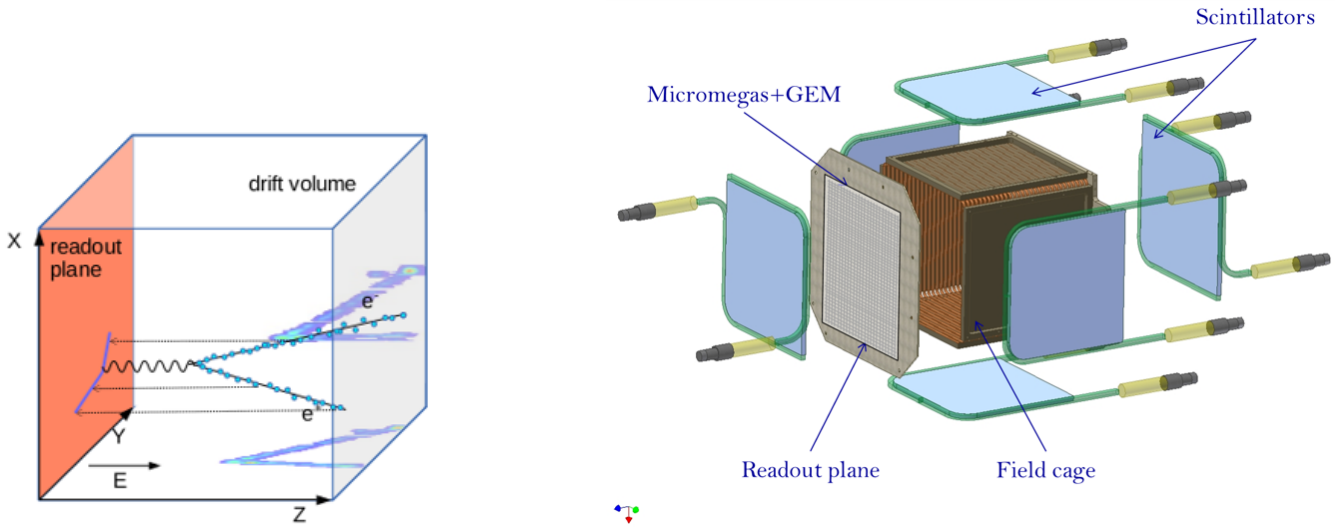


Figure 6.1: [Left] Cubic TPC principle with 2×1D (x,y)+z readout for 3D tracking. [Right] Description of HARPO TPC prototype.

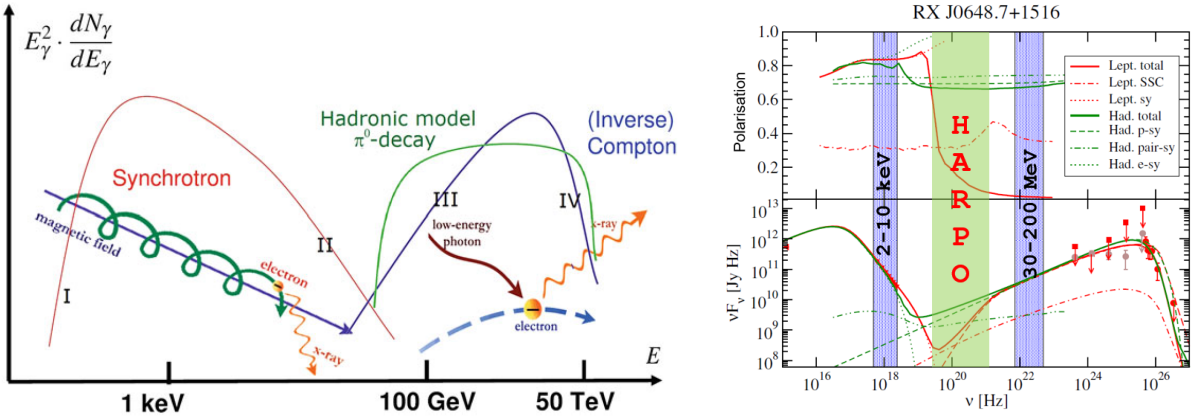


Figure 6.2: [Left] active galaxy nucleus model from [12] and [right] an example where polarimetry from HARPO could discriminate two models where the maximum degree of polarization for a high-synchrotron-peaked blazar RX J0648.7+1516 taken from [13].

### 6.1.2 Data taking

The HARPO detector prototype was exposed to the a high intensity $\gamma$ beam produced by inverse Compton scattering (LCS) of a laser beam on the electron beam with an energy of 0.6 to 1.5 GeV from the NewSUBARU storage ring [129]. The collimated $\gamma$ beam in front of the prototype has a fraction of P polarization almost identical to that of the original laser beam. Varying the wavelength of the laser and the energy of the electrons supply $\gamma$ from 1.7 to 74 MeV. A specific trigger was designed and used to acquire data with a signal event rate, i.e. the conversion of a photon from LCS in the gas into an $e^+e^-$ pair, of a few tens of Hz, while the incident background noise was a few tens of kHz, with a low dead time [126].

The experiment was fully simulated with a Monte Carlo based on Geant4 [130]. The highly non-symmetrical $x, y, t$ structure of the detector induces biases in the efficiency map and in the migration of events as a function of $\phi$. Biases were measured and corrected through a double trigger mechanism. Data was with polarized $\gamma$ taken by quarter with an orientation of the detector varying in steps of 45°.

Additional data with an unpolarized beam was also taken to be able to calculate the ratio of the distributions of the azimuth angle for (P=1) and for (P=0) and compared to the Monte Carlo simulation [131]. Under isotropic exposure, in orbit, these biases are naturally absent by long-term averaging (see Fig. 10 of [132]).

### 6.1.3 Track reconstruction

Due to large diffusion in the gas (no magnetic field), X(t) and Y(t) correlation and the important multiple scattering of the electrons and positrons make difficult the use of a straight line finding algorithm (Hough transform) or more sophisticated tracking method as a Kalman filter (see Sec. 4.5). So, in order to identify the pair vertices, an original method has been developed. Then by fitting the vertices of the two projections of X(t) and Y(t), the plan XY and XZ are associated with each other to recover the full 3D description of the vertex. The different steps are briefly described in the following the three steps below:

- **Search for 2D vertex**: a vertex is defined to be the starting point of two tracks where a photon is converted into a $e^+e^-$ pair. So, the angle defined by the tracks should strictly inferior to $\pi$. The vertex finder consists in looking for ellipse around each point of the event and in measuring the longest

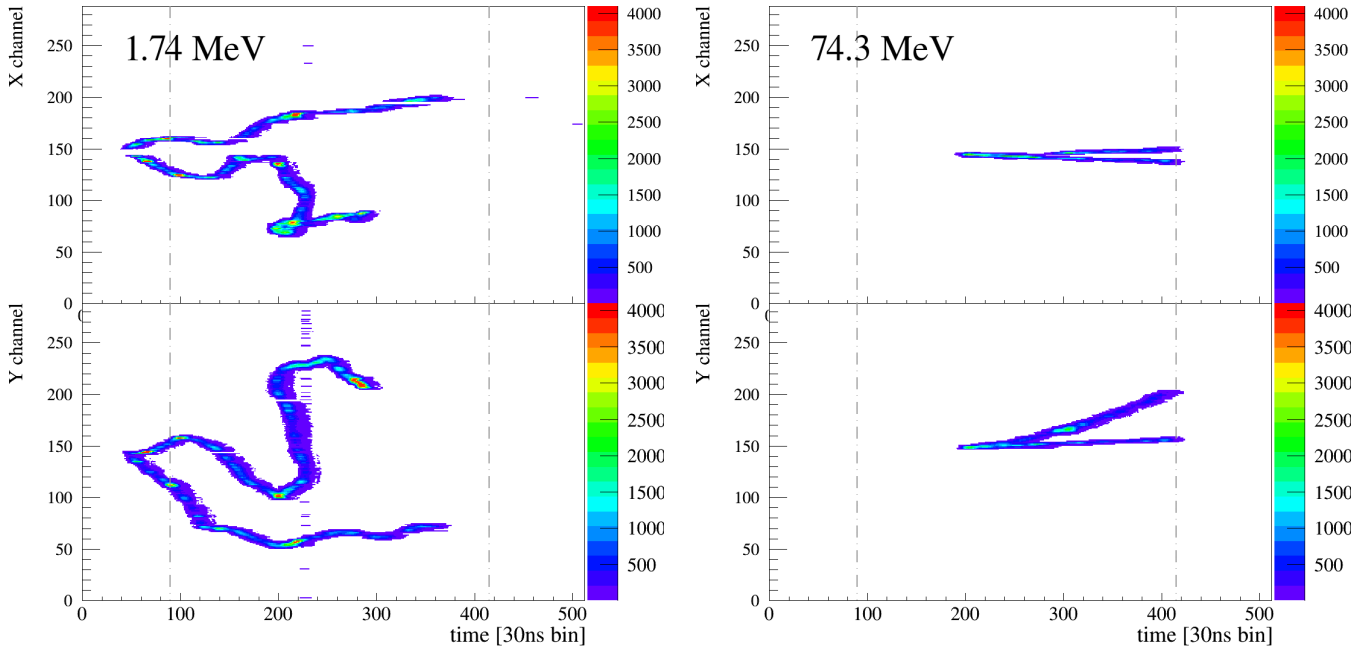


Figure 6.3: Gamma-ray conversion to e+e- pair at two different energies.

arc that does not cross any region containing signals. If this arc is longer more than $\pi$, it is identified as a vertex (see Fig. 6.4a).

- **Fit of the 2D vertex**: the next step is to map the charge distribution around the vertex in polar coordinates. Then only the regions with continuous signals from the vertex are selected. Most of the signal from the $\delta$-electron is removed. The peaks of the distribution obtained this way indicate the direction of the tracks originating from the vertex (Fig. 6.4b).

- **2D vertex matching for 3D reconstruction**: in each plan X(t) and Y(t), the signal contained in a region around the track direction is associated with each of the two tracks (Fig. 6.4c). Then, by comparing the charge profiles of the tracks as a function of the temporal coordinate ($t \propto Z$), the XZ projection of a vertex is associated with its YZ projection (Fig. 6.4d), so that finally the 3D vertex of the two tracks corresponding to the electron and the positron are recovered allowing to measure the incident photon direction and its polarisation.

A full description of the data analysis can be found in [133].

### 6.1.4 Results and spin-offs

After tracking, the $A \times P$ modulation of the incident photon azimuthal angle distribution can be extracted from a simple 1D distribution [134, 122]

$$\frac{d\sigma}{d\phi} \propto (1 + A \times P \cos(2(\phi - \phi_0)) \,. \tag{6.1}$$

Fig. 6.5 shows an example of the distribution of the azimuthal angle for the conversion of 11.8 MeV photons produced by the inverse Compton scattering of a linearly-polarised fiber erbium laser beam ($\lambda$=1.54 µm) on the 1 GeV electron beam of the NewSUBARU facility in argon-isobutane (95-5) gas mixture at 2.1 bar

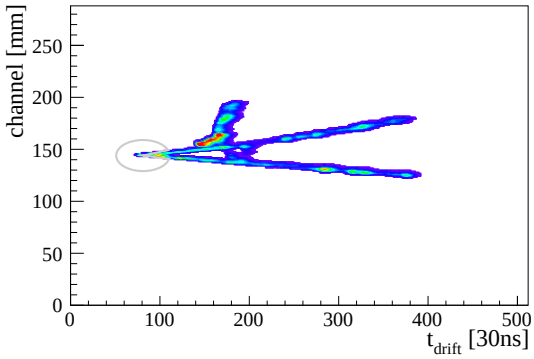


(a) 2D vertex finder procedure: circles are drawn around signal regions. If the longest arc without signal is larger than half an ellipse, the region is considered as a vertex candidate.

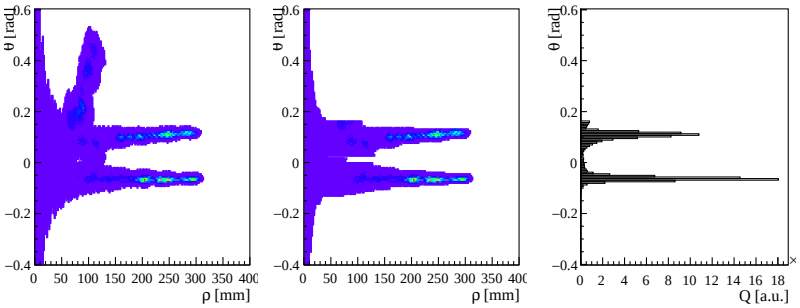


(b) 2D vertex fitting procedure: [Left] polar distribution of charge around the vertex candidate. [Middle] selection of regions nearly continuous signal from the vertex. [Right] angular distribution with two clear peaks corresponding to the two associated tracks.

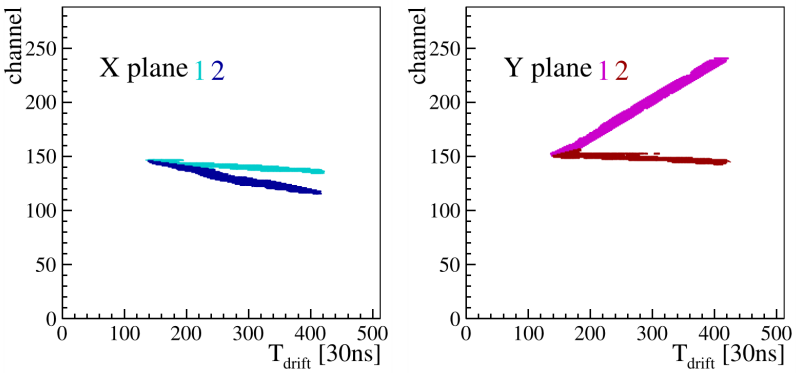


(c) Matching procedure: definition of the region associated to each of the two particles in the vertex

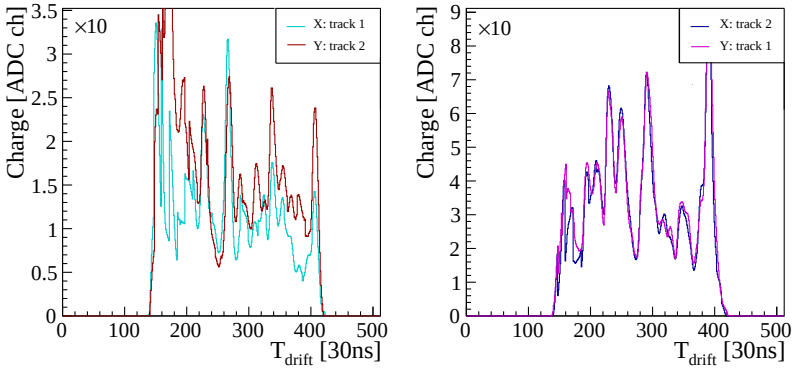


(d) Comparison of the charge profile (in $Z$ direction) of $X-Y$ track combinations.

Figure 6.4: Procedures to recontruct the vertex.

taken with the HARPO TPC prototype. The polarisation plot is obtained by the ratio of azimuthal angle distributions for polarised data (P=100%) and unpolarised data (P=0%).

The first gaseous demonstrator for gamma-ray polarimetry in the energy range between MeV and GeV has been built and operated. Furthermore the ability of a low-density active target to image precisely the conversion of low energy photons close to threshold ($2mc^2 \approx 1$ MeV) was demonstrated. These results were obtained while the background-noise rate from single tracks from upstream the beam was larger than the one expected in orbit.

This project also include the specific development of the first Monte Carlo event generator that samples the five-dimensional *Bethe-Heitler* differential cross section. This event generator has been submitted to the Geant4 Collaboration and after passing all qualification tests, it has been deployed within the 10.5beta Geant4 release.

Having a gaseous detector in orbit requires finding a solution for operation in sealed mode or semi-sealed mode. I then proposed the idea of recirculation to maintain the telescope performance over time while reducing the gas consumption. This led to a patent with the following number: EP3054168 (08/10/2016) [135].

A modified version of the AGET readout chip, named ASTRE *Asic with SCA and Trigger*, was designed, produced and tested [136]. The ASTRE chip is also resistant to ionizing radiation expected in space environment.

### 6.1.5 Gas circulation and purification system

To prevent the degradation of the gas during the space flight, a circulation and purification system (CAPS) have been developed.

The CAPS is composed of purification cartridge (an Oxisorb was chosen), a home-made circulator and the chamber to purify, here it was the HARPO TPC. The Oxisorb has an absorption capacitance of 0.5 L of $H_2O$ and 0.1 L of $O_2$ with an output purity as low as $< 5$ ppb for $O_2$ and 30 ppb for $H_2O$. The full schematics of the CAPS is shown on Fig. 6.7.

To study the CAPS, a gas flow was measured with a F-111B Bronkhorst mass flowmeter calibrated for Ar-i$C_4H_{10}$ gas mixture at 2 bar and 20 °C was added. Gas pressure and temperature were also monitored (I4 and I5) in the ranges of 0-50 °C and 0-10 bar with resolutions of 0.01 °C and 1 mbar.

After filling the vessel with new gas mixture at 2 bars, the monitoring of the CAPS parameters started. Cosmic data were taken once a week. After a period of time of 5 months, a regular degradation of the gain, the attenuation and the drift velocity are visible on Fig. 6.8.

On July 20, the purification was turned on. Several gas samples were taken for analysis with mass spectroscopy, which lead to density drops (lines 1, 2, and 3) on Fig. 6.8. Before and after every operation that affected the gas in the vessel, data was taken with the TPC for consistency checks. After purification, the drift velocity was measured to be 6.0±0.5% higher than its initial value. From the Garfield simulation, this can be explained by the cumulative effects of the reduced gas pressure from 2.1 to 1.9 bar (+4%) and of the measured decrease of the isobutane content from 5.1% to 4.5% (+3%). The residual oxygen content was found to be lower than the detection threshold of the spectrometer. A small but significant decrease of the amount of isobutane have been measured after starting the purification before to stabilization (probably after saturating atomic traps in the Oxisorb) see Tab. 6.1.

It has been proven as a flight solution for gaseous detector. Furthermore, $H_2O$ or $O_2$ permeation will not exist in space. Such purification and recirculation system have been used with a lighter system in the last telescopes developed for muon tomography reducing the gas flow down to 0.1 L/h.

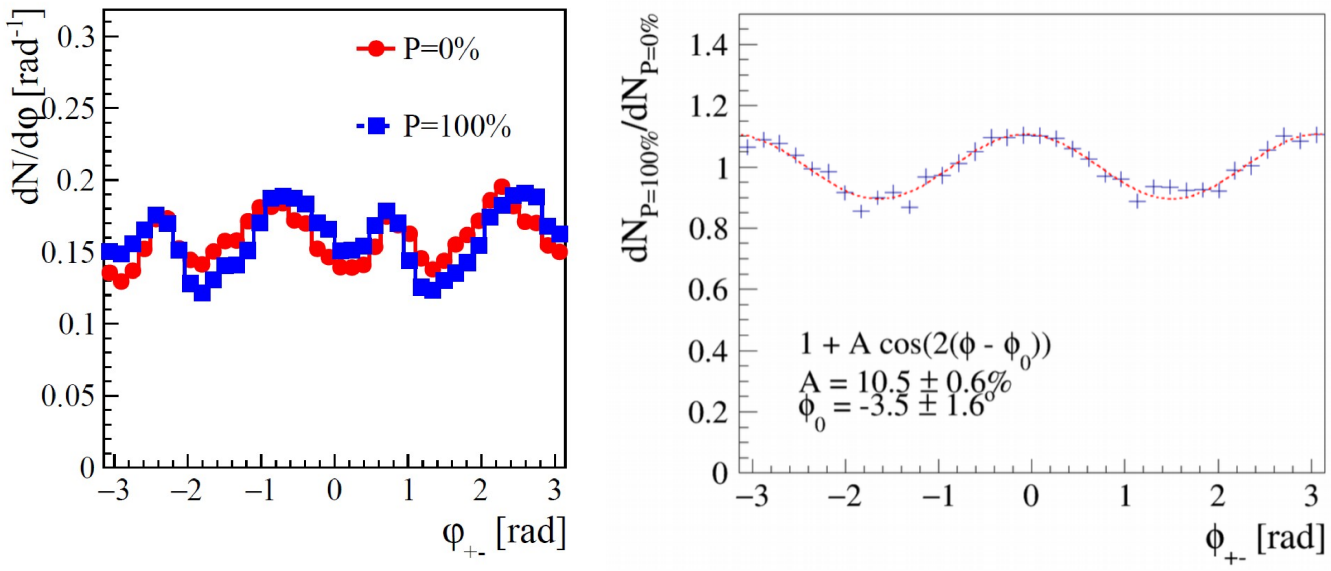


Figure 6.5: Polarisation plots from 11.8 MeV $\gamma$ with HARPO TPC oriented at 0° around the beam axis: [Left] distribution of $\Phi_{\pm}$ extracted from data of polarised and unpolarised beam in blue squares and red dots respectively. [Right] Ratio of the azimuthal angle distributions for polarised (P=100%) and unpolarised (P=0%). The systematic bias is cancelled by dividing the azimuthal angle distribution for polarised photons by the distribution for unpolarised photons from experimental data.

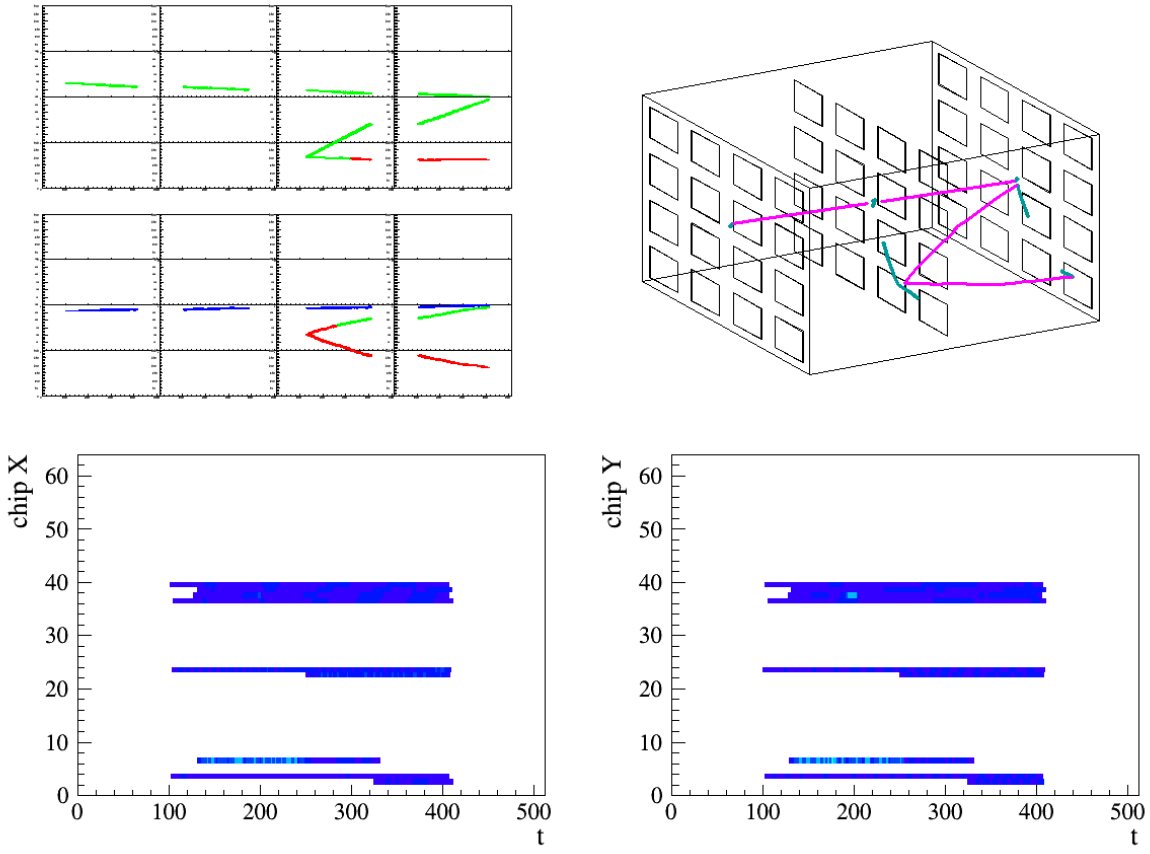


Figure 6.6: Simulation of an event seen in the ST3G telescope read by self-triggered ASTRE chips.

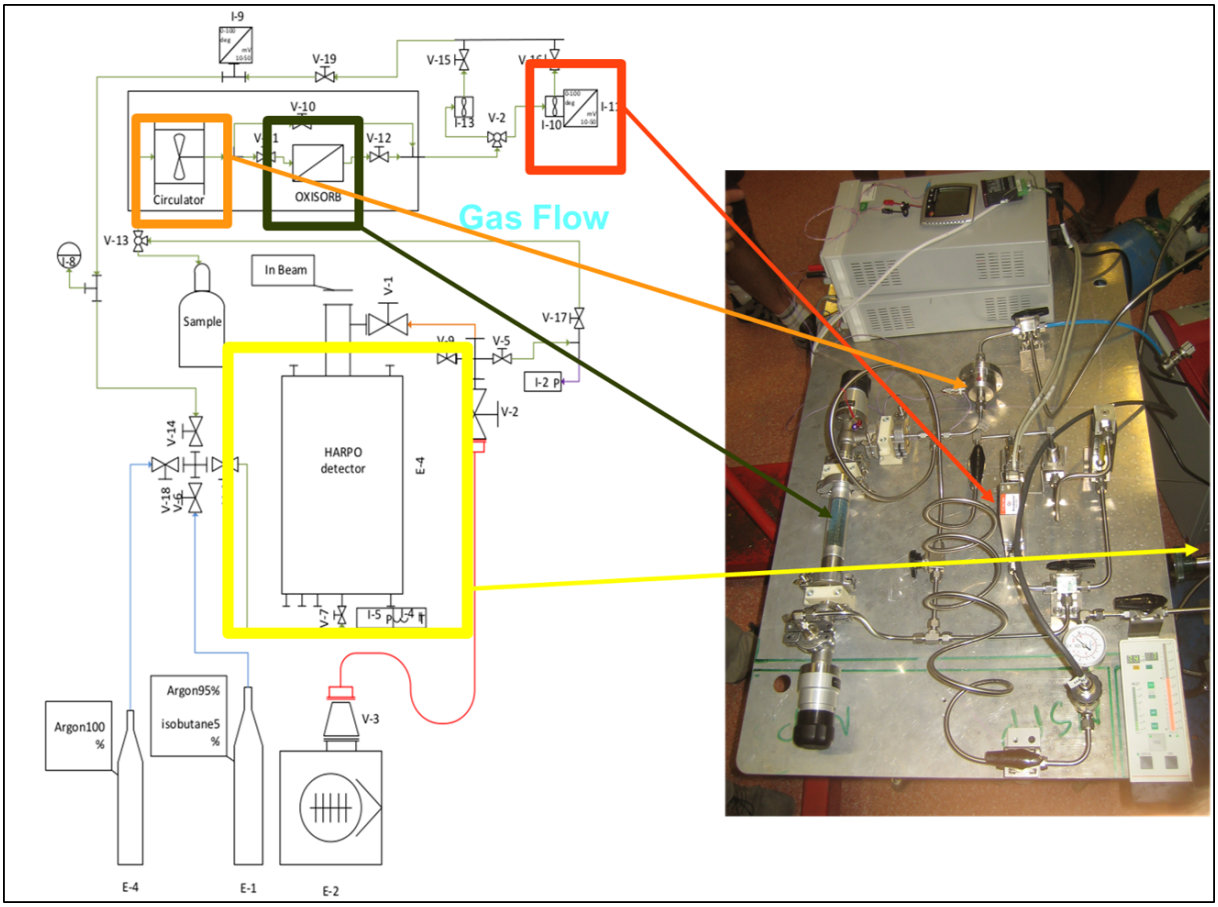


Figure 6.7: Gas circulation and purification diagram and the corresponding picture showing the different elements. The color red, green, orange and yellow show respectively the mass flowmeter, the Oxisorb purification cartridge, the circulator and the HARPO TPC chamber not visible here.

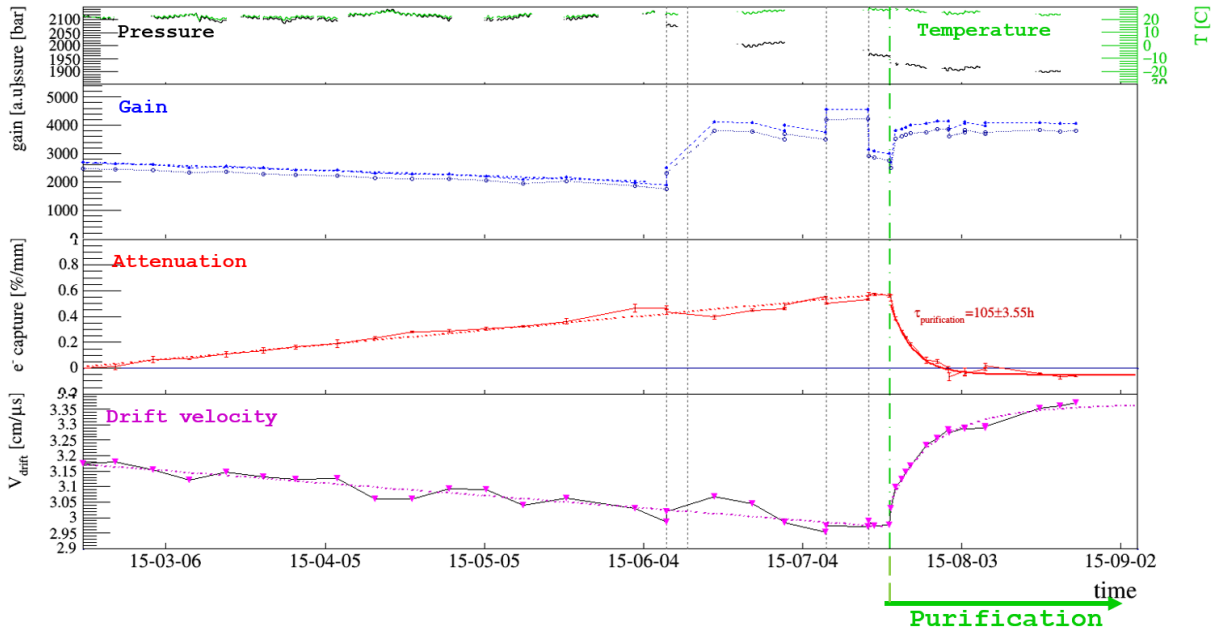


Figure 6.8: Time evolution of the gain, the attenuation an the drift velocity. For the first 5 months, a constant degradation of all three parameters with static sealed vessel. Several variations of the gain appeared (dotted line 1 to 4) due to pressure loss when gas sample were taken. On July 20 (dotted line 5), all the parameters started to recover when the CAPS was turned on.

| **Sample number** | | **1** | **2** | **3** |
|---|---|---|---|---|
| Compound / Date | | July 8 | Aug. 27 | Sept. 17 |
| $iC_4H_{10}$ | % | 5.10 | 4.42 | 4.49 |
| $O_2$ | ppm | 180 | <20 | <20 |
| CO | ppm | 190 | 250 | 130 |
| $CO_2$ | ppm | 120 | 160 | 130 |
| $N_2$ | ppm | 620 | 890 | 850 |

Table 6.1: Gas content measured by a mass spectrometer insensitive to $H_2O$.

### 6.1.6 Prospects

The HARPO prototype phase was successful. The design of a *flight* prototype named ST3G for *Self-Triggered TPC for $\gamma$-ray Telescope* for which a specific trigger has been studied at Irfu using the real-time information provided by the readout chips. Indeed, the main goal of the ST3G project is to develop a trigger system appropriate for gamma-ray detection with a TPC in space. This trigger should be tested in the realistic environment of a stratospheric balloon flight. Such a flight will contribute to evaluate and solve the challenges of running such a large gaseous detector in space. A scheme of $4 \times 4 \times 4 = 64$ modules for a total volume of 1.2 $m^3$ is foreseen for ST3G. It will be the first time sophisticated topological information from a TPC will be used to trigger itself in a high background environment.

A simulation toy has been initiated to study of behaviour of the ST3G event and find the appropriate algorithm to build the trigger [129].

Despite the lack of funding, the next step should focus on a very accurate description (full Monte Carlo including background) of the detector essential to describe and validate a trigger algorithm.

## 6.2 X-ray polarimetry using pixelated TPC

### 6.2.1 Advantages of a pixelated gaseous detector

A pixelized gaseous detector provides both photoelectric conversion of high energetic photon (start from a few keV) and high granularity allowing single electron sensitivity with tracking capability. That is why a small pixelated TPC prototype was made using Micromegas detector read out by a TimePix chip with pixel size of $50 \times 50$ µm$^2$ in a matrix of $256 \times 256$ (see Sec. 3.2.3.1). The chip was protected from sparks with a 20 µm amorphous silicon layer deposit by plasma process [137].

### 6.2.2 Digital Micro-TPC prototype for photoelectric absorption

Fig. 6.9 (left) shows the exploded view of the small detector built as a digital TPC prototype. The detector consists of an aluminium chamber containing a field cage ($2 \times 2 \times 6$ cm$^3$) mounted on a frame which holds a 50 µm gap Micromegas mesh on top of the chip (see Fig. 6.9). The field cage is folded kapton with 15 copper strips (4 mm pitch, 3 mm width). Each strip is connected to his neighbour with a 1 MΩ resistor to provide a uniform electric field.

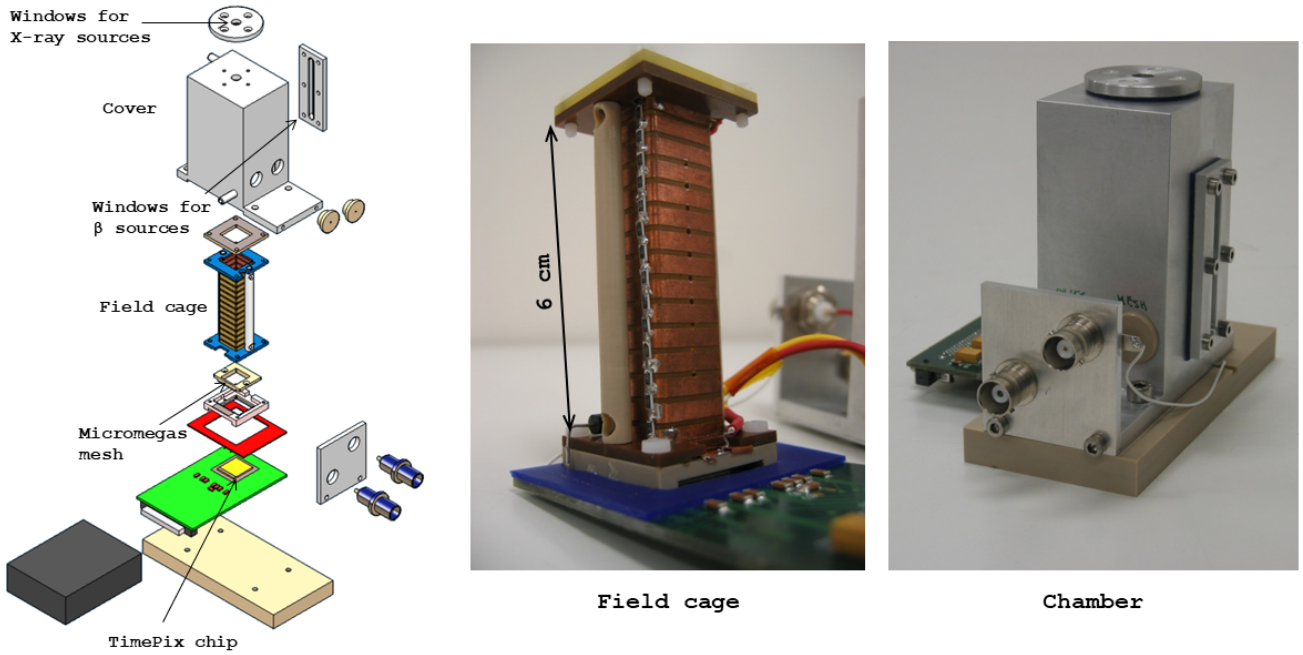


Figure 6.9: [Left] Exploded view of the small TPC using Cern TimePix board using [Middle] 6 cm field cage. [Right] Complete TPC chamber assembled.

Photoelectric x-ray polarimetry with gas-based detectors was first demonstrated in 1923 using a Wilson chamber [138] and recently by MPGDs using a Gas Electron Multiplier [139, 140]. They achieved a quantum efficiency up to 6% at 6.4 keV.

The technique consists in determining the emission angle of the photoelectron by imaging its track in a gas medium.

### 6.2.3 Data taken with $^{55}$ Fe

To demonstrate the capability of such detector, data were taken with a $^{55}$Fe radioactive source. A cut have been done with Neon(90%)-Isobutane(10%) (electron transverse diffusion coefficient $D_t \simeq 350\ \mu m/\sqrt{cm}$) and a drift distance of 5 mm. In this gas mixture the 5.9 keV photons absorption probability is 2.2%.

Fig. 6.10 shows events taken from the unpolarized source without trigger.

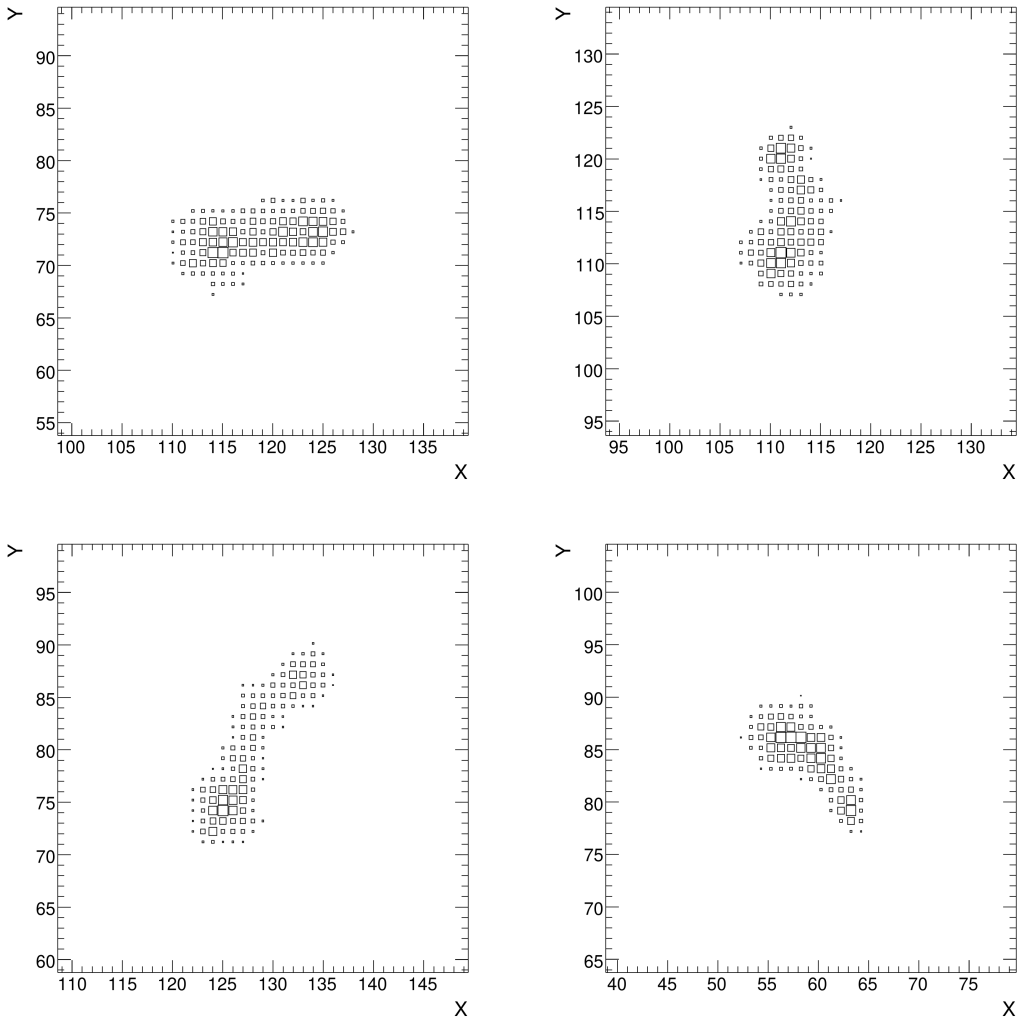


Figure 6.10: Examples of photoelectron tracks ($\simeq$ 1 mm) obtained with the 5.9 keV x-rays from $^{55}$Fe in Neon(90%)-Isobutane(10%) and a drift distance of 5 mm. The area of each square is proportional to the charge collected by the corresponding pixel set in TOT mode. The size of each image is 2.2×2.2 mm$^2$ (40×40 pixels).

The distribution of the direction angle given by the reconstruction of the photoelectric tracks gives the photon polarization. More details can be found in [27].

### 6.2.4 Caliste-MM with Piggyback detector

More recently, the association of the piggyback detector [141] and a Caliste readout (matrix of 16 × 16 pixels of 580 × 580 µm$^2$) with the setup called Caliste-MM [142] took data with polarized 8 keV beam at Soleil synchrotron facility [143]. The gas used was a mixture of He-i$C_4H_{10}$ (90-10). The helium-based

mixture allows to get photoelectron's tracks long enough to be reconstructed.

Fig. 6.12 shows the histogram of the reconstructed azimuthal angle for a 8 keV run with an estimated orientation of 50°. The red curve is the fitted function $A + B \times \cos^2(\phi - \phi_0)$, with $A$, $B$ and $\phi_0$ free parameters representing respectively the offset, the amplitude and the polarization direction.

As the incoming photon source is 100% polarized, the fit parameters allows to calculate the modulation factor of the detector $\mu = \frac{B}{2A+B}$. The factor $\mu = 92\tilde{\%}$ is relatively high despite the relatively big size of pixels used.

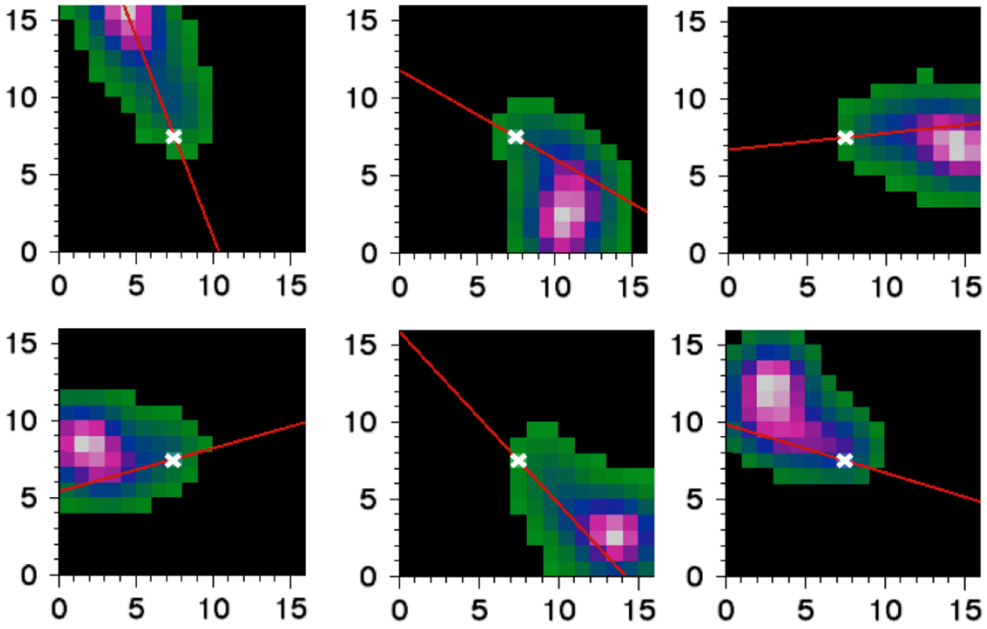

Figure 6.11: Example of track direction reconstructed on some 8 keV photoelectrons events on the CALISTE-MM. The reconstruction algorithm does not take into account the turns at the end due to multiple scattering of the photoelectron in the gas.

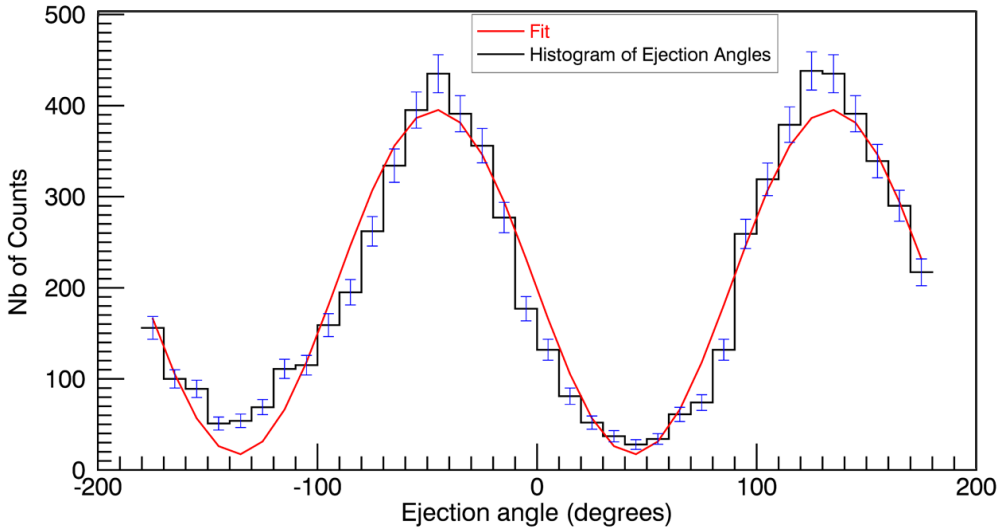


Figure 6.12: Histogram of the reconstructed azimuthal ejection direction, and the fitted function $A + B \times \cos^2(\phi - \phi_0)$ corresponding to the theoretical distribution.

# Third part

# Societal applications using Muon Tomography

*The only source of knowledge is experience.*

Albert Einstein

# Muon Tomography

Contents



Muon tomography is a non-destructive and non-invasive imaging technique using muons naturally generated in Earth's high atmosphere from cosmic rays. The reconstruction of the muons trajectories after crossing the object to be probed allows to generate a density map called *muography*. Although this idea was proposed several decades ago, the performances achieved by particle detectors in recent years, particularly in terms of stability, robustness and precision, have revived the interest of research laboratories developing these instruments for this topic.

## 7.1 Principle of the muon tomography

This technique is based on the Coulomb interaction of muons with matter (see Sec. 2.2.3). These muons come from the electromagnetic showers created during the interaction of high-energy (i.e. relativistic) particles (mainly protons) from the interstellar medium with the upper Earth's atmosphere. The collision with atmosphere nuclei generates hadronic showers including $K^{\pm}$ and $\pi^{\pm}$ that decay mostly into muons $\mu^{\pm}$ at a typical altitude of 15 km. The flux recorded at sea level is approximately 160 Hz/m$^2$, with a mean energy around 4 GeV and with a zenithal angle dependence. Low-energy muon flux decreases rapidly at large zenith angle because muons decay before reaching the ground (see Fig. 7.1).

The muons produced, being also of high energy, can pass through a large quantity of matter (up to a few hundred meters of rock) before being completely stopped. While interacting with matter, muons

can be diffused or absorbed. The angle of deviation and the probability of absorption depend not only on the length of material traversed, but also on its density. Gaseous detectors, sensitive to charged particle developed in our laboratory for particle physics and for nuclear physics experiments, give access to the directions of the muons passing through an object to be scanned. The reconstruction of their trajectories permits to deduce a map of its density. Thus, a muography (2D image from muon tomography) can be performed in several ways.

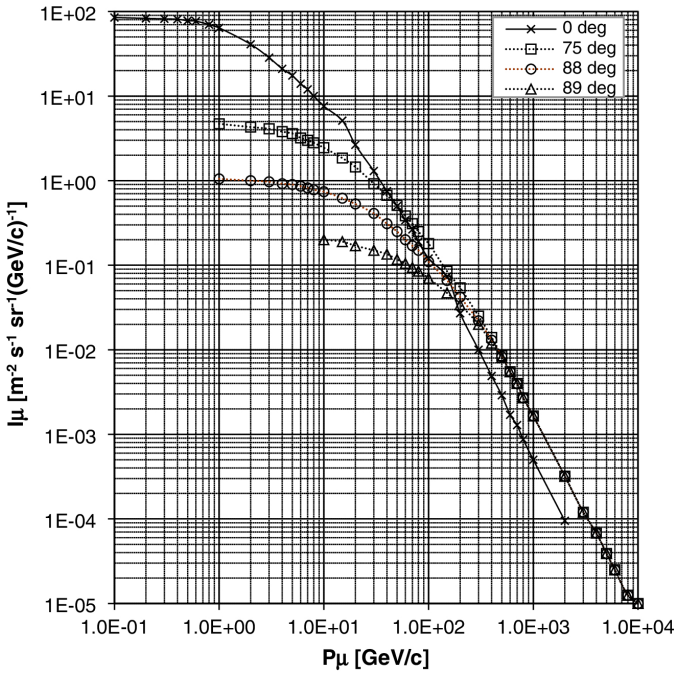


Figure 7.1: Integral spectra of cosmic-ray muons taken from [14]

The muon tomography can be done with three methods illustrated on Fig. 7.2:

- deviation muon tomography,
- transmission muon tomography,
- and absorption muon tomography.

### 7.1.1 Deviation muon tomography

Muon tomography using muon deviation angles can be obtained by placing the object between two telescopes that each measure the muon direction before and after crossing it (Fig. 7.2.a). The scattering angle and the position of the scattering point give access to the local density and make it possible to extract a 3D map of the density of the object.

### 7.1.2 Transmission muon tomography

If the object is large, a single telescope, necessarily placed below, is used to measure the flux of muons crossing the object. A 2D density map or muography (integrated density or opacity) can then be performed (Fig. 7.2.b). In the case of boreholes, by inserting one or more cylindrical instruments at a depth of a few

tens or even a few hundred meters (Fig. 7.2.d). The cylindrical shape of this instrument gives access to the near environment with a field of view of $2\pi$ (see Sec. 8.3).

Also, a 3D map is potentially accessible by placing several telescopes around the object or the place to image.

### 7.1.3 Absorption muon tomography

If the telescope is placed above the object, thus making it possible to measure the flux of muons having been stopped (absorption) by the object thanks to a detection plane (veto) placed below the object. The latter is necessary to identify the muons having been absorbed and thus reject the muons having crossed (Fig. 7.2.a).

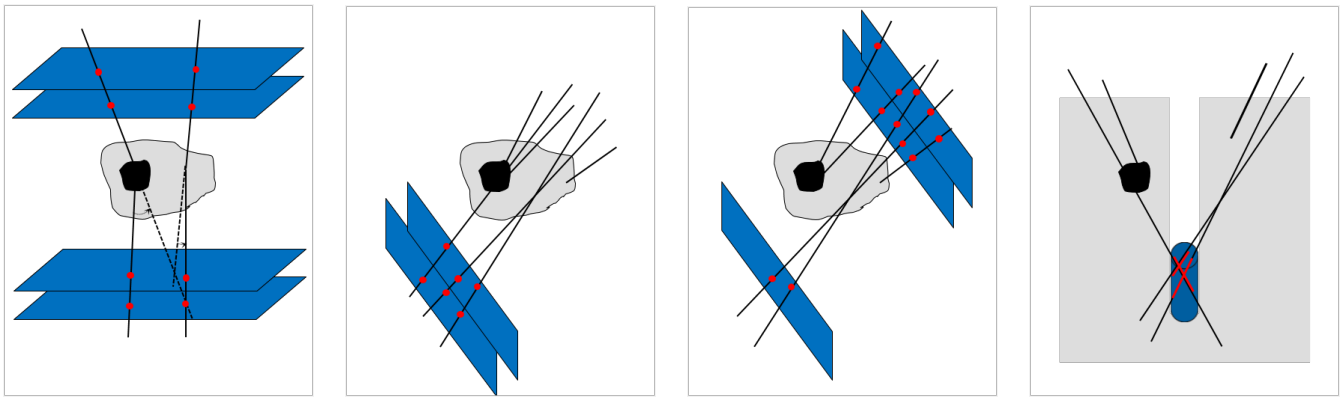

**(a)** **(b)** **(c)** **(d)**

Figure 7.2: Principles of muon tomography with deviation (a), with transmission (b) & (d) and with absorption (c). Black zones feature volumes with higher density, thus with higher deviation and absorption.

### 7.1.4 Muon metrology

The muon telescope built for muon tomography can also be used for muon metrology. If muons are generally scattered while interacting with matter, their deviation angle is on average small, even equal to zero. With a rectilinear propagation in the mean, muons offers a natural way of measuring the relative positions of two objects, like a natural, continuous and free laser system. Another advantage, such technique can be used even with objects separated by obstacles (roof, wall, ...). For muon metrology, a reference telescope is used in combination with a detector attached to the structure to be monitored (bridge, building, etc.). Muons crossing the two instruments allow relative positioning of the latter by making possible a continuous monitoring of the structure deformation. Metrology using muons is still very prospective but can offer many applications for monitoring structures and tracking in civil engineering. The POMME (*POsitionnement par Métrologie MuoniquE, or muon metrology positioning*) experiment have been successfully achieved in the laboratory as a proof of concept [144].

## 7.2 History and state of the art of muon tomography

The beginning of muon imaging took place in the 1950's by Eric George's experiment [145] in an Australian mine some Geiger counters to estimate the thickness of ice above a tunnel from the measurement of muon

| Detector Type | Spatial resolution | Large Scale | Industrial production capability | Production Cost | Electronics Cost | Ease of Operation |
|---|---|---|---|---|---|---|
| Drift Tubes | 0.1-1 mm | high | low | medium | low | complex fabrication process, depends on environmental parameters (T/p) |
| MWPC | 0.1-1 mm | medium | low | medium | medium | complex fabrication process, depends on environmental parameters (T/p) |
| RPC/MRPC | 0.1-1 mm | high | high | low | low | easy fabrication, process, depends on environmental parameters (T/p) |
| MPGD | 10-100 µm | high | high | high | medium | complex fabrication process, depends on environmental parameters (T/p) |
| Silicon Microstrips | 1-100 µm | low | low | high | high | robust, radiation hard |
| Scintillator Bars | 1-10 mm | high | high | low | high | robust, easy to handle |
| Scintillator fibres | 10-100 µm | medium | high | high | high | industrial fabrication process, bending of fibers to be avoided |
| Nuclear emulsion | 1 µm | high | meium | low | - | development needed, limited preservation |

Table 7.1: Comparison of several technologies used for muography.

flux. Later in 1970 Luis W. Alvarez deployed MPWC chambers to search for hidden chamber in the Khaphre pyramid [146] and in 1995 with K. Nagamine [147] with plastic scintillators to explore the inner-structure of a gigantic geophysical substance, the Mt Tsukuba as an example for a top region of volcano.

Since many decades, the use of particle detector technologies for muon tomography had the wind in one's sail and has been encourage by laboratory and government all over the world as new interesting solution to societal applications (volcanology, archaeology, industrial check-up, ...).

The Tab. 7.1 summarizes an exhaustive list of the various detector technologies coming from particle physics. Each of them has its advantages and disadvantages. In particular, MPGDs provide good spatial resolution (10-100 µm) for large scale. Recently, the industrial transfer made by CEA/Irfu to a French PCB company, ELVIA-PCB, to produce bulk Micromegas detectors decreased the production cost and improved the industrial production capability. Thanks to the multiplexing, the channel number can be divided by a factor up to 17, so the electronics cost can stay reasonable. A bulk Micromegas detector can be bought around 3 k€ and the electronics costs is about 10€/channel without including the development cost.

Here are the main many fields of application of muon tomography, the main ones being the following:

- Territorial security and border control: detection of contraband material for internal security (for example, inspection of containers or trucks), and in particular of nuclear materials. Many projects have been initiated around the world (USA, China, France, Russia, Italy, Canada, UK, etc.) with different technologies.
- Monitoring of large structures: whether natural (volcanoes) or not (tumuli, pyramids)
- Soil inspection: search for areas of interest (cavities for archaeology, uranium mining).
- Imagery of works of art: search for weaknesses and assessment of the need for restoration (statues, old buildings).
- Metrology: position and displacement measurement in cases where the instruments usually used are not suitable.

Since a few years, all these societal applications spawned worldwide the number of startups providing muon tomography service. Some of these startups are summarized in Tab. 7.2. Hoping that it is not just a niche market.

| **Name of the company** | **Origin** | **Goal** |
|---|---|---|
| Decision Sciences [148] | United States | Security applications |
| Gscan [149] | Europe | Security, border control, industry and medicine. |
| Ideon [150] | Canada | Geological and underground applications |
| IRIS Instruments [151] | France | Geological exploration |
| Muodim[152] | France | Civil engineering, industry, geoscience |
| Lingacom [153] | Israel | Security and underground applications |
| Lynkeos Technology [154] | United Kingdom | Imaging nuclear waste |
| Muon Solutions [155] | Finland | Geological exploration |
| Muon Systems [156] | Spain | Muon tomography for industrial applications |

Table 7.2: Companies providing muon tomography service.

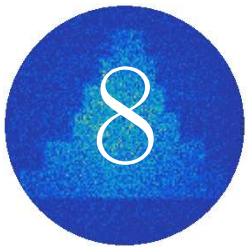

# From proofs of concept to societal applications

Contents



In 2014, the CEA/Irfu started to be involved in muon tomography by using multiplexed resistive Micromegas just invented in the laboratory. The following sections present the development of detectors and telescopes for muon tomography based on this technology, and their use for societal applications (homeland security, archaeology and nuclear survey and dismantling).

## 8.1 Brief history of the muon tomography at CEA/Irfu

After the invention of genetic multiplexing in 2012 [157], the first prototype of multiplexed bulk Micromegas detector was built and tested in 2013, as part of the development of a low-cost cosmic bench hodoscope (number of electronic channels significantly reduced) for the characterization of the detectors of the Clas12 project (see Sec. 5.2.2).

### 8.1.1 The M-Cube project

From 2014 to 2016, the M-Cube or $M^3$ (*Multiplexed Micromegas for Muon tomography*) project was funded by the NRBC-E program. This French program aims to develop new techniques dealing with nuclear, radiological, biological and chemical threats. The goal was to design, built and study a small (1 $m^2$ active area) muon tomography scanner using innovative Micromegas detectors to demonstrate the feasibility of detecting contraband special nuclear materials (SNM) in a few minutes.

The project allowed the development of two (v1 & v2) generations of 2D multiplexed resistive Micromegas detectors, called MultiGen [62]. These prototypes were used to verify the maximum degree of multiplexing, optimize dead zones, improve shielding and validate their performance (see Sec. 8.1.3.1).

The scanner was built with 16 MultiGen (v2) and operated with a 8 ft container (see Fig. 8.1), first, by putting lead bricks inside it (simply laid on a table). These data helped for detector and layer alignments absolutely required to make an accurate reconstruction with optimum sensitivity. The setup and the muography obtained by deviation is shown on Fig. 8.2.


Figure 8.1: Face view [left] and side view [right] of the M-Cube muon tomography 1 $m^2$ scanner. The two planes below the container and the two planes above comprised 4 MultiGen each are visible.

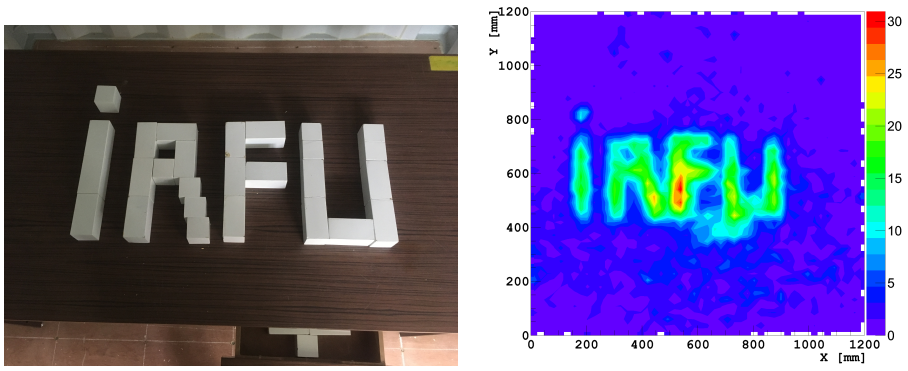


Figure 8.2: Muon tomography in deviation mode using the M-Cube project scanner. Left: picture of the lead blocks inside the container. Right: muon tomography.

Figure 8.3 shows the hit positions after demultiplexing of each MultiGen in the 4 layers composing the scanner. Thanks to a sustained manufacturing transfer, all the 14 over 16 MultiGens were built by the Elvia-PCB company [158]. Nevertheless some imperfections (cut strips, mesh defects and bus routing disjunctions) coming from the PCB fabrication are clearly visible. Only the two perfect detectors (C-09 & C-040) were manufactured by the CERN MPGD workshop of Rui de Oliveira. At that time, the resistive strips were all made by the CERN workshop using 100 kΩ/□ resistive ink (easier to manufacture and value low to spread the charge over several strips).

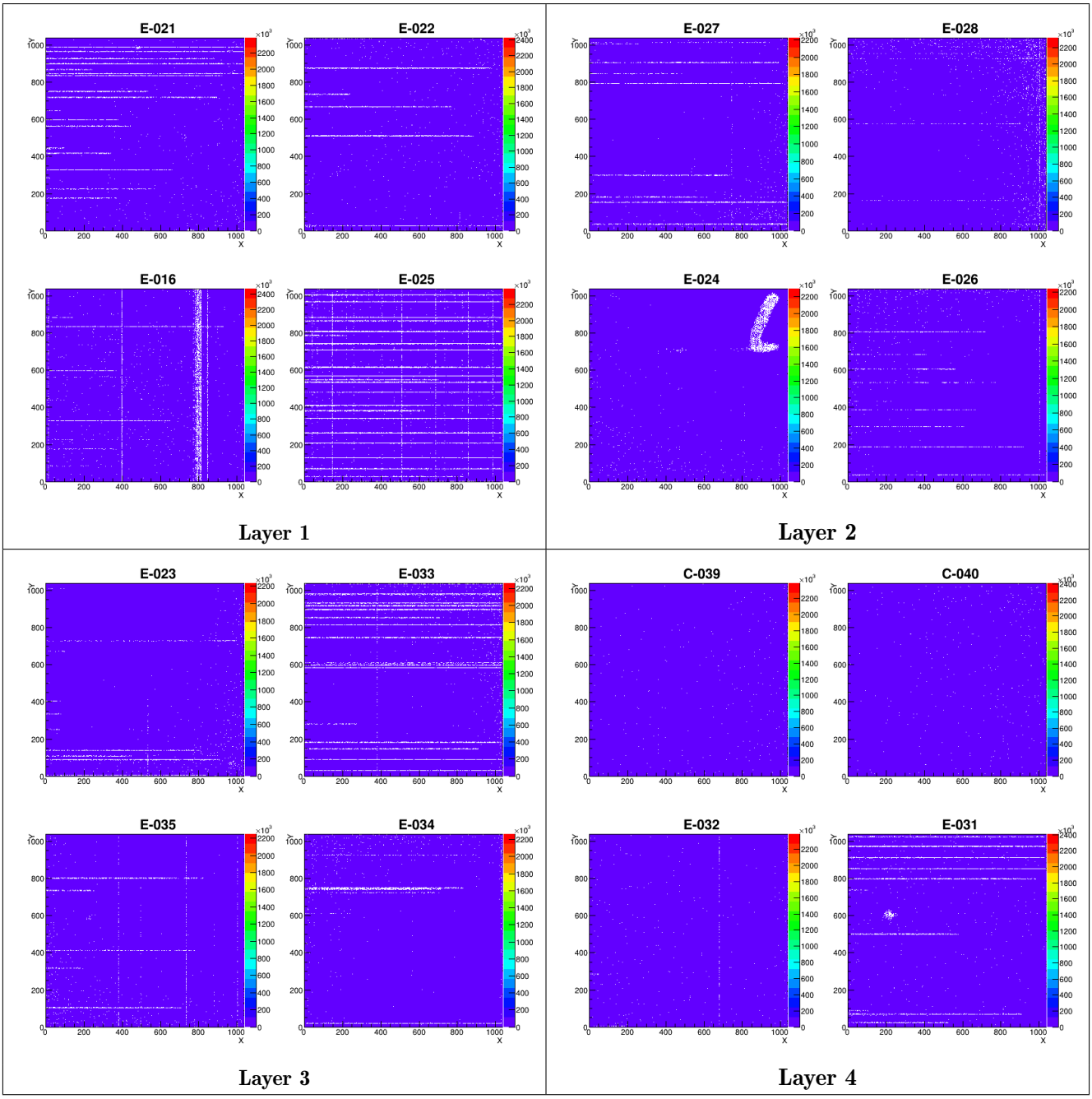


Figure 8.3: Hit positions for the sixteen detectors in the M-Cube bench separated layer by layer.

Then the container was filled of wood-chips and randomly with SNM. The SNM was 4 kg of depleted uranium rods. A Kolmogorov-Smirnov statistical test was used to compare two samples of a randomly distributed variable by computing the maximum distance of their cumulative distribution [15]. The results are shown in Fig. 8.4. This statistical test demonstrates the possibility to distinguish between a container filled with wood-chips bags and one also containing depleted uranium in $1.1 \times 10^5$ events. At this point the Kolmogorov probability (black curve of Fig. 8.4) converged below 2% which indicates that the two distributions are incompatible. If the active area of the bench is larger the time to accumulate $10^5$ events can reach about two minutes.

The M-Cube project showed that a scanner made of MultiGens can trigger an alarm in less than two minutes in the presence of 4 kg of nuclear material in a container. This threshold corresponds to the first criterion defined by the US DNDO (United State Domestic Nuclear Detection Office). Of course, to find the position of the SNM, the data taking has to be much longer (at least a few hours depending of the surrounding materials).

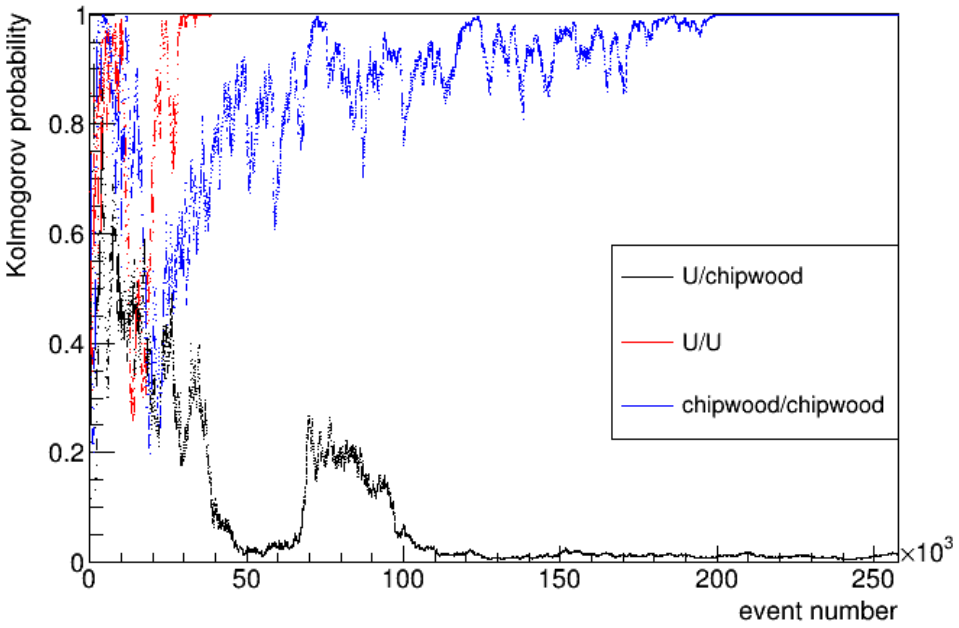


Figure 8.4: Kolmogorov probability in function of the accumulated event number in three different configurations. Taken from [15]

### 8.1.2 The WatTo demonstrator: first outdoor CEA telescope

In 2015, after the validation of the first MultiGen (v1) on the Clas12 cosmic bench, simultaneously to the M-Cube project, a first telescope was built and successfully operated outdoors close to the CEA/Saclay water tower (WatTo) to perform static and dynamic imaging [159].

This first CEA/Irfu field telescope was designed (see Fig. 8.14.a) to support 4 MultiGens (v1) with the following challenging requirements by descending order of priority:

1. Outdoor operation,
2. No additional detectors for triggering,

3. Low electric consumption allowing an autonomous mode,

4. Remotely monitored.

The WatTo telescope also benefited from the development of the Dream Front-End Unit (FEU) electronics card designed for the Clas12 project [29] (see Sec. A.2). The self-triggering mode of the FEU allows making coincidence between the 4 detectors of the telescope without external trigger system. Only 61 over 64 channels of a Dream ASIC are used per coordinate, so two ASICs for both coordinates of a detector and a FEU per telescope are needed.

A high voltage power supply (HVPS or High Voltage Power Supply) board for polarizing the detectors has been specifically developed to substitute the laboratory power supply usually installed in a crate. The HVPS is made of 5 DC-DC converters (from CAEN) transforming 5 V or 12 V low voltage into high voltages up to 800 V (with positive polarity for the resistive strips and negative for the cathodes).

The use of a single-board computer (Hummingboard board from Solid-Run [160]) to control and monitor the telescope by communicating via the Gigabyte Ethernet additional card to the FEU and the HVPS card and also to perform the acquisition and the storage of the data. Actually, at that time, the Raspberry Pi 3 was not able to handle Gigabyte Ethernet protocol. The total electric consumption did not excess 30 W. A 2-month gas autonomy was ensured with a B20 bottle of non-flammable T2K gas (Ar-Iso-$CF_4$, 95-2-3).

This configuration of FEU+HVPS and nano-PC for monitoring a telescope will be used in the next generations of CEA/Irfu's muography telescopes.

The telescope efficiency varied with time. A strong correlation was measured mainly with the temperature T and also with the pressure P but 3 times smaller amplitude. These effects were attributed to gain fluctuations with T and P combined to the use of the self-triggering function (see Fig. 8.5). By adding an USB barometer on the nano-PC, an on-line feedback was implemented to stabilize the efficiency.

The first campaign used an electrical supply from the closest building. After more than 2 months of operation, a second campaign of data taking was performed. The telescope was moved closer to the water tower, and it was supplied with a 160 Ah battery in combination and two 150 W solar panels. Due to the absence of any external grounding, the noise level appeared to be roughly 3 times larger, even with grounding to the Earth. In these conditions, the trigger purity decreased to 50% or less, but the efficiency did not seem to change significantly (see Fig 8.5).

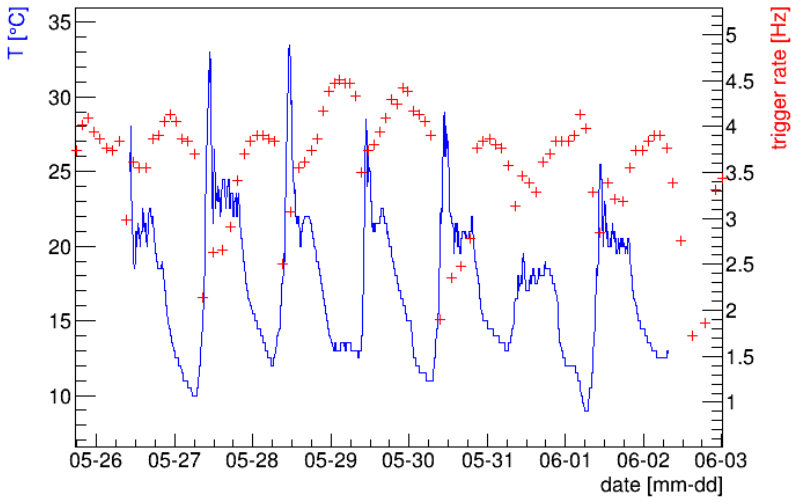


Figure 8.5: Variations of the trigger rate compared to the temperature before feedback corrections were implemented.

Fig. 8.6 (left) shows the image obtained after 4 days of data in the second configuration when the tank was full of water and (right) when the tank was empty during the same time [159].

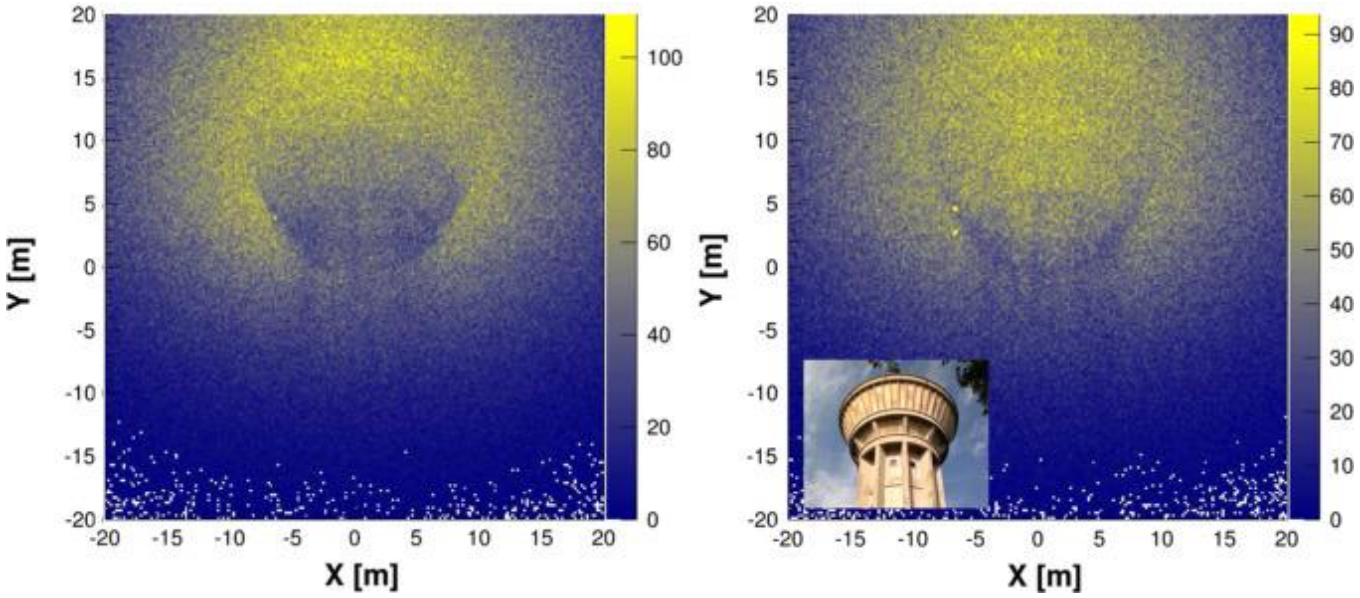


Figure 8.6: Left: muography of the Saclay water tower in 4 days of data when the tank was full. Right: muography of the same water tower in 4 days when the tank was emptied.

The WatTo experiment was the first absorption muography on which the probed object can be clearly recognized. In France, this image triggered a revival for the interest of this technique on various applications and lead the team to most of the projects described in the following paragraphs.

### 8.1.3 Detector and telescope continuous improvement

#### 8.1.3.1 Four generation of MultiGen

The MultiGen is a 2D resistive multiplexed bulk Micromegas readout by strips.

The active area of the MultiGen was limited by the maximal size available in French multilayer PCB industry ($600 \times 600$ mm$^2$ or $600 \times 1000$ mm$^2$). The square shape was chosen to enable mosaical assembling. At that time, it was the largest bulk Micromegas ever built. So, the active area of a MultiGen is defined as 1/4 m$^2$ ($50 \times 50$ cm$^2$) on a 6 layers PCB of $54.6 \times 54.6$ cm$^2$ size (see Fig 8.7). The number of strips in X & Y are identical with a pitch of about 500 µm. Each strip of each coordinate is connected to between to 12 (v4) and 17 times (v1-v3) via 61 internal bus lines. Each of the bus line is routed to a connector footprint in the PCB bottom side. The SAMTEC connector (reference MEC8-135-01-XX-D-RA1 corresponding to 70 pins) has been chosen to be compatible with the flat cable and the FEU electronics developed for Clas12 experiment. The first version was routed using a multiplexing correspondence table. The other versions are based on the first version with minor (v2-v3) or major (v4) modifications.

The figures 8.7 shows the MultiGen v2 and v3-4. Tab. 8.1 & Tab. 8.2 summarize the variations between the different versions of MultiGen.

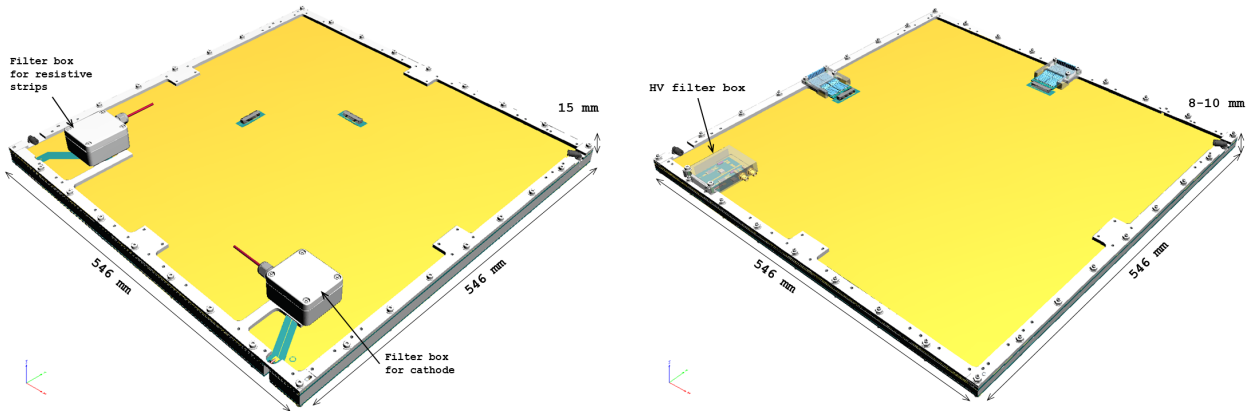


Figure 8.7: 3D CAD drawings of Mutigen v2 [left] and Multigen v3 & v4 [right].

| MultiGen version | Improvement from previous version |
|---|---|
| **v1** | Incomplete family: 13 missing strips |
| **v2** | Fully complete families; grounding layer added |
| **v3** | Connectors moved aside; filters added on PCB |
| **v4** | Number of families reduced to 12; strip resistivity increased |

Table 8.1: Improvement at each MultiGen version.

| Parameters \MultiGen version | v1 | v2 | v3 | v4 |
|---|---|---|---|---|
| **Year** | 2014 | 2015 | 2017 | 2019 |
| **Active area** ($cm^2$) | 50×50 | | | |
| **Total area** ($cm^2$) | 56×56 | 54.6×54.6 | | |
| **Number of channel per coordinate** | 61 | | | |
| **Number of multiplexing families** | 17* | 17 | | 12 |
| **Number of strips** | 1024 | 1037 | 1037 | 732 |
| **Pitch** (µm) | 488 | 482 | 482 | 683 |
| **Spatial resolution** (µm) | 280 | 250 | | 200 |
| **Drift gap** (mm) | 10 | 15 | 8 & 10 | 8 |
| **Efficiency** (%) | >96 | | | |

Table 8.2: Summary of the MutiGen characteristics. (*) One of the 17 multiplexing families was incomplete. The resistivity was progressively increased between the v3 and the v4.

The figure 8.8 shows raw signals recorded by a each of the 8 Dream Asic of a FEU. Each Dream is connected to a MultiGen coordinate X or Y. Thanks to the resistive strips the signal is shared over several strips allowing the demultiplexing and calculating the hit position for each coordinate. A common noise is clearly seen on the baseline due to the large strip capacitance ($\simeq$ 1.5 nF in X and $\simeq$ 0.8 nF in Y). Indeed, each channel is connected to the detector with a micro-coaxial cables is $\simeq$44 pF/m and each multiplexed strip family correspond to 6-8.5 m long strip. The inter-strip in X is only 100 µm while in Y the strip width is 100 µm. A common noise subtraction algorithm has been implemented to improve the signal/noise ratio.

The efficiency and the spatial resolution have been measured using a bench with the same version of MultiGen. The MultiGen v1 and v2 reach an efficiency about 96 % (see Fig. 8.9) when the voltage is above 470 V in Ar-i$C_4H_{10}$ gas mixture. Spatial resolution measurements have been done by fitting the distribution of measured position compared to muon track position with a Gaussian. For both, a degraded resolution is observed: the measured 280 µm (v1) and 250 µm (v2) are largely bigger than the minimum theoretical value expected to be pitch/$\sqrt{12}$ = 141 µm (v1) or 139 µm. MultiGen v3 & v4 have similar results with a spatial resolution measured at 200 µm thanks to their resistivity which were progressively increased from 100 kΩ/□ to a few MΩ/□ (see Sec. 8.1.3.2).

As the relatively low resistivity induces large cluster size numbers (up to 20 in Y direction and up to 50 in the X direction) shown in the Fig. 8.11 so it becomes difficult to match large cluster with a unique or precise position inside the detector and above all when it exceed the multiplexing family number (17 for v1-3 and 12 for v4). Furthermore, the resistivity inhomogeneities of the resistive layer degrade the time resolution, forbidding the use of enhanced clustering techniques such as the µ-TPC method [161, 162].

#### 8.1.3.2 MultiGen production

Since end of 2017, the resistive strips layers are produced in the CEA/Irfu MPGD workshop and the resistive layer lamination + bulk processes are done by the PCB manufacturer Elvia-PCB.

The resistive layer is a made with screen printing machine for depositing of a resistive ink (ESL resistive paste [102]) on a 50 µm polyimide film (usually Kapton from DuPont Corporation) through a screen. A mix of 100 kΩ/□, 1 MΩ/□ and neutral paste give access to higher resistivity (>1 MΩ/□) .

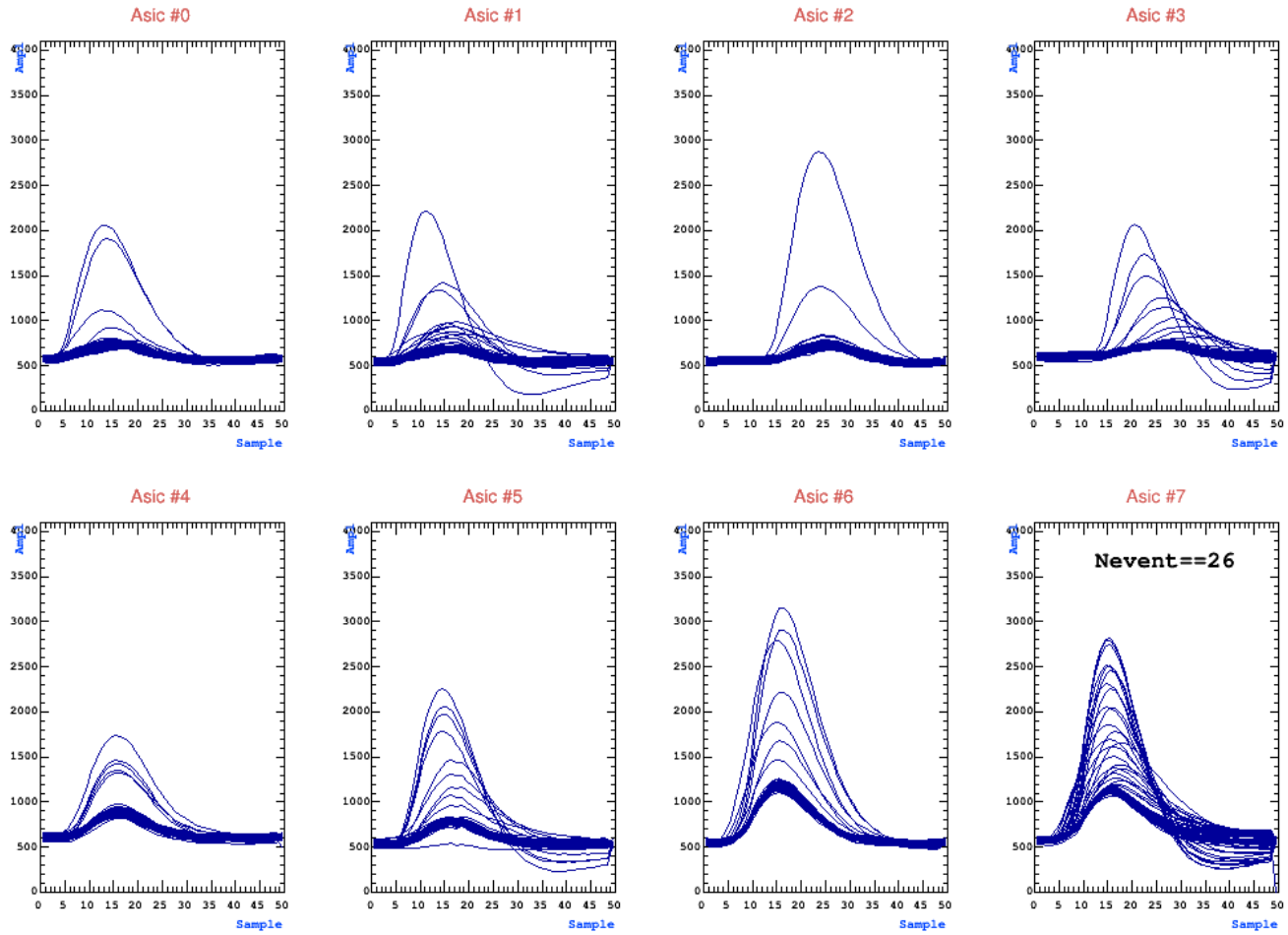


Figure 8.8: Auto-triggered signals seen by 4 MultiGen crossed by a muons.

A R&D effort was done between 2019 and 2021 to increase the resistivity value of the strips. Fig. 8.12 shows the evolution of the cluster size with the strip resistivity. A minimum cluster size of 10 is achieved after a resistivity of 5 MΩ/□. Beyond 3 MΩ/□, the dispersion increases, so the homogeneity and the reproducibility degrade. From 2020 to today all the MultiGens were produced with a resistivity above 1 MΩ/□. The spatial resolution reached 200 µm (v4) which is exactly the value expected for 683 µm strip without charge sharing.

The resistive Kapton foil pressing parameter also change the resistivity. Fig. 8.11 shows MultiGens built with resistive Kapton foils pressed at 12 bars by CERN (C-039 & C-040) and at 7 bars by Elvia-PCB (E-031 & E-032). So the cluster size distribution of the X coordinate from the CERN MultiGens are sharper than the Elvia-PCB ones. The time and the temperature used to polymerize the resistive paste also affect the resistivity. No simple and reproducible formula was found yet.

The resistivity increase is clearly correlated with the number of MultiGens produced by Elvia-PCB (up to 36 in 2021). Manufacturing defects (dust, insufficient rinsing, etc.) which usually lead to high leakage currents in the resistive Micromegas, give now leakage currents which have become very low thanks to higher resistivity values.

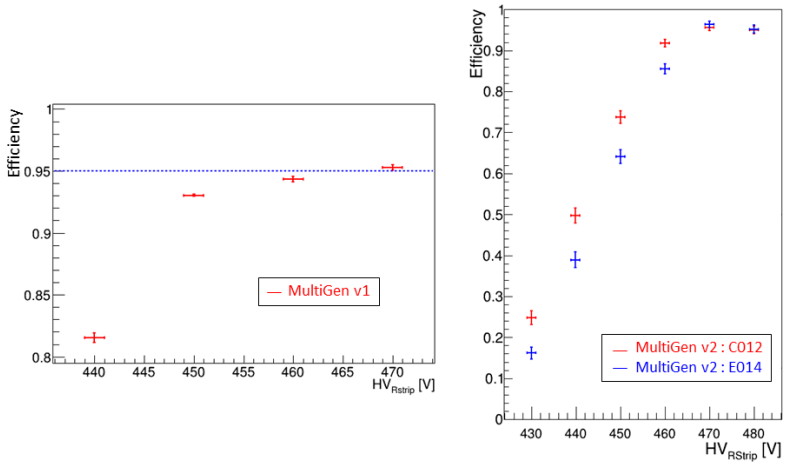


Figure 8.9: Efficiency for MultiGen v1 [left] and v2 [right] in Ar-i$C_4H_{10}$ gas mixture.

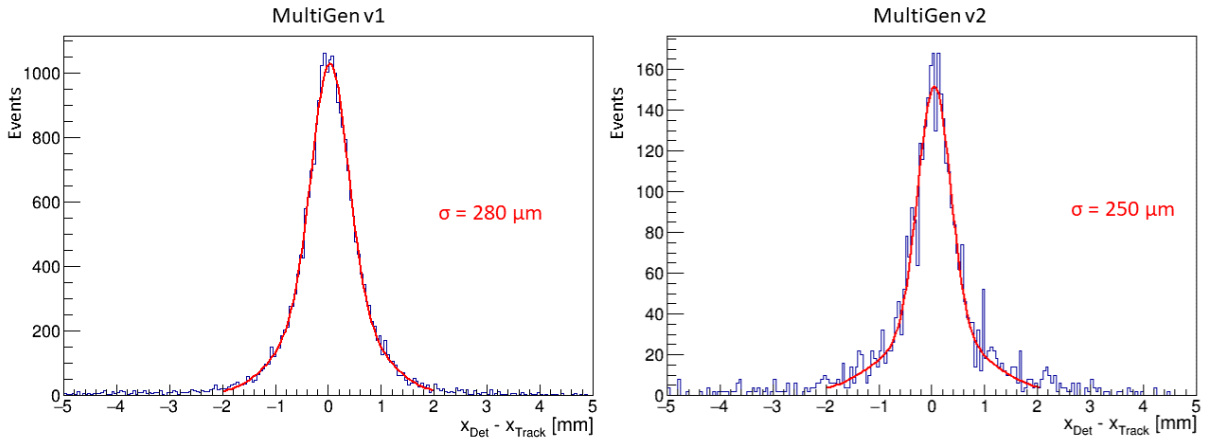


Figure 8.10: Spatial resolution given by distribution of measured position compared to muon track position for MultiGen v1 [left] and v2 [right] in Ar-i$C_4H_{10}$ gas mixture.

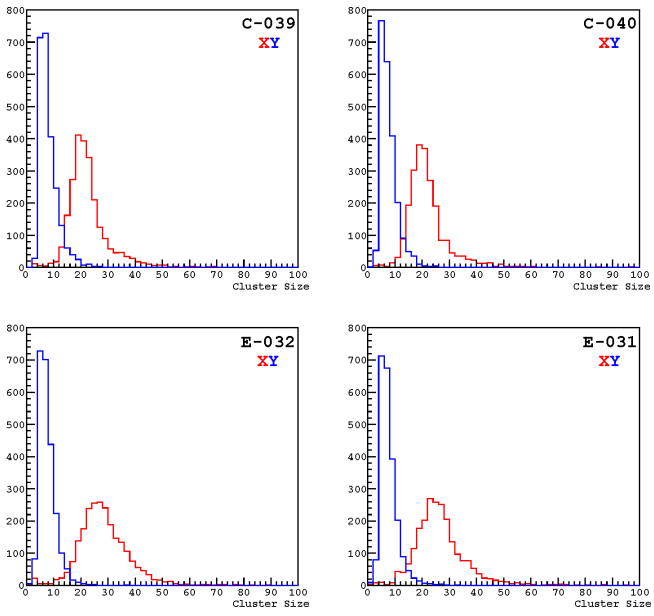


Figure 8.11: Cluster size distribution of X & Y coordinates for four MultiGens, two produced at CERN (C-039 & C-40) and two produced by Elvia (E-031 & E-032) .

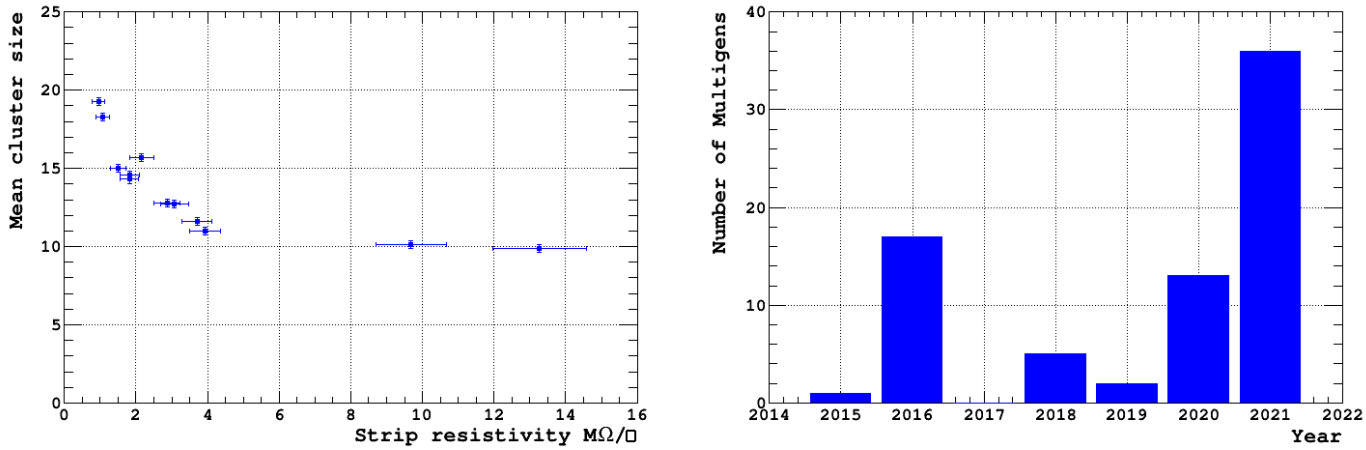


Figure 8.12: [Left] Cluster in function of the strip resistivity. [Right] Production of MultiGen at Elvia-PCB company during the past year.

| Telescope type | Year | Experiment | Number | Name |
|---|---|---|---|---|
| a | 2015 | WatTo | 1 | - |
| b | 2016 | ScanPyramids | 3 | *Alhazen, Alvarez, Brahic* |
| c | 2018 | ScanPyramids | 2 | *Charpak, Degennes* |
| c | 2019 | G2G3 | 1 | *Bose* |
| d | 2021 | G2G3 | 3 | *Dirac, Einstein, Fermi* |
| d | 2021-2022 | Various | 6 | *Fert, Blau, Leavitt, Meitner, Wu, Yulia* |

Table 8.3: List of telescopes built and operated.

#### 8.1.3.3 CEA/Irfu telescopes

Since the first outdoor telescope built for WatTo in 2015, the telescopes have also been improved alongside the MultiGens. They have become more compact, lighter and therefore more portable.

The figure 8.14 and Tab. 8.3 shows the four generations of telescope with the year and the number of objects built and operated. Each telescope has been named by an eminent scientist or personality. The WatTo telescope (a) was the largest followed by the 3 ScanPyramids telescopes deployed outside the Khufu's pyramids (b) and inside the Great Gallery (c). The dismantling project is using now the last version (d).

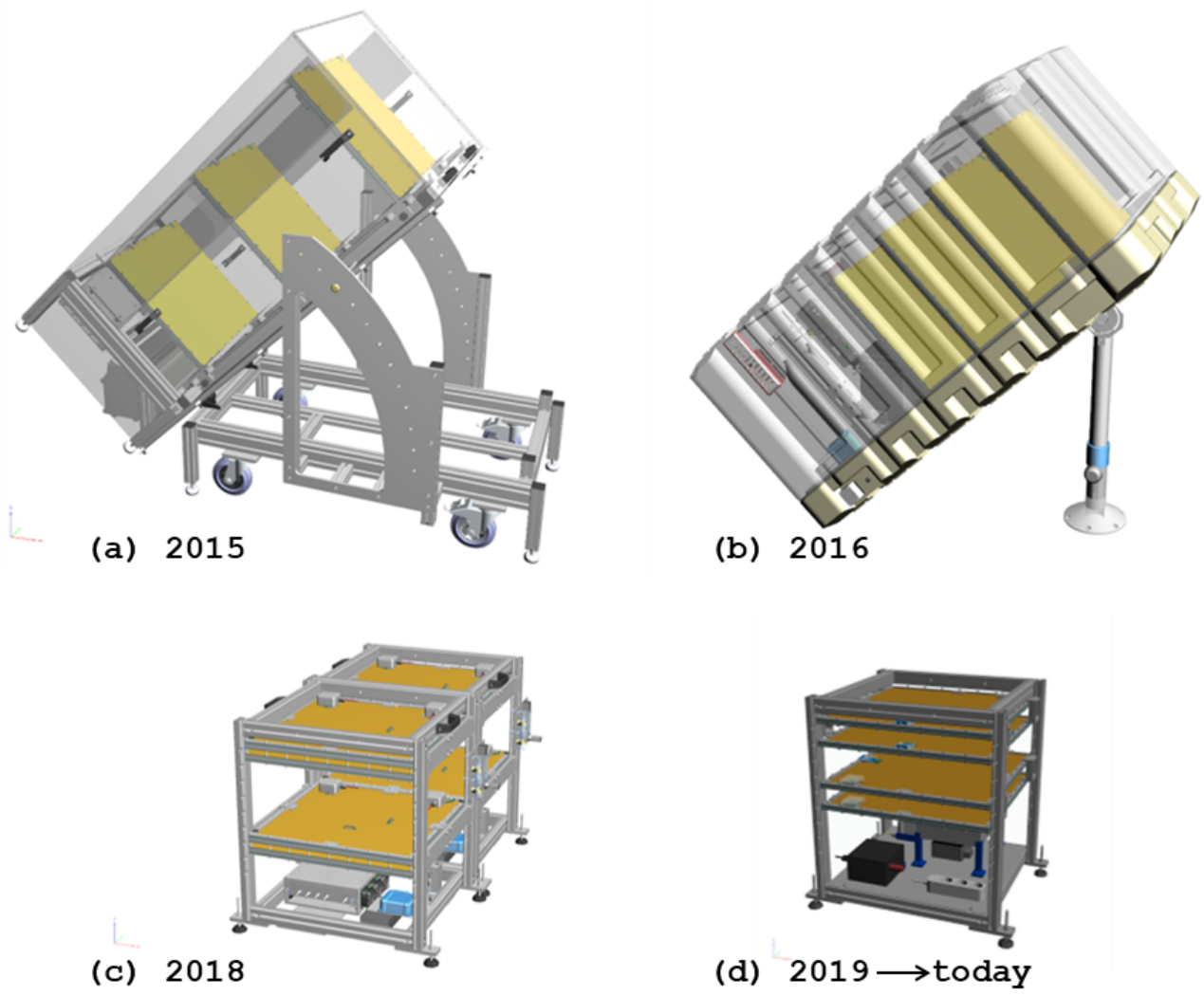


Figure 8.13: Evolution of the Micromegas-based telescope designs with time (same scale).

## 8.2 Applications

### 8.2.1 ScanPyramids Mission

The ScanPyramids mission is coordinated by the HIP (Heritage Innovation Preservation) institute and the Faculty of Engineering of Cairo. The goal is to image the 4 Egyptian pyramids (Khufu, Khafre) using the best non invasive technologies (radar, infrared thermography and muon tomography).

End of 2015, the coordinator of the ScanPyramid mission was reach out to participate to the Scanpyramids mission in collaboration with scientists all over the world (Egypt, Canada, Japan and France).

Two main campaigns were performed in collaboration with two Japanese teams (KEK and Nagoya University), the first was from outside and the second from inside the great pyramid.

| **Detection technology** | Gas detectors | Nuclear emulsion | Hodoscopes |
|---|---|---|---|
| **Laboratory** | CEA | Nagoya University | KEK |
| **Angular resolution [mrad]** | 0.8 - 4 | 2-14 | 7-10 |
| **Angular acceptance [Deg]** | 45 | 45 | 34-45 |
| **Active area [cm²]** | 50x50 | 30x25/unit | 120x120 |
| **Position resolution [um]** | 400 | 1 | 10 |
| **Height [cm]** | 60 | 0.02 | 100-150 |
| **Power requirement [W]** | 35 | 0 | 300 |
| **Data taking** | Real time | Development required | Real time |

Table 8.4: Comparison of the three technologies used for muography in the ScanPyramids mission.

#### 8.2.1.1 Proof of Concept: the notch

Three compact telescopes (*Alhazen*, *Alvarez* and *Brahic*) were built and operated outside the Khufu's pyramid between June 2016 and July 2017 in three configurations, while 2 Japanese teams with different muon technology were install in the Queen's Chamber (see Fig. 8.14-b). These new telescopes using only MultiGen v2 were more compact, more autonomous and fully controlled by 3G network compared to the WatTo telescope. The consumption was also around 40 W.

The first configuration aims to identify the known *Bob's Chamber* located on the North-East edge of the great pyramid in firstly the operation of the telescopes with temperatures close to 50°C (see Fig. 8.16). The results made it possible on the one hand to see the known cavity and the presence of another similar cavity a little higher on the same edge and on the other hand to confirm the existence and to triangulate from the outside the position of the *Big Void* seen by the Japanese from the inside [163].

#### 8.2.1.2 The Big Void discovery

The three techniques of muon tomography (see Tab. 8.4) were deployed towards the heart of the pyramid. The Japanese teams were installed inside (in the Queen's Chamber), while the CEA detectors were outside in the direction of center.

About 15 million events were recorded by the CEA/Irfu telescope. An excess of about 2 muons per day in the direction of the great gallery and this new void was measured.

After 2 months of data taking in the two telescopes (position G1 for *Alhazen* and G2 for *Brahic* in Fig. 8.15), the analysis reveals two statistically significant excesses of muons coming from the core of the

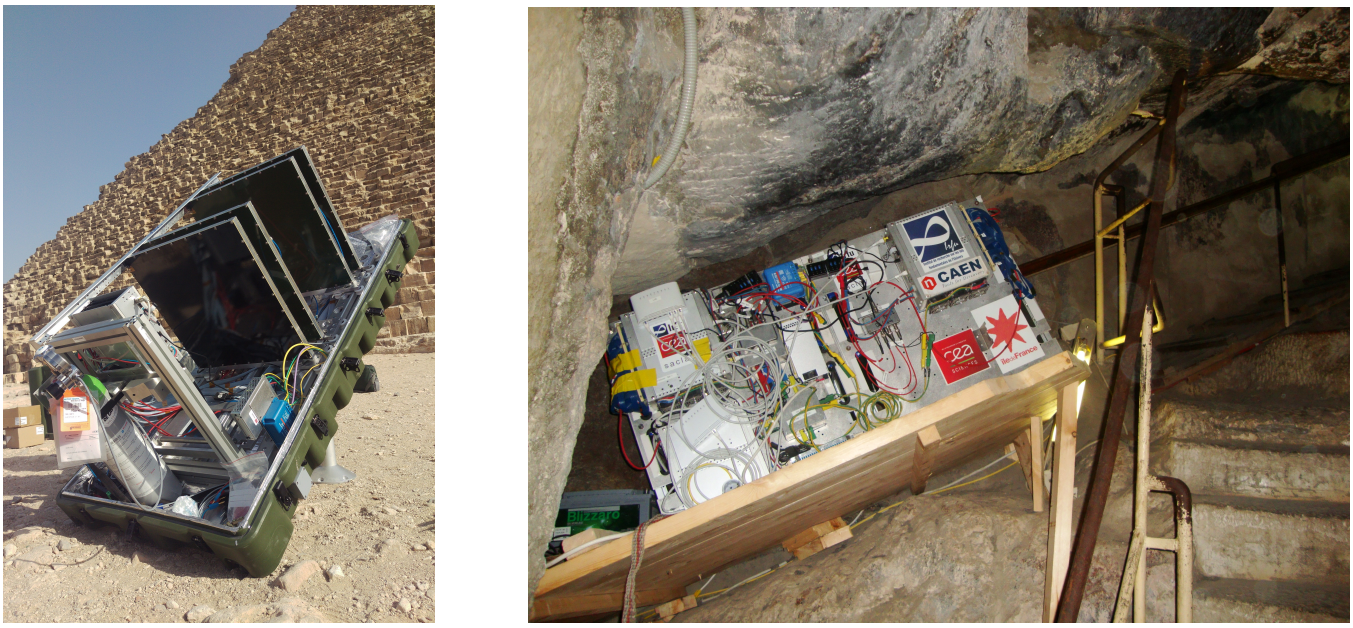


Figure 8.14: Telescope outside (north face) [left] and inside (at the bottom of the ascending corridor) [right] the Khufu's pyramid.

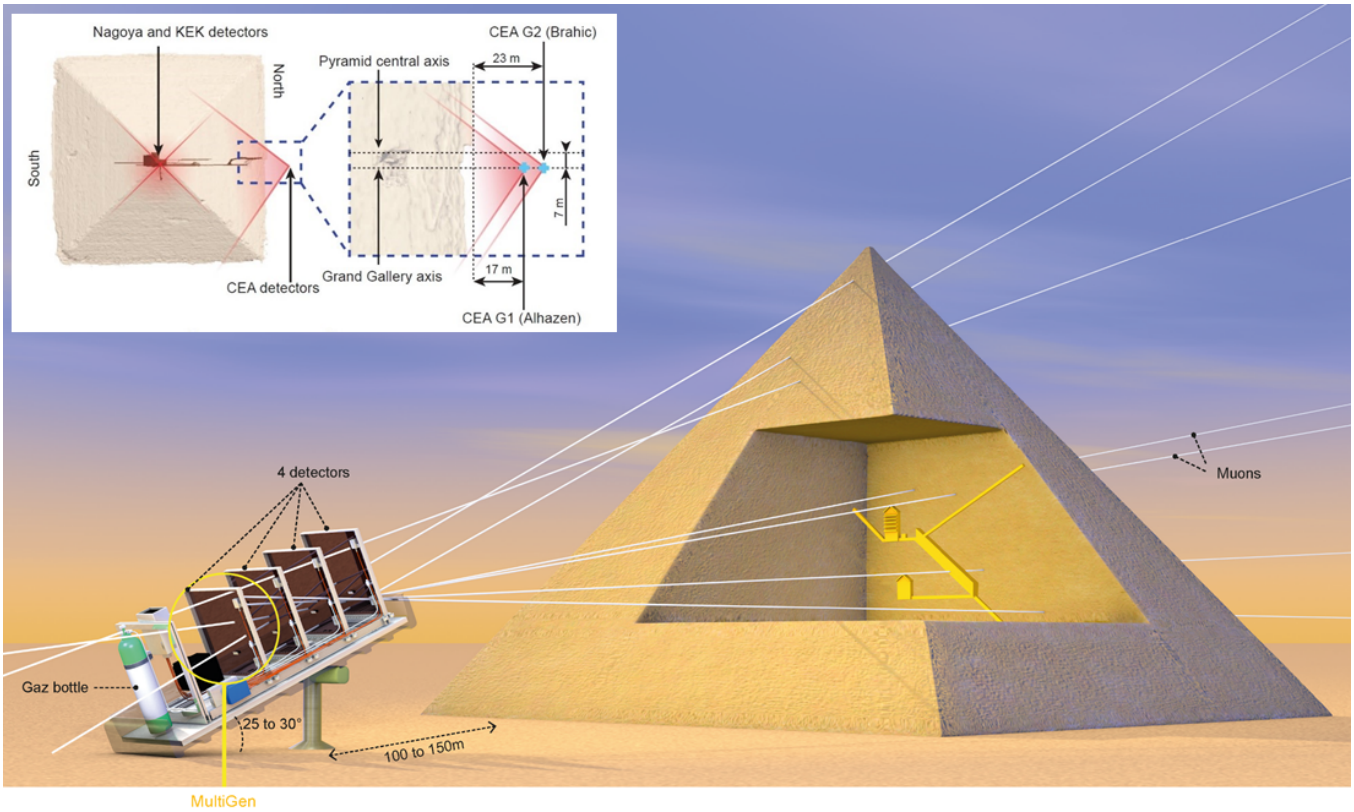


Figure 8.15: [Top left box] Position G1 of Brahic and G2 of Alhazen outsitde the Khufu's pyramid. Both telescopes were point out the pyramid center at respectively 23 m et 17 m.

pyramid (Fig. a, b, c, and d, e, f): an excess corresponding to the large gallery and the other corresponding to the new void. Their analysis model confirmed that the observation of the G1 and G2 telescopes converges on the same region as that obtained from the Queen's chamber with emulsion plates (figure h). The overall combined excesses give $8.4\sigma$ (respectively $5.8\sigma$) for the large gallery (respectively the new cavity).

The ScanPyramids Big Void dimensions is close to the large gallery one, an architectural structure located in the heart of the great pyramid (47 m long, 8 m high) below this new cavity. The latter has an estimate minimum length of 30 meters. The Big Void was first observed with nuclear emulsion films installed in the Queen's chamber (Nagoya University), then detected with a scintillator telescope installed in the same chamber (KEK), it was confirmed with gaseous detectors, Micromegas, located on the outside of the pyramid (CEA/Irfu). Therefore the very different angle of view from CEA/Irfu data made possible to refine the location of this void.

The three muography instruments were all able to detect this large void called ScanPyramids Big-Void from different angles and at different positions, with a level of confidence greater than $5\sigma$ (threshold level required for a discovery in particle physics). This level of certainty was confirmed for each muography result produced completely independently.

This is the first time that an instrument has detected a cavity located deep within a pyramid from the outside.

These results were published by the ScanPyramids team on November 2, 2017 in Nature [163].

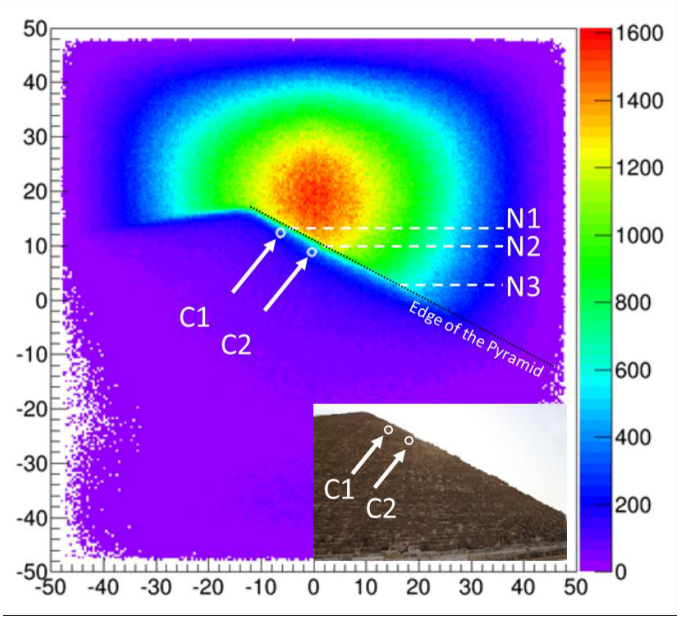


Figure 8.16: Muography of the north-east edge of the Cheops pyramid obtained by CEA/Irfu telescope. In addition to the notches N1, N2 and N3, and the cavity C2 already known, they highlighted a new cavity of about 9 $m^2$ named C1, about 105 meters high.)

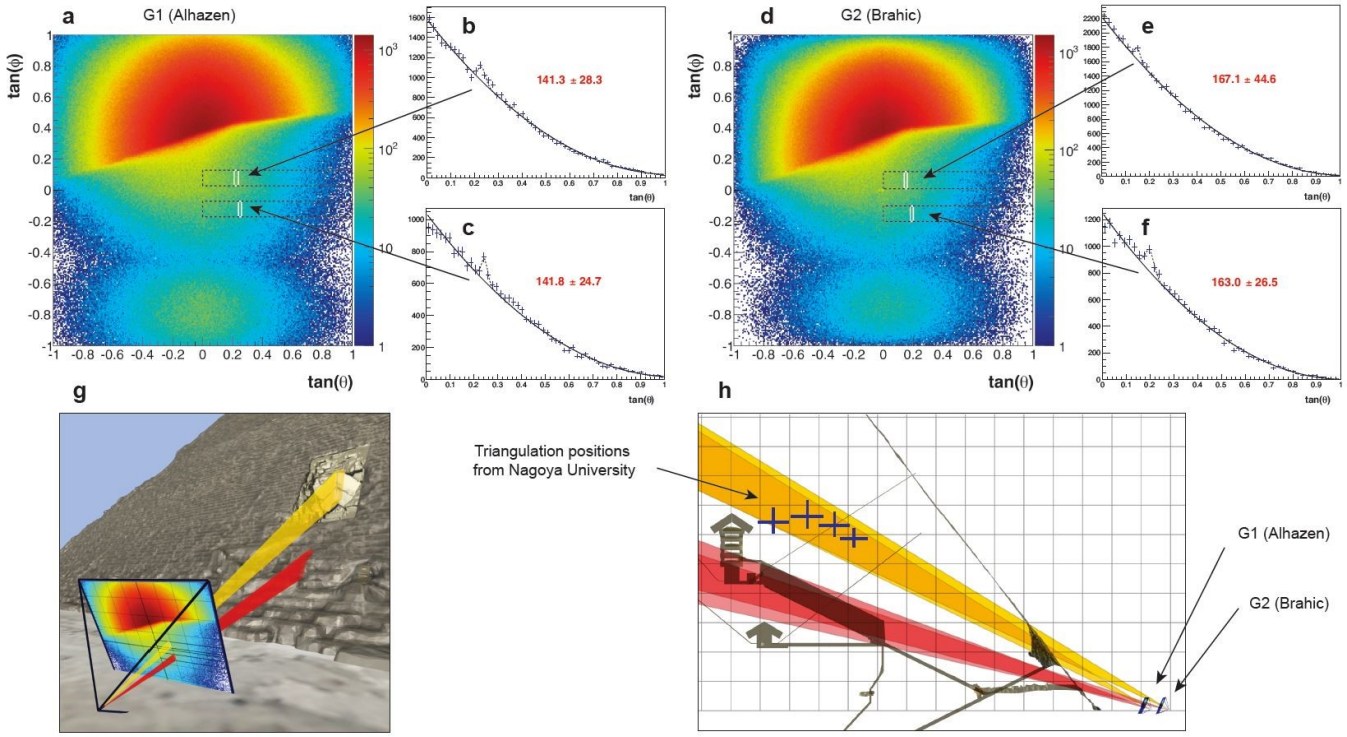


Figure 8.17: Results of analyses of data from the 2 Irfu telescopes placed outside the pyramid and at different positions G1 and G2. Each detects 2 muon excesses corresponding to the grand gallery and the other corresponding to the new void.

#### 8.2.1.3 The North Face Corridor

The discovery of the Big Void encouraged us to improve the compactness of the telescopes (reduced mechanical structure) and make them more gas-efficient (flow reduction down to 0.1 L/h) in order to deploy new telescopes inside the Khufu's pyramid (see Fig. 8.14-c). Initially, *Charpak* and *Degennes*, with a surface area of 1/2 $m^2$ each, were placed in the large gallery (from June 2018 to October 2019) to more precisely measure the position and dimensions of the *Big Void*. In a second step (from October 2019 to March 2020) they were redeployed with *Joliot* (1/4 $m^2$) at the bottom of the ascending corridor and in the descending corridor to precisely locate the North Face Corridor (NFC) discovered by the Japanese in 2016. The results of these measurements were submitted to the journal Nature Communications at the end of 2021.

End of 2019, the muon telescopes already inside the pyramid was moved to more optimal positions in order to allow for a precise triangulation and characterization of the North Face Corridor (NFC) first seen by the Japanese team of Nagoya University with nuclear emulsions previously deployed in the descending corridor and the Robbers's tunnel.

Three CEA/Irfu telescopes were installed, *Charpak* and *Joliot* in the descending corridor, and *Degennes* on a wooden platform built for this purpose at the bottom of the ascending corridor.

After 140 days of data taking (more than $116 \times 10^6$ muons reconstructed), raw muographies were obtained and compared GEANT4 simulations. Six cosmic muon parametrizations were implemented to normalize the data. All of them show an excess with a significance above $10\sigma$ corresponding to the NFC as shown on Fig. 8.18.

Its shape and location have been fully parametrized by: its width $W$, height $H$ and length $L$ and its position along the North-South axis $X$, East-West axis $Y$ and altitude $Z$, and finally its slope $\alpha$ and detailed in [164].

An important aspect of the simulation is the choice of the cosmic muon parametrization. Six of them were investigated, as shown in Fig. 8.18. The Guan parametrization [20] was found to provide the best agreement with CEA data in terms of relative and absolute muon flux, though Bogdanova [19], Reyna [17] and Tang [16] were also close. Matsuno [18] and Shukla [21] deviated significantly, but it's worth mentioning that the former was derived for nearly horizontal muons while the latter provided parameters at a given muon direction, a situation not adapted to our large acceptance instruments.

### 8.2.2 Nuclear applications

#### 8.2.2.1 G2G3 project

The G2G3 project corresponds to the monitoring of the two G2 & G3 reactors of the CEA of Marcoule which were built and use to enrich uranium to plutonium from end of the 1950's to beginning of the 1980's (see Fig. 8.19). This project took place in two phases: (1) a feasibility study of the use of muography by Monte Carlo simulation for monitoring using reactor CAD drawings (from 2018 to 2020) and (2) on-site measurement which highlighted an incompatibility between plans and reality (see Fig. 8.20). This defect was identified independently by the study of a team of engineers for several months. Also, the use of four telescopes of 1/4 $m^2$ (*Bose*, *Fermi*, *Dirac* and *Einstein*) positioned at several measuring points around the G2 reactor made it possible to make 27 different projections. Each projection corresponds to a transmission muography and the application of a SART algorithm (Simultaneous algebraic technical reconstruction) [165] made it possible to carry out the first 3D muon tomography of the interior of a nuclear reactor. Some tomographic sections are visible in Figure 8.21. The telescopes have been redeployed under the G3 reactor since the beginning of April 2022. They will periodically change position around the G3

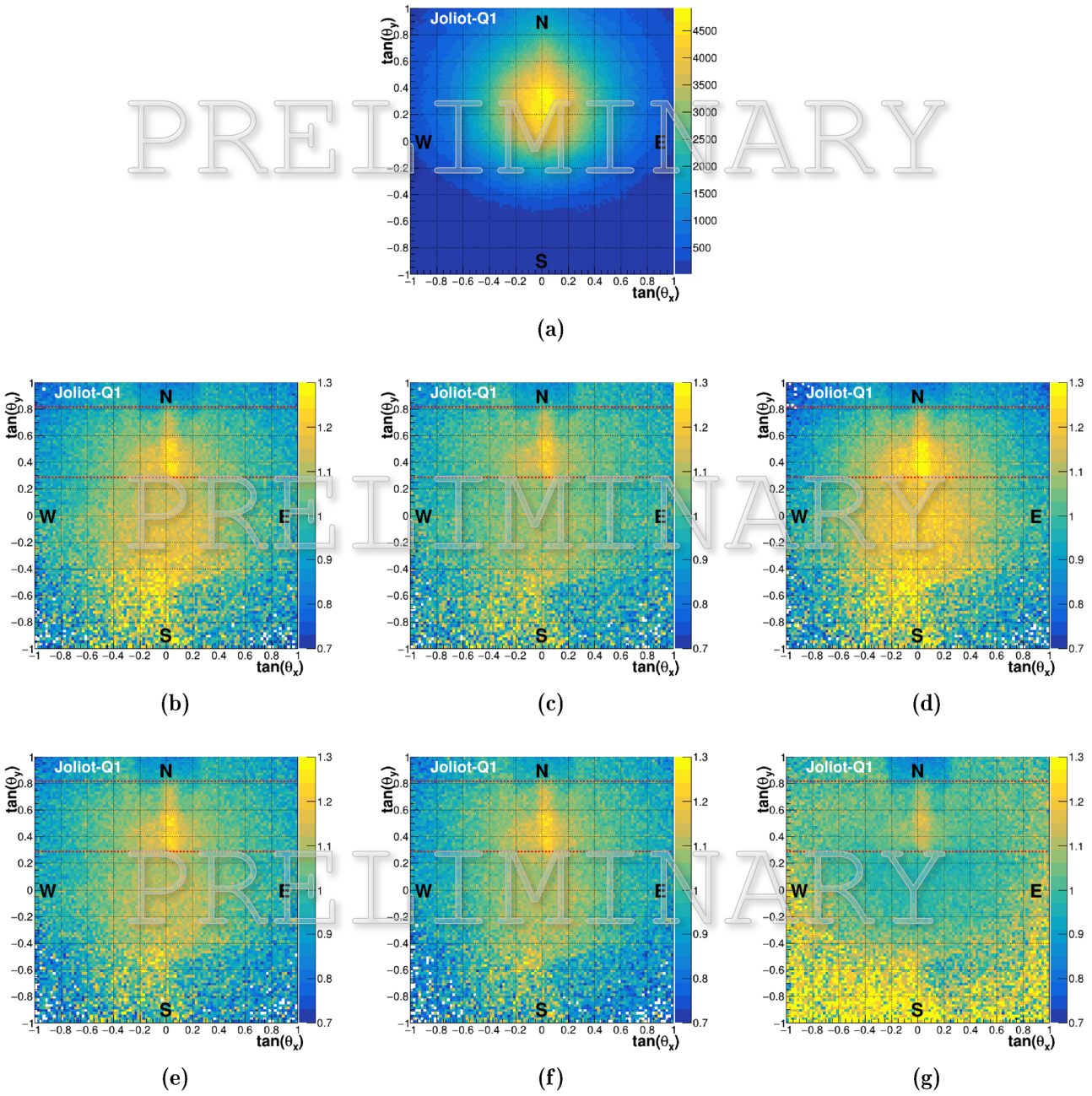


Figure 8.18: (a) Muography of the Joliot instrument; (b-g) Ratio between Joliot muography and GEANT4 simulations of the known structures, using parametrizations from Tang (b) [16], Reyna (c)[17], Matsuno (d) [18], Bogdanova (e) [19], Guan (f)[20] and Shukla (g) [21].

reactor (less accessible than G2) to maximize the number of projections to obtain a new 3D image (in publication [166]). The success of this project has aroused the interest of other teams of the CEA's Energy Department (DES) in Marcoule but also in Saclay.


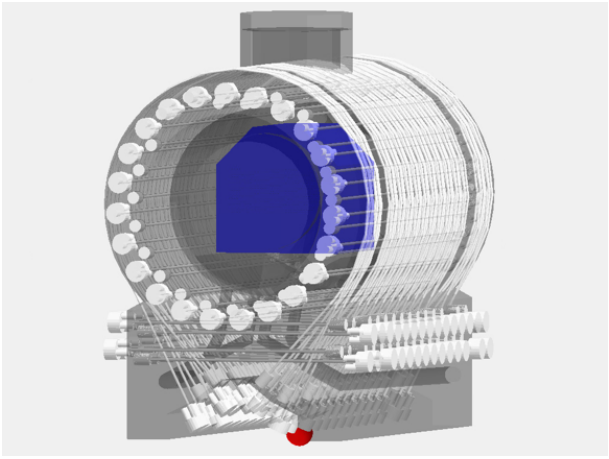

Figure 8.19: [Left] Nuclear reactor G2 in CEA/Marcoule. [Right] CAD model used for the GEANT4 simulation.

#### 8.2.2.2 IZEN

The objective of the IZEN project is to check the content and the integrity of more than a hundred nuclear waste packages stored in the CEA's Marcoule North Storage Zone Facility (IZEN). Packages of approximately 5 $m^3$ weighing between 12 and 15 tonnes must be positioned one by one on a table surrounded by a telescope (1/4 $m^2$) above and a 1 $m^2$ veto plan below. Monte-Carlo simulations made it possible to optimize the device, and to quantify the level of detail accessible inside these packages (presence of lead shells, defect in the concrete structure). Absorption muographies can then be performed by moving the veto plane underneath in order to scan the package. After validation of the bench in the laboratory at the end of 2022, it will be deployed in CEA's Marcoule at the start of 2023. The first validation and commissioning phase, which will last approximately 1 month, will be followed by an operating phase where the bench will be operated by Marcoule staff trained at a rate of approximately 1 package per week.

#### 8.2.2.3 INB72

End of 2020, the INB72 (Basic Nuclear Installation No. 72 of CEA/Saclay) project started. This INB houses nuclear waste storage wells 395 mm in diameter and 7 m deep. The aim of the project is to try to measure through transmission muography the height of air present between the plug and the elements of the well from a specific telescope located in a nearby unoccupied well. MC simulations have shown that a 6-month measurement can achieve a resolution of 5 to 10 cm on this height. Due to the confined environment, a new detector design, mini-Multigen, of 200 mm side was required (Fig. 8.22). The design of this new detector delayed the project by a few months. The new detectors were launched into production in early May and are expected to be delivered before summer 2022. After validation of the detectors and the telescope in the laboratory, an on-site installation could take place this fall.

## 8.3 D3DT

The D3DT project (*3D Detector for Muon Tomography*) aims to create a small diameter time projection chamber (TPC) dedicated to a confined environment such as boreholes for geosciences. The advantage of

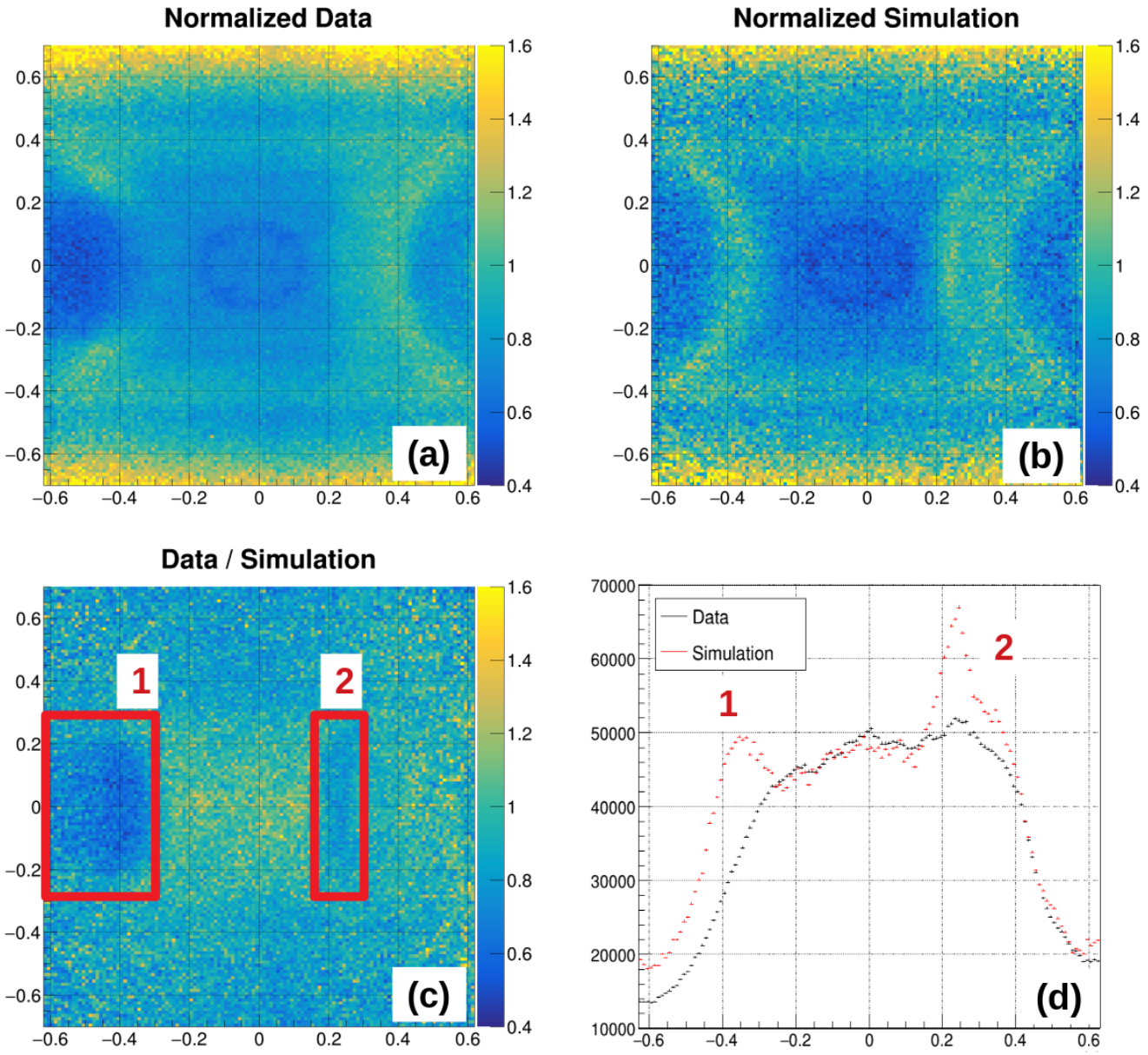


Figure 8.20: 2D image of the reactor obtained from the experimental measurement (a) and an equivalent simulation (b). Relationship between experimental measurement and simulation (c), two anomalies corresponding to excess muons detected in the simulation compared to the data are identified (red squares 1 and 2). The same anomalies are identified with a projection of the 2D comparison (d).

such device is the $2\pi$ acceptance with exception of the cylindrical direction where the TPC is blinded after the integration time of the electronics.

In 2017, a prototype TPC with a multiplexed pad Micromegas detector (1344 hexagonals in 3 mm pitch in active area of 12 cm), a 40 cm field cage integrated in a stainless steel chamber and a trigger system based on cylindrical plastic scintillator placed around the field cage has been designed to provide the muon crossing time ($t_0$) in the TPC which cannot be given by the electronics in self-triggering mode. As with MultiGen, the multiplexed pads reduce the number of electronic channels by a factor of 7. Defects on the

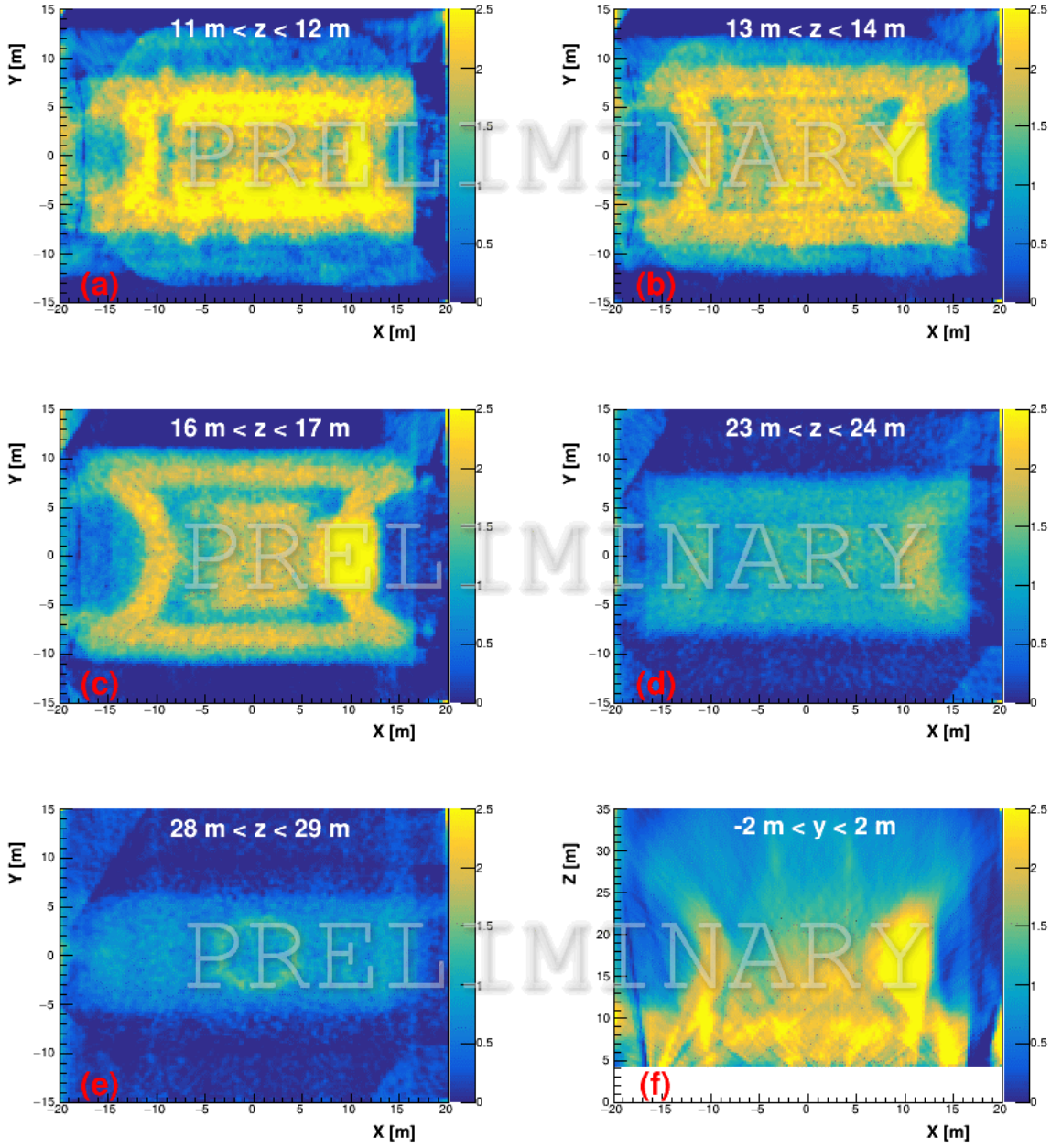


Figure 8.21: Some tomographic sections from the 3D reconstruction of the reactor, revealing several details of the structure. (a-e): horizontal slices x-y at different heights, (f): vertical slice x-z close to the y axis

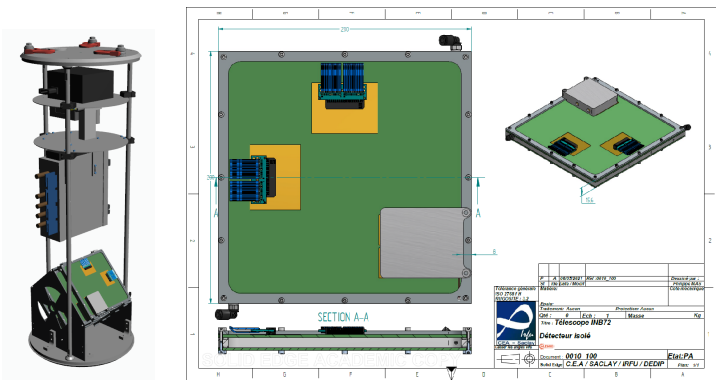

(a) (b)

Figure 8.22: (a) INB72 telescope design comprising 4 mini-Multigen (b) of 200x200 $mm^2$

multiplexed circuit were discovered during laboratory tests resulting in noise in the data thus degrading the quality of the data (see Figure 8.23). A RANSAC reconstruction of muon track are shown on Fig. 8.24.

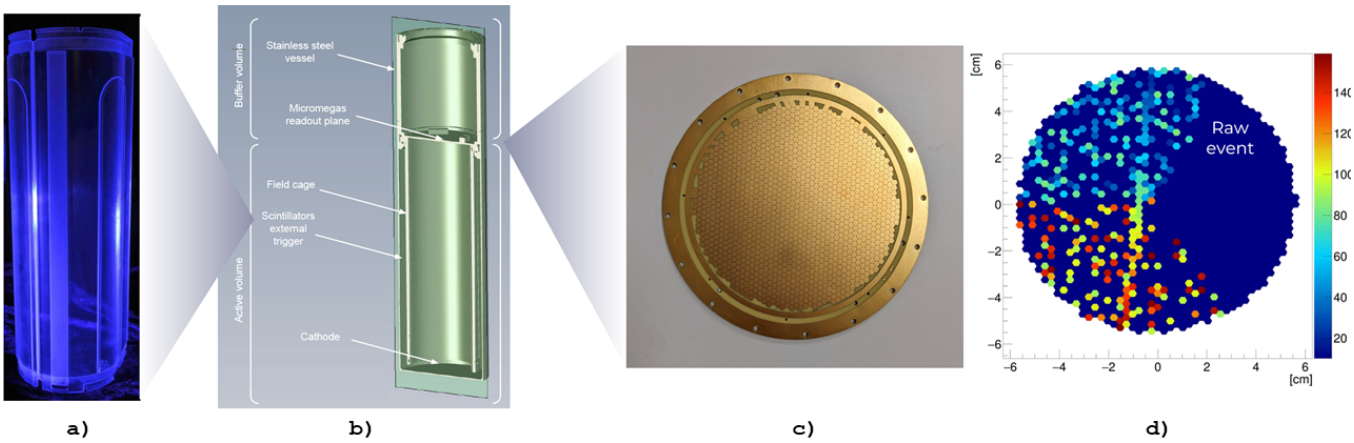


Figure 8.23: CAD 3D drawing of D3DT design (b). (a) View of the cylindrical-shape scintillator placed between the field cage and stainless steel vessel to provide an external trigger and timing information. (c) Readout plane with its 1344 multiplexed hexagonal pixels for signal readout.

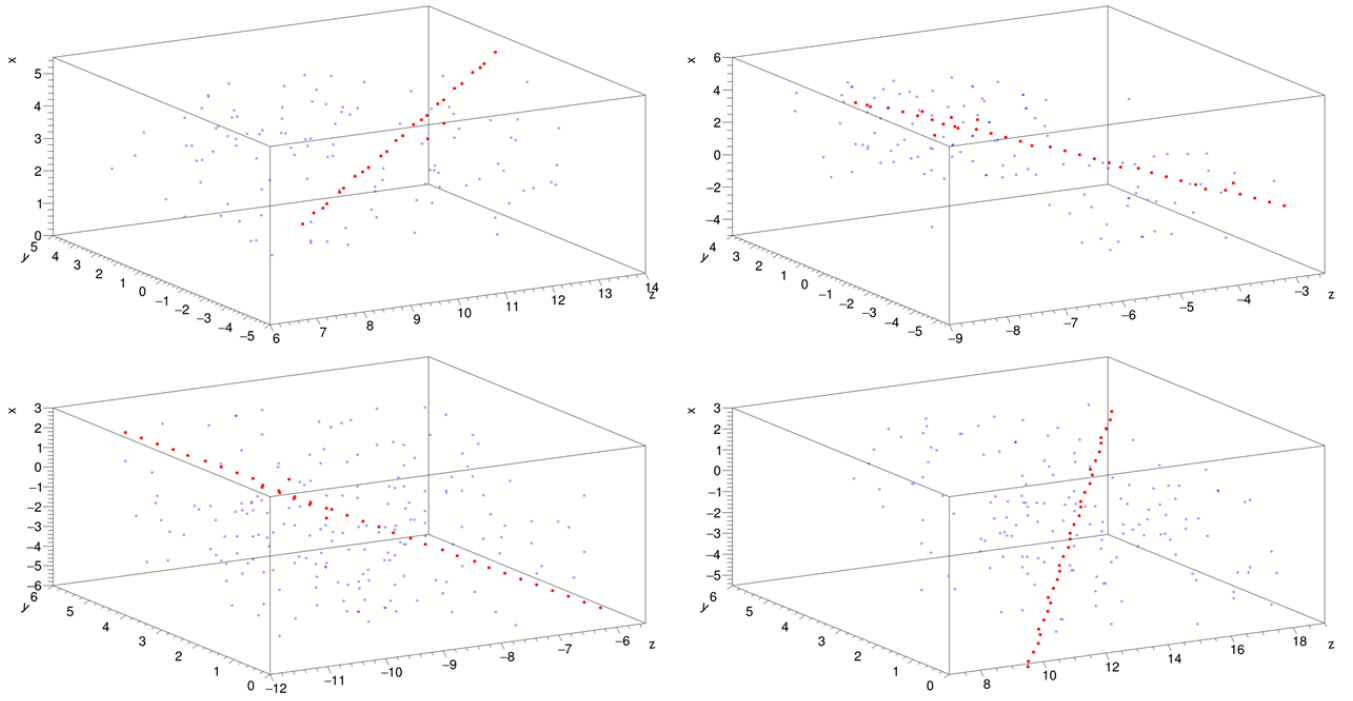

Figure 8.24: Four D3DT events reconstructed with a RANSAC algorithm.

## 8.4 Collaborative laboratory with IRIS Instruments

The collaboration with Iris-Instruments began in 2017 after the hiring on a fixed-term contract and then on a permanent contract of a former doctoral student of our team Simon Bouteille. Indeed, the company knowing the technique has rented for a year 4 Multigen detectors and an electronics box to carry out a transmission muography in a disused mine of the BRGM (France's reference public institution for Earth

Science applications) [167]. Satisfied with the result, the company then wanted to add to its catalogue a telescope based on Multigen. It is in this context that a joint laboratory was created in early 2020 with the aim of helping the commercialization in the academic world of a telescope based on CEA technology. Since the start of the collaborative laboratory, 3 common tasks have been launched, the first for the "construction of a prototype telescope", the second for the "development of power and control electronics" and the third for the improvement of "gas quality and consumption". The third task was completed in 2021, the other two will be finalized by the end of the year 2022. A fourth task for the "development of an optimized readout electronics" started with the hiring of an electronic engineer in November 2021.

# Fourth part

# Conclusion

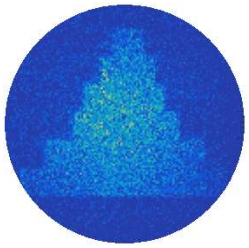

# Conclusions and perspectives

The last decade has been very productive in development around resistive MPGD and in particular with bulk Micromegas detectors, and it is certainly not over. This technology can be used in many domains of fundamental physics (particle physics, nuclear physics and high energy astrophysics) but also, thanks to muon tomography, it has found a way to profit to societal applications.

- **Perspective for resistive Micromegas detectors**

Since their invention, gaseous detectors evolve in parallel to high energy physics searches. Gaseous detectors are omnipresent in fundamental physics from the discovery of the first elementary particle (the electron) in 1897 with cathode-ray tube experiment by J. J. Thompson, to the constraint on the matter–antimatter symmetry-violating phase in neutrino oscillations in T2K experiment [117] where TPCs are operating since 2010 [104].

The future of neutrino physics is partly based on two long baseline experiments in which innovative detectors will operate and some of them are based on TPCs as tracking detector and as target. The first one is DUNE start-date in the early-2030's. The second one is Hyper-Kamiokande (Hyper-K), the Japanese neutrino detector scheduled to begin operations in 2028. Both main goals is to determine charge parity (CP) violation with neutrinos.

Since 2006, the association of pixelated readout with Micromegas amplification allowed the single electron imaging [78]. In 2010, a TPC with 500 000 pixels were operated in a test beam for the first time. This work was continued by Bonn University who operated up to 20 octoboards together (each containing 8 TimePix + Ingrid), that is 12 octoboards per LP-TPC module [168].

The recent development of resistive Micromegas can also let us dream of having gaseous detectors operating simply in air with relatively high fields [169] or an pixelated electronics with Piggyback Micromegas fully protected [141].

- **Experiment in future colliders**

After 10 years of R&D, the concept of spreading charge with resistive Micromegas has been demonstrated to be a robust solution for the readout of a TPC for ILC.

In 2018, the International Comitee for Future Accelerators (ICFA) supported a 20 km-long ILC operating at a centre-of-mass energy of 250 GeV – half the energy set out in the 2013 technical design report which was not convincing the MEXT (Japanese Ministry of Education, Culture, Sports, Science and Technology).

In June 2021, the ILC International Development Team (IDT) submitted a report to ICFA describing the organization of the Pre-Lab [170]. This IDT report has been studied by a Japanese government panel which released its evaluation on February 14, 2022 recognising the importance of a Higgs factory and the value of international collaborative research. However, this panel concluded that there is no progress in the international cost sharing for the ILC even if the Japanese government wishes to host the ILC facility. The engagements of related countries have to be more explicit, in particular in the context where the idea of building at CERN a Future Circular Collider (FCC) after LHC High-Luminosity phase (HL-LHC) that will end around 2040.

The growing FCC community examines scenarios for three different types of particle collisions: hadron (proton–proton and heavy ion) collisions, like in the LHC (FCC-hh) electron–positron collisions (FCC-ee); as in the former LEP; and other options include proton–electron collisions or proton-heavy ion collisions.

For both, FCC-ee and FCC-hh, conceptual design reports was submitted as input to the 2020 update of the European Strategy for Particle Physics [171, 172, 173]. Following adoption of this update by the CERN Council in 2020, CERN was mandated to carry out a technical and financial feasibility study for the FCC to be ready for the next update of the strategy, foreseen for 2027.

Event if the ILC-TPC will not be constructed, the continuous efforts have been used for the T2K-TPC upgrade. The choice of a DLC resistive bulk Micromegas was encouraged by the experience given by the tests made in the LP-TPC. Thirty two ERAM detectors are in production and will equipped the two HA-TPCs for the ND280 upgrade in 2023.

The CLAS12 Micromegas Central Tracker and the ATLAS-NSW using resistive Micromegas technologies have been build and operated. The success of these projects opens a new era where the use of resistive Micromegas detectors will become widespread.

- **TPC for high energy astrophysics**

The use of gas detectors for high energy astrophysics is not new (i.e. MSGCs of the X-ray monitor JEM-X in Integral observatory in space since 2003 [174]). Even if the HARPO demonstrator showed that a TPC is an interesting concept for the detection of photon energy between 1 Mev and 100 MeV, the community of high energy astrophysicists still has to be convinced.

The next step would be to perform a balloon flight with a full scale model before thinking of a space experiment.

Also, the pixelated readout of MPGDs offers a new generation of X-ray polarimeters as TimePix and CALISTE readout have been used with Micromegas.

- **Muon tomography**

Even if the CEA/Irfu was involved late in muon tomography, innovative breakthroughs catched up with the competitors. The first muography of a recognizable structure (WatTo experiment in 2015) was followed by the common discovery of the ScanPyramids Big Void in November 2017 (published in Nature [163]), the North Face Corridor in March 2023 (published in Nature Communications [164]) and the first (3D) muon tomography of a G2G3 reactor (published in Science [166] in February 2023) .

Thanks to the Ile-de-France region, the platform MIMOSA (*Maison de l'Imagerie Muonique Ouverte aux applications Sociétales et Académiques*) have been funded and the creation of the Common-Lab with the Iris-Instruments company should boost the Technological transfer. The first sale of CEA/Irfu muon tomography telescope is expected within two years.

- **Perspectives**

During the last decade, I have built and consolidated an expertise in instrumentation for high energy physics in particular in gaseous detectors and trackers.I also had the chance to transfer the tools developed in fundamental research to societal application thanks to muon tomography.

For the future collider experiments, time and spatial resolutions with long-term stability should be improved. Gaseous detectors should be also improved tracking with dE/dx and dN/dx capability in large volumes with very low material budget while developing environmentally friendly gaseous detectors. Building very large readout plane, with high-rate capability and high sensitivity in both low and high-pressure TPCs should be achievable.
So I will work on the the new challenges hoping that gaseous detectors will still be competitive.

# Fifth part

# Annexes

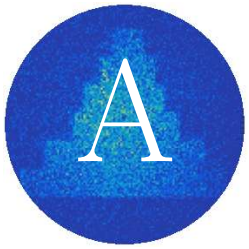

# Annexes

## A.1 Spatial resolution limitation

### A.1.1 First demonstration

The limitation of the spatial resolution defined by strips or pads consists of the standard deviation of an uniform distribution. Considering an uniform distribution on the interval from a to b defined by:

$$\begin{aligned} f(x) &= \frac{1}{b-a} \text{ for a} < \text{x} < \text{b} \\ &= 0 \text{ elsewhere.} \end{aligned}$$

The associated expected value (or mean) is written as E[f(X)] = S f(x)P(X=x)=E[X]:

$$\begin{aligned} E(X) &= \int_a^b \frac{x}{b-a} dx \\ &= \frac{1}{b-a}\left[\frac{x^2}{2}\right]_a^b \\ &= \frac{b^2-a^2}{2(b-a)} = \frac{a+b}{2} \\ E(X^2) &= \int_a^b \frac{x^2}{b-a} dx \\ &= \frac{1}{b-a}\left[\frac{x^3}{3}\right]_a^b \\ &= \frac{b^3-a^3}{3(b-a)} = \frac{a^2+ab+b^2}{3} \\ Var(X) &= E(X^2) - E(X)^2 \\ &= \frac{a^2+2ab+b^2}{3} - \frac{a^2+2ab+b^2}{4} \\ &= \frac{4b^2+4ab+4a^2-3b^2-6ab-3a^2}{12} \\ &= \frac{b^2-2ab+a^2}{12} \\ &= \frac{(b-a)^2}{12} \end{aligned}$$

and so the standard deviation is given by

$$\sigma = \frac{b-a}{\sqrt{12}} = \frac{w}{\sqrt{12}}. \tag{A.1}$$

### A.1.2 Second demonstration

The spatial resolution limitation can also be seen as a single hit on a particular pad or strip with number $n_{\mathrm{W}}$ recorded and its discrete coordinate $x_{\mathrm{measured}} = x_{\mathrm{in}} + n_{\mathrm{W}}dx$ is measured. The distribution function $D(x)$ is constant (normalized to 1) from $-\Delta x/2$ up to $+\Delta x/2$ corresponding to the pad size receiving the signal, and outside this interval the distribution function is zero (see Fig. A.1).

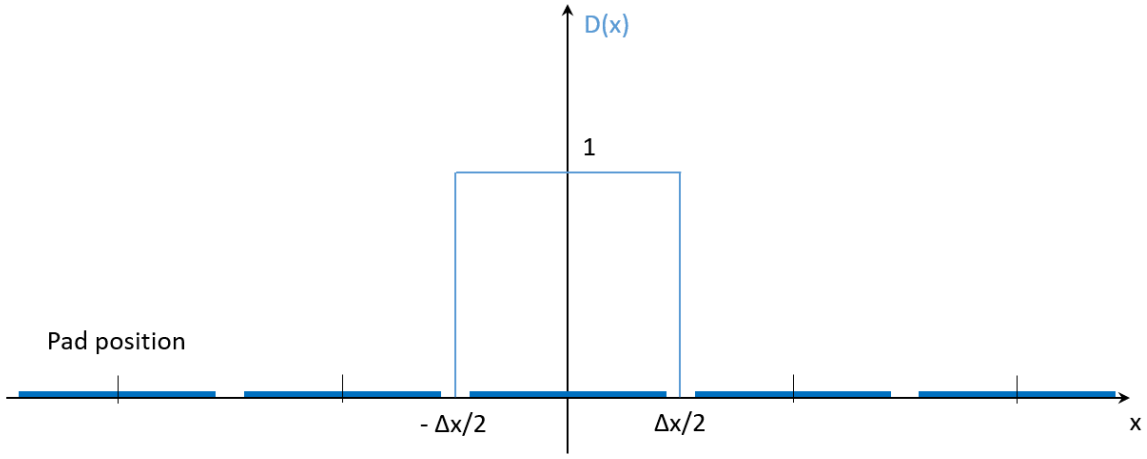


Figure A.1

The expected value for $x$ is 0 (position of the central pad/strip).

$$\langle x \rangle = \int_{-\Delta x/2}^{+\Delta x/2} x \cdot 1 dx = \left[ \frac{x^2}{2} \right]_{-\Delta x/2}^{+\Delta x/2} = 0 \tag{A.2}$$

The corresponding variance $\sigma^2$ is

$$\begin{aligned} \sigma_x^2 &= \int_{-\Delta x/2}^{+\Delta x/2} (x-0)^2 \cdot 1 dx \\ &= \left[ \frac{x^3}{3} \right]_{-\Delta x/2}^{+\Delta x/2} \\ &= \frac{(\Delta x/2)^3}{3} - \frac{(-\Delta x/2)^3}{3} \\ &= \frac{1}{3} \left[ \frac{\Delta x^3}{8} + \frac{\Delta x^3}{8} \right] \\ &= \frac{\Delta x^2}{12} \end{aligned}$$

So the spatial resolution for a pad/strip of size $\Delta x$ is given by

$$\sigma_x = \frac{\Delta x}{\sqrt{12}}. \tag{A.3}$$

### A.1.3 Energy lost per unit distance

Charged particles (alpha-particles, protons, pions, muons, atomic ions, ...) scatter electrons according to Rutherford scattering. Therefore scattering of the charged particles by free electrons is the same process, just in the rest frame of the electrons.

The Rutherford scattering formula is improved by the Mott scattering formula for electrons of momentum $p$ and velocity $v$ and particles with charge $Z_e$:

$$\left(\frac{d\sigma}{d\Omega}\right)_{\text{Mott}} = \left(\frac{Z\alpha\hbar c}{2pv}\right)^2 \text{cosec}^4\left(\frac{\theta}{2}\right)\left[1 - \frac{v^2}{c^2}\sin^2\left(\frac{\theta}{2}\right)\right] \tag{A.4}$$

$$\sin^2\left(\frac{\theta}{2}\right) = \left(\frac{q}{2p}\right) \tag{A.5}$$

using A.5, the $\text{cosec}(\theta/2)$ and $\sin^2(\theta/2)$ terms in the Mott scattering formula can be replaced by:

$$\left(\frac{d\sigma}{d\Omega}\right)_{\text{Mott}} = \left(\frac{Z\alpha\hbar c}{2pv}\right)^2 \left(\frac{2p}{q}\right)^4 \left[1 - \left(\frac{v}{q}\right)^2 \left(\frac{c}{2p}\right)^2\right] \tag{A.6}$$

Now convert the differential cross-section, $d\sigma/d\Omega$ into $d\sigma/dq^2$ and replace the differential solid angle $d\Omega$ in A.6 by $d\Omega = 4\pi\sin(\theta)d\theta$:

$$\frac{d\sigma}{\sin(\theta)d\theta} = 4\pi\left(\frac{Z\alpha\hbar c}{2pv}\right)^2 \left(\frac{2p}{q}\right)^4 \left[1 - \left(\frac{v}{c}\right)^2 \left(\frac{q}{2p}\right)^2\right] \tag{A.7}$$

The denominator $\sin(\theta)d\theta$ can be obtained by differentiating A.5 in the form $q^2 = 4p^2\sin^2(\theta/2)$ to give

$$\frac{dq^2}{d\theta} = 4p^2\sin\left(\frac{\theta}{2}\right)\cos\left(\frac{\theta}{2}\right) = 4p^2\left[\frac{1}{2}\sin\left(\frac{\theta}{2} + \frac{\theta}{2}\right)\right] = 2p^2\sin(\theta) \tag{A.8}$$

$$\Rightarrow \sin(\theta)d\theta = \frac{dq^2}{2p^2} \tag{A.9}$$

Substituting A.9 into (A.7) and cancelling terms yields:

$$\frac{d\sigma}{dq^2} = 8\pi\left(\frac{Z\alpha\hbar c}{q^2 v}\right)^2 \left[1 - \left(\frac{v}{c}\right)^2 \left(\frac{q}{2p}\right)^2\right] \tag{A.10}$$

In the electron referential being at rest with the charged particle moving towards it: $p_{\text{electrons}} \rightarrow p_{\text{nucleus}} = m_e v\gamma$

$$\frac{d\sigma}{dq^2} = 8\pi\left(\frac{Z\alpha\hbar c}{q^2 v}\right)^2 \left[1 - \left(\frac{v}{c}\right)^2 \left(\frac{q}{2m_e v\gamma}\right)^2\right] \tag{A.11}$$

The momentum transfert squared is the same in both referential and is related to the energy transfer $\delta$ by $q^2 = 2m_e\delta \rightarrow dq^2 = 2m_e d\delta$:

$$\frac{d\sigma}{2m_e d\delta} = 8\pi\left(\frac{Z\alpha\hbar c}{2m_e\delta v}\right)^2 \left[1 - \left(\frac{v}{c}\right)^2 \frac{2m_e\delta}{4(m_e c\gamma)^2}\right] \tag{A.12}$$

$$\frac{d\sigma}{d\delta} = 16\pi\left(\frac{Z\alpha\hbar c}{2m_e\delta v}\right)^2 \left[1 - \frac{m_e\delta}{2(m_e c\gamma)^2}\right] \tag{A.13}$$

So the cross-section for energy loss in the range $\delta \rightarrow \delta + d\delta$ is:

$$\frac{d\sigma}{d\delta} = \frac{4\pi}{m_e}\left(\frac{Z\alpha\hbar c}{2m_e\delta v}\right)^2 \left[1 - \frac{\delta}{2m_e c^2}\left(1 - \gamma^2\right)\right] \tag{A.14}$$

If the charged particle loses energy $-dE$ in a distance $dx$ in a material containing $n$ atoms of atomic number $Z$ material per unit volume then:

$$-dE = \begin{pmatrix}\text{number of electrons}\\ \text{per unit volume}\end{pmatrix} \times \begin{pmatrix}\text{energy loss}\\ \text{per unit volume}\end{pmatrix} \tag{A.15}$$

$$-dE = nZ_{\text{material}} \times dx \begin{pmatrix}\text{energy loss}\\ \text{per unit area}\end{pmatrix} \tag{A.16}$$

$$-dE = nZ_{\text{material}} \int_{\delta_{\min}}^{\delta_{\max}} \delta \frac{d\sigma}{d\delta} d\delta \tag{A.17}$$

Substitute A.13 into and integrate:

$$-dE = nZ_{\text{material}} \int_{\delta_{\min}}^{\delta_{\max}} \delta \frac{4\pi}{m_e} \left(\frac{Z\alpha\hbar c}{\delta v}\right)^2 \left[1 - \frac{\delta}{2m_e c^2}\left(1-\gamma^2\right)\right] d\delta \tag{A.18}$$

$$-dE = nZ_{\text{material}} \frac{4\pi}{m_e} \left(\frac{Z\alpha\hbar c}{v}\right)^2 \int_{\delta_{\min}}^{\delta_{\max}} \delta \left[\frac{1}{\delta} - \frac{1}{2m_e c^2}\left(1-\gamma^2\right)\right] d\delta \tag{A.19}$$

$$-dE = nZ_{\text{material}} \frac{4\pi}{m_e} \left(\frac{Z\alpha\hbar c}{v}\right)^2 \left[ln\left(\frac{\delta_{\max}}{\delta_{\min}}\right) - \frac{\delta_{\max}-\delta_{\min}}{2m_e c^2}\left(1-\gamma^2\right)\right] \tag{A.20}$$

The Bethe formula (A.21) describes the mean energy loss along the path for charged particles (protons, alpha particles, atomic ions) traversing matter. Its formula corresponds also to the stopping power of the material [64].

Because of their small masses, the energy loss by the electrons is different and require relativistic corrections taking into account the losses by Bremsstrahlung. High energy particles crossing matter interact with the electromagnetic field of the electrons of atoms in the material by exciting and ionizing the atoms leading to an energy loss of the particle. The electrons will emit photons which will reduce their energies (Bremsstrahlung radiation). This interaction depend not only on the number of electrons of the atom (atomic number Z) but also the size of the atom, represented by its atomic weight A.

$$-\left\langle \frac{dE}{dx} \right\rangle = \frac{4\pi n z^2}{m_e v^2} \cdot \left(\frac{e^2}{4\pi\varepsilon_0}\right)^2 \cdot \left[\ln\left(\frac{2m_e v^2}{I}\right)\right] \tag{A.21}$$

The non-relativistic version of the formula was found by Hans Bethe in 1930. The relativistic version was found by him in 1932. The most probable energy loss differs from the mean energy loss and is described by the Landau-Vavilov distribution.

## A.2 Electronics for gaseous detectors

The table A.1 summarizes all the characteristics of the analog chips designed at CEA/Irfu for MPGD. Except the AGET chip, the AFTER, DREAM and ASTRE chips were mentioned in this document.

| Parameter | AFTER | AGET | DREAM | ASTRE |
|---|---|---|---|---|
| **Polarity of detector signal** | Negative or Positive | Negative or Positive | Negative or Positive | Negative or Positive |
| **Number of channels** | 72 | 64 | 64 | 64 |
| **External Preamplifier** | No | Yes, access to the filter or SCA inputs | Yes, access to the filter or SCA inputs | Yes, access to the filter or SCA inputs |
| **Charge measurement** | | | | |
| **Input dynamic range gain/channel** | 120 fC, 240 fC, 360 fC, 600 fC | 120 fC, 240 fC, 1 pC, 10 pC | 50 fC, 100 fC, 200 fC, 600 fC | 120 fC, 240 fC, 1 pC, 10 pC |
| **Gain v.s Cdet (200pF) 200 fC tp = 230 ns** | -13% | -13% | -0.9% | -13% |
| **Sampling** | | | | |
| **Peaking time value** | 100 ns to 2 $\mu$s (16 values) | 50 ns to 1 $mu$s (16 values) | 50 ns to 900 ns (16 values) | 50 ns to 1 $\mu$s (16 values) |
| **Number of SCA Time bins** | 511 | 512 | 512 | 512 |
| **Sampling Frequency (WCk)** | 1 MHz to 100 MHz | 1 MHz to 100 MHz | 1 MHz to 50 MHz | 1 MHz to 100 MHz |
| **Triggering** | | | | |
| **Discriminator solution** | No | Leading edge | Leading edge | Leading edge |
| **HIT signal** | | OR of the 64 discri. outputs in LVDS level | OR of the 64 discri. outputs in LVDS level, 8 multiplicity levels | OR of the 64 discri. outputs in LVDS level |
| **Threshold Range** | | 5% or 17.5% of the dynamic range | 5% or 17.5% of the dynamic range | 5% or 17.5% of the dynamic range |
| **Threshold value** | | (3-bit + polarity bit) common DAC + 4-bit DAC / channel | (7-bit + polarity bit) DAC common to all channels | (3-bit + polarity bit) common DAC + 4-bit DAC / channel |
| **Readout** | | | | |
| **Readout frequency** | 20 MHz | 25 MHz | Up to 20 MHz | 25 MHz |
| **Channel Readout mode** | all channels | All, hit or selected | all channels SCA cell | All, hit or selected |
| **Readout mode** | all | 1 to 512 | Triggered columns only | 1 to 512 |
| **Trigger rate** | | | Up to 20kHz (4 samples read/trigger). | |
| **Counting rate** | <0.3 Hz/channel | <1 kHz/channel | <50 kHz/channel | <1 kHz/channel |
| **Power consumption** | <10 mW/channel | <10 mW/channel | <10 mW/N | <10 mW/channel |
| **Noise 120 fC, 200 ns peaking time** | 370 e- + 14.6 e- / pF (measured) | 580 e- + 9 e- / pF (measured) | | 580 e- + 9 e- / pF (measured) |
| **Noise 120 fC, 200 ns peaking time** | 700 e- + 8.5 e- / pF (measured) | | 610 e- + 9 e- / pF (measured) | |
| **Electronics** | T2K (AFTER + FEC + FEM ) | GET | DREAM + FEU + SSP | |
| | AFTER + FEC + evaluation kit | AGET + AsAd + rCoBo | DREAM + FEU + TCM | |
| | AFTER + FEC + STUC | FEMINOS | | |
| | AFTERSED | | | |

Table A.1: Summary of electronics ASICs developped at Irfu.

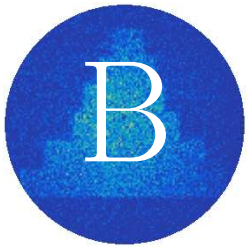

# Selected articles

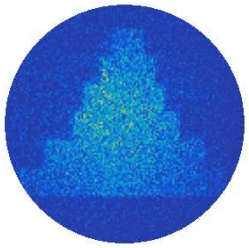

# *TPC review*

Nuclear Instruments and Methods in Physics Research A 598 (2009) 89–93

Contents lists available at ScienceDirect

Nuclear Instruments and Methods in Physics Research A

journal homepage: www.elsevier.com/locate/nima

# TPC review

D. Attié

*DSM/Irfu, CEA/Saclay, F-91191 Gif-sur-Yvette Cédex, France*

ARTICLE INFO

Available online 27 August 2008

ABSTRACT

The Time Projection Chamber (TPC) was invented by David Nygren 30 years ago. TPCs have been used as trackers in many particle and heavy ion physics experiments. There are also TPC projects for non-accelerator experiments such as double-beta decay and dark-matter searches. After a presentation of the original idea of the TPC, and the advantages of such a detector, the R&D for the TPC proposed for the future International Linear Collider will be reviewed. This work is being carried out by the LC-TPC collaboration formed recently by several labs from all over the world.



## 1. Introduction

A Time Projection Chamber (TPC) is typically a gas-filled cylindrical chamber (the gas could be at atmospheric pressure, pressurized or liquid) with one or two endplates and a long drift distance (up to a few meters). Proposed in 1974 [1], this detector provides a complete 3D picture of the ionization deposited in the chamber. The density of the ionization, along the track, depends on the momentum and type of the particle. By measuring the arrival, in space and in time $t$, of electrons moving at constant velocity $v$ to either of the two endplates due to the electric field **E** defined by a field cage, the TPC can reconstruct the paths of the original charged particles ($x-y$ are given by the projection and $z$ by $v \times t$). A magnetic field **B** parallel to **E** could furthermore be added as large as possible to minimize the transverse diffusion which limits the obtainable resolution. The TPC's 3D localization makes it extremely useful in tracking charged particles using approximately 100–200 measurement points along the track and for identifying particles by their ionization energy loss ($dE/dx$) measurements. In TPCs large track densities are possible due to the low occupancy.

After showing some examples of TPCs which have been used as tracking detectors in high energy physics, and recently for rare event detection, we discuss the new developments using Micro-Pattern Gaseous Detectors (MPGDs) and techniques to improve spatial resolution. These R&D are currently being performed by the international LC-TPC collaboration.

## 2. TPC in high energy Physics

### 2.1. Fields using TPC in the past

The first experiment in particle physics using a TPC was designed in 1976 at SLAC for the $e^+e^-$ PEP4 collider [2]. For the same physics, the TOPAZ TPC was proposed at KEK [3] in 1986 and the ALEPH TPC [4] and DELPHI TPC [5], in 1990 and 1992, respectively, for the LEP at CERN. Later, STAR [6] at BNL/RHIC and NA49 [7] at CERN were the first TPCs for heavy ion colliders. Most of the experiments that have used a TPC emphasize the importance of this type of detector for high energy physics.

### 2.2. Recent and future experiments

The Large Hadron Collider (LHC), currently in its final stages of construction, has one of its detectors designed to search for a quark-gluon plasma of heavy ion collisions named A Large Ion Collider Experiment (ALICE) [8]. Pb–Pb nuclei collisions will be studied with a center of mass energy of 5.5 TeV per nucleon. The main particle tracking device in ALICE is a TPC with a drift cavity measuring two times 2.5 m in length with a diameter of 2.5 m; in total containing 95 $m^3$ of $Ne/CO_2/N_2$ (90/10/5) of gas mixture. To read out the signal the endplates are equipped with wire planes which perform charge amplification and no less than 560 000 electronics channels for signal detection. Given a maximum sampling frequency of 11 MHz the entire TPC volume comprises of approximatively $6 \times 10^8$ pixels in three dimensions.

For the future International Linear Collider (ILC) a TPC is also an excellent candidate for the main tracking detector. A resolution on the momentum of $\sigma_{1/p} \simeq 5 \times 10^{-5}$/GeV is needed to provide precise and model-independent measurement of for instance the Higgs mass in the $Z \to \mu\bar{\mu}$ recoil reaction. The necessary

*E-mail address:* david.attie@cea.fr

0168-9002/$ - see front matter © 2008 Elsevier B.V. All rights reserved.
doi:10.1016/j.nima.2008.08.114

resolution is 10 times better than the one achieved at LEP. Also a high spatial resolution, better than 100 μm, is necessary differentiate between the high density tracks and final states with more than six jets. As such the LC-TPC must have high granularity and good two-track separation in addition to single track identification capability.

## 3. TPC for rare event detection

### 3.1. Liquid rare gas TPC

The first idea of using a TPC for rare event experiments came from Rubbia in 1977 who suggested a 300 t ultra-pure liquid argon TPC [9]. It is based on the fact that in highly pure argon, ionization tracks can be drifted over distances of the order of meters. Imaging is provided by position-segmented electrodes at the end of the drift path, continuously recording the signals induced. Recently, the experiment known as Imaging Cosmic And Rare Underground Signals (ICARUS) based on Gran Sasso is aimed at the direct detection of the neutrinos emitted from the Sun [10]. It should start collecting data in 2008. As well, the Giant Liquid Argon Charge Imaging ExpeRiment (GLACIER) is a powerful detector project for uniform and high accuracy imaging of massive active volume (100 kT) [11].

TPCs based on liquefied noble gases have already been proven to work reliably and are being increasingly used and proposed for particle physics experiments, especially for rare event detection. Indeed, the TPC medium can be used for many things at once, it can be used as a large volume target and/or a dense medium with inexpensive price.

All these experiments, generally underground experiments with low activity materials, explore neutrino (double-beta decay) and dark matter (axion, WIMPs) physics.

### 3.2. T2K long baseline experiment

The T2K long baseline experiment at Japan Proton Accelerator Research Complex (JPARC) [12] which will start next year has TPCs using argon : $CF_4$ : isobutane (95:3:2) gas mixture at atmospheric pressure. The near detector of T2K at 280 m (ND280) will contain three TPCs segmented in six readout planes of 12 modules ($34 \times 36\,cm^2$), for a total of 124 416 pads ($6.9 \times 9.7\,mm^2$ in size) [13].

These bulk detectors are simple and robust. They also have minimal inactive regions and can be produced in large surface area; these demonstrate that larger TPCs using such technologies can be manufactured. The T2K TPCs are under construction and will be operable by the time the neutrino is ready in May 2009.

## 4. New developments in TPC R&D

### 4.1. Micro-Pattern Gaseous Detectors

The current R&D for TPC readout focuses on the technology of MPGDs; the two new amplification systems replacing wire chambers are Gas Electron Multiplier (GEM) and Micromegas (see Fig. 1).

GEMs consist of two metal foils (e.g. copper) separated typically by 50 μm of isolated layer (e.g. kapton). GEM has typically bi-conical holes with 70 μm (50 μm) external (internal) diameter with a pitch of 140 μm. Electrons multiplication takes place in holes which are etched through the kapton [14]. The metal foils are charged to a potential difference of a few hundred volts thus creating a strong electric field (a few ten thousand V/cm) in the holes. Electrons drifting into these holes ionize the gas creating an avalanche. They are often cascaded in two or three stages.

MICROMEsh GASeous (Micromegas) amplification system use a thin metal mesh held in place by 50–150 μm high pillars. The mesh can be as simple as wire grid. The gas gain occurs between the mesh and the anode due to an applied potential difference where incoming electrons avalanche in the strong electric field. Operating very close to readout pads, the avalanche size is approximatively 15 μm rms [15].

MPGDs have several advantages over wire chambers: they do not suffer from the $\mathbf{E} \times \mathbf{B}$ effect, they are more robust, easily supported without wire sag and instability and positive ions generated in the avalanche are naturally collected before drifting away from the amplification region thus eliminating the build-up of space charge in the drift region which is known to distort the drift field.

In the last few years, GEMs and Micromegas have begun to replace wire chambers in some experiments and they are prominent in R&D for future colliders and for upgrades of the current experiment detectors.

### 4.2. Gas property studies

In a TPC, the gas mixture is generally a noble gas, with a low ionization potential, and a few percent of a quencher gas to absorb UV photons produced in the avalanche process in the strong electric field. The spatial resolution is limited by the electron diffusion in the gas which is determined by several properties: drift velocity, attachment, diffusion and multiplication of the electrons. Except for the multiplication (i.e. gain), the other properties can be relatively well simulated by MAGBOLTZ calculations [16].

Thus the gain of the gas mixture used in a TPC has to be studied and tuned to a specified operating state depending on each application.

The gain of a Micromegas-based detector (e.g. 50 μm gap) has been measured at Saclay as a function of the amplification electric field for nearly 50 gas mixtures showing the simulation limitations. To measure the gain the charge deposited by 5.9 keV X-rays was used as a standard for each gas. Using the same detector systematic measurements have been carried out with double mixtures and triple mixtures of gases (Ar, Ne, $CO_2$, $CH_4$, $C_2H_6$, Iso-$C_4H_{10}$, $CF_4$, etc.) at various concentrations.

Fig. 2 shows the gain curves as a function of the amplification field $E$ for many gas mixtures. Three groups of curves can be distinguished. The first group is formed by the Iso-$C_4H_{10}$ mixtures which yield the highest gains, up to $10^5$ ($50\,kV/cm < E < 70\,kV/cm$). The second group, mainly composed by *cold* gases ($CH_4$ and $CO_2$) have a maximum gain of a few $10^4$ ($70\,kV/cm < E < 100\,kV/cm$). Finally, between those two families ($60\,kV/cm < E < 80\,kV/cm$) is the $C_2H_6$ gas mixtures.

### 4.3. Spatial resolution measurement and techniques

Given that the avalanche charge distribution has a diameter of ~15 μm and the pad pitch $p$ limits the resolution to $\sigma_{z=0} \simeq p/\sqrt{12}$, if the pads are to large and collect all the charges on one pad, the spatial resolution must be improved by one of the three possibilities. One is to spread the charge using a resistive anode, another is to decrease the pad pitch as much as possible using for example a pixelized readout and we can quiet simply use GEMs by defocusing.

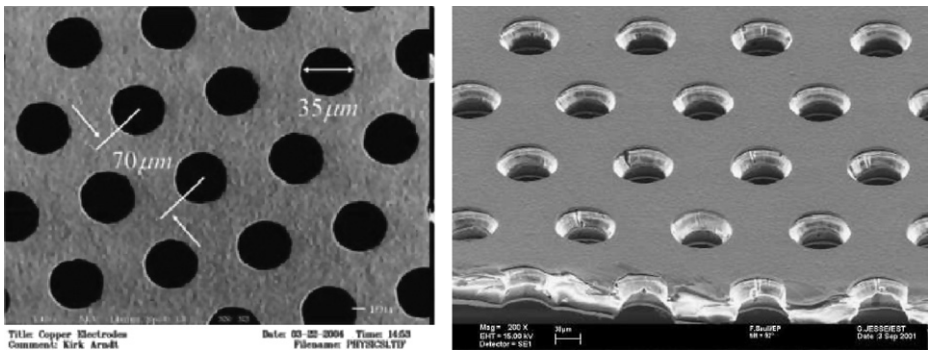


**Fig. 1.** The two main amplification system of Micro-Pattern Gas Detectors (MPGDs): Micromegas mesh (left) of Purdue University/3M (G. Bolla and I. Shipsey) and GEM (right) built at CERN (R. de Oliviera).

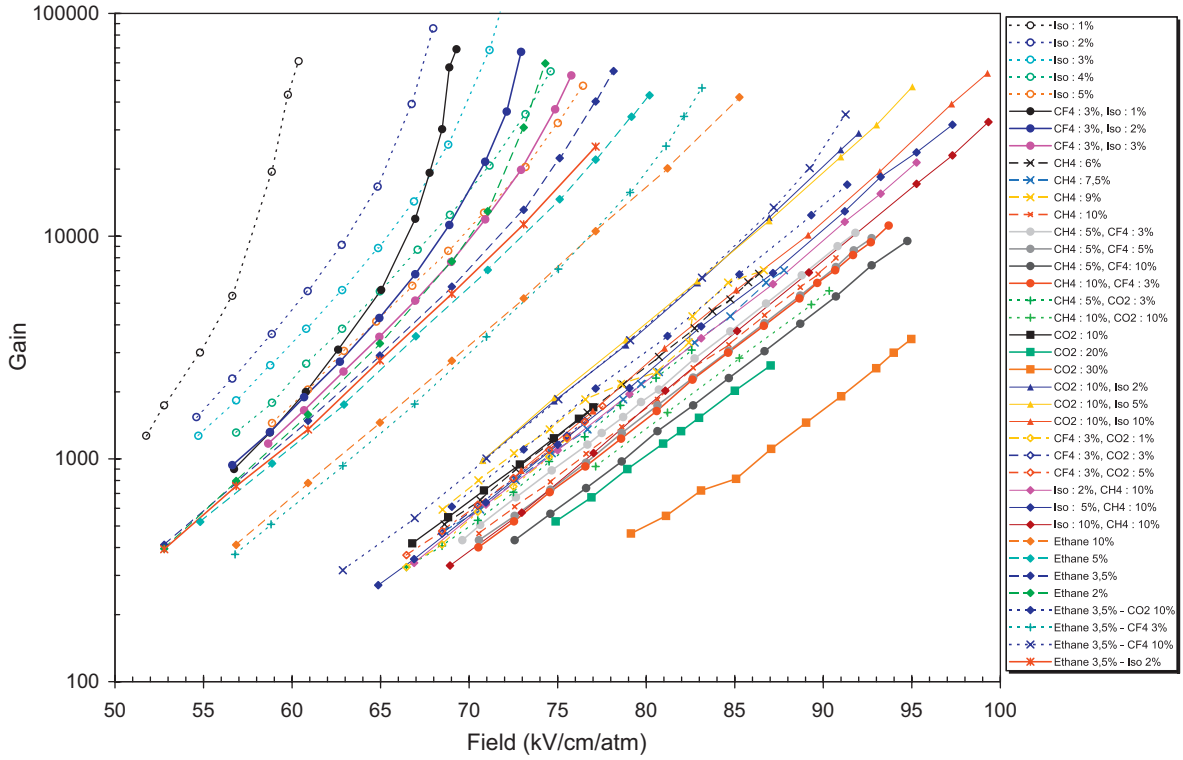


**Fig. 2.** Gain measurements as a function of the amplification electric field provided by a 50 μm gap Micromegas detector using gas mixtures containing argon and a few percent of other constituents ($CO_2$, $CH_4$, $C_2H_6$, Iso-$C_4H_{10}$, $CF_4$, etc.).

*4.3.1. Resistive anode*

Recent R&D at Carleton developed a new technique to improve the MPGD-TPC spatial resolution over that achievable with previous techniques. The new concept is based on the phenomenon of charge dispersion by a resistive film, placed on top of the readout anode, which enables one to approach the statistical limit of resolution as defined by the transverse diffusion. The resistive anode allows the dispersion of track avalanche charge over multiple pads to improve the determination of position centroids even with large pads (~2–3 mm). Recent studies with Micromegas detectors enhanced with a resistive anode are promising as a possible readout option for the LC TPC. Using 2 mm wide pads, they demonstrated better TPC resolution than has been achieved with conventional MPGD TPC readout systems with equally wide pads. The resolution achieved is near the diffusion limit of resolution for a gaseous TPC. In cosmic tests with no magnetic field the measured resolution follows the expectations of transverse diffusion and electron statistics [17,18]. Cosmic tests in a magnet have also demonstrate good resolution for a MPGD instrumented TPC in a magnetic field of 5 T (Fig. 3 in the case of Micromegas-TPC). The spatial resolution is independent of the drift distance over the 16 cm and reaches 50 μm. Extrapolating for the ILC TPC readout using ~2 mm wide pads and a magnetic field of $B = 4$ T with the same gas mixture, a resolution of ~80 μm for all tracks (2.5 m drift) appears achievable thanks to the possibility of using a resistive anode [19].

*4.3.2. Digital TPC*

A completely new approach for the readout of a TPC is to use a pixelized CMOS chip, such as the TimePix chip, combined with a MPGD. This chip contains a square matrix of 256 × 256 pixels as described in Llopart 2007 [20]. Due to the fine granularity (55 μm pitch) this system could be used to count primary clusters and primary electrons (see Fig. 4). Additionally the pixelized chips are useful for δ-ray recognition and suppression and also are sensitive

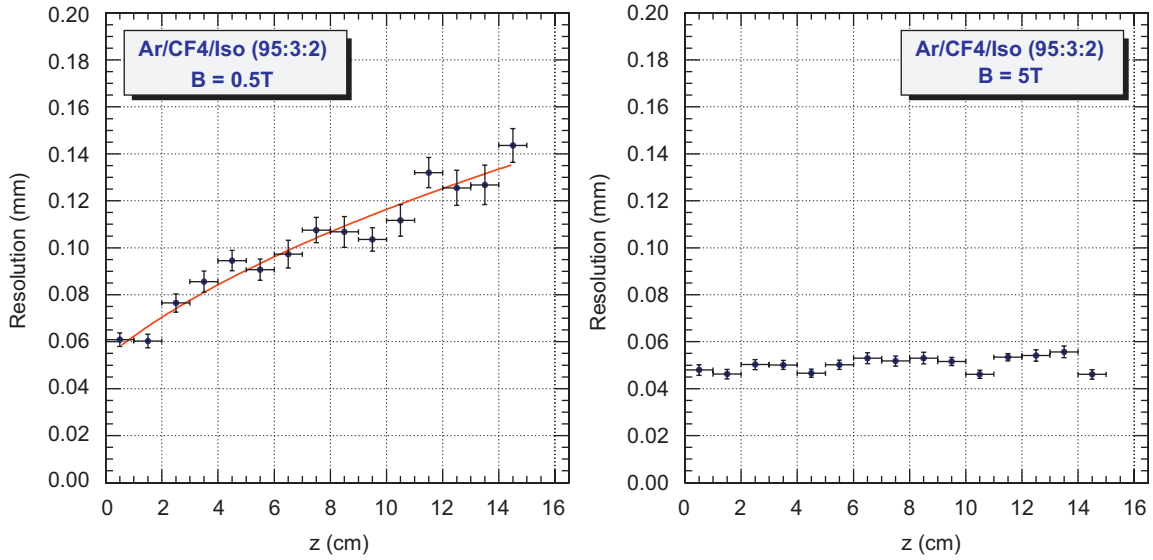


**Fig. 3.** Measured transverse resolution as a function of drift distance $z$ for 2 mm pitch pads using the $Ar/CF_4/iC_4H_{10}$ (95/3/2) gas mixture for magnetic field of 0.5 T (left) and 5 T (right). The data with charge dispersion (left figure) are fitted to the resolution $\sigma$ expected from diffusion in the TPC gas and electron statistics using the formula $\sigma(z) = \sqrt{\sigma_0^2 + (D^2/N_{\text{eff}})z}$ (where $\sigma$ is the resolution at $z = 0$, $D$ is the transverse diffusion and $N_{\text{eff}}$ is the effective number of electrons).

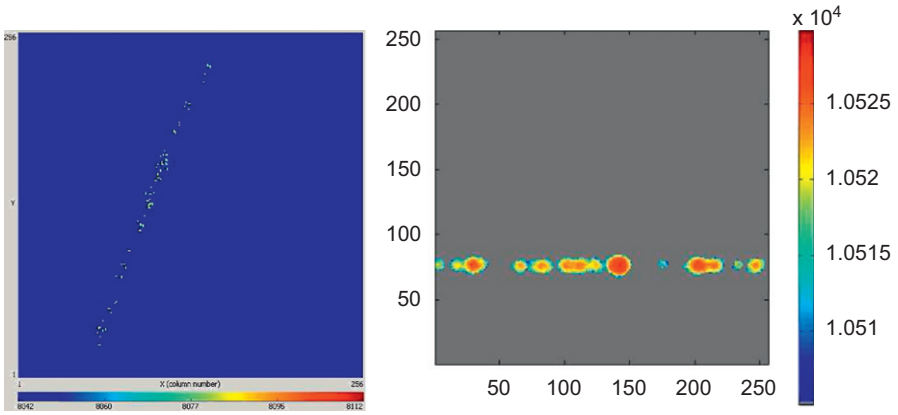


**Fig. 4.** Cosmic ray tack from a Micromegas-based TPC from Saclay in Ar/Iso-$C_4H_{10}$ 95:5 (left) and 5 GeV/$c$ $e^-$ beam from a Triple GEMs-based TPC in He/CO2 70:30 by Freiburg/Bonn (right, see also Ref. [21]). Both were taken using a TimePix chip readout which is was protected by amorphous-Si in the case of Micromegas.

to 3D directionality for other physics topics: nuclear recoils in WIMP or neutrino interactions, two electrons from double beta decay and X-ray polarimetry using low-energy electron.

*4.3.3. GEM defocusing effect*

Generally GEMs (two or three) are stacked one above the other at 1–2 mm distance (the transfer gaps) and positioned 1 mm above the readout pads (the induction gap). Due to the transverse diffusion in the gaps and to the electric field lines which are more compressed inside the holes than outside in the transfer gap, GEM create a defocusing effect. This intrinsic effect is tuned to spread charges over the readout pads. This result is that good resolution is possible with pads as small width as 1 mm.

## 5. LC-TPC collaboration

In order to unify the effort on the ILC TPC prototyping and design R&D a collaboration of about 40 groups was formed in October 2007 from three geographic regions (North America, Asia and Europe). The next goal of this collaboration is to set up a 60 cm × 80 cm TPC in a test beam at DESY as a technological demonstrator. This collaboration always is open to new members.

## 6. Summary

Over the last few decades large volume TPCs have been operated as the main tracking detectors in a wide range of physics experiments. With the recent R&D on MPGDs, gas property studies and spatial resolution techniques, we expect that this tracking detector will continue to be very useful in the present and the future of particle physics, heavy ion colliders and rare event experiments.

## Acknowledgments

I wish to thank the organizer of the 10th International Conference on Instrumentation for Colliding Beam Physics for inviting me, and the ILC-TPC collaboration for helping me for this review.

## References

[1] D.R. Nygren, A time projection chamber—1975, in: Presented at 1975 PEP Summer Study, PEP 198, 1975 and included in Proceedings.
[2] A.R. Clark, et al., Proposal for a PEP facility based on the time projection chamber, in: PEP-PROPOSAL-004, December 1976.
[3] T. Kamae, et al., Nucl. Instr. and Meth. A 252 (1986) 423.
[4] D. Decamp, et al., Nucl. Instr. and Meth. A 294 (1990) 121.
[5] Y. Sacquin, Nucl. Instr. and Meth. A 383 (1992) 209.
[6] K.H. Ackermann, et al., Nucl. Phys. A 661 (1999) 681.
[7] S. Afanasiev, et al., Nucl. Instr. and Meth. A 430 (1999) 210.
[8] ALICE TPC Technical Design Report, CERN/LHCC 2000-001, 2000.
[9] C. Rubbia, CERN-EP Internal Report 77-8, 1977.
[10] F. Arneodo, et al., Nucl. Phys. B 54 (1997) 95.
[11] A. Ereditato, A. Rubbia, arXiv:hep-ph/0510131.
[12] Y. Hayato, et al., Nucl. Phys. B 143 (2005) 269.
[13] A. Sarrat, Nucl. Instr. and Meth. A 581 (2007) 175.
[14] F. Sauli, Nucl. Instr. and Meth. A 386 (1997) 531.
[15] Y. Giomataris, et al., Nucl. Instr. and Meth. A 376 (1996) 29.
[16] S. Biaggi, Magboltz 2, version 7.1, CERN Library, 2004.
[17] M. Dixit, et al., Nucl. Instr. and Meth. A 518 (2004) 721.
[18] M. Dixit, A. Rankin, Nucl. Instr. and Meth. A 566 (2006) 28.
[19] M. Dixit, et al., Nucl. Instr. and Meth. A 518 (2004) 721.
[20] X. Llopart, et al., Nucl. Instr. and Meth. A 581 (2007) 485.
[21] A. Bamberger, et al., Nucl. Instr. and Meth. A 573 (2007) 361.

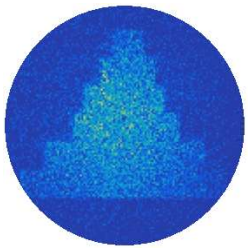

# *Gas pixel detector for X-ray observation*

Nuclear Instruments and Methods in Physics Research A 610 (2009) 178–182

Contents lists available at ScienceDirect

Nuclear Instruments and Methods in Physics Research A

journal homepage: www.elsevier.com/locate/nima

# Gas pixel detector for X-ray observation

D. Attié [a,*], M. Campbell [b], M. Chefdeville [c], P. Colas [a], E. Delagnes [a], Y. Giomataris [a], H. van der Graaf [c], X. Llopart [b], J. Timmermans [c], J. Visschers [c]

[a] CEA, Irfu, SPP, Centre de Saclay, F-91191 Gif-sur-Yvette, France
[b] CERN, CH-1211 Genève 23, Switzerland
[c] NIKHEF, Kruislaan 409, Amsterdam 1098 SJ, The Netherlands

ARTICLE INFO

Available online 13 June 2009

*Keywords:*
Diffusion in gases
Electronic circuits
Microelectronics
Gas-filled counters
Photolithography
Photon counting and statistics
Polarimeters
X-ray detectors

ABSTRACT

We report on the status of the R&D for a digital Time Projection Chamber (TPC) based on Micromegas (*MICRO MES*h *GA*seous *S*tructure) detectors using the CMOS chip TimePix as a direct readout anode protected by highly resistive a-Si:H layer. A small chamber was built as a demonstrator of the 2-D and 3-D imaging capabilities of this technique. We illustrate the new capabilities of this detector for X-ray observation with data taken from radioactive sources. This small TPC is a very useful tool both for studying gas properties thanks to its good efficiency for single electrons, and for reconstructing photoelectron direction for use as a soft X-ray polarimeter.



## 1. Introduction

By the recent advancement in microelectronics, the pixel readout chip technology achieved a granularity of a few tens of microns. When combined with a micro-pattern gas detector, such as Micromegas (*MICRO MES*h *GA*seous *S*tructure), for electron amplification [1], each pixel is sensitive to a single primary gas electron [2]. This ensures the ultimate spatial resolution for tracking images. Such a detector can also be used for soft X-ray observation ($1\,\mathrm{keV} < E_\gamma < 50\,\mathrm{keV}$).

After introducing the advantages of a digital Time Projection Chamber (TPC) we describe our prototype based on TimePix readout chips and Micromegas detectors. Afterwards we present two applications for X-ray observation: studies of primary electron statistics in gases and soft X-ray polarimetry or for high energy physics experiments.

## 2. Digital TPC based on TimePix and Micromegas

### 2.1. Advantages of a pixelized gas detector

Gas and solid detectors are able to collect and amplify the electrons released by ionizing radiation. But the gas medium has the advantage to affect less the incident radiation than the solid detector. Additionally, a pixelized detector provides a high granularity single electron sensitive readout which yields the ultimate spatial resolution. Gaseous trackers are sensitive to both minimally ionizing particles and photoelectric events on account of longer radiation lengths.

The incident particles interacts with the gas medium and produce electron–ion pairs. These pairs are separated by the electric field (a few hundred V/cm) and the electrons drift towards the anode plane. Thus, the electrons from ionization are projected on the readout plane providing 2-D localization. The information of the third dimension is given by the arrival time of the electrons, if the creation time and drift velocity is known. The total primary charge can be recorded to measure the energy lost by the incoming particles. For many applications, the pixelized gas detector is an excellent 2-D and 3-D imaging device with high spatial resolution.

### 2.2. Digital micro-TPC prototype

Fig. 1 shows the exploded view of the small detector we built as a digital TPC prototype. The detector consists of an aluminum chamber containing a field cage ($2 \times 2 \times 6\,\mathrm{cm}^3$) mounted on a frame which holds a 50 μm gap Micromegas mesh on top of the chip. The field cage is folded kapton with 15 copper strips (4 mm pitch, 3 mm width), between each is a 1 MΩ resistor to provide a uniform electric field. The TimePix chip and the Micromegas detector are described in the two following sections.

#### 2.2.1. TimePix chip

TimePix is a pixel readout chip designed in 0.25 μm CMOS ASIC technology which contains a square matrix of $256 \times 256$ pixels, each $55 \times 55$ microns [3]. Each pixel has a low noise

* Corresponding author.
*E-mail address:* david.attie@cea.fr (D. Attié).

0168-9002/$ - see front matter © 2009 Elsevier B.V. All rights reserved.
doi:10.1016/j.nima.2009.05.173

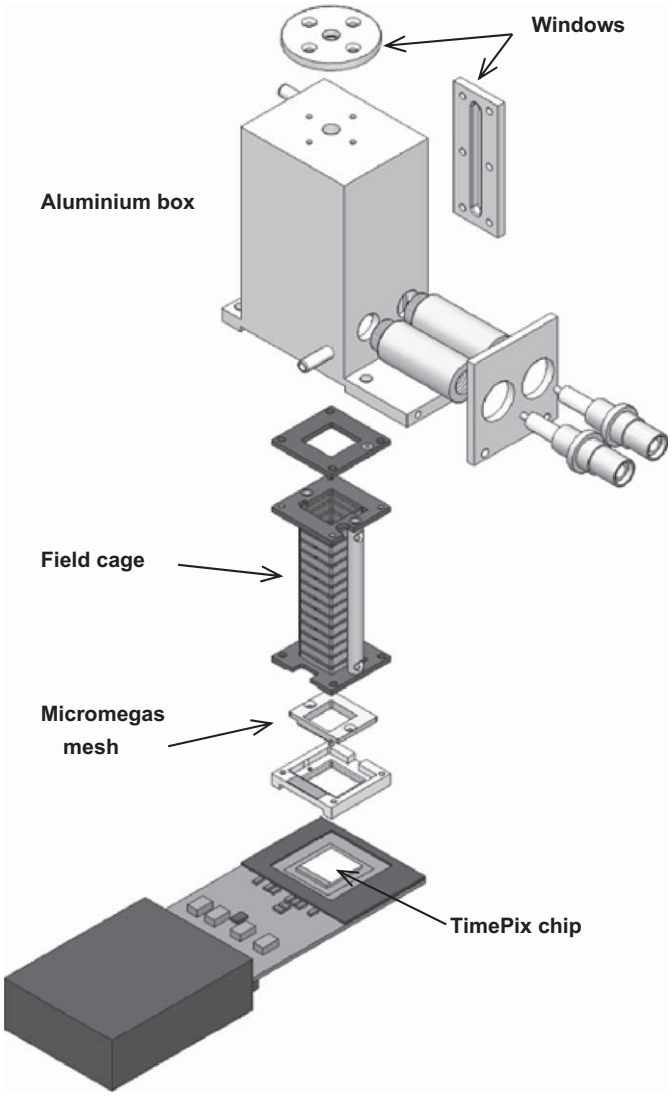


**Fig. 1.** Exploded view of Micro-TPC formed by a 6 cm field cage placed on the TimePix chip inside a small aluminium chamber.

preamplifier-shaper, a discriminator, a threshold DAC, a 14-bit counter and a TimePix Synchronization Logic (TSL) circuit. Each pixel can be independently set in one of five different modes (masked, hit counter, time-over-threshold (TOT), time and one-hit time). The TSL was designed to count clock pulses up to 100 MHz. During a user-defined time window (shutter time), every pixel that detects a signal crossing the threshold counts clock pulses unless it is masked; while the signal is above the threshold (*time-over-threshold* mode); or until the end of the shutter time (*time* mode). The *time-over-threshold* mode gives information regarding the total avalanche charge for each pixel, while the *time* (or *Timepix*) mode provides the electron arrival time.

The TimePix chip, based on Medipix2 chip [4], was designed for radiation tracking in gases for TPC applications.

#### 2.2.2. Micromegas and chip protection

Micromegas is an amplification system using a thin metal mesh held above the anode plane by pillars of 50−150 μm height. The gas gain occurs when incoming electrons multiply creating an avalanche in the strong electric field between the mesh and the anode, due to an applied potential difference [5]. In typical working conditions, the avalanche size is approximatively 15 μm rms assuring that one electron avalanche is collected on only one given pixel.

Post-processing technology makes it possible to integrate a Micromegas structure directly onto the chip (InGrid). The InGrid holes can be aligned precisely with the pixel pads while the pillar diameter can be made small enough ($\simeq 20\,\mu m$) to be placed between the holes [6].

In order to protect the chip against destructive sparks, a 20 μm thick highly resistive a-Si:H layer was deposited onto the chip by a plasma process at $\simeq 200\,^{\circ}C$ [7]. This protective cover, called *SiProt*, has a resistivity of $10^{11}\,\Omega\,cm$ and intends to protect the chip from high instantaneous spark currents which could destroy the chip.

## 3. Applications for X-ray observation

### 3.1. Measurements of primary statistics in gases

In gas detectors, the spatial resolution $\sigma_t$ is mainly determined by the electron diffusion, which can be described by factor $\sqrt{2 \cdot D \cdot t}$, where $D$ is the electron diffusion coefficient. This coefficient $D$ depends of the gas mixture and the electric field. To measure the number of primary electrons produced by soft X-ray photons we used the digital Micro-TPC filled with Argon(95%)–Isobutane(5%). In this mixture, which has a large transverse diffusion coefficient $D_t$, the primary electrons from the $^{55}$Fe's 5.9 keV photons are imaged into isolated clusters of 1–3 pixels (Fig. 2, left). Currently SiProt spreads by induction the electron avalanche over several pixels. Fig. 3 shows the spectrum of number of electrons for 2000 events (photons) using an InGrid on top of a TimePix chip covered with 15 μm of SiProt. The transverse diffusion coefficient $D_t$ is $500\,\mu m/\sqrt{cm}$ at 500 V/cm in Argon(95%)–Isobutane(5%). The spectrum has been fitted by two Gaussians to account for the $K_\alpha$ and $K_\beta$ lines. The mean of the $K_\alpha$ line corresponds to the specific number of electrons converted in this gas mixture (226 electrons). The measured energy resolution ~4%, defined as full width half maximum divided by peak position of the response function, shows that the electron number distribution is sub-poissonnian as expected from Fano theory. The energy resolution obtained using electron counting is slightly better than the energy resolution obtained when reading out the grid signal which is about 5% (rms). With an acquisition time of 100 μs, background from noise hits can be suppressed using the electrons arrival time which allows a very low detection threshold and thus a single electron efficiency (>90%) (Fig. 2, left). Some preliminary results show that the mean value corresponds to 232 electrons converted in the Argon(95%)–Isobutane(5%) gas mixture at an efficiency near 100%.

### 3.2. Polarimetry using photoelectric absorption

Photoelectric X-ray polarimetry with gas-based detectors was first demonstrated in 1923 using a Wilson chamber [8] and recently by micro-pattern gas detectors using a gas electron multiplier [9,10]. They achieved a quantum efficiency up to 6% at 6.4 keV.

The technique consists in determining the emission angle of the photoelectron by imaging its track in a gas medium.

This puts constraints on the gas mixture. On the one hand it should have enough absorption length to retain a good detection efficiency for few-keV X-rays, on the other hand, the diffusion limits the ability to measure the angle of the photoelectron. As a compromise, we choose a gas mixture of Neon(90%)–Isobutane(10%) (electron transverse diffusion coefficient $D_t \simeq 350\,\mu m/\sqrt{cm}$) and a

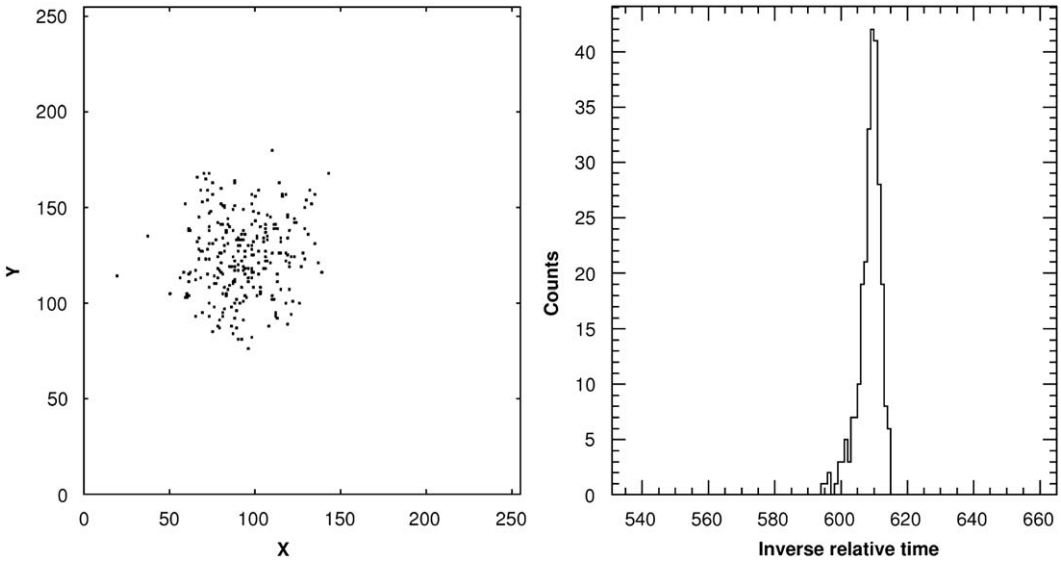


**Fig. 2.** Cluster of electrons from an X-ray photon $^{55}$Fe source converted in Argon(95%)–Isobutane(5%) gas mixture (left) and its corresponding time spectrum (right). A selection in time helps to suppress the background.

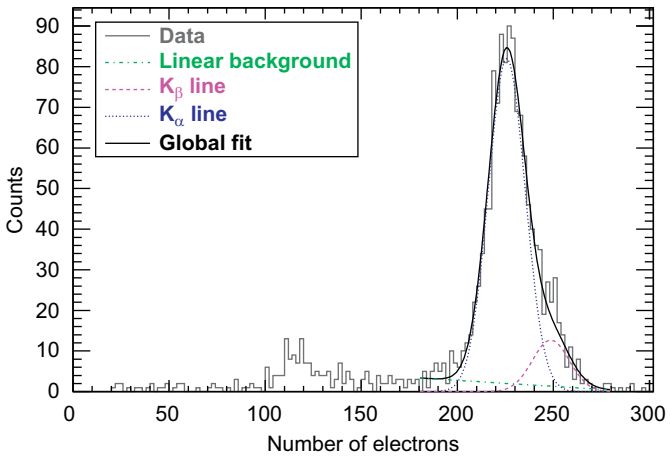


**Fig. 3.** Spectrum of the number of electrons obtained with each of 2000 photons from $^{55}$Fe source converted in Argon(95%)–Isobutane(5%) gas mixture. The $K_\alpha$ and $K_\beta$ lines have been fitted by two Gaussians. The mean of the line is 226 electrons and the RMS $\simeq$ 4%. The electron transverse diffusion coefficient was $D_t = 500\,\mu m/\sqrt{cm}$ at 500 V/cm.

drift distance of 5 mm. With this gas mixture the 5.9 keV photons absorption is 2.2%.

The photoelectric effect has a large cross-section at low energy making the process very sensitive to photon polarization. In the non-relativistic limit, the angular dependence of the differential cross-section is given by

$$\frac{d\sigma}{d\Omega} \propto \frac{\sin^2\theta\cos^2\phi}{(1-\beta\cos\theta)}$$

where $\beta = v/c$ is the electron velocity, $\phi$ is the polarization-dependent azimuthal angle, and $\theta$ is the polar angle with respect to the incident photon momentum (see Fig. 4). For linearly polarized photons, the differential photoelectron cross-section has a maximum probability ($\theta = 0$) in the plane orthogonal to the direction of the electric field of the incident photon with a $\cos^2\phi$ modulation. The polarization signature is given by the photoelectron angle distribution $N(\phi) = A + B\cos^2(\phi - \phi_{pol})$ and

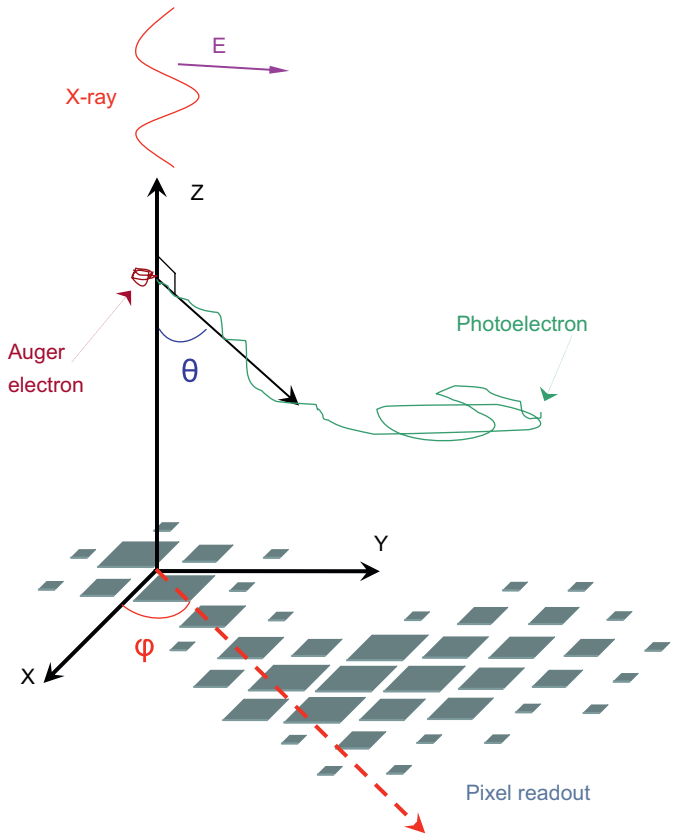


**Fig. 4.** Angular distribution and projection on the pixel readout of the detector plan ($XY$) obtained by an ejected photoelectron.

the modulation factor of a 100% linearly polarized radiation is

$$\mu = \frac{N_{max} - N_{min}}{N_{max} + N_{min}} = \frac{B}{2A + B}.$$

Using our digital TPC, with a drift distance of 5 mm, the photoelectron ejected after the absorption of $^{55}$Fe photon in the gas volume produces a track of electrons. The 55 μm pixel readout

chip allows a 2-D reconstruction of the photoelectron track ($\simeq 1$ mm).

The direction of emission of the photoelectron could be reconstructed by finding in first approximation the principal axis of the charge distribution on the pixels set in TOT mode (Fig. 5). The track image also contains information on the dynamics of the photoelectron energy loss; in case of asymmetric charge distribution, where the photoelectron track is seriously affected by Coulomb scattering, a better reconstruction of the photoelectron angle is possible by evaluating the absorption point after removing the final part of the track [11].

## 4. Summary

The principle of pixel gas detector has been demonstrated by combining Micromegas with the TimePix readout chip and resistive layer for protection. Beside the 3-D imaging capability, this small chamber is a very well suited for studying gas properties such as gain fluctuation and primary electron statistics. It could also be used as a soft X-rays polarimeter due to its ability to measure energy and directionality of photoelectrons with high spatial resolution, however with efficiency at a few percent level.

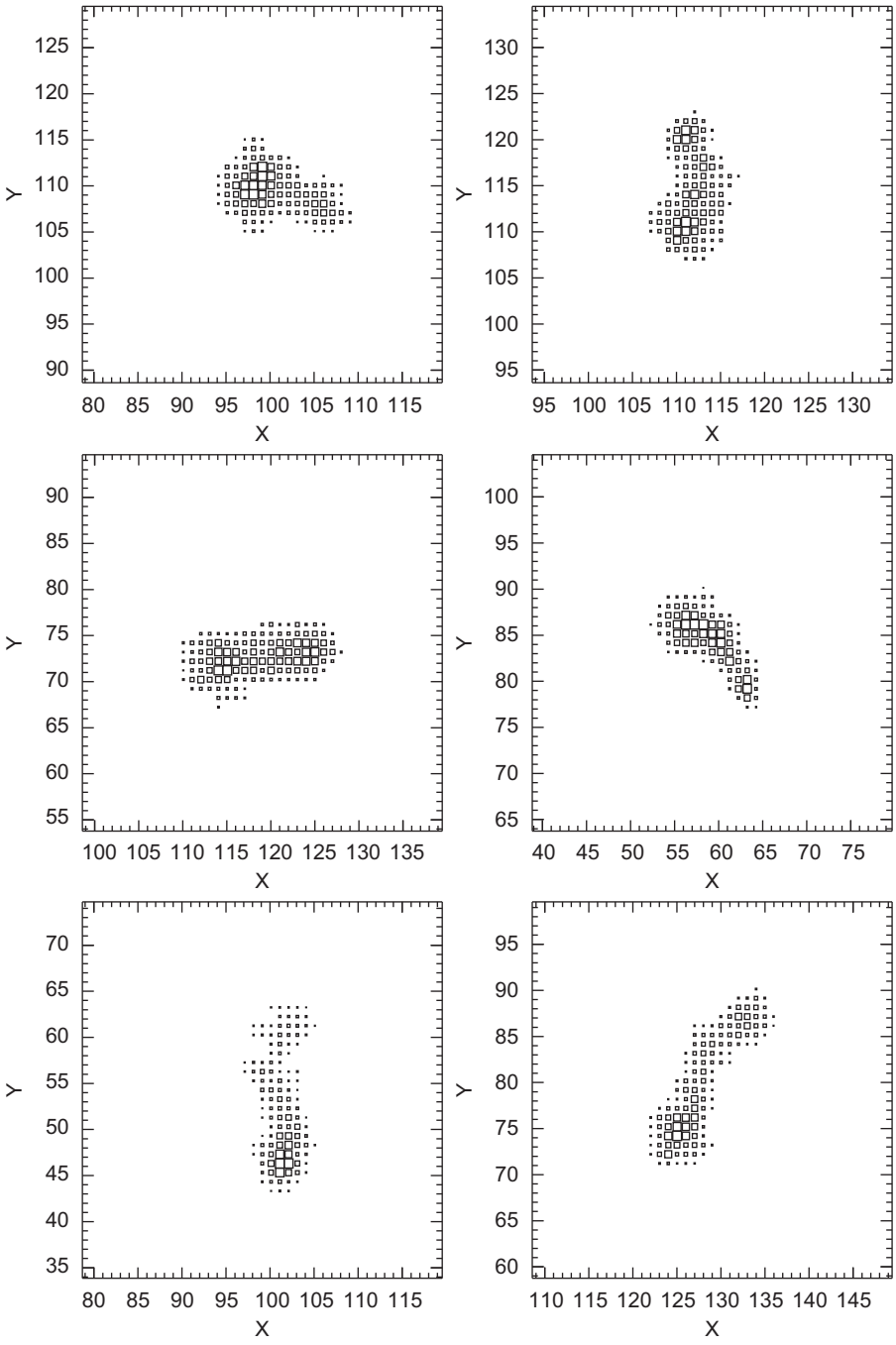


**Fig. 5.** Examples of photoelectron tracks ($\simeq 1$ mm) obtained with the 5.9 keV X-rays from $^{55}$Fe in Neon(90%)–Isobutane(10%) and a drift distance of 5 mm. The area of each square is proportional to the charge collected by the corresponding pixel set in TOT mode. The size of each image is 2.2 mm (40 pixels).

## Acknowledgments

This work is supported by the Commission of the European Communities under the 6th Framework Programme "Structuring the European Research Area", Contract number RII3-026126. We also thank the organizers of the 5th International Conference on New Developments In Photodetection 2008 for giving us the opportunity to present this work.

## References

[1] P. Colas, et al., Nucl. Instr. and Meth. A 535 (2004) 506.
[2] M. Campbell, et al., Nucl. Instr. and Meth. A 540 (2005) 295.
[3] X. Llopart, et al., Nucl. Instr. and Meth. A 581 (2007) 485.
[4] X. Llopart, et al., IEEE Trans. Nucl. Sci. NS-49 (2002) 2279.
[5] Y. Giomataris, et al., Nucl. Instr. and Meth. A 376 (1996) 29.
[6] M. Chefdeville, et al., Nucl. Instr. and Meth. A 556 (2006) 490.
[7] N. Wyrsch, et al., in: Proceedings of the MRS Symposium, vol. 869, 2005, pp. 3–14.
[8] C.T.R. Wilson, R. Soc. Proc. A 85 (1923) 1.
[9] R. Bellazzini, et al., Nucl. Instr. and Meth. A 572 (2007) 160.
[10] J.K. Black, et al., Nucl. Instr. and Meth. A 581 (2007) 755.
[11] R. Bellazzini, et al., Nucl. Instr. and Meth. A 510 (2003) 176.

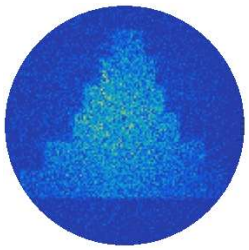

# *Beam tests of Micromegas LC-TPC large prototype*

PUBLISHED BY IOP PUBLISHING FOR SISSA

RECEIVED: *November 10, 2010*
ACCEPTED: *November 23, 2010*
PUBLISHED: *January 4, 2011*

1st INTERNATIONAL CONFERENCE ON MICRO PATTERN GASEOUS DETECTORS,
JUNE 12–15, 2009
KOLYMPARI, CRETE, GREECE



# Beam tests of Micromegas LC-TPC large prototype

**D. Attié**[1]

*CEA Irfu,*
*F-91191 Gif-Sur-Yvette, France*

*E-mail:* david.attie@cea.fr

ABSTRACT: Within the LC-TPC collaboration, a large TPC prototype for the International Linear Collider has been built and operated at DESY in a 1T superconducting magnet. Bulk Micromegas modules have been tested in a 5 GeV electron beam. Data have been taken with resistive anodes and standard anode pads at different operating conditions. Preliminary results on spatial resolution will be presented. In spite of wide pads ($3 \times 6.8$ mm$^2$) the intended spatial resolution, better than 100 microns, has been achieved. This recent result demonstrates and reinforces the technology potential for the resistive anode Bulk Micromegas.

KEYWORDS: Gaseous imaging and tracking detectors; Particle tracking detectors (Gaseous detectors); Time projection chambers

[1]On behalf of the LC-TPC collaboration, see http://www.lctpc.org for the full list of authors


doi:10.1088/1748-0221/6/01/C01007

## Contents



2011 JINST 6 C01007

## 1 Introduction

A gaseous central detector for the future International Linear $e^+e^-$ Collider (ILC) should measure up to 200 three-dimensional points along each track providing high performance in pattern recognition and in momentum determination. When operated in a high magnetic field (B=3.5T), a Time Projection Chamber has to achieve an r$\phi$ point resolution of about 100 microns per pad row on average along a track and thus allows decay mode independent tagging of Higgs bosons using the associated $Z$ decay into muon pairs [1].

In order to demonstrate a detector concept for the linear collider, the LC-TPC collaboration [2] has built and is testing Large Prototype of TPC based on readout systems using micro pattern gas detectors (MPGD), both Gas Electron Multipliers (GEM) and Micro Mesh Gas Amplifiers (Micromegas) described respectively in [3] and [4]. The EUDET TPC facilities (1 Tesla superconducting magnet PCMAG and a 60 cm long field cage) are described in [5].

## 2 Large prototype of TPC

Only the tests relating to the Micromegas module which was done in a 5 GeV/c collimated electron beam from the DESY II synchrotron are described here (figure 1). The GEM beam tests are reported in [6].

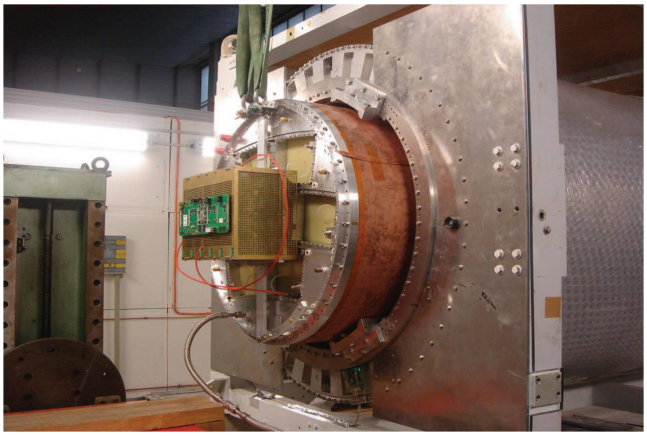

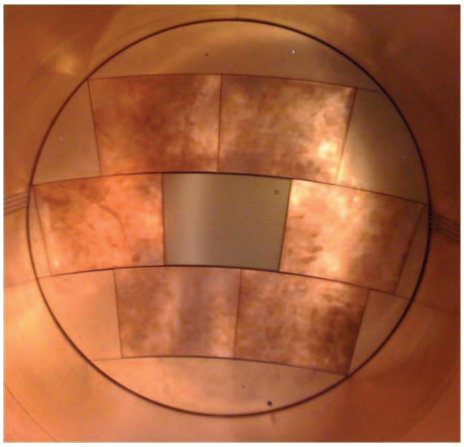

**Figure 1**. The TPC large prototype and AFTER electronics is pulled out from PCMAG (left figure). View from inside the TPC of the Micromegas module mounted in the middle of the endplate (right figure). Six other modules are dummy.

**Table 1**. Characteristics of the resistive Micromegas bulk tested with the Large Prototype TPC in DESY.

| Detector | Dielectric layer | Resistive layer | Resistivity (MΩ/□) |
|---|---|---|---|
| **Resistive Kapton** | $60-75\mu$m epoxy glass | $25\mu$m C-loaded polyimide | $\sim 4-8$ |
| **Resistive Ink** | $60-75\mu$m epoxy glass | $\sim 50\mu$m ink (3 layers) | $\sim 3$ |

### 2.1 Micromegas modules

The TPC endplate consists of seven interchangeable modules ($17 \times 23$ cm$^2$). Only a single detector module was mounted at the center of the TPC. Six other modules are dummy. Each module has 1726 pads arranged in 24 rows of 72 pads. Along the beam direction, the pads have a pitch of 6.8 mm and transverse to this direction, the pad pitch varies from 2.7 mm (bottom row) to 3.2 mm (top row) illustrated in figure 2. Two consecutive pads bring the high voltage to the mesh.

Three bulk Micromegas detectors have been tested successively in the TPC. The bulk technology, described in [7], consists of a stainless steel woven mesh held at 128 $\mu$m above the anode by insulated spacers (pillars). One of the detectors has standard conductive pads to collect the charge of the avalanches.

The two other detectors have a resistive coating, between the pads and the pillars, which is laminated (kapton i.e. polyimide) or painted (ink), on top of a 60 to 75 $\mu$m layer of print circuit board FR-4 glued to the anode using standard PCB procedures (lamination and heating). This dielectric layer is a composite of an epoxy resin reinforced with a woven fiberglass mat necessary to isolate the resistive coating.

For one of the detectors, the epoxy glass is covered by a 25 $\mu$m thick resistive Carbon-loaded kapton foil glued as before. Its resistivity was measured to be roughly 4-8 MΩ/□. The second detector has the epoxy glass covered by three layers of resistive ink ($\sim$50 $\mu$m of thickness in total) providing a resistivity of $\simeq 3$ MΩ/□. Both detector characteristics are summarized in table 1.



2011 JINST 6 C01007

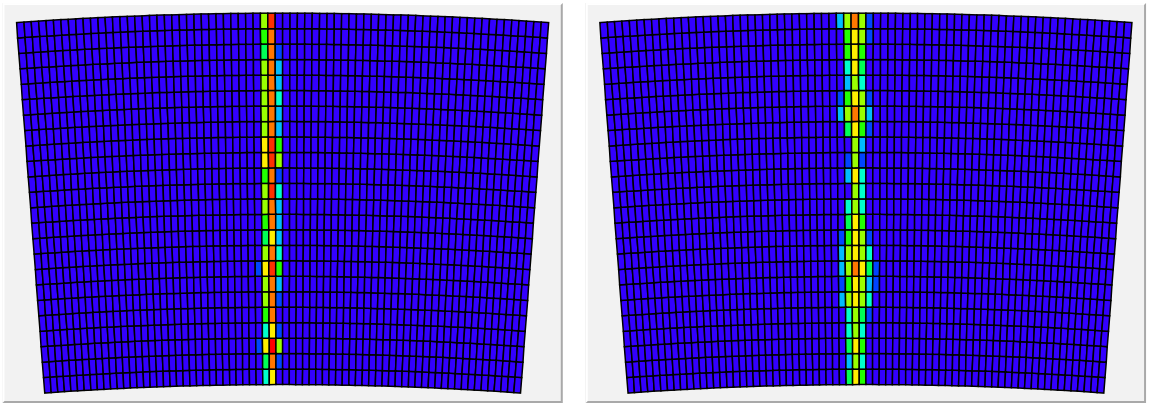

**Figure 2**. 5 GeV electrons beam events from resistive bulks with a magnetic field of 1T, with Carbon-loaded kapton (left figure) and resistive ink (right figure) technologies. Here, with the same Z position (5 cm), the second detector shows tracks with larger dispersion.

### 2.2 Readout electronics

The pads are read out with the AFTER-based electronics designed for the T2K experiment [9]. The sampling frequency can be varied between 10 and 100 MHz and the peaking time of the shaper can be set between 100 ns and 2 $\mu$s. Each channel provides a full-wave sampling over 511 time buckets and each sample is digitized by a 12-bit ADC.

## 3 Data taking

The Carbon-loaded Kapton bulk detector has been tested in the first period of data taking in November-December 2008. During the second period in May-June 2009, the resistive ink bulk module was tested for the first time and compared with the previous one (figure 2). During both periods, cosmics run, no magnetic field and B=1T data were taken. We varied the peaking time (200 ns, 500 ns, 1 $\mu$s and 2 $\mu$s) and the drift field ($E_{\text{low field}} = 140$V/cm and $E_{\text{standard field}} = 230$V/cm). The gas mixture was Ar:$CF_4$:iso-$C_4H_{10}$ (95:3:2), so-called T2K gas, in a premixed bottle.

In order to record data at several $z$ positions, the TPC was moveable inside PCMAG which was fixed with respect to the beam. For $z < 15$ cm and $z > 35$ cm the magnetic field is known to be inhomogeneous. The beam size was 3.9 mm (rms) in x and z.

## 4 Comparative analysis

### 4.1 Drift velocity

Figure 3 shows the drift times as function of the drift distance $z$ for several peaking times and at two different drift fields. The *low drift* field (140 V/cm) and the *standard drift* field (230 V/cm) give respectively drift velocities of 58 $\mu$m/ns and 76 $\mu$m/ns in the T2K gas mixture. At electric field $E_{drift}$ = 230 V/cm , the simulated drift velocity by Magboltz (75.48 $\pm$ 0.03 $\mu$m/ns for T2K gas with 140 ppm of water and a system pressure of $10^5$ Pa) was in agreement with the measured drift velocity (75.6 $\pm$ 0.2 $\mu$m/ns).



2011 JINST 6 C01007

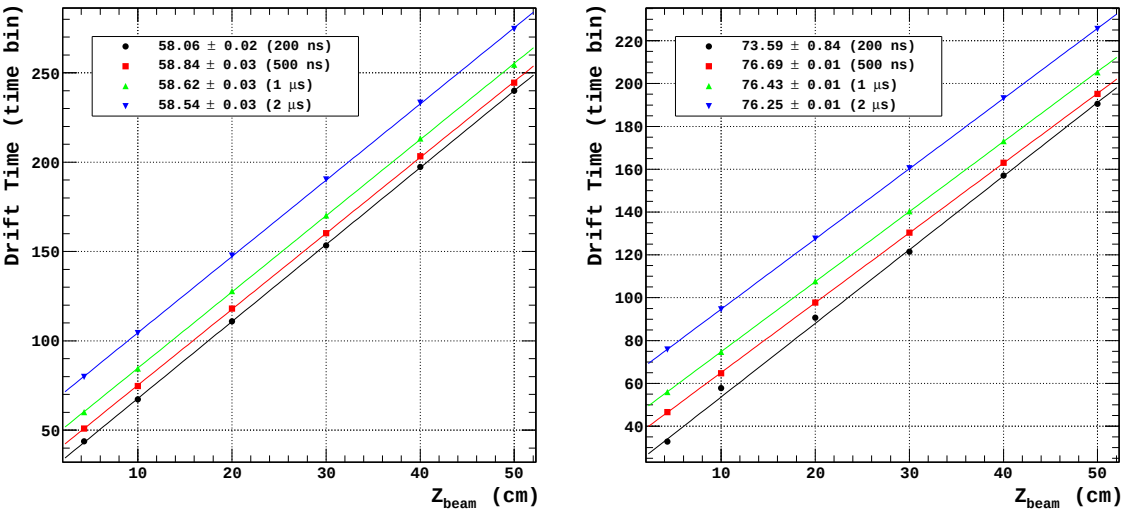


**Figure 3**. Determination of drift velocities (in $\mu$m/ns) for several electronics peaking times for two drift field conditions: low drift field condition (140 V/cm) on the left figure and standard drift field condition (230 V/cm) on the right figure. Each time bin is 40 ns for a sampling frequency of 25 MHz.

### 4.2 Spatial resolution

The resolution is determined from the residuals of track fits using the pad response function (PRF) extracted from the data. That is for each row, the normalized PRF is fitted by the function $f(x)$. This function is the ratio of two symmetric 4$^{\text{th}}$ order polynomials:

$$f(x,\Gamma,\Delta,a,b) = \frac{1+a_2x^2+a_4x^4}{1+b_2x^2+b_4x^4}. \tag{4.1}$$

The coefficients $a_2$ and $a_4$, and $b_2$ and $b_4$ can be expressed in terms of the full width half maximum $\Gamma$, the base width $\Delta$ of the PRF, and two scale parameters $a$ and $b$. The track fitting parameters $x_0$ and $\phi$ are determined by fitting the PRF to the pad amplitudes for the full event by $\chi^2$ minimization.

During the beam tests the comparison of the PRFs between resistive Kapton and resistive ink technologies (figure 4) made us decide to take more data of resistive Kapton detector rather than the other one. For instance, at drift distance $z = 5.7$ cm, the spatial resolution for the resistive ink detector is 130 $\mu$m compared to the 68 $\mu$m with the resistive Kapton detector.

The $z$ dependence of the resolution was parameterized as

$$\sigma^2 = \sigma_0^2 + \frac{C_{\text{D}}^2}{N_{\text{eff}}} z, \tag{4.2}$$

where $C_{\text{D}}$ is the diffusion constant, taken from Magboltz, and $\sigma_0$ and $N_{\text{eff}}$ are the resolution at zero drift distance and the number of effective electrons over the length of a pad. The zero drift resolution is found to be about 55 microns, which is 1/55 the size of the pad. $N_{\text{eff}}$ is in agreement with expectations and is given by the equation:

$$N_{\text{eff}} = \frac{1}{\langle 1/N \rangle} \left( \frac{1+\theta}{2+\theta} \right), \tag{4.3}$$



2011 JINST 6 C01007

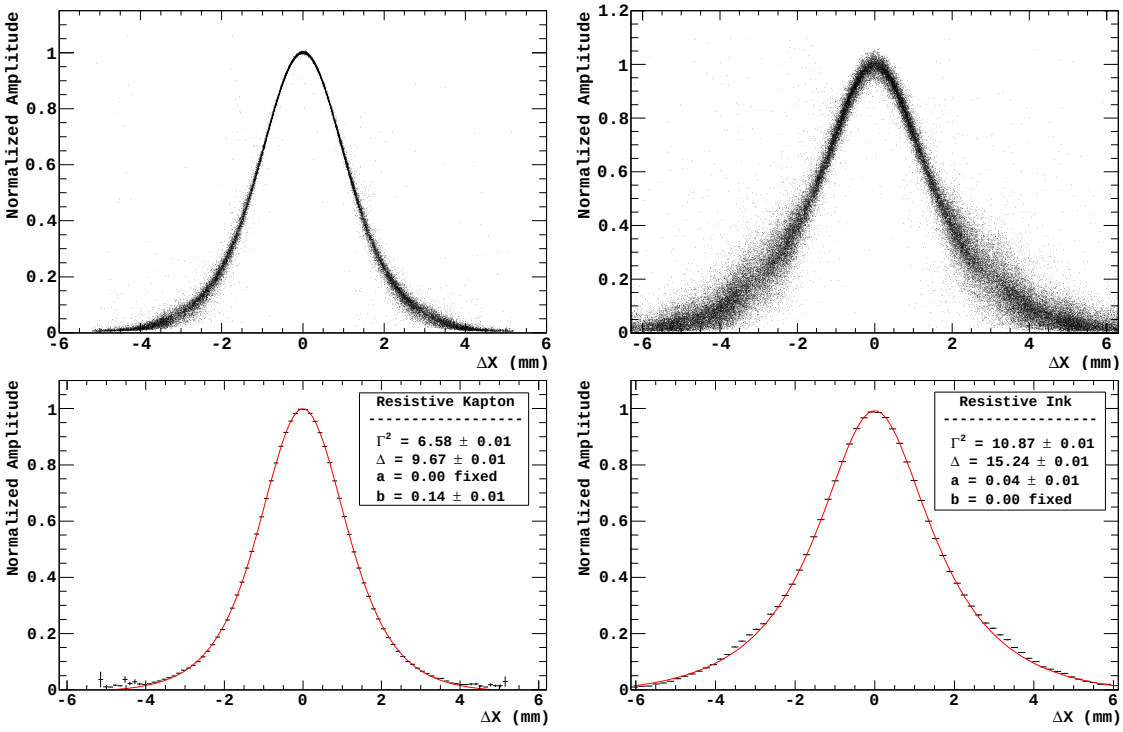


**Figure 4**. Comparison of the pad response functions from resistive bulks with a magnetic field of 1T, with Carbon-loaded kapton (left figure) and resistive ink (right figure) technologies.

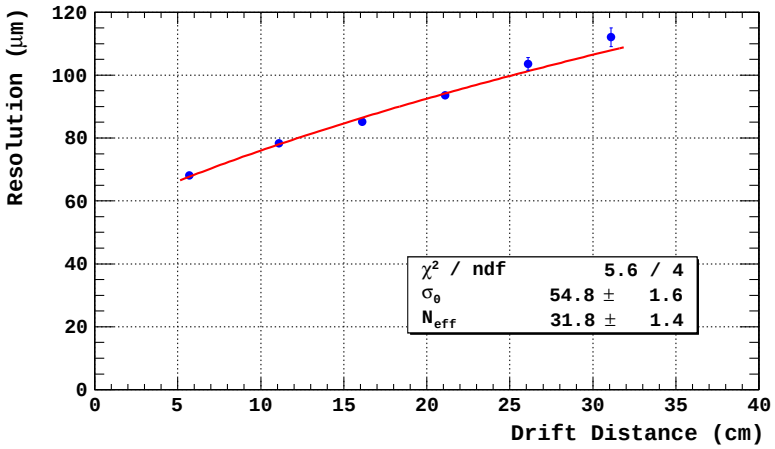


**Figure 5**. Measured point resolution as a function of drift distance for resistive Kapton Micromegas bulk using 500 ns of peaking time data. The data points are fitted by the eq. (4.2).

where $N$ is the number of electrons from ionization and the second term is a parametrization of the gas gain fluctuations [10]. $N$ is the number of electrons from the track ionization.

To determine the spatial resolution, the PRFs have been determined and used to fit the tracks as done before in previous data analysis. More information is available in [8, 11]. Figure 5 shows that the dependence of the spatial resolution on the drift distance with the Kapton resistive readout



2011 JINST 6 C01007

follows the expectation from transverse diffusion in the T2K gas ($C_{\mathrm{D}} = 104\ \mu\mathrm{m}/\sqrt{\mathrm{cm}}$) at $B = 1$ T and electron statistics.

## 5 Conclusion

Two resitive bulk Micromegas detectors have been tested in the TPC large prototype in a 1T magnetic field by the LC-TPC collaboration. The 55 $\mu$m of spatial resolution achieved by the C-loaded Kapton technology is very promising. The obtained spatial resolution as a function of drift distance reproduced well the expected equation. A lower resistivity ($\sim$1 M$\Omega/\square$) kapton technology will be tested in the next beam test and the design of a compact AFTER chip-based electronics is in progress and will be used in 2010.


## Acknowledgments

The LC-TPC collaboration thanks the DESY management for its hospitality, and the KEK cryogenic group for installation of the PC-MAG magnet. This work is partially supported by the Commission of the European Communities under the 6th Framework Programme *Structuring the European Research Area*, contract number RII3-026126.


## References


[1] LC-TPC collaboration, A. bellerive et al., *TPC R&D for an ILC detector*, LC-DET 2007-005 (DESY, Hamburg);
LC notes can be found on http.//flcweb01.desy.de/lcnotes/

[2] See http.//www.lctpc.org/.

[3] F. Sauli, *GEM: a new concept for electron amplification in gas detectors*, *Nucl. Instrum. Meth.* **A 386** (1997) 531.

[4] Y. Giomataris, P. Rebourgeard, J.P. Robert and G. Charpak, *MicrOMEGAs: a high-granularity position-sensitive gaseous detector for high particle-flux environments*, *Nucl. Instrum. Meth.* **A 376** (1996) 29.

[5] T. Behnke, K. Dehmelt, T. Matsuda and P. Schade, *A Large TPC Prototype with MPGD Readout: status and Plans*, arXiv:0903.2803.

[6] LC-TPC collaboration, T. Matsuda et al., *Results of the first beam test of a GEM TPC large prototype*, 2010 *JINST* **5** P01010.

[7] I. Giomataris et al., *MicrOMEGAs in a bulk*, *Nucl. Instrum. Meth.* **A 560** (2006) 405 [physics/0501003].

[8] M.S. Dixit et al., *Position sensing from charge dispersion in micro-pattern gas detectors with a resistive anode*, *Nucl. Instrum. Meth.* **A 518** (2004) 721.

[9] P. Baron et al., *AFTER, an ASIC for the readout of the large T2K time projection chambers*, *IEEE Trans. Nucl. Sci.* **55** (2008) 1744.

[10] D.C. Arogancia et al., *Study in a beam test of the resolution of a MicrOMEGAs TPC with standard readout pads*, *Nucl. Instrum. Meth.* **A 602** (2009) 403.

[11] M. Dixit et al., *MicrOMEGAs TPC studies at high magnetic fields using the charge dispersion signal*, *Nucl. Instrum. Meth.* **A 581** (2007) 254.




2011 JINST 6 C01007

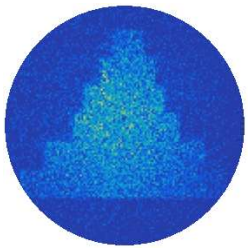

# *The CLAS12 Micromegas Vertex Tracker*

Nuclear Inst. and Methods in Physics Research, A 957 (2020) 163423

Contents lists available at ScienceDirect

Nuclear Inst. and Methods in Physics Research, A

journal homepage: www.elsevier.com/locate/nima

# The CLAS12 Micromegas Vertex Tracker

A. Acker, D. Attié, S. Aune, J. Ball, P. Baron, Q. Bertrand, D. Besin, T. Bey, F. Bossù *, R. Boudouin, M. Boyer, G. Christiaens, P. Contrepois, M. Defurne, E. Delagnes, M. Garçon, F. Georges, J. Giraud, R. Granelli, N. Grouas, C. Lahonde-Hamdoun, T. Lerch, I. Mandjavidze, O. Meunier, Y. Moudden, S. Procureur, M. Riallot, F. Sabatié, M. Vandenbroucke, E. Virique

*IRFU, CEA, Université Paris-Saclay, 91191, Gif-sur-Yvette, France*

ARTICLE INFO

*Keywords:*
CLAS12
Micromegas
Curved detectors
Particle tracking
DREAM ASIC

ABSTRACT

The Micromegas Vertex Tracker was designed to improve upon the tracking capabilities of the baseline design of the CLAS12 spectrometer in Hall B at Jefferson Laboratory. A Barrel Micromegas Tracker made with six concentric cylinders, each made of three 120°-sector tiles, surrounds the Silicon Vertex Tracker, and a Forward Micromegas Tracker composed of 6 disks is placed 30 cm downstream of the liquid-hydrogen target. Both trackers sit in a 5 T solenoid magnetic field. All Micromegas elements are based on resistive technology to withstand luminosities up to $10^{35}$ cm$^{-2}$ s$^{-1}$, as well as on bulk technology to enforce gain uniformity and mechanical robustness. Due to the high magnetic field, dedicated electronics have been designed and displaced ~2 m away from the detectors. The electronics readout is based on the DREAM ASICs that allow sustained operation up to 20 kHz trigger rate at the maximum luminosity.

## 1. Introduction

The baseline design of the Hall B CEBAF Large Acceptance Spectrometer for use at the 12 GeV Jefferson Laboratory (JLab) facility (CLAS12) [1] includes two tracking detector systems. A Silicon Vertex Tracker (SVT) [2] consists of a polyhedral arrangement around the target and resides in a 5 T solenoid magnetic field to detect particles emitted between 35° and 125° with respect to the beam direction. The forward tracking system consists of drift chambers [3] placed before, within, and after a toroidal magnetic field and covers the polar angle interval between 5° and 35°.

In 2010, a proposal submitted by the IRFU group at CEA-Saclay for an upgrade of the baseline CLAS12 design was accepted by JLab management. The upgrade of the central tracker consisted of replacing the fourth layer of the SVT baseline design with 6 layers of cylindrical Micromegas detectors, called the Barrel Micromegas Tracker (BMT). In addition, a Forward Micromegas Tracker (FMT) made of 6 Micromegas disks was placed ~30 cm downstream of the target to supplement the forward tracking system with the drift chambers. The FMT and BMT form the Micromegas Vertex Tracker (MVT). Simulations showed that the addition of the Micromegas detectors improved the vertex and polar angle resolutions both in the central and in the forward tracking systems compared to the baseline design [4,5].

Together, the SVT and the BMT form the Central Vertex Tracker (CVT). The CVT is surrounded by two scintillator-based detectors called the Central Time-Of-Flight (CTOF) [6] and the Central Neutron Detector (CND) [7] that provide particle identification information.

## 2. System description

### 2.1. Micromegas detectors

Micromegas detectors are micro-pattern gaseous detectors [8]. A schematic representation of a typical Micromegas detector is shown in Fig. 1. In the few-millimeter-wide conversion gap with an electric field of a few kV/cm, free electrons produced by the ionization of gas molecules by charged particles drift toward the micro-mesh and enter the amplification gap. In the amplification gap, the electric field reaches several hundreds of kV/cm, accelerating the electrons arriving from the conversion gap and making them ionize the gas, consequently creating an electromagnetic shower. The signal is then collected by the readout strips.

The MVT must sustain a high particle flux, which may induce sparks between the micromesh and the strips in its nominal running conditions. In order to quench these sparks and their associated temporary high voltages (HV) drops that "blind" the detector, all MVT detectors are based on the resistive technology. As depicted in Fig. 1, resistive strips and a thin layer of insulator are deposited on top of the readout strips [9]. The signals are transferred from the resistive to the readout

* Corresponding author.
*E-mail address:* francesco.bossu@cea.fr (F. Bossù).

https://doi.org/10.1016/j.nima.2020.163423
Received 18 December 2019; Accepted 7 January 2020
Available online 17 January 2020

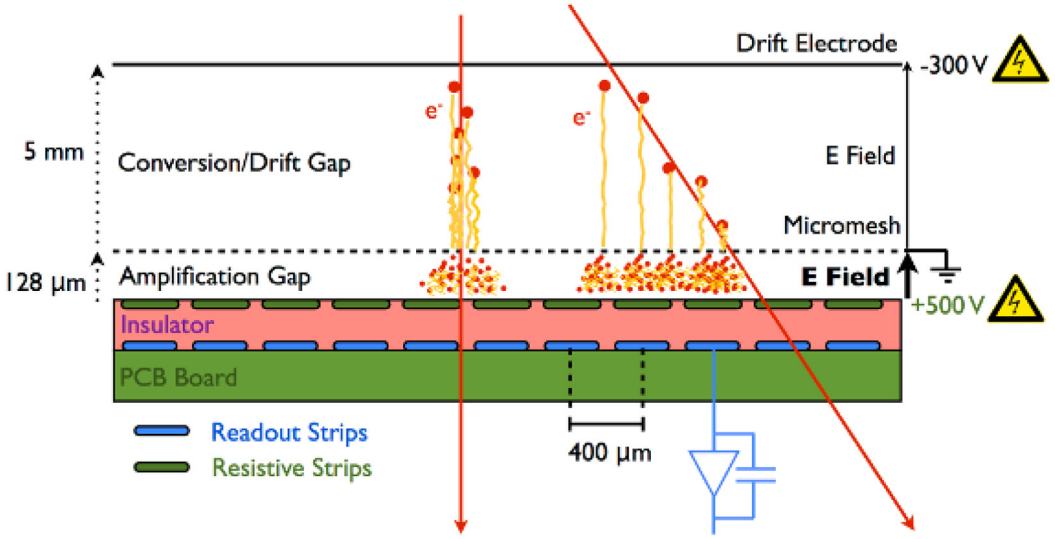


**Fig. 1.** Schematic view of a resistive Micromegas detector.

**Table 1**
Radius, pitch, and strip orientation of the different BMT layers.

| Radius (mm) | Pitch (µm) | Strip orientation |
|---|---|---|
| 146.146 | 330–860 | C |
| 161.146 | 487 | Z |
| 176.146 | 536 | Z |
| 191.146 | 340–770 | C |
| 206.146 | 529 | Z |
| 221.146 | 330–670 | C |

strips by capacitive coupling. Finally, the resistive technology allows for higher gains to be reached compared to regular detectors due to a lower probability of sparks in the amplification region. Consequently the resistive technology allows for higher signal to background ratios. In this configuration the mesh is grounded and the high voltage for amplification is positive on the resistive strips.

### 2.2. General

The Barrel Micromegas Tracker consists of six layers of cylindrical detectors, three with strips along the beam axis (Z strips) that provide information about the azimuthal angle of the particle and three with circular strips (C strips) perpendicular to the beam axis that significantly improve the polar angle determination with respect to that extracted from the SVT information alone. The strip orientation, the pitch, and the radial distance from the center are listed in Table 1. Each layer is made of three curved detectors covering 115° each. A total of 18 curved detectors is assembled on a carbon structure to complete the BMT. In addition to the resistive technology, these detectors make use of the bulk technology, meaning that the micromesh is embedded with the pillars on top of the resistive strips [10]. The bulk technology enforces a uniform distance between the micromesh and the strips, consequently maintaining a uniform gain over the detector surface, despite the mechanical stress induced by the curvature of the tile.

The Forward Micromegas Tracker consists of six flat Micromegas disks stacked together. The disks are all identical and assembled with a 60° rotation with respect to one another, giving 3 angles of strips (0°, 60°, and 120°). The FMT is attached to the downstream end flange of the BMT. Fig. 2 displays a cut view of both the BMT and FMT inside the CLAS12 solenoid magnet.

A separate CLAS12 subsystem called the Forward Tagger (FT) that is positioned just upstream of the torus magnet and covers polar angles from 2° to 5°, also includes a set of Micromegas trackers. The FT is

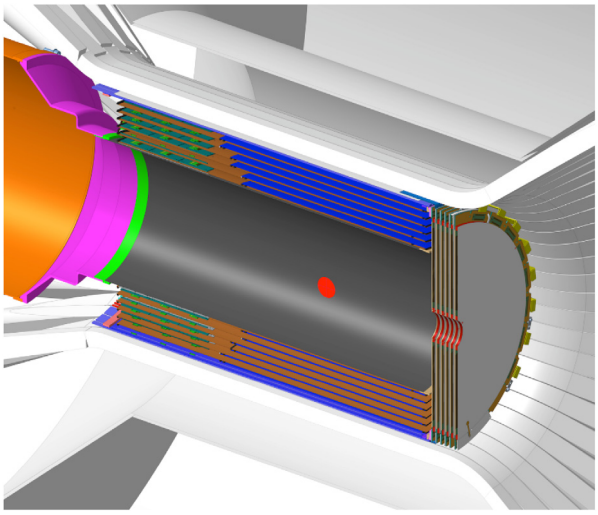

**Fig. 2.** Cut view showing the 6 different layers of the BMT and the 6 identical FMT disks. The detectors are inserted close to the Central Time-of-Flight, itself in the 5 T solenoid magnet. The SVT is inside the MVT and is not displayed in this view where the beam enters from the left. The red dot indicates the nominal target position. (For interpretation of the references to color in this figure legend, the reader is referred to the web version of this article.)

equipped with four Micromegas disks arranged in two pairs, called the FT Tracker (FT-Trk), which shares most of its design with the FMT. A detailed description can be found in Ref. [11].

### 2.3. Mechanical structure

In order to support the Micromegas Vertex Tracker in the magnet, a stainless-steel tube with the BMT and the FMT at its downstream end is attached to the flange of the SVT support tube, as shown in Fig. 3. This tube also holds 6 crates containing the 48 readout Front-End Unit (FEU) boards for the Micromegas detectors, as well as the service distributions for the gas, environmental sensors, and high-voltage distribution. The connection between the detectors and readout FEUs is done using assembled micro-coaxial cables that allow the signals to be read out from the upstream electronics crates. Each FEU is connected to a Back-End Unit with an optical fiber. The patch panels for the gas and the high voltage cables are located on the 6 crates.

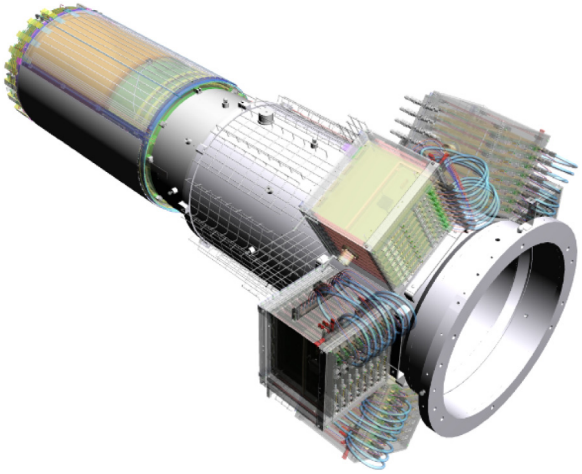

**Fig. 3.** Support tube with electronics rack and MVT detectors. The beam enters from the right.

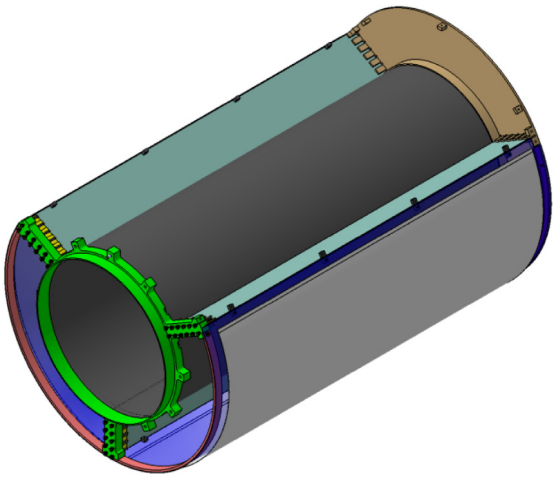

**Fig. 4.** BMT mechanical structure (shown with one sector open) that houses 6 curved detectors.

The mechanical structure of the BMT is made of a thin (1 mm) carbon cylinder with a glued PEEK flange downstream, and a glued stainless-steel flange upstream, as shown in Fig. 4. Since the main purpose of the barrel is to reconstruct protons with momentum as low as 300 MeV, the material budget must be as small as possible in order to reduce multiple scattering and energy loss. The stainless steel used for the tube and flanges is made of 904L (non-magnetic steel). The BMT structure is completed by an outer thin carbon-fiber cylinder that protects the BMT tiles during maintenance operations. The detector alignment is performed using particle tracks taken during zero magnetic field data taken either with cosmic rays (as described in Section 4.2) or with the electron beam.

### 2.4. Barrel Micromegas Tracker (BMT)

The Barrel detector tiles are made of a thin printed circuit board (PCB) (0.2 mm) transformed into Micromegas with the bulk process. Up to 16 MEC8 connectors are welded on the upstream end of the tile. The PCB is curved on a custom mandrel tool with the desired radius. The cylindrical shape is then maintained by gluing two carbon fiber arcs at each end of the active zone and two aluminum arcs on the MEC8 connector side. The thickness of the carbon and aluminum structure arcs (3 mm) was chosen to match the design drift gap of the detectors.

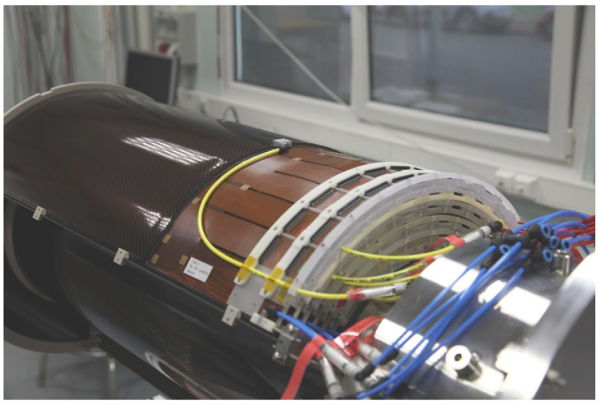

**Fig. 5.** Photograph of a full stack of 6 BMT layers. The two aluminum arcs are visible on top of the connectors. The blue and yellow plastic tubes are part of the gas plumbing. (For interpretation of the references to color in this figure legend, the reader is referred to the web version of this article.)

A Kapton foil (0.25 mm) with metallic coating is then glued on top of the carbon–aluminum structure to seal the detector and serves as the drift electrode of the detector. A curved 3D-printed plastic mechanical bracket is attached above the connectors to provide rigidity for the connection of the signal cables. The high voltage connections and the associated protection circuit are hosted inside 4 cm × 8 cm metallic boxes on the upstream side of the PCB, out of the active area. Gas is introduced in the middle of the connector side and flushed out on the edges of the connector side through the hollow carbon-aluminum mechanical structure. The leak rate of each detector is measured below $2\times10^{-3}$ l/h. Pins, serving both as fixation points and for alignment, are inserted and glued on both ends of each carbon tube. A geometrical survey was performed and the measured radii are within 1 to 2 mm of the design values. Fig. 5 shows a photograph of the curved BMT detectors.

As pointed out above, the BMT is located inside the CLAS12 5 T solenoid. The high magnetic field had a strong impact on the design and operation of the BMT detectors. Since the (detector) electric and the (solenoid) magnetic fields are essentially orthogonal, the primary electrons in the drift region of the Micromegas detectors are subject to Lorentz forces. Consequently, the electron trajectories form an angle with respect to the electric field direction, the so-called Lorentz angle. Hence, the charge is spread over a large area and this directly impacts the position resolution. Early studies showed that large Lorentz effects could be partly compensated for by using a 5–6 kV/cm drift high voltage [12]. This increase of the drift field impacts the efficiency through a loss of transparency of about ≈5%. The effect is worse in the case of the Z-type detectors with their strips parallel to the B-field direction. Finally, the gas mixture of 90% argon + 10% isobutane offers a reasonable trade-off between a limited drift velocity to reduce the Lorentz force effects and a high number of electrons generated in the conversion gap. The Lorentz angle is estimated to be about 40° in the 5 kV/cm drift electric field at 5 T.

### 2.5. Forward Micromegas Tracker (FMT)

The Forward Micromegas Tracker, shown in Fig. 6, consists of six identical Micromegas resistive detectors in the forward region from 30 cm to 36 cm downstream of the target center. Each Micromegas detector is a 450 mm diameter disk with an active area of 1024 parallel readout strips (525 μm pitch). The angle between the strip orientation of two adjacent disks is 60°. The distance between the readout strips of two consecutive disks is 10.5 mm. Each disk consists of an assembly of two 0.2-mm-thick PCBs glued on a 2 mm Rohacell foam backing to form the readout plane and a 0.2 mm PCB for the drift plane glued on

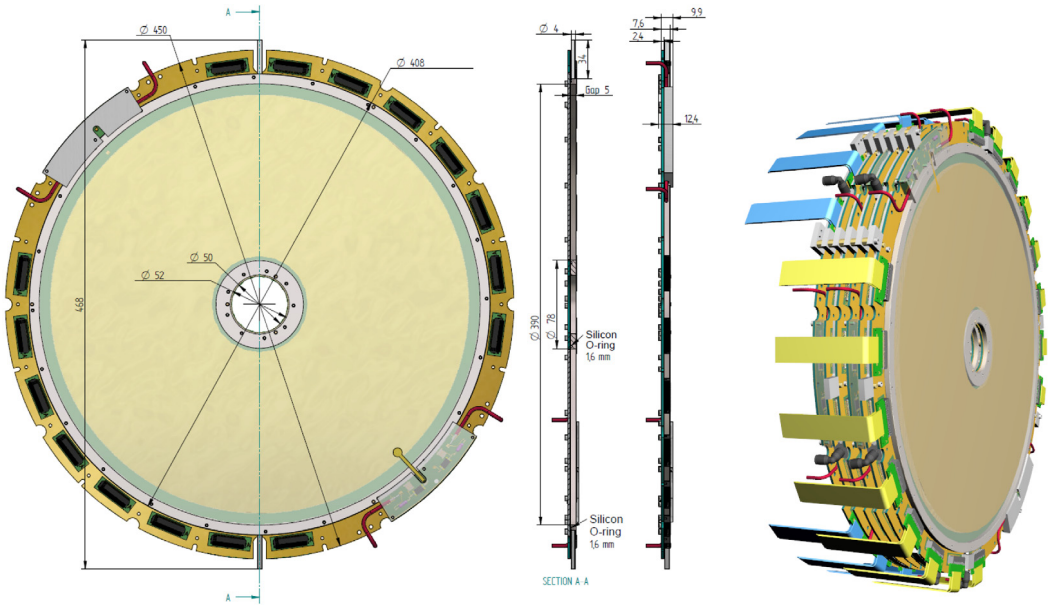


**Fig. 6.** CAD views of the FMT disks.

two cylindrical frames that define the gas volume (5 mm). The inner frame is made of PEEK and the outer frame of aluminum. Both define the chamber and are attached to the readout plane using stainless steel screws. High voltage connections and associated filter circuits are located on the disk edge diametrically opposed from one another. The signals are read out via 16 MEC8 connectors.

The active area of the FMT is divided in two parts, the inner part with diameter $86 < d < 166$ mm and the outer part with $168 < d < 380$ mm. Each of the two parts can be independently energized so that the inner region can be turned off in the case of a very high flux of charged particles.

Since the magnetic field is parallel to the drift field in the FMT, the drift electrons are not affected by the Lorentz angle effect. In order to improve the timing resolution, a mixture of 80% argon + 10% isobutane + 10% $CF_4$ allows for an increase of the drift velocity compared to 90% argon + 10% isobutane mixture used in the BMT [13].

### 2.6. Gas system

The Micromegas are continuously flushed with gas in order to maintain high purity and to overcome the normal outgassing of the detectors. As stated above, the gas used for the BMT is a flammable mixture, argon with 10% isobutane. Each layer of the barrel is fed with one gas line. The tiles of a given layer are connected in series, with a flow rate of about 1.5 l/h. For the FMT, the gas mixture is argon with 10% $CF_4$ and 10% isobutane with a flow rate of 2 l/h for a set of three disks connected in series. Thus a total of ∼13 l/h is used for both the FMT and BMT. Due to the low gas flow rate for the detectors, a gas recirculation system is not employed for the MVT.

A programmable logic controller controls the overall flow sent to the BMT and to the FMT, which is provided by a gas mixing system located outside of the experimental hall. As shown in Figs. 7 and 8, a gas control panel allows the gas distribution between the different lines for the BMT and FMT to be manually adjusted . Inside the gas control panel, the gas pressure and flow are measured at various points. The flow rate and pressure must be low and controlled to avoid any deformation of the detectors. Interlocks are set to close valves and stop the gas flow in the detector if pressures or flows are above the set thresholds. Finally, the total inflow and outflow are compared and trigger an interlock to stop the gas flow if they disagree, which could indicate a leak in the gas system or the detector volume.

## 3. Electronics

The MVT data acquisition system is designed to read out 6000 channels of the forward station and 18,000 channels of the barrel station. With the physics background as high as 20 MHz, the strip hit rates are about 60 kHz and 20 kHz in the forward detectors and in the barrel detectors, respectively. The readout system is compliant with the CLAS12 requirements of a 20 kHz maximum trigger rate and provides a sufficiently long data pipeline to cope with up to a 16 μs trigger decision latency. Timing precision of a few ns is sufficient to limit the number of ghost hits compatible with the timing of the trigger signals. A charge measurement with a 10-bit dynamic range is enough to cover the full span of the Micromegas detector signals and to discriminate accurately minimum-ionizing particles (MIPs) from noise. Note that the FT-Trk [11] uses the same readout electronics and architecture as the MVT.

### 3.1. Readout system architecture

The extremely compact and dense design of the CLAS12 Central Detector leaves a very narrow space between the MVT and its neighbor subsystems, as well as between the Micromegas detectors themselves. In addition to the stringent space limitations, the operational conditions of the tracker are harsh in terms of radiation and the high 5 T magnetic field. Keeping a low material budget is an obvious concern. Consequently, a readout architecture based on off-detector front-end electronics has been adopted. Lightweight micro-coaxial cable assemblies with low 40 pF/m linear capacitance carry bare, unamplified signals to the Front-End Units (FEUs) housed in crates ∼1.5–2 m upstream of the detectors.

The front-end electronics are responsible for the amplification and shaping of the detector signals, for holding the latter in a pipeline waiting for a trigger signal, for the digitization and compression of the selected event data, and for their delivery to the back-end electronics. The back-end is responsible for data concentration event by event. It provides an interface with the CLAS12 event building system, ensures a fixed latency path between the CLAS12 Trigger system [14] and the FEUs, and receives the system clock and trigger from the CLAS12 Trigger Supervisor and synchronously conveys them to the FEUs over bidirectional optical links. A schematic representation of the readout system architecture is shown in Fig. 9.

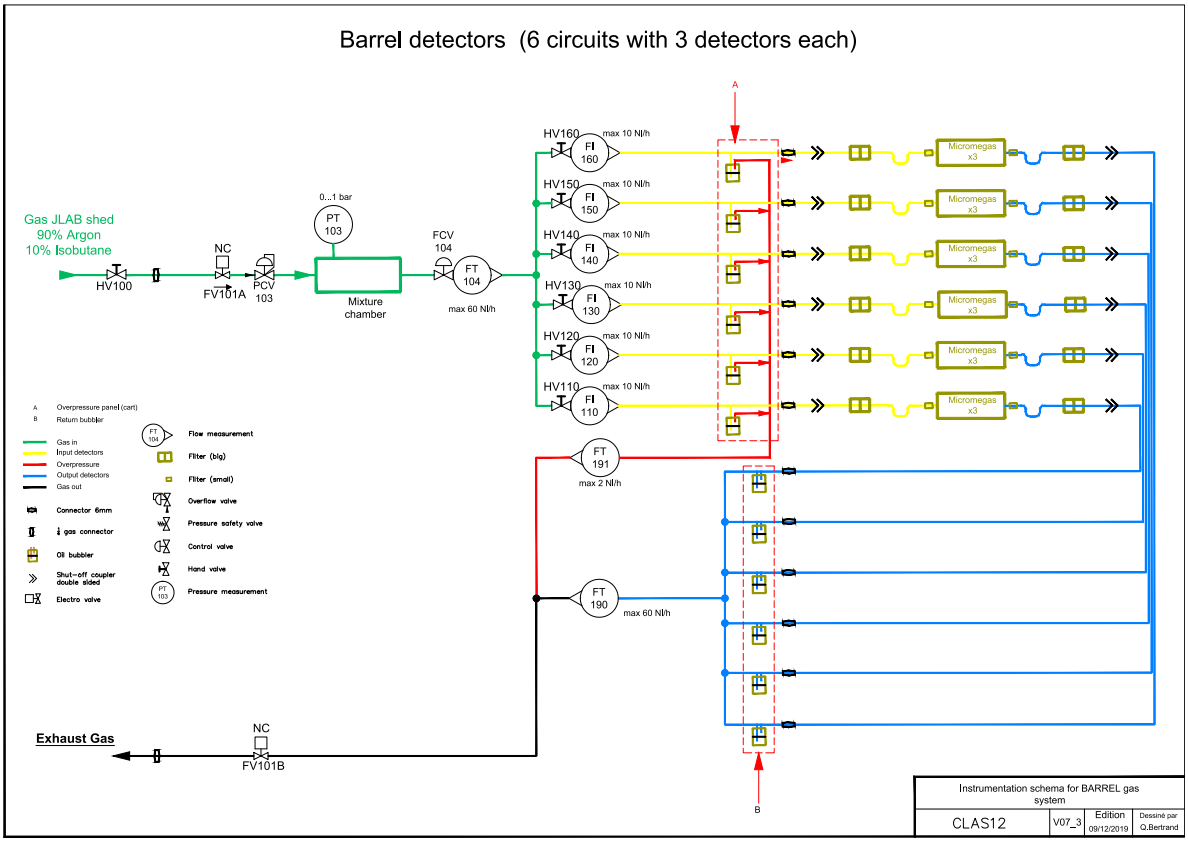


**Fig. 7.** Gas distribution diagram for the Barrel Micromegas Tracker.

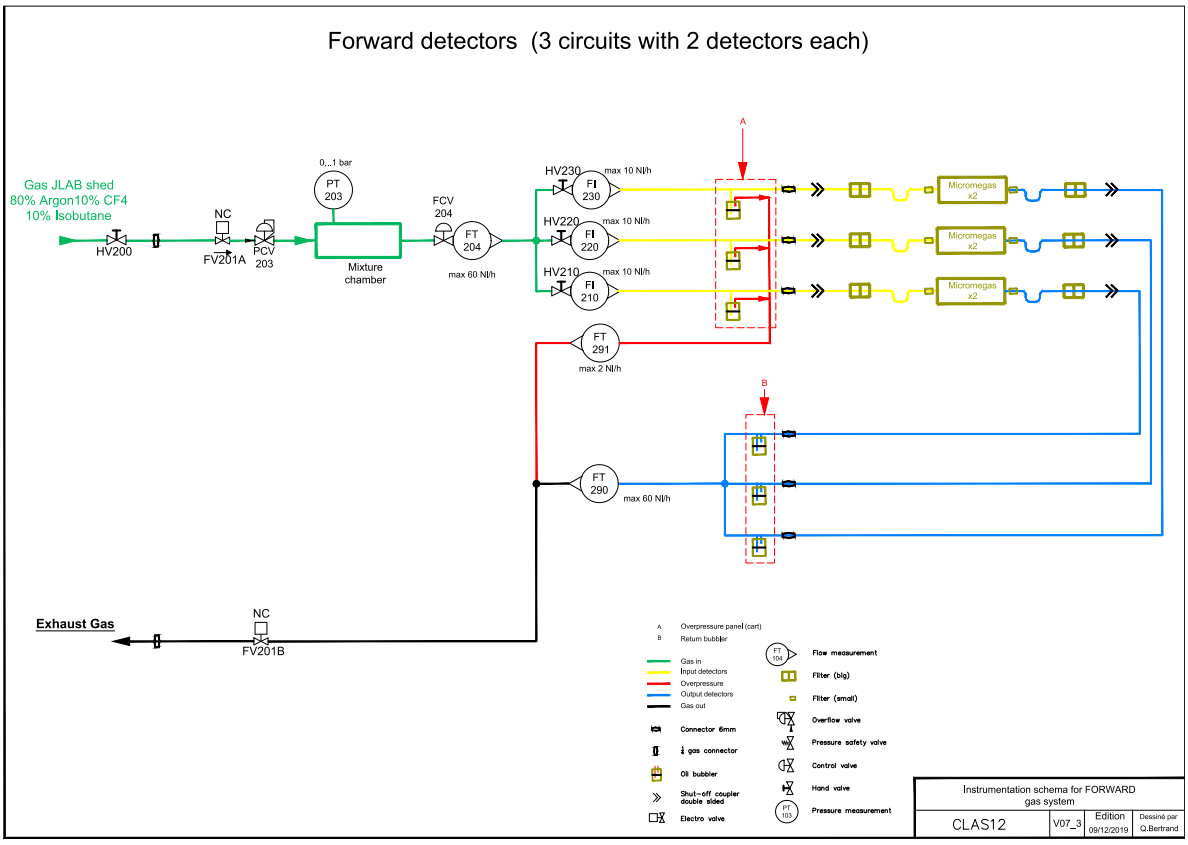


**Fig. 8.** Gas distribution diagram for the Forward Micromegas Tracker.

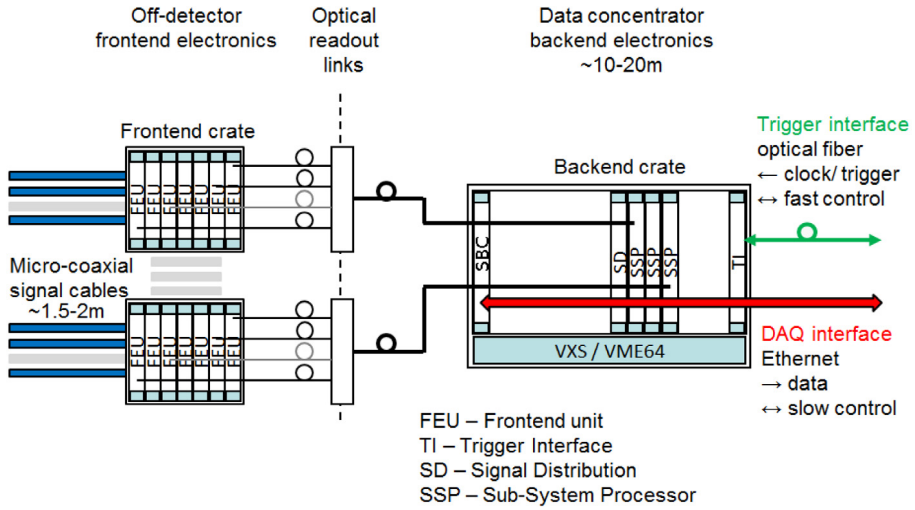


**Fig. 9.** Readout system for the MVT and FT-Trk detectors.

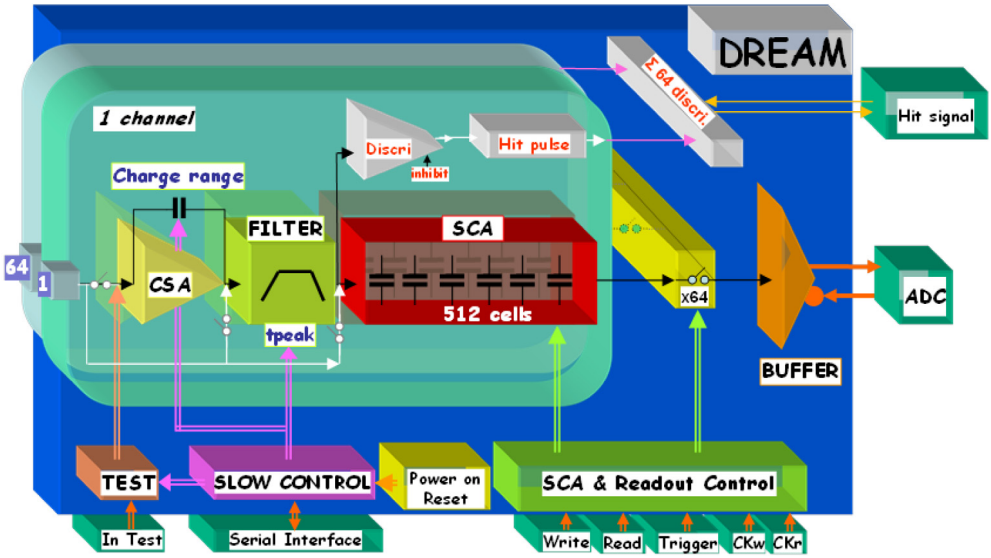


**Fig. 10.** Block diagram of the DREAM ASIC.

### 3.2. The 64-Channel DREAM ASIC

Depending on the type and size of the CLAS12 Micromegas detectors, the strip capacitances vary from 60 to 120 pF. The total capacitance seen by the front-end electronics input is even higher, up to 200 pF due to the contribution from the detector micro-coaxial cables. To achieve a comfortable signal-to-noise ratio (SNR) well above 10, the equivalent noise charge (ENC) of the detection chain should be ~2500 $e^-$ for the 140–200 pF range of the total input capacitance. At the time of the detector development, no existing ASICs could deliver the required performance while, in addition, sustain the 20 kHz readout rate and provide the 16 μs deep trigger pipeline required. A new 64-channel ASIC, called DREAM (for Dead-timeless Readout Electronics ASIC for Micromegas), has been developed [15].

The DREAM ASIC block diagram is shown in Fig. 10. Each channel includes a charge sensitive amplifier (CSA) adapted to a wide spread of detector capacitances (up to 1 nF) and four selectable charge measurement ranges (from 50 to 600 fC), a shaper with programmable peaking times (from 75 ns to 1 μs), and 512-cell deep Switched Capacitor Array (SCA) used as the trigger pipeline memory and a de-randomization buffer.

The input signals are continuously sampled and stored in the SCA at a rate of up to 50 MHz. Upon reception of the trigger signal, a programmable number of samples of all channels, corresponding in time to the event, is read out serially through a differential analog buffer capable of driving an external ADC at a frequency of up to 28 MHz. The sampling is not stopped during the readout process, which allows nearly dead-timeless operation. Other features, such as the ability to operate with both signal polarities, the possibility to inject input signals directly into the SCA memory bypassing the filter and/or CSA, and integrated per-channel discriminators (useful to form trigger primitives), make the chip extremely versatile. The integrated circuit is manufactured in the AMS CMOS 0.35 μm technology and is encapsulated in the 128-pin LQFP square package with a 1 mm side and a 0.4 mm pitch.

### 3.3. The 512-Channel Front-End Unit (FEU)

The FEU is a mixed analog–digital electronics board. The analog section comprises eight input connectors, protection circuits, DREAM ASICs, and an 8-channel flash ADC (see Fig. 11). The protection circuits are optional. They are installed on the FEUs to protect the DREAMs from the sparks of standard Micromegas detectors. When working with

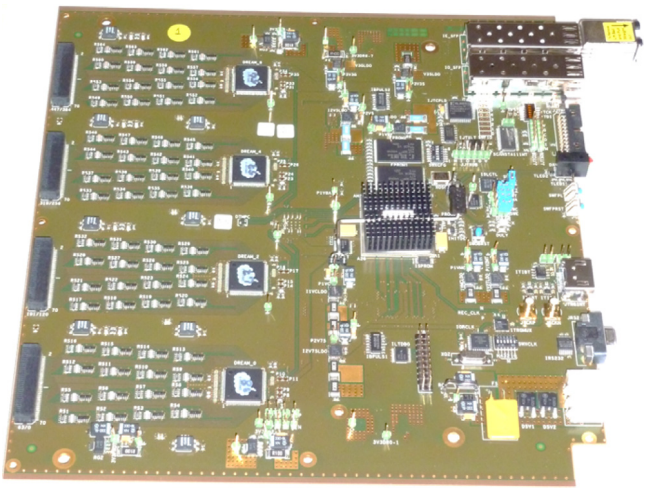

**Fig. 11.** Photograph of the 512-channel Front-End Unit.

resistive detectors, the input channels of the DREAM ASICs can be directly connected to the detector strips, improving the signal-to-noise ratio. The protected or non-protected type of FEUs are determined during their manufacturing.

As described above, the pre-amplification, shaping, and trigger pipeline functionalities are implemented in the DREAM chips. The analog samples from the eight DREAMs are digitized by an 8-channel 40 MHz 12-bit flash ADC AD9222 from Analog Devices [16]. The eight serial streams of digital data are delivered to the on-board FPGA. The digital section of the board comprises an xc6vlx75t-2-ff748 FPGA from the Xilinx Virtex-6 device family [17], its configuration memory, a 2 Mbyte synchronous SRAM, small form-factor pluggable (SFP) transceivers, an on-board clock synthesizer, and an auxiliary trigger interface circuit.

The FPGA controls the DREAM integrated circuits and the ADC, producing the sampling and readout clocks, as well as various required control signals. One of the SFP cages is populated with an optical transceiver module that is used to establish a synchronous communication channel with the back-end electronics over a 2.5 Gbit/s link. In the downstream direction, the link encodes the 125 MHz system clock, trigger signals, and fast synchronous commands.

Upon accepting the trigger signal, the FPGA reads the corresponding samples from the DREAMs and optionally applies the following digital data processing steps. First, after serial-to-parallel conversion, the pedestals are equalized. Next, for each sample, the coherent noise affecting the DREAM inputs is estimated and subtracted on a chip-by-chip basis. This greatly improves the noise immunity of the MVT readout system. Finally, the per-channel zero suppression is performed. The retained samples describe the signal development in the channel. Fitting their values with a known function allows an accurate estimation of the deposited charge and the signal timing. For each accepted trigger, the FPGA forms an event fragment from the retained channel data and delivers it to the back-end electronics via the optical channel. The optical channel is also used for setting and monitoring the run control parameters.

The FEU is a 6U (266 mm) high, 220 mm deep, and 5HP (25.4 mm) wide module. The thickness of its 12-layer PCB is 1.6 mm. It can be powered from either a 4.3 V or 5 V source and consumes slightly less than 20 W when all eight DREAMs operate in their most power-hungry mode. The FEUs have been operated in a magnetic field of up to 1.5 T without any perceptible change of their power consumption or functionality.

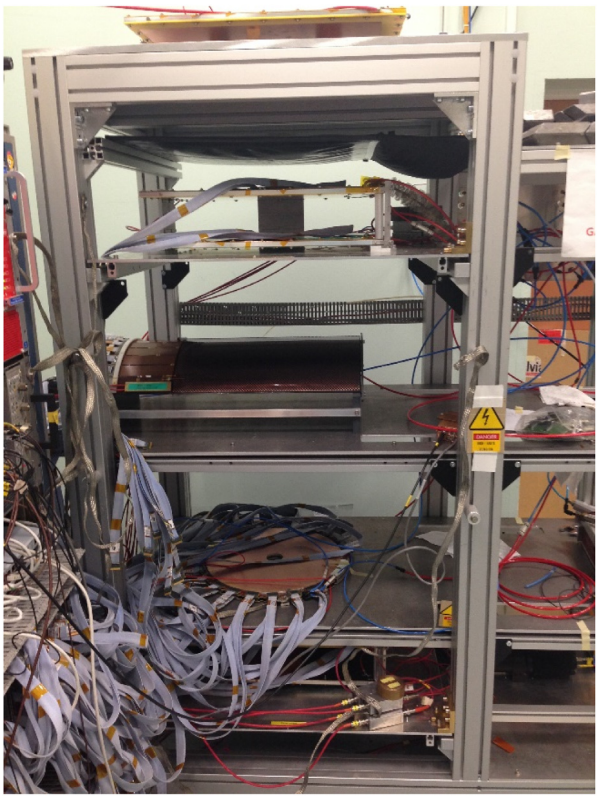

**Fig. 12.** The cosmic bench made of an external trigger from the coincidence of two scintillators and a hodoscope made of 4 reference trackers. The photograph shows the simultaneous operation of a BMT tile and a FMT disk under test.

### 3.4. The Back-End Unit (BEU)

The back-end of the data acquisition system of the MVT is based on the JLab standard VME/VXS hardware including a Trigger Interface (TI), a Signal Distribution (SD), a Subsystem Processor (SSP), and a crate controller single-board computer (SBC) [18]. The flow of the trigger, data, and control messages is shown in Fig. 9.

The TI receives a low-jitter, 250 MHz system clock and fixed-latency trigger signals from the CLAS12 Trigger Supervisor. It also delivers to the Trigger Supervisor the status information (e.g. busy) of the MVT readout system. The physical layer interface is based on parallel optic technology. The clock and trigger signals are delivered to the SD board over the VXS backplane. The SD board conveys properly delayed and aligned clock and trigger signals to the SSP boards. It also gathers their status information, and then combines and sends it to the TI board. These communications happen over the VXS backplane.

The SSP board was primarily designed to be a part of the hardware-level trigger logic for JLab experiments. Given the massive resources it provides (notably a Virtex-5 TX150T Xilinx FPGA, 32 multi-gigabit transceivers (GTX) routed to the front panel, 4 Gbyte DDR2 memory), it was considered for the readout of the MVT front-end electronics. The SSP firmware has been modified to fit the needs of the MVT Back-End Unit (BEU).

An SSP can distribute the global system clock, trigger, and synchronous commands to up to 32 FEUs. In practice, there are two Back-End Units each serving 24 front-ends. The trigger pulses and fast run control commands are broadcast synchronously to all FEUs over the synchronized fixed latency 2.5 Gbit/s links. The protocol between the FEUs and the BEU sets an 8 ns resolution on successive triggers and synchronous commands (125 MHz clock). However, the dispersion of their arrival times on the FEUs is well under 1 ns.

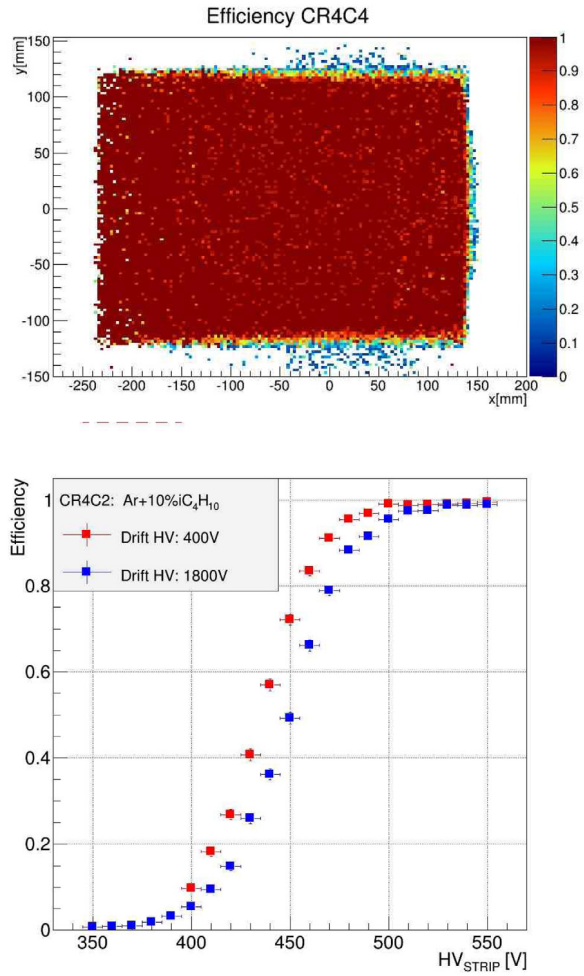


**Fig. 13.** Efficiency plateau (bottom) and 2D efficiency map (top) for a C-type barrel detector.

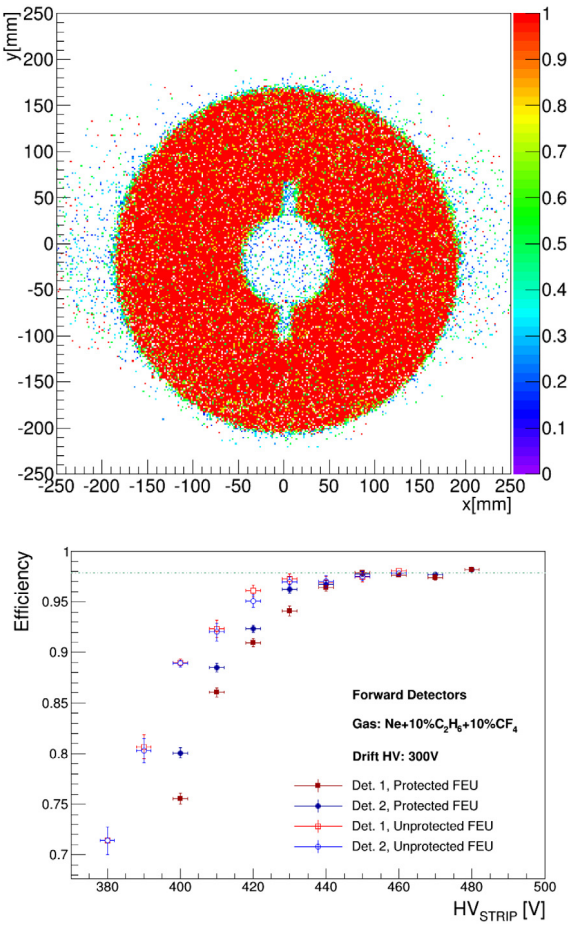


**Fig. 14.** Efficiency plateau (bottom) and 2D efficiency map (top) for a FMT disk.

On each trigger, the SSPs time stamp the event with the synchronous 125 MHz clock and assign it the event counter value. The 48-bit time stamp along with the 60-bit event identification (ID) is used for local event building. This process implies gathering from all FEUs the event data packets belonging to the same event (matching time stamps, and event IDs). Multi-event buffers, with a programmable number of events, are constructed in the external DDR2 memory. Upon the request from the crate controller SBC, the contents of the buffers are transferred to its memory over the VME64 backplane using the 2SST protocol. Transmission rates of ~200 Mbyte/s are routinely achieved.

The SBC executes the data collection and the run control tasks within the CODA software framework [18]. It also completes the data integrity checks performed in the SSP firmware, disentangles multi-event buffers, forms MVT events concatenating the FEU/SSP data with the corresponding TI data, and sends them to the CLAS12 Event Builder over a 10 GB/s Ethernet link.

The MVT readout electronics is continuously monitored by the CLAS12 detector monitoring system using the EPICS framework.

## 4. Detector performance

In order to calibrate the detectors and test their performance, a cosmic-ray test bench was designed and installed at Saclay early in the project. The goal of these tests was to determine the best operating conditions of the detectors and to compute their 2D efficiency maps using cosmic muons prior to their shipment to JLab.

The cosmic-ray test bench shown in Fig. 12 consists of a vertical stack of six detectors. Two scintillators are installed at the top and the bottom of the stack to provide the trigger. Four 50×50 $cm^2$ double-layer flat Micromegas were used as a tracker to provide the reference track of a cosmic ray. In the middle of the stack, empty trays receive the detectors to be characterized.

After alignment of the reference trackers and the detectors to be tested, the expected position of the particle in the test detector was provided by the reference trackers and compared with the measured signals, if any, in the test detector. If a cluster, i.e. a contiguous set of fired strips, matched the expected position within a millimeter, the test detector was considered to have seen the cosmic ray. The efficiency was then derived by repeating this test over a cosmic ray sample collected within a few hours. All MVT detectors were systematically characterized before shipment to JLab. These tests included a study of the efficiency as a function of the amplification voltage and a two-dimensional efficiency map, which required a cosmic ray sample collected over a day.

The results were found to be similar for all detectors. The efficiency plateau starts at about 500 V with a value between 98.5% and 99.5% at 510 V. It was shown that the plateau was slightly shifted to higher strip voltages when the drift plane was at higher voltage because the mesh loses electron transparency. The 2D-efficiency map was useful to look for any structural problems. All MVT detectors that were shipped to JLab had a uniform 2D-efficiency map. Examples of the efficiency plateau and the 2D efficiency map are shown in Figs. 13 and 14. Fig. 14 also shows the efficiency gained by removing the protection diodes before the Dream ASICs, not required with resistive Micromegas since sparks are quenched.

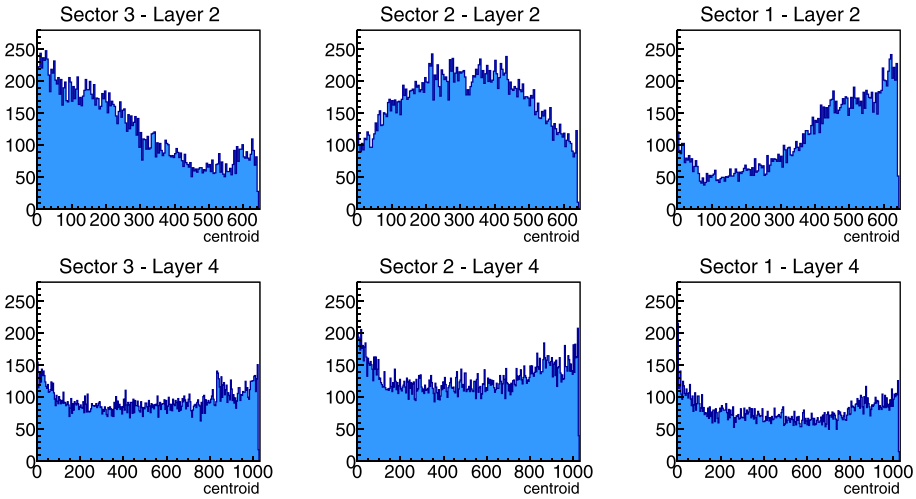


**Fig. 15.** Hit occupancies of a cosmic-ray run with the trigger delivered by the CTOF for layers 2 (Z tile) and 4 (C tile).

### 4.1. Commissioning

The Micromegas Vertex Tracker was delivered to JLab in June 2017. A team of 10 people assembled the MVT and integrated it with the SVT to form the final configuration of the CLAS12 Central Vertex Tracker. The MVT barrel was first commissioned with cosmic rays in the assembly room until mid-October 2017 and for the first two weeks after it was installed in Hall B. The final phase of the commissioning started in December 2017 with beam.

Before the start of data taking with beam, several cosmic ray runs were performed aimed at tuning and optimizing the integration of the data acquisition system and the slow controls (i.e. remote controls, interlocks, and monitoring) [18], and the gas delivery system. The online data monitoring system was developed to allow the inspection of raw quantities such as the hit maps, the pulse shape, and the timing of the signals. This system was tested and integrated into the standard CLAS12 online operation tools.

### 4.2. Cosmic ray data taking

Cosmic ray data with zero magnetic field were used not only for commissioning purposes, but also for the essential detector alignment. Given the absence of the solenoid magnetic field, the drift high voltages were set to about 400 V as the primary electrons do not experience the Lorentz-angle effect. The cosmic ray trigger for the Central Detector was provided by coincidences of CTOF signals in diametrically opposed scintillator bars. This CTOF trigger provides a quasi-uniform illumination along the BMT axis of the barrel with cosmic rays, not achievable in beam conditions because of the forward-peaked distribution due to the center-of-mass boost. The hit distribution on the Z tiles, instead, results from a convolution of the cosmic ray angular distribution with the trigger configuration, as shown in Fig. 15.

The distributions of cluster size for the three sectors (see Fig. 16) show, on average, larger clusters in Sectors 1 and 3 with respect to Sector 2. Indeed, since cosmic rays are mostly vertical, the projection of their path in the drift gap onto the strip surface is longer for Sectors 1 and 3 than for Sector 2.

A BMT stand-alone straight-track reconstruction algorithm based on least-squares minimization has been developed to reconstruct cosmic rays. A typical reconstructed event is shown in Fig. 17 using the CLAS12 event display package [19]. This tracking algorithm is also used to perform the alignment of the BMT tiles: the distance between the hit in a tile excluded from the tracking and the reference track provided by the other tiles is minimized by introducing rotations and translations.

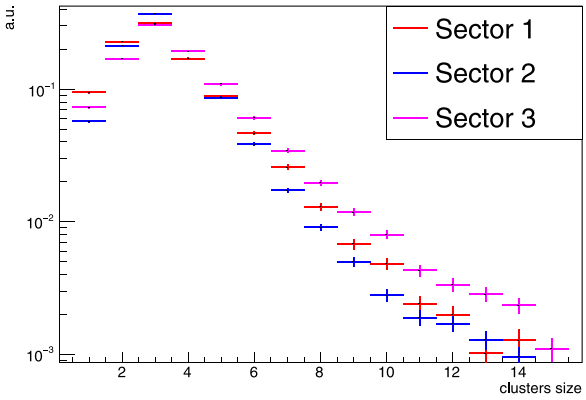


**Fig. 16.** Cluster size distributions, i.e. the number of strips fired in a tile by a cosmic ray, during cosmic ray data taking for the three sectors of the Z tiles.

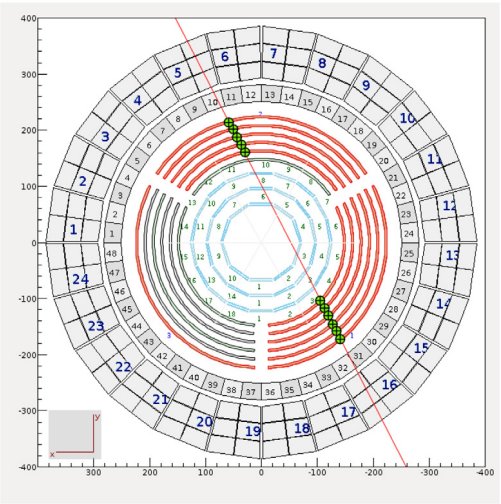

**Fig. 17.** Event display of a cosmic ray track reconstructed in the BMT detectors. The six tiles on the top are called Sector 2, the six on the bottom right are Sector 1 and the bottom left six tiles are the Sector 3.

Fig. 18 shows the distributions of track residuals, i.e. the distance of a hit with respect to the particle trajectory, for three Micromegas tiles

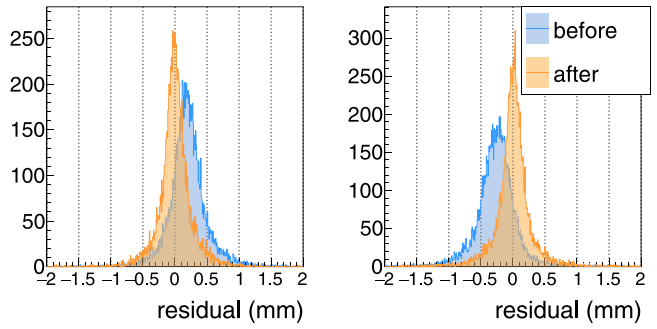


**Fig. 18.** Example of residuals for two BMT tiles with cosmic ray data before and after a preliminary alignment procedure obtained with a BMT stand-alone reconstruction.

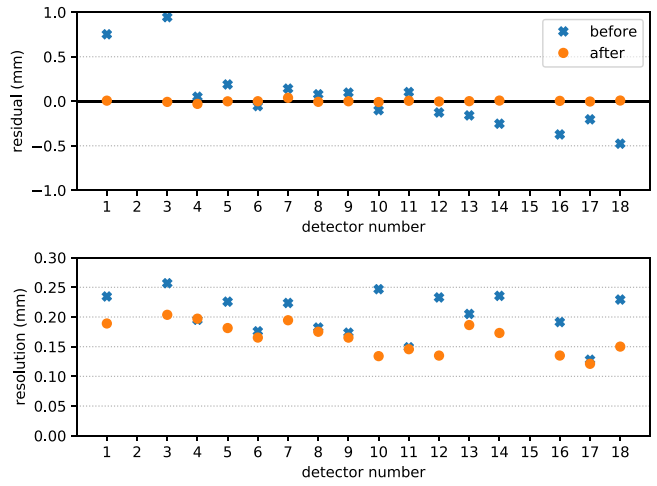


**Fig. 19.** Preliminary BMT residuals (top) and resolutions (bottom) with cosmic-ray data before and after an alignment procedure obtained with a BMT stand-alone reconstruction.

before and after alignment corrections. Fig. 19 shows the summary of the preliminary results for all BMT detectors: after the alignment procedure all residual distributions are centered around zero. Preliminary detector resolutions, defined as the standard deviations of Gaussian fits to the residual distributions, are improved and below 200 μm.

### 4.3. Data taking with beam

With the start of beam operations, the behavior of the detectors has been carefully monitored and the working parameters such as high voltage settings have been tuned. The working point for the strip high voltage has been studied by performing a scan with a 20 V step. Due to delays in the offline data reconstruction for a proper efficiency measurement, the cluster multiplicity per electron trigger was used as an alternative observable accessible online that can be used to exhibit a plateau. Indeed, as shown in Fig. 20, this observable was found to flatten out where the efficiency plateau was determined from the commissioning with cosmic rays. For the FMT, the plateau was found from 460 V to 490 V. Above 490 V, the cluster multiplicity and the current on the strips increases suddenly, potentially due to a Corona effect. It was decided to set 460 V as the nominal HV settings for the FMT, which allows safe operations for luminosities up to $10^{35}$ cm$^{-2}$ s$^{-1}$. The nominal HV setting was set to be 520 V for the BMT, although the plateau was not as clear as for the FMT.

Preliminary efficiencies for the Micromegas detectors were measured by performing tracking without the detector layer under study to determine for each track going through the studied detector layer, if a hit was found close to the expected intersection. The efficiency plateau

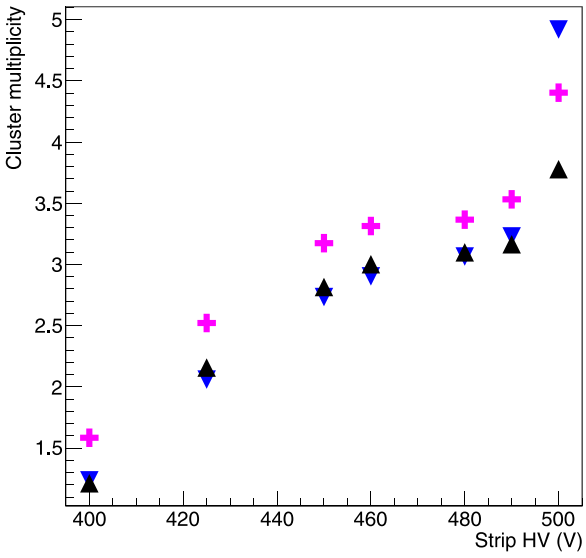


**Fig. 20.** Cluster multiplicity in 3 FMT disks as a function of HV on the strips.

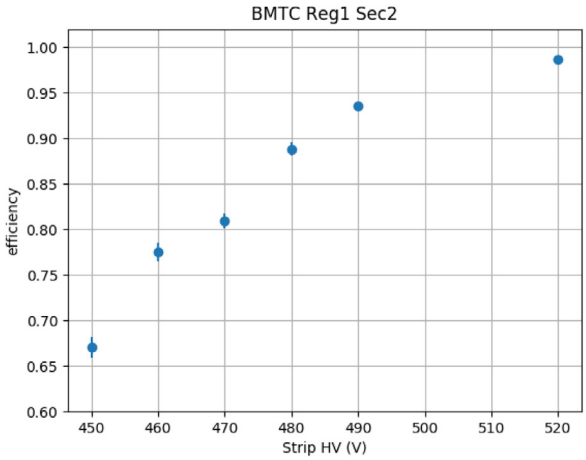


**Fig. 21.** Efficiency measurement as a function of the strip high voltage for one BMT tile in beam conditions.

was found to be at the same position as the plateau with the cluster multiplicities, thus validating the HV settings used. An example of the efficiency scan for one BMT tile is shown in Fig. 21.

Strip currents and detector occupancy have been measured during a beam intensity scan up to the instantaneous luminosity of about $10^{35}$ cm$^{-2}$ s$^{-1}$. Fig. 22 shows the correlation between the currents drawn by the BMT strips and the beam current. The slope coefficient resulting from a linear regression is 0.02 μA/nA. At the maximum beam current of 78 nA, two BMT tiles reached the safety threshold of 2 μA and they were automatically turned off. The detector occupancy shows as well a linear correlation with the beam current, reaching values of about 3.5% for the FMT disks and 2.5% for the BMT tiles at nominal luminosity, as shown in Fig. 23.

During the first year of operations with beam, CLAS12 took data at several electron beam energies (2.2, 6.4, 7.5, and 10.6 GeV) with a liquid-hydrogen target. An example of a rare event at 10.6 GeV with five tracks reconstructed in the CVT is shown in Fig. 24. At 2.2 GeV, the large elastic cross section and the trigger configuration allowed for the visualization of the recoil protons in the raw occupancies of the BMT-C tiles as seen in Fig. 25.

The largest data set has been collected at an electron beam energy of 10.6 GeV and at 50 nA intensity. Fig. 26 shows the distributions

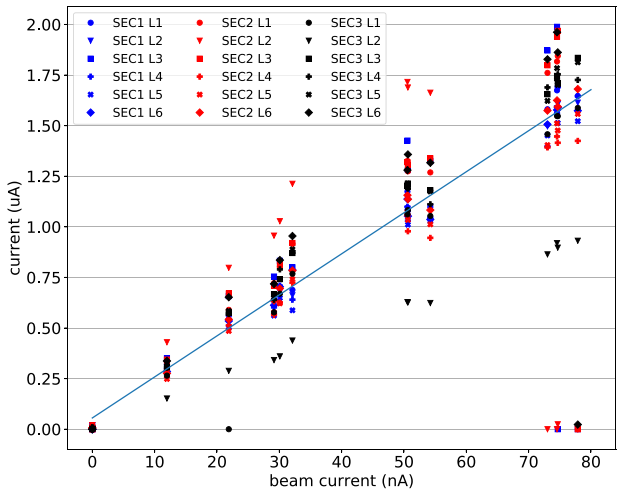


**Fig. 22.** Currents on the BMT strips as a function of beam current on a 5-cm-long liquid-hydrogen target. All detectors have similar currents. The nominal luminosity of $10^{35}$ cm$^{-2}$ s$^{-1}$ corresponds to 75 nA on target.

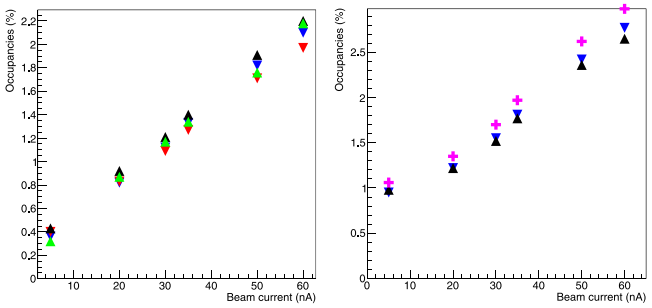


**Fig. 23.** Hit occupancy as a function of the beam current for 4 BMT layers (left) and 3 FMT disks (right).

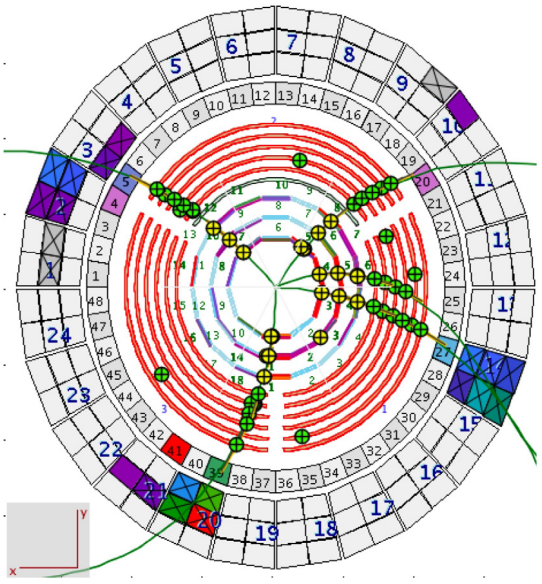

**Fig. 24.** Event display of a rare five-track event in the CVT.

of the number of clusters on all six BMT layers and their cluster size distribution. Although most of the events present a very low number of clusters with clusters of small size, the long tails are mainly due to knock-off electron "loopers" and beam-induced soft photons.

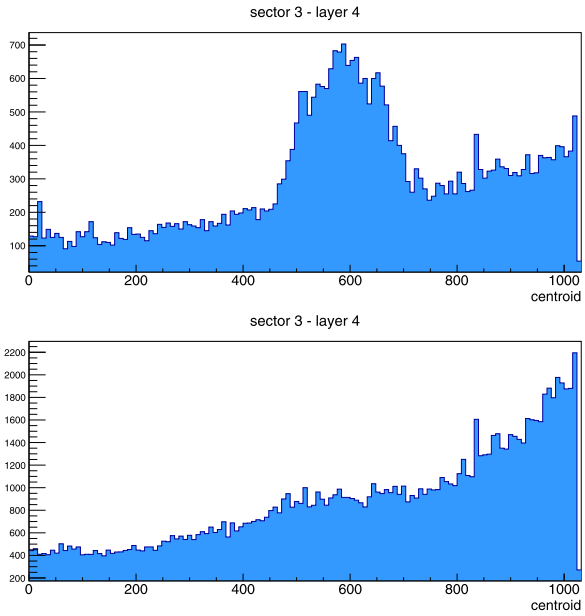


**Fig. 25.** Hit occupancy for C tiles at 2.2 GeV (top) and 10.6 GeV (bottom) in events triggered by an electron in the forward CLAS12 detectors. The elastic recoil protons are responsible for the large excess of events at 2.2 GeV between strip number 400 and 700. At 10.6 GeV, the elastic cross section is too small and no clear proton excess is visible.

Each MVT hit has an associated time stamp that can be used to compute the time difference of the signal with respect to the trigger. Consequently, a minimum time $T_{min}$ can be associated with each cluster as the minimum time of the hits in the cluster. Fig. 27 clearly shows that the clusters that have been associated with a reconstructed track have similar $T_{min}$ distributions over the six BMT layers, i.e. the clusters associated with a triggered physics event are strongly correlated in time. However, the $T_{min}$ distributions of background clusters, i.e. clusters that are not associated with reconstructed tracks, are uniform in time except for very low $T_{min}$ values. The excess of events at low $T_{min}$ for all layers is explained by the asymmetric shape of the pulse: since the tail of the pulse is much longer than the leading edge of the pulse, it is more likely to get out-of-time clusters prior to than after the trigger.

Special data taking runs with an empty target cell have been performed for calibration purposes, as well as low-luminosity runs with zero magnetic field for detector alignment studies. The stand-alone straight-track algorithm used for cosmic ray reconstruction has been adapted and extended to use SVT hits. Using preliminary alignment corrections for both the SVT and BMT, a zero-field empty-target run was reconstructed in SVT-stand-alone mode and CVT (i.e. SVT+BMT) mode. The preliminary results are shown in Fig. 28. The aluminum target walls are clearly visible in both reconstruction modes. There is a significant improvement from ~4.5 mm to 2.5 mm of the vertex position resolution ($1\sigma$) along the beam axis when the BMT information is used in the track reconstruction. Indeed the BMT-C tiles largely improve the polar angle of the particle with respect to the SVT-stand-alone mode. Concerning the azimuthal angle, the resolution of the BMT-Z tiles is not as good as that of the SVT modules since the strip pitch is larger and they are further away from the beam axis. Therefore the improvement of the resolution on the azimuthal angle of the track and related quantities like the vertex transverse coordinates is limited. On the other hand, the BMT-Z tiles provide an essential redundancy for tracks that cross a limited number of SVT layers.

## 5. Conclusions

In this paper, the CLAS12 Micromegas Vertex Tracker system is presented. The mechanical structure of the Forward and the Barrel

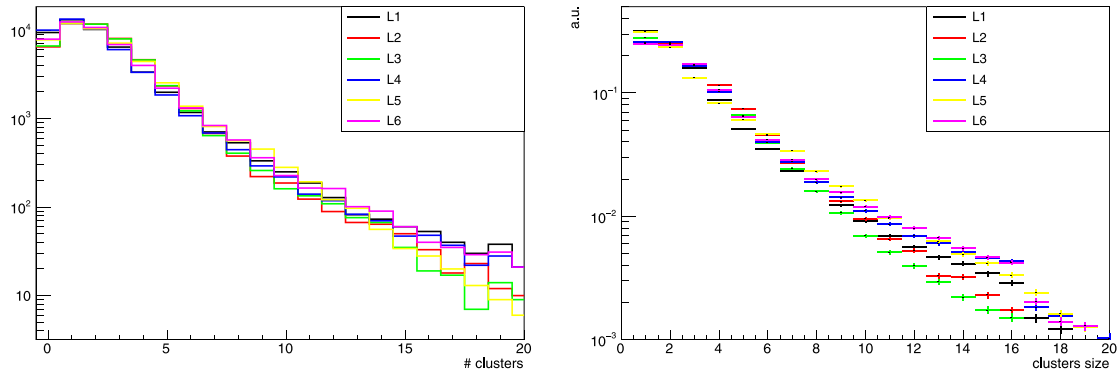


**Fig. 26.** (left) Number of clusters per event and (right) cluster size distribution in the BMT layers. The beam current was 50 nA.

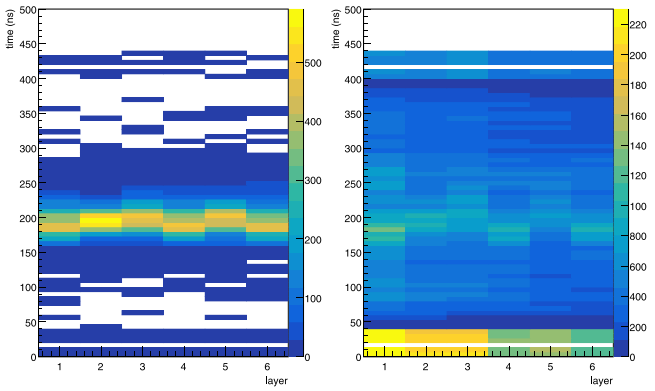


**Fig. 27.** (left) Time distribution in the six BMT layers for clusters associated with a track; (right) Time distribution for clusters not associated with a reconstructed track.

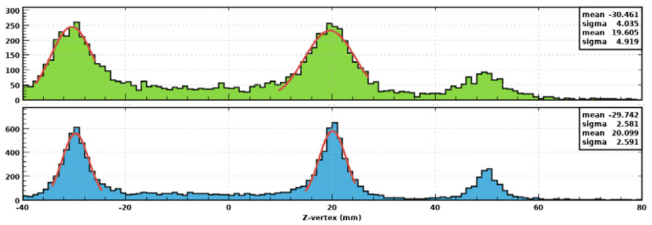


**Fig. 28.** Preliminary vertex position along the beam axis reconstructed with the SVT-stand-alone reconstruction (top-green distribution) and the CVT reconstruction (bottom-blue distribution) for an empty-target and no solenoid field. The target walls are located at −30 and 20 mm with gaseous hydrogen in-between. At 50 mm, the scattering chamber endcap is clearly visible. The improvement in the resolution from the SVT to the CVT reconstruction is mainly due to the BMT-C tiles.

Micromegas Trackers, the first curved detector of this size using the Micromegas technology, is described. The architecture and performance of the readout electronics are presented, including the DREAM ASIC, developed to achieve the performance required by the CLAS12 specifications. The Micromegas Vertex Tracker performance with cosmic rays is shown, as well as some preliminary results with beam data to demonstrate a significant improvement in the reconstruction in the central tracker.

## Acknowledgments

We are grateful to D. Abbott, S. Boiarinov, C. Cuevas, J. W. Gu, B. Moffit and A. Stepanyan from JLab for their continuous help at various phases of the project. We would like to thank the Hall B staff, the JLab Detector Support Group, and Y. Gotra for their support on the MVT project.

This material is based upon work supported by the U.S. Department of Energy, Office of Science, Office of Nuclear Physics under contract DE-AC05-06OR23177. This research was funded in part by the French Agence Nationale de la Recherche contract no. 37.

## References

[1] V.D. Burkert, et al., The CLAS12 spectrometer at Jefferson laboratory, Nucl. Instrum. Methods Phys. Res. A (2020) in this issue.
[2] M.A. Antonioli, et al., The CLAS12 silicon vertex tracker, Nucl. Instrum. Methods Phys. Res. A (2020) in this issue.
[3] M.D. Mestayer, The CLAS12 drift chamber system, Nucl. Instrum. Methods Phys. Res. A (2020) in this issue.
[4] S. Procureur, Simulation of micromegas detectors for the CLAS12 central tracker, 2007, CLAS-Note 2007-004.
[5] S. Aune, et al., Simulation of micromegas detectors for the CLAS12 central tracker, 2010, CLAS-Note 2010-003.
[6] D.S. Carman, et al., The CLAS12 central time-of-flight system, Nucl. Instrum. Methods Phys. Res. A (2020) in this issue.
[7] P. Chatagnon, et al., The CLAS12 central neutron detector, Nucl. Instrum. Methods Phys. Res. A (2020) in this issue.
[8] Y. Giomataris, P. Rebourgeard, J. Robert, G. Charpak, MICROMEGAS: A high-granularity position-sensitive gaseous detector for high particle-flux environments, Nucl. Instrum. Methods Phys. Res. A 376 (1) (1996) 29–35, URL http://www.sciencedirect.com/science/article/pii/0168900296001751.
[9] T. Alexopoulos, J. Burnens, R. de Oliveira, G. Glonti, O. Pizzirusso, V. Polychronakos, G. Sekhniaidze, G. Tsipolitis, J. Wotschack, A spark-resistant bulk-micromegas chamber for high-rate applications, Nucl. Instrum. Methods Phys. Res. A 640 (1) (2011) 110–118, http://dx.doi.org/10.1016/j.nima.2011.03.025, URL http://www.sciencedirect.com/science/article/pii/S0168900211005869.
[10] I. Giomataris, R. De Oliveira, S. Andriamonje, S. Aune, G. Charpak, P. Colas, G. Fanourakis, E. Ferrer, A. Giganon, P. Rebourgeard, P. Salin, Micromegas in a bulk, Nucl. Instrum. Methods Phys. Res. A 560 (2) (2006) 405–408, http://dx.doi.org/10.1016/j.nima.2005.12.222, URL http://www.sciencedirect.com/science/article/pii/S0168900205026501.
[11] M. Battaglieri, et al., The CLAS12 forward tagger, Nucl. Instrum. Methods Phys. Res. A (2020) in this issue.
[12] P. Konczykowski, S. Aune, J. Ball, M.E. Yakoubi, C. Lahonde-Hamdoun, O. Meunier, S. Procureur, F. Sabatié, S. Cazaux, E. Delagnes, S. Lhenoret, A. Mohamed, Measurements of the lorentz angle with a micromegas detector in high transverse magnetic fields, Nucl. Instrum. Methods Phys. Res. A 612 (2) (2010) 274–277, http://dx.doi.org/10.1016/j.nima.2009.10.105, URL http://www.sciencedirect.com/science/article/pii/S0168900209020567.
[13] S. Procureur, Micromegas: A tracking detector for high energy physics and beyond, 2015, Habilitation à Diriger des Recherches, IRFU-15-73, 10 decembre 2015.
[14] B. Raydo, et al., The CLAS12 trigger system, Nucl. Instrum. Methods Phys. Res. A (2020) in this issue.
[15] C. Flouzat, et al., Dream: a 64-channel front-end chip with analog trigger latency buffer for the micromegas tracker of the CLAS12 experiment, in: TWEPP 2014 Topical Workshop on Electronics for Particle Physics, Centre des Congrès - Aix en Provence, France, 2014.
[16] Analog Devices, AD9222: Octal, 12-Bit, 40/50/65 MSPS Serial LVDS 1.8 V A/D Converter, Datasheet, Rev. D.
[17] Xilinx, Virtex-6 family overview, 2012, DS150, v2.4.
[18] S. Boyarinov, et al., The CLAS12 data acquisition system, Nucl. Instrum. Methods Phys. Res. A (2020) in this issue.
[19] V. Ziegler, et al., CLAS12 event reconstruction, Nucl. Instrum. Methods Phys. Res. A (2020) in this issue.

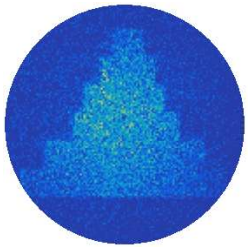

# *Muon tomography with Micromegas: Archaeology, nuclear safety and new developments for Geotechnics*

IOP Conf. Series: Journal of Physics: Conf. Series **1312** (2019) 012013 doi:10.1088/1742-6596/1312/1/012013

# Muon tomography with Micromegas: Archaeology, nuclear safety and new developments for Geotechnics.

**H. Gómez, D. Attié, D. Calvet, X. Coppolani, B. Gallois, M. Kebbiri, M. Lehuraux, P. Magnier, I. Mandjavidze, S. Procureur and M. Vandenbroucke**

Commissariat à l'Énergie Atomique et aux Énergies Alternatives (CEA), Centre de Saclay, IRFU, 91191 Gif-sur-Yvette, France

E-mail: hector.gomez@cea.fr

**Abstract.** Muon tomography, or muography, stands out as a non-invasive technique for the scanning of big objects' internal structure. It relies on the measurement of the direction changes or absorption of atmospheric muons when crossing the studied object. Proposed several decades ago, the performance achieved in particle detectors in the last years, specially in terms of stability, robustness and precision, has enlarged the possible applications of this technique. Bulk Micromegas represent a well-known technology suitable for the construction of muon telescopes based on these detectors. Thus autonomous and portable instruments have been conceived and constructed at Commissariat à l'Énergie Atomique et aux Énergies Alternatives (CEA), being able to perform muography measurements in-situ, next to the studied objects. At present, a new muon telescope concept is being developed at CEA, combining a Time Projection Chamber (TPC) readout by a 2D multiplexed bulk Micromegas. This new generation of detectors will enlarge the possible application fields of muography, being specially interesting for geotechnics.

## 1. Introduction

Muon tomography, or muography, was proposed as scanning method of big structures [1] soon after the discovery of muons produced at the Earth's atmosphere by cosmic rays [2, 3, 4]. Muons have the capability to pass through hundreds of metres or even kilometres suffering an attenuation or a trajectory deviation mainly related to the opacity of the traversed material, defined as the product of the crossed length by its mean density [5]. Two main methods arise for muography. First is the so-called transmission method [6, 7]. It relies on the well-known radiography concept, as it is used with X-rays in medicine. The attenuation of muons crossing the studied object depends on the opacity of the materials traversed by muons along their path before their detection. Based on this principle, a 2D mean density image can be obtained studying the directions of all detected muons after crossing the studied object. Furthermore, the combination of measurements done at different points would provide information to obtain a 3D image. The second one is the deviation method [8, 9]. It studies the muon direction changes when they traverse the scanned object, which are driven by the Coulomb multiple scattering. The deviation angle, as described by Moliere's theory [10], mainly depends on the opacity of the traversed object. Assuming that the direction change has been produced by a main diffusion process, the diffusion point can be deduced from the intersection of muon trajectories before and

after crossing the object, obtaining this diffusion point and its associated deviation angle hence the local opacity. Therefore a 3D density map can be obtained from all reconstructed events.

Being complementary, both muography techniques provide a non-invasive scanning method utilisable for big objects, with an application range from few metres to hundreds of meters depending on the used technique. While the deviation method is more sensitive to opacity variations, it can only be used for smaller objects with limited opacity, since it is necessary to place muon detectors upstream and downstream the studied object. On the other hand, transmission method requires longer measurement times, but it is capable to scan bigger objects.

During the last years the application fields of muon tomography have increased significantly. Nowadays there exist projects related to vulcanology [11, 12], archaeology [13], engineering [14], homeland security or nuclear safety applications. One of the main reasons for this enlargement is the improvement of the detectors used for the muon tracks reconstruction. At present several techniques provide instruments with good enough angular resolution, while keeping the required robustness, autonomy and portability to perform long measurements in varying environmental conditions. Among these techniques, the *Commissariat à l'Énergie Atomique et aux Énergies Alternatives* (CEA) group conceived a muon telescope based on the operation of bulk Micromegas detectors, which has allowed the group to perform different muography measurements and to work in several projects at present.

## 2. Micromegas-based muon telescopes

The main requirement for muography measurements is the precise reconstruction of the incident muons direction. The detectors used with this purpose must provide excellent angular and spatial resolution. Moreover, these detectors should be integrated in a detection system, commonly referred to as muon telescopes, which also have some requisites. Because of the type and location of the structures commonly scanned by muon tomography, measurements take place outdoors, exposed to environmental conditions and during long periods of time, often several months. This requires a telescope based on a robust technology besides its performance. Furthermore, the telescope should be preferably portable, autonomous and with a stable operation despite measurement conditions. The CEA group took Micromegas detectors [15] as basis to develop a muon telescope.

These telescopes mainly consist of several planes of Micromegas (usually 3 or 4) placed in parallel. When a muon crosses the telescope, the induced signals in the Micromegas are used to determine the muon interaction point in each of them. From these points the incoming muon trajectory can be reconstructed. Thus, the most important part of the telescope is the Micromegas readouts themselves. Nowadays, these gaseous detectors are largely used in nuclear and particle physics, representing a stable and robust technology offering an excellent performance. For these telescopes, bulk Micromegas [16] with an active surface of $50 \times 50$ cm$^2$ are used in an Argon-i$C_4H_{10}$-$CF_4$ (95-2-3) gas mixture at atmospheric pressure. The active surface is readout by 1037 strips (with 482 micrometres pitch) both in X and Y coordinates, *i.e.* 2074 channels must be registered to readout a single Micromegas. In order to simplify the signal acquisition system, adapting it to the telescope requirements, readout strips have been multiplexed following a genetic algorithm [17] which reduces the readout channels of each coordinate from 1037 to 61. Besides the multiplexing, the Micromegas are also equipped with a screen-printing resistive layer on top of the readout strips [18]. This allows a more stable operation since this layer protects from possible sparks. Moreover it also diffuses the charge distribution, which can improve the position of the muon interaction point and, consequently, the resolution of the telescope.

As mentioned, the rest of the telescope components have been conceived and made to optimize the portability and autonomy of the instrument. Light materials as aluminium have been used for the telescope structure while the DAQ components, including the high-voltage module,

have been miniaturized reducing their power consumption. The whole instrument is controlled and monitored by a Hummingboard nano-PC running GNU/Linux, which also performs the events online reconstruction and manages the data transfer via a 3G connection. With all these features, the overall consumption of a telescope composed by 4 planes of 50 $\times$ 50 cm$^2$ active surface is around 35 W, being possible to supply them by batteries or solar panels. With this configuration, a position resolution of 400 micrometers can be achieved, leading to an angular resolution between 0.8 to 4 mrad depending on the distance between the Micromegas planes.

### *2.1. Applications and results*

The CEA group has already performed different muography measurements using these instruments. Mainly using transmission methods, they have covered some of the potential applications of muon tomography. Among them, three projects could be highlighted because of their interest and their importance on the development of muography activities at CEA.

First of them is the WatTo experiment [19]. It scanned by muography a water-tower deposit located at CEA-Saclay campus. It entailed the proof-of-concept of Micromegas-based telescopes built at CEA since it was the first muography measurement done outdoors, next to the scanned object. The good behaviour of the telescope and all the ancillary systems during the measurement period allowed the obtention of an image of the water deposit structure. Moreover it was also possible to determine a clear anti-correlation between the water level in the deposit and the detected muon flux. This showed the capabilities of muography as a continuous monitoring technique.

Most relevant results obtained by CEA Micromegas-based telescopes come from the ScanPyramids project [20], which scanned the Khufu's pyramid in Egypt by muography using three different detection techniques. Different telescopes were installed inside and outside the pyramid looking for its internal structure. Micromegas telescopes were installed at different positions outside the pyramid to complement the measurements of other detectors placed inside. These measurements, carried out over several months in different data taking campaigns, confirmed the good behaviour of the instruments in terms of autonomy, robustness and stability. Moreover, the combination of all the measurements, including those made with Micromegas telescopes, pointed out to the existence of an unexplored cavity over the Grand Gallery of the pyramid [21]. New measurements are currently ongoing with the Micromegas telescopes inside the pyramid, optimizing the detectors position with respect to the void, in order to better determine its size, position and orientation.

The third project is the so-called G2G3. In an internal collaboration between CEA groups, it aims to scan by muography two nuclear reactors (G2 and G3) dated form the 60s and located at the CEA site of Marcoule (south of France). Two goals are pursued in this project: first, to cross-check the reactors structure with the corresponding plans, and second, to explore the reactors internal structure and their parts, specially those made of concrete. If measurements sensitivity is good enough, fissures in the concrete as well as other damages in different parts could be identified. The project is divided in two main phases. The first one is devoted to the performance of feasibility studies by Monte Carlo simulations to explore muography capabilities for this application. In a further phase, on-site measurements will be carried out to compare with previous simulations. A first phase of this project revealed the necessity to perform a simulation framework devoted for muography studies and represented the first application of a simulation framework performed at CEA with this purpose.

Based on Geant4 [22] and C++/ROOT [23] routines, this simulation framework has been conceived in a modular and versatile way. It optimizes the computing time but also makes the framework adaptable to any muography application as well as to any muon telescope. Mainly, the first module is devoted to the simulations of the propagation of muons through the studied object while the second generates muons events at the telescope corresponding to those which

have traversed the studied structure. Finally, the third module generates the corresponding signal from the events registered in the previous module. A more detailed description of the framework and its main features can be found at [24]. For the case of G2G3 project one of the most important aspect is that the whole geometry of the nuclear reactor have been transformed from the 3D CAD model into GDML format for its further implementation on the first module of the framework. This accurate definition of the studied object geometry will provide a more precise comparison between experimental data and simulations. Results of preliminary simulations of this project can be found at [24].

## 3. 3D tomography using TPCs

Going further about other muography applications would require the development of new muon telescope concepts. They should keep the features of the current designs trying to overcome some of their limitations. With this aim a new muon telescope concept has been conceived at CEA. It is based on the operation of a gaseous Time Projection Chamber (TPC) with a small-diameter cylindrical shape. As TPC readout, a 2D pixelized Micromegas will be used. The main improvement of this detector with respect to current telescopes is its acceptance, being possible to cover almost $2\pi$ sr solid angle with a smaller single detector. The reduced diameter of the TPC, of around 15 cm, makes possible to fit these detectors at the bottom of conventional boreholes to scan the surroundings by muography or in any other reduced-space location. Furthermore, installing a network of TPCs at several measurement points would provide enough information to obtain a 3D image. Thus this TPC-based telescope has potential applications in mining exploration or geothermal sounding when installed in a borehole as well as in civil engineering or even monitoring structures as buildings, dykes or bridges when operating a detector network.

The principle of a muography measurement using this detector is equivalent to that performed with the telescopes described in Section 2. In this case the track direction is fully determined from the information provided by the TPC. From the registered directions the angular distribution of the detected muons can be obtained trying to identify any anomaly (excess or deficiency of muons) for a given direction, pointing to the identification of an internal structure. A preliminary simulation to illustrate this principle has been done using the dedicated framework developed by CEA and presented in Section 2.1. Figure 1(a) shows the simulated case. A TPC of 15 cm diameter and 40 cm height is defined at the bottom of 30 m depth borehole dug in standard rock. Some cavities with volumes from 18 to 90 $m^3$ where defined and filled with air or water. 20 millions of muons where simulated following the parametrization proposed by Shukla [25]. As result the angular distribution of the detected muons can be obtained as showed in figure 1(b). If this distribution is projected to 1 dimension, it should follow the distribution given by the muon parametrization. Any anomaly identified is associated to the presence of internal structures as showed in figure 1(c).

The main component of this telescope is the 2D pixelized bulk Micromegas detector. It covers a circular active surface of 12 cm diameter by 1344 hexagonal pads. These pads are multiplexed grouping 7 of them in a single channel. To carry out this multiplexing, a 12 layers PCB with an overall thickness of 3.2 mm has been designed. This leads to 192 channels which are divided into 3 symmetric sectors of 64 channels each, being possible to readout them by a single ASIC. Figure 2 shows the layout of the hexagonal pads divided in 3 sectors, as well as the routing for the pads multiplexing. This routing has been designed using in 2D a similar technique as the presented in [17]. It respects different contiguity restrictions to avoid ambiguities in the muon track reconstruction process.

First tests of Micromegas detectors have been performed in a test bench. Detectors have been operated at atmospheric pressure with Argon-i$C_4H_{10}$-$CF_4$ (95-2-3) gas mixture with 3 cm drift length but without any field cage. A photograph of the experimental set-up is presented in figure 3. Voltage at the cathode has been fixed to -1000 V, while the voltage at the mesh varied from

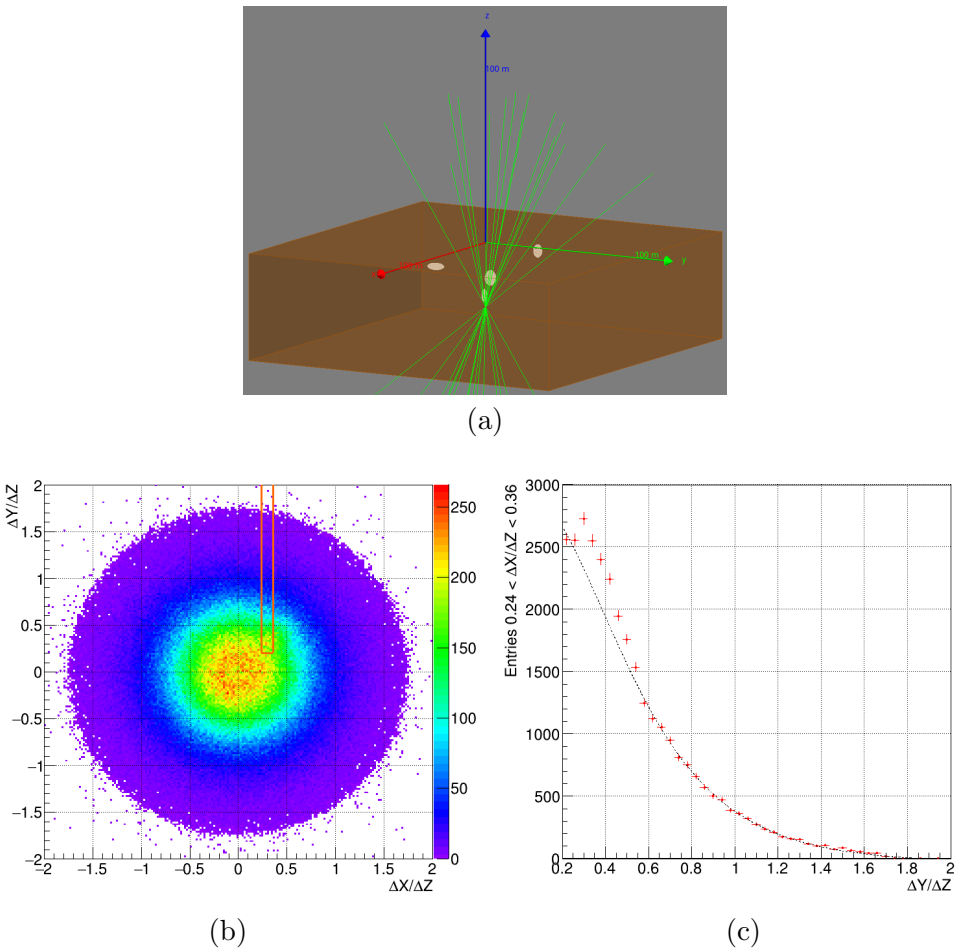


(a)

(b) (c)

**Figure 1.** Picture of the simulated case of the tomography using a TPC (a). The detector is located at the bottom of a borehole dug in standard rock with the presence of some cavities filled of air or water. Simulations results are presented in the plots at the bottom. (b) shows the angular distributions of the detected muons from a 20 millions simulated muons following the parametrization proposed by Shukla [25]. (c) presents the 1D projection of the angular distribution in the range $0.24 < \Delta X/\Delta Z < 0.36$ and $\Delta Y/\Delta Z > 0.2$, marked in orange in plot (b). An excess of muons with respect to the overall trend is identifiable at $\Delta Y/\Delta Z \sim 0.4$, corresponding to one of the cavities defined.

-380 V to -400 V, keeping the Micromegas pads grounded. Pads signals have been registered using the same DAQ as for Micromegas telescopes described in Section 2. Figure 4 presents some examples of events registered with this test bench. For these examples raw signals are showed (i.e. any treatment as pedestal subtraction have been applied). Pulses over an arbitrary threshold are considered. Even if several pixels are triggered because of the multiplexing, in both presented cases a single long track is identifiable. The third component of the track, this corresponding to the drift field direction, can be reconstructed analysing the time difference of the registered pulses. Even with a preliminary analysis, these tests already demonstrated the capabilities of multiplexed Micromegas to reconstruct muon tracks.

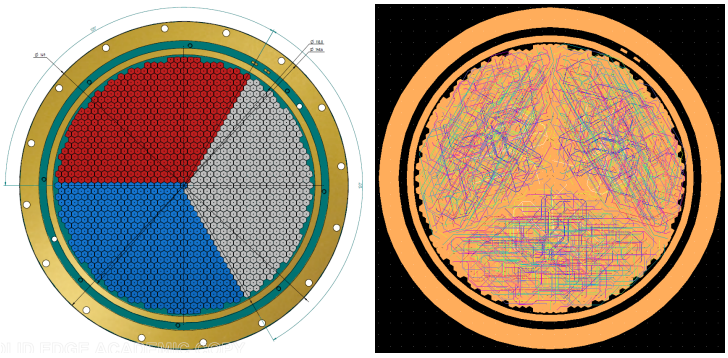

(a) (b)

**Figure 2.** Design of the hexagonal pads of the 2D multiplexed Micromegas of the cylindrical TPC divided in 3 sectors (a). Layout of the routing of each of the pads along the 12 layers of the PCB to multiplex the 1344 pads into 192 readout channels divided into 3 sectors. Lines of the same colour means that they are routed to the same channel (b).

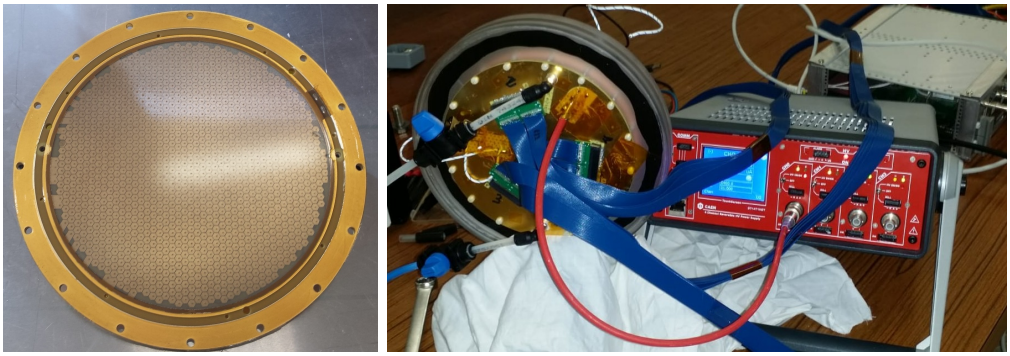

(a) (b)

**Figure 3.** Photograph of a 2D multiplexed Micromegas before its installation on the test bench (a). General photograph of the Micromegas test bench (b). Rear part of the Micromegas is visible with the readout and high voltage cables as well as the gas input and output tubes.

## 4. Outlook and conclusions

Nowadays muon tomography, or muography, stands out as a method for the scanning of the internal structure of big objects. Some of its main advantages are that it is non-invasive, versatile and safe, being possible to perform measurements far from the studied objects. The increase of the number of its potential applications is related to the improvement of the detectors used, specially in terms of spatial and angular resolution, stability and robustness. Among them, Micromegas-based telescopes, as those conceived and developed at CEA, have revealed their capabilities and have been successfully used in several projects. However, new potential applications of muography requires the development of new instruments capable to overcome some of the limitations of the current ones. CEA group proposes a new muon telescope concept based on a gaseous TPC readout by a 2D multiplexed Micromegas. As main advantages, these instruments provide a bigger acceptance with a single telescope, smaller than current versions. Furthermore the installation of a network of these TPCs would provide information to make a 3D reconstruction of the scanned object. These features make these detectors specially interesting for mining or civil engineering.

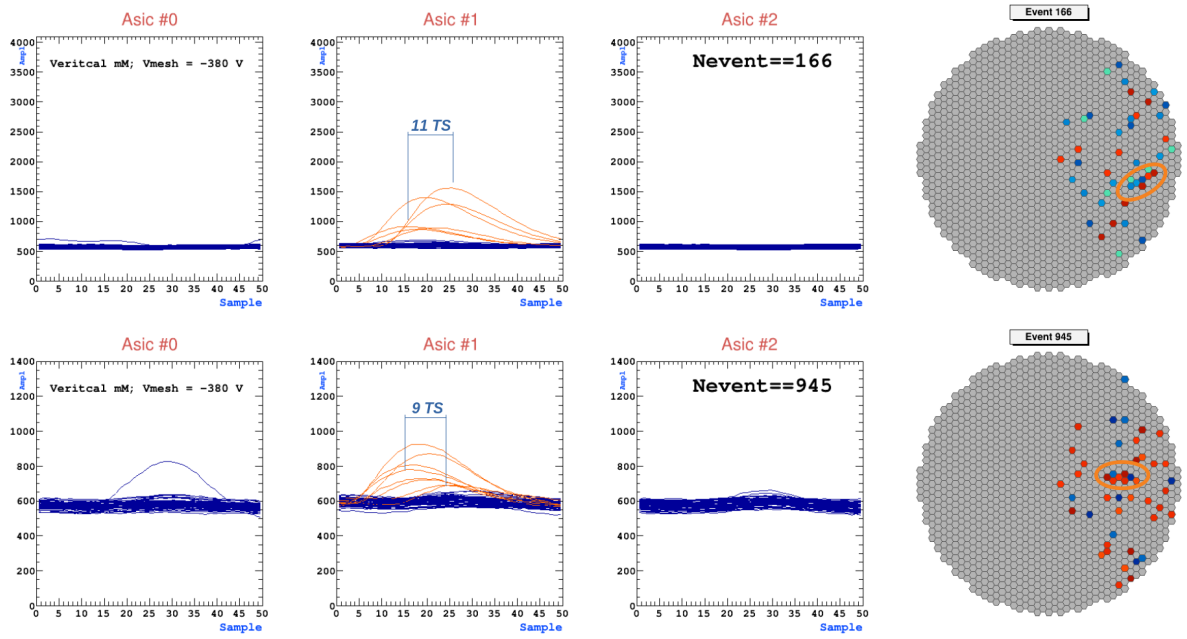


**Figure 4.** Two examples of muons registered in the Micromegas test bench. The three plots on the left shows the registered signals in each ASIC, corresponding to each sector of the Micromegas. Signals in orange are those over an arbitrary threshold. Time difference between pulses provides information about the track direction in the coordinate perpendicular to the Micromegas plane. Plots on the right show the pads corresponding to the signals over threshold. Due to the multiplexing the triggered pads are 7 times the triggered pulses. However a single continue track is identifiable (circled in orange) corresponding to the muon track projection on the Micromegas plane.

One of the most important components of these telescopes is the 2D multiplexed Micromegas. As first step, a preliminary checking of the performance of these detectors in a devoted test bench has been done. At this stage, next steps will consist on the construction of a first prototype to be operated at the laboratory. It will include all the remaining detector components, mainly the whole drift length (∼40 cm) with the corresponding field cage, as well as all the ancillary systems as DAQ or gas system. Future measurements carried out with this prototype will represent the proof of concept of this new telescope. In a further step, and based on the outcome of the first prototype, a final design and construction of a TPC capable to perform on-site measurements will be carried out.

In parallel, feasibility studies by Monte Carlo simulations will continue to evaluate the capabilities of these detectors depending on the size of the structures to scan, the depth where the TPCs will be installed or the measurement time. They will be performed using the framework developed for muon tomography studies mentioned in Section 2.1. These studies will consider measurements with a single TPC as well as with a detector network. The latter case will provide enough information to perform 3D tomography measurements. Moreover, simulations will also be used to develop the analysis tools, mainly focused on track identification and reconstruction algorithms.

## References

[1] George E P 1955 *Commonwealth Engineer* **455**

[2] Neddermeyer S H and Anderson C D 1937 *Phys. Rev.* **51** 884
[3] Neddermeyer S H and Anderson C D 1938 *Phys. Rev.* **54** 88
[4] Auger P 1941 *PUF, Paris* **136**
[5] Nagamine K 2003 *Cambridge University Press, Cambridge*
[6] Lesparre N et al 2010 *Geophysical Journal International* **183** 1348
[7] Marteau J et al 2012 *Nucl. Instrum. Meth. A* **695** 23
[8] Borozdin K N et al 2003 *Nature* **422** 277
[9] Procureur S 2018 *Nucl. Instrum. Meth. A* **878** 169
[10] Bethe H A 1953 *Physical Review* **89** 1256
[11] Oláh L 2018 *Scientific Reports* **8** 3207
[12] Ambrosino F et al 2015 *J. Geophys. Res. Solid Earth* **120** 7290
[13] Saracino G et al 2017 *Scientific Reports* **7** 1181
[14] Guardincerri E et al 2017 *Pure and Applied Geophysics* **174** 2133
[15] Giomataris Y et al 1996 *Nucl. Instrum. Meth. A* **376** 29
[16] Giomataris Y et al 2006 *Nucl. Instrum. Meth. A* **506** 405
[17] Procureur S et al 2013 *Nucl. Instrum. Meth. A* **729** 888
[18] Alexopoulos T et al 2011 *Nucl. Instrum. Meth. A* **640** 110
[19] Bouteille S et al 2016 *Nucl. Instrum. Meth. A* **834** 223
[20] ScanPyramids project, `www.scanpyramids.org`
[21] Morishima K et al 2017 *Nature* **552** 386
[22] Agostinelli S et al (GEANT4 collaboration) 2003 *Nucl. Instrum. Meth. A* **506** 250,
Agostinelli S et al (GEANT4 collaboration) 2006 *IEEE Trans. Nucl. Sci.* **53** 270,
Allison J et al 2016 *Nucl. Instrum. Meth. A* **835** 186
[23] Brun R and Rademakers F 1997 *Nucl. Instrum. Meth. A* **389** 81
Antcheva I et al 2009 *Comp. Phys. Comm.* **12** 1499
[24] Gómez H 2018 `https://doi.org/10.1016/j.nima.2018.10.011`
[25] Shukla P and Sankrith S 2016 Energy and angular distributions of atmospheric muons at the Earth Preprint hep-ph/1606.06907

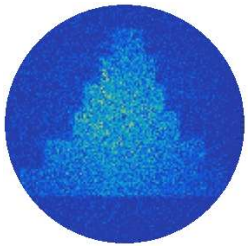

# Bibliography


[1] C.G. Montgomery and D.D. Montgomery. Geiger-mueller counters. *Journal of the Franklin Institute*, 231(5):447 – 467, 1941. https://doi.org/10.1016/S0016-0032(41)90498-2. – Cited pages vii & 13.

[2] M.S. Dixit and A. Rankin. Simulating the charge dispersion phenomena in micro pattern gas detectors with a resistive anode. *Nuclear Instruments and Methods in Physics Research Section A: Accelerators, Spectrometers, Detectors and Associated Equipment*, 566(2):281–285, 2006. https://doi.org/10.1016/j.nima.2006.06.050. – Cited pages vii, 20 & 21.

[3] Hansjörg Fischle, Joachim Heintze, and Bernhard Schmidt. Experimental determination of ionization cluster size distributions in counting gases. *Nuclear Instruments and Methods in Physics Research Section A: Accelerators, Spectrometers, Detectors and Associated Equipment*, 301(2):202–214, 1991. https://doi.org/10.1016/0168-9002(91)90460-8. – Cited pages vii, 25 & 26.

[4] What is x-ray attenuation definition. https://www.radiation-dosimetry.org/what-is-x-ray-attenuation-definition/. – Cited pages vii & 31.

[5] Xcom: Photon cross sections database. https://physics.nist.gov/PhysRefData/Xcom/html/xcom1.html. https://doi.org/10.18434/T48G6X. – Cited pages vii & 31.

[6] Ángel Yanguas-Gil, José Cotrino, and Luís L Alves. An update of argon inelastic cross sections for plasma discharges. *Journal of Physics D: Applied Physics*, 38(10):1588–1598, may 2005. https://doi.org/10.1088/0022-3727/38/10/014. – Cited pages vii & 34.

[7] Magboltz - transport of electrons in gas mixtures. https://magboltz.web.cern.ch/magboltz/. – Cited pages viii, 33 & 35.

[8] Hamid Mounir, Mustapha Haddad, and Seddik Bri. Micromegas performance based in argonisobutane and argon-demethyl-ether. *European Scientific Journal, ESJ*, 9(10), Jan. 2014. https://doi.org/10.19044/esj.2013.v9n10p\%25p. – Cited pages viii & 38.

[9] Luigi Rolandi, Werner Riegler, and Walter Blum. *Particle Detection with Drift Chambers - 2nd Edition*. Springer, 2008. https://doi.org/10.1007/978-3-540-76684-1. – Cited pages ix, 13, 14 & 74.

[10] A G Drutskoy. Physics at ILC. *Journal of Physics: Conference Series*, 675(2):022019, feb 2016. https://doi.org/10.1088/1742-6596/675/2/022019. – Cited pages ix, 82 & 83.

[11] H. Li, R. Pöschl, and F. Richard. Hz recoil mass and cross section analysis in ild, 2012. https://arxiv.org/abs/1202.1439v1. – Cited pages ix & 83.

[12] Maurizio Spurio. *Particles and Astrophysics*. Astronomy and Astrophysics Library. Springer, 2015. https://doi.org/10.1007/978-3-319-08051-2. – Cited pages xii & 129.

[13] H. Zhang and M. Böttcher. X-Ray and Gamma-Ray Polarization in Leptonic and Hadronic Jet Models of Blazars. *The Astrophysical Journal*, 774(1):18, September 2013. https://doi.org/10.1088/0004-637X/774/1/18. – Cited pages xii & 129.

[14] Haruo Miyadera and Christopher L. Morris. Muon scattering tomography: review. *Appl. Opt.*, 61(6):C154–C161, Feb 2022. https://doi.org:10.1364/AO.445806. – Cited pages xii & 142.

[15] Simon Bouteille. *Développement et applications de détecteurs gazeux à micro-pistes pour la tomographie muonique*. PhD thesis, 2017. Thèse de doctorat dirigée par Procureur, Sébastien Physique des particules Université Paris-Saclay (ComUE) 2017. https://tel.archives-ouvertes.fr/tel-01759508. – Cited pages xiii & 150.

[16] Alfred Tang, Glenn Horton-Smith, Vitaly A. Kudryavtsev, and Alessandra Tonazzo. Muon simulations for super-kamiokande, kamland, and chooz. *Phys. Rev. D*, 74:053007, Sep 2006. https://doi.org/10.1103/PhysRevD.74.053007. – Cited pages xiii, 163 & 164.

[17] D. Reyna. A simple parameterization of the cosmic-ray muon momentum spectra at the surface as a function of zenith angle, 2006. https://doi.org/10.48550/ARXIV.HEP-PH/0604145. – Cited pages xiii, 163 & 164.

[18] S. Matsuno, F. Kajino, Y. Kawashima, T. Kitamura, K. Mitsui, Y. Muraki, Y. Ohashi, A. Okada, T. Suda, Y. Minorikawa, K. Kobayakawa, Y. Kamiya, I. Nakamura, and T. Takahashi. Cosmic-ray muon spectrum up to 20 tev at 89° zenith angle. *Phys. Rev. D*, 29:1–23, Jan 1984. https://doi.org/10.1103/PhysRevD.29.1. – Cited pages xiii, 163 & 164.

[19] L. N. Bogdanova, M. G. Gavrilov, V. N. Kornoukhov, and A. S. Starostin. Cosmic muon flux at shallow depths underground. *Physics of Atomic Nuclei*, 69(8):1293–1298, aug 2006. https://doi.org/10.1134/s1063778806080047. – Cited pages xiii, 163 & 164.

[20] Mengyun Guan, Ming-Chung Chu, Jun Cao, Kam-Biu Luk, and Changgen Yang. A parametrization of the cosmic-ray muon flux at sea-level, 2015. https://doi.org/10.48550/ARXIV.1509.06176. – Cited pages xiii, 163 & 164.

[21] Prashant Shukla and Sundaresh Sankrith. Energy and angular distributions of atmospheric muons at the earth, 2016. https://doi.org/10.48550/ARXIV.1606.06907. – Cited pages xiii, 163 & 164.

[22] Calculation of radiation length in materials. 2010. https://cds.cern.ch/record/1279627/files/PH-EP-Tech-Note-2010-013.pdf. – Cited pages xv, 29 & 30.

[23] P. A. Zyla et al. Review of Particle Physics. *PTEP*, 2020(8):083C01, 2020. https://doi.org/10.1093/ptep/ptaa104. – Cited pages xv & 34.

[24] H. J. Hilke. Time projection chambers. *Reports on Progress in Physics*, 73(11):116201, oct 2010. https://doi.org/10.1088/0034-4885/73/11/116201. – Cited pages xv, 70 & 71.

[25] Peter J. Mohr, David B. Newell, and Barry N. Taylor. Codata recommended values of the fundamental physical constants: 2014. *J. Phys. Chem. Ref. Data*, 45:043102, Nov 2016. https://doi.org/10.1063/1.4954402. – Cited page xix.

[26] D. Attié. Tpc review. *Nuclear Instruments and Methods in Physics Research Section A: Accelerators, Spectrometers, Detectors and Associated Equipment*, 598(1):89–93, 2009. Instrumentation for Collding Beam Physics. https://doi.org/10.1016/j.nima.2008.08.114. – Cited page 4.

[27] D. Attié, M. Campbell, M. Chefdeville, P. Colas, E. Delagnes, Y. Giomataris, H. van der Graaf, X. Llopart, J. Timmermans, and J. Visschers. Gas pixel detector for x-ray observation. *Nuclear Instruments and Methods in Physics Research Section A: Accelerators, Spectrometers, Detectors and Associated Equipment*, 610(1):178–182, 2009. New Developments In Photodetection NDIP08. https://doi.org/10.1016/j.nima.2009.05.173. – Cited pages 4 & 137.

[28] D Attié. Beam tests of micromegas LC-TPC large prototype. *Journal of Instrumentation*, 6(01):C01007–C01007, jan 2011. https://doi.org/10.1088/1748-0221/6/01/c01007. – Cited page 4.

[29] A. Acker, D. Attié, S. Aune, J. Ball, P. Baron, Q. Bertrand, D. Besin, T. Bey, F. Bossù, R. Boudouin, M. Boyer, G. Christiaens, P. Contrepois, M. Defurne, E. Delagnes, M. Garçon, F. Georges, J. Giraud, R. Granelli, N. Grouas, C. Lahonde-Hamdoun, T. Lerch, I. Mandjavidze, O. Meunier, Y. Moudden, S. Procureur, M. Riallot, F. Sabatié, M. Vandenbroucke, and E. Virique. The clas12 micromegas vertex tracker. *Nuclear Instruments and Methods in Physics Research Section A: Accelerators, Spectrometers, Detectors and Associated Equipment*, 957:163423, 2020. https://doi.org/10.1016/j.nima.2020.163423. – Cited pages 4, 111 & 151.

[30] J. J. Thomson M.A. F.R.S. Xl. cathode rays. *The London, Edinburgh, and Dublin Philosophical Magazine and Journal of Science*, 44(269):293–316, 1897. https://doi.org/10.1080/14786449708621070. – Cited page 7.

[31] Ernest Rutherford and Hans Geiger. An electrical method of counting the number of $\alpha$-particles from radio-active substances. *Proceedings of the Royal Society of London. Series A, Containing Papers of a Mathematical and Physical Character*, 81(546):141–161, 1908. https://doi.org/10.1098/rspa.1908.0065. – Cited pages 11 & 12.

[32] Hans Geiger and Walthe Müller. Das elektronenzälrohr. *Physikalische Zeitschrift*, 29:839–841, 1928. – Cited page 12.

[33] S. Ramo. Currents induced by electron motion. *Proceedings of the IRE*, 27(9):584–585, 1939. – Cited page 12.

[34] W. Shockley. Currents to conductors induced by a moving point charge. *Journal of Applied Physics*, 9(10):635–636, 1938. https://doi.org/10.1063/1.1710367. – Cited page 12.

[35] J. Warren Keuffel. Parallel-plate counters. *Review of Scientific Instruments*, 20(3):202–208, 1949. https://doi.org/10.1063/1.1741489. – Cited page 12.

[36] G.D. Alkhazov. Mean value and variance of gas amplification in proportional counters. *Nuclear Instruments and Methods*, 75(1):161 – 162, 1969. https://doi.org/10.1016/0029-554X(69)90671-5. – Cited page 12.

[37] G.D. Alkhazov. Statistics of electron avalanches and ultimate resolution of proportional counters. *Nuclear Instruments and Methods*, 89:155–165, 1970. https://doi.org/10.1016/0029-554X(70)90818-9. – Cited pages 12 & 60.

[38] G. Charpak, R. Bouclier, T. Bressani, J. Favier, and Č. Zupančič. The use of multiwire proportional counters to select and localize charged particles. *Nuclear Instruments and Methods*, 62(3):262 – 268, 1968. https://doi.org/10.1016/0029-554X(68)90371-6. – Cited page 12.

[39] CHARPAK, G. La détection des particules au moyen des décharges dans les gaz. *J. Phys. Colloques*, 30:C2–86–C2–96, 1969. https://doi.org/10.1051/jphyscol:1969213. – Cited page 13.

[40] J. Saudinos, J.-C. Duchazeaubeneix, C. Laspalles, and R. Chaminade. Localisation de particules par computeur à migration. *Nuclear Instruments and Methods*, 111(1):77 – 81, 1973. https://doi.org/10.1016/0029-554X(73)90099-2. – Cited page 13.

[41] A.H. Walenta. A system of large multiwire driftchambers. *Nuclear Instruments and Methods*, 111(3):467 – 475, 1973. https://doi.org/10.1016/0029-554X(73)90204-8. – Cited page 13.

[42] A. Breskin, G. Charpak, F. Sauli, M. Atkinson, and G. Schultz. Recent observations and measurements with high-accuracy drift chambers. *Nuclear Instruments and Methods*, 124(1):189 – 214, 1975. https://doi.org/10.1016/0029-554X(75)90403-6. – Cited page 13.

[43] R. Hammarström, O. Runolfsson, and M. Uldry. Multitube proportional chambers for high counting rates. *Nuclear Instruments and Methods*, 176(1):181 – 187, 1980. https://doi.org/10.1016/0029-554X(80)90700-4. – Cited page 14.

[44] R. Santonico and R. Cardarelli. Development of Resistive Plate Counters. *Nucl. Instrum. Meth.*, 187:377–380, 1981. https://doi.org/10.1016/0029-554X(81)90363-3. – Cited page 14.

[45] R. Santonico, R. Cardarelli, A. Di Biagio, and A. Lucci. Progress in Resistive Plate Counters. *Nucl. Instrum. Meth. A*, 263:20–25, 1988. https://doi.org/10.1016/0168-9002(88)91011-X. – Cited page 14.

[46] Fabio Sauli. *Principles of operation of multiwire proportional and drift chambers*. CERN, Geneva, cern edition, 1977. CERN, Geneva, 1975 - 1976. https://doi.org/10.5170/CERN-1977-009. – Cited pages 14 & 37.

[47] A. Oed. Position-sensitive detector with microstrip anode for electron multiplication with gases. *Nuclear Instruments and Methods in Physics Research Section A: Accelerators, Spectrometers, Detectors and Associated Equipment*, 263(2):351–359, 1988. https://doi.org/10.1016/0168-9002(88)90970-9. – Cited page 14.

[48] S Dalla Torre. MPGD developments: historical roadmap and recent progresses in consolidating MPGDs. *Journal of Instrumentation*, 8(10):C10020–C10020, oct 2013. https://doi.org/10.1088/1748-0221/8/10/c10020. – Cited page 14.

[49] Y. Giomataris, Ph. Rebourgeard, J.P. Robert, and G. Charpak. Micromegas: a high-granularity position-sensitive gaseous detector for high particle-flux environments. *Nuclear Instruments and Methods in Physics Research Section A: Accelerators, Spectrometers, Detectors and Associated Equipment*, (1):29 – 35, 1996. https://doi.org/10.1016/0168-9002(96)00175-1. – Cited pages 14 & 16.

[50] F. Sauli. Gem: A new concept for electron amplification in gas detectors. *Nuclear Instruments and Methods in Physics Research Section A: Accelerators, Spectrometers, Detectors and Associated Equipment*, 386(2):531 – 534, 1997. https://doi.org/10.1016/S0168-9002(96)01172-2. – Cited page 14.

[51] R. Chechik, A. Breskin, C. Shalem, and D. Mörmann. Thick gem-like hole multipliers: properties and possible applications. *Nuclear Instruments and Methods in Physics Research Section A: Accelerators, Spectrometers, Detectors and Associated Equipment*, 535(1):303 – 308, 2004. Proceedings of the 10th International Vienna Conference on Instrumentation. https://doi.org/10.1016/j.nima.2004.07.138. – Cited page 15.

[52] A. Badertscher, L. Knecht, M. Laffranchi, D. Lussi, A. Marchionni, G. Natterer, P. Otiougova, F. Resnati, A. Rubbia, and T. Viant. Operation of a double-phase pure argon large electron multiplier time projection chamber: Comparison of single and double phase operation. *Nuclear Instruments and Methods in Physics Research Section A: Accelerators, Spectrometers, Detectors and Associated Equipment*, 617(1):188 – 192, 2010. 11th Pisa Meeting on Advanced Detectors. https://doi.org/10.1016/j.nima.2009.10.011. – Cited page 15.

[53] V.M. [Blanco Carballo], Y. Bilevych, M. Chefdeville, M. Fransen, H. [van der Graaf], C. Salm, J. Schmitz, and J. Timmermans. Gemgrid: a wafer post-processed gem-like radiation detector. *Nuclear Instruments and Methods in Physics Research Section A: Accelerators, Spectrometers, Detectors and Associated Equipment*, 608(1):86 – 91, 2009. https://doi.org/10.1016/j.nima.2009.06.023. – Cited page 15.

[54] Fabio Sauli. The gas electron multiplier (gem): Operating principles and applications. *Nuclear Instruments and Methods in Physics Research Section A: Accelerators, Spectrometers, Detectors and Associated Equipment*, 805:2 – 24, 2016. Special Issue in memory of Glenn F. Knoll. https://doi.org/10.1016/j.nima.2015.07.060. – Cited page 15.

[55] I. Giomataris, R. De Oliveira, S. Andriamonje, S. Aune, G. Charpak, P. Colas, G. Fanourakis, E. Ferrer, A. Giganon, Ph. Rebourgeard, and P. Salin. Micromegas in a bulk. *Nuclear Instruments and Methods in Physics Research Section A: Accelerators, Spectrometers, Detectors and Associated Equipment*, 560(2):405 – 408, 2006. https://doi.org/10.1016/j.nima.2005.12.222. – Cited pages 16, 19 & 118.

[56] M.S. Dixit, J. Dubeau, J.-P. Martin, and K. Sachs. Position sensing from charge dispersion in micropattern gas detectors with a resistive anode. *Nuclear Instruments and Methods in Physics Research Section A: Accelerators, Spectrometers, Detectors and Associated Equipment*, 518(3):721–727, 2004. https://doi.org/10.1016/j.nima.2003.09.051. – Cited pages 16 & 20.

[57] S Andriamonje, D Attié, E Berthoumieux, M Calviani, P Colas, T Dafni, G Fanourakis, E Ferrer-Ribas, J Galan, T Geralis, A Giganon, I Giomataris, A Gris, C Guerrero Sanchez, F Gunsing, F J Iguaz, I Irastorza, R De Oliveira, T Papaevangelou, J Ruz, I Savvidis, A Teixera, and A Tomás. Development and performance of microbulk micromegas detectors. *Journal of Instrumentation*, 5(02):P02001–P02001, feb 2010. https://doi.org/10.1088/1748-0221/5/02/p02001. – Cited pages 16 & 47.

[58] V. M. Blanco Carballo, M. Chefdeville, M. Fransen, H. van der Graaf, J. Melai, C. Salm, J. Schmitz, and J. Timmermans. A radiation imaging detector made by postprocessing a standard cmos chip.

*IEEE Electron Device Letters*, 29(6):585–587, June 2008. https://doi.org/10.1109/LED.2008.925649. – Cited page 16.

[59] D. Attié, S. Aune, E. Berthoumieux, F. Bossù, P. Colas, A. Delbart, E. Dupont, E. Ferrer-Ribas, I. Giomataris, A. Glaenzer, H. Gómez, F. Gunsing, F. Jambon, F. Jeanneau, M. Lehuraux, D. Neyret, T. Papaevangelou, E. Pollacco, S. Procureur, M. Revolle, P. Schune, L. Segui, L. Sohl, M. Vandenbroucke, and Z. Wu. Current status and future developments of micromegas detectors for physics and applications. *Applied Sciences*, 11(12), 2021. https://doi.org/10.3390/app11125362. – Cited page 16.

[60] Y. Giomataris. Development and prospects of the new gaseous detector "micromegas". *Nuclear Instruments and Methods in Physics Research Section A: Accelerators, Spectrometers, Detectors and Associated Equipment*, 419(2):239 – 250, 1998. https://doi.org/10.1016/S0168-9002(98)00865-1. – Cited pages 17 & 51.

[61] T. Alexopoulos, J. Burnens, R. de Oliveira, G. Glonti, O. Pizzirusso, V. Polychronakos, G. Sekhniaidze, G. Tsipolitis, and J. Wotschack. A spark-resistant bulk-micromegas chamber for high-rate applications. *Nuclear Instruments and Methods in Physics Research Section A: Accelerators, Spectrometers, Detectors and Associated Equipment*, 640(1):110–118, 2011. https://doi.org/10.1016/j.nima.2011.03.025. – Cited page 20.

[62] S. Bouteille, D. Attié, P. Baron, D. Calvet, P. Magnier, I. Mandjavidze, S. Procureur, and M. Riallot. Large resistive 2d micromegas with genetic multiplexing and some imaging applications. *Nuclear Instruments and Methods in Physics Research Section A: Accelerators, Spectrometers, Detectors and Associated Equipment*, 834:187 – 191, 2016. https://doi.org/10.1016/j.nima.2016.08.006. – Cited pages 20 & 148.

[63] Werner Riegler. Electric fields, weighting fields, signals and charge diffusion in detectors including resistive materials. *Journal of Instrumentation*, 11(11):P11002–P11002, nov 2016. https://doi.org/10.1088/1748-0221/11/11/p11002. – Cited page 21.

[64] H. A. Bethe. Molière's theory of multiple scattering. *Phys. Rev.*, 89:1256–1266, Mar 1953. https://doi.org/10.1103/PhysRev.89.1256. – Cited pages 25 & 183.

[65] H. H. Andersen and J. F. Ziegler. *Hydrogen Stopping powers and ranges in all elements*. Pergamon Press, United States, 1977. – Cited page 28.

[66] J. Lindhard, M. Scharff, and H.E. Schiøtt. *Range Concepts and Heavy Ion Ranges: (Notes on Atomic Collisions, II)*. Kongelige Danske Videnskabernes Selskab: Matematisk-fysiske meddelelser. Munksgaard, 1963. – Cited page 28.

[67] Jens Lindhard, V Nielsen, M Scharff, and PV Thomsen. Integral equations governing radiation effects. *Mat. Fys. Medd. Dan. Vid. Selsk*, 33(10):1–42, 1963. – Cited page 28.

[68] William T. Scott. The theory of small-angle multiple scattering of fast charged particles. *Rev. Mod. Phys.*, 35:231–313, Apr 1963. https://doi.org/10.1103/RevModPhys.35.231. – Cited page 28.

[69] O. Klein and Y. Nishina. Über die streuung von strahlung durch freie elektronen nach der neuen relativistischen quantendynamik von dirac. *Zeitschrift für Physik*, 52(11):853–868, Nov 1929. https://doi.org/10.1007/BF01366453. – Cited page 32.

[70] Garfield++ toolkit. https://garfieldpp.web.cern.ch/garfieldpp/. – Cited page 37.

[71] M. Tosaki, T. Kawano, and Y. Isozumi. Measurements of electron attachment by oxygen molecule in proportional counter. *Nuclear Instruments and Methods in Physics Research Section B: Beam Interactions with Materials and Atoms*, 315:72–75, 2013. 25th International Conference on Atomic Collisions in Solids (ICACS-25). https://doi.org/10.1016/j.nimb.2013.04.081. – Cited page 38.

[72] G.D. Alkhazov, A.P. Komar, and A.A. Vorob'ev. Ionization fluctuations and resolution of ionization chambers and semiconductor detectors. *Nuclear Instruments and Methods*, 48(1):1–12, 1967. https://doi.org/10.1016/0029-554X(67)90455-7. – Cited page 41.

[73] K Ueda, E Shigemasa, Y Sato, A Yagishita, M Ukai, H Maezawa, T Hayaishi, and T Sasaki. Threshold behaviour of the multiply-charged photoion yields near the ar k edge. *Journal of Physics B: Atomic, Molecular and Optical Physics*, 24(3):605–613, feb 1991. 10.1088/0953-4075/24/3/016. – Cited page 44.

[74] D D Ryutov. The physics analysis of a gas attenuator with argon as a working gas. 12 2010. https://doi.org/10.2172/1000329. – Cited page 44.

[75] Preamplifier ortec 142b. https://www.ortec-online.com/products/electronics/preamplifiers/142a-b-c. – Cited page 46.

[76] D Attié, L Boilevin-Kayl, T Dafni, E Ferrer-Ribas, S Ferry, Y Giomataris, D C Herrera, F J Iguaz, I G Irastorza, M Kebbiri, T Papaevangelou, R de Oliveira, L Seguí, and A Tomás. Towards smaller gap microbulks. *Journal of Instrumentation*, 9(04):C04013–C04013, apr 2014. https://doi.org/10.1088/1748-0221/9/04/c04013. – Cited page 47.

[77] X. Llopart, R. Ballabriga, M. Campbell, L. Tlustos, and W. Wong. Timepix, a 65k programmable pixel readout chip for arrival time, energy and/or photon counting measurements. *Nuclear Instruments and Methods in Physics Research Section A: Accelerators, Spectrometers, Detectors and Associated Equipment*, 581(1):485 – 494, 2007. VCI 2007. https://doi.org/10.1016/j.nima.2007.08.079. – Cited page 58.

[78] M. Chefdeville, P. Colas, Y. Giomataris, H. van der Graaf, E.H.M. Heijne, S. van der Putten, C. Salm, J. Schmitz, S. Smits, J. Timmermans, and J.L. Visschers. An electron-multiplying 'micromegas' grid made in silicon wafer post-processing technology. *Nuclear Instruments and Methods in Physics Research Section A: Accelerators, Spectrometers, Detectors and Associated Equipment*, 556(2):490–494, 2006. https://doi.org/10.1016/j.nima.2005.11.065. – Cited pages 59 & 173.

[79] Maximilien Chefdeville. Development of micromegas-like gaseous detectors using a pixel readout chip as collecting anode. 01 2009. https://cds.cern.ch/record/1169417. – Cited page 59.

[80] Hartland S. Snyder. The electromagnetic field in quantized space-time. *Phys. Rev.*, 72:68–71, Jul 1947. https://doi.org/10.1103/PhysRev.72.68. – Cited page 60.

[81] Werner Legler. Zur statistik der elektronenlawinen. *Zeitschrift für Physik*, 140(2):221–240, Mar 1955. 10.1007/BF01349380. – Cited page 60.

[82] H. Schindler, S.F. Biagi, and R. Veenhof. Calculation of gas gain fluctuations in uniform fields. *Nuclear Instruments and Methods in Physics Research Section A: Accelerators, Spectrometers, Detectors and*

*Associated Equipment*, 624(1):78–84, 2010. https://doi.org/10.1016/j.nima.2010.09.072. – Cited page 60.

[83] P. Bhattacharya, D. Sankar Bhattacharya, S. Mukhopadhyay, S. Bhattacharya, N. Majumdar, S. Sarkar, P. Colas, and D. Attie. Investigation of ion backflow in bulk micromegas detectors. *Journal of Instrumentation*, 10(09):P09017, sep 2015. https://doi.org/10.1088/1748-0221/10/09/P09017. – Cited page 64.

[84] F. Kunn, P. Abbon, J. Ball, Y. Bedfer, C. Bernet, E. Delagnes, A. Giganon, J.-M. Le Goff, A. Magnon, D. Neyret, H. Pereira, S. Platchkov, P. Rebourgeard, G. Tarte, and D. Thers. The gaseous microstrip detector micromegas for the compass experiment at cern. *Nuclear Physics A*, 721:C1087–C1090, 2003. https://doi.org/10.1016/S0375-9474(03)01291-0. – Cited page 64.

[85] F Thibaud, P Abbon, V Andrieux, M Anfreville, Y Bedfer, E Burtin, L Capozza, C Coquelet, Q Curiel, N d'Hose, D Desforge, K Dupraz, R Durand, A Ferrero, A Giganon, D Jourde, F Kunne, A Magnon, N Makke, C Marchand, D Neyret, B Paul, S Platchkov, M Usseglio, and M Vandenbroucke. Performance of large pixelised micromegas detectors in the COMPASS environment. *Journal of Instrumentation*, 9(02):C02005–C02005, feb 2014. https://doi.org/10.1088/1748-0221/9/02/c02005. – Cited page 64.

[86] D Thers, Ph Abbon, J Ball, Y Bedfer, C Bernet, C Carasco, E Delagnes, D Durand, J.-C Faivre, H Fonvieille, A Giganon, F Kunne, J.-M.Le Goff, F Lehar, A Magnon, D Neyret, E Pasquetto, H Pereira, S Platchkov, E Poisson, and Ph Rebourgeard. Micromegas as a large microstrip detector for the compass experiment. *Nuclear Instruments and Methods in Physics Research Section A: Accelerators, Spectrometers, Detectors and Associated Equipment*, 469(2):133–146, 2001. https://doi.org/10.1016/S0168-9002(01)00769-0. – Cited page 64.

[87] Fabien Jeanneau, T. Alexopoulos, D. Attie, M. Boyer, J. Derre, G. Fanourakis, E. Ferrer-Ribas, J. Galan, E. Gazis, T. Geralis, A. Giganon, I. Giomataris, S. Herlant, J. Manjarres, E. Ntomari, Ph. Schune, M. Titov, G. Tsipolitis, and W. Wang. Performances and ageing study of resistive-anodes micromegas detectors for hl-lhc environment. *IEEE Transactions on Nuclear Science*, 59(4):1711–1716, 2012. https://doi.org/10.1109/TNS.2012.2198492. – Cited page 66.

[88] David R. Nygren. Proposal to investigate the feasibility of a novel concept in particle detection. *LBL Internal Report*, 1974. – Cited page 68.

[89] David R. Nygren. The time-projection chamber - a new $4\pi$ detector for charged particles. *PEP*, 144, 1974. – Cited page 68.

[90] R.L. Gluckstern. Uncertainties in track momentum and direction, due to multiple scattering and measurement errors. *Nuclear Instruments and Methods*, 24:381 – 389, 1963. https://doi.org/10.1016/0029-554X(63)90347-1. – Cited page 73.

[91] R. Frühwirth. Application of kalman filtering to track and vertex fitting. *Nuclear Instruments and Methods in Physics Research Section A: Accelerators, Spectrometers, Detectors and Associated Equipment*, 262(2):444–450, 1987. https://doi.org/10.1016/0168-9002(87)90887-4. – Cited page 75.

[92] Martin A. Fischler and Robert C. Bolles. Random sample consensus: A paradigm for model fitting with applications to image analysis and automated cartography. *Commun. ACM*, 24(6):381–395, jun 1981. https://10.1145/358669.358692. – Cited page 77.

[93] Ilc technical design report. https://linearcollider.org/technical-design-report/. – Cited page 81.

[94] Mikael Berggren. New physics searches with the international large detector at the ilc, 2021. https://doi.org/10.48550/ARXIV.2111.02386. – Cited page 81.

[95] Keisuke Fujii, Christophe Grojean, Michael E. Peskin, Tim Barklow, Yuanning Gao, Shinya Kanemura, Hyungdo Kim, Jenny List, Mihoko Nojiri, Maxim Perelstein, Roman Poeschl, Juergen Reuter, Frank Simon, Tomohiko Tanabe, Jaehoon Yu, James D. Wells, Hitoshi Murayama, and Hitoshi Yamamoto. Physics case for the international linear collider, 2015. https://doi.org/10.48550/arXiv.1506.05992. – Cited page 82.

[96] Desy 5t magnet. https://flc.desy.de/tpc/projects/infrastructure/5t_magnet/index_eng.html. – Cited page 83.

[97] D.C. Arogancia, A.M. Bacala, K. Boudjemline, D.R. Burke, P. Colas, M. Dixit, K. Fujii, H. Fujishima, A. Giganon, I. Giomataris, H.C. Gooc, M. Habu, T. Higashi, Y. Kato, M. Kobayashi, H. Kuroiwa, V. Lepeltier, T. Matsuda, S. Matsushita, K. Nakamura, O. Nitoh, R.L. Reserva, Ph. Rosier, K. Sachs, R. Settles, A. Sugiyama, T. Takahashi, T. Watanabe, A. Yamaguchi, H. Yamaoka, and Th. Zerguerras. Study in a beam test of the resolution of a micromegas tpc with standard readout pads. *Nuclear Instruments and Methods in Physics Research Section A: Accelerators, Spectrometers, Detectors and Associated Equipment*, 602(2):403–414, 2009. https://doi.org/10.1016/j.nima.2009.01.014. – Cited page 83.

[98] M. Dixit, D. Attié, A. Bellerive, K. Boudjemline, P. Colas, A. Giganon, I. Giomataris, V. Lepeltier, S. Liu, J.-P. Martin, K. Sachs, Y. Shin, and S. Turnbull. Micromegas tpc studies at high magnetic fields using the charge dispersion signal. *Nuclear Instruments and Methods in Physics Research Section A: Accelerators, Spectrometers, Detectors and Associated Equipment*, 581(1):254–257, 2007. VCI 2007. https://doi.org/10.1016/j.nima.2007.07.099. – Cited page 83.

[99] Lc-tpc memorandum of agreement. https://www.lctpc.org/e9/e56939/. – Cited page 84.

[100] Eudet: Detector r&d towards the international linear collider. https://www.eudet.org/. – Cited page 86.

[101] The ILD Concept Group. The international large detector: Letter of intent, 2010. https://doi.org/10.48550/arXiv.1006.3396. – Cited page 86.

[102] Esl resistive catalogue. http://www.lichuangxin.cn/pdf/all.pdf. – Cited pages 86 & 154.

[103] P Baron, J Beucher, D Calvet, Xavier de la Broise, E Delagnes, A Delbart, F Druillole, A Le Coguie, E Mazzucato, E Monmarthe, and M Zito. After, the front end asic of the t2k time projection chambers. 2009. https://doi.org/10.5170/CERN-2009-006.596. – Cited page 87.

[104] N. Abgrall, B. Andrieu, P. Baron, P. Bene, V. Berardi, J. Beucher, P. Birney, F. Blaszczyk, A. Blondel, C. Bojechko, M. Boyer, F. Cadoux, D. Calvet, M.G. Catanesi, A. Cervera, P. Colas, X. De La Broise,

E. Delagnes, A. Delbart, M. Di Marco, F. Druillole, J. Dumarchez, S. Emery, L. Escudero, W. Faszer, D. Ferrere, A. Ferrero, K. Fransham, A. Gaudin, C. Giganti, I. Giomataris, J. Giraud, M. Goyette, K. Hamano, C. Hearty, R. Henderson, S. Herlant, M. Ieva, B. Jamieson, G. Jover-Mañas, D. Karlen, I. Kato, A. Konaka, K. Laihem, R. Langstaff, M. Laveder, A. Le Coguie, O. Le Dortz, M. Le Ross, M. Lenckowski, T. Lux, M. Macaire, K. Mahn, F. Masciocchi, E. Mazzucato, M. Mezzetto, A. Miller, J.-Ph. Mols, L. Monfregola, E. Monmarthe, J. Myslik, F. Nizery, R. Openshaw, E. Perrin, F. Pierre, D. Pierrepont, P. Poffenberger, B. Popov, E. Radicioni, M. Ravonel, J.-M. Reymond, J.-L. Ritou, M. Roney, S. Roth, F. Sánchez, A. Sarrat, R. Schroeter, A. Stahl, P. Stamoulis, J. Steinmann, D. Terhorst, D. Terront, V. Tvaskis, M. Usseglio, A. Vallereau, G. Vasseur, J. Wendland, G. Wikström, and M. Zito. Time projection chambers for the t2k near detectors. *Nuclear Instruments and Methods in Physics Research Section A: Accelerators, Spectrometers, Detectors and Associated Equipment*, 637(1):25–46, 2011. https://doi.org/10.1016/j.nima.2011.02.036. – Cited pages 87, 116 & 173.

[105] Common software packages developed for the international linear collider ilc. https://ilcsoft.desy.de/portal. – Cited page 94.

[106] Lcio: Linear collider input output. https://ilcsoft.desy.de/portal/software_packages/lcio/. – Cited page 94.

[107] Denis Calvet. T2k tpc read-out electronics digital front-end mezzanine card design notes, 2007. – Cited page 94.

[108] Marlin based simulation, digitisation, reconstruction and analysis code for the tpc. https://ilcsoft.desy.de/portal/software_packages/marlintpc/. – Cited page 95.

[109] K. Boudjemline, M.S. Dixit, J.-P. Martin, and K. Sachs. Spatial resolution of a gem readout tpc using the charge dispersion signal. *Nuclear Instruments and Methods in Physics Research Section A: Accelerators, Spectrometers, Detectors and Associated Equipment*, 574(1):22–27, 2007. https://doi.org/10.1016/j.nima.2007.01.017. – Cited page 96.

[110] Nicholi M. Shiell. A New Analysis Technique to Improve Spatial Resolution for a Resistive Anode Time Projection Chamber. Master's thesis, Carleton University, Canada, January 2012. – Cited page 96.

[111] Wenxin Wang. *Etude d'un grand détecteur TPC Micromegas pour l'ILC*. PhD thesis, 2013. Thèse de doctorat dirigée par Colas, Paul Physique des particules Paris 11 2013. – Cited page 100.

[112] G. Bardelloni, E. Bertolucci, A.L.J. Boerkamp, D. Calvet, M. Conti, M. Maiorino, P. Russo, and J.L. Visschers. A new read-out system for an imaging pixel detector. In *2000 IEEE Nuclear Science Symposium. Conference Record (Cat. No.00CH37149)*, volume 2, pages 12/57–12/60 vol.2, 2000. https://doi.org/10.1109/NSSMIC.2000.949940. – Cited page 104.

[113] V.D. Burkert, L. Elouadrhiri, K.P. Adhikari, S. Adhikari, M.J. Amaryan, D. Anderson, G. Angelini, M. Antonioli, H. Atac, S. Aune, H. Avakian, C. Ayerbe Gayoso, N. Baltzell, L. Barion, M. Battaglieri, V. Baturin, I. Bedlinskiy, F. Benmokhtar, A. Bianconi, A.S. Biselli, P. Bonneau, F. Bossù, S. Boyarinov, W.J. Briscoe, W.K. Brooks, K. Bruhwel, D.S. Carman, A. Celentano, G. Charles, P. Chatagnon, T. Chetry, G. Christiaens, S. Christo, G. Ciullo, B.A. Clary, P.L. Cole, M. Contalbrigo, M. Cook, V. Crede, R. Cruz-Torres, C. Cuevas, A. D'Angelo, N. Dashyan, M. Defurne, A. Deur, R. De Vita,

S. Diehl, C. Djalali, G. Dodge, R. Dupre, M. Ehrhart, L. El Fassi, B. Eng, T. Ewing, R. Fair, G. Fedotov, A. Filippi, T.A. Forest, M. Garçon, G. Gavalian, P. Ghoshal, G.P. Gilfoyle, K. Giovanetti, F.X. Girod, D.I. Glazier, E. Golovatch, R.W. Gothe, Y. Gotra, K.A. Griffioen, M. Guidal, V. Gyurjyan, K. Hafidi, H. Hakobyan, C. Hanretty, N. Harrison, M. Hattawy, F. Hauenstein, T.B. Hayward, D. Heddle, P. Hemler, O.A. Hen, K. Hicks, A. Hobart, J. Hogan, M. Holtrop, Y. Ilieva, I. Illari, D. Insley, D.G. Ireland, B.S. Ishkhanov, E.L. Isupov, G. Jacobs, H.S. Jo, R. Johnston, K. Joo, S. Joosten, T. Kageya, D. Kashy, C. Keith, D. Keller, M. Khachatryan, A. Khanal, A. Kim, C.W. Kim, W. Kim, V. Kubarovsky, S.E. Kuhn, L. Lanza, M. Leffel, V. Lucherini, A. Lung, M.L. Kabir, M. Leali, S. Lee, P. Lenisa, K. Livingston, M. Lowry, I.J.D. MacGregor, I. Mandjavidze, D. Marchand, N. Markov, V. Mascagna, B. McKinnon, M. McMullen, C. Mealer, M.D. Mestayer, Z.E. Meziani, R. Miller, R.G. Milner, T. Mineeva, M. Mirazita, V. Mokeev, P. Moran, A. Movsisyan, C. Munoz Camacho, P. Naidoo, S. Nanda, J. Newton, S. Niccolai, G. Niculescu, M. Osipenko, M. Paolone, L.L. Pappalardo, R. Paremuzyan, O. Pastor, E. Pasyuk, W. Phelps, O. Pogorelko, J. Poudel, J.W. Price, K. Price, S. Procureur, Y. Prok, D. Protopopescu, R. Rajput-Ghoshal, B.A. Raue, B. Raydo, M. Ripani, J. Ritman, A. Rizzo, G. Rosner, P. Rossi, J. Rowley, B.J. Roy, F. Sabatié, C. Salgado, S. Schadmand, A. Schmidt, E.P. Segarra, V. Sergeyeva, Y.G. Sharabian, U. Shrestha, Iu. Skorodumina, G.D. Smith, L.C. Smith, D. Sokhan, O. Soto, N.Sparveris, S. Stepanyan, P. Stoler, S. Strauch, J.A. Tan, M. Taylor, D. Tilles, M. Turisini, N. Tyler, M. Ungaro, L. Venturelli, H. Voskanyan, E. Voutier, D. Watts, X. Wei, L.B. Weinstein, C. Wiggins, M. Wiseman, M.H. Wood, A. Yegneswaran, G. Young, N. Zachariou, M. Zarecky, J. Zhang, Z.W. Zhao, and V. Ziegler. The clas12 spectrometer at jefferson laboratory. *Nuclear Instruments and Methods in Physics Research Section A: Accelerators, Spectrometers, Detectors and Associated Equipment*, 959:163419, 2020. https://doi.org/10.1016/j.nima.2020.163419. – Cited page 107.

[114] Jefferson lab. https://www.jlab.org/. – Cited page 108.

[115] A. Acker, D. Attié, S. Aune, J. Ball, P. Baron, M. Bashkanov, M. Battaglieri, R. Behary, F. Benmokhtar, A. Bersani, Q. Bertrand, D. Besin, T. Bey, P. Black, P. Bonneau, F. Bossù, R. Boudouin, M. Boyer, P. Campero Rojas, A. Casale, A. Celentano, R. Cereseto, A. Ciarma, F. Cipro, G. Charles, G. Christiaens, P. Contrepois, M. Cook, A. D'Angelo, R. De Vita, M. Defurne, E. Delagnes, E. Fanchini, S. Fegan, J. Fleming, A. Filippi, M. Garçon, F. Georges, K.L. Giovanetti, D.I. Glazier, R. Granelli, N. Grouas, K. Hicks, A. Hoebel, S.M. Hughes, C. Lahonde, L. Lanza, M. Leffel, T. Lerch, T. Lemon, K. Livingston, A. Manco, I. Mandjavidze, H.S. Mann, B. McKinnon, O. Meunier, R. Miller, G. Miní, Y. Mouden, P. Musico, M. Osipenko, G. Ottonello, F. Parodi, E. Pasyuk, P. Pollovio, F. Pratolongo, S. Procureur, R. Puppo, C. Rossi, M. Riallot, M. Ripani, A. Rizzo, F. Sabatié, C. Salgado, G.D. Smith, D. Sokhan, I. Stankovic, M. Taiuti, A. Trovato, M. Vandenbroucke, V. Vigo, E. Virique, D. Watts, C. Wiggins, N. Zachariou, and L. Zana. The clas12 forward tagger. *Nuclear Instruments and Methods in Physics Research Section A: Accelerators, Spectrometers, Detectors and Associated Equipment*, 959:163475, 2020. https://doi.org/10.1016/j.nima.2020.163475. – Cited page 110.

[116] K. Abe, N. Abgrall, Y. Ajima, H. Aihara, J. B. Albert, C. Andreopoulos, B. Andrieu, S. Aoki, O. Araoka, J. Argyriades, A. Ariga, T. Ariga, S. Assylbekov, D. Autiero, A. Badertscher, M. Barbi, G. J. Barker, G. Barr, M. Bass, F. Bay, S. Bentham, V. Berardi, B. E. Berger, I. Bertram, M. Besnier, J. Beucher, D. Beznosko, S. Bhadra, F. d.M. M. Blaszczyk, A. Blondel, C. Bojechko, J. Bouchez, S. B. Boyd, A. Bravar, C. Bronner, D. G. Brook-Roberge, N. Buchanan, H. Budd, D. Calvet, S. L. Cartwright, A. Carver, R. Castillo, M. G. Catanesi, A. Cazes, A. Cervera, C. Chavez, S. Choi,

G. Christodoulou, J. Coleman, W. Coleman, G. Collazuol, K. Connolly, A. Curioni, A. Dabrowska, I. Danko, R. Das, G. S. Davies, S. Davis, M. Day, G. De Rosa, J. P. A. M. de André, P. de Perio, A. Delbart, C. Densham, F. Di Lodovico, S. Di Luise, P. Dinh Tran, J. Dobson, U. Dore, O. Drapier, F. Dufour, J. Dumarchez, S. Dytman, M. Dziewiecki, M. Dziomba, S. Emery, A. Ereditato, L. Escudero, L. S. Esposito, M. Fechner, A. Ferrero, A. J. Finch, E. Frank, Y. Fujii, Y. Fukuda, V. Galymov, F. C. Gannaway, A. Gaudin, A. Gendotti, M. A. George, S. Giffin, C. Giganti, K. Gilje, T. Golan, M. Goldhaber, J. J. Gomez-Cadenas, M. Gonin, N. Grant, A. Grant, P. Gumplinger, P. Guzowski, A. Haesler, M. D. Haigh, K. Hamano, C. Hansen, D. Hansen, T. Hara, P. F. Harrison, B. Hartfiel, M. Hartz, T. Haruyama, T. Hasegawa, N. C. Hastings, S. Hastings, A. Hatzikoutelis, K. Hayashi, Y. Hayato, C. Hearty, R. L. Helmer, R. Henderson, N. Higashi, J. Hignight, E. Hirose, J. Holeczek, S. Horikawa, A. Hyndman, A. K. Ichikawa, K. Ieki, M. Ieva, M. Iida, M. Ikeda, J. Ilic, J. Imber, T. Ishida, C. Ishihara, T. Ishii, S. J. Ives, M. Iwasaki, K. Iyogi, A. Izmaylov, B. Jamieson, R. A. Johnson, K. K. Joo, G. V. Jover-Manas, C. K. Jung, H. Kaji, T. Kajita, H. Kakuno, J. Kameda, K. Kaneyuki, D. Karlen, K. Kasami, I. Kato, E. Kearns, M. Khabibullin, F. Khanam, A. Khotjantsev, D. Kielczewska, T. Kikawa, J. Kim, J. Y. Kim, S. B. Kim, N. Kimura, B. Kirby, J. Kisiel, P. Kitching, T. Kobayashi, G. Kogan, S. Koike, A. Konaka, L. L. Kormos, A. Korzenev, K. Koseki, Y. Koshio, Y. Kouzuma, K. Kowalik, V. Kravtsov, I. Kreslo, W. Kropp, H. Kubo, Y. Kudenko, N. Kulkarni, R. Kurjata, T. Kutter, J. Lagoda, K. Laihem, M. Laveder, K. P. Lee, P. T. Le, J. M. Levy, C. Licciardi, I. T. Lim, T. Lindner, R. P. Litchfield, M. Litos, A. Longhin, G. D. Lopez, P. F. Loverre, L. Ludovici, T. Lux, M. Macaire, K. Mahn, Y. Makida, M. Malek, S. Manly, A. Marchionni, A. D. Marino, J. Marteau, J. F. Martin, T. Maruyama, T. Maryon, J. Marzec, P. Masliah, E. L. Mathie, C. Matsumura, K. Matsuoka, V. Matveev, K. Mavrokoridis, E. Mazzucato, N. McCauley, K. S. McFarland, C. McGrew, T. McLachlan, M. Messina, W. Metcalf, C. Metelko, M. Mezzetto, P. Mijakowski, C. A. Miller, A. Minamino, O. Mineev, S. Mine, A. D. Missert, G. Mituka, M. Miura, K. Mizouchi, L. Monfregola, F. Moreau, B. Morgan, S. Moriyama, A. Muir, A. Murakami, M. Murdoch, S. Murphy, J. Myslik, T. Nakadaira, M. Nakahata, T. Nakai, K. Nakajima, T. Nakamoto, K. Nakamura, S. Nakayama, T. Nakaya, D. Naples, M. L. Navin, B. Nelson, T. C. Nicholls, K. Nishikawa, H. Nishino, J. A. Nowak, M. Noy, Y. Obayashi, T. Ogitsu, H. Ohhata, T. Okamura, K. Okumura, T. Okusawa, S. M. Oser, M. Otani, R. A. Owen, Y. Oyama, T. Ozaki, M. Y. Pac, V. Palladino, V. Paolone, P. Paul, D. Payne, G. F. Pearce, J. D. Perkin, V. Pettinacci, F. Pierre, E. Poplawska, B. Popov, M. Posiadala, J.-M. Poutissou, R. Poutissou, P. Przewlocki, W. Qian, J. L. Raaf, E. Radicioni, P. N. Ratoff, T. M. Raufer, M. Ravonel, M. Raymond, F. Retiere, A. Robert, P. A. Rodrigues, E. Rondio, J. M. Roney, B. Rossi, S. Roth, A. Rubbia, D. Ruterbories, S. Sabouri, R. Sacco, K. Sakashita, F. Sánchez, A. Sarrat, K. Sasaki, K. Scholberg, J. Schwehr, M. Scott, D. I. Scully, Y. Seiya, T. Sekiguchi, H. Sekiya, M. Shibata, Y. Shimizu, M. Shiozawa, S. Short, M. Siyad, R. J. Smith, M. Smy, J. T. Sobczyk, H. Sobel, M. Sorel, A. Stahl, P. Stamoulis, J. Steinmann, B. Still, J. Stone, C. Strabel, L. R. Sulak, R. Sulej, P. Sutcliffe, A. Suzuki, K. Suzuki, S. Suzuki, S. Y. Suzuki, Y. Suzuki, Y. Suzuki, T. Szeglowski, M. Szeptycka, R. Tacik, M. Tada, S. Takahashi, A. Takeda, Y. Takenaga, Y. Takeuchi, K. Tanaka, H. A. Tanaka, M. Tanaka, M. M. Tanaka, N. Tanimoto, K. Tashiro, I. Taylor, A. Terashima, D. Terhorst, R. Terri, L. F. Thompson, A. Thorley, W. Toki, T. Tomaru, Y. Totsuka, C. Touramanis, T. Tsukamoto, M. Tzanov, Y. Uchida, K. Ueno, A. Vacheret, M. Vagins, G. Vasseur, T. Wachala, J. J. Walding, A. V. Waldron, C. W. Walter, P. J. Wanderer, J. Wang, M. A. Ward, G. P. Ward, D. Wark, M. O. Wascko, A. Weber, R. Wendell, N. West, L. H. Whitehead, G. Wikström, R. J. Wilkes, M. J. Wilking, J. R. Wilson, R. J. Wilson, T. Wongjirad, S. Yamada, Y. Yamada, A. Yamamoto, K. Yamamoto, Y. Yamanoi, H. Yamaoka, C. Yanagisawa,

T. Yano, S. Yen, N. Yershov, M. Yokoyama, A. Zalewska, J. Zalipska, L. Zambelli, K. Zaremba, M. Ziembicki, E. D. Zimmerman, M. Zito, and J. Żmuda. Indication of electron neutrino appearance from an accelerator-produced off-axis muon neutrino beam. *Phys. Rev. Lett.*, 107:041801, Jul 2011. https://doi.org/10.1103/PhysRevLett.107.041801. – Cited page 116.

[117] K. Abe, R. Akutsu, A. Ali, C. Alt, C. Andreopoulos, L. Anthony, M. Antonova, S. Aoki, A. Ariga, T. Arihara, Y. Asada, Y. Ashida, E. T. Atkin, Y. Awataguchi, S. Ban, M. Barbi, G. J. Barker, G. Barr, D. Barrow, C. Barry, M. Batkiewicz-Kwasniak, A. Beloshapkin, F. Bench, V. Berardi, S. Berkman, L. Berns, S. Bhadra, S. Bienstock, A. Blondel, S. Bolognesi, B. Bourguille, S. B. Boyd, D. Brailsford, A. Bravar, D. Bravo Berguño, C. Bronner, A. Bubak, M. Buizza Avanzini, J. Calcutt, T. Campbell, S. Cao, S. L. Cartwright, M. G. Catanesi, A. Cervera, A. Chappell, C. Checchia, D. Cherdack, N. Chikuma, M. Cicerchia, G. Christodoulou, J. Coleman, G. Collazuol, L. Cook, D. Coplowe, A. Cudd, A. Dabrowska, G. De Rosa, T. Dealtry, P. F. Denner, S. R. Dennis, C. Densham, F. Di Lodovico, N. Dokania, S. Dolan, T. A. Doyle, O. Drapier, J. Dumarchez, P. Dunne, A. Eguchi, L. Eklund, S. Emery-Schrenk, A. Ereditato, P. Fernandez, T. Feusels, A. J. Finch, G. A. Fiorentini, G. Fiorillo, C. Francois, M. Friend, Y. Fujii, R. Fujita, D. Fukuda, R. Fukuda, Y. Fukuda, K. Fusshoeller, K. Gameil, C. Giganti, T. Golan, M. Gonin, A. Gorin, M. Guigue, D. R. Hadley, J. T. Haigh, P. Hamacher-Baumann, M. Hartz, T. Hasegawa, S. Hassani, N. C. Hastings, T. Hayashino, Y. Hayato, A. Hiramoto, M. Hogan, J. Holeczek, N. T. Hong Van, F. Iacob, A. K. Ichikawa, M. Ikeda, T. Ishida, T. Ishii, M. Ishitsuka, K. Iwamoto, A. Izmaylov, M. Jakkapu, B. Jamieson, S. J. Jenkins, C. Jesús-Valls, M. Jiang, S. Johnson, P. Jonsson, C. K. Jung, X. Junjie, P. B. Jurj, M. Kabirnezhad, A. C. Kaboth, T. Kajita, H. Kakuno, J. Kameda, D. Karlen, S. P. Kasetti, Y. Kataoka, T. Katori, Y. Kato, E. Kearns, M. Khabibullin, A. Khotjantsev, T. Kikawa, H. Kikutani, H. Kim, J. Kim, S. King, J. Kisiel, A. Knight, A. Knox, T. Kobayashi, L. Koch, T. Koga, A. Konaka, L. L. Kormos, Y. Koshio, A. Kostin, K. Kowalik, H. Kubo, Y. Kudenko, N. Kukita, S. Kuribayashi, R. Kurjata, T. Kutter, M. Kuze, L. Labarga, J. Lagoda, M. Lamoureux, M. Laveder, M. Lawe, M. Licciardi, T. Lindner, R. P. Litchfield, S. L. Liu, X. Li, A. Longhin, L. Ludovici, X. Lu, T. Lux, L. N. Machado, L. Magaletti, K. Mahn, M. Malek, S. Manly, L. Maret, A. D. Marino, L. Marti-Magro, J. F. Martin, T. Maruyama, T. Matsubara, K. Matsushita, V. Matveev, K. Mavrokoridis, E. Mazzucato, M. McCarthy, N. McCauley, J. McElwee, K. S. McFarland, C. McGrew, A. Mefodiev, C. Metelko, M. Mezzetto, A. Minamino, O. Mineev, S. Mine, M. Miura, L. Molina Bueno, S. Moriyama, J. Morrison, Th. A. Mueller, L. Munteanu, S. Murphy, Y. Nagai, T. Nakadaira, M. Nakahata, Y. Nakajima, A. Nakamura, K. G. Nakamura, K. Nakamura, S. Nakayama, T. Nakaya, K. Nakayoshi, C. Nantais, C. E. R. Naseby, T. V. Ngoc, K. Niewczas, K. Nishikawa, Y. Nishimura, E. Noah, T. S. Nonnenmacher, F. Nova, P. Novella, J. Nowak, J. C. Nugent, H. M. O'Keeffe, L. O'Sullivan, T. Odagawa, K. Okumura, T. Okusawa, S. M. Oser, R. A. Owen, Y. Oyama, V. Palladino, J. L. Palomino, V. Paolone, M. Pari, W. C. Parker, S. Parsa, J. Pasternak, P. Paudyal, M. Pavin, D. Payne, G. C. Penn, L. Pickering, C. Pidcott, G. Pintaudi, E. S. Pinzon Guerra, C. Pistillo, B. Popov, K. Porwit, M. Posiadala-Zezula, A. Pritchard, B. Quilain, T. Radermacher, E. Radicioni, B. Radics, P. N. Ratoff, E. Reinherz-Aronis, C. Riccio, E. Rondio, S. Roth, A. Rubbia, A. C. Ruggeri, C. A. Ruggles, A. Rychter, K. Sakashita, F. Sánchez, G. Santucci, C. M. Schloesser, K. Scholberg, J. Schwehr, M. Scott, Y. Seiya, T. Sekiguchi, H. Sekiya, D. Sgalaberna, R. Shah, A. Shaikhiev, F. Shaker, A. Shaykina, M. Shiozawa, W. Shorrock, A. Shvartsman, A. Smirnov, M. Smy, J. T. Sobczyk, H. Sobel, F. J. P. Soler, Y. Sonoda, J. Steinmann, S. Suvorov, A. Suzuki, S. Y. Suzuki, Y. Suzuki, A. A. Sztuc, M. Tada, and The T2K Collaboration. Constraint on the matter–antimatter symmetry-violating phase in neutrino oscillations. *Nature*,

580(7803):339–344, Apr 2020. https://doi.org/10.1038/s41586-020-2177-0. – Cited pages 116 & 173.

[118] Bopp, steel mesh producer. https://www.bopp.com/. – Cited page 118.

[119] D. Attié, M. Batkiewicz-Kwasniak, P. Billoir, A. Blanchet, A. Blondel, S. Bolognesi, D. Calvet, M.G. Catanesi, M. Cicerchia, G. Cogo, P. Colas, G. Collazuol, A. Delbart, J. Dumarchez, S. Emery-Schrenk, M. Feltre, C. Giganti, F. Gramegna, M. Grassi, M. Guigue, P. Hamacher-Baumann, S. Hassani, F. Iacob, C. Jesús-Valls, R. Kurjata, M. Lamoureux, M. Lehuraux, A. Longhin, T. Lux, L. Magaletti, T. Marchi, A. Maurel, L. Mellet, M. Mezzetto, L. Munteanu, Q.V. Nguyen, Y. Orain, M. Pari, J.-M. Parraud, C. Pastore, A. Pepato, E. Pierre, B. Popov, H. Przybiliski, T. Radermacher, E. Radicioni, M. Riallot, S. Roth, A. Rychter, L. Scomparin, J. Steinmann, S. Suvorov, J. Swierblewski, D. Terront, N. Thamm, F. Toussenel, V. Valentino, G. Vasseur, U. Yevarouskaya, M. Ziembicki, and M. Zito. Characterization of resistive micromegas detectors for the upgrade of the t2k near detector time projection chambers. *Nuclear Instruments and Methods in Physics Research Section A: Accelerators, Spectrometers, Detectors and Associated Equipment*, 1025:166109, 2022. https://doi.org/10.1016/j.nima.2021.166109. – Cited page 119.

[120] D. Attié, M. Batkiewicz-Kwasniak, J. Boix, S. Bolognesi, S. Bordoni, D. Calvet, M.G. Catanesi, M. Cicerchia, G. Cogo, P. Colas, G. Collazuol, A. Dabrowska, A. Delbart, J. Dumarchez, S. Emery-Schrenk, C. Giganti, F. Gramegna, M. Guigue, P. Hamacher-Baumann, F. Iacob, C. Jesús-Valls, U. Kose, R. Kurjata, N. Lacalamita, M. Lamoureux, A. Longhin, T. Lux, L. Magaletti, T. Marchi, M. Mezzetto, J. Michalowski, J. Mundet, L. Munteanu, Q.V. Nguyen, M. Pari, J.-M. Parraud, C. Pastore, A. Pepato, B. Popov, H. Przybiliski, E. Radicioni, M. Riallot, C. Riccio, S. Roth, A.C. Ruggeri, A. Rychter, F. Sánchez, J. Steinmann, S. Suvorov, J. Swierblewski, D. Vargas, G. Vasseur, T. Wachala, A. Zalewska, M. Ziembicki, and M. Zito. Performances of a resistive micromegas module for the time projection chambers of the t2k near detector upgrade. *Nuclear Instruments and Methods in Physics Research Section A: Accelerators, Spectrometers, Detectors and Associated Equipment*, 957:163286, 2020. https://doi.org/10.1016/j.nima.2019.163286. – Cited page 119.

[121] D. Bernard. Tpc in $\gamma$-ray astronomy above pair-creation threshold. *Nuclear Instruments and Methods in Physics Research Section A: Accelerators, Spectrometers, Detectors and Associated Equipment*, 701:225–230, 2013. https://doi.org/10.1016/j.nima.2012.11.023. – Cited page 127.

[122] D. Bernard. Polarimetry of cosmic gamma-ray sources above e+e- pair creation threshold. *Nuclear Instruments and Methods in Physics Research Section A: Accelerators, Spectrometers, Detectors and Associated Equipment*, 729:765–780, 2013. https://doi.org/10.1016/j.nima.2013.07.047. – Cited pages 127 & 130.

[123] H. Zhang and M. Böttcher. X-RAY AND GAMMA-RAY POLARIZATION IN LEPTONIC AND HADRONIC JET MODELS OF BLAZARS. *The Astrophysical Journal*, 774(1):18, aug 2013. https://doi.org/10.1088/0004-637x/774/1/18. – Cited page 128.

[124] Denis Calvet. A versatile readout system for small to medium scale gaseous and silicon detectors. *IEEE Transactions on Nuclear Science*, 61(1):675–682, 2014. https://doi.org/10.1109/TNS.2014.2299312. – Cited page 128.

[125] J E Campagne, S Conforti Di Lorenzo, S Drouet, D Duchesneau, F Dulucq, N Dumont-Dayot, A El Berni, J Favier, A Gallas, B Genolini, K Hanson, N Hauchecorne, R Hermel, M Imre, B Ky,

C de La Taille, J Maltese, A Maroni, G Martin-Chassard, T Nguyen Trung, J Peyré, J Pouthas, E Rindel, P Rosier, L Séminor, J Tassan, C Théneau, E Wanlin, and A Zghiche. Pmm$^2$: R&d on triggerless acquisition for next generation neutrino experiments. *Journal of Instrumentation*, 6(01):C01081–C01081, jan 2011. https://doi.org/10.1088/1748-0221/6/01/c01081. – Cited page 128.

[126] Yannick Geerebaert, Denis Bernard, Philippe Bruel, Mickaël Frotin, Berrie Giebels, Philippe Gros, Deirdre Horan, Marc Louzir, Patrick Poilleux, Igor Semeniouk, Shaobo Wang, David Attié, Denis Calvet, Paul Colas, Alain Delbart, Patrick Sizun, Diego Götz, Sho Amano, Satoshi Hashimoto, Takuya Kotaka, Yasuhito Minamiyama, Shuji Miyamoto, Akinori Takemoto, Masashi Yamaguchi, Schin Daté, and Haruo Ohkuma. Electronics for harpo: Design, development and validation of electronics for a high performance polarised-gamma-ray detector. In *2016 IEEE-NPSS Real Time Conference (RT)*, pages 1–8, 2016. https://doi.org/10.1109/RTC.2016.7543098. – Cited pages 128 & 129.

[127] Philippe Gros. HARPO - TPC for High Energy Astrophysics and Polarimetry from the MeV to the GeV. In *Technology and Instrumentation in Particle Physics 2014 (TIPP2014)*, volume TIPP2014, page 133, 2014. https://doi.org/10.22323/1.213.0133. – Cited page 128.

[128] Alain Delbart. HARPO, TPC as a gamma telescope and polarimeter: First measurement in a polarised photon beam between 1.7 and 74 MeV. *PoS*, ICRC2015:1016, 2016. https://doi.org/10.22323/1.236.1016. – Cited page 128.

[129] D. **Attié**, Sho Amano, Pascal Baron, David Baudin, Denis Bernard, Philippe Bruel, Denis Calvet, Paul Colas, Schin Daté, Alain Delbart, Mickaël Frotin, Yannick Geerebaert, Berrie Giebels, Diego Gotz, Philippe Gros, Satoshi Hashimoto, Deirdre Horan, Takuya Kotaka, Marc Louzir, Frederic Magniette, Yasuhito Minamiyama, Shuji Miyamoto, Haruo Ohkuma, Patrick Poilleux, Igor Semeniouk, Patrick Sizun, Akinori Takemoto, Masashi Yamaguchi, Ryo **Yonamine**, and Shaobo Wang. HARPO, prototype of a gamma-ray polarimeter: Results of a polarised photon beam test between 1.7 and 74 MeV. In *35th International Cosmic Ray Conference (ICRC2017)*, volume 301 of *Proceedings of 35th International Cosmic Ray Conference*, page 818, 2017. https://doi.org/10.22323/1.301.0818. – Cited pages 129 & 135.

[130] P. Gros, S. Amano, D. Attié, P. Baron, D. Baudin, D. Bernard, P. Bruel, D. Calvet, P. Colas, S. Daté, A. Delbart, M. Frotin, Y. Geerebaert, B. Giebels, D. Götz, S. Hashimoto, D. Horan, T. Kotaka, M. Louzir, F. Magniette, Y. Minamiyama, S. Miyamoto, H. Ohkuma, P. Poilleux, I. Semeniouk, P. Sizun, A. Takemoto, M. Yamaguchi, R. Yonamine, and S. Wang. A TPC as high performance gamma-ray telescope and polarimeter: polarisation measurement in a beam between 1.7 and 74mev with HARPO. *Journal of Physics: Conference Series*, 1029:012003, may 2018. https://doi.org/10.1088/1742-6596/1029/1/012003. – Cited page 129.

[131] P. Gros, S. Amano, D. Attié, P. Baron, D. Baudin, D. Bernard, P. Bruel, D. Calvet, P. Colas, S. Daté, A. Delbart, M. Frotin, Y. Geerebaert, B. Giebels, D. Götz, S. Hashimoto, D. Horan, T. Kotaka, M. Louzir, F. Magniette, Y. Minamiyama, S. Miyamoto, H. Ohkuma, P. Poilleux, I. Semeniouk, P. Sizun, A. Takemoto, M. Yamaguchi, R. Yonamine, and S. Wang. Performance measurement of harpo: A time projection chamber as a gamma-ray telescope and polarimeter. *Astroparticle Physics*, 97:10–18, 2018. https://doi.org/10.1016/j.astropartphys.2017.10.008. – Cited page 129.

[132] Mikael Frosini and Denis Bernard. Charged particle tracking without magnetic field: Optimal measurement of track momentum by a bayesian analysis of the multiple measurements of deflections due to multiple scattering. *Nuclear Instruments and Methods in Physics Research Section A: Accelerators, Spectrometers, Detectors and Associated Equipment*, 867:182–194, 2017. https://doi.org/10.1016/j.nima.2017.06.030. – Cited page 129.

[133] P. Gros, S. Amano, D. Attié, D. Bernard, P. Bruel, D. Calvet, P. Colas, S. Daté, A. Delbart, M. Frotin, Y. Geerebaert, B. Giebels, D. Götz, S. Hashimoto, D. Horan, T. Kotaka, Marc Louzir, Y. Minamiyama, S. Miyamoto, H. Ohkuma, Patrick Poilleux, I. Semeniouk, P. Sizun, A. Takemoto, M. Yamaguchi, and S. Wang. First measurement of the polarisation asymmetry of a gamma-ray beam between 1.7 to 74 MeV with the HARPO TPC. 9905:893 – 905, 2016. https://doi.org/10.1117/12.2231856. – Cited page 130.

[134] P. Gros and D. Bernard. γ-ray polarimetry with conversions to e+e- pairs: Polarization asymmetry and the way to measure it. *Astroparticle Physics*, 88:30–37, 2017. https://doi.org/10.1016/j.astropartphys.2016.12.006. – Cited page 130.

[135] D. A. Attié and P. Magnier. A radiation imaging detector made by postprocessing a standard cmos chip. *Institut national de la propriété industrielle*, June 2016. https://data.inpi.fr/brevets/EP3054168. – Cited page 132.

[136] D. Baudin, D. Attié, P. Baron, D. Bernard, D. Calvet, A. Delbart, Y. Geerebaert, and P. Gros. Astre: Asic with switched capacitor array (sca) and trigger for detector readout electronics hardened against single event latchup (sel). *Nuclear Instruments and Methods in Physics Research Section A: Accelerators, Spectrometers, Detectors and Associated Equipment*, 912:66–69, 2018. New Developments In Photodetection 2017. https://doi.org/10.1016/j.nima.2017.10.043. – Cited page 132.

[137] A.A. Aarts, V.M. Blanco Carballo, M. Chefdeville, P. Colas, S. Dunand, M. Fransen, H. van der Graaf, Y. Giomataris, F. Hartjes, E. Koffeman, J. Melai, H. Peek, W. Riegler, C. Salm, J. Schmitz, S. M. Smits, J. Timmermans, J.L. Visschers, and N. Wyrsch. Discharge protection and ageing of micromegas pixel detectors. In *2006 IEEE Nuclear Science Symposium Conference Record*, volume 6, pages 3865–3869, 2006. https://doi.org/10.1109/NSSMIC.2006.353833. – Cited page 136.

[138] Charles Thomson Rees Wilson. Investigations on x-rays and $\beta$-rays by the cloud method. part 1.$\beta$;x-rays. *Proceedings of the Royal Society of London. Series A, Containing Papers of a Mathematical and Physical Character*, 104(724):1–24, 1923. https://doi.org/10.1098/rspa.1923.0090. – Cited page 136.

[139] R. Bellazzini and G. Spandre. Micropattern gas detectors with pixel read-out. *Nuclear Instruments and Methods in Physics Research Section A: Accelerators, Spectrometers, Detectors and Associated Equipment*, 513(1):231–238, 2003. Proceedings of the 6th International Conference on Position-Sensitive Detectors. https://doi.org/10.1016/j.nima.2003.08.038. – Cited page 136.

[140] R. Bellazzini, L. Baldini, A. Brez, F. Cavalca, L. Latronico, M.M. Massai, M. Minuti, N. Omodei, M. Pesce-Rollins, C. Sgró, G. Spandre, E. Costa, and P. Soffitta. Gas pixel detectors. *Nuclear Instruments and Methods in Physics Research Section A: Accelerators, Spectrometers, Detectors and Associated Equipment*, 572(1):160–167, 2007. Frontier Detectors for Frontier Physics. https://doi.org/10.1016/j.nima.2006.10.171. – Cited page 136.

[141] D Attié, A Chaus, D Durand, D Desforge, E Ferrer-Ribas, J Galán, Y Giomataris, A Gongadze, F J Iguaz, F Jeanneau, R de Oliveira, T Papaevangelou, A Peyaud, and A Teixeira. Piggyback resistive micromegas. *Journal of Instrumentation*, 8(11):C11007–C11007, nov 2013. https://doi.org/10.1088/1748-0221/8/11/c11007. – Cited pages 137 & 173.

[142] Paul Serrano. *Caliste-MM : a new spectro-polarimeter for soft X-ray astrophysics*. Theses, Université Paris-Saclay, October 2017. https://tel.archives-ouvertes.fr/tel-01723432. – Cited page 137.

[143] Soleil synchrotron facility. https://www.synchrotron-soleil.fr/. – Cited page 137.

[144] S. Procureur, D. Attié, H. Gomez, M. Lehuraux, P. Magnier, I. Mandjavidze, and P. Mas. Muon metrology and positioning: the POMME experiment. *Journal of Instrumentation*, 16(07):P07013, jul 2021. https://doi.org/10.1088/1748-0221/16/07/p07013. – Cited page 143.

[145] E. P. George. Cosmic rays measure overburden of tunnel. *Commonwealth Engineer*, 43:455–457, Januray 1955. – Cited page 143.

[146] Luis W. Alvarez, Jared A. Anderson, F. El Bedwei, James Burkhard, Ahmed Fakhry, Adib Girgis, Amr Goneid, Fikhry Hassan, Dennis Iverson, Gerald Lynch, Zenab Miligy, Ali Hilmy Moussa, Mohammed Sharkawi, and Lauren Yazolino. Search for hidden chambers in the pyramids. *Science*, 167(3919):832–839, 1970. https://doi.org/10.1126/science.167.3919.832. – Cited page 144.

[147] K Nagamine, M Iwasaki, K Shimomura, and K Ishida. Method of probing inner-structure of geophysical substance with the horizontal cosmic-ray muons and possible application to volcanic eruption prediction. *Nuclear Instruments and Methods in Physics Research Section A: Accelerators, Spectrometers, Detectors and Associated Equipment*, 356(2):585–595, 1995. https://doi.org/10.1016/0168-9002(94)01169-9. – Cited page 144.

[148] Decision sciences. https://decisionsciences.com/. – Cited page 145.

[149] Gscan. https://gscan.eu/technology/. – Cited page 145.

[150] Ideon. https://ideon.ai/. – Cited page 145.

[151] Iris-instruments. http://www.iris-instruments.com/. – Cited page 145.

[152] Muodim. https://www.pulsalys.fr/startup/muodim. – Cited page 145.

[153] Lingacom ltd. https://lingacom.com. – Cited page 145.

[154] Lynkeos technology ltd. https://www.lynkeos.co.uk/. – Cited page 145.

[155] Muon solutions. http://muon-solutions.com/. – Cited page 145.

[156] Muon systems. https://muon.systems/. – Cited page 145.

[157] S. Procureur, R. Dupré, and S. Aune. Genetic multiplexing and first results with a 50×50cm2 micromegas. *Nuclear Instruments and Methods in Physics Research Section A: Accelerators, Spectrometers, Detectors and Associated Equipment*, 729:888–894, 2013. https://doi.org/10.1016/j.nima.2013.08.071. – Cited page 147.

[158] Elvia. https://www.pcb-elvia.com/. – Cited page 149.

[159] S. Bouteille, D. Attié, P. Baron, D. Calvet, P. Magnier, I. Mandjavidze, S. Procureur, M. Riallot, and M. Winkler. A micromegas-based telescope for muon tomography: The watto experiment. *Nuclear Instruments and Methods in Physics Research Section A: Accelerators, Spectrometers, Detectors and Associated Equipment*, 834:223 – 228, 2016. https://doi.org/10.1016/j.nima.2016.08.002. – Cited pages 150 & 152.

[160] Solid-run hummingboard card. https://www.solid-run.com/embedded-industrial-iot/nxp-i-mx6-family/hummingboard/. – Cited page 151.

[161] Georgios Iakovidis. Research and Development in Micromegas Detector for the ATLAS Upgrade, Oct 2014. Presented 13 Oct 2014. https://cds.cern.ch/record/1955475. – Cited page 154.

[162] Konstantinos Ntekas. Performance characterization of the Micromegas detector for the New Small Wheel upgrade and Development and improvement of the Muon Spectrometer Detector Control System in the ATLAS experiment, 2016. Presented 2016. https://cds.cern.ch/record/2143887. – Cited page 154.

[163] Kunihiro Morishima, Mitsuaki Kuno, Akira Nishio, Nobuko Kitagawa, Yuta Manabe, Masaki Moto, Fumihiko Takasaki, Hirofumi Fujii, Kotaro Satoh, Hideyo Kodama, Kohei Hayashi, Shigeru Odaka, Sébastien Procureur, David Attié, Simon Bouteille, Denis Calvet, Christopher Filosa, Patrick Magnier, Irakli Mandjavidze, Marc Riallot, Benoit Marini, Pierre Gable, Yoshikatsu Date, Makiko Sugiura, Yasser Elshayeb, Tamer Elnady, Mustapha Ezzy, Emmanuel Guerriero, Vincent Steiger, Nicolas Serikoff, Jean-Baptiste Mouret, Bernard Charlès, Hany Helal, and Mehdi Tayoubi. Discovery of a big void in khufu's pyramid by observation of cosmic-ray muons. *Nature*, 552(7685):386–390, 2017. https://doi.org/10.1038/nature24647. – Cited pages 159, 161 & 174.

[164] Sébastien Procureur, Kunihiro Morishima, Mitsuaki Kuno, Yuta Manabe, Nobuko Kitagawa, Akira Nishio, Hector Gomez, David **Attié**, Ami Sakakibara, Kotaro Hikata, Masaki Moto, Irakli Mandjavidze, Patrick Magnier, Marion Lehuraux, Théophile Benoit, Denis Calvet, Xavier Coppolani, Mariam Kebbiri, Philippe Mas, Hany Helal, Mehdi Tayoubi, Benoit Marini, Nicolas Serikoff, Hamada Anwar, Vincent Steiger, Fumihiko Takasaki, Hirofumi Fujii, Kotaro Satoh, Hideyo Kodama, Kohei Hayashi, Pierre Gable, Emmanuel Guerriero, Jean-Baptiste Mouret, Tamer Elnady, Yasser Elshayeb, and Mohamed Elkarmoty. Precise characterization of a corridor-shaped structure in khufuâ€™s pyramid by observation of cosmic-ray muons. *Nature Communications*, 14(1):1144, March 2023. https://doi.org/10.1038/s41467-023-36351-0. – Cited pages 163 & 174.

[165] A.H. Andersen and A.C. Kak. Simultaneous algebraic reconstruction technique (sart): A superior implementation of the art algorithm. *Ultrasonic Imaging*, 6(1):81–94, 1984. https://doi.org/10.1016/0161-7346(84)90008-7. – Cited page 163.

[166] Sébastien Procureur, David **Attié**, Laurent Gallego, Hector Gomez, Philippe Gonzales, Baptiste Lefèvre, Marion Lehuraux, Bertrand Lesage, Irakli Mandjavidze, Philippe Mas, and Daniel Pomarède. 3d imaging of a nuclear reactor using muography measurements. *Science Advances*, 9(5):eabq8431, 2023. https://doi.org/10.1126/sciadv.abq8431. – Cited pages 164 & 174.

[167] France's reference public institution for earth science applications. https://www.brgm.fr/en. – Cited page 169.

[168] Michael Lupberger, Yevgen Bilevych, Hubert Blank, Daniel Danilov, Klaus Desch, Alexander Hamann, Jochen Kaminski, Walter Ockenfels, Johann Tomtschak, and Susanne Zigann-Wack. Toward the pixel-tpc: Construction and operation of a large area gridpix detector. *IEEE Transactions on Nuclear Science*, 64(5):1159–1167, 2017. https://doi.org/10.1109/TNS.2017.2689244. – Cited page 173.

[169] S. Procureur, D. Attié, S. Aune, J. Ball, P. Baron, M. Boyer, G. Charles, E. Delagnes, R. Dupré, V. Gautard, A. Giganon, C. Lahonde-Hamdoun, I. Mandjavidze, and O. Meunier. Operation of a resistive micromegas in air. *Nuclear Instruments and Methods in Physics Research Section A: Accelerators, Spectrometers, Detectors and Associated Equipment*, 688:75–79, 2012. https://doi.org/10.1016/j.nima.2012.06.013. – Cited page 173.

[170] International Linear Collider International Development Team. Proposal for the ilc preparatory laboratory (pre-lab). 2021. https://doi.org/10.5281/ZENODO.4742043. – Cited page 174.

[171] **The FCC Collaboration**. FCC-ee: The Lepton Collider. Future Circular Collider Conceptual Design Report Volume 2, June 2019. 10.1140/epjst/e2019-900045-4. – Cited page 174.

[172] **The FCC Collaboration**. FCC-hh: The Hadron Collider. Future Circular Collider Conceptual Design Report Volume 3, July 2019. 10.1140/epjst/e2019-900087-0. – Cited page 174.

[173] **The FCC Collaboration**. HE-LHC: The High-Energy Large Hadron Collider. Future Circular Collider Conceptual Design Report Volume 4, July 2019. 10.1140/epjst/e2019-900088-6. – Cited page 174.

[174] Lund, N., Budtz-Jørgensen, C., Westergaard, N. J., Brandt, S., Rasmussen, I. L., Hornstrup, A., Oxborrow, C. A., Chenevez, J., Jensen, P. A., Laursen, S., Andersen, K. H., Mogensen, P. B., Rasmussen, I., Omø, K., Pedersen, S. M., Polny, J., Andersson, H., Andersson, T., Kämäräinen, V., Vilhu, O., Huovelin, J., Maisala, S., Morawski, M., Juchnikowski, G., Costa, E., Feroci, M., Rubini, A., Rapisarda, M., Morelli, E., Carassiti, V., Frontera, F., Pelliciari, C., Loffredo, G., Martínez Núñez, S., Reglero, V., Velasco, T., Larsson, S., Svensson, R., Zdziarski, A. A., Castro-Tirado, A., Attina, P., Goria, M., Giulianelli, G., Cordero, F., Rezazad, M., Schmidt, M., Carli, R., Gomez, C., Jensen, P. L., Sarri, G., Tiemon, A., Orr, A., Much, R., Kretschmar, P., and Schnopper, H. W. Jem-x: The x-ray monitor aboard integral*. *A&A*, 411(1):L231–L238, 2003. https://doi.org/10.1051/0004-6361:20031358. – Cited page 174.

université PARIS-SACLAY | ÉCOLE DOCTORALE PHENIICS

**Titre:** Détecteurs gazeux de particules pour des applications sociétales et académiques

**Mots clés:** TPC, Micromegas, tomographie muonique

**Résumé:** Le développement récent de détecteurs gazeux de particules à base de la technologie Micromegas (inventée au CEA en 1996) a entrainé l'utilisation de couches résistive dans les détecteurs depuis 2004. Ces couches résistives permettent d'une part d'étaler la charge pour obtenir une résolution spatiale avec peu de voies d'électronique et d'autre part d'augmenter le flux de particules. Le développement de chambres à projection temporelle ou détecteur 3D basée sur la technologie Micromegas à lecture résistive avec des pixels est présenté dans le cadre de la R&D pour le futur collisionneur $e^+e^-$ et dans le cadre de la mise à jour du détecteur proche ND280 de l'expérience T2K. Des détecteurs plans (2D) de particules lues avec des pistes résistives ont aussi été développés et installés pour l'expérience CLAS12 au laboratoire Jefferson pour la physique nucléaire. Depuis 2014, ces mêmes détecteurs ont été utilisés en version 2D multiplexée dans des télescopes pour réaliser des tomographies muoniques pour répondre à des enjeux sociétaux.

**Title:** Gaseous tracking detectors for academic and societal applications

**Keywords:** TPC, Micromegas, Muon tomography

**Abstract:** The recent development of gaseous particle detectors based on Micromegas technology (invented at the CEA in 1996) has led to the use of resistive layers in detectors since 2004. These resistive layers help to spread the charge to obtain spatial resolution with few electronic channels and allow the operation in high particle rate. The development of time projection chambers or 3D detector based on resistive Micromegas technology using pads is presented in the R&D for the future collider $e^+e^-$ and in the upgrade of the ND280 near detector of the T2K experiment. Planar (2D) particle detectors with resistive strips have also been developed and installed for the CLAS12 experiment at the Jefferson Laboratory for Nuclear Physics. Since 2014, these same detectors have been used in a 2D multiplexed version in telescopes to perform muon tomography to meet societal challenges.

**Université Paris-Saclay**
Espace Technologique / Immeuble Discovery
Route de l'Orme aux Merisiers RD 128 / 91190 Saint-Aubin, France